

**XXIII<sup>RD</sup>**

**I  
N  
T  
E  
R  
N  
A  
T  
I  
O  
N  
A  
L  
  
C  
O  
N  
F  
E  
R  
E  
N  
C  
E  
 O  
N  
  
P  
H  
E  
N  
O  
M  
E  
N  
A I  
N  
  
I  
O  
N  
I  
Z  
E  
D  
  
G  
A  
S  
E  
S**



**INVITED PAPERS**

EDITED BY  
M.C. BORDAGE AND A. GLEIZES

  
**EDP**  
SCIENCES

Public reporting burden for this collection of information is estimated to average 1 hour per response, including the time for reviewing instructions, searching existing data sources, gathering and maintaining the data needed, and completing and reviewing the collection of information. Send comments regarding this burden estimate or any other aspect of this collection of information, including suggestions for reducing this burden to Washington Headquarters Services, Directorate for Information Operations and Reports, 1215 Jefferson Davis Highway, Suite 1204, Arlington, VA 22202-4302, and to the Office of Management and Budget, Paperwork Reduction Project (0704-0188), Washington, DC 20503.

1. AGENCY USE ONLY (Leave blank)		2. REPORT DATE 1 December 1998	3. REPORT TYPE AND DATES COVERED Conference Proceedings	
4. TITLE AND SUBTITLE XXIII International Conference on Phenomena in Ionized Gases, <i>INVITED PAPERS</i>			5. FUNDING NUMBERS F6170897W0048	
6. AUTHOR(S) Conference Committee				
7. PERFORMING ORGANIZATION NAME(S) AND ADDRESS(ES) Universite Paul Sabatier 118 Route de Narbonne Toulouse Cedex 31062 France			8. PERFORMING ORGANIZATION REPORT NUMBER N/A	
9. SPONSORING/MONITORING AGENCY NAME(S) AND ADDRESS(ES) EOARD PSC 802 BOX 14 FPO 09499-0200			10. SPONSORING/MONITORING AGENCY REPORT NUMBER CSP 97-1013	
11. SUPPLEMENTARY NOTES One book of Invited Papers and five volumes of Proceedings and Contributed Papers				
12a. DISTRIBUTION/AVAILABILITY STATEMENT Approved for public release; distribution is unlimited.			12b. DISTRIBUTION CODE A	
13. ABSTRACT (Maximum 200 words)  The Final Proceedings for XXIII International Conference on Phenomena in Ionized Gases, 17 July 1997 - 22 July 1997  kinetic, thermodynamics, and transport phenomena; elementary processes; low pressure glows; coronas, sparks, surface discharges, and high pressure glows; arcs; high frequency discharges; ionospheric magnetospheric, and astrophysical plasmas; plasma diagnostic methods; plasma surface effects; plasma processing; plasma flows; non ideal plasmas; waves and instabilities; non-linear phenomena; particle and laser beam interactions with plasmas; plasma sources of radiation; modeling; plasma for environmental issues; plasma thrusters; surface treatment; high pressure, non-thermal plasmas.				
14. SUBJECT TERMS  EOARD, Space Environment, Pulsed Power, Aerodynamics, Coatings, Fluids & Lubrication, Electromagnetics, High Power Generation, Lasers			15. NUMBER OF PAGES Too Many to Count	
			16. PRICE CODE N/A	
17. SECURITY CLASSIFICATION OF REPORT UNCLASSIFIED	18. SECURITY CLASSIFICATION OF THIS PAGE UNCLASSIFIED	19. SECURITY CLASSIFICATION OF ABSTRACT UNCLASSIFIED	20. LIMITATION OF ABSTRACT UL	

NSN 7540-01-280-5500

Standard Form 298 (Rev. 2-89)  
Prescribed by ANSI Std. Z39-18  
298-102

JOURNAL DE PHYSIQUE IV

Volume 7

Colloque C4

Octobre 1997

Supplément au Journal de Physique III, n°10

# XXIII<sup>rd</sup> International Conference on Phenomena in Ionized Gases

CSP 97-1013

F61708-97-W0048



19981216 002

*Edited by:*

M.C. Bordage and A. Gleizes



7, avenue du Hoggar  
ZA de Courtabœuf, B.P. 112  
91944 Les Ulis cedex A, France

AQF99-03-0344

---

## Organizers

Centre de Physique des Plasmas et de leurs Applications de Toulouse (CPAT)  
Laboratoire de Génie Électrique de Toulouse (LGET)  
From the Université Paul Sabatier, Toulouse, France

## International Scientific Committee

R. d'Agostino, Italy  
J. Allen, Great Britain  
A. Bouchoule (*Chairman*), France  
E. Desoppere, Belgium  
H. Kikuchi, Japan  
E.E. Kunhardt, U.S.A.

J. Mentel, Germany  
B. Milic, Yugoslavia  
D. Morrow, Australia  
A.H. Oien, Norway  
A.A. Rukhadze, Russia  
M. Sicha, Czech Republic

## Local Organizing Committee

J.P. Bœuf  
M.C. Bordage (*Sec.*)  
H. Brunet (*co-Chair.*)  
J.P. Couderc  
B. Despax  
M. Dziadowiec  
A. Gleizes

B. Held  
F. Massines  
L.C. Pitchford (*co-Chair.*)  
Y. Segui  
S. Vacquie  
M. Yousfi  
G. Zissis



## Sponsors

Association pour le Développement de la Physique Atomique (ADPA)  
International Union of Pure and Applied Physics (IUPAP)  
Centre National de la Recherche Scientifique (CNRS)  
Université Paul Sabatier (UPS) de Toulouse  
Direction de la Recherche et Technologie (DRET)  
Commissariat à l'Énergie Atomique (CEA), Cycle de Combustible  
Électricité de France through: Club Arc Électrique, Club Chimie des Hautes Températures and Novelect  
Conseil Régional de la Région Midi-Pyrénées  
Conseil Général du Département de la Haute-Garonne  
Mairie de Toulouse  
CRT Plasma-Laser  
Union Radio Scientifique Internationale (URSI)  
US Air Force through the EOARD

*The Local Organizing Committee wishes to express appreciation to the following corporations for their support*

AGA S.A.  
Motorola Semiconducteurs S.A.  
Osram-Sylvania Inc.

Thomson Tubes Électroniques  
Schneider Electric  
Philips Lighting (for the Penning Award)

### IUPAP Sponsorship

*"To secure IUPAP sponsorship, the organizers have provided assurance that ICPIG XXIII will be conducted in accordance with IUPAP principles as stated in the ICSU-Document "Universality of Science" (sixth edition, 1989) regarding the free circulation of scientists for international purposes. In particular, no bona fide scientist will be excluded from participation on the grounds of national origin, nationality, or political considerations unrelated to science".*

## Preface

This special issue contains the texts of the invited talks presented at the XXIIIrd International Conference on Phenomena in Ionized Gases (ICPIG) which was held in Toulouse, July 17-22, 1997. A short article presenting an overview of the conference is also presented in this special issue.

The articles here are divided into two groups, the plenary lectures (for general lectures of broad interest) and the topical lectures (for more specialized topics). Within each group, the articles are ordered alphabetically by presenting author's name. Along with the plenary lectures is the text of the lecture given by Professor Takada, the recipient of the 1997 Penning Prize. The Penning Prize, which was again sponsored by Philips Lighting, is awarded every two years to an individual for contributions in the subject areas covered by the ICPIG. Also included with the topical lectures is the text of one of the talks given during the workshop "Applications of Low Temperature Plasmas" which was held in the middle of the conference and open to all participants. The articles published here were reviewed by two members of the community, and the review procedure was organized and coordinated by the members of the International Scientific Committee of the XXIIIrd ICPIG.

The technical program of the XXIIIrd ICPIG included, in addition to the invited talks, more than 500 contributed papers which were presented in poster sessions. The contributed papers, a maximum of 2 pages in length, were reviewed by the Local Organizing Committee. Those contributed papers which were presented at the conference are included in the five volumes of conference proceedings. These were distributed at the conference and additional copies of the proceedings are available through the guest editors of this special issue.

We would like to thank these authors for having made the extra effort of putting their lectures on paper, and we hope that this publication of the invited talks of the XXIIIrd ICPIG as articles in a refereed journal will give them a wide diffusion. We also thank "EDP Sciences" for arranging publication in this special issue of Journal de Physique.

Marie-Claude Bordage and Alain Gleizes  
Guest Editors  
Centre de Physique des Plasmas et Applications de Toulouse (CPAT)  
Université Paul Sabatier  
118, route de Narbonne  
31062 Toulouse cedex 4, France

## Summary of the XXIII ICPIG

A. Bouchoule, H. Brunet\* and L.C. Pitchford\*

*GREMI, Université d'Orléans, UMR 6606 du CNRS, 45067 Orléans, France*

*\* CPAT, Université Paul Sabatier, ESA 5002 du CNRS, 118 route de Narbonne, 31062 Toulouse, France*

### 1. INTRODUCTION

The International Conference on Phenomena in Ionized Gases (ICPIG) is a biannual conference which covers most aspects of phenomena in ionized gases, with emphasis on low to moderate temperature plasmas. The tremendous growth in applications of low and moderate temperature plasmas (surface treatment, pollution control, microelectronics fabrication, and many others) makes this field dynamic, interdisciplinary, and rapidly evolving. The ICPIG series provides an international forum for presentation and discussion of fundamental physics of ionized gases and applied research underlying the newer as well as the more mature plasma-based technologies. There is no other international conference which covers the range of topics of the ICPIG.

Until 1995 the ICPIG venue traditionally alternated between sites in Eastern and Western Europe. The 1995 ICPIG at Stevens Institute in Hoboken, New Jersey, marked the first time the conference was held outside Europe, and this served the very useful purpose of making the conference truly international.

We, in France, were happy to have the chance to welcome the ICPIG back to Europe for the 1997 meeting, the twenty-third in the series. The XXIII ICPIG was held on the downtown campus of the University of Toulouse, from Thursday, July 17, to Tuesday, July 22, 1997. This campus is located in the historic center of Toulouse, and the central location proved to be especially attractive to participants and their accompanying persons. Every effort was made to keep the cost low so that participants who could not attend the meeting in the USA for financial reasons were able to be present in Toulouse. The attractive location and the low cost were key factors in the large participation at the meeting.

The local organization was assured by members of two laboratories from the University of Toulouse, the Centre de Physique des Plasmas et Applications de Toulouse (CPAT) and the Laboratoire de Genie Electrique de Toulouse (LGET). Continuity from meeting to meeting and guidance are provided by the ICPIG International Scientific Committee (ISC) which meets annually. The members of the ISC and of the Local Organizing Committee (LOC) are listed in the front of this special issue.

### 2. PARTICIPATION

The attendance at the XXIII ICPIG was larger than for the several previous meetings. A total of 561 participants took part in this meeting. The number of participants from each of the 36 countries represented at the ICPIG is shown in Table 1.

Country	number of participants	Country	number of participants
Algeria	3	Mexico	2
Australia	6	Netherlands	10
Austria	2	Norway	5
Belarus	1	Poland	4
Belgium	4	Portugal	11
Brazil	1	Republic of Moldova	1
Bulgaria	3	Romania	8
Canada	6	Russian Federation	60
Chili	1	Slovakia	8
Czech Republic	32	Slovenia	1
Egypt	4	Spain	5
Estonia	2	Switzerland	1
France	183	Turkey	1
Germany	53	UK	16
Iran	1	Ukraine	5
Ireland	3	USA	31
Israel	7	Yugoslavia	6
Italy	16		
Japan	58	TOTAL	561

**Table 1.** Geographical distribution of participants at the XXIII ICPIG

One of the goals of the organization was to encourage student participation. To this end, low cost rooms were available for participants and the registration fee was reduced for students. These two factors were contributed to the large student participation (138 students were present). The generous support of the sponsors and contributors of the XXIII ICPIG enabled the Local Organizing Committee to support in full or in part a number of participants from Eastern European countries.

### 3. TECHNICAL PROGRAM

The technical sessions of the XXIII ICPIG consisted of invited talks and poster presentations. The invited talks were given in either plenary sessions (for general lectures of broad interest) or in parallel sessions (for more specialized topics). The invited speakers were selected by the ISC. There were 31 invited speakers at the 1997 meeting, including 7 plenary lectures and 24 topical lectures. The international character of the ICPIG was reflected in the participation of 17 countries in the invited talks. The articles in this special issue include the texts of the invited talks at the XXIII ICPIG.

There were 513 contributed papers presented in the form of posters at the meeting. The poster sessions were arranged not to overlap with the presentation of the invited talks in order to give participants ample opportunity to meet and discuss with the presenters of the posters. The contributed papers themselves are short, a maximum of two pages in length, and these were printed and distributed to participants at the meeting. These ICPIG proceedings are organized in 5 volumes, one for each meeting day and a fifth one for 'late papers'. A requirement for inclusion of the papers in conference proceedings is that at least one of the authors be registered. The 'late papers' are those for which the authors registered after the deadline for printing the first 4 volumes. Additional copies of the proceedings are available and can be ordered from the LOC. Contributed papers from the proceedings of the XXIII ICPIG will appear in the INSPEC data base.

A short overview on the contents of these contributions is given in table 2 which summarizes the list of subjects covered at the conference, as updated in 1996 by the ISC, and the number of contributions in each. At their meeting in 1996, the ISC decided to feature two subjects for special emphasis in 1997, (a) highly ionized, low pressure plasmas, and (b) high pressure, non-thermal plasmas.

TOPIC	number of posters
Kinetics, thermodynamics and transport phenomena	30
Elementary processes	27
Low pressure glows	42
Coronas, sparks, surface discharges and high pressure glows	35
Arcs	42
High frequency discharges	36
Ionospheric, magnetospheric, and astrophysical plasmas	7
Plasma diagnostic methods	50
Plasma wall interactions, electrode and surface effects	20
Physical aspects of plasma chemistry, plasma processing of surfaces, plasma wall interaction and thin film technology	40
Generation and dynamics of plasma flows	6
Non-ideal plasmas. Clusters and dusty plasmas	17
Waves and instabilities, including shock waves	22
Non-linear phenomena and self-organizing processes	22
Particle and laser beam interaction with plasmas	6
Plasma sources of radiation	29
Numerical modeling	41
Plasmas for environmental issues	15
<u>Special topics emphasized at the 1997 meeting:</u>	
Highly ionized, low pressure plasmas	16
High pressure, non-thermal plasma	10
TOTAL	513

**Table 2.** Number of contributed papers in each of the subject areas covered by the XXIII ICPIG

The poster sessions were very well attended in spite of the warm weather, and there were numerous animated discussions in the poster session area and in the gardens just outside where the coffee breaks and lunches were held.

A total of 661 contributed papers were submitted to and reviewed by the Local Organizing Committee. About 5% were rejected, mostly on the grounds that they were outside the subject area of the conference. A large number of papers, mostly from Eastern European countries, were accepted by the LOC, but the authors were unable to attend the meeting and present their papers. These papers were therefore not printed in the proceedings.

#### 4. PENNING PRIZE AND POSTER PRIZES

The Penning Prize is awarded every two years, at the occasion of ICPIG, to an individual for work in the field of physics and technology of plasmas and ionized gases. The 1997 Penning prize, again sponsored by Philips Lighting, was awarded to Professor S. Takeda from Japan. The citation for the 1997 Penning

Prize to Professor Takeda reads "for his many, long-standing contributions to the field of plasmas and ionized gases, and in particular, for his work on an extension of Paschen's law to high-frequency discharges and waves in plasmas". Professor Takeda accepted the Penning Prize, consisting of \$1000 and a certificate, and presented a lecture on gas discharge work in Japan. He also received a gold medal from the city of Toulouse in recognition of his having been awarded the Penning Prize. Professor Takeda was selected by the ISC from the 12 nominations which were submitted by members of the scientific community.

For the first time the ICPIG Conference distinguished two contributed papers with awards, one for theory/modeling and the other for experimental work. The 1997 ICPIG poster prize winners were E. Robert, C. Cachoncinlle, A. Khacef, R. Viladrosa and J.M. Pouvesle from GREMI, CNRS/Université d'Orléans, France for experimental work and A. Bogaerts and R. Gijbels from University of Antwerp, Belgium for theory/modeling.

## 5. WORKSHOPS

An industrial workshop has traditionally been organized to coincide with the ICPIG. This year the industrial workshop, open to all registered participants of the ICPIG, was held in the middle of the conference on Saturday afternoon. Six leaders in research and development in large companies accepted invitations to speak, and attendance at the workshop was very good. The following topics were presented :

- Plasma Processing of Semiconductors (J.N. Bardsley, LLNL, USA)
- Plasma Display Panels (H. Doyeux, Thomson Tube Electronics, France)
- Plasma Addressed Liquid Crystal Displays (K. Ilcisin, Technical Visions, USA) .
- Electromagnetic Propulsion (A. Cadiou, CNES, France)
- Circuit Breakers and Switches (M. Barrault, Schneider, France)
- Waste Treatment with Thermal Plasmas (M. Labrot, Aérospatiale, France).

The organizers wish to express again their appreciation to these speakers for their participation in the workshop.

Another special industrial workshop on plasma technologies for environmental issues was organized the day before the conference. More than 50 specialists, mainly from Europe and USA, attended this special workshop. This workshop was organized by the Center of Technological Ressources (CRT) in Plasmas and Lasers which was recently established in France. Reports will be available though the CRT (B. Bergaya, CRT Plasma-Laser, UFR Sciences, 45067 Orléans, France ).

## 6. SOCIAL EVENTS

Very important parts of any conference are the social events, and we were happy to have this opportunity to share some of the pleasures of life in southern France with the attendees at the XXIII ICPIG. A welcome reception was held outside in the garden of the campus on Wednesday evening, July 16. For the accompanying persons, there was a 2-hour walking tour of Toulouse on Thursday afternoon and bus trips on Friday and Monday to Albi and Cordes and to Carcassonne which were 'sold-out'. The conference banquet was held in the Hotel Dieu, a Toulouse landmark on the banks of the Garonne River in the center of city. The after-dinner talk was a hilarious tale of the « baguette laser » given by Dr. Jean-Michel Pouvesle (who, incidentally, was one of the poster prize winners !). A conference excursion to the countryside around Toulouse was organized on Sunday, and there were about 240 people who made this excursion. On Monday evening, the mayor of Toulouse hosted a reception for all ICPIG participants in the magnificent 'Salle des Illustres' in the Toulouse City Hall. At this event, medals from the city of Toulouse were presented to the Professor Takeda and the poster prize winners.

## **7. SPONSORS AND CONTRIBUTORS**

The success of this conference is due in part to the generous support of our sponsors. It is thanks to this support that the cost for participants was a minimum thereby allowing more people to attend. We gratefully acknowledge the sponsors of XXIII ICPIG, the list of which appears in the front of this volume.

## **8. XXIV ICPIG**

The 24th ICPIG will be held in Warsaw in July 1999. We hope to see you all again there !

# Contents<sup>1</sup>

Summary of the XXIII ICPIG	
A. Bouchoule, H. Brunet and L.C. Pitchford.....	VII

## General

Physics and Modeling of Plasma Display Panels	
<u>J.P. Bœuf</u> , C. Punset, A. Hirech and H. Doyeux .....	C4-3
A Guide to Laser-Induced Fluorescence Diagnostics in Plasmas	
T.G.M. Freegarde and <u>G. Hancock</u> .....	C4-15
Properties of Arc Cathode Spots	
<u>B. Jüttner</u> .....	C4-31
Dielectric-Barrier Discharges. Principle and Applications	
<u>U. Kogelschatz</u> , B. Eliasson and W. Egli .....	C4-47
Nonequilibrium in Thermal Plasmas with Applications to Diamond Synthesis	
<u>C.H. Kruger</u> , T.G. Owano, C.O. Laux and R.N. Zare .....	C4-67
Ectons and their Role in Electrical Discharges in Vacuum and Gases	
<u>G.A. Mesyats</u> .....	C4-93
The Birkeland Terrella Experiments and their Importance for the Modern Synergy of Laboratory and Space Plasma Physics	
<u>K. Rypdal</u> and T. Brundtland.....	C4-113
Gas Discharges Studies in Japan and some of my Own Researches	
<u>S. Takeda</u> .....	C4-133

## Topical

Nonlocal Electron Kinetics in DC Discharges	
<u>L.L. Alves</u> , G. Gousset and C.M. Ferreira.....	C4-143
Crystal and Fluid-Like Assemblies in Plasma Sheaths	
B.M. Annaratone .....	C4-155
Modelling of the Parametric Behaviour of a Self-Heated Copper Vapour Laser: Issues Governing the Thermal Runaway Behaviour of the Plasma Tube Wall Temperature	
<u>R.J. Carman</u> .....	C4-167
Application of Non-Linear Optical Methods to Plasma Diagnostics	
<u>U. Czarnetzki</u> .....	C4-175
Transient Phenomena in Plasma Torches and in Plasma Sprayed Coating Generation	
<u>P. Fauchais</u> , J.F. Coudert and M. Vardelle .....	C4-187
Grafting of Chemical Groups onto Polymers by Means of RF Plasma Treatments: a Technology for Biomedical Applications	
<u>P. Favia</u> , R. d'Agostino and F. Palumbo .....	C4-199

<sup>1</sup> Underlined names in the contents and in paper headings correspond to authors who presented orally the corresponding communications.



Time Resolved Spectroscopy of RF Plasmas: A Comparison of Hydrogen and Deuterium Plasmas <u>W.G. Graham</u> and C.M.O. Mahony.....	C4-209
Interaction of Grains in Dusty Plasmas <u>A.M. Ignatov</u> .....	C4-215
The Switching Dynamics of the Plasma Addressed Liquid Crystal Display <u>K.J. Ilcisin</u> , T.S. Buzak and G.J. Parker .....	C4-225
Production of Large Diameter ECR Plasma <u>Y. Kawai</u> and Y. Ueda.....	C4-235
Emission Spectroscopy of the Cathode Fall Region of an Analytical Glow Discharge <u>N. Konjević</u> , I.R. Videnović and M.M. Kuraica.....	C4-247
Triggering of Negative Corona <u>M. Laan</u> , P. Paris and V. Repán.....	C4-259
The Coupling of PIC/MCC Models of Discharge Plasmas with Vibrational and Electronic Kinetics <u>S. Longo</u> , M. Capitelli and K. Hassouni.....	C4-271
A Unified Theory of Arcs and their Electrodes <u>J.J. Lowke</u> .....	C4-283
High-Frequency Magnetoplasmas in Electronegative Gases <u>J. Margot</u> , M. Chaker, L. St-Onge, M. Tabbal, A. Aliouchouche, O. Pauna, C. Alinot and C. Kliagine .....	C4-295
Laboratory Observations of Wave-Induced Radial Transport within an "Artificial Radiation Belt" <u>M.E. Mauel</u> .....	C4-307
Measurements of High Density Plasmas after Pulsed Discharges in Liquid Helium W. Qin, <u>K. Minami</u> , A.W. DeSilva and F. Tomimoto .....	C4-319
Generation of Supersonic Plasma Flow by Means of Unipolar RF Discharges M. Novák, M. Šícha, V. Kapička, L. Jastrabík, L. Soukup, Z. Hubička, M. Klíma, P. Slaviček and A. Brablec .....	C4-331
Negative Differential Resistance, Oscillations and Constrictions of Low Pressure, Low Current Discharges <u>Z.Lj. Petrović</u> , I. Stefanović, S. Vrhovac and J. Živković.....	C4-341
Progress in the Development of Table-Top Discharge-Pumped Soft X-Ray Lasers <u>J.J. Rocca</u> , F.G. Tomasel, C.H. Moreno, V.N. Shlyaptsev, M.C. Marconi, B.R. Benware, J.J. Gonzalez, J.L.A. Chilla and C.D. Macchietto .....	C4-353
Quasistatic Plasma Sources: Physical Principles, Modelling Experiments, Application Aspects <u>K.P. Shamrai</u> , A.F. Aleksandrov, G.E. Bougrov, V.F. Virko, V.P. Katiukha, S.K. Koh, E.A. Kralkina, G.S. Kirichenko and A.A. Rukhadze .....	C4-365
The Oscillations of the Positive Glow Corona R.S. Sigmond.....	C4-383
Langmuir Probe Diagnostics for Medium Pressure and Magnetised Low-Temperature Plasma <u>M. Tichý</u> , P. Kudrna, J.F. Behnke, C. Csambal and S. Klage .....	C4-397
Nonlinear Wave Phenomena in an Electron-Beam Plasma <u>K. Yamagiwa</u> , T. Itoh and T. Nakayama.....	C4-413
<b>Author Index</b> .....	C4-421

# General

## Physics and Modeling of Plasma Display Panels

J.P. Bœuf, C. Punset, A. Hirech and H. Doyeux\*

*Centre de Physique des Plasmas et Applications de Toulouse, Université Paul Sabatier, 118 route de Narbonne, 31062 Toulouse, France*

*\* Thomson Tubes Électroniques, ZI Centr'Alp, Moirans, France*

**Abstract:** We discuss physical phenomena which take place in an AC Plasma Display Panel (PDP) cell for matrix and coplanar electrode geometries. The effect of the gas mixture and the electrode geometry on the breakdown voltage is first analyzed using a fluid discharge model. We then compare solutions from simple fluid models and more accurate hybrid models for a 1D cell, and discuss the sensitivity of the models to the uncertainties on the charged particle transport coefficients. Finally we present typical results showing the space and time evolution of a discharge in AC matrix and coplanar cells.

### 1. INTRODUCTION

Plasma display panels (PDP's) are now the best candidate on the market in the competition for large size, wall hanging television displays [1], [2]. The feasibility of high quality 42 in. color plasma displays has been demonstrated by several companies, and mass production of these displays started in 1996. However, some of the characteristics of these displays can be improved, and basic research is needed to guide improvements in, for example, the luminous efficiency of PDP's [3] which is low, but acceptable, in today's devices. Modeling is an important part of this research effort since accurate and detailed models of the discharge and plasma formation in PDP cells are now available and have considerably improved our understanding of the physical mechanisms governing the light emission from a picture element [4], [5], [6], [7], [8], [9].

In this paper we give a general presentation, based on numerical results from fluid and hybrid models, of the physical processes occurring in the plasma which forms in the PDP. In section 2 we describe the typical matrix and coplanar electrode geometries which are used in AC PDP's. The breakdown voltage in a PDP cell must be small in order to limit the cost of the electronic drivers. The breakdown voltage depends on the gas mixture and on the surface, which provides secondary electrons under ion bombardment. In a simple parallel plate geometry, the breakdown voltage is a function of the  $pd$  product - gas pressure times gap length (Paschen curve). This is no longer true in a coplanar geometry where the position of the third (address) electrode plays an important role. These questions are discussed in section 3. In section 4, results from fluid and hybrid models of a transient discharge occurring in a matrix PDP cell are compared. The aim of this comparison is to estimate the accuracy of simple fluid models based on the local field approximation (LFA). Although the LFA models are based on a very rough approximation, they are much more practical to use (much faster) than hybrid or particle models. This aspect is essential when the models are used for computer aided design. We show that in the conditions of a typical AC plasma display cell, the LFA model provides a good qualitative picture of the discharge, with a reasonable quantitative accuracy. We also show that the errors introduced by this approximation are not larger than those due to uncertainties in the data characterizing charged particle transport and secondary electron emission. In section 5 we describe the space and time evolution of a discharge in matrix and coplanar electrode geometry, on the basis of a 2D fluid model.

## 2. MATRIX AND COPLANAR AC PLASMA DISPLAYS

In AC plasmas displays, the discharges occur between electrode stripes which are deposited on a glass plate and covered with a dielectric layer. In a matrix display, each discharge cell is at the intersection of a line electrode and a column electrode which are deposited on two parallel glass plates. The sets of line electrodes and column electrodes are orthogonal to each other. The matrix electrode geometry is represented in Figs. 1 and 2a. A discharge is fired by applying a large enough voltage between a line electrode X, and a column electrode Y.

In a coplanar display [10], [11], the discharges occur between electrodes which are parallel and are deposited on the same glass plate. A third electrode, the address electrode, is used to define the position of the discharge in the direction perpendicular to the parallel electrodes, and to trigger the discharge (see Fig. 2b). Dielectric barrier ribs are used to prevent electrical and optical interaction (cross-talk) between the cells. The barrier ribs also play an important role in the UV-visible photon conversion since a layer of phosphor is deposited on the rib walls. A picture element consists of three discharge cells with phosphors in the three fundamental colors.

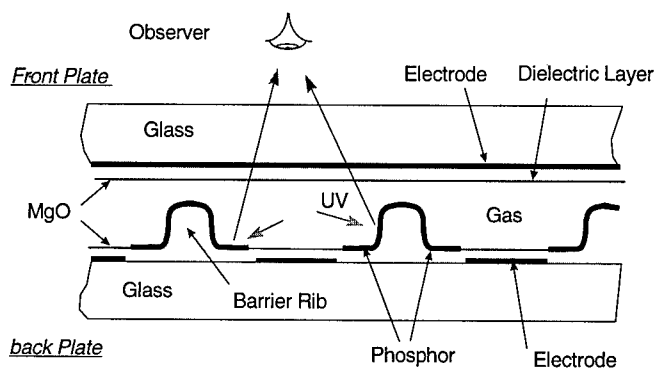


Figure 1: Schematic of an AC Matrix display (Thomson geometry)

The dielectric barrier ribs are parallel to the planes of Figs. 2a and 2b and therefore do not appear on these figures (they are perpendicular to the plane of Fig. 1).

The dielectric layer above the electrodes is generally made of enamel and is typically 20-25  $\mu\text{m}$  thick. It is covered with a MgO layer (less than 1  $\mu\text{m}$  thick). The MgO layer is extremely important because 1) it protects the dielectric layer, and 2), its large secondary emission coefficient under neon or helium ion bombardment helps maintain a low breakdown voltage.

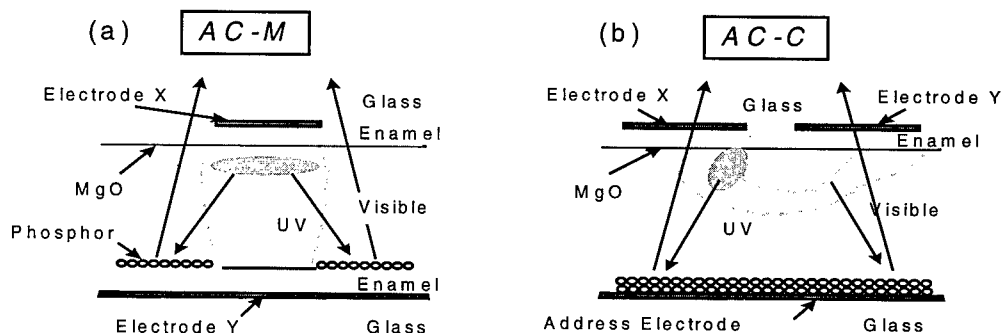


Figure 2: AC matrix (a), and coplanar (b) cells (cut in a plane parallel to the barrier ribs and perpendicular to the plane of Fig. 1)

Intense research efforts have been devoted to identifying materials which are resistant to sputtering and have a large secondary electron emission coefficient under ion bombardment. Magnesium oxide,

MgO, has been used for more than 30 years and is still the best known material for protecting the dielectric layer and providing secondary electrons. Uniform layers of MgO can be deposited on large areas by electron beam evaporation. An important advantage of MgO is that its secondary emission coefficient properties do not change significantly even after hundreds of nanometers are removed from the surface by ion sputtering. The life time of the display is limited by the sputtering of the MgO layer but can be larger than 10000 hours. The matrix and coplanar geometries are also called, respectively, double substrate and single substrate structures. We will not discuss here the advantages and drawbacks of each structure. However, let us mention that in the coplanar structure the electrodes on the front plate occupy a large area and must therefore be transparent (ITO, indium tin oxide). Due to the resistivity of ITO, a small width metal electrode (bus electrode) is generally deposited on the edge of each coplanar electrode to maintain a constant voltage along the electrodes.

### 3. BREAKDOWN VOLTAGE

In AC plasma displays, a square wave voltage, the sustaining voltage, is applied constantly between the X and Y electrodes. The amplitude of the sustaining voltage is less than the breakdown voltage. In a matrix display, a discharge is turned on in a given cell by applying, between the electrodes of that cell, a voltage larger than the breakdown voltage (the writing voltage). The discharge forms and is quickly quenched because of the charging of the dielectric surfaces. At the next half cycle, when the sustaining voltage reverses, the field in the gas gap due to the charges deposited on the dielectric surfaces by the previous pulse now adds to the field due to the voltage across the electrodes and a new discharge is initiated. This discharge is in turn quenched by the charging of the dielectric surfaces and so on. If the charges on the dielectric layers at the end of a discharge pulse are  $+Q$  and  $-Q$ , the next discharge must transfer  $-2Q$  and  $+2Q$  respectively on these surfaces, to maintain a steady state. The voltages of the writing and erasing pulses are such as to transfer exactly  $+Q$  and  $-Q$  to the dielectric surfaces. The sustaining voltage must be smaller than the breakdown voltage (otherwise all the cells would be constantly in an "ON" state). The sustaining voltage must also be large enough to maintain a written cell in the ON state. The minimum and maximum values of the sustaining voltage define the margin of the display. It is important to operate in conditions where the margin is large because the operating value of the sustaining voltage must be within the margins of all the cells of the panel (which are not perfectly identical). As we have seen, the maximum value of the sustaining voltage is the breakdown voltage. The minimum value of the margin is related to (but always larger than) the minimum, normal glow discharge voltage. The calculations [4] show that the margin increases when the  $pd$  (pressure - gap length) product is increased. Therefore, the  $pd$  product must be large enough to have a large margin, but low enough to have a reasonably low breakdown voltage and sustain voltage.

In plasma displays, the sustaining and addressing pulses are generated by high-voltage transistors. High -voltage integrated drivers switch the addressing pulses to the appropriate electrodes. Choosing a gas mixture and electrode geometry leading to low operating voltages is therefore essential.

#### 3.1 Breakdown in Xe-Ne mixtures

Although xenon is an efficient UV emitter, the breakdown voltage in pure xenon is impractically large and mixtures of xenon with neon or helium are generally used in plasma displays.

Adding neon or helium to xenon decreases the breakdown voltage for two reasons: 1) neon and helium ions are much more efficient than xenon at extracting secondary electrons from a MgO surface, and, 2) the total ionization coefficient in some xenon-neon mixtures for example, can be larger than the ionization coefficient in pure xenon and in pure neon (this is because the momentum cross-section for electron-neutral collisions is much larger in xenon than in neon so that in a mixture containing a large concentration of neon, the electrons can gain energy more easily and reach the excitation and ionization thresholds of xenon for lower values of the reduced electric field).

The above properties appear on Fig. 3 which shows the calculated Paschen curves for xenon-neon mixtures in a parallel plate geometry. The secondary electron emission coefficients in Fig. 3 are supposed

to be independent of the reduced electric field (or ion energy). This figure shows that xenon-neon mixtures with xenon concentrations less than 10% are much more appropriate than pure xenon for plasma display cells. The secondary emission coefficients for neon and xenon ions on MgO are not well known although a value between 0.3 and 0.5 for neon ions seems reasonable [4]. The value of the secondary emission coefficients of xenon ions is not accurately known but it is undoubtedly much smaller than that of neon ions. We generally use a value of 0.05 in the calculations for xenon ions on MgO, but this value is just a guess. Figure 3b shows how the breakdown curve depends on the xenon secondary emission coefficient.

The breakdown curves of Fig. 3 have been obtained by from the self-sustaining condition in the gas mixture. If  $\alpha_{Ne}$  and  $\alpha_{Xe}$  are the partial ionization coefficients for neon and xenon, and if  $\gamma_{Ne}$  and  $\gamma_{Xe}$  are the secondary emission coefficients of MgO under neon and xenon ion bombardment this condition can be written:

$$M = e^{[\alpha_{Ne} + \alpha_{Xe}]d} = 1 + \frac{\alpha_{Ne} + \alpha_{Xe}}{\alpha_{Ne}\gamma_{Ne} + \alpha_{Xe}\gamma_{Xe}}$$

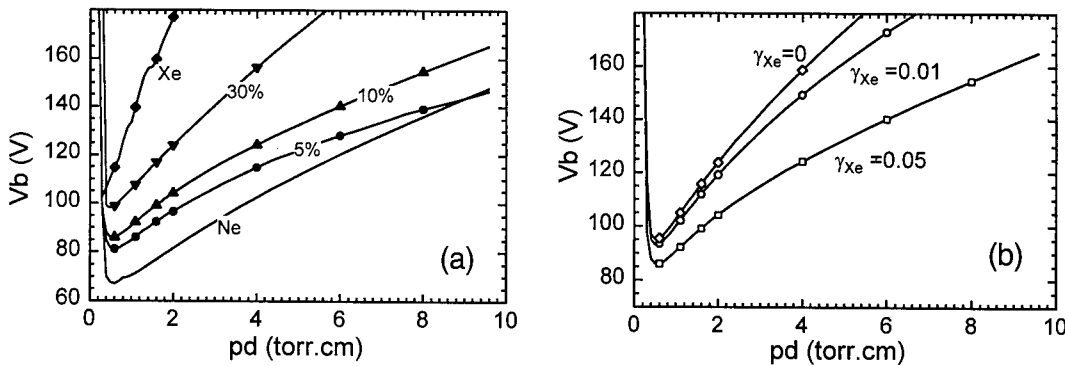


Figure 3: Breakdown curves in Xe-Ne mixtures for a parallel plate geometry (no dielectric layer above the electrodes). The secondary electron emission coefficient for neon ions on MgO is set to 0.5 in both figures. The secondary electron emission coefficient for xenon ions on MgO is set to 0.05 in (a) and is varied in (b). The gas mixture is Xe-Ne (10%-90%) in (b).

Note that Penning effect does not play a significant role in mixtures of neon with more than a few percent of xenon because most of the electron energy in these mixtures is spent into xenon excitation and ionization. Penning effect starts to become much more important when the concentration of xenon is less than 1%. This is because for very low concentrations of xenon, most of the electron energy is deposited in excitation and ionization of neon. A lot of energy is stored in neon excited states and the ionization of a xenon atom by an excited neon atom becomes very probable. (Mixtures of neon with typically 0.1% argon have been used to lower the operating voltage in monochrome plasma display panels.)

### 3.2 Breakdown in a coplanar geometry

The breakdown condition above, for a parallel plate geometry, is a relation between the breakdown voltage and the  $pd$  product. This is because  $\alpha/p$  is a function of the reduced electric field  $E/p = V/(pd)$ . This is exact for a parallel plate geometry (and if direct ionization by electron impact is the only ionization mechanism). In a matrix electrode geometry one can expect this to be true to first order. In a coplanar geometry the breakdown voltage no longer depends on the  $pd$  product alone, because the electric field distribution in the cell also depends on the position of the address electrode. The breakdown curves can still be plotted as a function of  $pd$ , but different curves are found for different  $d$  and different  $h$  where  $d$  is the distance between the coplanar electrodes and  $h$  is the distance between the dielectric surfaces.

The results displayed in Fig. 4 have been obtained with a 2D fluid model of the discharge cell shown in Fig. 4. Breakdown was said to have occurred when the ion density in the cell reached  $5 \cdot 10^{12} \text{ cm}^{-3}$  (for

this value of the density, the plasma had not yet formed but the distortion of the geometric field due to the ion space charge was large enough to always lead to a further increase of the current).

We see on Fig. 4a that the breakdown voltage increases considerably when the  $d/h$  ratio is increased. This is because the low potential region between the bottom sustaining electrode and the address electrode becomes larger for larger  $d/h$ , and the secondary electrons are not efficiently drawn to the high field region between the two coplanar electrodes. A non-negligible fraction of the electrons emitted from the surface may be lost by diffusion for large  $d/h$ . We also see on Fig. 4a that the minimum of the breakdown curve is shifted toward larger  $pd$  when  $d$  is increased. These tendencies have been observed in experiments [12], [13] but very few experimental data are available, and systematic comparisons are still to be done.

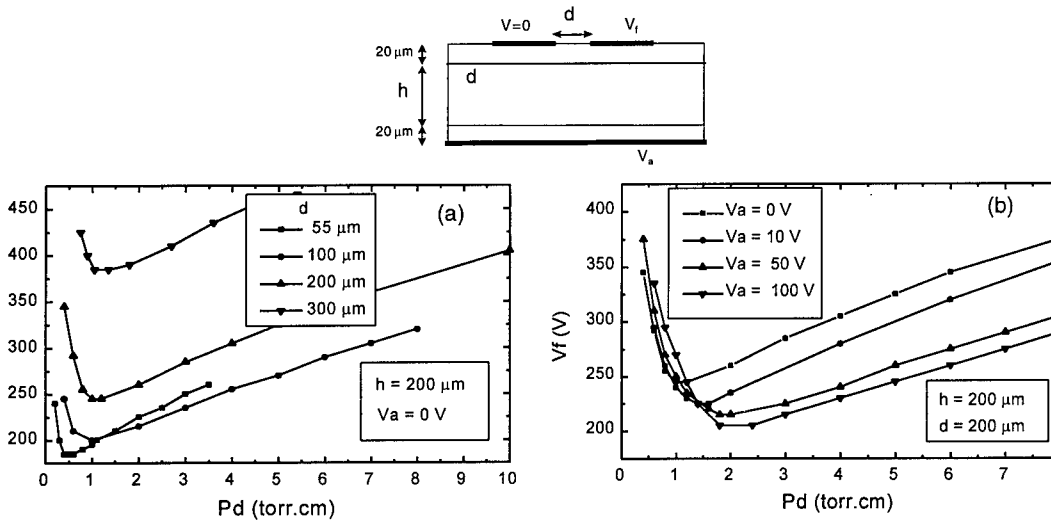


**Figure 4:** Breakdown curves in Xe-Ne mixtures in a coplanar structure (2 dimensional, Cartesian geometry). The secondary electron emission coefficient is set to zero on the dielectric surface above the addressing electrode. The thickness of both dielectric layers is set to  $20\ \mu\text{m}$ , and their relative permittivity is 12. The secondary electron emission coefficients for neon and xenon ions on the MgO surface above the sustaining electrodes are supposed to be 0.5 and 0.05, respectively.

The effect of the addressing voltage on the breakdown curve can be seen on Fig. 4b where the gap length  $d$  and the distance between the plates  $h$  are kept constant. A non-zero voltage on the addressing electrode helps draw the secondary electrons emitted above the grounded sustaining electrode to the high field, multiplication region. The breakdown voltage can therefore be significantly decreased when  $V_a$  is increased. We also observe a saturation effect on Fig. 4b: when the voltage of the addressing electrode is increased from 50 V to 100 V, the effect on the breakdown voltage is relatively small.

The distances  $d$  and  $h$  characterizing the coplanar geometry must be chosen extremely carefully since 1) when  $d/h$  is too large, the breakdown voltage becomes too large, and 2), when  $d/h$  is too small, the value of  $V_a$  does not affect strongly the discharge between the sustain electrodes and addressing becomes difficult. Note that 3D effects may also affect the breakdown curves in a real cell.

#### 4. PRINCIPLES AND ACCURACY OF THE MODELS

The aim of the models is to provide a good qualitative understanding of the physical mechanisms occurring in a discharge cell and to help define the optimal cell geometry and operating conditions. It is clear that exact descriptions of such a complex system are not possible, and the main task of the modeler is to choose the necessary approximations in such a way that all the elements are on similar levels of accuracy. In this section we first try to estimate the accuracy of a simple fluid model by comparing its results with those from a more sophisticated (but much more time consuming) hybrid fluid - Monte Carlo model. The approximate description of the charged particle transport is the first source of error in the

results. A second source of errors is related to the data which are used in the model (cross-sections, transport coefficients, secondary electron emission coefficients etc.). In the second part of this section we estimate the errors in the results which are due to uncertainties in the data and show that they are as large or larger as those due to the approximations in the transport equations implied by the LFA fluid model.

#### 4.1 Fluid and Hybrid models

The models we are using to describe the discharge evolution in a plasma display cell have been previously described in Meunier et al. [4], Boeuf and Pitchford [6], and Punset et al. [9]. Similar models have been developed by other groups [7], [14], [8]. They are based on solutions of the charged particle transport equations coupled with Poisson's equation for the electric field. They can be coupled to a model of the excited species kinetics in the xenon-neon mixture (see Meunier et al. [4]) but the results show that, in typical conditions, the concentration of excited species in the discharge is relatively low and that second kind collisions (e.g. stepwise ionization) or Penning ionization do not play a significant role. The electric part of the model (charged particle transport and field) can therefore, to the first order, be decoupled from the excited species kinetics and the photon transport model.

The discharge is strongly collisional and fluid models seem more appropriate, under these conditions, than particle models. We choose to represent the charged particle momentum transport equation by the usual drift-diffusion approximation which is well suited to collisional situations. We also often replace the electron energy equation with the so-called local field approximation (LFA) which assumes that the electron energy losses exactly balance the electron energy gain, locally in space and time. This approximation is excellent in the case of a swarm of charged particles moving in a uniform or slightly non uniform field. It is, however, well known that it becomes less suitable when the relative variations of the electric field are not negligible over lengths on the order of the electron mean free path for energy exchange or during times on the order of the electron energy relaxation time. The cathode region of a DC or RF glow discharge is a typical example of where the LFA is not valid.

Since the discharge in an AC plasma display cell is quickly quenched because of the charging of the dielectric layers, the sheath length is not as small as it would be in DC conditions, and it is interesting to study quantitatively the errors which are induced by the local field approximation in that case. We therefore compared the results from two different discharge models. The first one is a fluid model based on the LFA and is similar to the models used in Meunier et al. [4] and Punset et al. [9].

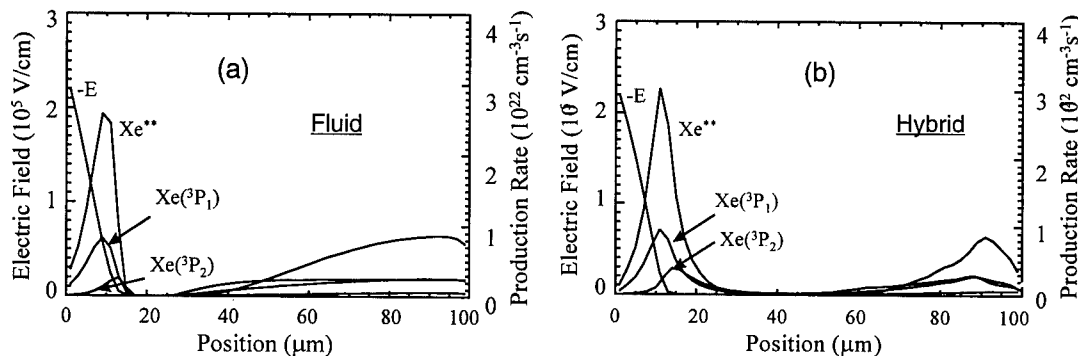


**Figure 5:** Spatial distributions of the excitation rates and electric field at the time of peak current from (a), the fluid, LFA model, and (b), from the hybrid fluid - Monte Carlo model (see text for the conditions).

The second model we have developed is a hybrid fluid - Monte Carlo model where the LFA is no longer used to calculate the ionization rate. The ionization rate in the hybrid model is obtained from a Monte Carlo simulation of the electrons which are energetic enough to ionize and excite the xenon and neon atoms. In other words the tail of the electron distribution function is described with a particle, Monte Carlo simulation, while the transport of the bulk electrons is described with a simple, drift-diffusion, fluid



model. Similar hybrid models have been described previously in J.P. Boeuf and L. Pitchford [15], and Fiala et al. [16]. The Monte Carlo simulation is run each time the electric field profile has changed by more than a given amount (a few percent). Each Monte Carlo simulation is performed assuming quasi-steady state. This is possible because the relaxation time of the tail of the electron distribution function is fast compared to the characteristic time of variations of the electric field in the cell (this time is on the order of 1 ns in typical conditions while the electron collision time is on the order of  $10^{-12}$  s and the energy exchange time for inelastic collisions is on the order of  $10^{-10}$  s).

We have compared the results of the fluid and hybrid model for a 1D (matrix) cell in the following conditions: Xe-Ne 10%-90% mixture, gas pressure 560 torr, 100  $\mu\text{m}$  gas gap, equivalent capacitance of the dielectric layers 230 pF/cm<sup>2</sup>, applied voltage between the electrodes 330 V and no memory charges on the dielectric surface. The ionization coefficients which have been used in the fluid LFA model in the results of Figs. 5, 6, and 8a have been obtained from Monte Carlo simulations in a uniform field. In the results of Figs. 7 and 8b, the ionization coefficients are those of Meunier et al. [4] which were derived from a multiterm Boltzmann equation. They are slightly different (up to 10% at high reduced field) from the ionization coefficients obtained with the Monte Carlo simulation in the hybrid model, under conditions of uniform electric field. This point will be discussed in a forthcoming paper.

Figure 5 shows a comparison between the predictions of the fluid and hybrid models at the instant of peak current. The spatial distributions of the electric field and xenon excitation rates at that time are represented. At this time, the sheath length is at its minimum and the electric field on the dielectric surface is maximum. These conditions are therefore the worst possible conditions for the local field approximation. We see that the field profiles predicted by the two models are very similar. The xenon excitation rates have similar profiles although, as expected, the hybrid model predicts a significant excitation in the zero field region, at the entrance of the negative glow plasma, while excitation on the cathode side occurs only in the sheath, in the fluid model.

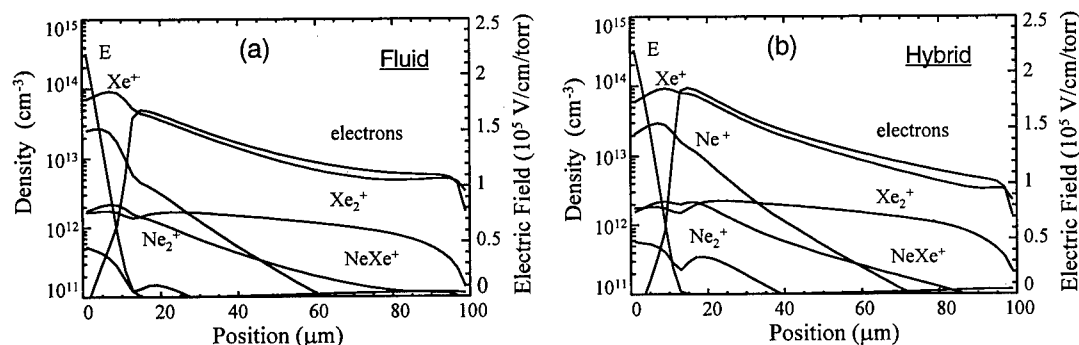


Figure 6: Spatial distributions of the charged particle densities and electric field at the time of peak current from (a), the fluid, LFA model, and (b), from the hybrid fluid - Monte Carlo model

It is also interesting to note that the increase of xenon excitation in the plasma, on the anode side, which had been observed and discussed in Meunier et al. [4] (and attributed to a transient effect at the instant of peak current) is also predicted by the hybrid model. The profile and intensity of excitation in the plasma predicted by the hybrid and fluid models are however not identical.

Figure 6 shows the spatial profiles of the charged particle densities in the same conditions as Fig. 5, at the instant of peak current. The comparison is quite satisfactory although some differences can be observed between the predictions of the fluid and hybrid models: as expected, the ion density in the sheath is larger in the results from the fluid models than in those of the hybrid model, and the reverse is true for the plasma density.

Figure 7 shows the mid-margin and current half-width as a function of xenon concentration, deduced from the fluid and hybrid models. It appears from Fig. 7a that the mid-margin voltage predicted by the

fluid model is 15-20 V below the mid-margin voltage deduced from the hybrid model. However the trends predicted by both models are in good agreement. The current half-width is about 3 ns longer in the hybrid model. The current pulse is shorter in the fluid case because the ions are created closer to the dielectric layer; they are created deeper in the plasma, due to non local effects, in the hybrid model.

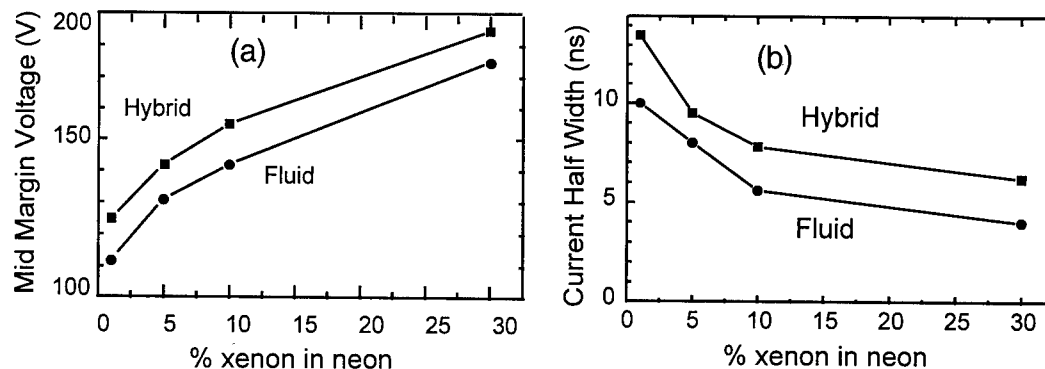


Figure 7: Comparisons of (a) the mid-margin voltage and (b), the current half width (at mid-margin) as a function Xe concentration, calculated with the fluid LFA model, and with the hybrid model

The current pulse and voltage across the gas gap are displayed in Fig. 8a. They are very similar to the results predicted by the fluid model (see Meunier et al. [4]). The times to breakdown predicted by both models may however be quite different if the ionization coefficients used in the fluid models are not identical to those which would be calculated under uniform field conditions with the Monte Carlo simulation (this is the case in the calculations above since the ionization coefficients in the fluid model have been obtained from solutions of a Boltzmann equation corresponding to a Pulsed Townsend swarm experiment and not to a Steady State Townsend experiment).

Note finally that the UV efficiency of the discharge calculated with the fluid and hybrid models is practically identical (Fig. 8b).

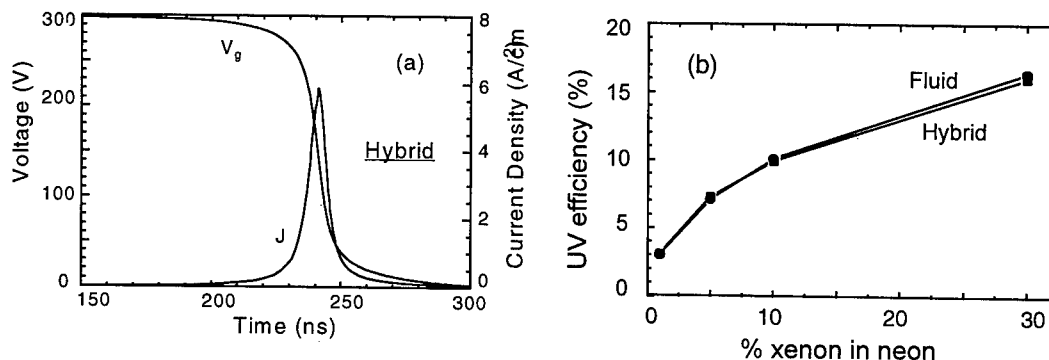
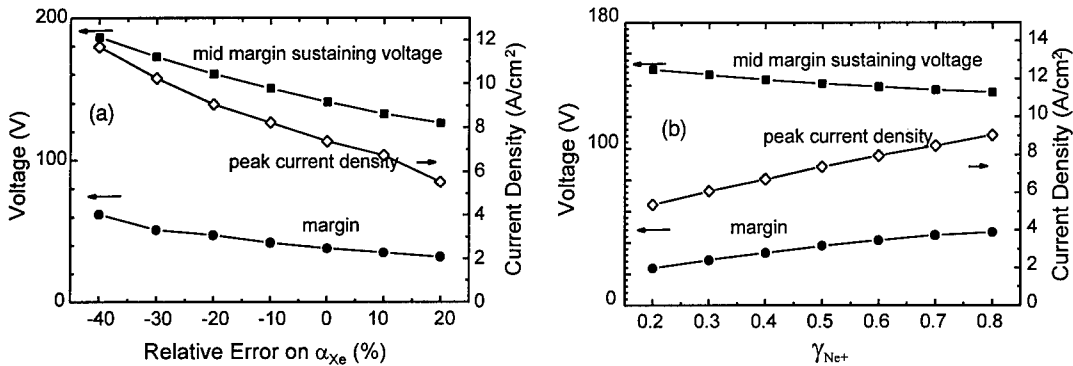


Figure 8: (a) Time evolution of the current and gas gap voltage obtained with the hybrid model (conditions of Fig. 5); (b) comparisons of the UV discharge efficiency calculated at mid-margin with the hybrid and fluid models for different xenon-neon mixtures.

#### 4.2 Sensitivity to uncertainties in data

The approximations made in the transport equations are a source of error as discussed in the previous section. Another source of error which is often more difficult to quantify is related to the uncertainties in

the basic data which are used in the models. In our problem these data are the electron neutral cross-sections (used in the hybrid model, or to calculate the transport coefficients), the transport coefficients (ionization coefficients, mobility ...), and the secondary electron emission coefficients. The most important unknown in a PDP discharge model is undoubtedly related to the secondary emission coefficient. We have only a rough estimation of the secondary emission due to neon ions on MgO ( $\gamma_{Ne} \sim 0.3-0.5$ ) but we do not know at all how this coefficient depends on ion energy in the energy range of interest. The secondary emission coefficient for xenon ions on MgO is not known although it seems reasonable to assume that it is at least 10 times smaller than  $\gamma_{Ne}$ . The ionization coefficients and other charged particle transport coefficients are known with a better accuracy. The accuracy of these coefficients is, roughly speaking, not better than  $\pm 10\%$  even in the relative simple case of rare gases.



**Figure 9:** Sensitivity of the results (from the fluid LFA model) to the uncertainties in (a) xenon ionization coefficient, and (b), secondary electron emission by impact of neon ions on MgO

In order to estimate the errors in the results which are due to uncertainties in the data, we have performed simulations where one of these parameters (ionization coefficient, secondary emission coefficient ...) was varied by a given percentage. Figure 9 shows the results of this study in the case of the xenon ionization coefficient (Fig. 9a) and the neon secondary electron emission coefficient (Fig. 9b). We see on this figure that the margin changes by a factor of 2 when the secondary emission coefficient of neon is changed between 0.2 and 0.5. The mid-margin voltage decreases typically by 20 V when the xenon ionization coefficient is increased by 10%.

#### 4.3 Are the fluid models accurate enough ?

The conclusion of this section is that although the fluid LFA model does not capture all the complexity of the non local electron transport in the conditions of a plasma display panel cell, it can predict correctly the qualitative behavior and the trends. On a more quantitative point of view, the inaccuracies introduced by the fluid LFA model seem to be not larger than the inaccuracies introduced by the uncertainties in the basic data. Finally we mention that the computation time of the fluid LFA model is about 20-50 times shorter than the computation time needed by the hybrid model. This is an essential point for practical applications.

We believe that an efficient way to use discharge simulations in the optimization of plasma display panels is to use simple fluid models. These should be validated, for a few operating points, by comparisons with simulations based on hybrid or particle models.

### 5. DISCHARGE AND PLASMA FORMATION IN MATRIX AND COPLANAR GEOMETRY

Figures 10 and 11 show typical results from a 2D fluid model of the discharge for matrix and coplanar structures, respectively.

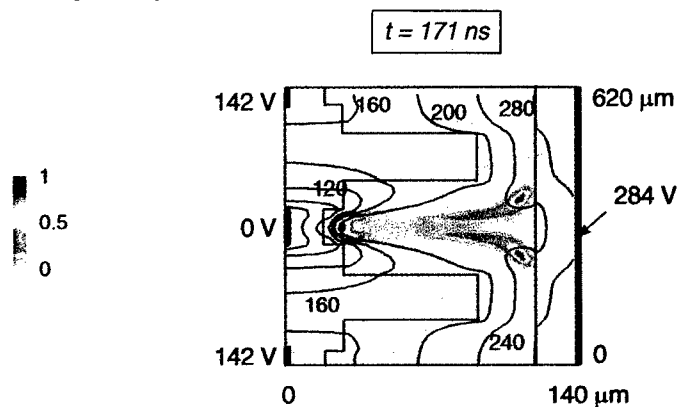


**Figure 10:** Equipotential curves and power dissipated in xenon excitation (unit  $7.4 \cdot 10^4 \text{ W.cm}^{-3}$ ) at the instant of maximum current of a discharge in a matrix PDP (Xe-Ne 10%-90%, 560 torr). No memory charges are present before the discharge pulse.

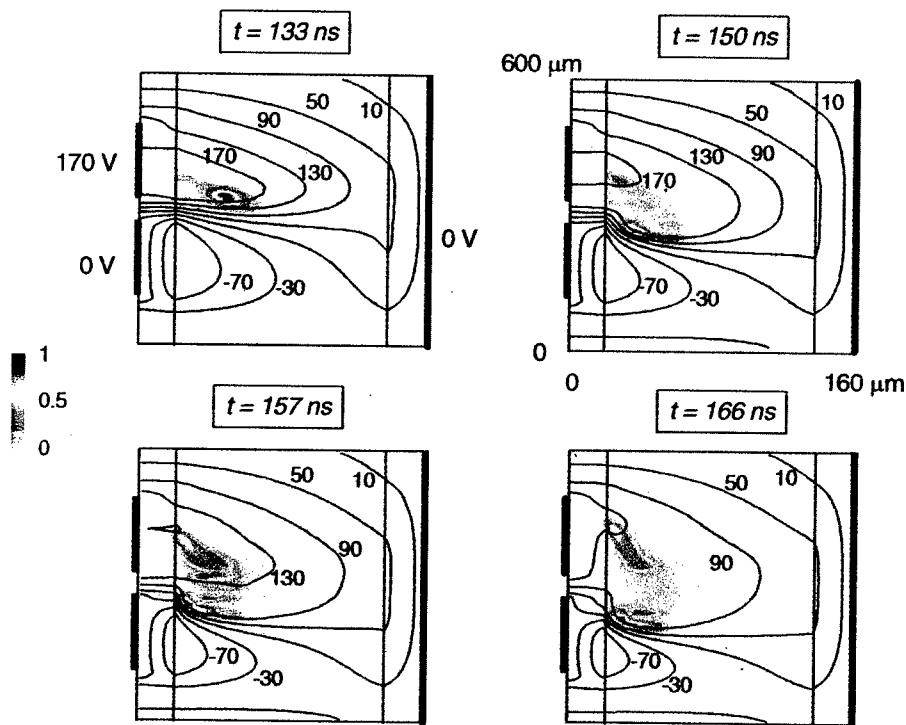


**Figure 11:** Equipotential curves and power dissipated in xenon excitation at four different times of a discharge pulse in a coplanar PDP cell (Xe-Ne 10%-90%, 500 torr). Memory charges are present before the discharge pulse and the discharge operates in the ON state of the sustaining regime. The units of the color scale for the power dissipated into xenon excitation are  $1.8, 5.5, 7.9, 3.8 \cdot 10^4 \text{ W.cm}^{-3}$ , for  $t=133, 150, 157, \text{ and } 166 \text{ ns}$  respectively.

In the simulation of Fig. 10 the discharge was supposed to be in the OFF state before the voltage pulse, and no memory charges were present on the dielectric surfaces before the pulse. One cell and two half-cells are included in the simulation domain. Symmetric boundary conditions are assumed on the top and bottom of the simulation domain. We see in Fig. 10 the intense xenon excitation in the cathode region next to the left electrode. The equipotential curves show the high field sheath next to the dielectric surface on the left side. Xenon excitation also occurs next to the dielectric surface on the anode side. This is related (see, e.g. [6], [9]) to the charging of the dielectric layers by electrons. The charging of the surface induces a local drop of the potential. The electrons which continue to flow to the surface move to the higher potential region along the dielectric surface. The electric field associated with the potential gradient along the surface appears clearly in Fig. 10 (see the shape of the potential line at 240 V, next to the right dielectric surface) and is large enough to accelerate the electrons and induce significant xenon excitation.

The simulation of Fig. 11 corresponds to a discharge pulse in the sustaining regime of a coplanar cell. Periodic boundary conditions are assumed on the top and bottom of the simulation domain. Memory charges have been deposited by the previous pulse and are present on the dielectric surfaces at the beginning of the pulse of Fig. 11. The equipotential curves at the beginning of the current pulse ( $t=133$  ns) show the effect of the presence of the memory charges on the dielectric surface. The potential on the dielectric surface above the cathode (left electrode at 0 potential) is below -70 V and the potential on the dielectric surface above the anode (left electrode at 170 V) is larger than 170 V. The applied voltage (sustain voltage, 170 V) between the coplanar electrodes is smaller than the breakdown voltage in these conditions. The combination of the potential drop due to the memory charges and the voltage across the electrodes lead to a total voltage drop larger than the breakdown voltage in the gas gap above the coplanar electrode. A discharge is therefore initiated. At  $t=133$  ns, the plasma has already formed above the anode. Xenon excitation is maximum above the anode, at the boundary between the large field region between the coplanar electrodes and the lower field region above the anode. At  $t=150$  ns the plasma has expanded, as shown by the extension of the low field region above the anode. The ion sheath tends to bend the equipotential curves above the cathode and the position of maximum excitation moves with the high field region. This motion continues at time  $t=157$  ns and  $t=166$  ns. The potential along the dielectric surface decreases above the anode because of the charging by electrons and increases slowly above the cathode due to the charging by ions. It is interesting to note that significant xenon excitation also occurs above the anode after  $t=150$  ns. This increase in xenon excitation above the anode is due to the same phenomena as in the matrix case (Fig. 10). The potential quickly drops above the anode due to electron charging of the dielectrics and the resulting electric field parallel to the surface (see the first potential line above the anode at  $t=166$  ns) is large enough to accelerate the electrons and induce xenon excitation.

Simultaneous emission of the plasma above the cathode and anode of a coplanar plasma display cell has been observed by the group of Prof. Uchiike at Hiroshima University [17]. These authors used an ultra-high-speed electronic camera to measure the space and time evolution of the infrared emission of xenon. We believe that the observed emission above the anode in the experiments of Zhang et al. [17] is due to the electric field induced by the charging of the dielectric, as described above. Further work is however needed to confirm this point.

## 6. CONCLUSION

Physical models of the discharge occurring in plasma display panels are now being used in research laboratories as well as in industry. They provide very useful guidance in the design of the discharge cell and in the choice of operating conditions. They may, in the near future, play a key role in the search for better and more efficient plasma display panels.

Very few results from plasma diagnostic experiments have been published in the conditions of plasma displays, and there is a lack of reliable, published experimental data even on relatively simple questions such as the breakdown curves in a coplanar geometry. Since space and time resolved spectroscopic measurements are difficult in the conditions of a plasma display cell, we believe that

experiments on larger cells and for lower pressure could be very useful to validate the models, to guide the optimization of the cell geometry, and to aid in the research of more efficient structures.

Although acceptable for practical use in some applications, several characteristics of PDPs need to be improved in order to achieve better accepted products and increase the market share [1][2]:

- luminous efficacy, which is about 1 lm/W today, and must be increased up to a goal of 2 lm/W.
- life time, about 10 000 hours now, must be more than 20 000 hours in the mid term.
- image quality, related to addressing speed and priming issues, is not yet equivalent to that of Cathode Ray Tubes.

In order to move forward in the above characteristics, engineers need a better understanding of the physics underlying PDPs:

- an accurate energy budget of the complete system including discharge, phosphors, and cell geometry [18] shares is needed.
- a better knowledge about surface mechanisms: secondary emission and sputtering on MgO
- a better view on addressing mechanisms and limitations: minimum time between two writing or erase operations, priming problems at low duty cycles.

The effort and results presented in this paper contribute to some of these items.

### Acknowledgments

This work is partially supported by Thomson Tubes Electroniques.

### References

- [1] Deschamps J. and Doyeux H., *Physics World* June 1997 p. 39
- [2] Deschamps J. and Doyeux H., "Color PDP development: an exciting and ever progressing story", International Display Workshop, IDW'96 (1996) p. 275
- [3] Shinoda T., Wakitani M., Nanto T., Kurai T., Awaji N., and Suzuki M., "Improvement of Luminance and Luminous Efficiency of Surface Discharge Color AC PDP", Proceedings of the Society for Information Display Symposium, SID 91 Digest (1991) p. 724
- [4] Meunier J., Belenguer P., and Boeuf J. P., *J. Appl. Phys.* **78** (1995) 731
- [5] Boeuf J. P. and Doyeux H., *Europhysics News* **27** (1996) 46
- [6] Boeuf J. P. and Pitchford L. C., *IEEE Trans. Plasma Sci.* **24** (1996) 95
- [7] Campbell R. B., Veerasingam R., and McGrath R. T., *IEEE Trans. Plasma Sci.* **23** (1995) 698
- [8] Veerasingam R., Campbell R. B., and McGrath R. T., *IEEE Tran. Plasma Sci.* **24** (1996) 1411
- [9] Punset C., Boeuf J.-P., and Pitchford L. C., *J. Appl. Phys.* (1997) (submitted)
- [10] Shinoda T., "The AC plasma display panel", International Display Workshop, IDW'95 (1995) p. 29
- [11] Takayama O., "Innovation and commercial viability of large area plasma display through Fujitsu's continued R&D activities", International Display Workshop, IDW'96 (1996) p. 7
- [12] Sato S., Yamamoto H., Shirouchi Y., Iemori T., Nakayama N., and Morita I., *IEEE Trans. Electron Devices* **23** (1976) 328
- [13] Makino M., Yoshioka T., Ueoka M., and Saito T., "Non-uniform electric field influence on firing voltage of surface discharge AC-PDPs", International Display Workshop, IDW'96 (1996) p. 259
- [14] Choi K. C. and Whang K. W., *IEEE Trans. Plasma Sci.* **23** (1995) 399
- [15] Boeuf J. P. and Pitchford L. C., *IEEE Trans. Plasma Sci.* **19** (1991) 286
- [16] Fiala A., Pitchford L. C., and Boeuf J. P., *Physical Review E* **49** (1994) 5607
- [17] Zhang S., Uchiike H., Harano Y., and Yoshoda K., "Consideration to improve luminance of AC plasma displays based on the discharge characteristics by using an electronic camera", Proceedings of the Society for Information Display Symposium, SID 97 Digest (1997) p. 225
- [18] Doyeux H., "Luminance and luminous efficacy of PDPs", International Display Workshop, IDW'95 (1995) p. 53

## **A Guide to Laser-Induced Fluorescence Diagnostics in Plasmas**

T.G.M. Freegarde and G. Hancock

*Physical and Theoretical Chemistry Laboratory, Oxford University, South Parks Road, Oxford OX1 3QZ, U.K.*

**Abstract.** A brief guide is presented for the use of laser induced fluorescence (LIF) as a diagnostic for reactive species in plasmas. The technique can determine concentrations, energies, and kinetics of atoms, radicals and ions, and can also be used to measure the fields which influence the motion of the charged particles. Measurements can be made in a spatially selective fashion within the plasma reactor, and in a way which is non-invasive. The review gives examples of all these types of measurements, with emphasis on how quantitative information can be extracted from the LIF signals. Guides are given to the limits of species detectivity, and to the pitfalls which need to be avoided if the technique is to be used reliably.

### **1. INTRODUCTION**

An understanding of the physics and chemistry of plasmas requires information on identities, concentrations and energies of the species present - atoms, ions, electrons, radicals, molecules. This information needs to be quantitative, spatially resolved with respect to the active area of the plasma, and needs to be carried out in a fashion that does not disturb the plasma. If the plasma can be modulated then time resolution (on a scale which may run from seconds to ns) will provide additional information. No single technique can achieve all of these requirements, and a list of the various ways in which information of this kind has been gathered would probably encompass all techniques used in species diagnostics.

Plasmas glow, and much can be learned from observations of the wavelength resolved emission [1]. Emission reveals properties of the excited species, and is generally used in the visible and UV regions to observe electronically excited quantum states. Emission of course does not reveal the behaviour of the ground states of the species, which in most plasmas (and certainly in the low temperature plasmas used for materials processing) are in concentrations orders of magnitude higher than those of the excited states, and which are generally the major species responsible for the technologically important phenomena such as plasma etching, deposition or ion implantation. All ground state atoms, molecules and ions (with the exception of  $H^+$ ) can absorb light in transitions between eigenstates, and hence are detectable by this effect. Measurement of the absorption (the fraction of the incident light absorbed by the species) gives the concentration of the absorber directly, and is an extremely general technique, but suffers two drawbacks. First, the absorption is necessarily measured over the whole of the path of the interrogating light beam, and thus may mask spatial inhomogeneities. This can be overcome by viewing different paths through the plasma and using suitable inversion techniques to reconstruct the spatial variations in species concentrations. The second disadvantage is one of detectivity. Here we need to be quantitative: the limits of measurements of absorption depend crucially upon the noise characteristics of the source and detector, and the time interval over which the measurements are averaged. Some of the most careful estimates of this have come from experiments (generally not carried out in plasmas, but applicable to them) which use diode lasers as the light source. An absorption of  $10^{-6}$  over a 1s time period is a quoted detectivity limit with a signal to noise (S/N) ratio of unity [2], and to translate this into practical detectivity terms we consider a specific example. The

quantum state resolved absorption features in the OH radical in its  $A^2\Sigma^+ - X^2\Pi$  transition near 308 nm have cross sections of the order of  $5 \times 10^{-16} \text{ cm}^2$  [3]. In a plasma of length 10 cm, an absorption of  $10^{-6}$  would be achieved by a concentration of  $2 \times 10^8 \text{ cm}^{-3}$ , a very respectable detectivity limit. However we reiterate that this is a limit, achieved with a well characterised laser source, and measured over a 1s time period with unity S/N. Higher measurement periods increase the problems of drift in the experimental parameters. In practice such limits would be hard to achieve in a noisy plasma environment, and a couple of orders of magnitude leeway in the absorption measurements should be allowed. We note for example that an absorption of  $2 \times 10^{-4}$  has been suggested as a limit for absorption measurements of the  $\text{CH}_3$  radical with a Xe arc lamp as an excitation source near 216 nm [4].

Absorption measures the loss of photons, but makes no statement about their fate. Any absorption process will be accompanied by emission (fluorescence) from the excited state, and if the fluorescence quantum yield is "reasonable" (we consider what is meant by this later) then the emission can be used as a marker for the excited species, and hence for the species in the original lower quantum level. Any light source of the correct frequency can induce fluorescence, and we consider the use of a laser to do so. Fluorescence has an immediate advantage over absorption in that it is not a relative technique - in an ideal case the fluorescence is observed against a zero background. Ideal cases must give way to pragmatism, and we discuss in this review the application of laser induced fluorescence (LIF) to the noisy environment of a plasma. We first note the requirement of a "reasonable" fluorescence quantum yield. The ideal value of unity can be reduced by quenching, but this does not generally cause a major detectivity problem for low pressure ( $< 100$  Torr) plasmas. What are far more troublesome are the unimolecular decay processes which can compete with fluorescence, and, for the vast majority of electronically excited polyatomic species, processes such as dissociation or internal conversion render LIF impractical. Our example of the  $\text{CH}_3$  radical considered above is a case in point - the absorption step at 216 nm is followed by overwhelming predissociation and essentially no useful fluorescence.

**Table 1:** Laser armoury. Characteristics of typical laser systems available for laser-induced fluorescence studies of plasma species. Powers and pulse energies are of course wavelength and system dependent, and the list is not intended to be exhaustive. The generation of harmonics below 200 nm is generally in gas phase media; the practical lower limit for third harmonic generation is taken to be the lithium fluoride transmission cut-off, although shorter wavelengths are achievable.

laser type	medium	excitation	c.w./ pulsed	fundamental power/energy @ wavelength/nm		second harmonic power/energy @ wavelength/nm		third harmonic power/energy @ wavelength/nm	
Pump lasers									
Nd:YAG	crystal	optical	c.w.	10 W	1064	0.1 W	532		355
Ar <sup>+</sup>	gas	discharge	c.w.	3 W	514, 488				
Kr <sup>+</sup>	gas	discharge	c.w.	3 W	676, 338				
Nd:YAG	crystal	optical	pulsed	1 J	1064	0.2 J	532	0.1 J	355
excimer: XeCl	gas	discharge	pulsed	2 J	308				
excimer: KrF	gas	discharge	pulsed	1 J	248				
copper vapour	gas	discharge	pulsed	10 mJ	511, 578	1 mJ	255, 289		
Tunable lasers									
dye	liquid	optical	c.w.	1 W	320-1000	10 mW	220-500		
Ti:sapphire	crystal	optical	c.w.	1 W	670-1100	10 mW	350-470	1 nW	260
diode	semi-cond	electrical	c.w.	100 mW	630-700 740-870 900-1060 1180-1580	1 mW	330-340 380-435 450-530		
dye	liquid	optical	pulsed	100 mJ	320-970	10 mJ	190-310	1 μJ	108-210
Ti:sapphire	crystal	optical	pulsed	1 J	680-1070	10 μJ	350-470		
diode	semi-cond	electrical	pulsed	100 μJ	630-1580	1 μJ	330-530		

Electronic transitions which lead to observable fluorescence lie roughly in the 100 - 1000 nm region, and laser sources are available (at varying output energies and powers) at all of these wavelengths. Most experiments are carried out with tunable lasers, and the starting point is often the tunable dye laser pumped



with the visible or u.v. fixed frequency output of a Nd:YAG or excimer system. Various frequency conversion schemes extend the output range, and examples of the laser armoury with typical output conditions are given in Table 1. Longer wavelengths take us into the excitation range of vibration-rotation transitions, and although fluorescence is still observable from these species, the relatively low Einstein A coefficients (in comparison with those at shorter wavelengths) coupled with the lower sensitivity of commonly available i.r. detectors have meant that few LIF studies of plasmas have been carried out at these longer wavelengths (although spontaneous i.r. emission can be a useful diagnostic under such conditions [5]). The characteristics of laser radiation that make the LIF technique useful are easily listed: tunability means that the absorption and hence the fluorescence is species selective, spatial coherence means that spatial selectivity within a plasma chamber is achievable with ease, intensity gives the possibility of multiphoton excitation leading to fluorescence. We shall give examples of the use of these properties in detecting atoms, radicals and ions in plasmas.

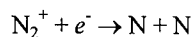
This guide seeks to be realistic. We discuss four sets of examples of the type of information that can be obtained from lasers, stressing at all times that the observations can be quantitative, but that they do have disadvantages. We first discuss the measurement of spatially resolved species concentrations in plasmas, paying particular attention to detectivity limits and to the problem of determining the absolute species concentration from the LIF signal. The next section discusses energy distributions, both translational and internal, that can be obtained by LIF, and gives an opportunity for discussion of the thorny problem of saturation by laser irradiation and how it can affect the interpretation of LIF data. We then discuss what can be learnt from temporal variations of the LIF signal, in particular commenting on the measurement of parameters such as the loss rates of species on surfaces in the plasma reactor. Finally, measurements of electric fields by LIF are briefly discussed. Several examples will be taken from the LIF measurements conducted over the past ten years in our research group.

## 2. MEASUREMENT OF CONCENTRATIONS

Figure 1 shows an example of the kind of LIF signal that can be straightforwardly obtained in plasmas [6]. Here we use a conventional RF capacitatively coupled parallel plate reactor with feedstock gases of either  $\text{CF}_4$  or  $\text{CHF}_3/\text{Ar}$ , at total pressures of 50 mTorr, and the species observed is the  $\text{CF}_2$  radical.  $\text{CF}_2$  has long been recognised as an important species leading to polymerisation in fluorinated hydrocarbon plasmas, and in these experiments it is excited at 234 nm in the strong A - X band system with fluorescence detected off resonance (to remove problems of scattered laser light) at 248 nm [7]. We note several pieces of information which come from these data. First, the spatial variations of the species concentrations measured as a function of height above the RF driven electrode surface are different close to the electrode for the two feedstock gases. For an understanding of this we need to realise that the processes which form the radicals appear not to be confined to electron impact of the parent molecule: surface formation (which would give rise to an enhanced concentration close to the electrode, observed in this case for  $\text{CHF}_3/\text{Ar}$  and noticeable in  $\text{CF}_4$  at higher pressures) can also play a major role [8]. Secondly, the concentrations of the radicals appear to be approximately constant in the plasma bulk (at distances above 10 mm from the electrode), and reflect the importance of fast diffusion ironing out any local changes in production rates. Thirdly, the data here are given on a relative scale, and this indicates one of the major problems of LIF: measurements of relative concentrations are facile, but putting these onto an absolute scale needs great care.

In principle if the characteristics of the excitation source are known, the spectroscopy of the transition is quantitatively understood, and the absolute value of the detected fluorescence can be measured, then the concentration can be determined. In practice this method is full of pitfalls, and rarely provides a convincing result. Here we first note that measurements of absolute spectral intensities of both the laser source and the fluorescence are not straightforward, and in section 3 below we shall dwell on another of the problems, that of saturation of the transition. To overcome the former difficulty, a variety of relative methods have been derived. One of these is to use a "fluorescence actinometer", a molecule whose concentration can be measured, and whose fluorescence intensity under similar conditions of laser excitation can be compared with that of the unknown species. Nitric oxide has been used in this way both for  $\text{CF}_2$  and for CF [9] and this

fixes the absolute concentrations of the  $\text{CF}_2$  radicals which are given in the caption to Figure 1. We note in passing that these absolute values are determined by the balance between the radical formation and loss rates, and that both of these processes can be extremely reactor specific, because of their dependences on surface processes. The problem of saturation affecting these calibrations has been cleverly addressed [10] and we return to this below. Other relative methods have included a comparison of the LIF signal with that from Raman scattering [11], and an elegant comparison of the LIF intensities of an unknown concentration of the CH radical with that from the  $\text{N}_2^+$  ion, the concentration of the latter being equal to that of electrons in a nitrogen discharge, with the electron concentration measured by microwave interferometry [12]. The equality of the  $\text{N}_2^+$  ion concentration  $c$  with that of the electrons in a nitrogen discharge can be used to make an estimate of  $c$  by kinetic means [13]. If the discharge is extinguished, and conditions are chosen such that the ion loss process is dominantly dissociative recombination with electrons



then the rate of loss of the ions is described by a second order equation

$$-\frac{dc}{dt} = k_1 c^2$$

where  $k_1$  is the known recombination rate constant under the given experimental conditions. Analysis of the decay of the relative LIF signal thus gives the absolute rate constant: this has been used to determine the absolute concentration of the  $\text{N}_2^+$  ion in the bulk of a parallel plate reactor as  $1 \times 10^{10} \text{ cm}^{-3}$  at a molecular nitrogen concentration of  $6.5 \times 10^{14} \text{ cm}^{-3}$  [14].

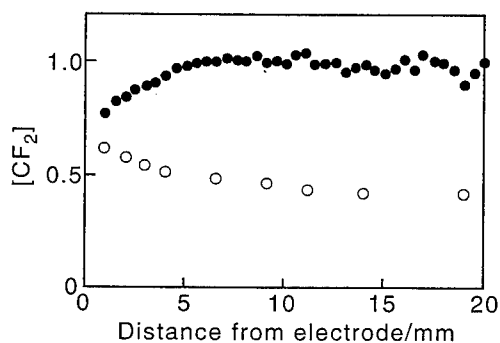


**Figure 1:**  $\text{CF}_2$  radical signals observed by LIF as a function of height above the RF driven electrode in a parallel plate reactor. Two separate sets of results are shown for a plasma in  $\text{CF}_4$  (filled circles) and an equimolar mixture of  $\text{CHF}_3/\text{Ar}$  (open circles), both at a total pressure of 50 mTorr and the same applied power. As can be seen, the LIF signals behave very differently close to the electrode. The radical concentrations have been put on an absolute basis as explained in the text: for the data at 20 mm the concentrations in  $\text{CF}_4$  and  $\text{CHF}_3/\text{Ar}$  are  $1 \times 10^{13}$  and  $1.4 \times 10^{13} \text{ cm}^{-3}$  respectively. Reproduced with permission from [6].

Figure 2 shows how the concentration of the  $\text{N}_2^+$  ion varies with height above the driven electrode in a parallel plate reactor. The plasma sheath in this case is observed visually to extend about 12.5 mm above the electrode surface, and it can be seen that as the surface is approached and the ions are accelerated to it, their concentration drops as a consequence of their increased velocities. The limiting concentration that we have been able to measure in these experiments is about  $2 \times 10^8 \text{ cm}^{-3}$ , and we now consider whether or not this number can be considered a "reasonable" detectivity limit for LIF in plasmas.

## 2.1 Detectivity

In principle, it is possible to detect a single atom or ion by LIF. With a reasonably intense continuous-wave laser it is possible to saturate the absorption transition resulting in a maximum spontaneous fluorescence rate whilst the laser is active of half a photon per upper level radiative lifetime. Taking the example of atomic caesium, excitation by a laser diode at 852 nm will saturate at an intensity of  $65 \mu\text{W}.\text{mm}^{-2}$ , and fluorescence photons will be emitted at a rate of  $16 \text{ million s}^{-1}$ . The emission from thermal population of the upper level will in comparison be negligible. By measuring the change in detected fluorescence signal in phase with wavelength modulation of the laser on and off the resonance wavelength, the background emission and laser scatter are rejected.

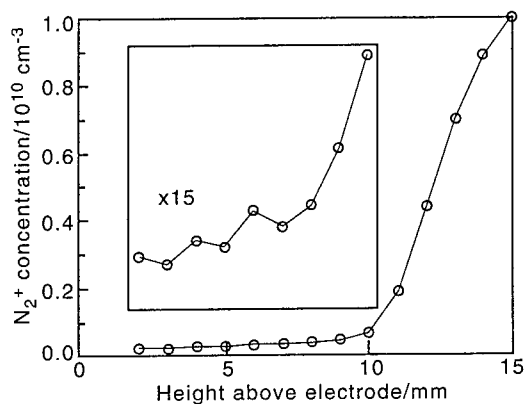


**Figure 2:** Measurements of the variation of  $\text{N}_2^+$  ion concentrations as a function of height above the driven electrode in an RF capacitatively coupled parallel plate reactor. LIF signals were put onto an absolute basis by measurements of the  $\text{N}_2^+$  decay rates under conditions where this was dominated by dissociative recombination. The smallest concentrations measured were approximately  $2 \times 10^8 \text{ ions cm}^{-3}$ . Total pressure 20 mTorr. Reprinted with permission from *J. Appl. Phys.* **81** (1997) 5945. © 1997 American Institute of Physics.

Our first estimate of the detectivity limit for species in a plasma is thus one atom, ion or molecule in the appropriate electronic, vibrational and rotational state within the observed volume. Taking a required spatial resolution of  $1 \text{ mm}^3$  and assuming that we are dealing with a molecular species with 1% of the population in the required initial state, we arrive at a density of  $10^5 \text{ cm}^{-3}$ , although the signal will at such concentrations vary as the single species diffuse into and out of the observed volume. Of course, the efficiency of detection of the fluorescent photons will not be unity - typically, because of the solid angle subtended by the detector and the detector efficiency, we shall collect less than 1% of the emitted light, even with F/2.8 optics. If we increase the species concentration to achieve once again the full single-atom count rate, and thus also reduce the statistical signal variation, we arrive at a concentration of the order of  $10^8 \text{ cm}^{-3}$ , which proves in practice to be a good rule of thumb.

For pulsed laser excitation, the pulse length is generally of the order of or less than the radiative lifetime, and thus the saturated spontaneous fluorescence signal will not exceed one photon per atom or ion per laser pulse. Single photon detection is nonetheless possible, and the above logic thus continues to apply: Goeckner *et al* [15] have measured argon ions by pulsed laser-induced fluorescence with a precision of the order of  $10^7 \text{ cm}^{-3}$ , whilst for molecular species some of our own results are shown in fig 2 at a total concentration of  $2 \times 10^8 \text{ cm}^{-3}$  [14], and we shall see later that it is possible to achieve some degree of velocity resolution at this level. Both cases are typical of ion densities in plasma sheaths. The low duty cycle of a pulsed laser however requires a longer averaging time than for c.w. experiments: Sadeghi *et al* [16] have compared c.w. and pulsed LIF, and found an immediate improvement in signal-to-noise ratio upon changing to the c.w. system, even though the species sensitivity was reduced as a result of improved Doppler velocity resolution.

Signal fluctuations are not, unfortunately, the sole sources of noise in LIF measurements of plasma species, for the plasma - unlike single trapped ions, for example - radiates light of its own accord. This plasma emission, due principally to electron impact excitation of the observed species, occurs at a much lower level than that due to saturated LIF, but a typical imaging system will be sensitive to plasma emission at all points within the field of view. The effective contributing volume may be several orders of magnitude larger than that observed by LIF; it may also correspond to regions of higher species concentration, for example if the plasma sheath is observed through, or partly through, the plasma bulk. Plasma emission which occurs at wavelengths other than that at which LIF is observed may be removed by suitable filters placed before the detector. That which occurs at the observed wavelength is then eliminated from the signal by phase-sensitive measurement as the laser is switched or tuned on and off resonance, although it will continue to add to the measurement noise.

There are, in addition, two routes through which the laser may contribute to the observed signal: scatter of the laser beam by the plasma and plasma chamber, and scatter of fluorescence induced outside the observed region. Direct laser scatter may be attenuated by the detector filters if we are observing off-resonance, but potentially has a much larger initial intensity: care should therefore be taken to eliminate scattering objects from the line of sight, and to reduce their reflectivity wherever possible. Scattered LIF cannot be so removed, although it should be attenuated by the scattering process itself. Nonetheless, if we again consider LIF measurements of sheath species probed by a laser beam entering through the plasma bulk, it is clear that the longer path length through the bulk and the higher species density there will result in a far larger yield than from the small and rarefied region being probed. If the laser beam runs along the axis of the plasma chamber, then the cylindrical walls will reflect some of the emission onto the axial region of observation. If it is then scattered, it will be indistinguishable from true LIF unless careful diagnostic tests are carried out.

Sensitive LIF experiments will therefore use carefully designed imaging to collect the fluorescence without accepting too much background plasma emission or laser scatter, and the light will be passed through filters to remove both plasma emission and laser wavelengths. Wavelength modulation allows direct laser scatter to be eliminated, and background emission may be rejected by either wavelength or intensity modulation of the laser. Finally, comparison with the signal when the plasma has been extinguished will often confirm that the observed signal is indeed laser-induced fluorescence from the species and region of interest.

### 3. ENERGIES

LIF is a quantum state resolved measurement, and thus can be used to determine the distribution of the species over the populated quantum states. If the species are in Boltzmann equilibrium then this distribution will correspond to a temperature, but we should note that there is no *a priori* reason to assume that this will be true in a plasma. For a temperature to be established within a given degree of freedom we need the rate of formation of a specific quantum state to be slow in comparison with the rates of the energy transfer processes within that degree of freedom. The latter processes may take place in 10-100 collisions for equilibration within translational and rotational degrees of freedom, but may require many more than this for vibrational energy transfer. Furthermore, although different degrees of freedom may be characterised by temperatures they need not necessarily be the same. This will be particularly true for vibrational distributions in comparison with those for rotational and translational degrees of freedom owing to the relatively slow rates of energy transfer out of vibration into these modes.

Figure 3 shows part of what is known as a fluorescence excitation spectrum of the  $N_2^+$  ion near 400 nm, in which the total fluorescence is gathered as the laser wavelength is swept. The main structure can be identified as lines in the R branch of the  $B^2\Sigma^+ - X^2\Sigma^+ (0,0)$  band, and the intensities of these can be converted into relative populations if the following factors are known or understood. First, a knowledge of the line strengths (equivalent to the absorption cross sections) is needed - these are straightforwardly calculable. Secondly, the excitation process is not isotropic in the laboratory frame, as the laser has a propagation vector and is normally linearly polarised. Even for an isotropic sample (by isotropic here we mean a random

distribution of the transition dipoles of the absorbing species) this means that the fluorescence itself is not spatially isotropic and is often polarised. Corrections should be applied to take this into account, and a "user friendly" guide to the extraction of populations under these conditions [17] has been extensively used in the fields of photodissociation and reaction dynamics where the distribution of transition dipoles probed by LIF can be markedly non-isotropic. In plasmas the distributions are assumed to be isotropic, and the polarisation corrections assumed to be small. Neither is necessarily true: energy transfer processes involving drifting ions have been shown to lead to molecular frame alignment [18], and polarisation corrections can be of the order of  $\pm 10\%$  if transitions from different branches or from quantum states with low values of  $J$  are measured. For neutral species these effects however are generally small. Thirdly, saturation can again be a problem, and we consider its effect later on in this section.

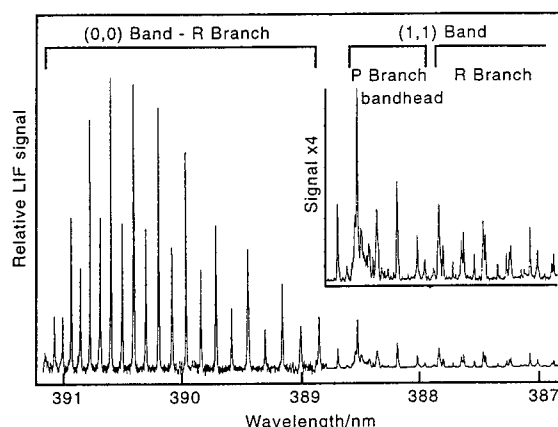
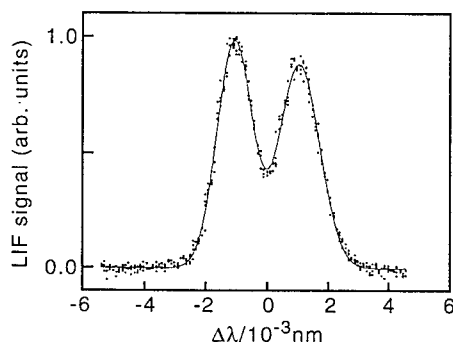


**Figure 3:** Laser excitation spectrum between 387 and 391 nm of the  $N_2^+$  ion excited in the (0,0) band of the  $B^2\Sigma^+ - X^2\Sigma^+$  transition in the bulk of a plasma of nitrogen at 50 mTorr. The R branch of the (0,0) band can be analysed to reveal the rotational distribution of the ground state ions, which in this case corresponds to a Boltzmann temperature of 355 K. At the low wavelength end of the spectrum part of the (1,1) band can be seen, and this allows an estimate of the relative vibrational populations of the  $v=0$  and 1 levels to be made.

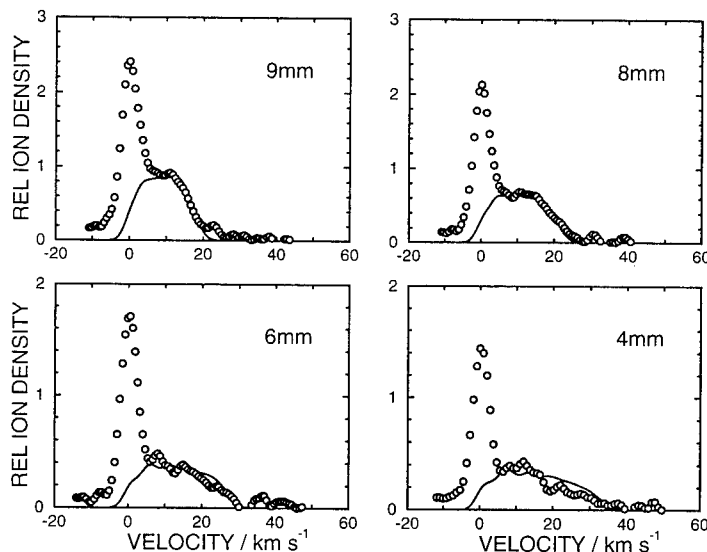
An analysis of the data in Figure 3 shows that in the plasma bulk the  $N_2^+$  ions have a distribution which corresponds closely to a temperature, in this case  $355 \pm 15$  K. This is not surprising: rotational equilibration in this ion is expected to be rapid under the experimental conditions (50 mTorr total pressure in this case), and we would expect this degree of freedom to be equilibrated with the local translational temperature. We note that in Figure 3 at shorter wavelengths, signal is seen in the (1,1) band of the transition, and this allows us to estimate the relative vibrational populations of  $v=0 : v=1$  as  $1 : 0.07$ . If this corresponded to a temperature (we cannot confirm this, as our detectivity precludes observations of higher vibrational levels) it would be around 1200 K, showing the marked difference between the rotational and vibrational degrees of freedom. Vibrational distributions are little studied in plasmas, and the importance of such excited species warrants investigation. For example, the electron impact cross section for a dissociation or ionisation process may be considerably enhanced by vibration, owing to a better overlap of geometries between the vibrationally excited state and the electronically excited state which leads to fragmentation (the electron impact equivalent of a Franck-Condon factor in photon absorption). The process requires electrons of lower energy than for the ground state, another factor which would enhance the rate of the excitation process. Further investigation of such effects is required.

Figure 4 shows a high resolution scan of the R(6) line of the (0,0) band of  $N_2^+$ , taken in the plasma bulk with the laser beam propagating parallel to the electrodes (and thus perpendicular to any DC fields in the chamber). The double-peaked structure is caused by the spin rotation doubling in the  $^2\Sigma^+$  states of the transition, and the widths are the result of the speed distribution of the ions in the laser propagation direction. The fit is that which would be expected if the translational distribution corresponded to the same

temperature, within experimental error, as that of the rotational distribution. We note that this is not a very precise measurement of temperature, as the Doppler width scales as  $T^{1/2}$ . We note also that ions are affected by fields, and we expect this to be manifested in the speed distributions perpendicular to the electrodes. Within the plasma bulk we find the velocity distribution to be isotropic (and well represented by a temperature) within our experimental precision, but as the ions are driven through the sheath their speeds in this perpendicular direction increase. Figure 5 shows data as a function of height above the driven electrode: fast ions are seen, increasing in importance as the electrode is approached. These fast ions are always accompanied by an unexpected component of slow ions, the origin of which is still unclear but which may have been from ionisation by secondary electrons emitted from the electrode surface [14]. The non-intrusive nature of the laser beam means here that the velocity distributions can be measured throughout the plasma, and because the technique measures concentrations of particles as well as their speeds, particle fluxes can be estimated throughout the range of particle energies.



**Figure 4:** High resolution LIF scan over the R(6) line of the  $N_2^+$  band shown in Figure 3. The two peaks result from spin doubling of the rotational levels in the  $^2\Sigma^+$  states, and the fit is that which would be expected from a Boltzmann distribution of the ions velocities at the same temperature as for the rotational distribution of Figure 3.



**Figure 5:** Measured relative  $N_2^+$  ion densities as a function of velocity component perpendicular to the electrode surface at distances of 9, 8, 6 and 4 mm above the driven electrode and at a pressure of 20 mTorr. The total ion concentrations are respectively  $4.6$ ,  $3.9$ ,  $3.0$  and  $2.6 \times 10^8 \text{ cm}^{-3}$  and the curves are plotted in the same relative units. The solid curves are theoretical predictions, which, whilst reproducing well the velocity distributions of the fast ions, are unable to account for the persistent slow component. The latter may be caused by ionisation from fast electrons emitted from the driven electrode. Reprinted with permission from *J. Appl. Phys.* **81** (1997) 5945. © 1997 American Institute of Physics.

### 3.1 Pitfalls of saturation

At low laser intensities, the processes of laser-induced excitation and subsequent fluorescence are simply related: for each laser photon absorbed an atom, ion or molecule is excited, and there is a constant probability that the subsequent decay will be via spontaneous radiation of a fluorescence photon, the detectability of which will depend upon the solid angle subtended by the detector and any loss processes or inefficiencies therein. Provided that the probabilities and loss mechanisms are known and that the sample is optically thin, the ratio of fluorescent signal to laser intensity will hence give the absolute species concentration; if the sample is not optically thin then attenuation of the exciting laser beam and reabsorption of the fluorescence must of course be taken into account. Such is the basis for measurement of absolute species concentrations by LIF. The calibration parameters may be established experimentally in a number of ways, as has been discussed in Section 2.

When the same principle is used to determine the vibrational and rotational distributions, it must be noted that the fluorescence yield depends upon rotational and vibrational quantum number as well as electronic state. The vibrational dependence is characterised by the Franck-Condon factor  $F(v_1, v_2)$ , which simply depends upon the overlap of the initial and final vibrational wavefunctions. The rotational dependence of the fluorescence yield is described similarly by the Hönl-London factor  $S(J_1, J_2)$ , which accounts for the initial and final state angular momenta  $J_{1,2}$  and the requirement that this be conserved ( $\Delta J = J_1 - J_2 = 0, \pm 1$ ). The total absorption rate  $B_{12}$  (per unit spectral radiation density) from state 1 to state 2 is thus proportional to the product

$$B_{12} \propto R_{12} F(v_1, v_2) \frac{S(J_1, J_2)}{g_1} \quad (1)$$

where  $R_{12}$  is the square of the dipole matrix element between the two electronic states and  $g_1$  the initial state degeneracy (here the conventional notation is taken that the  $S(J_1, J_2)$  sum over all  $J_2$  to  $g_1$ ). If the rotational distribution is required - it is often a good measure of the species translational temperature - then measurement is often made at high  $J_1, J_2$  when the factor  $S(J_1, J_2)/g_1$  loses its  $J$  dependence. This is not however always possible, and with diatomic hydrides, for example, the rotational level spacing may be large enough that only the low  $J$  states are thermally populated. In such cases, correction for the Hönl-London factors will be essential.

At high laser intensities typical of pulsed excitation, saturation occurs: the rate of excitation is sufficient that the ground (or lower) state population is depleted by the laser excitation before the end of the laser pulse or, in the continuous-wave case, before the atoms have had a chance to decay. The excitation rate is thus reduced whilst the converse process of stimulated emission competes with spontaneous fluorescence, and the signal becomes a sub-linear function of laser intensity. Ultimately, the strong laser field induces Rabi oscillations of population between the upper and lower levels: the mean excitation probability will be a half, and the fluorescence rate (if radiative decay is dominant) will be constant at half a photon per atom per radiative lifetime. Such saturation is, in principle, reproducible, and may therefore be calibrated, but the nonlinearity means that care must be taken if fluctuating signals are averaged, and in general it is necessary that the laser be stable for reliable results to be obtained.

#### 3.1.1 Saturation of homogeneously broadened species by monochromatic illumination

For monochromatic illumination (laser linewidth  $< A_{12}$ ) of a homogeneously broadened sample of atoms, ions or molecules, by a laser of intensity  $I(\nu)$  and frequency  $\nu$ , the fraction of the population in the excited state will be given simply by [19, 20]

$$\frac{\sigma_{12}(\nu) \beta}{(1 + g_1 / g_2) h \nu} \frac{I(\nu)}{1 + I(\nu) / I_s} \quad (2)$$

$I_s$  is the saturation intensity for the species, given by

$$I_s(\nu) = \frac{h\nu A_{12}}{\sigma_{12}(\nu)\beta} \quad (3)$$

where  $A_{12}$  is Einstein coefficient of spontaneous emission between the final and initial states,  $\sigma_{12}(\nu)$  is the absorption cross-section for the transition and  $\beta = \tau_2 A_{12} [1 + (1 - \tau_2 A_{12}) g_2 \tau_1 / g_1 \tau_2]$  where  $\tau_{1,2}$  and  $g_{1,2}$  are respectively the lifetimes and degeneracies of the initial and final states. With fully-allowed atomic transitions, the saturation intensity can be a few tens or hundreds of watts per  $m^2$ , easily reached by c.w. lasers. Note that the saturation intensity depends, through  $\beta$ , upon the upper and lower level lifetimes, which are reduced at pressures high enough to broaden the natural atom or ion linewidth: the LIF yield, as well as the saturation characteristics, may thus be functions of the plasma pressure and other parameters which affect the population and quenching rates.

Vibrational and rotational structure typically raises the saturation intensity due to the Franck-Condon and Hönl-London factors by an order of magnitude or more, but saturation nonetheless remains possible with pulsed dye lasers, even when of broad bandwidth. Saturation has a somewhat different meaning with pulsed lasers, as we shall see in Section 3.1.3. First, however, we consider the effect of inhomogeneities in the laser-species interaction, and show that a linear dependence of LIF signal upon laser intensity by no means implies that saturation may be neglected.

### 3.1.2 Saturation of inhomogeneously broadened species

The fluorescence intensity from a homogeneously-broadened sample (*i.e.* indistinguishable species) will rise with the laser intensity at low levels to a shoulder at  $I_s$ , and approach a constant fluorescence intensity thereafter. The situation is not, however, so simple when the sample is inhomogeneously broadened - *i.e.* the absorption lines of the plasma species are distributed due to thermal Doppler shifts, fine spectroscopic structure or spatial variations in field-induced Stark or Zeeman shifts. In such circumstances, different classes of species will be saturated to different extents for a given laser wavelength. In the case of a Doppler-broadened sample, for example, the fluorescence signal will continue to increase with laser intensity even once the on-resonance species are strongly saturated: the signal essentially depends upon the proportion of species for which the process is saturated, which proves to vary as  $I/(1+I/I_s)^{1/2}$  [20].

Inhomogeneities in the interaction between the plasma species and the laser may also be due to spatial variations in the laser intensity, so that saturation is achieved at the centre of the laser beam before it occurs at the edges. In such cases, the fluorescence signal will increase with laser intensity even if the plasma species are homogeneously broadened [21].

It should thus be clear that a linear dependence of fluorescence upon laser intensity will not necessarily indicate the absence of saturation.

### 3.1.3 Saturation by non-monochromatic illumination: laser linewidth $> A_{21}$

For the general case of broad-band c.w. laser excitation, it is necessary to integrate equation (2) across the laser emission spectrum:

$$\frac{\beta}{(1 + g_1 / g_2) h \nu} \int \sigma_{12}(\nu) \frac{I(\nu)}{1 + I(\nu) / I_s} d\nu \quad (4)$$

where  $I(\nu)$  is the laser emission spectrum. The absorption cross-section  $\sigma_{12}(\nu)$  contains the spectral sensitivity of the species, and a given species class thus sees only that part of the laser intensity which lies within its homogeneous linewidth. For specific cases, a saturation intensity may thus be calculated, and it is



clear that an intense laser may be sufficiently broad in bandwidth that it avoids saturating the species because the spectral intensity is low.

For pulsed laser excitation with a duration shorter than the excited state lifetime, saturation of the fluorescence signal will not occur until intensities rather higher than those indicated above, which correspond to significant excitation within an atomic lifetime rather than the shorter laser pulse duration: the  $A_{12}$  term should be replaced by the reciprocal of the pulse length. In such cases, account must also be taken of the laser bandwidth which will, by virtue of the finite pulse duration alone, be broader than the atomic absorption lineshape; the saturation intensity thus becomes proportional to the inverse square of the pulse length. If relaxation and spontaneous emission during the laser pulse duration  $\tau_{\text{pulse}}$  may be neglected, then we may define a pulsed saturation intensity - at which the initial state population becomes significantly depleted - by

$$I_s = \frac{h \nu \tau_{12}}{\sigma_{12} \tau_{\text{pulse}}^2} \quad (5)$$

where  $\tau_2$  is the upper level lifetime. For the 308.0 nm  $Q_1(2)$  transition between the  $A^2\Sigma^+(v=0)$  and  $X^2\Pi(v=0)$  states of the OH radical, excited by a dye laser pulse of 10 ns duration, the saturation intensity will be  $700 \text{ kW.cm}^{-2}$ , corresponding to a fluence of  $70 \text{ }\mu\text{J.mm}^{-2}$ , easily achieved by the output of a commercial pulsed dye laser. This transition is not exceptionally strong; the upper state radiative lifetime is 700 ns, and in species such as CF, NO or  $\text{CF}_2$  saturation will occur at lower fluence levels. The above expression assumes, of course, that the laser bandwidth is entirely due to the finite pulse duration: this is a reasonable approximation for many lasers, whose single-pulse spectra are dominated by one or two longitudinal modes.

Modification of equation (4) for pulsed lasers is in many cases of only academic interest. Broad-band pulsed lasers owe their spectral distributions to shot-to-shot jitter and multiple longitudinal (and transverse) resonator modes. The above expression is valid for a single-pulse laser spectrum, across which there is assumed to be no phase coherence, and in general the difficulty of obtaining appropriate data and performing such integrations will not be sufficiently worthwhile. For the case of a constant and uniform intensity Gaussian lineshape, the significance of saturation for LIF measurements in Doppler-broadened plasma species has been carefully considered by Goeckner and Goree [22]; the reader should nonetheless be aware that for many lasers the approximation to an incoherent Gaussian may be very poor.

### 3.1.4 Dealing with saturation in laser-induced fluorescence

It is apparent that at low intensities, the fluorescence yield is directly proportional to the product of laser intensity and species concentration, with a proportionality constant which may be derived either theoretically or by calibration, as discussed in Section 2. In such circumstances, the use of LIF to determine absolute species concentrations is straightforward. If the sample species are inhomogeneously broadened, then sweeping the laser wavelength gives the relative populations of the corresponding classes, enabling velocity distributions and so on to be determined. It is clear, nonetheless, that the exciting laser must be narrow or at least reproducible in bandwidth: if the laser bandwidth is broad, the effective laser intensity is only that fraction which lies within the homogeneous linewidth of the observed species.

If the laser spectral intensity is sufficient to saturate any of the species, then considerably more care is required in the interpretation of laser-induced fluorescence measurements, for the laser lineshape and the inhomogeneity of the laser-species interaction play crucial rôles in determining the fluorescence yield. Provided that the laser parameters are stable, a pragmatic calibration is nonetheless possible, as has been shown by Engelhard [21]; Cunge [10] meanwhile has demonstrated a neat method of cross-referencing the LIF yields from two different species by scaling according to the saturation parameter. It is also possible to compare the relative yields of two transitions of differing cross-section which originate from the same quantum level, such as the main and sub-branch transitions of the OH molecule [23].

The pitfalls of saturation in laser-induced fluorescence are two-fold. Firstly, saturation may go unrecognised because the fluorescence signal intensity continues to show a roughly linear dependence upon laser intensity: if a low-intensity calibration is applied to such data, the species concentration will be underestimated. Secondly, if the relation between laser and signal intensities is non-linear, then the average of a jittering or noisy signal may reflect the variation in laser intensity as well as the mean, and true calibration will in such circumstances be complex. The practitioner of LIF needs to be fully aware of these problems.

#### 4. TEMPORAL BEHAVIOUR

Modulation of the power source applied to a plasma clearly will result in a change of the rate of formation of the active species produced as a result of electron impact processes. The steady-state equilibrium concentration of these species depends upon the balance of the formation and loss rates, and if the time scale of the modulation is slower than that on which the equilibrium is re-established, then the time history of the reactive species can be followed with ease and kinetic information extracted. Section 2 above demonstrates how 100% modulation of a  $N_2$  plasma can lead to information on the concentration of the dominant  $N_2^+$  ion when the loss process is dissociative recombination. One of the most useful pieces of information that can be derived from experiments on radicals in plasmas concerns the loss rates that can be measured on surfaces - processes which are often the dominant removal steps in plasmas and are significant in technologically important processes such as plasma etching, polymerisation and ion implantation.

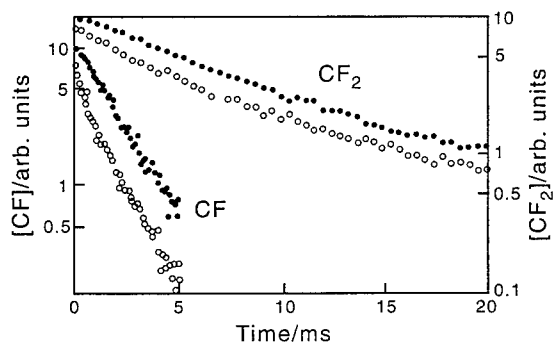


**Figure 6:** Semi-logarithmic plots of the variation in concentration of the  $CF_2$  and  $CF$  radicals, observed by LIF, after the extinction of a plasma of 50 mTorr  $CF_4$ . Closed and open circles represent the decay of the species measured at two different locations, 20 and 2 mm above the driven electrode respectively. Under these conditions the decays are seen to be reasonably well represented by exponential loss processes, with that for  $CF$  being markedly faster than for  $CF_2$ . Reprinted with permission from *J. Appl. Phys.* **66** (1989) 5251. © 1989 American Institute of Physics.

We give an example of the decay characteristics of radicals probed in a cylindrically symmetric RF excited parallel plate reactor [7] when the excitation source is removed. Under some conditions the resultant decay is well represented by a single exponential, and an example for both  $CF$  and  $CF_2$  radicals in a  $CF_4$  plasma is given in Figure 6. The time history of the radicals contains contributions from diffusion processes, losses in the gas phase by chemical reaction, and losses to the walls, and under some conditions the contribution from the wall loss process can be put on a quantitative basis. What can be estimated is a "phenomenological loss coefficient" [24], defined as the fraction of the particle flux to the surface which does not return to the gas phase on the time scale of the experiment. In Figure 1 we noted that radicals can have a marked spatial distribution within a reactor, and that this reflected formation and loss at the surfaces. For a full understanding of these processes both the spatial and temporal behaviour are required [8], and the complex behaviour that can occur is illustrated in Figure 7 where the spatially dependent loss phenomena of the  $CF_2$  radical in a  $CHF_3/Ar$  plasma are shown. Plasma extinction leads to an initial rise of the concentration in the plasma bulk (20 mm from the electrode surface) because of diffusion from the higher

concentrations of species present in the steady state near the electrode (illustrated in Figure 1). On re-ignition this concentration drops markedly, suggesting a homogeneous loss process involving other species formed in the plasma.

These results illustrate the type of information that can be found from such time dependent measurements, but we finish this section with two caveats. The first is that the determination of the loss coefficient tells us nothing about the chemical fate of the species lost on the surface. Some information can be obtained by looking for product molecules, for example the  $\text{SiF}_2$  radical formed by F atom etching of Si substrates [25], and observable by LIF near 225 nm. The second more general point concerns LIF detection, and is illustrated by observations of ground state  $\text{O}(^3\text{P})$  atoms, for which a convenient detection scheme is two photon excitation at 226 nm which populates the  $3p\ ^3\text{P}$  level and is followed by fluorescence to the lower  $3s\ ^3\text{S}$  level at 845 nm. Dye lasers can produce considerable output at 226 nm, and this is enough to create a population inversion between these fluorescing levels, which then can result in amplified stimulated emission (ASE) along the axis of the laser beam. The process is well understood, but can in some cases have an effect on the LIF diagnostic signal, as the ASE process will compete with spontaneous fluorescence which is thus reduced. This can be a problem when the depletion is a non-linear function of atom density, and an effect of this kind, causing a fluorescence reduction of the order of 30%, has been reported [26]. Our own measurements of the decay rates of O atoms following plasma extinction have demonstrated that erroneous results can be obtained if ASE is strong, as the fluorescence depletion is non-linear in O atom concentration and hence in time [27]. The problem is solved (at the expense of signal) by using a lower laser power, and illustrates that care needs to be taken to ensure that the laser diagnostic is not itself adversely affecting the quantity being observed.

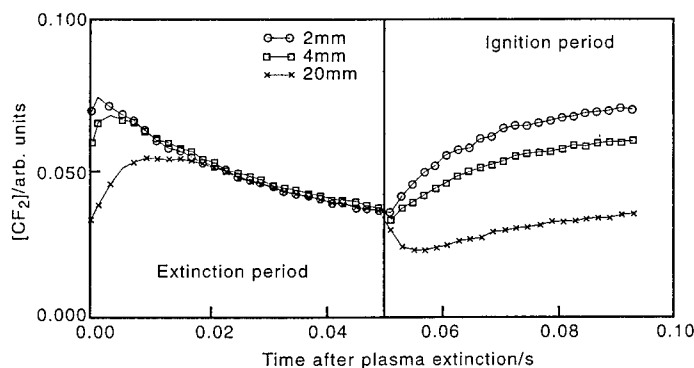


**Figure 7:** Variation of the time dependence of the LIF signal from  $\text{CF}_2$  with height above the driven electrode for a plasma of 200 mTorr equimolar  $\text{CHF}_3/\text{Ar}$  as the power is switched off (extinction period) and on (ignition period). Close to the electrode the behaviour is similar to that seen in Figure 6, but in the bulk it is very different; an initial rise is seen following extinction and caused by diffusion of the higher concentration of radicals from close to the electrode. Re-ignition causes a noticeable fast drop in bulk concentration.

## 5. FIELDS

Charged particles react to fields, and a measurement of the field distribution in a plasma is crucial for understanding the methods by which energetic ions and electrons are formed, and the energies with which they collide with other species and with surfaces. LIF can do this in two ways. The first involves the Stark effect, in which energy levels are altered in the presence of an electric field. An example is given in Figure 8 from the work of Muraoka *et al* [28], in which LIF is observed following the excitation of the  $11\ ^1\text{P}$  state of He from the metastable  $2\ ^1\text{S}$  level in a DC glow discharge. Here advantage is taken of the fact that Stark splittings in He increase with principle quantum number  $n$ , and for the  $n=11$  level the clear resolution in Figure 8 was obtained for an electric field of 90 V/mm, with the detection limit, determined simply by the laser bandwidth, being 21.5 V/mm. Excitation to higher  $n$  with a spectrally narrowed source improves this

by a factor of 2. More recently Stark shifts in atomic H excited to  $n=3$  by two-photon excitation of the ground state atom at 205 nm have yielded a sensitivity limit of 5 V/mm [29].

The second method for LIF measurement of electric fields relies on the field mixing of levels of opposite parity in the upper electronic level [30]. The method is illustrated with reference to the best studied example, that of the BCl radical excited in its  $A^1\Pi - X^1\Sigma$  transition, the (0,0) band of which is at 272 nm. The upper  $A^1\Pi$  state has its rotational levels split into opposite parity components, depending upon whether the  $\Pi$  electron is in an orbital which is symmetric or antisymmetric with respect to reflection through the plane of rotation ('lambda doubling'). In the absence of a field (and of collisions), excitation of for example an R branch transition yields fluorescence only on R and P branch lines ( $\Delta J=\pm 1$ ), owing to the parity selection rules. Electric fields cause mixing of the states of opposite parity, and in the presence of a field a Q branch ( $\Delta J=0$ ) is seen, the intensity of which relative to the fully allowed R and P branches gives a measure of the electric field. The field detectivity limits are of the same order as those measured by Stark splittings, and a useful list of the appropriate species for which this technique is possible has been published [28]. One of the most notable pieces of information that can be obtained through this technique is a measure of how the electric field changes with the phase of the applied voltage, for example during an RF cycle [31]. The limitation however is that the species needs to have a  $\Sigma$  ground state, and this restricts the range of diatomic species that can be studied, eliminating for example radicals such as OH, CF and SiF which have unpaired electrons but  $^2\Pi$  ground electronic states.

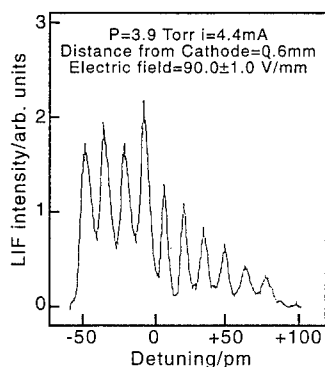


**Figure 8:** LIF spectrum near 321.25 nm of the He  $11^1P \leftarrow 2^1S$  transition in a DC discharge, against laser detuning from centre wavelength. The peaks arise from the Stark splitting in the upper state, and from these data the DC field can be calculated. Reproduced with permission from [28]

## 6. CONCLUSIONS

Densities, spatial distributions, energies, fields and interaction kinetics of plasma species can all be measured in a non-invasive fashion by LIF: information crucial for the refinement of models low temperature plasmas. Yet lasers are only rarely used as diagnostics in the technological plasmas used for industrial processing, partly because lasers have hitherto been bulky, expensive and - in spite of their manufacturers' claims - in need of the attention of skilled operators.

The examples of laser-induced fluorescence measurements that we have given in this article all involve the use of laser radiation in the visible and u.v. spectral regions. These wavelengths can now be reached by efficient upconversion of the output of c.w. diode lasers manufactured in vast quantities for communications and optical reader systems. Efficient frequency doubling of c.w. radiation in  $\text{KNbO}_3$ , for example, can yield several mW of light in the 430 nm region [32], and carefully designed resonators allow similar powers to be generated with few gaps from as low as 330 nm up to 500 nm and beyond. Even frequency quadrupling, which extends the range of these sources to below 250 nm, has been reported. Such systems are already being considered for balloon-borne atmospheric measurements, where their small size, relatively low cost and ruggedness make laser-based diagnostics attractive. Diode lasers have an additional advantage over

conventional devices in that their emission wavelength is directly controllable electrically, permitting extremely high stability to be maintained and allowing complex modulation and signal processing schemes to be tailored to the spectroscopic application.

Diode laser systems, only just emerging from the laboratory, may represent the future of *in situ* processing diagnostics, but their conventional cousins continue to be capable workhorses for plasma investigations, provided that the price and expertise can be afforded. A pulsed dye laser, pumped by an excimer or Nd:YAG source, or a continuous-wave system with the dye pumped by an argon ion or c.w. Nd:YAG laser, will put at its owners' disposal most of the techniques that we have described.

## References

- [1] The application of optical diagnostics to low pressure plasmas has been reviewed by Dreyfus R. W., Jasinski J. M., Walkup R. E., Selwyn G. S., *Pure & Appl. Chem.* **57** (1985) 1265.
- [2] Werle P., Mücke R. and Slemr F., *Appl. Phys. B* **57** (1993) 131; Güllück T., Wagner H. E. and Slemr F., *Rev. Sci. Instrum.* **68** (1997) 230.
- [3] Dorn H. P., Neuroth R. and Hofzumahaus A., *J. Geophys. Res.* **100** (1995) 7397.
- [4] Childs M. A., Menningen K. L., Toyoda H., Anderson L. W. and Lawler J. E., *Europhys. Lett.* **25** (1994) 729.
- [5] Hancock G. and Sucksmith J. P., *J. Vac. Sci. Technol.* **A13** (1995) 2945.
- [6] Hancock G., Lanyi L., Sucksmith J. P., and Woodcock B. K., *Pure and Appl. Chem.* **66** (1994) 1207.
- [7] Booth J. P., Hancock G., Perry N. D. and Toogood M. J., *J. Appl. Phys.* **66** (1989) 5251.
- [8] Booth J. P., *to be published*.
- [9] Hancock G., *Proc. Int. Symp. Laser-Aided Plasma Diagnostics* **5** (1991) 254.
- [10] Cunge G., Booth J. P., Derouard J., *Chem. Phys. Lett.* **263** (1996) 645.
- [11] Bischel W., Bamford D. and Jusinski L., *Appl. Optics* **25** (1986) 1215.
- [12] Jacob W., Engelhard M., Möller W. and Koch A., *Appl. Phys. Lett.* **64** (1994) 971.
- [13] Borysow J. and Phelps A. V., *Phys. Rev. E* **50** (1994) 1399; Visser R. J., Baggerman J. A. G., Poppelaars J. P. J. and Collart E. J. H., *J. Appl. Phys.* **71** (1992) 5792.
- [14] Woodcock B. K., Busby J. R., Freegarde T. G. M. and Hancock G., *J. Appl. Phys.* **81** (1997) 5945.
- [15] Goeckner M. J., Goree J., Sheridan T. E., *Phys. Fluids B* **4** (1992) 1663.
- [16] Sadeghi N., Nakano T., Trevor D. J., Gottscho R. A., *J. Appl. Phys.* **70** (1991) 2552.
- [17] Greene C. H. and Zare R. N., *J. Chem. Phys.* **78** (1983) 6741.
- [18] Anthony E. B., Schade W., Bastian M. J., Bierbaum V. M. and Leone S. R., *J. Chem. Phys.* **106** (1997) 5413.
- [19] Corney A. *Atomic and Laser Spectroscopy* (Oxford University Press, Oxford, 1977)
- [20] Demtröder W., *Laser Spectroscopy - basic concepts and instrumentation* (Springer-Verlag, Berlin, 1996)
- [21] Engelhard M., Jacob W., Möller W., Koch A. W., *Appl. Opt.* **34** (1995) 4542.
- [22] Goeckner M. J., Goree J., *J. Vac. Sci. Technol. A* **7** (1989) 977.
- [23] Brouard M., Lambert H. M., Short J. and Simons J. P., *J. Phys. Chem.* **99** (1995) 13571.
- [24] Booth J. P. and Hancock G., *Mat. Sci. Forum* **140** (1993) 219.
- [25] Vanhaelermersch S., van Hoeymissen J., Vermeylen D. and Peeters J., *J. Appl. Phys.* **70** (1991) 3892.
- [26] Tserepi A. D., Wurzburg E. and Miller T. A., *Chem. Phys. Lett.*, **265** (1997) 297.
- [27] Toogood M. J., D.Phil. thesis, Oxford University, 1991.
- [28] Muraoka K. and Maeda M., *Mat. Sci. Forum* **140** (1993) 191.
- [29] Booth J. P., J Derouard, Fadlallah M., Cabaret L. and Pinard J., *Opt. Commun.* **132** (1996) 363.
- [30] Moore C. A., Davis G. P. and Gottscho R. A., *Phys. Rev. Lett.* **52** (1984) 538. Mandich M. L., Gaebel C. E. and Gottscho R. A., *J. Chem. Phys.* **83** (1985) 3349.
- [31] Yamagata Y., Miyama M., James B. W., Muraoka K., Maeda M. and Akazaki M., *Proc. 10th Int. Symp. Plasma Chem.* **2** (1991) paper 2.1-49.
- [32] Lodahl P., Sorensen J. L. and Polzik E. S., *Appl. Phys. B* **64** (1997) 383.

## Properties of Arc Cathode Spots

B. Jüttner

*Humboldt-Universität zu Berlin and Max-Planck-Institute for Plasma Physics, Mohrenstrasse 41,  
10117 Berlin, Germany*

**Abstract.** Arc cathode spots operating by formation of surface-microplasmas are reviewed for discharges in vacuum and in gases. New experimental studies using advanced optical methods (image converter cameras and laser absorption techniques) reveal that the spot is composed of fragments with a size below  $10\text{ }\mu\text{m}$ . In vacuum these are highly mobile, for copper on a time scale  $< 50\text{ ns}$ . The motion and the rapid sequences of extinctions and re-ignitions determine the behavior of the whole spot. Cu-spots in vacuum exhibit displacements in times  $< 100\text{ ns}$ . A tentative explanation of the spot movement is given on the base of the fragment dynamics. In gases the fragments are more separated than in vacuum. The ignition of fragments is discussed in the framework of recent studies on the glow-to-arc transition in high pressure discharges. Finally, new mechanisms for enhanced field electron emission are mentioned.

### 1. INTRODUCTION

Trivially, in a gas discharge the areas of the electrodes are limited, so the cathodic region is necessarily finite. Frequently the discharges do not use the whole available surface, they contract to a more or less circular footpoint at the cathode. This contraction can be understood by processes in the gas plasma and in the space charge sheath that separates the plasma from the surface. In recent years considerable progress has been achieved in the understanding of gaseous arcs with hot cathodes [1-8]. Here the arc heats the cathode to temperatures sufficient to transfer the current by thermionic emission. While in the past the models were incomplete, necessitating arbitrary assumptions such as the minimum principle or empirical parameters such as the cathode fall, by including the non-stationary heat conduction in the cathode body the modern theories achieve a self-consistent description of the whole discharge system [1-7]. In this way, without using empirical parameters, spot radii can be determined, having values of  $0.5\text{-}2\text{ mm}$ , surface and plasma temperatures can be calculated, having values of  $3000\text{-}4000$  and  $2\text{-}3\text{ eV}$ , respectively, and the cathode fall is obtained as  $10\text{-}20\text{ V}$  [6, 7]. These values are in sometimes excellent agreement with the experiment [7], so it seems that the research has reached its final stage. At present, even 3D-calculations are possible [5] yielding still more exact data.

However, this comfortable situation does not hold for all kind of spots. With cold cathodes the current can no longer be transferred by thermionic emission. Also with hot cathodes there may arise transient situations where the temperature does not suffice. Then the discharge contracts to a submillimeter region. When the local energy transfer to the surface surpasses a certain limit the surface starts to evaporate. From the vapor a dense microplasma is formed, being highly non-stationary. The resulting cathode spots constitute a qualitatively new phenomenon, because they allow the transfer of virtually unlimited currents between discharge plasma and cathode at relatively small voltages  $< 50\text{ V}$ , without external electrode heating, and for all conducting electrode materials.

The present paper restricts itself to such vapor-producing cathode spots. They are most common with cold cathodes, but can be found at hot cathodes, too. They occur in numerous applications: Electric arcs, sparks, welding devices, or switches. They are welcome in vacuum arc coating devices and ion sources, but a nuisance at inner walls of fusion machines or at the electrodes of gas discharge lamps. Their physical parameters are still subjected to sometimes vivid disputes, but it is not necessary to take care for the

production of the spots, because they occur as a self-organizing phenomenon. This may be one of the reasons why the lack of understanding is widely tolerated. However, sometimes it is desirable but difficult to avoid them. There is hope to improve this situation by better knowledge.

The experimental difficulty is due to the small size and the variability of the spots, the latter being controlled by surface effects. Theoretical problems arise by nonlinear feedbacks, nonstationary processes and poorly known material parameters at high temperatures and pressures. Modern optical methods yielding information with high spatial and time resolution and new theoretical concepts promise a more satisfactory explanation of the basic spot phenomena.

## 2. DEFINITIONS AND PRINCIPLES OF THE THEORY

The cathode spot is defined as an ensemble of heated surface and metal vapor plasma. Energy sources for surface heating are the Joule heat produced by the current and the impinging plasma particles (ions and energetic electrons). The hot surface emits electrons and evaporates metal, the latter constituting the medium for the spot plasma. Details of these processes are treated by numerous authors, the most recent presentation being given by Hantzsche [9]. The details are combined to complete theories on various levels: from the construction of possible existence areas for the spot parameters by Ecker [10] until the elaborated 1D-theory of Beilis [11].

The spot radius is determined by the size of the heated surface region. Leaving the cathode in direction of the anode one has a small ballistic zone defined by the Debye length (space charge sheath). Here the cathode fall is situated (15-20 V) that forms the emitted electrons to an energetic beam, and here the plasma ions gain the main part of the energy that is transmitted to the surface. Electrons and plasma ions cross this zone without suffering collisions. Directly at the surface the evaporated atoms have a uni-directional velocity distribution. It is transformed to a shifted Maxwellian distribution at the end of the heavy particle relaxation zone, extending beyond the ballistic zone. Still more distant from the surface ends the electron beam relaxation zone where the emitted electrons are thermalized by collisions. It is at the end of this zone that the vapor is ionized forming a dense plasma. The plasma then expands, in vacuum up to the anode, in gases up to some mm in dependence on the gas pressure (Drouet and Meunier [12]).

Relevant equations are (Beilis [11, 13]): for the plasma the Saha-equation, the energy balance of the electrons and the equations of state; for the evaporated atoms the Langmuir-equation and the conservation of mass; and for the surface the energy balance, the thermo-field emission and the electric field, the last from the Poisson-equation.

Typically for this kind of theories, the time enters via the surface heating, assuming that non-stationary heat conduction is the slowest process that governs the development [10]. Beilis [13] calculates the spot parameters as a function of time without specifying a fixed time value. Fig. 1 gives an example for the plasma density (electron density) and the spot radius. In the time range 50 ns to 1 ms the density decreases from  $4 \times 10^{26} \text{ m}^{-3}$  to  $1 \times 10^{26} \text{ m}^{-3}$  whereas the radius increases from 16 to 56  $\mu\text{m}$  (correspondingly, the current density decreases from  $5 \times 10^{10} \text{ A/m}^2$  to  $4 \times 10^9 \text{ A/m}^2$ ). In the same time span, the surface temperature decreases from 4600 K to 4000 K and the electric field from  $4 \times 10^9 \text{ V/m}$  to  $1.3 \times 10^9 \text{ V/m}$ .

In practice, evaporating spots are basically non-stationary. They are born during a formation time, change

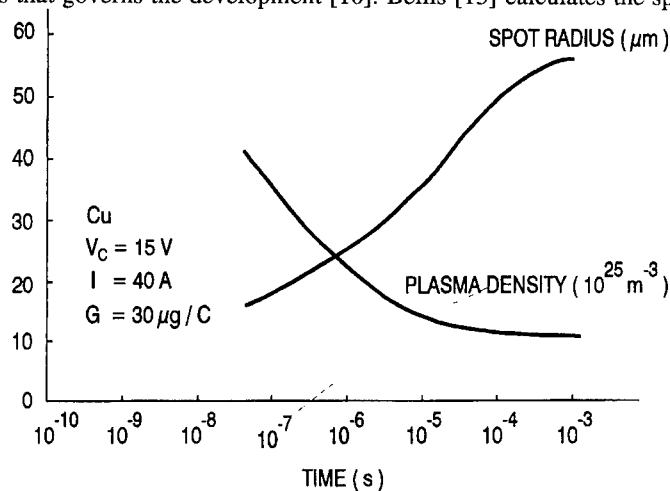


Fig. 1: Spot radius and plasma density as a function of time after Beilis [13]

their size during a residence time, and then they are displaced. Any displacement of the discharge to a cold surface location means the end of the spots life and the formation of a new spot, because heating and evaporation must start again. During several decades of spot research, the boundaries given by the formation and the residence time are displaced to smaller values, in fig. 1 to the left (with some random component).

A somewhat different approach is proposed by Mesyats [14]. According to his model the spot operates on a sequence of nanosecond acts. Delivering quickly an energy amount of about  $10^7$  J/kg into a microscopic surface volume (corresponding to  $10^{10} - 10^{11}$  J/m<sup>3</sup>), a burst of ionized matter and of emitted electrons occurs. The duration of this burst and the amount of ejected material little depend on the means of energy deposition and the material. So the spot processes are divided in nanosecond periods having some kind of fundamental character. Mesyats called them ECTONS ("Explosive Center"). If the energy is deposited by Joule heating of the surface with a current density  $j$ , the formation time  $t_f$  is obtained from

$$\int_0^{t_f} j^2 dt = h_m. \quad (1)$$

The value of  $h_m$  is nearly constant, amounting to  $1.8 \times 10^{17}$  A<sup>2</sup> s m<sup>-4</sup> for W and to  $4.1 \times 10^{17}$  A<sup>2</sup> s m<sup>-4</sup> for Cu. It is clear that in this case  $j$  must surpass  $10^{12}$  A/m<sup>2</sup> to reach nanosecond formation times. Relation (1) is known from the physics of exploding wires. Already Rothstein [15] suggested the analogy of the spots with exploding wires, but Mesyats and his colleagues were able to derive quantitative expressions for spot size, surface temperature, plasma density, erosion rate and plasma expansion velocity. Compared to fig. 1, the values are situated at the left-hand side where Beilis stopped his calculation.

Knowing the time scale of the spot processes, one can decide which theoretical conception is valid. One has to deal with the question: is the spot a microsecond or a nanosecond phenomenon? The answer should be given by the experiment as discussed in the following sections.

### 3. SPOTS IN VACUUM

#### 3.1 Experiments with the emitted light

Registering the emitted light by photographic methods seems to be the most straightforward way to measure spot size and time constants, especially in vacuum where the spot is the only light source. However, as shown by Hantzsche et al. [16], in vacuum the plasma expansion imposes a limit of about 10  $\mu$ m to the spatial resolution. During the radiative lifetime of excited states the particles move in an average over distances  $\geq 10$   $\mu$ m, thus blurring the spot appearance. This effect hides spot displacements over distances  $< 10$   $\mu$ m and, therefore, constitutes also a limit to the time measurement. Using continuum radiation the effect is absent, but then the intensity of the light does not suffice for nanosecond exposure times. So the results with the total light presented in the following give but upper limits of time and size.

In [17, 18] arc spots were produced at the rounded end of cylindrical cathodes having diameters of 0.3 - 0.5 mm. The current was 50-100 A, the discharge duration about 200  $\mu$ s. The surfaces were free from contamination layers (oxides, hydrocarbons), the residual gas pressure amounted to  $10^{-7}$  Pa. 1 - 100  $\mu$ s after arc ignition the cathode was photographed by a high speed image converter camera (IMACON 468) via a long distance microscope (QUESTAR QM 1) having a nominal resolution of 3  $\mu$ m. Fig. 2 shows

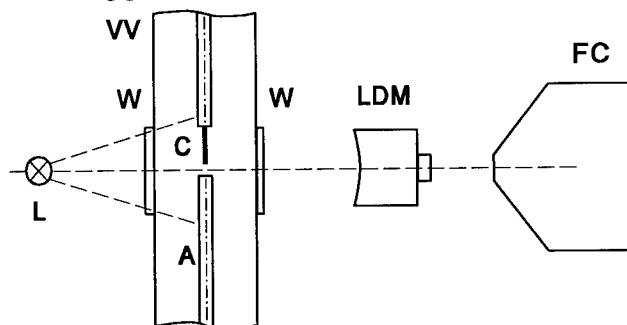


Fig. 2: Experimental setup from [17, 18]. C-cathode, A-anode, VV-vacuum vessel, W-sapphire windows, L-lamp, LDM-long distance microscope, FC-framing camera



the schematic of the device. The camera has eight channels that can freely be programmed in the time range 10 ns - 1 ms. In a later version, the eighth channel was exchanged for a streak unit allowing to continuously observe the spot displacement. If not stated otherwise, the arc current amounted to 70 A, the electrode material was copper.

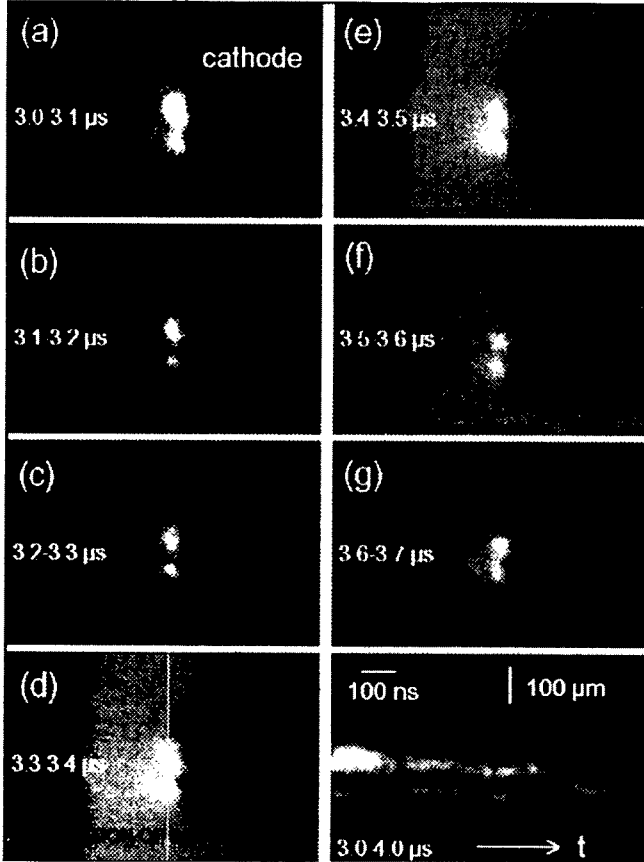


Fig. 3: Vacuum arc between Cu-electrodes. Framing time 100 ns, no pause between the frames, streak sweep 1  $\mu$ s

Fig. 3 shows a picture taken 3  $\mu$ s after arc ignition, with a framing time of 100 ns, no pause between the frames, and a streak sweep of 1  $\mu$ s. Two spots can be seen in front of the cathode that seem to be stationary during 1  $\mu$ s. However, with a certain probability positional changes can be found in the submicrosecond range, especially when looking with higher magnification. This can be seen in fig. 4 where eight frames were used to display an arc 15  $\mu$ s after ignition (framing time 100 ns, no pause between the frames). A single spot appears somewhat distant from the cathode apex, having clear internal structures that change in times  $\leq 100$  ns. In the following these structures will be called fragments. Their apparent diameter is 10-20  $\mu$ m. The fragments seem to periodically attract each other. Merging of some of the fragments leads to increased brightness [17, 18]. Fig. 5 displays the signal of a fast photodiode showing brightness peaks with intervals of about 15 ns (for Cu). When adding the streak channel to the frames one observes that during this dynamics the spot center is displaced. Fig. 6 gives an example with only 50 ns framing time. Finally, fig. 7 shows a sequence of frames where two spots distinctly changed their relative position

within 50 ns. For titanium, such changes could even be found during 20 ns [17].

Immobile spots as in fig. 3 do not represent a different species. Because the displacement occurs at random, for a given direction displacement zero is most probable. Fig. 8 shows the probability for displacements in y-direction within time intervals  $t=100$  ns, 200 ns, and 500 ns. Already for  $t=100$  ns the distributions obey the random walk law

$$W(Y)dY = \frac{1}{\sqrt{\pi \langle R^2 \rangle}} \exp\left(-\frac{Y^2}{\langle R^2 \rangle}\right) dY, \quad \frac{\langle R^2 \rangle}{t} = \text{const.}, \quad (2)$$

$W(Y)dY$  being the probability for a displacement between  $Y$  and  $Y+dY$  and  $\langle R^2 \rangle$  the mean square value of the two-dimensional displacement, ( $\langle R^2 \rangle = 2\langle Y^2 \rangle$ ).

Hence, the spot displacement takes place on a submicrosecond timescale. Sometimes it is argued that the spots behave differently on broad area cathodes, especially at higher currents where spot grouping leads to stationary scenarios. To test this, in ref. [13] the movement was analysed on copper cathodes of 65 mm diameter with currents up to 1.5 kA. Fig. 9 shows a streak of spots at 980 A. Table 1 gives the random walk data from this experiment together with the values according to fig. 8 for 70 A.

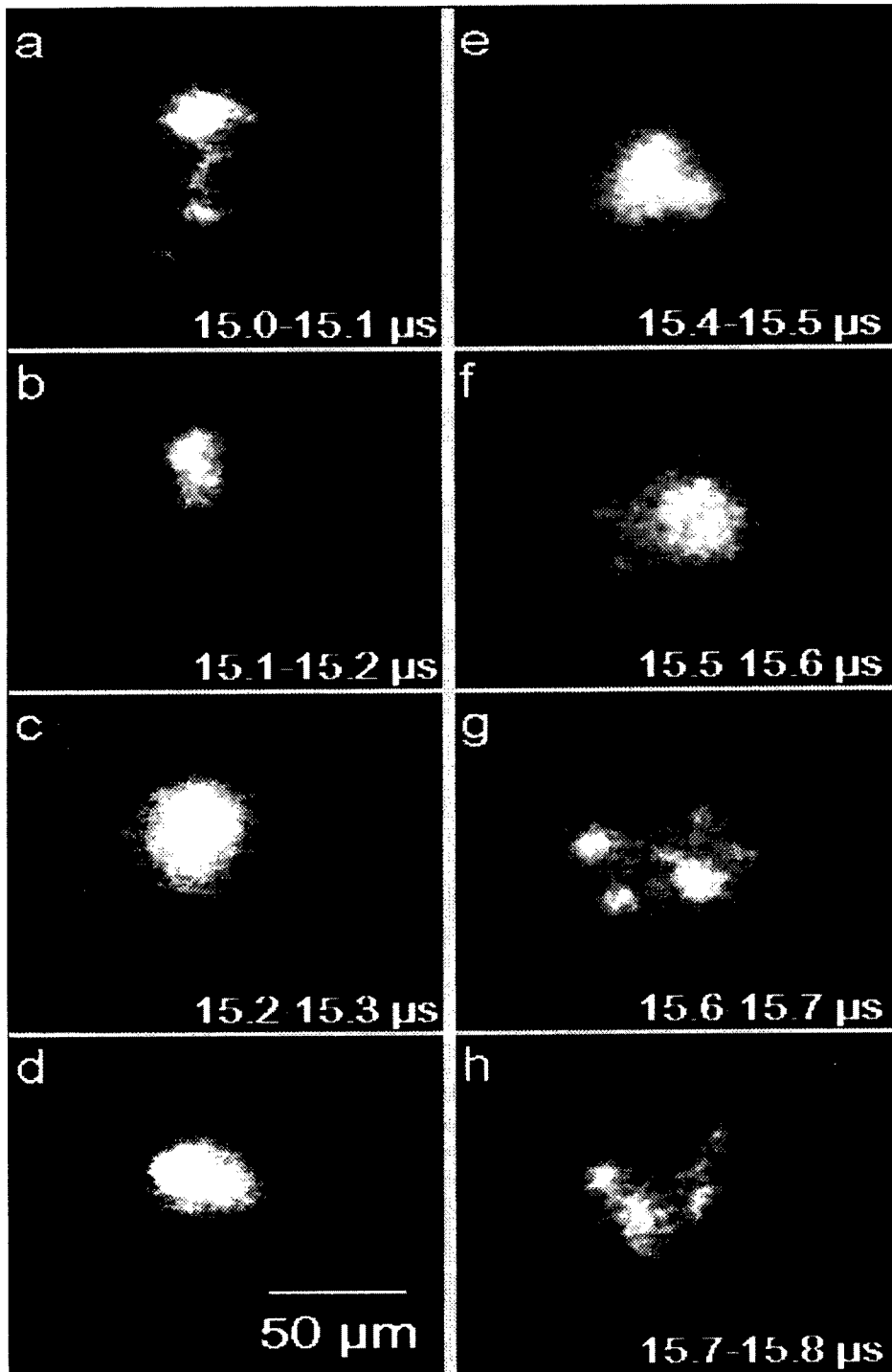


Fig. 4: Arc spot with inner fragments. Frame exposure time 100 ns, no pause between the frames, delay to ignition 15  $\mu\text{s}$ . Cu, 70 A.

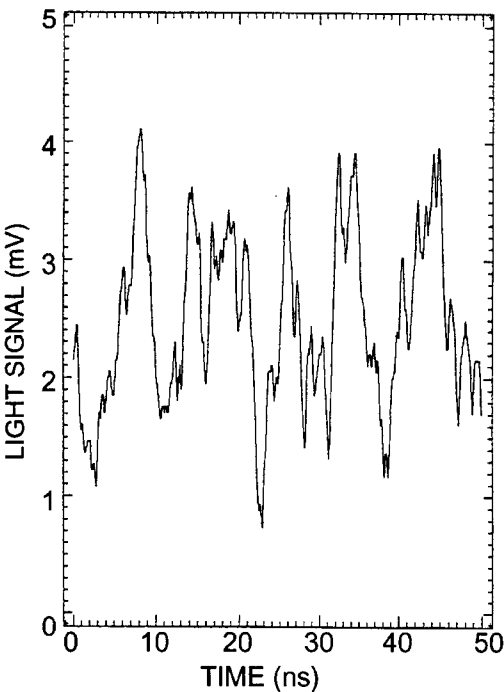


Fig. 5: Fluctuations of the light emitted by an arc spot in vacuum

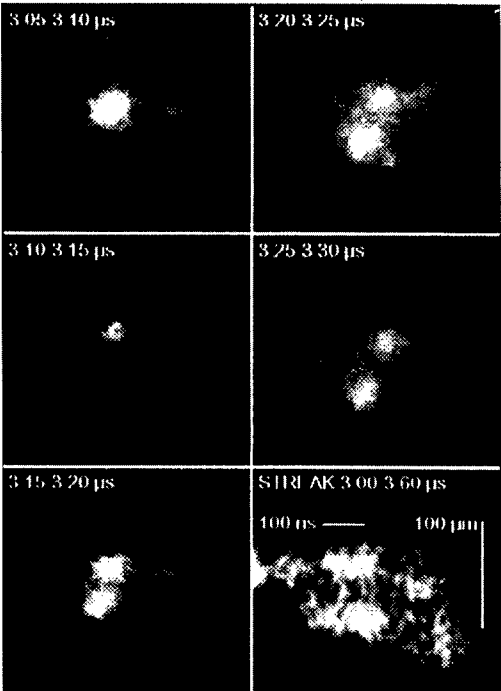


Fig. 6: Submicrosecond spot displacement. Frame exposure time 50 ns, no pause between the frames, streak sweep 600 ns, delay to ignition 3 μs. Cu, 70 A

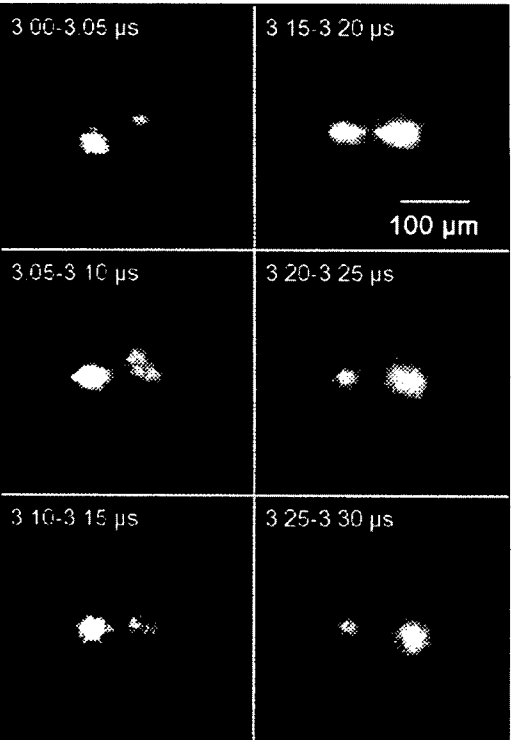


Fig. 7: Positional changes of two cathode spots on Cu. Frame exposure time 50 ns, no pause between the frames

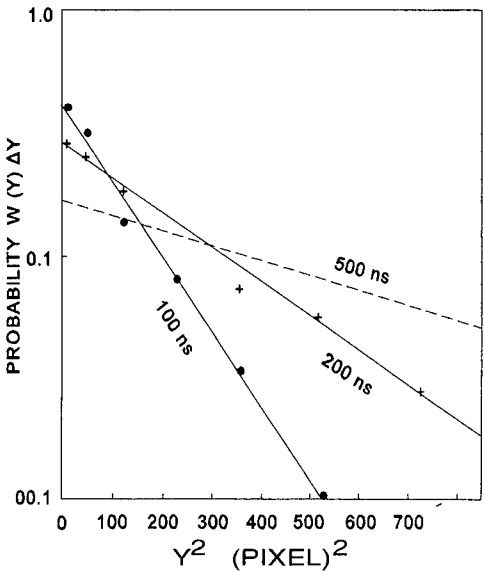


Fig. 8: Probability for one-dimensional spot displacements for time intervals of 100 ns, 200 ns and 500 ns. One pixel equals 1.2 μm [18]

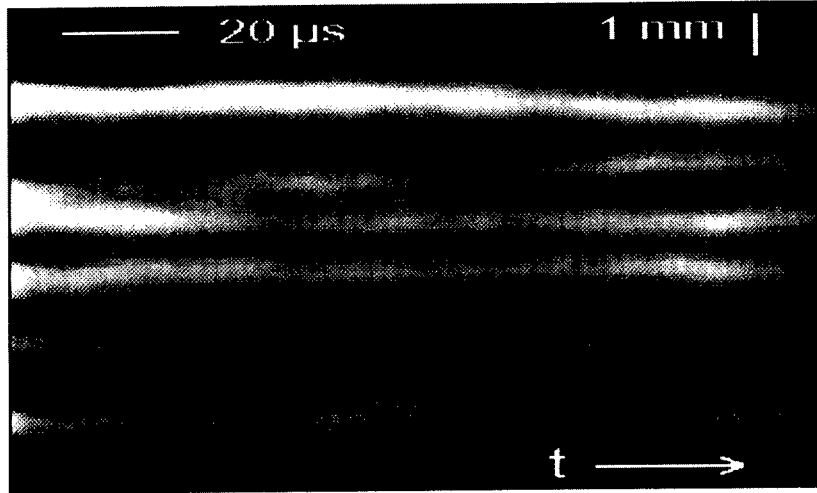


Fig. 9: Streak of arc cathode spots on a Cu-cathode of 65 mm diameter. Total current 980 A, 3 ms after ignition [13]

Table 1: Random walk data for extended and small Cu-cathodes  
N-number of events, t-observation time,  $\langle R^2 \rangle$ -mean square value of two-dimensional displacement

Cathode Diameter (mm)	Reference	Current (A)	N	t ( $\mu$ s)	$\langle R^2 \rangle / t$ ( $10^{-3} \text{ m}^2/\text{s}$ )
65	[13], fig. 9	40-100	56	25	$1.3 \pm 0.5$
65	[13], fig. 9	150-1500	343	25	$1.0 \pm 0.3$
65	[13], fig. 9	40-1500	229	75	$1.0 \pm 0.3$
0.47	[18], fig. 8	70	145	0.1	$2.2 \pm 0.6$
0.47	[18], fig. 8	70	310	0.2	$2.3 \pm 0.6$
0.47	[18], fig. 8	70	725	0.5	$2.2 \pm 0.6$

Although in table 1 the ratio of the mean square displacement  $\langle R^2 \rangle$  to the measuring time is somewhat smaller for broad area cathodes, the order of magnitude is the same, thus no principal change of the spot behavior can be stated.

### 3.2 Experiments with absorbed light

Absorption of laser light yields pictures of the spot plasma having advantages over the technique using the emitted light: the broadening of the image by the plasma expansion is minimized [16], and the hot surface cannot contribute. Also, with short laser pulses the exposure time can be  $< 1 \text{ ns}$ . Fig. 10 gives an example for a Cu-arc of 90 A, taken 232 ns after ignition with an exposure time of 0.4 ns [19]. Structures with a size down to  $5 \mu\text{m}$  can be seen. From the absorption coefficient, in [19] electron densities  $\geq 6 \times 10^{26} \text{ m}^{-3}$  have been estimated. No principal changes have been observed when delaying the picture by up to 50  $\mu\text{s}$  after ignition.

Vogel [20] registered density profiles after Abel-inversion as shown in fig. 11. A long-distance microscope with a resolution of about  $1 \mu\text{m}$  was used, thus showing more details as in [17, 18]. Obviously

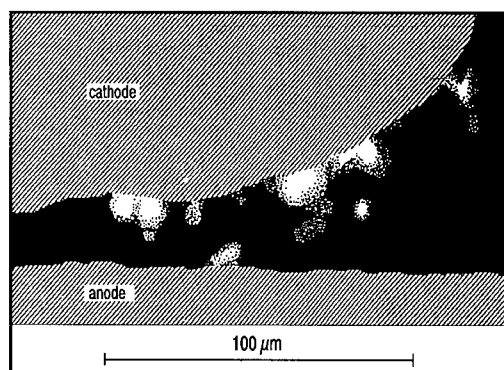


Fig. 10: Absorption picture of Cu-spots, 90 A, taken 232 ns after ignition with 0.4 ns exposure time [19]

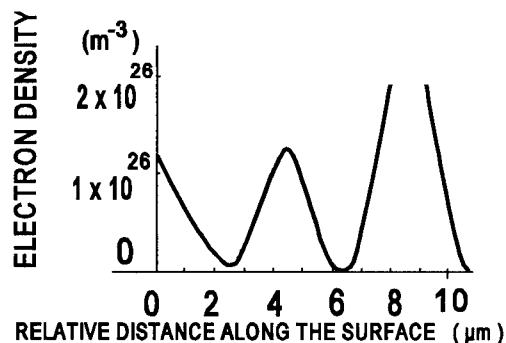


Fig. 11: Linear scan of the electron density of a Cu-spot in vacuum obtained from absorption profiles taken 18 ns after ignition with 0.1 ns exposure time. Current 9 A [20]

the figure depicts the fragment structure at an early phase. Three fragments are observed having a half-width of 3-5 μm and distances of about 5 μm. With the emitted light they would have appeared as a single spot.

### 3.3 Contradictions

As can be seen in the preceding sections, the fragments of vacuum arc spots are small and fast as well. There are, however, papers being at variance to this statement. Siemroth et al. [21] studied copper arc spots in vacuum at currents of about 3-5 kA with a high speed framing camera. With such currents numerous spots and fragments are present. The fragments (the authors called them subspots) were found to be small, having a half-width of about 10 μm [21], thus one might assume that they are similar to those depicted in fig. 4. However, Siemroth et al. found little changes for times <10 μs. The present author believes that this is due to the evaluation method used in ref. [21]. Siemroth et al. exposed the four framing channels of their camera to the same event using increasing exposure times for each channel and suggesting that the spot movement will broaden the picture if the exposure time surpasses the residence time. Fig. 12 shows the luminous fragment profile for exposure times of 10 ns, 100 ns, 1 μs, and 10 μs. Obviously the profile width increases when the time exceeds 10 ns, but probably the background must be subtracted, being itself a function of the exposure time.

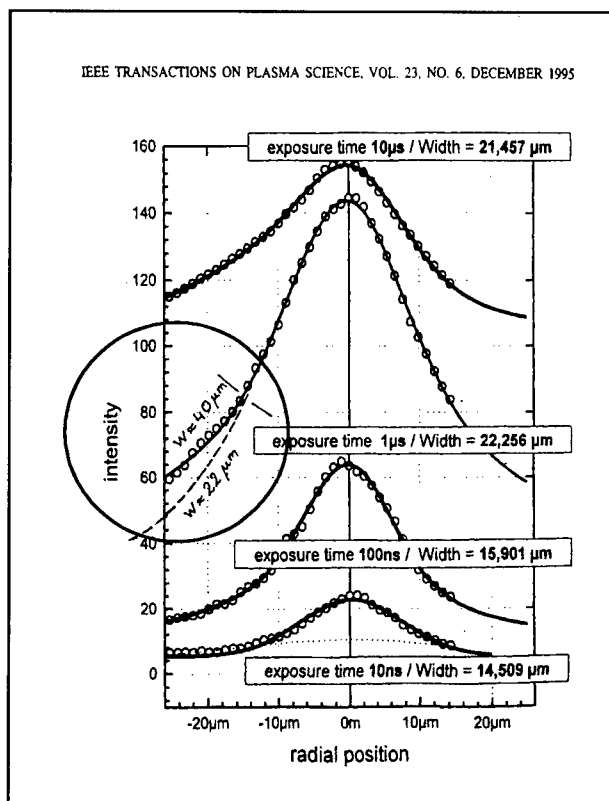


Fig. 12: Luminous fragment profiles at different exposure times after Siemroth et al. [21]

This background arises from the presence of numerous spots at high current. Although the subtraction might produce arbitrary profile forms and widths, it seems natural to look for a Gaussian profile. In [21] this was possible for the center of the measured curves, yielding half-widths of about  $20\text{ }\mu\text{m}$  for all exposure times. However, this does not hold for the wings, as indicated in the circle at the  $1\text{ }\mu\text{s}$ -curve (drawn by the present author). Fitting the wing by a Gaussian curve would yield the half-width of about twice as much. Thus, as pointed out in ref. [18], the method underestimates the movement because of the neglect of the outer zones of the luminous profile. The invariability of the deduced half-width led Siemroth et al. to the conclusion that  $\langle R^2 \rangle / t < 10^{-5}\text{ m}^2/\text{s}$ , in contrast to Tab. 1. Using the wings of the profiles, much higher values would have been obtained. Hence, the difference between [18] and [21] might be due to different evaluation methods rather than to different phenomena.

#### 4. SPOTS IN GASES

With the same system as described in figs. 2-7, preliminary experiments have been carried out at atmospheric pressure. In these cases the bright gas plasma covered the whole apex of the cathodes, so with the emitted light cathode spots could only be observed at the boundary of this plasma. Fig. 13 shows this for air and fig. 14 for argon. Numerous isolated spots can be seen with a size  $\leq 5\text{ }\mu\text{m}$ , i. e. at the limit of the spatial resolution. Such structures are found occasionally even at hot cathodes as demonstrated in fig. 15 for a high pressure sodium lamp.

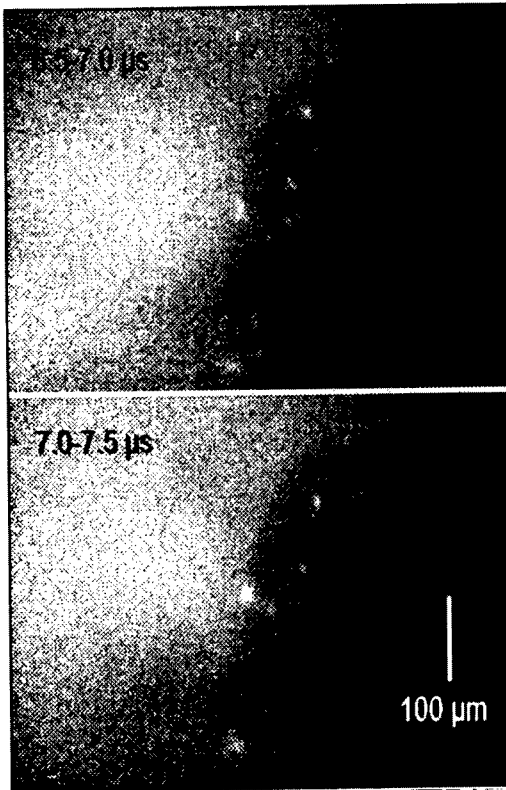


Fig. 13: Spots in air,  $6.5\text{ }\mu\text{s}$  after ignition,  $0.5\text{ }\mu\text{s}$  exposure time. Cu,  $70\text{ A}$

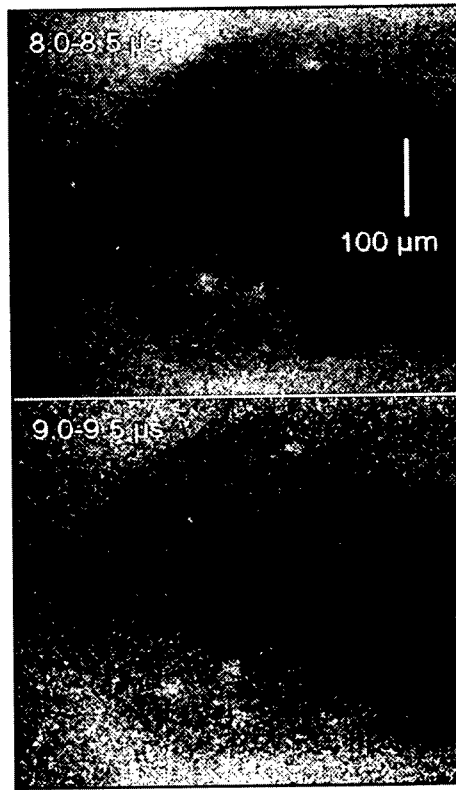


Fig. 14: Spots in argon, at atmospheric pressure,  $8\text{ }\mu\text{s}$  after ignition,  $0.5\text{ }\mu\text{s}$  exposure time. Cu,  $70\text{ A}$

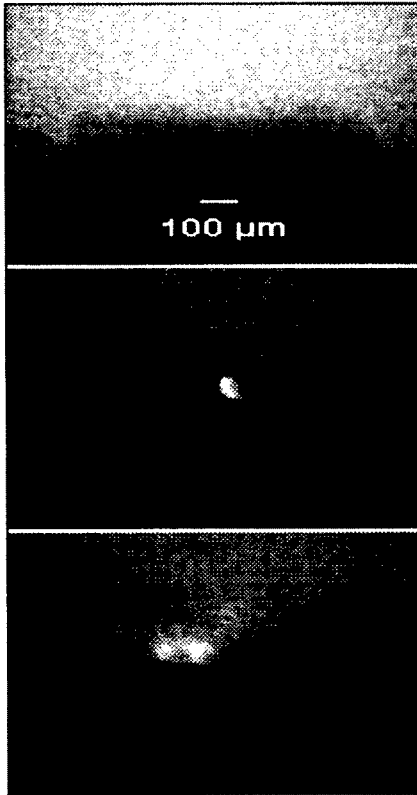


Fig. 15: Spots at the hot cathode of a high pressure sodium lamp after about one hour burning at 50 Hz. Snapshots in different half-cycles, exposure time 2  $\mu$ s

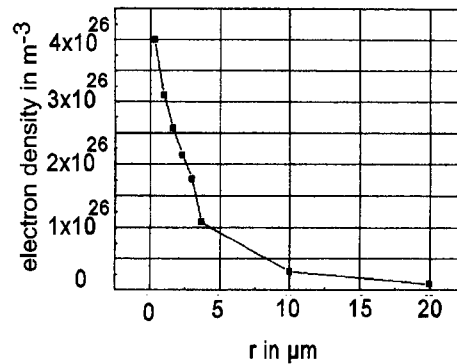


Fig. 16: Electron density profile obtained from laser absorption in atmospheric air. Cu, 9 A, exposure time 0.1 ns, delay to ignition 9 ns [22]

The absorption technique avoids the interference of the gas plasma. Fig. 16 shows a density profile for a Cu-spot in air obtained by Vogel [22]. The half-width amounts to about 3  $\mu$ m, the density reaches  $4 \times 10^{26} m^{-3}$ . At the cathode of pseudo-sparks, Frank et al. [23] found spots  $< 15 \mu$ m with a minimum density of  $10^{27} m^{-3}$ .

## 5. CONSEQUENCES

In vacuum the emitted light yields information on the time scales. In our measurements for the fragments and the whole spot the time constants are definitely  $< 50$  ns and  $< 100$  ns, respectively. These short times do not refer to an initial phase followed by a more stationary regime, but they describe the whole phenomenon. Delaying the frame pictures by 10 ns through 100  $\mu$ s did not result in longer time constants at higher delays. Thus, the ECTON-conception formulated by Mesyats [14] seems to be near the truth.

Absorption pictures of vacuum spot fragments indicate diameters of less than 5  $\mu$ m. So the fragment plasmas are smaller than the surface craters found after the discharges. It seems plausible that the small spots in gases are of similar nature as the fragments in vacuum. The difference is: they are not free to move and to merge, and they can carry currents  $< 1$  A. Because of the limited expansion of the spot plasma, in our experiments spots in gases appear small also in the emitted light. Tab. 2 compares spots in vacuum and in gases. Probably the fragments in vacuum are still composed structures, while at atmospheric pressure one observes the most elementary spot components.

Table 2: Comparison of Cu-arc spots in vacuum and in gases (figs. 4, 6, 7, 10, 13, 14)

FEATURE	AIR, ARGON	VACUUM
current per fragment	$< 1 \text{ A}$	5-10 A
apparent plasma diameter	$\leq 5 \text{ }\mu\text{m}$	10-20 $\mu\text{m}$
distance between fragments	50-100 $\mu\text{m}$	10-50 $\mu\text{m}$
displacement	oscillation and rotation in areas of 50-100 $\mu\text{m}$ diameter within times $< 500 \text{ ns}$	random movement within times $< 100 \text{ ns}$ : $R^2/t \approx 10^{-3} \text{ m}^2/\text{s}$ , $v \propto 1/\sqrt{t}$

The division into fragments helps the spot to survive: if one fragment dies the other fragments take over the current until a new fragment is formed. Also, the spot motion can be explained by the action of the fragments. The Lorentz-force causes them to attract each other. The framing pictures (comp. fig. 4) indicate a scenario as depicted in fig. 17: The fragments move into the spot center. When they are close together, an instability occurs like an explosion, accompanied by increased brightness (comp. fig. 5). This results in the formation of new fragments at the periphery, and the cycle starts again. Here one could speculate on the reason for the spot movement: If one fragment dies before merging, the configuration becomes non-symmetric and the center of gravity of the spot is displaced (in fig. 17 to the right). An external magnetic field will tend to remove a fragment in forward direction, causing to displace the remainder in a retrograde way. A gas reduces the interaction between the fragments and can, therefore, reverse the direction. This idea, however, must be examined by further experiments.

## 6. SPOT IGNITION

If the spots life is a sequence of nanosecond acts of birth and death of the constituents, the question arises how new fragments can be ignited. Directly in the spot this process is difficult to investigate. There are, however, some recent works that study ignition processes in much detail [24, 25]. In these experiments, a plasma is brought into contact with a negatively biased electrode, thus observing the processes preceding the spot formation. The problem is related to the question of glow-to-arc transition.

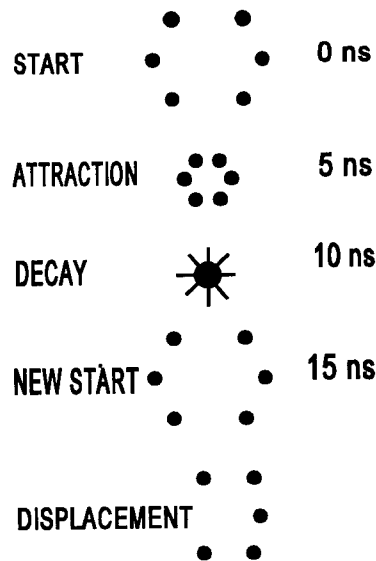


Fig. 17: Schematic of fragment dynamics and spot displacement

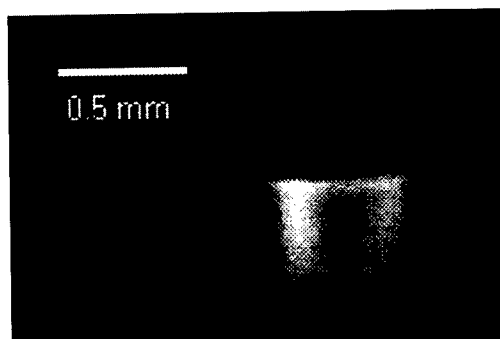


Fig. 18: Luminous cathodic layer preceding spot formation [24]. Cu-electrode, argon at atmospheric pressure, exposure time 100 ns



Mentel and co-workers [24, 25] found that at first a luminous cathodic layer is formed having a width of 75-200  $\mu\text{m}$ . Fig. 18 gives an example. The contraction to spots is already indicated at two locations. In this phase, a current up to some 100 mA is flowing that exceeds the ion saturation current from the plasma. (Such precurrents have also been found at negatively biased electrodes in a tokamak [26, 27]). After some time the spots start to operate as bright localized structures. As fig. 19 shows, at the surface one finds a homogeneously changed region (due to the plasma layer), intersected by craters (due to the spots) [25].

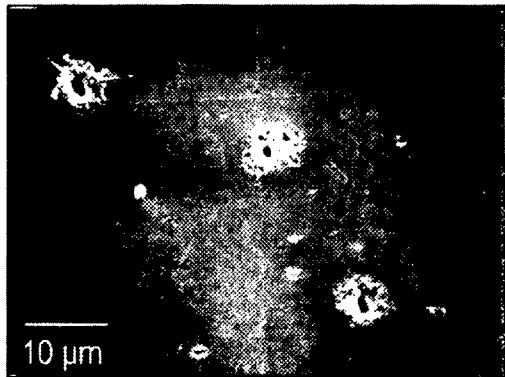


Fig. 19: Erosion of a Cu-cathode by a predischage followed by a short arc [25]

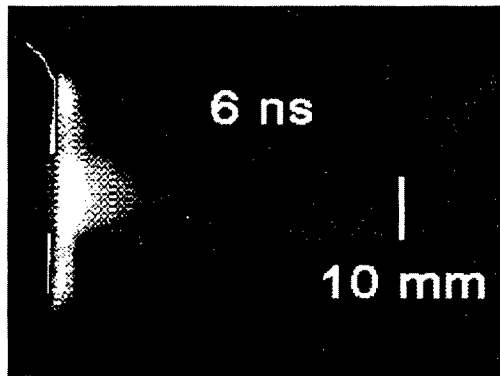


Fig. 20: Luminous sheath at the cathode as a precursor to spot formation in high pressure discharges [28]

Luminous sheaths have also been found at the cathode of excimer lasers [28] as demonstrated in fig. 20. Korolev and Mesyats [29] reported that the duration of such predischages decreases with increasing pressure. It decreases also with increasing bias voltage. Fig. 21 compiles results from [24, 27-29]. Near a cathode spot, where the pressure may reach values  $>10$  bar, the times will be  $< 5$  ns, so the delay of fragment formation can be sufficiently small.

Elaborated theories have been published by Belasri and co-workers [30] and Simon and Böttcher [31]. According to these works, the electric field at the cathode may reach values in excess of  $10^8$  V/m at the stage of sheath formation. From experiments on vacuum breakdown it is known that such fields are sufficient to cause explosive field emission at the surface.

Regarding the field emission, two new ideas have been emerged in recent years: (i) Jimenez and co-workers [32] were able to show that in vacuum the combination of micrometer surface structures with submicrometer protrusions causes local field enhancement by factors  $>100$ . Such structures will be intense emitters in the electric field of the luminous cathodic layer. (ii) The individual field of plasma ions approaching the surface can enhance

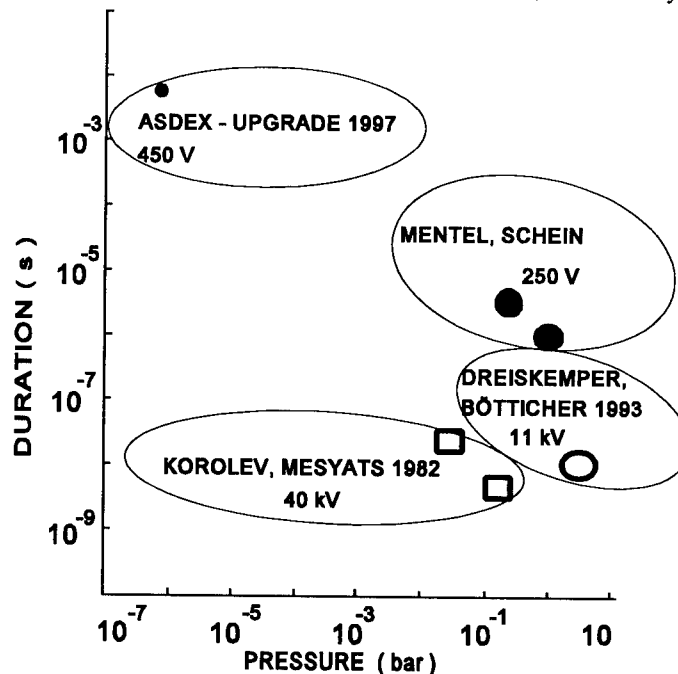


Fig. 21: Duration of predischages as a function of pressure and voltage [24, 27-29]

the emission. This effect of ion-field or ion-thermo-field emission has recently been studied by Testé and Chabrier [33] and by Vasenin and co-workers [34]. Fig. 22 from ref. 34]

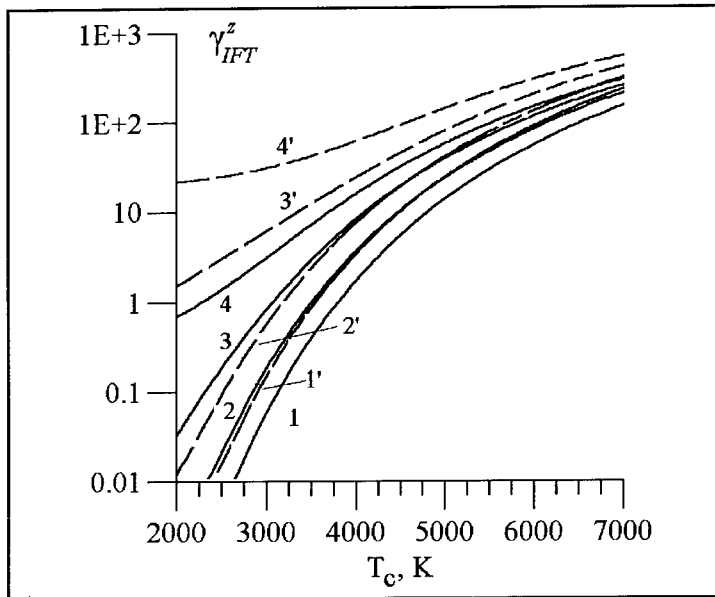


Fig. 22: Electron yield of I-F-T-emission as a function of the cathode temperature [34]. The numbers indicate the field strength: (1)- $2.5 \times 10^8$  V/m, (2)- $5 \times 10^8$  V/m, (3)- $1 \times 10^9$  V/m, (4)- $1.5 \times 10^9$  V/m. Solid and dashed lines: ion charge number 1 and 2, respectively

shows the electron yield  $\gamma_{IFT}^z$  caused by the effect in addition to thermo-field emission (number of electrons per ion with charge  $z$ ). As a consequence, in a plasma field emission is possible at smaller electric fields than in vacuum.

Hence, the ignition process can be assumed as follows: When the spot decays, transient voltages are developed that cause the formation of a sheath outside the center with high electric fields. Field electron emission enhanced by ion impact leads to surface explosions that produce new fragments within a nanosecond or less.

## 7. CONCLUDING REMARKS

The well known conception of fragments [35] promises to yield the key for the understanding of the cathode spots. Probably the nature of the fragments does not so much depend on the external conditions, while the variety of cathode spots will be due to varying combinations of fragments and different processes of their mutual interaction. To study the nature of the spot substructure, one needs spatial resolution  $< 10 \mu\text{m}$  and time resolution  $< 50 \text{ ns}$ , thus the present experimental devices are operating at the technical limit. In vacuum, and with clean surfaces, several fragments combine to a single spot that then reaches a size of about  $50 \mu\text{m}$ . At atmospheric pressure the fragments remain separated, having a size too small to be resolved yet. In the past it has often been argued that the spot must be much greater than a surface crater [36], the latter having diameters of a few  $\mu\text{m}$ , but now it turns out that the size of the fragment plasma is even smaller than the crater.

In vacuum the formation and residence time of the fragments are below the available resolution. Probable values are of the order of 1 ns. The fragment ensemble as a whole that forms the spot is slower, though in vacuum time constants  $< 50 \text{ ns}$  could be observed for the whole spot (compare fig. 7). This supports the concept of cyclic reproduction on a nanosecond timescale as proposed by Mesyats (ECTONS), though the base process is not necessarily an explosion, because to evaporate a piece of matter with a size of  $1 \mu\text{m}$  a time of 10 ns is sufficient. The explosion models have a long history, starting with Rothstein in 1948 [15] and Nekrashevich and Bakuto in 1955 [37]. The further development is marked by Fursey and co-workers [38], Mitterauer [39], and Mesyats and co-workers [14, 40]. However, these models are often hypothetical, and many physicists and engineers have doubts that the seemingly stationary discharges are composed of short individual acts. So they admit nanosecond processes as a phenomenon of ignition at the highest. More research is needed to clarify the relevance of nanosecond spots in gases and with hot cathodes, but for cold cathodes in vacuum they have always been found in our experiments.

The existence of nanosecond fragments promises the understanding of the paradoxical behavior of the arc spot: Why does it move to cold locations, why the direction is retrograde in a magnetic field, why external gas with pressures far below the spot pressure can influence the movement, what are the forces that repel the spots from each other? The answer could be: there are no repelling forces, only the attracting Lorentz-force, the movement being due to a loss of symmetry in the fragment configuration as indicated in fig. 17. It is hoped to test this idea in near future.

If the cyclic nature is true, the ignition processes deserve more attention. Here the experiments in Bochum [24, 25] and the theory in Toulouse [30] and Hannover [31] yielded valuable results, especially with respect to the formation of transient plasma sheaths. It must still be examined whether this can be generalised to the high pressure metal vapor plasma of the cathode spots. There is already some experimental evidence that the surface in the neighbourhood of a spot can be modified by intense ion bombardement [41], in analogy to fig. 19.

In spite of the experimental progress of the recent years, we are but at the beginning to understand the vapor producing spots. At present it seems hopeless to develop theoretical models where the properties of the spots can be calculated from their interconnection with the other parts of the discharge without introducing empirical data, in contrast to the situation with quasistationary spots on hot cathodes [1-8]. However, there may exist mixed cases: vacuum arc spots can become more stationary when the cathode is sufficiently hot or when they are anchored at special surface structures as for example in the work of Djakov [42, 43], and transient microspots can occasionally be found at thermionic cathodes (fig. 15).

### Acknowledgements

The author is indebted to the Deutsche Forschungsgemeinschaft for the grants Ju 227/5-1 and Ju 227/7-1; to the Bundesministerium für Bildung und Forschung for the grants 13N6616 and 13N7108/1; and to E. Hantzsche, Berlin, and B. E. Djakov, Sofia, for helpful comments. Also, he thanks the referees for stressing the importance of spots on hot cathodes and suggesting to discuss the work of Siemroth et al. [21].

### References

- [1] Delalandre, C. and Simonin O. J., *Physique Coll.* **51** (1990) 199-206.
- [2] Zhu, P., Lowke, J. J., and Morrow, R., *J. Phys. D: Appl. Phys.* **25** (1992) 1221-30.
- [3] Morrow, R. and Lowke, J. J., *J. Phys. D: Appl. Phys.* **26** (1993) 634-642.
- [4] Zhu, P. and Lowke, J. J. R., *J. Phys. D: Appl. Phys.* **26** (1993) 1073-1076.
- [5] Kaddani, A., "Modélisations 2D and 3D des Arcs Electriques dans l'Argon à la Pression Atmosphérique avec la prise en compte du Couplage Thermique et Electrique Arc-Electrodes et de l'Influence des Vapeurs Métalliques", Thesis Paris 1995, also Report EDF HE-44/95/012/A.
- [6] Benilov, M. S. and Marotta, A., *J. Phys. D: Appl. Phys.* **28** (1995) 1869-1882.
- [7] Lowke, J. J., Morrow, R., and Haidar, J., *J. Phys. D: Appl. Phys.* **30** (1997) 2033-2042.
- [8] Rethfeld, B., Wendelstorf, J., Klein, T., and Simon, G., *J. Phys. D: Appl. Phys.* **29** (1996) 121-128.
- [9] Hantzsche, E., "Theories of Cathode Spots" in: *Handbook of Vacuum Arc Science and Technology*, Eds. Boxman, R. L., Martin, P. J., and Sanders, D. M., (NOYES Publications New Jersey 1995), pp. 151-208.
- [10] Ecker, G., "Theoretical Aspects of the Vacuum Arc" in: *Vacuum Arc. Theory and Application*, Ed. Lafferty, J. M. (Wiley NY 1980), pp. 228-320.
- [11] Beilis, I., "Theoretical Modeling of Cathode Spot Phenomena" in: *Handbook of Vacuum Arc Science and Technology*, Eds. Boxman, R. L., Martin, P. J., and Sanders, D. M., (NOYES Publications New Jersey 1995), pp. 208-264.
- [12] Drouet, M. G., and Meunier, J. L., *IEEE Trans. Plasma Sci.* PS-13 (1985) 285-287.
- [13] Beilis I., Djakov B. E., Jüttner B., and Pursch, H., *J. Phys. D: Appl. Phys.* **30** (1997) 119-130.
- [14] Mesyats, G. A., "Properties of ectons in a vacuum discharge", XVth Int. Symp. Discharges and Electr. Insul. in Vacuum, Ed. Mesyats, G. A. (SPIE vol. 2259, Washington 1994), pp. 22-29.

- [15] Rothstein, J., Phys. Rev. **73** (1948) 1214.
- [16] Hantzsch E., Jüttner, B., and Ziegenhagen, G., IEEE Trans. Plasma Sci. **23** (1995) 55-64.
- [17] Jüttner, B., J. Phys. D: Appl. Phys. **28** (1995) 516-522.
- [18] Jüttner, B., J. Phys. D: Appl. Phys. **30** (1997) 221-229.
- [19] Anders, A., Anders S., Jüttner, B., Böttcher, W., Lück, H., and Schröder, G., IEEE Trans. Plasma Sci. **20** (1992) 466-472.
- [20] Vogel, N. and Skvortsov, V., XVIIth Int. Symp. Discharges and Electr. Insul. in Vacuum, Eds. Anders, A. and Anders, S. (LBL Berkeley 1996), pp. 89-98.
- [21] Siemroth, P., Schülke, T., and Witke, T., IEEE Trans. Plasma Sci. **23** (1995) 919-925.
- [22] Vogel, N., private communication.
- [23] Frank, K., Felsner, P., Christiansen, J., Hintz, G., Mehr, T., Prucker, U., Stenzenberger, J., Stetter, M., Tkotz, R., and Hoffmann, D. H. H., XVIIth Int. Symp. Discharges and Electr. Insul. in Vacuum, Eds. Anders, A. and Anders, S. (LBL Berkeley 1996), pp. 1029-1033.
- [24] Schein, J., Schumann, M., Nandelstädt, D., and Mentel, J., IEEE Trans. Plasma Sci. **25** (1997), to be published
- [25] Nachtigall, K. P. and Mentel, J., IEEE Trans. Plasma Sci. **19** (1991) 947-953.
- [26] Ertl, K. and Jüttner, B., Nuclear Fusion **25** (1985) 1413-1419.
- [27] Jüttner, B., "Electrical Breakdown and Arcs in a Tokamak", unpublished report, Berlin 1997.
- [28] Dreiskemper, R., Schröder, G., and Böttcher, W., IEEE Trans. Plasma Sci. **23** (1995) 180-187.
- [29] Korolev, Yu. D. and Mesyats, G. A., "Field Emission and Explosive Processes in a Gas Discharge", Ed. Koval'chuk, B. M. (Nauka Publishers Novosibirsk 1982).
- [30] Belasri, A., Boeuf, J. P., and Pitchford, L. C., J. Appl. Phys. **74** (1993) 1553-1567
- [31] Simon, G. and Böttcher W., J. Appl. Phys. **76** (1994) 5036-5046
- [32] Jimenez, M., Noer, R. J., Jouvet, G., Jodet, J., and Bonin, B., J. Phys. D: Appl. Phys. **27** (1994) 1038-1045.
- [33] Testé, P. and Chabrierie, J. P., J. Phys. D: Appl. Phys. **29** (1996) 697-705
- [34] Vasenin, Yu. L., Gvozdetsky, V. S., Krivtsun, I. V., Zel'nichenko, A. T., Vladimirov, V. V., Jüttner, B., and Pursch, H., "Theory of the cathodic region of electric arcs in vacuum", Report BMBF 13N6616 (Berlin 1997).
- [35] Kesaev, I. G., "Cathode processes of an electric arc" (Nauka Publishers Moscow 1968).
- [36] Rakhovsky, V. I., IEEE Trans. Plasma Sci. **4** (1976) 81-102.
- [37] Nekrashevich, I. G., and Bakuto, I. A., Bull. Byelorussian Acad. Sci., Phys. Techn. Inst. **2** (1955) 167-177.
- [38] Fursey, G. N. and Vorontsov-Vel'yaminov, P. N., Sov. Phys.-Tech. Phys. **12** (1967) 1370-1382.
- [39] Mitterauer, J., Acta Physica Austriaca **37** (1973) 175-192.
- [40] Bugaev, S. P., Litvinov, E. A., Mesyats, G. A., and Proskurovsky, Sov. Phys. Usp. **18** (1975) 51-61.
- [41] Puchkarev, V. F. and Bochkarev, M. B., XVth Int. Symp. Discharges and Electr. Insul. in Vacuum, Ed. König, D. (VDE Verlag Berlin 1992), pp. 359-363.
- [42] Djakov, B. E., Contrib. Plasma Phys. **33** (1993) 201-207.
- [43] Djakov, B. E., Contrib. Plasma Phys. **33** (1993) 307-316.

## Dielectric-Barrier Discharges. Principle and Applications

U. Kogelschatz, B. Eliasson and W. Egli

*ABB Corporate Research Ltd., Baden, Switzerland*

**Abstract:** Dielectric-barrier discharges (silent discharges) are non-equilibrium discharges that can be conveniently operated over a wide temperature and pressure range. At about atmospheric pressure electrical breakdown occurs in many independent thin current filaments. These short-lived microdischarges have properties of transient high pressure glow discharges with electron energies ideally suited for exciting or dissociating background gas atoms and molecules. The traditional application for large-scale ozone generation is discussed together with novel applications in excimer UV lamps, high power CO<sub>2</sub> lasers and plasma display panels. Additional applications for surface treatment and pollution control are rapidly emerging technologies. Recent results on greenhouse gas recycling and utilisation in dielectric-barrier discharges are also discussed.

### 1. INTRODUCTION

Dielectric-barrier discharges (DBDs), also referred to as barrier discharges or silent discharges have for a long time been exclusively related to ozone generation. Detailed investigations into the properties of this non-equilibrium discharge which can be conveniently operated at about atmospheric pressure led to a number of new applications: The generation of powerful coherent infrared radiation in CO<sub>2</sub> lasers and of incoherent VUV or UV excimer radiation in excimer lamps are two examples that became commercially available within a few years. Other processes like pollution control or surface treatment with DBDs show great promise for the future. As far as market potential is concerned the most important use of DBDs will be in ac plasma display panels. In 1996 multi-billion dollar investments in production facilities for large-area flat television screens in Japan and South Korea started a new age of large-scale industrial dielectric-barrier applications.

The most important characteristic of dielectric-barrier discharges is that non-equilibrium plasma conditions can be provided in a much simpler way than with other alternatives like low pressure discharges, fast pulsed high pressure discharges or electron beam injection. Its flexibility with respect to geometrical configuration, operating medium and operating parameters is unprecedented. Conditions optimised in laboratory experiments can easily be scaled up to large industrial installations. Efficient low cost power supplies are available up to very large powers.

First introduced by W. Siemens in 1857 [1] for the purpose of "ozonizing" air DBDs have for a long time been regarded as the ozonizer discharge. Important new insight into the structure of the discharge was gained by high voltage engineers studying gas breakdown. In 1932 Buss [2] observed that in a plane parallel gap with insulated electrodes air breakdown occurs in a number of individual tiny breakdown channels. More detailed information about these current channels was collected by Klemenc et al. in 1937 [3], by Honda and Naito in 1955 [4] and later by Gobrecht et al. [5], by Bagirov et al. [6], by Tanaka et al. [7], Hirth [8] and by Heuser [9].

More recently it was realised that the plasma parameters in these breakdown channels, now frequently referred to as microdischarges, can be influenced and modelled and consequently can be optimised for a given application [8,10-17]. Advanced plasma diagnostics and computer modelling has put us in a position to understand and tailor microdischarge properties for an intended purpose. Our present understanding of dielectric-barrier discharges is described starting with an overview of overall discharge characteristics and microdischarge properties. Ways of influencing microdischarge properties are discussed. Models of different degrees of sophistication are presented for computing plasma physical details about microdischarge formation during breakdown, plasma chemical reactions following breakdown, or both. A number of novel applications based on DBDs are described.

## 2. DISCHARGE STRUCTURE AND MICRODISCHARGE PROPERTIES

Dielectric-barrier discharges are characterised by the presence of one or more insulating layers in the current path between metal electrodes in addition to the discharge space. Different planar or cylindrical configurations are common (Fig. 1). Closely related are surface discharge configurations in which discharges are initiated at a dielectric surface due to strong electric fields generated by imbedded metal electrodes. The presence of the dielectric(s) precludes dc operation. Although DBD configurations can be operated between line frequency and microwave frequencies the typical operating range for most technical DBD applications lies between 500 Hz and 500 kHz.

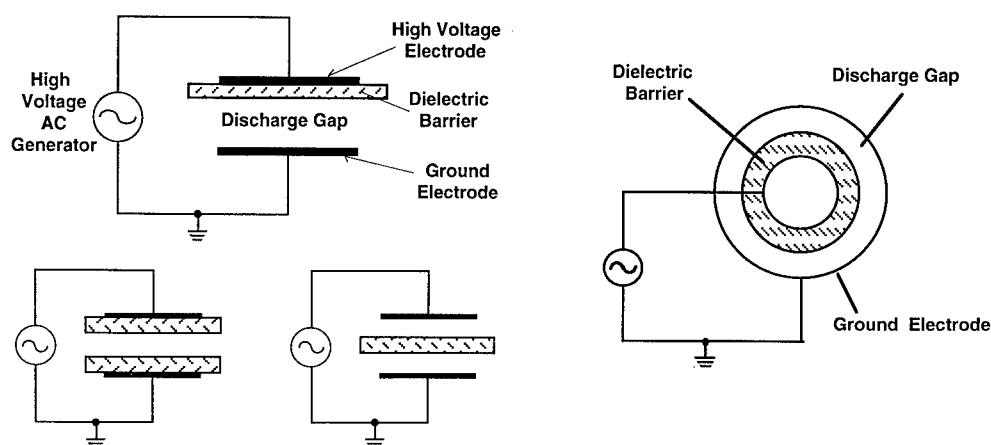


Fig. 1: Common dielectric-barrier discharge configurations

Gas spaces bounded by one or two dielectrics have practically the same breakdown voltage as if they were between metal electrodes. Typical clearances vary from less than 100  $\mu\text{m}$  to several cm. For atmospheric pressure discharges gap spacings of a few mm are common thus requiring alternating driving voltages with amplitudes of typically 10 kV. Low loss dielectrics of high breakdown strength such as glass, quartz or ceramic plates or tubes are used to which metal electrode coatings can be applied. On the other hand, also metal electrodes with dielectric coatings, e. g. steel tubes with enamel layers can be used.

### 2.1 Microdischarge Properties

The most interesting property of DBDs is that in most gases at about atmospheric pressure breakdown is initiated in a large number of independent current filaments or microdischarges. Fig. 2 shows a snapshot of such microdischarges in a 1 mm air gap photographed through a transparent electrode.

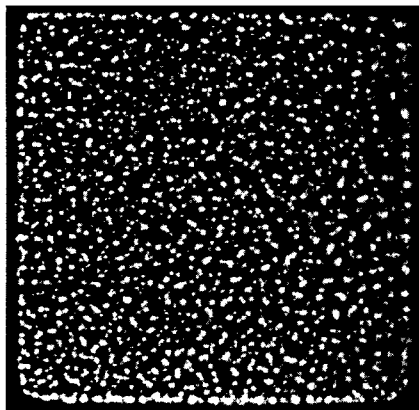


Fig. 2: End-on view of microdischarges  
Original size: 6 x 6 cm, exposure time: 20 ms

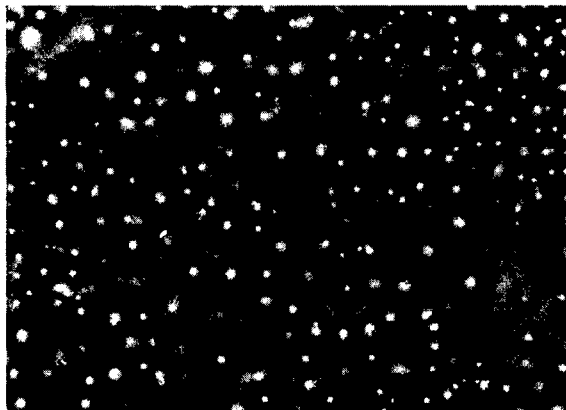


Fig. 3: Lichtenberg figure showing footprints of individual microdischarges, original size: 7 x 10 cm

Fig. 3 shows footprints of individual microdischarges left on a photographic plate with the emulsion facing the discharge gap and the glass plate serving as the dielectric. After applying a high voltage halfwave the plate was developed in the dark room. This photographic technique had already been used by Buss [2] in 1932 who found that we can expect about 10 microdischarges of submicrosecond duration per  $\text{cm}^2$  and that the channel diameter is roughly 0.1 mm. These findings are in accordance with later more sophisticated measuring and modelling techniques.

At the dielectric surface a microdischarge channel spreads into a surface discharge covering a region much larger than the original channel diameter. Typical microdischarge properties (order of magnitude) for a 1 mm air gap at 1 bar can be summarised as follows:

Table 1: Characteristic Microdischarge Properties.

Duration:	1-10 ns	Total Charge:	0.1 - 1 nC
Filament Radius:	about 0.1 mm	Electron Density:	$10^{14} - 10^{15} \text{ cm}^{-3}$
Peak Current	0.1 A	Electron Energy:	1-10 eV
Current Density:	100 - 1000 A/cm <sup>2</sup>	Gas Temperature:	close to average gap temperature

The microdischarge filaments can be characterised as weakly ionised plasma channels with properties resembling those of transient high pressure glow discharges. They ignite when the breakdown field is reached and extinguish not far below the same field value when electron attachment and recombination reduce plasma conductivity. Due to charge build up on the dielectric the field at the location of a microdischarge is reduced within a few ns after breakdown thus terminating the current flow at this location. Detailed measurements about microdischarge properties have been performed [8-10,14,18-21]. The transported charge is proportional to the gap spacing and the permittivity of the dielectric but does not depend on pressure. The current density in a microdischarge channel can reach 100 to 1000 Acm<sup>-2</sup>. Due to the short duration this normally results in very little transient gas heating in the remaining channel. Humidity tends to increase the strength of a microdischarge while irradiating the cathode with UV photons tends to decrease it. The dielectric barrier limits the amount of charge and energy deposited in a microdischarge and distributes the microdischarges over the entire electrode surface. As long as the external voltage is rising additional microdischarges will occur at new positions because the presence of residual charges on the dielectric has reduced the electric fields at positions where microdischarges have already occurred. When the voltage is reversed, however, the next microdischarges will form in the old microdischarge locations. So, high voltage low frequency operation tends to spread the microdischarges, while low voltage high frequency operation tends to reignite the old microdischarge channels every half period. This memory effect due to charge deposition on the dielectrics is extensively used in ac plasma displays.

Over a wide range of operating frequencies and voltage shapes microdischarge properties do not depend on the external driving circuit. They are determined by the gas properties, the pressure and the electrode configuration. Raising the power for a given configuration means generating more microdischarges per unit of time and/or per unit of electrode surface area. This characteristic of DBDs is very important because it allows us to investigate and optimise microdischarge properties for a given application in a fairly small laboratory set-up. Scale-up even to very large electrode surfaces in industrial applications normally does not present a problem if gap spacing and power density is not changed.

Individual microdischarge properties can however be changed for a given configuration when extremely fast rising voltages are applied. When the rise time of the voltage becomes comparable to the duration of a microdischarge a large number of microdischarges may be started simultaneously. In this case there may not be enough surface area available on the dielectric to accommodate all surface discharges of the initiated microdischarges. As a consequence weaker microdischarges result. The pulsed DBD mode offers additional flexibility by synchronising the microdischarges, by overshooting the stationary breakdown voltage and by adapting the pauses between pulses in accordance with the process under investigation.

## 2.2 Overall Discharge Characteristics

The described uniformity of individual microdischarges leads to a well defined overall discharge behaviour. This can be shown, for example, by recording voltage/charge Lissajous figures (Fig. 4). Suppose we apply a sinusoidal voltage. Initially, without discharge, the total capacitance  $C_{\text{tot}}$  is charged with rising voltage. When the breakdown voltage of the gas space is reached microdischarges occur that start to charge the capacitance of the dielectric  $C_p$  while the discharge voltage  $U_{\text{Dis}}$ , the average voltage

across the gas space, remains constant. This stops when the maximum of the voltage  $\hat{U}$  is reached and the reverse situation occurs in the second half wave. In many DBD applications the voltage/charge Lissajous figure is an almost ideal parallelogram (oscillogram in Fig. 4). From the slopes the effective capacitances  $C_{\text{tot}}$  and  $C_D$  can be derived, and  $U_{\text{Min}}$  and  $\hat{U}$  can be immediately determined [22]. The form of the voltage/charge Lissajous figure is independent of the form of the applied voltage as long as the notion of a constant discharge voltage holds. The enclosed area is always proportional to the power independent of such assumptions. According to Müller and Zahn [23] DBDs can exhibit different modes depending on the gas and the operating conditions.

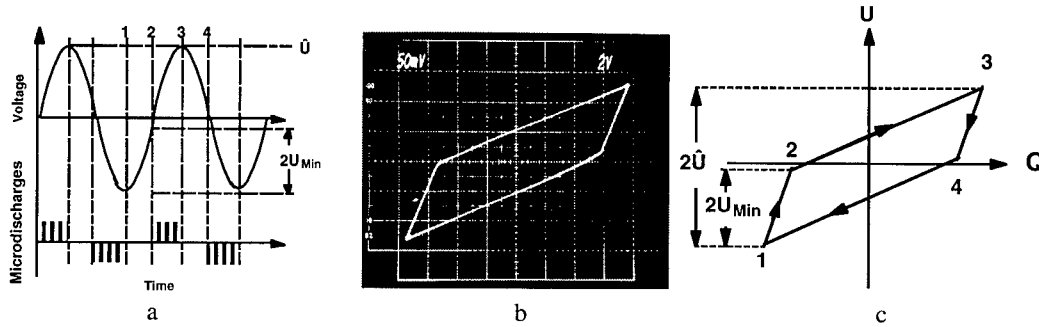


Fig. 4: Schematic diagram of applied voltage and microdischarge activity (a) and recorded (b) and schematic representation (c) of voltage/charge Lissajous figure

From voltage/charge diagrams Manley in 1943 [24] derived the power formula for ozonizers which applies to many DBDs. The enclosed area corresponds to the energy dissipated during one period of the applied voltage. According to Manley the total power is given by:

$$P = 4 f C_D U_{\text{Dis}} \{ \hat{U} - C_D^{-1} (C_D + C_g) U_{\text{Dis}} \}, \quad \hat{U} \geq C_D^{-1} (C_D + C_g) U_{\text{Dis}} \quad (1)$$

where  $f$  is the frequency and  $C_g$  the capacitance of the discharge gap. Since the fictitious discharge voltage  $U_{\text{Dis}}$  cannot be measured directly, it is sometimes advantageous to express the power  $P$  by measurable quantities [22].

$$P = 4 f C_D^2 (C_D + C_g)^{-1} U_{\text{Min}} (\hat{U} - U_{\text{Min}}), \quad \hat{U} \geq U_{\text{Min}} \quad (2)$$

where  $U_{\text{Min}}$  is the minimum external voltage required to maintain a discharge. The voltages are related by  $U_{\text{Dis}} = C_D (C_D + C_g)^{-1} U_{\text{Min}}$ .

The applied voltage/charge Lissajous figure and corresponding gap voltage/current presentations are very useful instruments for characterising the discharge behaviour and designing power supplies and matching circuits. Tanaka and co-workers have extensively used these tools to characterise different modes of dielectric-barrier discharges [25, 26]. At very high operating frequencies, e. g. a 10 MHz sine wave, or also for wide gaps at reduced pressure, the parallelogram of Fig. 4 turns into an ellipse, indicating that plasma conductivity no longer decays between successive halfwaves. The voltage/charge Lissajous figure of a plasma display panel driven by a 100 kHz square wave, on the other hand, shows a well defined jump of the charge whenever an applied voltage of  $\pm 200$  V is reached [26].

### 3. MODELLING DIELECTRIC-BARRIER DISCHARGES

#### 3.1 Modelling of the Reaction Kinetics

Different aspects of dielectric barrier discharge modelling can be addressed. For a rough determination of the different time constants involved it is often convenient to disregard spatial gradients in the beginning and treat a homogeneous plasma as a first step. To simulate the action of a short-lived microdischarge either a short high voltage pulse is applied [10, 12] or an electron beam is injected [27, 28]. In both cases it is necessary to derive the rate coefficients for electron impact collisions in the gas mixture under consideration by solving the Boltzmann equation. This requires a reliable set of electron collision cross sections. For DBD calculations the local field approximation is normally used, assuming that the electron energy distribution is in equilibrium with the electric field and that all rate coefficients can be tabulated as a sole function of the mean electron energy or the reduced field  $E/n$ .

Although these assumptions appear rather crude they have been used extensively and rather successfully in optimising ozone generators. The physical reason for this success is as follows. At atmospheric pressure electrons accelerated in the electric field perform so many collisions with the background gas that they approach equilibrium values within about 10 ps. Appreciable voltage changes



and corresponding electric field changes are much slower, typically in the ns range. So, in many cases it is justified to work with stationary solutions of the Boltzmann equation. Excitation and dissociation by electron collision are again extremely fast processes followed by free radical reactions that occur at an intermediate time scale, typically 1 to 100  $\mu\text{s}$  at atmospheric pressure. Most free radical reactions will therefore be completed before any substantial displacement of the involved species by diffusion or convection can take place. These processes take much longer and occur at ms time scales. So, in many cases where the final product is formed essentially by free radical reactions, simulating what happens within the microdischarge filament can give already a fairly good approximation. In simulating the action of many microdischarges in complicated gas mixtures a first approach neglecting the electron kinetics may also be to repetitively inject certain concentrations of free radicals and then compute the following chemical reactions [13, 29]. This approach is normally taken if reliable electron collision cross sections are missing for some components of the gas mixture under consideration.

### 3.2 Two-Dimensional Modelling

Modelling microdischarge formation is closely related to computing gas breakdown at atmospheric pressure. In the early phases of discharge development there is little difference between breakdown between metal electrodes and breakdown in a gap with one or two dielectric walls. When an overvoltage is applied to a discharge gap at atmospheric pressure an electron avalanche starting at the cathode soon reaches a critical stage where the local "eigenfield" caused by space charge accumulation at the avalanche head leads to a situation where extremely fast streamer propagation towards both electrodes becomes possible. Breakdown between metal electrodes was treated by Kline and Siambis [30], Lozanskii [31, 32], Gallimberti [33], Kunhardt et al. [34 - 35], Marode and co-workers [36], Dhali and Williams [37, 38], Yoshida and Tagashira [39] and more recently also by Kulikovsky [40] and by Babaeva and Naidis [41], among others. Computations of propagating streamers in atmospheric air and  $\text{SF}_6$  were also presented by Morrow and Lowke [42 - 44] and very detailed numerical investigations about streamer morphology in nitrogen were published by Vitello and co-workers. [45]. All these computations come to the conclusion that extremely high electric fields occur at the streamer head, that a reasonably thin conductive channel (diameter of the order 100  $\mu\text{m}$ ) is formed with maximum electron densities in the range  $10^{14}$  to  $10^{15} \text{ cm}^{-3}$ . Propagation is caused by ionisation waves travelling at a speed much higher than the electron drift velocity.

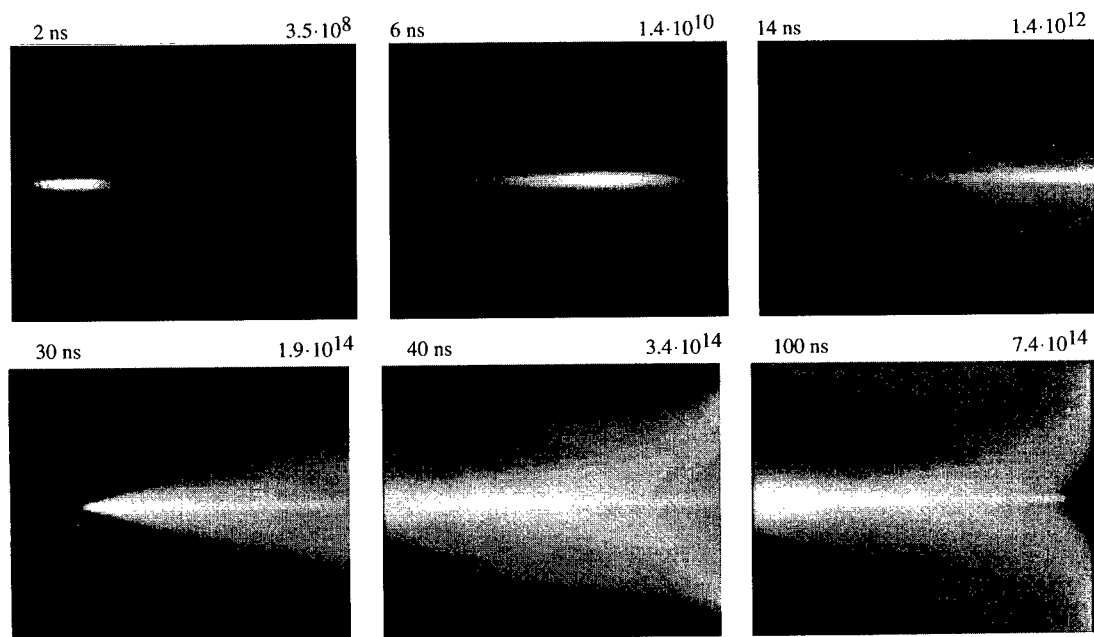


Fig. 5: Development of a microdischarge in an atmospheric pressure  $\text{H}_2/\text{CO}_2$  mixture (4/1). The 1 mm discharge gap is bounded by a plane metal cathode (left) and a 0.8 mm thick dielectric of  $\epsilon = 3$  (right). A constant voltage is applied, that results in an initially homogeneous reduced field of 125 Td in the gas space which corresponds to an overvoltage of 90% in this mixture. The numbers in the right upper corner indicate the maximum electron density in  $\text{cm}^{-3}$  reached in that picture. The maximum current of 35 mA is reached at 40 ns.

Numerical simulation of microdischarge formation in a gap bounded by a dielectric has to include the process of charge accumulation on the dielectric surface. As a consequence of this deposited charge the electric field in the gap is reduced and the microdischarge is choked, typically within a few ns. This process has been extensively studied in connection with ozone research [12,15,46-50]. These calculations show that upon arrival of the cathode directed streamer within a fraction of a ns a cathode layer is formed with extremely high reduced fields of several thousand Td. In air at atmospheric pressure the thickness of this cathode layer is about 10  $\mu\text{m}$  and the current density at its outer boundary is about 250  $\text{A cm}^{-2}$ . For a 1 mm air gap the maximum current of 0.1 A peaks at the time of the cathode layer formation. At this time a conductive channel of about 200  $\mu\text{m}$  radius is established which expands in front of the dielectric barrier. The current then decays due to charge accumulation on the dielectric surface where a maximum charge density of about 20  $\text{nC cm}^{-2}$  is found. The total energy dissipated by the microdischarge amounts to about 5  $\mu\text{J}$  leading to mean overtemperature in the column of about 5 K only [15]. In recent years such 2D models have also been applied to other gases like xenon [12], carbon dioxide [13,29] or combustion flue gases [16,51].

#### 4. OZONE GENERATION

##### 4.1 Properties and Applications of Ozone

For industrial purposes ozone is exclusively generated in large installations using dielectric-barrier discharges [22, 52]. Ozone is a potent germicide and one of the strongest known oxidants. In many applications it can replace chlorine thus causing less environmental concern. Because ozone is only moderately stable it will eventually decay to form  $\text{O}_2$  or, in the presence of organic substances, perhaps  $\text{CO}_2$ . In the absence of oxidisable substances this decay occurs within a few days. Elevated temperatures, ultraviolet radiation, or the presence of catalysts accelerate ozone destruction considerably. Although ozone itself is toxic, ozone treatment leaves no toxic residues that have to be treated or disposed of.

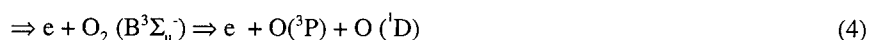
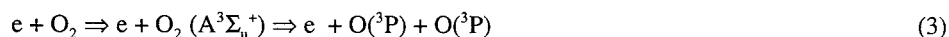
Ozone has a characteristic pungent odour and is a practically transparent colourless gas. In the ultraviolet spectral region, however, it exhibits extremely strong absorption peaking around 250 nm (Hartley band). This property is responsible for the strong filtering action of the stratosphere. The ozone layer, which apparently is endangered by anthropogenic emissions, protects the biosphere against dangerous short-wavelength radiation from the sun.

The traditional application of ozone is for water treatment which has a long tradition especially in Europe. About one hundred years ago it was realised that the germicidal and viricidal effects of ozone can provide safe drinking water in areas previously endangered by cholera and typhus epidemics. The first major ozone installations went into operation in Nice in 1907 and in St. Petersburg in 1910. Although up to recently many countries have preferred chlorine chemistry for water treatment because of its lower cost there is a strong tendency now to switch to ozone. The main targets for using ozone in water treatment are disinfection, control of disinfection by-products (trihalomethanes), colour, taste, odours, pesticides or the removal of iron and/or manganese. The second important growing large-scale use of ozone is in the paper industry. By combining oxygen, ozone and hydrogen peroxide bleaches, pulp can be treated in a closed circuit without using chlorine.

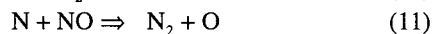
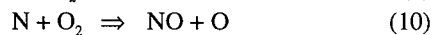
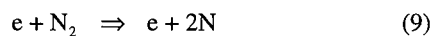
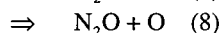
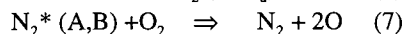
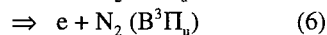
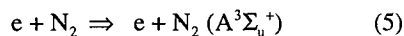
##### 4.2 Plasma Chemistry of Ozone Formation

As mentioned above many investigations on dielectric-barrier discharges in general and especially on microdischarge properties were motivated by research activities aimed at improving ozone generation. Many of the very extensive Russian contributions to this subject are summarised in the (Russian) books by Filippov et al. 1987 [53] and by Samoilovich et al. 1989 [54]. Overviews of the historical aspects and the physics and chemistry involved have been given in some review papers and handbook articles by Eliasson and Kogelschatz [12,13,22,55-57].

Local electrical breakdown in narrow discharge gaps leads to microdischarge formation and short current pulses. Detailed calculations of the electronic and ionic processes and the following neutral particle reactions in oxygen as well as in air show that mainly the electrons are important for ozone formation [10,14]. So one of the secrets of efficient ozone generation is to generate microdischarges with negligible energy losses to ions. The role of the electrons is then to excite and dissociate oxygen and nitrogen molecules. In pure oxygen two dissociation path ways are available:



with energy thresholds of 6 eV and 8.4 eV, respectively. In air naturally also nitrogen molecules are subjected to electron collisions which results in excitation and subsequent energy transfer to  $O_2$  molecules or direct dissociation and subsequent reaction:



These reactions show that part of the energy lost in collisions with nitrogen molecules can be utilised for the generation of oxygen atoms and second that NO formation cannot be avoided [58]. As a matter of fact, in air roughly half the ozone concentration of that in pure oxygen is obtained. The electron kinetics in oxygen and air has been treated by several authors [58 - 66]. Also its application to DBDs has been treated [10, 12, 14, 15, 54, 56, 67]. Ozone is formed almost exclusively from oxygen atoms, a process which, at atmospheric pressure, takes about 10  $\mu s$  in oxygen and about 100  $\mu s$  in air.



Computations at low ozone concentrations predict maximum efficiencies of slightly over 30% in pure oxygen and roughly half of that in air. Based on the enthalpy of formation of 1.48 eV per  $O_3$  molecule 100% efficiency corresponds to a yield of 0.68 ozone molecules/eV or 1.22 kg/kWh. The optimum reduced field for ozone formation in oxygen is about 140 Td in pure oxygen and closer to 200 Td in air [10,14,55].

Microdischarge properties can be tailored by optimising operating pressure, gap spacing and the dielectric barrier. If the microdischarges get too strong recombination of oxygen atoms reduces the chemical efficiency of ozone formation. At 1% atom concentration, for example, every second oxygen atom recombines to  $O_2$  instead of forming  $O_3$ . If the microdischarges are too weak, on the other hand, energy losses to ions become important. A reasonable compromise in oxygen is found when the degree of dissociation in the microdischarge channel reaches about 0.2%. The corresponding current density peaks at about 500  $Acm^{-2}$ , a current density at which the electron component dominates and energy losses by ions can be neglected. In oxygen about 80% of the energy transferred to electrons can be utilised for the dissociation of  $O_2$  [10,22].

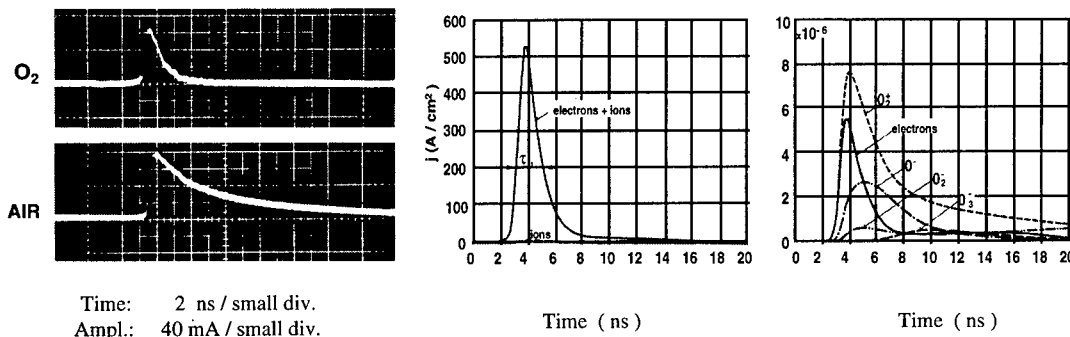
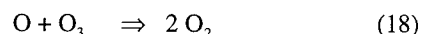
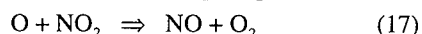
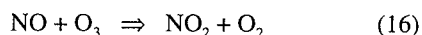
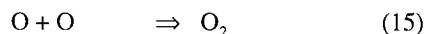


Fig. 6: Measured microdischarge current pulses in  $O_2$  and air, simulated total and ion current density and charged particle concentrations in  $O_2$

### 4.3 Nitrogen Oxide Formation

Since the  $N_xO_y$  reaction kinetics has recently again attracted attention in connection with plasma remediation of flue gases a few facts about air fed in ozonizers shall be briefly mentioned. At the output of an ozone generator in the presence of ozone only the highest oxidation state  $N_2O_5$  is detected together with traces of the fairly inert nitrous oxide  $N_2O$  [68].  $N_2O$  results from a reaction of excited  $N_2^*(A)$  with  $O_2$  at early times during discharge development [63].  $N_2O_5$  is formed in slow reactions from the intermediate species  $NO_2$  and  $NO_3$  if no water vapour is present. Otherwise  $HNO_3$  is formed. If the power density or the temperature is raised  $N_xO_y$  concentrations increase and ozone production decreases. When the  $N_xO_y$  reach a certain level ozone generation breaks down completely, an effect which has been referred to as "discharge poisoning". The reason is a catalytic reaction cycle also known from stratospheric chemistry:



The left cycle leads to enhanced "catalytic" recombination of oxygen atoms, the right cycle results in enhanced ozone destruction. The effect can easily be demonstrated with an ozone generator operating on dry air or oxygen. If as little as 0.1% NO or NO<sub>2</sub> is added to the feed gas ozone production breaks down completely [8, 22, 52, 55, 69, 70].

#### 4.4 Industrial Ozone Generation

Most technical ozone generators make use of cylindrical discharge tubes of about 20-50 mm diameter and 1-2 m length. Glass tubes are mounted inside stainless steel tubes to form a narrow annular discharge space (Fig. 7). The high voltage electrode is formed by a conductive coating, e.g. a thin aluminium film on the inside of the glass tubes. The preferred dielectric material is borosilicate glass (Pyrex, Duran). In advanced ozone generators also layered enamel coatings with optimised dielectric characteristics are used on steel tubes. Large ozone generators use several hundred tubes and produce up to 100 kg ozone per hour.

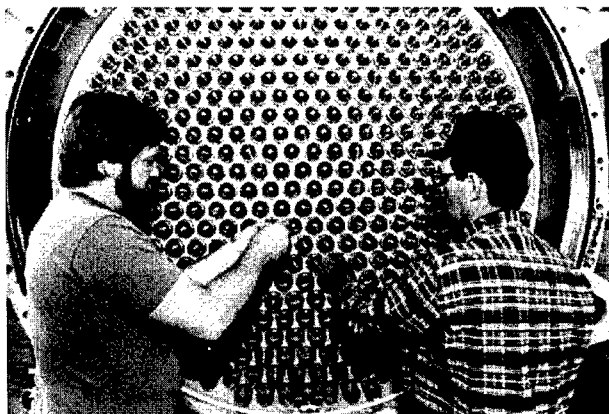
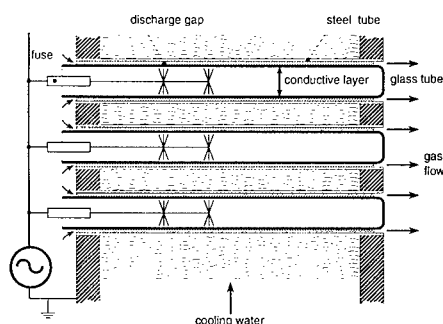


Fig. 7: Schematic diagram of discharge tubes [52] and photograph of large ozone generator at the Los Angeles Aqueduct Filtration Plant (Courtesy K. L. Rakness)

Since the efficiency of ozone formation decreases strongly with rising temperature modern ozone generators use narrow discharge gaps to ensure efficient heat removal. Typical gap spacings are in the range of 0.5 to 2 mm. Recently also extremely narrow gaps of 0.1 mm width have been proposed. The average increase of gas temperature  $\Delta T_g$  is determined by a balance of the discharge power not used for ozone formation - unfortunately the major part - and heat removal by radial heat conduction to the cooled steel electrode [10, 22, 52]

$$\Delta T_g = \frac{1}{3} \frac{d}{\lambda} \frac{P}{F} (1-\eta) \quad (19)$$

where  $d$  is the gap spacing,  $\lambda$  the heat conductivity of the feed gas,  $P/F$  the power density referred to the electrode area and  $\eta$  the efficiency of ozone generation. If the power, on a time average, is evenly dissipated in the gap volume the resulting radial temperature profile is a half parabola with its peak value at the (uncooled) glass tube. The wall temperature  $T_w$  of the steel tube is determined by the cooling water. The average temperature in the discharge gap is given by

$$T_g = T_w + \Delta T_g = T_w + \frac{1}{3} \frac{d}{\lambda} \frac{P}{F} (1-\eta) \quad (20)$$

With typical values for the operating parameters ( $T_w = 20^\circ\text{C}$ ,  $d = 2 \times 10^{-3}$  m,  $\lambda = 2.5 \times 10^{-2}$  W/mK,  $P/F = 2$  kW/m<sup>2</sup>,  $\eta = 10\%$ ) we arrive at an average temperature of about  $70^\circ\text{C}$  in the gap. The peak value at the glass tube reaches approximately  $90^\circ\text{C}$ . According to eq. (20) lowering  $T_w$  and using narrower discharge

gaps will reduce the gas temperature. The most effective way of cooling the gap is the introduction of a second cooling circuit for the glass tubes which would reduce  $\Delta T_g$  by a factor of four. Since this requires cooling of the high voltage electrode it is rarely done in technical ozone generators.

Traditionally, ozone generators were operated at line frequency. For smaller low cost ozone installations this technique is still used. Modern high-power ozone generators use thyristor-controlled frequency converters generating square wave currents at frequencies between 0.5 and 5 kHz. This way power levels up to 1 MW/unit can be handled.

## 5. INCOHERENT EXCIMER ULTRAVIOLET SOURCES

As mentioned earlier the plasma in a microdischarge can be characterised as a transient high pressure glow discharge. When a dielectric-barrier discharge is operated in rare gases or a rare gas/halogen mixture plasma conditions in a microdischarge channel are similar to those in pulsed excimer lasers. As a consequence each microdischarge can act as an intense source of ultraviolet (UV) or vacuum ultraviolet (VUV) radiation. Excimer formation is favoured by high collision rates requiring a high pressure and efficient excitation or ionisation of precursor species which requires a non-equilibrium discharge. DBDs conveniently combine these two requirements. Typical examples are the formation of  $\text{Xe}_2^*$  or  $\text{XeCl}^*$  excimer complexes, one of which is formed essentially from neutral excited atoms the other mainly via recombination of ions. The most important reactions are [11]:



### 5.1 Typical Excimer Lamp Configurations and Gas Mixtures

When these gases are filled in quartz vessels whose walls act as dielectric barriers and transparent or perforated electrodes are applied excimer lamps can be built [11,72-75]. Fig. 8 shows a water cooled cylindrical version and a planar configuration. These lamps can be operated at high power densities using gap spacings of a few mm, voltages of a few kV and frequencies of a few hundred kHz. Reliable switch-mode power supplies can be matched to the characteristics of the discharge to reach plug efficiencies of 90% regarding the energy deposited in the plasma. In a practical device typically 5 - 15% of the discharge power can be converted to UV or VUV radiation.

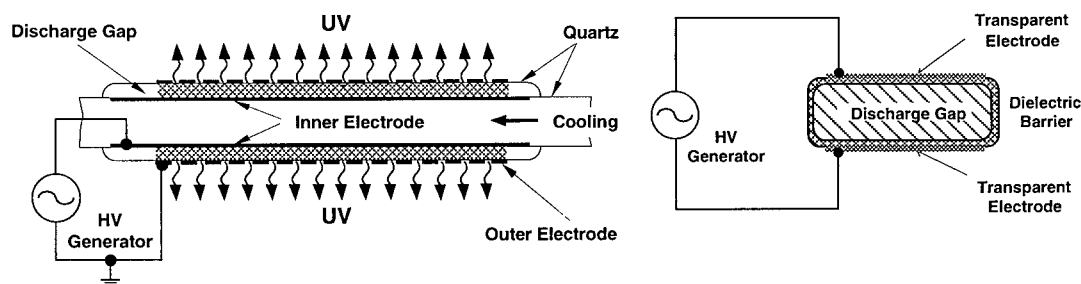


Fig. 8.: Cylindrical and planar excimer UV lamp configurations [73]

A large variety of excimer forming gas mixtures have successfully been tried out. Fig. 9 shows six representative excimer lamp spectra all of which show extremely clean spectra with narrow-band excimer emission in only one wavelength region.

The xenon excimer spectrum in Fig. 9 shows the emission of the second excimer continuum peaking around 172 nm. Its width at half intensity is 14 nm. Since this radiation is used not only in excimer UV lamps but also in mercury-free fluorescent lamps and plasma displays we mention some of the more important aspects. In low pressure xenon discharges an extremely narrow resonance line at 147 nm is emitted. Its intensity increases with pressure and peaks around 100 Pa [77]. The decay above this pressure is due to self absorption of the emitted radiation and quenching of the excited atoms. If the pressure is further increased a wider spectral emission appears in the same spectral range with a shoulder

towards longer wavelengths. This emission is referred to as the first excimer continuum of xenon. At pressures above about 10 kPa the second excimer continuum around 172 nm appears and completely dominates above 50 kPa. It results from a transition of the lower vibrational levels of the excimer states  $^1\Sigma_u^+$ ,  $^3\Sigma_u^+$  to the repulsive ground state. From electron beam experiments and numerical simulations it is known that this emission can reach an efficiency of 40 - 50% [78-80] and that extremely high power densities  $>1 \text{ MW cm}^{-3}$  can be achieved. Our own calculations indicate that similar efficiencies can be reached in DBDs [11]. Fig. 10 shows computations of the efficiency for different assumed electron densities at 100 kPa and the pressure dependence of the different emission features neglecting radiation trapping of the resonance line. Recorded emission spectra, also presented in Fig. 10, show that at 68 kPa only the second excimer continuum is emitted. At this pressure excimer formation is faster than any decay or quenching processes of the excited precursor species  $\text{Xe}^*(^3P_{1,2})$ .

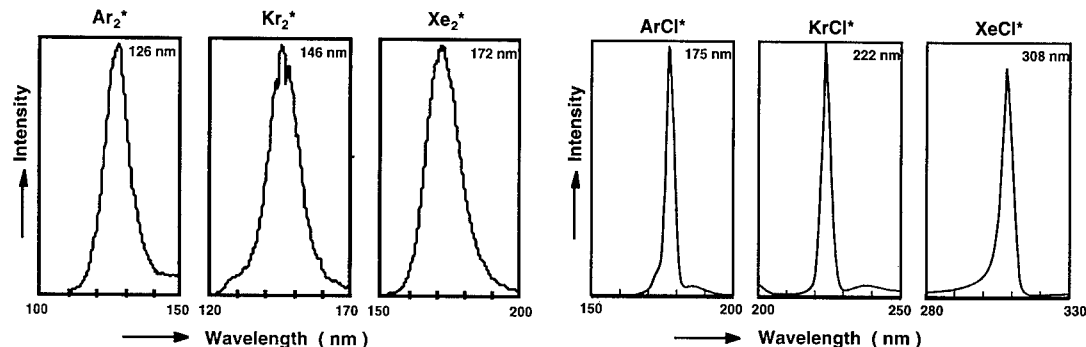


Fig. 9: Emission spectra of different excimer lamps [73]

Quite a few additional DBD lamps with excimer emission in the VUV, UV or visible spectral range have been investigated [73-76,81]. In addition to the simple geometrical configurations of Fig. 8 also large-area and windowless excimer lamps have been proposed [73,82-84]. The main advantage of excimer lamps is that they provide high-intensity narrow-band radiation that, due to the absence of a stable excimer ground state, can leave the plasma without reabsorption. If properly cooled this high radiation output can be obtained at low lamp temperature. The excimer formation process is completed within some ns and the excimer radiation decays in about 100 ns. As a consequence, excimer lamps can be switched on and off at extremely fast rates. A lamp driven at a fundamental frequency of 100 kHz, for example, emits bursts of short light pulses at a repetition rate of 200 kHz. Excimer lamps need no warm-up time and can be operated even at cryogenic temperatures. Another important advantage is the flexibility of the sandwich like electrode configuration which can be formed to any desired shape. Excimer lamps found a number of interesting novel applications and, within a short period of time, became commercially available in Germany, in Japan and in the United States.

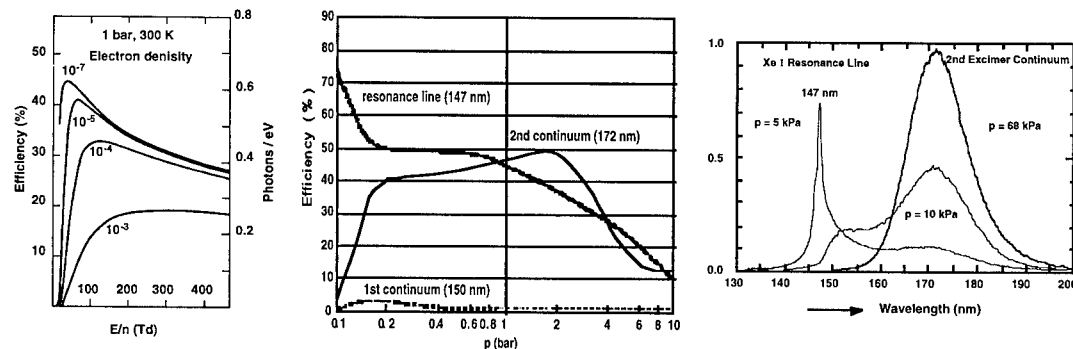


Fig. 10: Computation of the UV efficiency at 172 nm and pressure dependence and measured emission spectrum of a xenon dielectric-barrier discharge (in the computations radiation trapping of resonance radiation is neglected) [11, 12, 73]

## 5.2 Novel Applications of Excimer Lamps

Soon after the first prototypes of excimer lamps became available it was realised that these novel UV and VUV sources will find a number of interesting industrial applications [57,71,73,85]. As opposed to most other lamps excimer UV sources provide selective intense UV radiation at specific wavelengths. This narrow-band UV radiation can initiate chemical reactions, break molecular bonds or modify surface properties. At shorter wavelengths the absorption coefficient of most substances increases. So, in many cases the UV radiation is absorbed in a very thin surface layer. Like other UV sources excimer lamps can be used to induce photo-polymerisation of special paints, varnishes, adhesives, a process called UV curing. The special capabilities of excimer lamps in providing large-area intense narrow-band UV irradiation at low temperature, without producing ozone at the same time, immediately led to first applications on printing machines for high speed drying of UV printing inks. For this application the XeCl<sup>+</sup> lamp is used. Novel applications, especially for the shorter UV and VUV wavelengths, were found in materials processing and pollution control.

### 5.2.1. Material Deposition with Excimer Lamps

Excimer lamps emitting UV or VUV radiation have proved very useful tools for the photo cleavage of precursor substances that lead to the deposition of metallic, dielectric or semiconducting layers. Substantial work has been reported on the mechanism of area-selective deposition of copper structures following UV induced palladium nucleation from palladium(II) acetate precursor films [57,71,85-92]. By irradiating a spin coated or dip coated Pd acetate film with UV radiation from an excimer lamp palladium nucleation of the surface is obtained. This well adhering Pd interface of a few nm thickness serves as the starting point for a subsequent electroless plating process. This low temperature metallisation has potential applications in microcircuits, multichip interconnects and prototype fabrication. Within a few years this process was brought to technical maturity in the Brite/EuRam PACE project focusing on Photo Assisted Catalysis of Electroless Plating.

Photo-induced deposition of insulating films has also become an important application of excimer lamps. Low temperature deposition of good quality silicon dioxide and silicon nitride films were obtained by irradiating silane/nitrous oxide/ammonia mixtures [93-96]. By carefully adjusting the gas mixture any desired SiO<sub>x</sub>N<sub>y</sub> composition could be obtained. The dielectric constant of the deposited film could be varied between that of pure SiO<sub>2</sub> and that of pure Si<sub>3</sub>N<sub>4</sub>. The oxides of silicon, lanthanum and aluminium have also been obtained by irradiating sol-gel metal organic precursor films [87,96,97]. Also tantalum oxide films were obtained by irradiating tantalum ethoxide sol-gel films with a xenon excimer lamp. Due to its high dielectric constant of about 25 it is a promising candidate as a capacitor dielectric in high density dynamic access memories (DRAMs) and in ultra-large scale integrated (ULSI) devices [98]. Recently also the photoinduced deposition of polyimide films was demonstrated [99]. Polyimide is of great interest as a low dielectric constant material ( $\epsilon = 3.1$ ) for faster semiconductor devices in which it could replace the SiO<sub>2</sub> ( $\epsilon = 4.2$ ) as an interlayer dielectric. With the aid of UV radiation from a xenon excimer lamp thin polyimide films were obtained from polyamic acid precursor coatings spun onto a silicon substrate. With UV irradiation complete imidisation could be achieved at low temperature. Sample metal-insulator semiconductor diodes incorporating these new UV cured polyimides showed much lower leakage current than diodes with thermally cured polyimide.

Also the UV induced deposition of amorphous semiconductor layers from gaseous precursors was demonstrated. Again the 172 nm radiation of the xenon excimer lamp was used. Good quality a-Si:H films were obtained by irradiating Si<sub>2</sub>H<sub>6</sub> [101-103], semiconducting silicon carbide films by adding C<sub>4</sub>H<sub>10</sub> and a-Ge:H films from GeH<sub>4</sub> as a precursor.

### 5.2.2. Surface Modification with Excimer Lamps

As soon as excimer lamps became available it was realised that these novel VUV and UV sources offered enormous potential for materials processing [84,85,87]. Among the first applications were surface modification and polymer etching [84,87-89]. Irradiation of PTFE (polytetrafluoroethylene, Teflon) with VUV radiation from xenon or krypton excimer lamps under ammonia atmosphere results in hydrophilic surfaces. The changes are attributed to the incorporation of nitrogen, hydrogen and oxygen atoms into the surface [107]. Also dry photochemical selective etching of InGaAs on InAlAs was demonstrated with a xenon excimer lamp [108]. In this case a HBr gas atmosphere at a pressure of 12 kPa was used. An excellent selectivity of over 100 was achieved for this material system. Important applications are foreseen for the fabrication of electrical as well as optical devices using InGaAs/InAlAs heterojunctions, e.g. high electron mobility transistors (HEMTs) for microwave applications as well as monolithic integration of photodiodes. Very recently also the direct oxidation of silicon at fairly low temperatures was demonstrated by Boyd and Zhang with a xenon excimer lamp [109]. At 250°C direct photooxidation

of silicon was achieved at a rate of 0.1 nm/min which was about 100 times faster than thermal oxidation at 612 °C. The grown films had excellent electrical properties with respect to fixed oxide charge density, leakage current and breakdown field, comparable to those of thermally grown oxide on Si. This new photo assisted oxidation process can become a fast fabrication process for integrated circuits with only moderate increase of the thermal budget of the treated device.

### 5.2.3. Pollution Control with Excimer UV and VUV Radiation

The availability of new intense VUV and UV sources prompted a number of investigations in the photodegradation of pollutants in gaseous [110-113] and aqueous media [110,114-118]. Many of the common pollutants (TCE; PCE, DCE,  $\text{CCl}_4$ ,  $\text{CH}_3\text{Cl}$ ) absorb strongly in the ultraviolet spectral range close to 200 nm. Their molecular absorption cross sections can be well in excess of  $10^{-17} \text{ cm}^2$ . This value is more than million times larger than that of water or air in this spectral range. Consequently selective photodegradation of micropollutants at low concentration becomes possible [110]. The VUV radiation of the xenon excimer lamp is energetic enough to induce photocleavage of water and oxygen. Both substances absorb strongly at 172 nm. In both cases highly reactive radicals  $\text{O}(^1\text{D})$ ,  $\text{O}(^3\text{P})$ , OH are generated that can be utilised for pollution control. In general, the VUV process is very simple and has the particular advantage that no chemicals need to be added. The process represents a real challenge to other photochemical water treatment processes [119]. Treatment of contaminated surface water, ground water as well as waste water containing biocidal or nonbiodegradable components is under investigation. Oxidative degradation following VUV photolysis of water, due to its simplicity, has fast become an attractive alternative to other advanced oxidation (AOP) processes [119-121].

## 6. FLUORESCENT LAMPS AND PLASMA DISPLAYS

Efficient generation of VUV excimer radiation can also be utilised for fluorescent lamps. With the aid of phosphors visible radiation can be generated for a number of different applications. It is possible to produce mercury free fluorescent lamps with obvious advantages for the environment. The efficiencies obtained so far do not reach those of lamps based on the 254 nm resonance line of mercury. The advantage of fluorescent lamps based on  $\text{Xe}_2^*$  excimer radiation could be much higher luminescence intensities that can be reached due to the absence of radiation trapping in the lamp. A second advantage over mercury-based lamps is that operating conditions are practically independent of ambient temperature and that the excimer formation process is extremely fast. There are a number of applications where instant availability and short pulse operation is of advantage, for example in copying machines. A third advantage is the flexibility of dielectric-barrier discharges with respect to conceivable geometries. Some interesting work has been performed with respect to ultra flat fluorescent lamps that have been developed for LCD backlighting [122, 123]. This way large-area panels of uniform luminance can be realised. Typical gap spacings are 0.5 - 2 mm and the filling pressure is about 10 - 40 kPa. Pure xenon or also xenon/neon mixtures can be used. The DBD is enclosed between two soda-lime glass plates. The back electrode is a silver layer covered with a printed dielectric and a phosphor layer. The front glass plate is covered by phosphor on the inside and by a transparent ITO (indium/tin oxide) electrode on the front side. Such panels can be operated by 30 kHz sine wave or square wave excitation at about 1000 V<sub>rms</sub>. Phosphor layers containing e. g.  $\text{Y}_2\text{O}_3:\text{Eu}$  or  $(\text{Y,Gd})\text{BO}_3:\text{Eu}$  for red light,  $\text{LaPO}_4:\text{Ce,Tb}$ ,  $\text{BaAl}_{12}\text{O}_{19}:\text{Mn}$  or  $\text{Zn}_2\text{SiO}_4:\text{Mn}$  for green light and  $\text{BaMgAl}_{14}\text{O}_{23}:\text{Eu}$  or  $\text{BaMgAl}_{16}\text{O}_{27}:\text{Eu}$  for blue light have been proposed [123,129]. Blends of different phosphors yield white light. Luminous efficiencies of about 30 lm/W at a relatively high luminance of 3500 cd/m<sup>2</sup> and at power densities of 40 mW/cm<sup>2</sup> were reported [123].

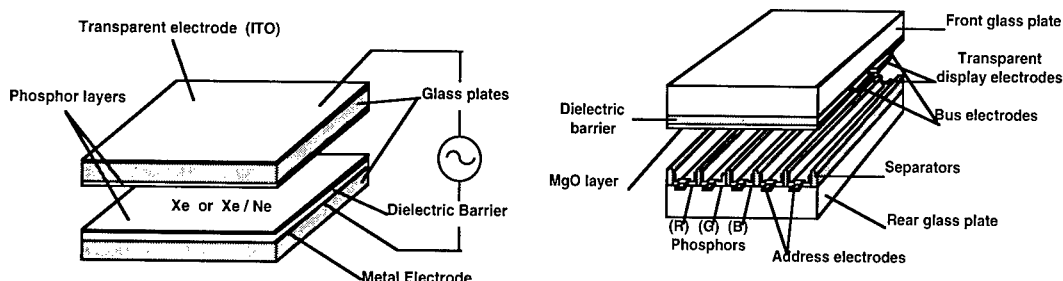


Figure 11: Flat fluorescent lamp and ac plasma display cell based on excimer radiation generated in a dielectric-barrier discharge.



One of the most fascinating recent applications of DBDs results from its enormous potential for miniaturisation. The new generation of large-area ac plasma displays just entering the market are based on dielectric-barrier discharges. Each colour pixel is a miniature excimer fluorescent lamp. It now appears that large-area displays for flat HDTV displays will use plasma display panels (PDPs) rather than TFT (thin film transistor) liquid crystal technology. The manufacturing of plasma displays profits from low material costs, inexpensive high throughput thick film processes and moderate cleanroom requirements. Prototype PDPs of excellent resolution and brilliance have been presented and mass production has started in Japan at several manufacturing sites. These displays with currently 40 inch diagonal are expected to eventually replace cathode ray tubes (CRTs) in television and large-area monitor applications. The plasma display itself can be made as thin as 6 mm although the whole package still measures 5 - 10 cm in thickness. The viewing angle is  $140^\circ$ , comparable to that of CRTs and superior to that of LCDs. The power consumption is comparable to that of conventional TV sets, about 200 - 300 W. The weight of a PDP is about 10 - 30 kg compared to more than 150 kg for a CRT display of comparable size. In addition to the obvious use as a flat TV set there are a number of important other uses for bright large-area displays in industrial, medical and military applications [124-127].

The discharge gap width in PDPs is reduced to 80 - 100  $\mu\text{m}$  and the width of each cell is about 200  $\mu\text{m}$ . Adjacent cells are separated by ribs of typically 50  $\mu\text{m}$  thickness and 100  $\mu\text{m}$  height to reduce cross talk between neighbour cells (Fig. 11). These cells can be sandblasted or etched into a flat glass plate or formed by thick film printing processes, relatively inexpensive manufacturing technologies. The filling gas is a helium/xenon or neon/xenon mixture at filling pressures between 10 and 100 kPa. Two sets of perpendicular rows of thin electrode strips allow to address each individual cell. In ac PDPs the electrodes are coated by dielectrics and thin protective layers of magnesium oxide. MgO's low sputtering rate assures long life times and its high coefficient of secondary electron emission is taken advantage of for lowering the operating voltage. PDPs can be operated by 200 V integrated driver circuits.

UV radiation of excited xenon atoms and excimers activates appropriate phosphor layers deposited on the inner wall of the gas cells. Colour triples RGB (red green blue) or quadruplets RGBG form one image point of the display. The pitch of these pixels is about 0.3 - 0.6 mm. While neon and helium are used as buffer gases xenon is used for the generation UV radiation. Mainly the Xe resonance line at 147 nm ( $\text{Xe}^3\text{P}_1$ ) and the first and second excimer continua at 150 nm and 172 nm originating from  $\text{Xe}_2^+$  excimer molecules ( $\text{O}_u^+$ ,  $^3\Sigma_u^+$  and  $^1\Sigma_u^+$ ) are detected in the emission spectrum. While the resonance radiation is subjected to strong self absorption in the gas, a process referred to as radiation trapping or radiation imprisonment, the excimer radiation can escape from the plasma with practically no absorption. Higher pressures favour the second excimer continuum at 172 nm. Above about 10 kPa the three body reaction of excited xenon atoms leading to the formation of xenon excimer complexes becomes faster than de-excitation of  $\text{Xe}^*$  [11,12]. The main reason for using a buffer gas is to lower the operating voltage to levels that can be handled by transistors. MgO has an extremely large secondary electron emission coefficient for impinging  $\text{Ne}^+$  ions resulting in a cathode fall voltage drop of only 95 V. Mole fractions up to 95% neon can be used. Detailed 1D [128-130] or 2D [125,131,132] computer models of discharge development and radiation characteristics in xenon/neon mixtures in PDP cells have been presented. A review of the physics and modelling of plasma display panels can be found in the paper by J.-P. Boeuf in this volume.

Typical sustaining frequencies for ac displays are of the order 50 - 100 kHz with current pulse duration of about 20 ns, depending on the rise time of the square wave driving voltage, gas mixture and geometry. The intensity of a cell is adjusted by using duty cycle modulation. 256 grey levels and 16 million colours can be obtained, resulting in extremely bright and colourful pictures. So far the luminance and luminous efficiency of PDPs reach 400  $\text{cd/m}^2$  and 1  $\text{lm/W}$ , respectively. This corresponds to an energy conversion of only about 0.3%. For a good display these values should be raised to 700  $\text{cd/m}^2$  and 5  $\text{lm/W}$  to match the performance of CRTs [127]. The basic structure and the exposed materials are extremely durable so that panel lifetimes should eventually reach those of monochrome PDPs, reported to be close to 100 000 hours.

The technological breakthrough that recently led to massive investment in large-volume production facilities for flat plasma display panels is based on three developments: Overcoming the limitations of self-absorption by using  $\text{Xe}_2$  excimer radiation, developing phosphors that are immune to VUV radiation damage and making prudent use of MgO protective coatings in combination with the buffer gas neon to keep the discharge voltage low at pressures high enough to ensure excimer formation. Expectations are that this most recent application of dielectric-barrier discharges, within a few years, will become the most important one as far as sales volumes are concerned.

## 7. SD CO<sub>2</sub> LASERS

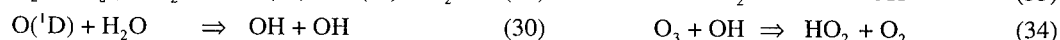
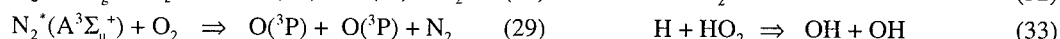
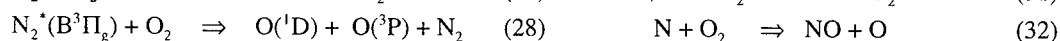
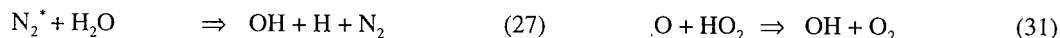
Dielectric-barrier discharges are extensively used today to pump high power CO<sub>2</sub> lasers. Ishchenko, 1978 [133] and Christensen, 1979 [134] were probably the first to use pulsed DBDs to obtain CO<sub>2</sub> laser pulses.

Only two years later the concept of a high power quasi-DC CO<sub>2</sub> laser excited by DBDs was presented by Yagi and Tabata [135], a team that could build on its experience with ozone generation. This SD CO<sub>2</sub> laser (SD for silent discharge) soon became the most successful commercial laser for material processing on the Japanese market. The water cooled plane metal electrodes are covered by glass or alumina dielectrics and are separated by 20 - 50 mm. A high-velocity cross flow passes the discharge gap at 50 - 80 m/s for heat removal and discharge stabilisation. Typical gas mixtures are CO<sub>2</sub>/N<sub>2</sub>/He (1/8/4) at a total pressure of 6.5 - 20 kPa [136 - 138]. The discharge looks fairly homogeneous and has been referred to as an ion trapping discharge. There is not enough time for the ions to decay or be removed between succeeding half waves. As a consequence, the discharge behaves very much like a resistive load. The current/voltage diagram is almost a straight line and the voltage/charge Lissajous figure looks like an ellipse. The discharge is maintained by a high voltage sine wave supplied by transistorised power supplies operating at between 100 and 500 kHz, typically at 170 kHz. Nearly diffraction limited infrared radiation is obtained at a power level of 5 kW and an efficiency surpassing 10%. High speed welding and cutting of metal plates and other materials is the main application of this SD CO<sub>2</sub> laser.

## 8. POLLUTION CONTROL WITH DBDs

Applications of DBDs to the destruction of poisonous compounds and to pollution control in general has received growing attention. After initial work on military toxic wastes by Clothiaux et al. in 1984 [139] and Fraser and Sheinson in 1986 [140] an increasing number of investigations were devoted to the decomposition of nitrogen oxides and sulphur oxides, and of volatile organic compounds (VOCs) such as hydrocarbons, chlorocarbons and chlorofluorocarbons (CFCs) in silent discharges. Contamination of exhaust air with gaseous hydrocarbons or organic solvent vapours occurs in many industrial processes, e. g. in chemical processing, in print and paint shops, in semiconductor processing as well as in soil remediation and water treatment. Much of the more recent work was discussed at the 1992 NATO Advanced Research Workshop on Non-Thermal Plasma Techniques for Pollution Control [141]. An up-to-date review by L. A. Rosocha exclusively devoted to the use of silent discharges for processing hazardous chemicals was published earlier this year [142].

Many hazardous organic chemical are readily attacked by free radicals, electrons or UV photons. DBDs are used to provide reactive species such as N<sub>2</sub><sup>+</sup>(A<sup>3</sup>Σ<sub>u</sub><sup>+</sup>), N<sub>2</sub><sup>+</sup>(B<sup>3</sup>Π<sub>g</sub><sup>-</sup>), O<sub>2</sub><sup>+</sup>(a<sup>1</sup>Δ<sub>g</sub>), O(<sup>1</sup>D), O(<sup>3</sup>P), H, OH, and N. These species initially formed by electron collisions in the microdischarge filaments subsequently provide a number of reaction paths to generate additional O, OH or HO<sub>2</sub> radicals:



These radicals can subsequently react with hazardous compounds to form non-hazardous or less hazardous substances such as O<sub>2</sub>, O<sub>3</sub>, CO, CO<sub>2</sub>, H<sub>2</sub>O, simple acids or, upon addition of ammonia for example, solid salt particles. In humid gas streams like combustion exhaust gases the hydroxyl radical (OH) plays an important role. This radical is also responsible for the cleaning of the troposphere [143].

In the case of chlorinated compounds typical destruction products are also chlorine and hydrochloric acid. In this case catalytic reaction schemes involving ClO and ClO<sub>2</sub> can become important. Care must be taken to avoid formation of even more toxic compounds. A famous example is the formation of extremely toxic phosgen (COCl<sub>2</sub>), a combat gas of the first world war, when decomposing chlorocarbons in dry air streams. So safety precautions and good diagnostics are essential for such investigations. Quite a few successful laboratory and pilot investigations have been reported in the literature. The removal of NO<sub>x</sub> and SO<sub>2</sub> from air and flue gas streams or exhausts was investigated by several groups [144-151]. Also the destruction of formaldehyde (HCHO) [151,152], carbon tetrachloride (CCl<sub>4</sub>) [142,157], trichloroethylene (TCE, ClHC=CCl<sub>2</sub>) [142,154,155], perchloroethylene (PCE, C<sub>2</sub>Cl<sub>4</sub>) [51], methylene chloride (CH<sub>2</sub>Cl<sub>2</sub>), benzene (C<sub>6</sub>H<sub>6</sub>) [153], toluene (methylbenzene, C<sub>6</sub>H<sub>5</sub>CH<sub>3</sub>) and xylene (dimethylbenzene, C<sub>6</sub>H<sub>4</sub>(CH<sub>3</sub>)<sub>2</sub>) [156], H<sub>2</sub>S and NH<sub>3</sub> [158, 159] and methanol (CH<sub>3</sub>OH) [155] was given special attention.

As compared to incineration and thermal plasma treatment the advantage of using a non-equilibrium discharge is that most of the discharge energy can be utilised to accelerate electrons and generate free radicals. In dielectric-barrier discharges the conditions in the microdischarges can be optimised to produce sufficient free radicals for the intended destruction reaction and avoid concentrations where radical-radical reassociation or annihilation reactions become important. This can be achieved at gas temperatures close to room temperature and atmospheric pressure, a condition which is of utmost importance for flue gas or off gas treatment. DBDs are considered especially if pollutant concentrations

are low, say in the 10 to 1000 ppm range. The main reason is that for dilute pollution concentrations raising the temperature of the complete carrier gas stream to incineration temperatures or only to temperatures where catalytic destruction can be initiated (200 - 500°C) becomes uneconomic. DBDs may also have advantages over conventional methods when different pollutants have to be treated simultaneously. Also additional effects caused by UV radiation [21,149,157,160] or inserted dielectric pellets [153,161,162] are under investigation.

When compared to pulsed positive corona and electron beam treatment DBDs have the advantage of much easier up-scaling and simpler power supply units. Electron beams have to be accelerated under high vacuum conditions and then transferred through special windows to the reaction chamber, which again has to be sized with respect to the penetration depth of the electrons. Pulsed corona discharges according to many investigations reach removal efficiencies similar to those of DBDs but require special pulsed power supplies to initiate and terminate the pulsed streamer corona. The microdischarge mechanism active in DBDs, on the other hand, is self-terminating and works over a large range of supply frequencies with different voltage or current shapes. As a consequence, non-thermal plasma remediation of air pollutants using dielectric-barrier discharges has become a promising fast growing technology.

## 9. SURFACE MODIFICATION WITH DBDs

Many plastic surfaces are not easily wetted so that it may be difficult or even impossible to glue, paint or print on them. In many cases it is possible to activate such surfaces by a plasma treatment, a process often referred to as "corona treatment" [163]. In most applications in reality a dielectric-barrier discharge is used. Typically, the work piece or a coating on the transport rolls or high voltage electrodes serves as a dielectric barrier. To treat large foils on one or both sides they are passed at high speed under a silent discharge maintained by an alternating high voltage applied between a knife edge electrode and a drum covered by a dielectric (Fig. 12). In many applications electrode assemblies of several parallel knife edges are used. Foils up to 10 m width are treated at a speed of about 10 m/s. This requires a discharge power of about 100 kW. Useful operating frequencies are in the range of 10 - 50 kHz.

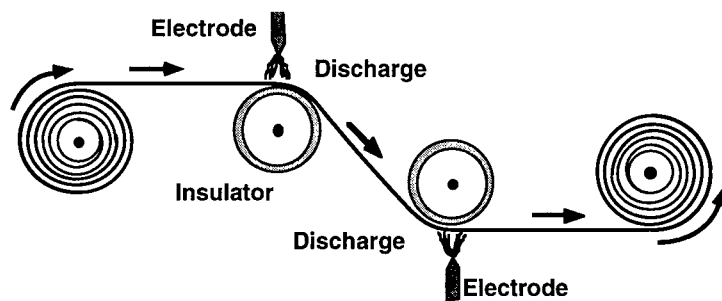


Fig. 12: Schematic diagram of high speed DBD treatment of plastic foils

Also the deposition of thin films in dielectric-barrier discharges has been investigated. In 1979 Donohoe and Wydeven [164] described a plasma polymerisation reactor operating at atmospheric pressure. One group around S. Okazaki and M. Kogoma [165-168] felt that the discrete microdischarges are not ideal for this purpose and tried to get a homogeneous discharge which they called APG (atmospheric pressure glow) discharge. The spatial homogeneity of DBDs can be influenced by using two dielectric barriers and specially shaped metal electrodes, by the operating frequency, by using large fractions of helium or neon or certain other additives like acetone or methane in argon. This work on homogeneous DBDs was further investigated by Massines and co-workers [169,170]. An alternative approach was presented in recent years by J. Salge and co-workers [171-174]. They showed that by using pulsed dielectric-barrier discharges the properties of microdischarges can be influenced in such a manner that superior surface modification and coatings of excellent quality can be obtained. Special power supplies were developed to generate repetitive pulse trains resulting in improved statistical distribution of the microdischarges across the surface, a prerequisite for more uniform treatment. Working in acetylene pin-hole-free polymeric films with properties resembling those of polyacetylene were obtained. Also thin deposits of silicon oxide were obtained at atmospheric pressure in a atmosphere of propargyl alcohol vapour and silane. In both cases the surface tension of polypropylene foils could be doubled from 30 mN/m to more than 70 mN/m [174].

The possibility to treat or coat surfaces at low temperature and close to atmospheric pressure is an important advantage for large-scale industrial applications. It is to be expected that coating techniques

using vapour or gas phase deposition in DBDs and also the annealing and oxidation of sol-gel films subjected to DBDs will be further developed.

## 10. GREENHOUSE GAS RECYCLING WITH DBDs

Recent research activities in the field of dielectric-barrier discharges address the problem of global warming and threatening climate changes. Global warming due to anthropogenic emissions of greenhouse gases has long been discussed among scientists as a possible cause for observed climate changes. The  $\text{CO}_2$  concentration in the atmosphere that had been constant at approximately 280 ppm for at least 1000 years started to rise around 1750 with the advent of industrialisation and increased use of fossil fuels. Within only 200 years the  $\text{CO}_2$  concentration in the atmosphere rose to 360 ppm and is rising at an increasing rate. As a result of a full evaluation of the available scientific evidence the United Nation's Intergovernmental Panel on Climate Change (IPCC) recently came to the conclusion that current warming "is unlikely to be entirely natural in origin" and that "the balance of evidence suggests a discernible human influence on global climate." The IPCC recommends a 50% reduction of global  $\text{CO}_2$  emissions within the next fifty years. This goes far beyond the commitments made by many industrial nations at the 1992 Rio World Environmental Summit. The recommendation then was to stabilise  $\text{CO}_2$  emissions at the level of that of 1990 by the year 2000. As far as emitted quantities are concerned the major greenhouse gases are carbon dioxide and methane. Close to 60% of the man-made greenhouse effect can be attributed to  $\text{CO}_2$  emissions which amount to 30 Gt per year. Of this amount about 22 Gt result from the combustion of fossil fuels. World wide about two thirds of the power plants run on fossil fuels and their flue gases contain typically between 4 and 14%  $\text{CO}_2$ . The availability of coal and the need of additional electric power especially in China and India will result in many new coal-fired power plants in the next decades. Concern about possibly irreversible climate changes and impending international legislation restricting or penalising these emissions has prompted extensive research activities aimed at  $\text{CO}_2$  disposal and  $\text{CO}_2$  utilisation. One proposal is to recycle  $\text{CO}_2$  as an energy carrier, perhaps combined with hydrogen in the form of a liquid fuel, or as a feed stock in the chemical industry [175].

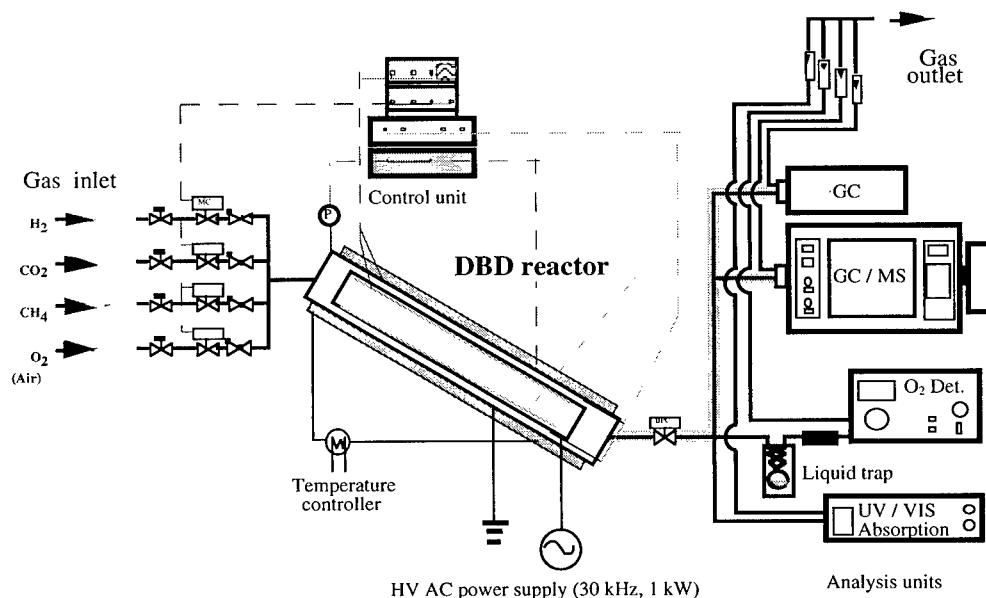


Fig. 13: Dielectric-barrier discharge reactor for greenhouse gas investigations

To investigate the decomposition of greenhouse gases and possible routes to their utilisation we designed a DBD reactor that can be operated over a wide temperature and pressure range. We studied the decomposition of the greenhouse gases  $\text{CO}_2$  and  $\text{CH}_4$  under different operating conditions. It could be demonstrated that both gases can be decomposed in the discharge and that new products are formed. The DBD reactor can be operated at pressures up to 1 MPa and regulated wall temperatures up to  $400^\circ\text{C}$ . A high voltage power supply operating close to 30 kHz can adjust the discharge power between 100 W and 1 kW. Under different operating conditions the decomposition of the main greenhouse gases  $\text{CO}_2$  and  $\text{CH}_4$

was studied [176]. Formation of CO, O<sub>2</sub> and O<sub>3</sub> is observed when CO<sub>2</sub> is treated. H<sub>2</sub>, C<sub>2</sub>H<sub>6</sub> and higher alkanes are detected when pure CH<sub>4</sub> is used. In methane/oxygen mixtures methanol is formed together with CO and H<sub>2</sub>O [176-178]. We could show that methanol can also be synthesised from CH<sub>4</sub>/air mixtures. MeOH is an attractive synthetic fuel which has twice the energy density of liquid hydrogen. Being a liquid at ambient conditions it can readily be stored and transported. It has a large potential for being used as a fuel in motor vehicles and stationary combustion sources or as a chemical storage medium for electrical energy. In our labs also methanol synthesis from CO<sub>2</sub> and hydrogen, or possibly a hydrogen donor, is investigated. The CO<sub>2</sub> could be recovered from the exhaust of a power plant operating on fossil fuels. In addition to DBDs and catalytic reactors also the suspension of fine grain catalysts in a dielectric-barrier discharge is studied [179]. It could be demonstrated that the presence of the discharge plasma can substantially reduce the activation energy of the catalyst and, on the other hand, the presence of the catalyst can substantially increase the selectivity of the dielectric-barrier discharge with respect to methanol formation.

## 11. CONCLUSIONS

Dielectric-barrier discharges have ideal properties for establishing non-equilibrium plasma conditions in high pressure gases in a controllable way. Operation close to atmospheric pressure is an absolute necessity when large combustion flue gas streams or large mass flows have to be treated and when the reaction kinetics requires high pressure operation. Also the handling and DBD treatment of large parts is facilitated at atmospheric pressure. The properties of individual microdischarges can be tailored to suit a given application. In the microdischarges transient electron energies can be obtained that are comparable to those of low pressure volume discharges. In many applications the free radicals generated by electronic collisions are more important than the electrons and ions themselves. Free radical chemistry at atmospheric pressure is extremely fast and thus allows high production or destruction rates as well as high speed treatment of surfaces. The novel applications described in this paper were brought about by a better understanding of the discharge physics and the plasma chemistry involved on one side and on recent developments of power electronics on the other side. There is no doubt that the described industrial applications of dielectric-barrier discharges will continue to grow at a fast rate and that additional novel applications will emerge in the future.

## References

- [1] Siemens W., Poggendorfs Ann. Phys. Chem. **102** (1857) 66-122.
- [2] Buss K., Arch. Elektrotech. **26** (1932) 261--265.
- [3] Klemenc A., Hinterberger H. and Höfer H., Z. Elektrochem. **43** (1937) 261-265.
- [4] Honda K. and Naito Y., J. Phys. Soc. Japan **10** (1955) 1007-1011.
- [5] Gobrecht H., Meinhardt O. and Hein F., Ber. Bunsenges. phys. Chem. **68** (1964) 55-63.
- [6] Bagirov M. A., N. A. Nuraliev and M. A. Kurbanov, Sov. Phys.-Tech. Phys. **17** (1972) 495-498.
- [7] Tanaka M., Yagi S. and Tabata N., Trans. IEE Japan **98A** (1978) 57-62.
- [8] Hirth M., Beitr. Plasmaphys. **20** (1981) 1-27.
- [9] Heuser C., "Zur Ozonerzeugung in elektrischen Gasentladungen", PhD Thesis, RWTH Aachen, 1985.
- [10] Eliasson B., Hirth M. and Kogelschatz U., J. Phys. D: Appl. Phys., **20** (1987) 1421-1437.
- [11] Eliasson B. and Kogelschatz U., Appl. Phys. B. **46** (1988) 299-303.
- [12] Eliasson B. and Kogelschatz U., IEEE Trans. Plasma Sci. **19** (1991) 309-322.
- [13] Eliasson B., Egli W. and Kogelschatz U., Pure & Appl. Chem. **66** (1994), 1275-1286.
- [14] Braun D., Küchler U. and Pietsch G., J. Phys. D: Appl. Phys. **24** (1991) 564-572.
- [15] Braun D., Gibalov V. and Pietsch G., Plasma Sources Sci. Technol. **1** (1992) 166-172.
- [16] Gentile A.C. and Kushner M.J., J. G. Appl. Phys. **79** (1996) 3877-3885.
- [17] Boeuf J.-P. and Pitchford L.C., IEEE Trans. Plasma Sci. **24** (1996) 95-96.
- [18] Tanaka M., Yagi S. and Tabata N., Trans. IEE of Japan, **98A** (1978) 57-62.
- [19] Drimal J., Gibalov V.I. and Samoilovich V.G., Czech. J. Phys. **B 37** (1987) 1248-1255.
- [20] Falkenstein Z. and Coogan J.J., J. Phys. D: Appl. Phys. **30** (1997) 817-825.
- [21] Falkenstein Z., J. Appl. Phys. **81** (1997) 5975-5979.
- [22] Kogelschatz U., "Advanced Ozone Generation" in: Process Technologies for Water Treatment S. Stucki Ed. (Plenum Press, New York, 1988) pp.87-120.
- [23] Müller S. and Zahn R.-J., Contrib. Plasma Phys. **36** (1996), 6, 697 - 709.
- [24] Manley T.C., Trans. Electrochem. Soc. **84** (1943) 83-96.
- [25] Tanaka M., Yagi S. and Tabata N., "High frequency silent discharge and its application to cw CO<sub>2</sub> laser application", Gas Discharges and their Applications (GD 85), Oxford 1985 (Leeds University Press) pp. 551 - 554.
- [26] Tamida T., Iwata A. and Tanaka M., "Characteristics and modeling of discharge in ac plasma display panels", Gas Discharges and their Applications (GD 97), Greifswald 8. - 12. September 1997.
- [27] Peyroux R., "Simulation de l'évolution temporelle de diverses espèces gazeuses créées par l'impact d'une impulsion électronique dans de l'oxygène ou de l'air, sec ou humide", Dissertation, Université de Pau (France) 1986.
- [28] Peyroux R., Pignolet P. and Held B., J. Phys. D.: Appl. Phys. **22** (1989) 1658-1667.

- [29] Eliasson B., Simon F. G. and Egli W., "Hydrogenation of CO<sub>2</sub> in a silent discharge" in Non-Thermal Plasma Techniques for Pollution Control, NATO ASI Series, Vol. G 34, Part B, Non-Thermal Plasma Techniques for Pollution Control, B.M. Penetrante and S.E. Schultheis Eds. (Springer, Berlin, 1993) pp. 321-338.
- [30] Kline L.E. and Siambis J. G., Phys. Rev. **A5** (1972) 794-805.
- [31] Lozanskii E.D., Sov. Phys. - Tech. Phys. **13** (1969) 1269-1272.
- [32] Lozanskii E.D., Sov. Phys. - Usp. **18** (1976) 893-908.
- [33] Gallimberti I., J. Phys. D: Appl. Phys. **5** (1972) 2179-2189.
- [34] Kunhardt E.E. and Byszewski W.W., Phys. Rev. **21**(1980) 2069-2077.
- [35] Kunhardt E.E. and Tzeng Y., Phys. Rev. A **38** (1988) 1410-1421.
- [36] Djermoune D., Samson S., Marode E. and Ségur P. "A time resolved two dimensional modelling of the electrical behaviour and the chemical yield of streamer induced discharge", Gas Discharges and Their Applications (GD 95), Tokyo 11 - 15 September 1995, pp.II-484 - II-487.
- [37] Dhali S.K. and Williams P.F., Phys. Rev. **A31**(1987) 1219-1221.
- [38] Dhali S. and Williams P.F., J. Appl. Phys. **62** (1987) 4696-4707.
- [39] Yoshida K. and Tagashira H., J. Phys. D: Appl. Phys. **12** (1979) L3-L7.
- [40] Kulikovskiy A.A., J. Phys. D: Appl. Phys. **27** (1994) 2556-2569.
- [41] Babaeva N.Yu. and Naidis G.V., J. Phys. D: Appl. Phys. **29** (1996) 2423-2431.
- [42] Morrow R., Phys. Rev. A **35**(1987) 1778-1785.
- [43] Morrow R. and Lowke J.J., Austr. J. Phys. **48** (1995) 453-460.
- [44] Morrow R. and Lowke J.J., J. Phys. D: Appl. Phys. **30** (1997) 614-627.
- [45] Vitello P.A., Penetrante B.M. and Bardsley J.N., Phys. Rev. **E49** (1994) 5574-5598.
- [46] Gibalov V.I., Samailovich V.G. and Filippov Yu.V., Russ. J. Phys. Chem. **55** (1981) 471-479.
- [47] Egli W. and Eliasson B., Helv. Phys. Acta **62** (1989) 302-305.
- [48] Eliasson B. and Egli W., "The silent discharge: numerical simulation of microdischarge formation", Phenomena in Ionized Gases (ICPIG XIX), Belgrade, July 1989, pp. 1024-1025.
- [49] Pietsch G.J., Braun D. and Gibalov V. I., "Modeling of dielectric barrier discharges", NATO ASI Series, Vol. G 34, Part A, Non-Thermal Plasma Techniques for Pollution Control, B.M. Penetrante and S.E. Schultheis Eds. (Springer, Berlin, 1993) pp. 273-286.
- [50] Pietsch G.J., J. Adv. Oxid. Technol. **1**(1996) 1 61-66.
- [51] Gentile A.C., "Kinetic Processes and Plasma Remediation of Toxic Gases" PhD Thesis, University of Illinois at Urbana-Champaign, 1995.
- [52] Kogelschatz U. and Eliasson B., "Ozone Generation and Applications" in Handbook of Electrostatic Processes, J.S. Chang, A.J. Kelly and J.M. Crowley Eds. (Marcel Dekker, New York 1995) pp. 581-605.
- [53] Filippov Yu.V., Boblikova V.A. and Pantelev V.I., Electrosynthesis of Ozone (Russ.), (Moscow State University 1987).
- [54] Samoilovich V.G., Gibalov V.I. and Kozlov K.V., Physical Chemistry of the Barrier Discharge (Russ.), (Moscow State University, 1989).
- [55] Kogelschatz U., "Ozone synthesis in gas discharges", Phenomena in Ionized Gases (ICPIG XVI), Düsseldorf, Aug. 1983, W. Böttcher, H. Wenk and E. Schulz-Gulde, Eds., Invited Papers, pp.240-250.
- [56] Eliasson B. and Kogelschatz U., IEEE Trans. Plasma Sci. **19** (1991) 1063-1077.
- [57] Kogelschatz U., "Silent discharges and their applications", Gas Discharges and Their Applications (GD92), Swansea 13-18 September 1992, W.T. Williams Ed. Vol. II p. 972 - 980.
- [58] Eliasson B., Kogelschatz U. and Baessler P., J. Phys. B: At. Mol. Phys. **17** (1984) L797-L801.
- [59] Yagi S. and Tanaka M., J. Phys. D: Appl. Phys. **12** (1979) 1509-1520.
- [60] Bonnet J., Fournier G., Pigache D. and Lécuyer M., J. Phys. Lettr. France **41** (1980)L477-L478.
- [61] Penkin N.P., Smirnov V.V., and Tsygir, O.D., Sov. Phys. - Techn. Phys. **27** (1982) 945-949.
- [62] Rutscher A. and Wagner H.E., Beitr. Plasmaphys. **25** (1985) 336-350.
- [63] Eliasson B. and Kogelschatz U., J. Chim. Phys. France **83** (1986) 279-282.
- [64] Yoshida K. and Tagashira H., Mem. Kitami Inst. Technol. **18** (1986) 11-20.
- [65] Okazaki S., Sugimitsu H., Niwa H., Kogoma M., Moriaki T., and Inomata, T., Ozone Sci. & Eng. **10** (1988) 137-151.
- [66] Nilsson J.O. "Numerical modeling of pulsed volume discharges for the generation of ozone", PhD Thesis, Royal Institute of Technology, Stockholm, 1997.
- [67] Samoilovich V.G. and Gibalov V.I., Russ. J. Phys. Chem. **60** (1986) 1107-1116.
- [68] Kogelschatz U. and Baessler P., Ozone Sci. & Eng. **9** (1987) 195-206.
- [69] Braun D., Küchler U. and Pietsch G., Pure & Appl. Chem. **60** (1988) 741-746.
- [70] Yagi S., Tanaka M., and Tabata N., Trans. IEE of Japan **97A** (1977) 609-616.
- [71] Kogelschatz U., Pure & Appl. Chem. **62** (1990) 1667-1674.
- [72] Eliasson B. and Gellert B., J. Appl. Phys. **68** (1990) 2026-2037.
- [73] Kogelschatz U., "Excitation of excimer radiation in silent discharges", Phenomena in Ionized Gases (ICPIG-XX), Barga Italy 8-12 July 1991, Invited Papers pp. 218 -227.
- [74] Gellert B. and Kogelschatz U., Appl. Phys. **B 52** (1991)14-21.
- [75] Neiger M. "Dielectric barrier discharges: An unusual new light source", Science & Technology of Light Sources (LS 6), Budapest 10.8 - 3.9. 1992, L. Bartha and, F.J. Kedves, Eds. pp. 75-82.
- [76] Falkenstein Z. and Coogan J.J., subm. to J. Phys. D: Appl. Phys. (May 1997).
- [77] Okabe H., Photochemistry of small molecules (J. Wiley & Sons, New York, 1978), p. 36.
- [78] Werner C. W. "Radiative and kinetic mechanisms in bound-free excimer systems", Ph D Thesis, MIT, 1975.
- [79] Rhodes Ch.K. Ed., Excimer Lasers (Springer, New York, 1979).
- [80] Eckstrom D.J., Nakano H.H., Lorents D.C., Rothem T., Betts J.A., Lainhart M.E., Dakin D.A. and Maenchen J.E., J. Appl. Phys. **64** (1988) 1679-1690.
- [81] Zhang J.-Y. and Boyd I.W., J. Appl. Phys. **80** (1996) 633-638.

- [82] Esrom H. and Kogelschatz U., Appl. Surf. Sci. **54** (1992) 440-444.
- [83] Bergonzo P., Patel P., Boyd I.W. and Kogelschatz U., Appl. Surf. Sci. **54** (1992) 427-429.
- [84] Boyd I. W. and Zhang J.-Y., Nucl. Instr. **B121** (1997) 349-356.
- [85] Kogelschatz U., Eliasson B. and Esrom H., Materials & Design **12** (1992) 251-258.
- [86] Esrom H., Demny J. and Kogelschatz U., Chemtronics **4** (1989) 202-208.
- [87] Kogelschatz U., Appl. Surf. Sci. **54** (1992) 410-423.
- [88] Zhang J.Y. "Photochemische Modifizierung von Oberflächen durch Excimer-UV-Strahlung", PhD Thesis, University Karlsruhe, 1993.
- [89] Esrom H. and Kogelschatz U., Thin Solid Films **218** (1992) 231-246.
- [90] Esrom H. and Kogelschatz U., Mat. Res. Soc. Symp. Proc. **158** (1990) 189-198.
- [91] Esrom H. and Kogelschatz U., Appl. Surf. Sci. **46** (1990) 158-162.
- [92] Zhang J.-Y., H. Esrom H. and Boyd I.W., Appl. Surface Sci. **96-98** (1996) 399-404.
- [93] Bergonzo P., Kogelschatz U. and Boyd I.W., Appl. Surf. Sci. **69** (1993) 393-397.
- [94] Bergonzo P. and Boyd I.W., J. Appl. Phys. **76** (1994) 4372-4376.
- [95] Bergonzo P. and I. W. Boyd I. W., Appl. Phys. Lett. **63** (1993) 1757-1759.
- [96] Bergonzo P., New Applications of excimer lamps to the low temperature photo-decomposition of thin films, Ph D Thesis, University College London, 1994.
- [97] Van de Leest, R.E., Appl. Surf. Sci. **86**(1995), 278 - 285.
- [98] Zhang J.-Y., Bie L.-J., Boyd I.W. and Dusastre V., "Thin tantalum oxide films prepared by 172 nm excimer lamp irradiation using sol-gel method", E-MRS Spring Meeting, Strasbourg, 16-20 June 1997, Paper B-VII.3.
- [99] Zhang J.-Y. and Boyd I.W., Electronic Lett. **33** (1997) 911-912.
- [100] Kessler F. and Bauer G.H., Appl. Surf. Sci. **54** (1992) 430-434.
- [101] Manfredotti C., Fizzotti F., Bocro M. and Piatti G., Appl. Surf. Sci. **69** (1993) 127-132.
- [102] Manfredotti C., Fizzotti F., Osenga C., Amato G. and Boarino L., Phys. Stat. Sol. (a) **135** (1993) 191-198.
- [103] Esrom H., Zhang J.-Y. and Kogelschatz U., Mat. Res. Proc. **236** (1992) 39-45.
- [104] Zhang, J.-Y. and Boyd I.W., Surf. Interf. Anal. **24** (1996) 718-722.
- [105] Zhang J.-Y., Esrom H., Emig G. and Kogelschatz U., Modification of polymers with UV excimer radiation from lasers and lamps in Polymer Surface Modification: Relevance to Adhesion, K. L. Mittal Ed. (VSP International Science Publishers, Utrecht, The Netherlands, 1996) pp. 153-185.
- [106] Esrom H., Zhang J.-Y. and Kogelschatz U., Photochemical modification and etching of PTFE with excimer VUV/UV radiation in Polymer Surfaces and Interfaces: Characterization, Modification and Application, K.L.Mittal and K.-W. Lee Eds. (VSP International Science Publishers, The Netherlands, 1996) pp 27-35.
- [107] Heitz J., Niino H. and Yabe A., Appl. Phys. Lett. **68** (1966) 2648-2650.
- [108] Habibi S., Totsuka M., Tanaka J., Kinoshita T. and Matsumoto S., J. Vac. Sci. Technol. **B 13** (1995) 247-252.
- [109] Boyd I.W. and Zhang J.-Y., "Low temperature Si oxidation with excimer lamp sources", Invited Paper, MRS Spring Meeting, San Francisco, April 1997.
- [110] Kogelschatz U., "UV production in dielectric barrier discharges for pollution control", ASI Series, Vol. G 34, Part B, Non-Thermal Plasma Techniques for Pollution Control, B.M. Penetrante and S.E. Schultheis Eds. (Springer, Berlin, 1993) pp. 339 -354.
- [111] Loraine G. A. and Glaze W. H., "Destruction of vapor phase halogenated methanes by means of ultraviolet photolysis", 47th Purdue Industrial Waste Conference (Lewis Publishers, Inc. Chelsea, Michigan, U. S. A. 1992) pp. 309-316.
- [112] Scheytt H. "Untersuchungen zur UV-photoinduzierten Oxidation chlorierter Kohlenwasserstoffe in der Gasphase", Ph D Thesis, University of Erlangen, 1995.
- [113] Scheytt H., Esrom H., Prager L., Mehnert R. and von Sonntag C., Ultraviolet light and electron beam induced degradation of trichloroethylene, NATO ASI Series, Vol. G 34, Part B, Non-Thermal Plasma Techniques for Pollution Control, B.M. Penetrante and S.E. Schultheis Eds. (Springer, Berlin, 1993) pp. 91-102.
- [114] Jakob L., Traitement des eaux par photocatalyse et photolyse V-UV: Degradation oxydative de polluants organiques, PhD Thesis, Ecole Polytechnique Fédéral de Lausanne, Switzerland, 1992.
- [115] Jacob L., Hashem T.M., Bürki S., Guindy N.M. and Braun A.M., J. Photochem. Photobiol. A: Chem. **75** (1993) 97-113.
- [116] Loraine G.A., Hazard. Waste & Hazard. Mater. **10** (1993), 185-194.
- [117] Nohr R.S., MacDonald J.G., Kogelschatz U., Mark G., Schuchmann H.-P. and von Sonntag C., J. Photochem. Photobiol. A: Chem. **79** (1994) 141-149.
- [118] Oppenländer T., Europ. Photochem. Ass. Newslett., **50** (1994) 2-8.
- [119] Legrini O., Oliveros E. and Braun A.M., Chem. Rev. **93** (1993) 671-698.
- [120] Oppenländer T., Baum G., Egle W. and Hennig T., Indian Acad. Sci. (Chem. Sci.) **107** (1995) 621-636.
- [121] Baum, G. and Oppenlaender T., Chemosphere **30** (1995) 1781-1790.
- [122] Beneking C., Dannert H., Neiger M., Schorpp V., Stockwald K. and Müller H. "Neuartige UV-Lampen auf der Basis stiller Entladungen", BMFT (Bundesministerium für Forschung und Technologie) Forschungsbericht FKZ 12N5695, 1992.
- [123] Urakabe T., Harada S., Saikatsu T. and Karino M. "A flat fluorescent lamp with dielectric barrier discharges", Science and Technology of Light Sources (LS 7), Kyoto, 27-31 August 1995, R. Italani and S. Kamiya Eds. (The Illuminating Engineering Institute of Japan, 1995) pp. 159-160.
- [124] Sobel A., IEEE Trans. Plasma Sci. **19** (1991) 1032-1047.
- [125] Boeuf J.-P. and Doyeaux H., Europhys. News **27** (1996) 46-49.
- [126] Mikoshiba S., Informations Display **10** (1994) 21-23.
- [127] Mikoshiba S., "Color Plasma Displays", SID International Symposium, Boston 12-16 May 1997, Seminar Lecture Notes, J. Morreale Ed., Vol. 1, pp. M-4/1 - M-4/36.
- [128] Meunier J., Belenguer Ph. and Boeuf J.P., J. Appl. Phys. **78** (1995) 731-745.
- [129] Meunier J., Etude numérique et expérimentale d'une cellule de panneau à plasma alternatif couleur, Thèse No. 1014, C.P.A.T. Toulouse, 1995.

- [130] Veerasingham R., Campbell R.C. and McGrath R.T., *IEEE Trans Plasma Sci.* **23** (1995) 688-697.
- [131] Boeuf J.-P. and Pitchford L.C., *IEEE Trans. Plasma Sci.* **24** (1996) 95-96.
- [132] Campbell R.C., Veerasingham R. and McGrath R.T., *IEEE Trans. Plasma Sci.* **23** (1995) 698-708.
- [133] Ishchenko V.N., Lisitsyn V.N. and Sorokin A. R., *Sov. J. Quant. Electron.* **8** (1978) 453-457.
- [134] Christensen, C.P., *Appl. Phys. Lett.* **34** (1979) 211-213.
- [135] Yagi, S. and Tabata N., *IEEE/OSA Conf. on Lasers and Opto-Electronics*, Washington DC 1989, Paper WE5.22.
- [136] Tanaka M., Yagi S. and Tabata N., "High frequency silent discharge and its application to cw CO<sub>2</sub> laser application", *Gas Discharges and their Applications (GD 85)*, Oxford 1985 (Leeds University Press) pp. 551-554.
- [137] Yasui K., Kuzumoto M., Ogawa S., Tanaka M. and Yagi S., *IEEE J. Quantum Electron.* **25** (1989) 836-840.
- [138] Takenaka Y., Kuzumoto M., Yasui K., Yagi S. and Tagashira M., *IEEE J. Quantum Electron.* **27** (1991) 2482-2487.
- [139] Clothiaux E. J., Koropchak J. A. and Moore R.R., *Plasma Chem. & Plasma Proc.* **4** (1984) 15-20.
- [140] Fraser, M.E. and R. Sheinson R., *Plasma Chem. & Plasma Proc.* **6** (1986) 27-38.
- [141] Penetrante B.M. and Schultheis S.E. Eds., "Non-Thermal Plasma Techniques for Pollution Control", NATO ASI Series G: Ecological Sciences Vol. 34A, and B (Springer, Berlin, 1993).
- [142] Rosocha L. A., Processing of hazardous chemicals using silent-discharge plasmas in *Plasma Science and the Environment*, W. Manheimer, L.E. Sugiyama and T.H. Stix Eds. (American Institute of Physics, Woodbury, New York, 1997) pp. 261-298.
- [143] Comes F.J., *Angew. Chem.* **106** (1994) 1900-1910.
- [144] Sardja, I. and Dhali S. K., *Appl. Phys. Lett.* **56** (1990) 21-23.
- [145] Dhali, S.K. and Sardja I., *J. Appl. Phys.* **69** (1991) 6319-6324.
- [146] Chang M.B., Balbach J.H., Rood M. J. and Kushner M.J., *J. Appl. Phys.* **69** (1991) 4409-4417.
- [147] Chang M.B., Kushner M.J. and Rood M.J., *Plasma Chem. & Plasma Proc.* **12** (1992) 565-580.
- [148] Chang M.B., Kushner M.J. and Rood M.J., *Environ. Sci. Technol.* **26** (1992) 777-781.
- [149] Chang M.B., Kushner M.J. and Rood M.J., *J. Environm. Eng.* **119** (1993) 414-423.
- [150] Higashi M., Uchida S., Suzuki N. and Fujii K., *IEEE Trans. Plasma Sci.* **20** (1992) 1-12.
- [151] Gentile A.C. and Kushner M.J., *J. Appl. Phys.* **78** (1995) 2074-2085.
- [152] Storch D.G. and M. J. Kushner M.J., *J. Appl. Phys.* **53** (1993) 51-55.
- [153] Neely, W.C., Newhouse E.I., Clothiaux E.J. and Gross C.A., Decomposition of complex molecules using silent discharge processing, NATO ASI Series, Vol. G 34, Part B, *Non-Thermal Plasma Techniques for Pollution Control*, B.M. Penetrante and S.E. Schultheis Eds. (Springer, Berlin, 1993) pp. 309-320.
- [154] Evans D., Rosocha L.A., Anderson G.K., Coogan J.J. and Kushner M.J., *J. Appl. Phys.* **74** (1993) 5378-5386.
- [155] Hsiao M.C., Merrit B.T., Penetrante B.M. and Vogtlin G.E., *J. Appl. Phys.* **78** (1995) 3451-3456.
- [156] Bugaev S.P., Kushinov V.A., Sochugov N.S. and Khryapov P.A., *Plasma Chem. & Plasma Process.* **16** (1996) 669-677.
- [157] Falkenstein Z., *J. Adv. Oxid. Technol.* **1**(1997) 3 1-16.
- [158] Traus I. and Suhr H., *Plasma Chem. & Plasma Proc.* **12** (1992) 275-285.
- [159] Chang M.B. and Tseng T. D., *J. Environm. Eng.* **122** (1996) 41-46.
- [160] Falkenstein, Z., *Fundamental Studies on the Combined (V)UV-Non-Thermal Plasma Treatment of Air Pollutants*, Ph D Thesis, University of Karlsruhe 1996 (Los Alamos Report LAUR-96-2219).
- [161] Chang J.-S., Lawless P. A. and Yamamoto T., *IEEE Trans. Plasma Sci.* **19** (1991) 1152-1166.
- [162] Nunez C.M., Ramsey G.H., Ponder W.H., Abbott J.H., Mammel L.E. and Kariher P.H., *Air & Waste* **43** (1993) 242-247.
- [163] Linsley Hood J.L., "The corona treatment of plastic films", *Gas Discharges and Their Applications (GD 80)*, Edinburgh 8-11 September 1980, pp.86-90.
- [164] Donohoe K.G. and Wydeven T., "Plasma polymerisation of ethylene in an atmospheric pressure discharge", *Plasma Chemistry (ISPC-4)*, Zürich 27. August - 1. September 1979, S. Veprek and J. Hertz, Eds., pp. 765-771.
- [165] Kanazawa S., Kogoma M., Moriwaki T. and Okazaki S., *J. Phys. D: Appl. Phys.* **21** (1988) 838-840.
- [166] Yokoyama T., Kogoma M., Kanazawa S., Moriwaki T. and Okazaki S., *J. Phys. D: Appl. Phys.* **23** (1990) 374-377.
- [167] Okazaki S., Kogoma M., Uehare M. and Kimura Y., *J. Phys. D:Appl. Phys.* **26** (1993) 889-892.
- [168] Kogoma M. and Okazaki S., *J. Phys. D:Appl. Phys.* **27** (1994) 1985-1987.
- [169] Massines F., Mayoux C., Messaoudi R., Rabehi A. and Ségur P., *Gas Discharges and Their Applications (GD 92)*, Swansea 13-18 September 1992, W. T. Williams Ed., Vol II, pp 730-733.
- [170] Massines F., Gadri R.B., Decomps P., Rabehi A., Ségur P. and Mayoux C. "Atmospheric pressure dielectric controlled glow discharges: diagnostics and modelling", *Phenomena in Ionized Gases (XXII ICPIG)*, 31 July -4 August, Hoboken, NJ 1995, K.H.Becker, W.E.Carr and E.E. Kunhardt Eds. (AIP Press Woodbury, N. Y., 1996,Conference Proceedings 363) Invited Papers pp. 306-315.
- [171] Reitz U., *Barrierentladungen zur plasmagestützten Oberflächenbehandlung*, PhD Thesis, TU Braunschweig, 1992.
- [172] Schwarz R., *Über die Beschichtung von Oberflächen mit Barrierentladungen bei Atmosphärendruck*, PhD Thesis, Technical University Braunschweig 1995.
- [173] Salge J., *Surf. Coat. Technol.* **80** (1996) 1-7.
- [174] Meiners S., Salge J.G.H., Prinz E. and Förster F. "Surface modification of polymer materials by transient gas discharges at atmospheric pressure", *Plasma Surface Engineering*, Garmisch-Partenkirchen 9-13 September 1996.
- [175] Eliasson B., CO<sub>2</sub> Chemistry: An Option for CO<sub>2</sub> Emission Control ? in *Carbon Dioxide Chemistry: Environmental Issues*, J. Paul and C.-M. Pradier Eds. (The Royal Society of Chemistry, Cambridge, G.B., 1994) pp. 5-15.
- [176] Bill A., Wokaun A., Eliasson B., Killer E. and Kogelschatz U., *Energy Convers. Mgmt.* **38** (1997) S415- S422.
- [177] Okazaki K., Nozaki T., Uemitsu Y. and Hijikata K., "Direct conversion from methane to methanol by a pulsed silent discharge plasma", *Plasma Chemistry (ISPC-12)*, Minneapolis, Aug. 21-25, 1995, J.V.Heberlein, D.W.Ernie and J.T.Roberts Eds. (University of Minnesota) Vol. II, 581-586.
- [178] Shepelev S.S., Gesser H.D. and Hunter N.R., *Plasma Chem. & Plasma Proc.* **13** (1993) 479-488.
- [179] Eliasson B., Kogelschatz U., Xue B. and Zhou L.M., "Application of dielectric barrier discharges to the decomposition and utilisation of greenhouse gases", *Plasma Chemistry (ISPC-13)*, Beijing, Aug. 18 - 22, 1997, C.K.Wu Ed. (Peking University Press) Vol. IV, 1784-1789.



## Nonequilibrium in Thermal Plasmas with Applications to Diamond Synthesis

C.H. Kruger, T.G. Owano, C.O. Laux and R.N. Zare\*

*Mechanical Engineering Department, High Temperature Gasdynamics Laboratory, Stanford University, Stanford, California 94305, U.S.A.*

*\* Chemistry Department, Stanford University, Stanford, California 94305, U.S.A.*

**Abstract** - Atmospheric pressure plasmas are frequently considered to be in local thermodynamic equilibrium due to the high frequency of collisional processes which drive the plasma state towards a Maxwell-Boltzmann equilibrium. However, various forms of thermodynamic, ionizational, and chemical nonequilibrium have been demonstrated and investigated in atmospheric pressure plasma environments over the last several years, and the nonequilibrium behavior of such systems can be quite significant. The investigation, understanding, and exploitation of atmospheric pressure nonequilibrium plasma chemistry is necessary to the further expansion of plasma-based systems into mainstream manufacturing and processing applications. Several experimental programs to investigate the fundamental processes of atmospheric pressure nonequilibrium plasma chemistry, and the application of this nonequilibrium to various chemical systems have been undertaken in our laboratories. The results of these investigations have shed light on the kinetics behind various forms of atmospheric pressure nonequilibrium chemistry, and provided insights into the beneficial control of nonequilibrium plasma chemistry for processing applications.

### 1. INTRODUCTION

Nonequilibrium chemistry in atmospheric and near atmospheric pressure plasmas has emerged as an important factor in the understanding and design of plasma processing systems. Although atmospheric pressure thermal plasmas have been regarded in the past as equilibrium systems for which equilibrium diagnostic interpretations are suitable, and have been used primarily for high-enthalpy processes, recent research has shown that both naturally occurring and induced nonequilibrium chemistry can dramatically change the properties and capabilities of these plasmas. This nonequilibrium plasma chemistry offers challenges to current diagnostic techniques and their interpretation, as well as the opportunity to expand the range and scale of current plasma processing systems. The benefits of nonequilibrium plasma chemistry have been known and applied in low pressure plasma processing systems, and in fact those particular properties are responsible for making many of these processes possible (such as anisotropic etching in semiconductor manufacturing). Recent efforts to bring the unique capabilities of plasma processing into mainstream manufacturing have been hampered by the need to accomplish these processes on larger scales, with higher throughput, and at atmospheric or near atmospheric pressure.

In this paper we will illustrate our recent research in several plasma systems for purposes of fundamental radiation and kinetic studies, thermal plasma CVD, and aerothermal applications. In these studies we have encountered various forms of electronic, vibrational, ionizational, and chemical nonequilibrium that required experimental characterization using a variety of complementary diagnostic techniques ranging from emission spectroscopy to advanced laser-based diagnostics. We will describe these techniques and discuss various models that have been developed and applied to interpret and predict the observed nonequilibrium. We will demonstrate how this new understanding of nonequilibrium behavior can be applied to the synthesis of advanced materials, and to the improvement of nonequilibrium radiation models. Finally, we will present preliminary results from a novel plasma processing technique that selectively enhances desirable nonequilibrium chemistry by means of targeted

energy addition to the free electrons. The combination of appropriate plasma diagnostic techniques and detailed interpretive tools is essential for the further understanding of nonequilibrium plasma environments and the advancement of plasma processing technology.

## 2. EXPERIMENTAL FACILITIES

The research described here has been carried out in the laboratories of the High Temperature Gasdynamics Laboratory, Department of Mechanical Engineering, at Stanford University. In this laboratory, we currently operate two large-scale atmospheric pressure plasma facilities, one low pressure reactor, and several state-of-the-art laser-based diagnostic facilities. In this section we will briefly review these facilities.

### 2.1 RF Plasma Torch Facility

The RF plasma torch facility is centered around a 50 kW TAFE model 66 RF induction plasma torch, powered by a LEPEL model t-50-3 power supply operating at a frequency of 4 MHz. The torch head itself (shown schematically in Figure 2.1) consists of a 5-turn copper induction coil (mean radius 8.6 cm and height 8.6 cm) surrounding a 3 mm thick quartz tube (inner radius approx. 7.6 cm) and encased in a Teflon body with brass end plates. Overall size of the torch head is approximately 15 cm diameter and 35 cm height. Deionized cooling water is circulated around the load coil in the annular region between the Teflon body and the inner quartz tube. This provides cooling for both the load coil and the inner quartz tube which contains the generated plasma. Deionized water is used to prevent electrical breakdown between adjacent coils and to limit corrosion and mineral deposits within the cooling system. Copper exit nozzles of 0.5, 1.27, 2.0, 2.54, 3.81, 5.0, and 7.0 cm exit diameter can be utilized at the top of the upward firing torch (with the nozzle exit being approximately 11 cm above the uppermost coil) to provide flowing plasmas of various size and velocity.

The induction torch can operate completely on gases such as argon, air, and nitrogen as well as mixtures involving trace species such as methane, hydrogen, and oxygen. Atmospheric pressure plasmas at temperatures up to 10,000K can be generated, with soft vacuum and super-atmospheric operation also possible with modification. The torch, being relatively large, provides for more realistic conditions not dominated by wall effects, but at the same time is compatible with university-scale research conducted by Ph.D. students. Several flow reactors can also be used in conjunction with the plasma torch. These flow reactors consist of a double walled, water cooled, synthetic fused silica or brass test section (also shown schematically in Figure 2.1) mounted on the exit nozzle of the plasma torch. There are several sizes currently in use, varying from 1 to 7 cm in diameter, with flow lengths from approximately 5 cm to 100 cm. The quartz test sections consist of approximately 2 mm thick walled synthetic fused silica tubes (grade GE214 selected for minimum surface defects and maximum smoothness) separated by an approximately 2 mm thick annular water cooling passage. This arrangement prevents entrainment of room air into the flowing plasma as well as providing almost complete optical access to the plasma. The brass test sections are also of a double-walled, water-cooled design, but are modular in construction and can be assembled to any length desired. Without the test section in place, the luminous tail flame of the torch is quenched by room air entrainment within approximately 8-10 cm for the highest power argon cases, and thus the test sections enable the plasma to flow a much longer distance in a relatively well controlled environment.

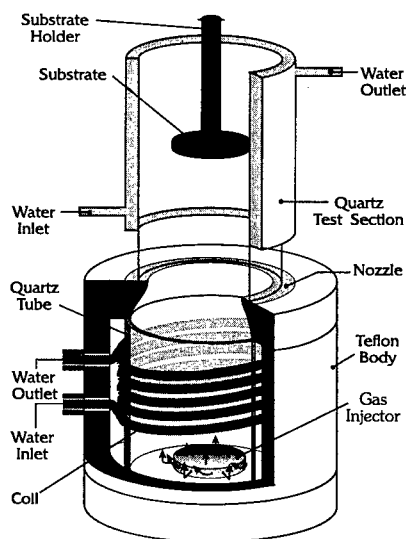


Figure 2.1 Schematic cross-section of torch head.

In addition to the plasma torch itself, the facility is well equipped for spectroscopic diagnostics. Several, multi-level optical tables, two monochromators, PMTs, optics, translators, and an optical chopper / lock-in amplifier combination coupled to a dedicated computer permit study of the plasma by emission spectroscopy. The facility is also complemented by a state-of-the-art laser diagnostic facility described below.

## 2.2 DC Arcjet Facility

The DC arcjet facility is based around a 150 kW DC arcjet (shown schematically in Figure 2.2). The DC arcjet facility is capable of providing uniform, moderate to high speed atmospheric pressure plasma flows, at temperatures up to approximately 8000 K. The arcjet itself is a Thermal Dynamics Model F-5000 swirl stabilized direct current arcjet, with up to 200 kW of electrical power available from three rectifier banks. It utilizes a molten spot tungsten cathode and a water-cooled copper anode/nozzle. The arcjet typically operates on argon, with process gases injected into the plasma in a small plenum below the arcjet exit. The mixture plasma is directed through an interchangeable nozzle into the process reactor test section. The interchangeable nozzle design allows for varying exit diameters and thus varying plasma velocities. It is important to note that this plasma/nozzle design provides a uniform plasma flow over the substrate in contrast to conventional configurations of DC arcjets for plasma synthesis.

Inside the process reactor test section, substrates are typically mounted in a stagnation point flow geometry, perpendicular to the oncoming plasma. The substrate is separated from its water-cooled holder by means of an adjustable thickness insulator, thus giving control of the substrate temperature, which is monitored pyrometrically through a cooled window. The substrate can be biased with respect to the arcjet and plasma by means of a separate power supply. In preliminary discharge experiments this biasing has been accomplished using a bank of four Kepco Model ATE 100-10M power supplies in parallel, each rated at 100 V - 10 A.

## 2.3 Hot-Filament Reactor System

The hot-filament reactor is shown schematically in Figure 2.3, and consists of a 5-way stainless steel cross 4 inches in diameter. A two-stage mechanical pump (E2M40, Edwards) is used to evacuate the chamber to the minimum pressure of  $4 \times 10^{-3}$  Torr. Inside this reactor, a tungsten filament is positioned horizontally inside the chamber using two tungsten posts, 4 cm long and 1.5 mm in diameter, mounted on water-cooled copper electrodes. The tungsten filament is typically 20 mm long and 200  $\mu$ m in diameter, and is resistively heated with dc current while its temperature is monitored with a disappearance pyrometer (Pyro Micro-Optical Pyrometer). Substrates can be mounted near the filament via a similar post support system, and are typically made of a molybdenum strip (4 mm x 20 mm x 250  $\mu$ m). The substrate is also resistively heated via an AC power source. The substrate temperature is monitored with a K Type thermocouple which is welded to the rear surface of the substrate, and also by an infra-red optical pyrometer (Minolta Cyclops).

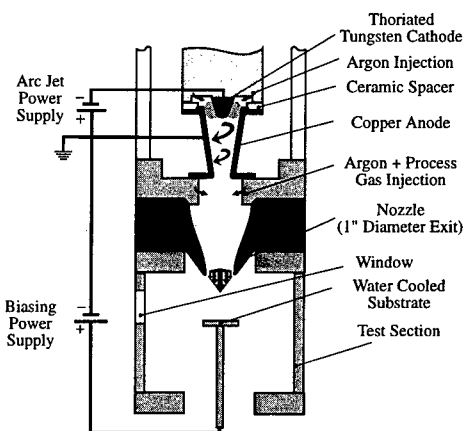


Figure 2.2 Schematic of DC arcjet.

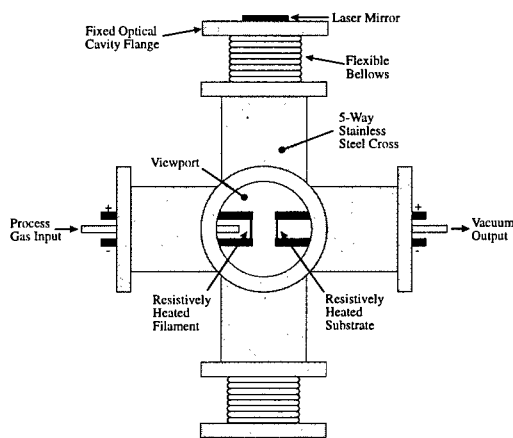


Figure 2.3 Schematic of the Hot-Filament Reactor.

## 2.4 Visible/UV Laser Facility

A complete nano-second laser facility is currently in operation at the RF plasma torch facility, and is comprised of a Spectra-Physics DCR-4G Nd:YAG laser (modified for temperature stabilized 20 Hz operation), a Spectra-Physics PDL-2 dye laser, a Spectra-Physics WEX frequency doubler and mixer, a Lumonics HD-500 narrow linewidth dye laser modified with a special Bethune cell amplifier, and a Lumonics HT-1000 frequency doubler (Figure 2.4). Associated equipment for the laser facility includes four gated integrators/boxcar averagers, a four channel digital delay/pulse generator, fast pre-amplifiers, analog processors, an HP 54510A digitizing oscilloscope, associated optics, and a dedicated Pentium based laboratory microcomputer. In its present configuration, the laser system is capable of delivering two independently tunable source beams for simultaneous spectroscopic interrogations.

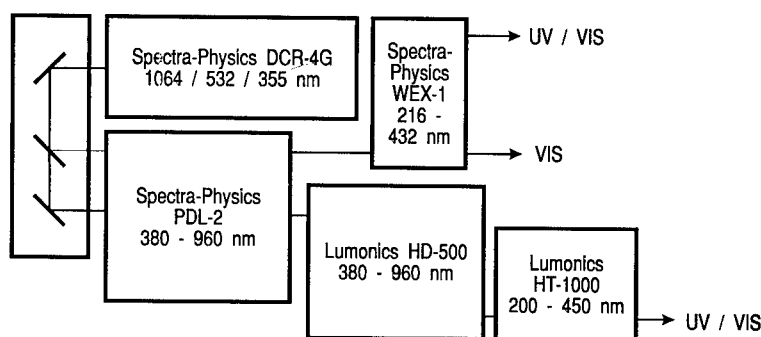


Figure 2.4 Schematic of laser facility.

## 2.5 Infra-Red OPO Laser Facility

We have also developed an infra-red Optical Parametric Oscillator (OPO) laser facility (shown schematically in Figure 2.5). These infra-red OPO systems have only recently become commercially available and represent instrumentation that exists at only a few facilities nationwide. The infrared OPO system produces near transform-limited nanosecond pulses ( $0.017 \text{ cm}^{-1}$  bandwidth) that are continuously tunable from 1.5 to  $10 \mu\text{m}$ , with pulse energies varying from approximately 10 mJ in the near infrared to approximately 100  $\mu\text{J}$  at  $10 \mu\text{m}$ . The laser system consists of an injection seeded Nd:YAG pump laser (Continuum Powerlite 8000) coupled to an optical parametric master oscillator operated in the near-infrared followed by two successive parametric converter stages (Continuum MIRAGE 3000) and a difference frequency generation stage to extend the accessible wavelength range to  $10 \mu\text{m}$  (Continuum MX-1). The single mode operation of the laser system is assured by continuous monitoring of the master oscillator and use of an actively stabilized cavity.

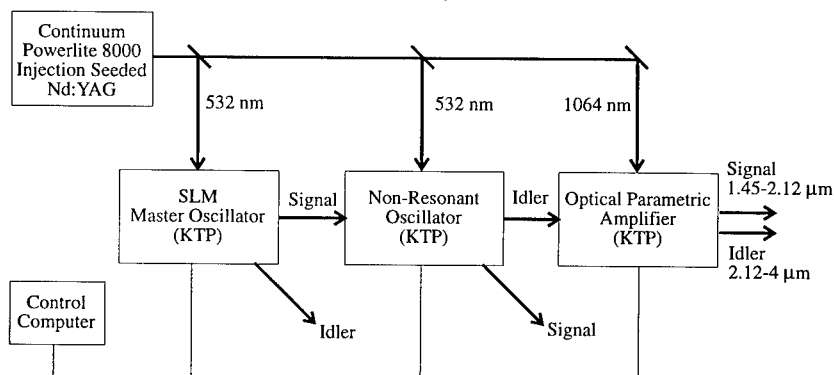


Figure 2.5 Schematic of the infra-red OPO laser facility.

### 3. INVESTIGATIONS AND DIAGNOSTICS OF NONEQUILIBRIUM PLASMA CHEMISTRY

In recent years, we have investigated the nature and chemistry of atmospheric pressure plasmas. In this effort, fundamental information on the plasma state, excitation temperatures, electron densities, radiation escape, recombination rates, and electronic quenching of excited levels have been investigated. The plasmas studied have ranged from simpler noble gas plasmas, to more complex admixtures involving diatomics such as hydrogen and nitrogen, to very complex reacting environments such as air plasmas and the diamond producing argon-hydrogen-methane system. As part of these fundamental investigations, we have developed and applied advanced, laser based diagnostic techniques in order to understand realistic plasma synthesis and plasma processing environments.

#### 3.1 Noble-Gas and Dilute Mixture Plasmas

Atmospheric pressure argon plasmas have been used to investigate the applicability of LTE assumptions to noble gas plasmas of moderate temperatures and electron densities ( $< 10,000$  K,  $10^{22}$  m $^{-3}$  respectively). In these experiments, emission diagnostics are used to assess the plasma state at several locations downstream of the excitation source. Absolute line intensities, relative line intensities, and absolute continuum intensities are used to determine electronic state populations, electron density, and associated temperatures. The measurement of excited electronic state populations and electron density allows the applicability of LTE assumptions to be tested at the conditions of interest.

If a plasma is truly in a state of LTE, temperatures describing the absolute and relative electronic level populations, as well as their relation to the density of free electrons, will be the same. Recombining argon plasmas in the temperature and electron density range of 5000 - 8500 K,  $10^{20}$  -  $10^{22}$  m $^{-3}$  respectively, downstream of the inductively coupled plasma torch, have been investigated in this manner and found to exhibit non-LTE behavior.[1, 2] This is due to the relatively slow electron-ion three-body recombination rates. Nevertheless the plasma is found to maintain partial local thermodynamic equilibrium, or PLTE. In this state of PLTE, excited electronic states and free electrons are mutually in partial equilibrium at the Boltzmann temperature  $T_B$ , as given by the excited state Saha equation:

$$\frac{n_e^2}{n_j} = \frac{2g_i}{g_j} \left( \frac{2\pi m_e k T_B}{h^2} \right)^{3/2} \exp \left( \frac{-\epsilon_{ji}}{k T_B} \right)$$

where  $\epsilon_{ji}$  is the ionization energy of the  $j$ th excited level,  $g_i$  represents the ion partition function, and the other symbols have their usual meaning. The absolute populations of bound and free electrons, however, deviate from LTE with the ground state by a nonequilibrium factor,  $\alpha$ , given by:

$$\frac{n_i}{g_i} = \alpha \left( \frac{1}{g_1} \right) \left( \frac{p}{k T_B} \right) \exp \left( \frac{-\epsilon_i}{k T_B} \right)$$

$$\left( \frac{n_e^2}{n_1} \right) = \alpha \left( \frac{2g_i}{g_1} \right) \left( \frac{2\pi m_e k T_B}{h^2} \right)^{3/2} \exp \left( \frac{-\epsilon_i}{k T_B} \right)$$

Although emission measurements allow only confirmation of PLTE in the argon plasmas to electronic levels as low as  $j=3$ , absorption measurements indicate that PLTE in fact extends to  $j=2$  for the range of conditions investigated. Since the partial equilibrium is maintained by collisions between excited electronic states and free electrons, the Boltzmann temperature  $T_B$  should agree with the free electron translational temperature  $T_e$ . This is supported by detailed collisional-radiative models which show equilibration, at sufficiently high electron densities, between the electron temperature  $T_e$  and the Boltzmann slope temperature  $T_B$  of high lying bound electronic levels. Analysis of the electron energy equation in the regions downstream of the excitation source indicates relatively small differences between the electron temperature  $T_e$  and the heavy particle gas temperature  $T_g$ . Detailed investigation of the electron-ion three body recombination coefficient of argon[2] shows it to be insufficiently high to

allow ionizational equilibrium to be maintained for even the slow moving, atmospheric pressure plasmas under study. This emphasizes the importance of understanding recombining plasmas so common in plasma chemistry.

The importance of accurately accounting for deviations from LTE can be illustrated by the interpretation of argon radiative source strength measurements. Measurements of the volumetric radiative source strength of argon[1] are shown in Figure 3.1 as interpreted with the assumption of LTE as opposed to those interpreted taking into account effects of the observed PLTE. Since the bound and free electrons responsible for the radiative emission of the plasma are, for the most part, overpopulated with respect to their LTE values, we can see that the value obtained using LTE assumptions drastically overpredicts the low temperature values of radiative source strength. Also shown in Figure 4.1 are the measurements of Emmons, who made use of LTE arguments in his data reduction, as well as a proposed upper bound curve, based on the argument that the observed radiation must fall off with decreasing temperature at least as fast as a Boltzmann factor corresponding to the population of the second excited level at 13.1 eV. We see in this case that the use of LTE temperatures for determining the plasma state and interpreting measurements is unsatisfactory.

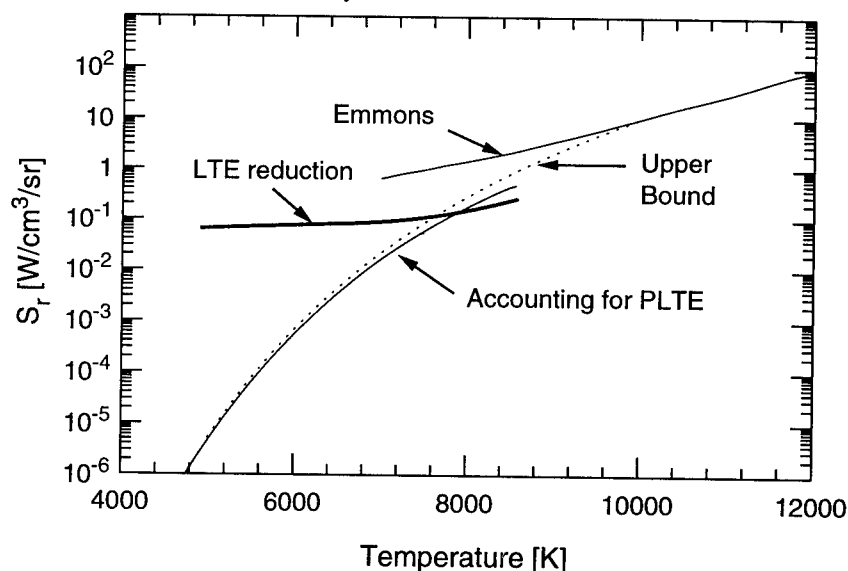
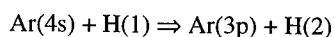


Figure 3.1 Radiative source strength of argon.

As a step toward more complex systems, we have mixed small amounts of nitrogen or hydrogen with argon under conditions similar (but not necessarily identical) to those of the noble-gas experiments. It is found that under conditions where the plasma is still strongly recombining at the test-section exit the presence of the diluent causes marked departures from partial local thermodynamic equilibrium between the bound and free electrons.[3] Typical results are shown in Figure 3.2 where the normalized population of the 4p bound state of argon is shown for varying diluent concentrations. In this Figure, an ordinate value of 1 indicates that the 4p level population is in partial equilibrium with the free electrons, while a value of 0 indicates that the 4p level population is in LTE with the ground state. The decrease of the normalized values from unity as the diluent concentration is increased can be described as quenching of the bound-state populations. This quenching will lower the effective radiation source strength and invalidate PLTE diagnostics, such as the line to continuum temperature method.[4] It seems likely that this quenching results from exothermic exchange reactions such as:



An approximate collisional/radiative model, incorporating four levels of argon and four levels of hydrogen with reactions such as the foregoing, has been successful in interpreting the qualitative behavior shown in Figure 3.2.

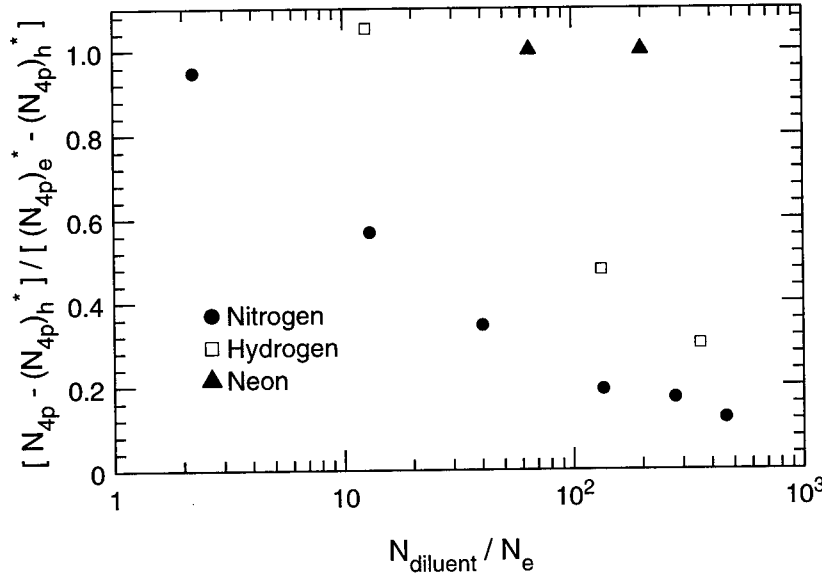


Figure 3.2 Quenching of argon 4p bound electronic level.

An interesting aspect of these experiments is that for the plasmas with nitrogen addition the elevated nonequilibrium electron density appears to be governed not by the usual electron three-body recombination, but rather by the (neutral) recombination of N to N<sub>2</sub>. Based on calculations for these conditions using CHEMKIN[5] with rates from the literature,[6, 7] the concentration of electrons and ionic species is governed by rapid dissociative recombination of N<sub>2</sub><sup>+</sup> and charge exchange between N<sub>2</sub><sup>+</sup>, N<sup>+</sup>, and Ar<sup>+</sup>. According to the CHEMKIN calculations, a partial equilibrium of these reactions establishes the charged-particle concentrations relative to N<sub>2</sub> and N, at least for nitrogen concentrations greater than 1%. More specifically, the CHEMKIN calculations for our conditions support to a good approximation the readily derived result that for partial equilibrium of the dissociative-recombination and charge exchange reactions:

$$\frac{n_e \text{Ar}^+ / \text{Ar}}{(n_e \text{Ar}^+ / \text{Ar})^*} = \frac{N^2 / N_2}{(N^2 / N_2)^*}$$

Here ( )<sup>\*</sup> denotes the equilibrium value of the concentration ratio in question. Similar results are obtained for N<sub>2</sub><sup>+</sup> and N<sup>+</sup>, with Ar<sup>+</sup>/Ar on the left-hand side replaced by N<sub>2</sub><sup>+</sup>/N<sub>2</sub> or N<sup>+</sup>/N. It is then the relatively slow recombination of N to N<sub>2</sub> through the test section that maintains and governs the electron-density overpopulation. This effect, if substantiated, may be of considerable importance for a range of plasma chemistry applications where molecular ions are present.

Our experience with recombining inductively coupled plasmas at temperatures below 10,000 K and electron densities below  $5 \times 10^{21} \text{ m}^{-3}$  indicates that LTE is not a reliable assumption for plasma diagnostics or plasma modeling. However, for a pure argon plasma partial equilibration between bound and free electrons can be a useful and practical approximation. Under PLTE conditions, electron density and electron temperature must be separately measured, for example, by continuum radiation and the line to continuum temperature method. The validity of this approximation can be checked by accessing several bound states with sufficient energy separation. Under PLTE conditions, the nonequilibrium

radiation source strength is independent of the ground-state density and proportional to the square of the nonequilibrium electron concentration.

Plasmas consisting of mixtures of species including molecules are considerably more complex. The addition of relatively small amounts of nitrogen or hydrogen to a recombining plasma otherwise in PLTE has been shown to produce a quenching of excited state populations, invalidating the usefulness of the PLTE approximation. Under such circumstances, one must resort to direct measurements. Stark broadening and absolute continuum intensities in the visible (as well as other methods) can be used for a direct measurement of the electron density. For the electron temperature, we have used the variation of the recombination radiation intensity with wavelength in the UV.[8] This method assumes only a Maxwellian electron translational velocity distribution function and a satisfactory knowledge of the recombination cross section through the so-called Biberman factor. Application of this method to our well-diagnosed argon plasmas shows good agreement under PLTE conditions with Boltzmann and line to continuum temperatures. For the gas temperature, since rotational equilibrium is likely for many conditions of interest, measurement of the relative intensities of rotational lines will in principle yield a rotational temperature which often can safely be assumed equal to the gas translational temperature. However, if this is done by conventional emission spectroscopy the usual Abel inversion of multiple lines can lead to unreliable results. A promising alternative is the measurement of rotational temperature (as well as species concentration) using laser-induced fluorescence. However, these laser-based point measurements are notably difficult to perform in a luminous plasma, as evidenced by the scarcity of reported verified results. The scattering measurements of line width reported by Snyder and Reynolds[9] are a notable exception. Another possibility for the measurement of the gas temperature is the use of wavelength tunable diode lasers to obtain Doppler line widths. Because of the weak temperature dependence and occurrence of other forms of broadening this measurement must be performed with unusual precision to provide useful results.[10]

### 3.2 More Complex Plasmas

Departures from equilibrium in the population of free-electrons in recombining thermal plasmas are normally attributed to finite rates for three-body electron recombination. Indeed, in atomic or fully dissociated molecular plasmas electrons recombine via reactions of the type  $X^+ + e + M \rightleftharpoons X + M$  (where  $X = N$  or  $O$ , and  $M$  is a third-body electron or heavy particle) which are relatively slow as they involve ternary collisions. If molecular ions are present in the plasma, electrons can recombine instead via the dissociative recombination reactions  $XY^+ + e \rightleftharpoons X + Y$ . The latter reactions are typically much faster and equilibrate more rapidly than three-body electron recombination reactions. Likewise, charge exchange reactions are generally fast as well. As a result, the preferential channel for electron recombination in molecular plasmas is via dissociative recombination, and the degree of ionizational nonequilibrium is ultimately determined by the rates of (three-body) atom recombination reactions:



Since these reactions are generally slow, we have the surprising result[11] that ionizational nonequilibrium in air plasmas is caused by finite-rate neutral chemistry. Reliable rates for atom recombination reactions are therefore required to correctly predict the extent of ionizational nonequilibrium. Unfortunately, many of these rates are not known with good accuracy, in particular at temperatures below 7000 K.[7]

In our laboratory, experiments have been conducted to assess the various rates proposed in the literature.[12-14] To this end, electron recombination was measured as a function of residence time in recombining plasmas flowing through water-cooled, 1 cm diameter brass test-sections mounted on the exit nozzle of the torch as shown in Fig. 2.1. As discussed below, three types of plasmas (air, nitrogen/argon, and air/argon) were investigated, each yielding an assessment of the rates of reactions 1 and 2 above.



### 3.2.1 Air Plasma Experiments

An air plasma flow, initially in equilibrium at a temperature of 7,160 K at the nozzle exit, was cooled to ~4,900 K within ~400  $\mu$ s over a distance of 25 cm. Temperature, electron number density, and line-of-sight spectral emission measurements were made at the exit of test-sections with lengths between 10 and 25 cm in 5 cm increments in order to examine plasma recombination as a function of residence time. Radial temperature profiles were obtained by Abel-inverting lateral profiles of the absolute intensity of the atomic oxygen triplet at 777.4 nm, and electron number densities were measured from the Stark broadening of the  $H_\beta$  line at 486.2 nm (to this end, a small quantity of ~1 slpm of  $H_2$  was premixed with 100 slpm of air before injection into the torch).

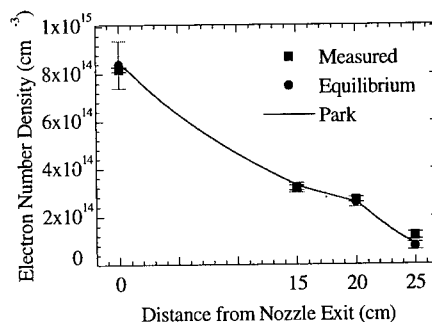


Figure 3.3 Measured and predicted electron number densities in air at 0, 15, 20, and 25 cm.

As can be seen in Fig. 3.3, the measured electron number densities were found to be close to their equilibrium values. Furthermore, the emission spectra were compared with equilibrium simulations performed with the accurate radiation code NEQAIR2[15, 16] recently developed by our group as an extension to the NASA code NEQAIR.[17] Differences between the measurements and LTE simulations would be indicative of nonequilibrium conditions in the experiment.[18] At all locations, however, the equilibrium radiation calculations reproduced all measured spectral features originating from the B state of  $N_2^+$ , the B and C states of  $N_2$ , the A, B, and C states of NO and the B state of  $O_2$  within experimental and modeling uncertainties. Thus the plasma remains close to equilibrium throughout the reaction zone.

These experimental observations were used to assess the reaction mechanisms proposed by Dunn and Kang,[12] Gupta et al.,[13] and Park.[14] To this end, the dynamic evolution of species concentrations along the axis of the plasma flow was modeled using the chemical kinetics solver CHEMKIN[19] and the three sets of ~30 reactions and rates.[12-14] Figure 3.4 shows the predicted nonequilibrium concentration factors, defined as the ratio of predicted to equilibrium mole fractions. Thus a value of unity indicates equilibrium, and a value greater than 1 indicates an overpopulation of the given species. Figure 3.4 also illustrates the rather poor understanding of the controlling rates of ionizational nonequilibrium, and the resulting uncertainty in the predicted electron concentration. As can be seen in Fig. 3.4, the mechanism of Park predicts that the air plasma remains close to equilibrium throughout the reaction zone, in agreement with our experimental observations, whereas the mechanisms of Dunn and Kang, and Gupta et al. predict departures from equilibrium in the electron number density by up to a factor 3 at the exit of the 25 cm test-section. Since overall plasma recombination, and in

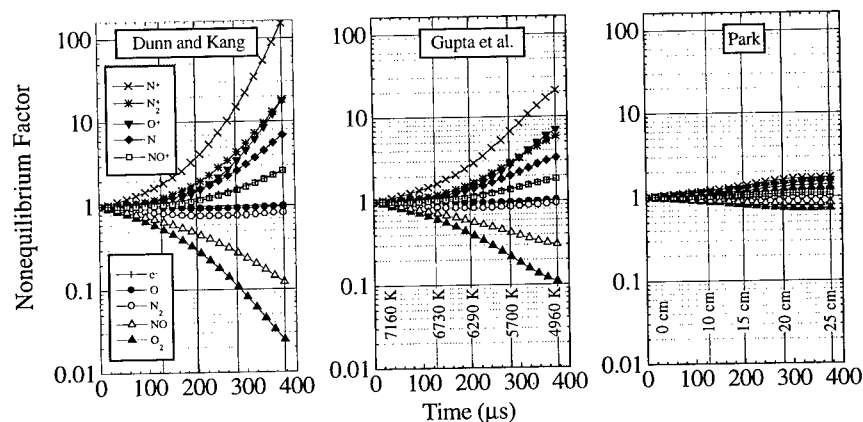


Figure 3.4 Nonequilibrium factors predicted by three reaction mechanisms for the recombining air plasma.

particular electron recombination, is mainly controlled by the rate of Reaction 1 under these conditions, it appears that the rate of Reaction 1 should be at least as fast as the rate proposed by Park.[14]

### 3.2.2. Nitrogen/argon plasma

To assess the rate of  $N + N + M \rightleftharpoons N_2 + M$  (Reaction 2), separate experiments were conducted with a nitrogen plasma (100 slpm  $N_2$ ), premixed before injection into the torch with 50 slpm of argon to provide stable operating conditions, and 2.3 slpm of  $H_2$  for electron density measurements. The plasma recombined over a length of 15 cm and within 250  $\mu s$  from 7200 to 4700 K. Measurements were made at the 0, 10 and 15 cm locations. Temperature profiles were obtained from the Abel-inverted intensities of lines of argon (763.5 nm) and hydrogen ( $H_\alpha$  and  $H_\beta$ ), and of the band head of the  $N_2^+$  (B-X) transition. As shown in Fig. 3.5, electron number densities at 0 and 10 cm were found to be close to equilibrium. In contrast, at 15 cm an electron overpopulation factor of  $135 \pm 60$  was observed, consistent with (although higher than) the value of 45 predicted with Park's mechanism (see Fig. 3.5). Since here electron recombination is controlled by the rate of Reaction 2, we concluded that the rate proposed by Park for that reaction is accurate to within approximately a factor three over the considered temperature range. Further work is in progress[20] using a quantitative coupled flow-chemistry model to provide a definite assessment and, if necessary, a corrected value for this rate.

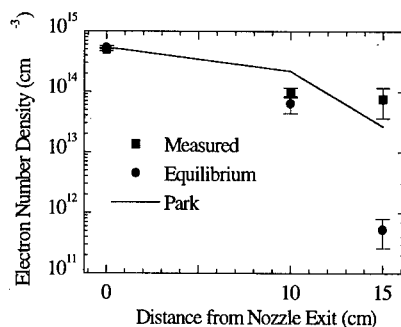


Figure 3.5 Electron number densities in the nitrogen/argon plasma.

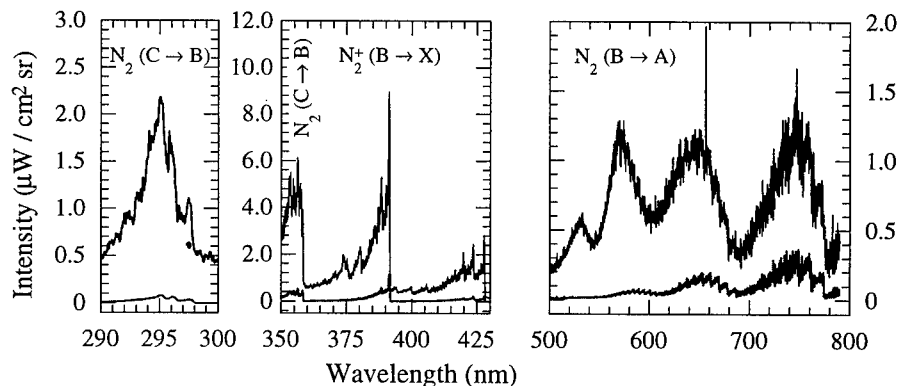


Figure 3.6 Nitrogen/argon plasma at 15 cm downstream of nozzle exit: Measured spectrum (black) and computed LTE spectrum (grey).

We obtained experimental confirmation of the slow recombination of N atoms from spectral emission measurements at 15 cm where the excess free electrons appears conjointly with a significant enhancement of the populations of the B and C states of  $N_2$ . This can be seen in Fig. 3.6 wherein the measured spectrum appears much more intense than the computed equilibrium spectrum, unlike the case at 0 and 10 cm where the two spectra agree to within better than 10%.<sup>9</sup> For the B state of  $N_2$ , the observed difference indicates large departures from a Boltzmann distribution in the vibrational levels. The measured vibrational overpopulation distribution (Fig. 3.7) is characteristic of the Lewis-Rayleigh afterglow mechanism[21] by which N atoms recombine preferentially into levels 10-12 of the B state of  $N_2$  and thus produce the observed vibrational distribution when an excess of N atoms exists. Similarly,

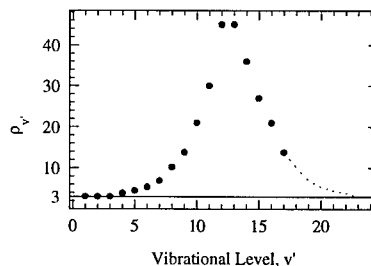


Figure 3.7 Measured vibrational overpopulation in the  $N_2$  B state.

the populations of the  $N_2$  C state vibrational levels are partially coupled to the population of N atoms as a result of fast inverse predissociation.[18] The overpopulation factors for these levels, measured to be approximately 32, therefore confirm the presence of N overpopulation.

The foregoing observations clearly show that under nonequilibrium conditions great care must be exercised when interpreting both temperatures and concentration measurements.

### 3.2.3. Air/argon experiments

To provide a better assessment of the rate of Reaction 1 (on which the pure air studies permitted us to place a lower limit), experiments were conducted with a ~10% air - 90 % argon plasma cooled from 7,900 K to approximately 2,700 K over a time of ~1.3 ms and a distance of 65 cm. Dilution of ~10% air in argon causes the recombination of nitrogen atoms to be about one order of magnitude slower than in the pure air plasma case as the third body efficiency of argon in Reaction 1 is approximately 20 times smaller than the third body efficiencies of N and O atoms. By slowing the overall N atom recombination, it should be possible to observe significant chemical and ionizational nonequilibrium, and thus to place an upper limit on the rate of Reaction 1. Even at this relatively high dilution level, the electron recombination path remains the same as in pure air because electrons still recombine preferentially via the dissociative recombination reaction  $NO^+ + e \rightarrow N + O$ , even though  $NO^+$  is no longer the dominant ion here.

Experiments were conducted with 15.6 slpm of air premixed with 162 slpm of argon and a small quantity (2.3 slpm) of  $H_2$  for electron number density determinations. Optical emission was collected at the end of test sections ranging from 0 cm (nozzle exit) to 65 cm in length. Because the temperature varies from ~8000 K at the nozzle exit to ~2500 K at the 65 cm test section exit, various techniques were employed to obtain temperatures and electron number densities. At 0, 10, and 15 cm, temperature profiles were obtained from the Abel-inverted line intensities of oxygen (777.3 nm), argon (763.5 nm) and hydrogen ( $H_\alpha$ ). At each location, the temperatures determined from the three atomic lines were found to agree within 150 K. At 40, 50, and 65 cm, the excited state populations of atomic species could not be seen in emission, but the temperatures could still be accurately measured from the temperature sensitive shape of the measured OH  $A^2\Sigma^+ \rightarrow X^2\Pi_i$  band. This was done by comparing numerical OH spectra[22] at various temperatures normalized to the 309.2 nm peak to the measured line of sight spectra. This shape-matching technique yields centerline temperatures with an accuracy of ~200 K. The remainder of the temperature profile was obtained from the Abel-inverted intensity of the 306.8 nm peak relative to the 304 nm baseline. More details can be found in Ref.[23].

The overpopulation factors shown in Fig. 3.8 were computed with CHEMKIN using the rates of Park[14] for air and appropriate rates for reactions with argon and hydrogen.[18] In Fig. 3.9, the measured electron number densities are compared with those predicted using Park's mechanism. At 0, 10, and 15 cm, direct measurements of  $n_e$  were made via the Stark broadening of the  $H_\beta$  line at 486.1 nm. Error bars on these data points (Fig. 3.9) reflect uncertainties on measured electron number densities and on centerline temperatures. At the exit of longer test-sections, the intensity of the  $H_\beta$  line was very weak and therefore no direct measurements of electron number densities could be made. However, as discussed in Ref.[23], the electron number density at these locations could be determined from the measured overpopulation factors of the C state of NO.

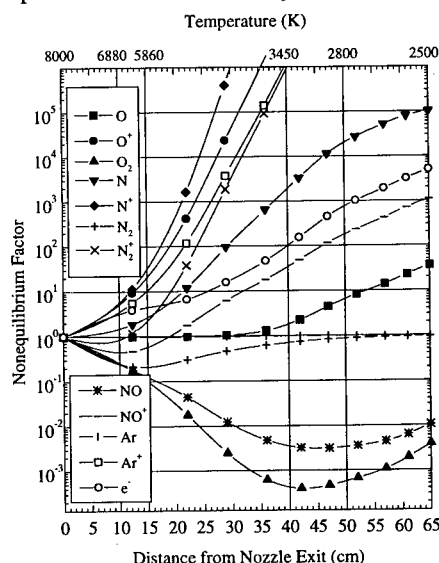


Figure 3.8 Predicted nonequilibrium factors for the recombining air/argon plasma (Park's mechanism).

Since the three body recombination of NO accounts for about 38 to 20 % of the total N atom consumption between 15 and 60 cm downstream of the nozzle exit (the balance being due to the Zeldovich reactions whose rates can be considered well known), the rate of  $N + O + M \leftrightarrow NO + M$  may be too slow. While Park concludes that this rate is known within a factor three,[7] examination of his compilation of relevant NO thermal dissociation rate measurements seem to warrant a factor ten uncertainty on this rate. As discussed in Ref.[23], multiplying the third body efficiencies in Reaction 1 by a factor 10 improves the agreement between measurements and predictions for test-sections  $\leq 45$  cm, but produces a recombination rate that is too fast at longer distances. Several issues must be examined in order to draw more definite conclusions about these third body efficiencies. First, a detailed collisional-radiative model is warranted to better determine the degree of coupling between the NO C state and N and O atoms. And second, possible departures from a Maxwellian distribution for the free-electrons and their consequences on rate coefficients must be considered. A preliminary analysis of these effects indicates that departures from a Maxwellian distribution may occur at locations  $> 35$  cm.[23] These various issues are currently being examined in order to provide a better assessment of the rate of NO three-body recombination.

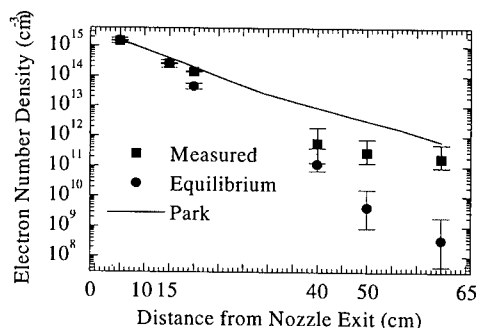


Figure 3.9 Electron number densities in the air/argon plasma.

### 3.3 Diagnostics of Diamond Synthesis Environments

Over the past several years, we have investigated the nonequilibrium synthesis of diamond thin films in several high and low pressure facilities. Although the diamond synthesis environment is quite challenging to investigate due to its highly nonequilibrium neutral and plasma chemistry, it is also within reach of state-of-the-art numerical simulations based on relatively well established systems research. We have made extensive use of laser-based diagnostics and comparisons with sophisticated models to learn about the process of diamond Chemical Vapor Deposition (CVD).

#### 3.3.1 Degenerate Four-Wave Mixing (DFWM)

It is quite difficult, for many diagnostic techniques, to provide useful and accurate information in the harsh and nonequilibrium environment of atmospheric pressure PACVD of diamond thin films. Sensitive measurement of temperature and trace radical concentrations within a reacting boundary layer is a challenging problem due to the highly luminous environment, small spatial scales, and steep thermal and concentration gradients. It is in this environment where the application of sensitive, laser based diagnostic techniques can allow the detailed measurement of temperature and trace radical concentrations to be made, and compared to models of the deposition environment. The application of a powerful non-linear laser spectroscopy, degenerate four wave mixing (DFWM), as a gas-phase optical diagnostic has opened the door for significant advancement in the area of atmospheric pressure plasma chemistry, since it can provide high sensitivity and spatial resolution with a coherent, phase conjugate signal which can be readily discriminated against the plasma.[24-27]

The DFWM technique[28] utilizes three laser beams of a single wavelength interacting with the plasma to produce a fourth spatially coherent, polarized signal beam that can be collected with high efficiency, and effectively filtered from the intense plasma luminosity. This feature is perhaps the greatest advantage of DFWM over other traditional diagnostic tools of atmospheric pressure plasmas which are often disabled or corrupted by the intense background luminosity. In thermal plasma CVD, we find DFWM to be an extremely useful nonintrusive probe of the plasma, capable of providing high spectral and spatial resolution, and permitting measurements of temperature and relative species concentrations of trace radicals under conditions in which other spectroscopic techniques fail. Since DFWM can be used to probe the ground state of electronic transitions, it is much less subject to

misinterpretation as a result of nonequilibrium effects[29] than conventional techniques such as optical emission spectroscopy (OES).

In a program to investigate the thermal plasma diamond CVD environment, experiments were conducted using the RF plasma torch facility, inside a water cooled quartz test section which is shown in schematic cut-away along with the plasma torch head in Figure 3.10. Open-ended laser access ports, approximately 6.5 cm downstream of the nozzle exit, enable the DFWM pump and probe beams to enter and exit the reactor unhindered, and to cross at a location directly below the stagnation point of a diamond growth substrate. Substrates are supported within the quartz test section in a stagnation point flow geometry by means of a water cooled holder. The substrate can be vertically translated in-situ to allow laser measurements to be made at various points through the boundary layer. Substrate temperature is monitored with a Minolta/Land Cyclops 152 infra-red optical pyrometer. Reactant gases (hydrogen and methane) are premixed with the carrier gas (argon) before passage through the RF discharge.

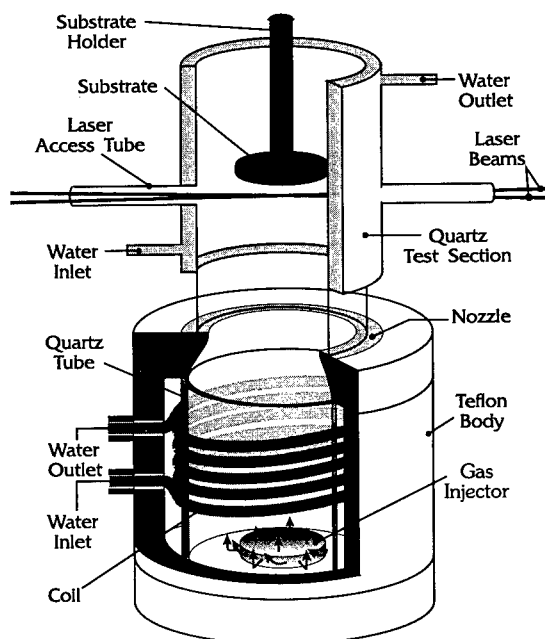


Figure 3.10 Schematic of RF-ICP reactor.

In these studies, DFWM was used to perform in-situ measurements of the trace radical CH to determine vibrational temperatures, rotational temperatures, and relative species concentration measurements (including profiles of these quantities through the reacting boundary layer above the growth substrate), and compared to results of a detailed one-dimensional model[30] of the deposition environment. It was desired to make in-situ measurements during normal operation of the atmospheric pressure RF-ICP diamond synthesis reactor - with a substrate in place, and growing diamond. The conditions chosen for these studies were indeed diamond growth conditions (although they were not optimized for best possible growth) and all measurements reported here were taken with the growing substrate in place. The reactor gas feed mixture was comprised of 106.5 l/min Ar, 12.0 l/min H<sub>2</sub>, and 0.8% to 10% CH<sub>4</sub> (in H<sub>2</sub>) premixed before introduction to the plasma torch. Calorimetric energy balance of the reactor indicates a net plasma enthalpy of 6 kW leaving the nozzle exit. The molybdenum substrate had a measured surface temperature of 1035°C.

The CH radical was probed with in-situ DFWM measurements of the CH  $A^2\Delta \leftarrow X^2\Pi$  (0,0) system near 431 nm. A comparison of measured CH vibrational and rotational temperatures along the stagnation line of the substrate with values from the computational simulation is shown in Figure 3.11. Boundary conditions for the simulation are the measured freestream temperature of 3900 K, an estimated freestream velocity of 8 m/s, and the measured substrate temperature of 1035°C. We can see in Figure 6 the predicted thermal boundary layer ( $\approx 6$ mm thick) with a steep fall off in temperature very close to the substrate. The measured CH vibrational temperatures are in close agreement with the predictions, although the loss in signal of the  $v=1$  transitions in the cooler region very near the substrate prevents accurate vibrational temperature measurement for distances  $< 2$ mm. Rotational temperatures measurements from the CH  $v=0$  lines, which remain strong enough for accurate measurement closer to the substrate are in good agreement with both the measured vibrational temperatures and the computational simulation. It is possible to make rotational temperature measurements even closer to the substrate than shown in Figure 3.11, but for these experimental conditions the CH concentration in that region has dropped below approximately 2 ppm, which is our current detection limit.

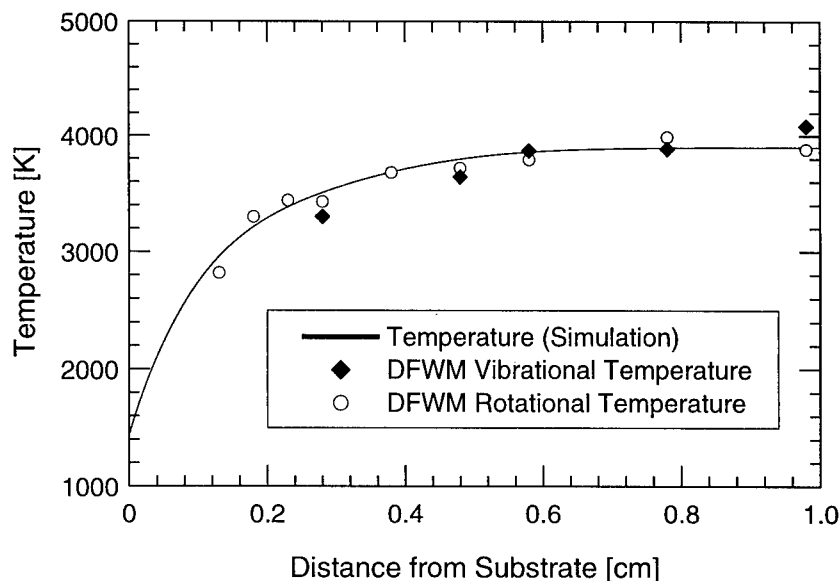


Figure 3.11 Boundary layer temperature profiles.

Measurements of the relative CH mole fraction within the substrate boundary layer are compared to results of the computational simulation in Figure 3.12. The CH mole fraction is approximately 30 ppm in the freestream (3900 K) and is predicted to first rise within the approximately 6 mm thick boundary layer (due to production) as the plasma cools toward approximately 3700 K, reaching a peak of approximately 52 ppm at 2.5 mm from the substrate surface, then to be destroyed as the plasma cools further on its approach to the substrate surface.

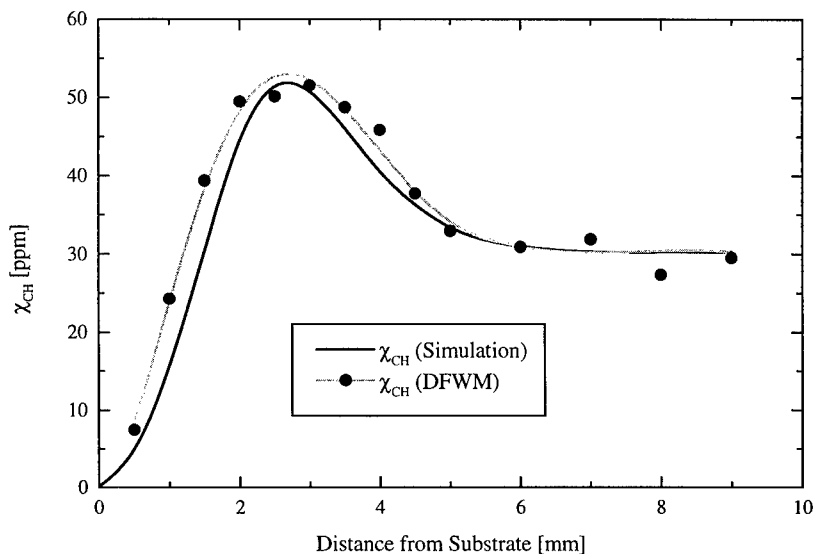


Figure 3.12 CH concentration profile.

A more direct insight into the boundary layer chemistry can be gained by comparing the CH mole fraction throughout the boundary layer to its equilibrium value at the measured local temperature. This is displayed in Figure 3.13a where we can observe the CH to remain near its equilibrium values until approximately 2 mm from the substrate surface where it then rises to approximately 1000 times the

equilibrium value close to the surface. The measured nonequilibrium is in close agreement with the predicted values. By studying the numerical simulation, we find that this nonequilibrium observed in the CH mole fraction is in fact driven by the atomic hydrogen chemistry. The timescale of transit through the boundary layer is insufficient for the atomic hydrogen recombination mechanisms to maintain atomic hydrogen concentration in equilibrium with the local gas temperature. The calculated atomic hydrogen nonequilibrium is shown in Figure 3.13b. The fast reactions between atomic hydrogen and the  $\text{CH}_x$  hydrocarbons maintains a partial equilibrium amongst these species, and thus an overpopulation of atomic hydrogen maintains an overpopulation of all  $\text{CH}_x$  hydrocarbons (notably  $\text{CH}_3$ , thought to be the major growth precursor). The interrogation of this environment using DFWM has thus allowed us to see that the nonequilibrium behavior of atomic hydrogen chemistry is a critical component to the atmospheric pressure synthesis of diamond thin films.

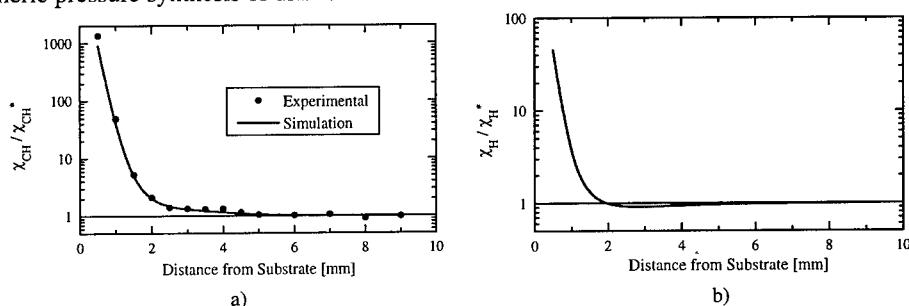


Figure 3.13 a) CH nonequilibrium profile, b) atomic hydrogen nonequilibrium profile.

### 3.3.2 Cavity Ring-Down Spectroscopy (CRDS)

The methyl radical has fundamental importance for studies of diamond film growth by chemical vapor deposition (CVD) because it is regarded as a gas-phase precursor of the diamond film.[31-33] Therefore, starting with the first report in 1988[34] on infrared detection of  $\text{CH}_3$  during filament-assisted growth of diamond, several techniques have been applied to monitor methyl radicals in a CVD reactor, including REMPI spectroscopy [35-39], UV absorption spectroscopy [40, 41], and mass spectrometry [42]. These techniques, however, can be intrusive (as in the case of REMPI) and of limited spatial resolution (mass spectrometry) and sensitivity (absorption). The  $\text{CH}_3$  mole fraction in a CVD reactor has been also modeled,[43] and the relation between the model predictions and growth rate and film quality has been studied.[44, 45]

We have developed diagnostics for the methyl radical based on the cavity ring-down technique (CRDS).[46-50] CRDS is a highly sensitive absorption spectroscopy that determines the absolute absorbance of a laser pulse passing through a sample. In a manner similar to single-pass laser absorption spectroscopy, this measurement is performed with two-dimensional spatial resolution; however, unlike the case of single-pass absorption spectroscopy, CRDS measures absorbance as low as  $10^{-5}$  -  $10^{-7}$  and is insensitive to shot-to-shot power fluctuations in the laser pulses. These features make CRDS suitable for high sensitivity measurements.

The hot-filament reactor (shown in Figure 2.3) consists of a 5-way stainless steel cross 4 inches in diameter. A two-stage mechanical pump (E2M40, Edwards) is used to evacuate the chamber to the minimum pressure of  $4 \times 10^{-3}$  Torr. The chamber is filled with 20 Torr mixture of  $\text{H}_2$  with 0.5 % of  $\text{CH}_4$  flowing at a rate of 100 sccm. The tungsten filament is 20 mm long and 200  $\mu\text{m}$  in diameter. It is positioned horizontally inside the chamber using two tungsten posts, 4 cm long and 1.5 mm in diameter, mounted on water-cooled copper electrodes. The filament is resistively heated with dc current to a brightness temperature of 2300 K, which is monitored with a disappearance pyrometer (Pyro Micro-Optical Pyrometer). The substrate is made of a molybdenum strip (4 mm x 20 mm x 250  $\mu\text{m}$ ) and is resistively heated. The substrate temperature is monitored with a K Type thermocouple which is welded to the rear surface. The front surface is scratched with 10  $\mu\text{m}$  diamond paste. The reactor condition is stabilized for more than 12 hours before CRDS measurement. In these studies, the ring-down cavity is

62 cm long with mirrors mounted in 1.5 inch thick aluminum blocks separated with four stainless steel rods 3/4 inch in diameter for cavity stability. The reactor is placed inside this cavity frame and connected to the mirror mounts by means of flexible bellows. A laser pulse injected into the cavity circulates back and forth along the same path between the cavity mirrors, crossing the reactor parallel to the filament and substrate. The distance between the filament and the pulse path is controlled with a micrometer that moves the reactor on a translation stage.

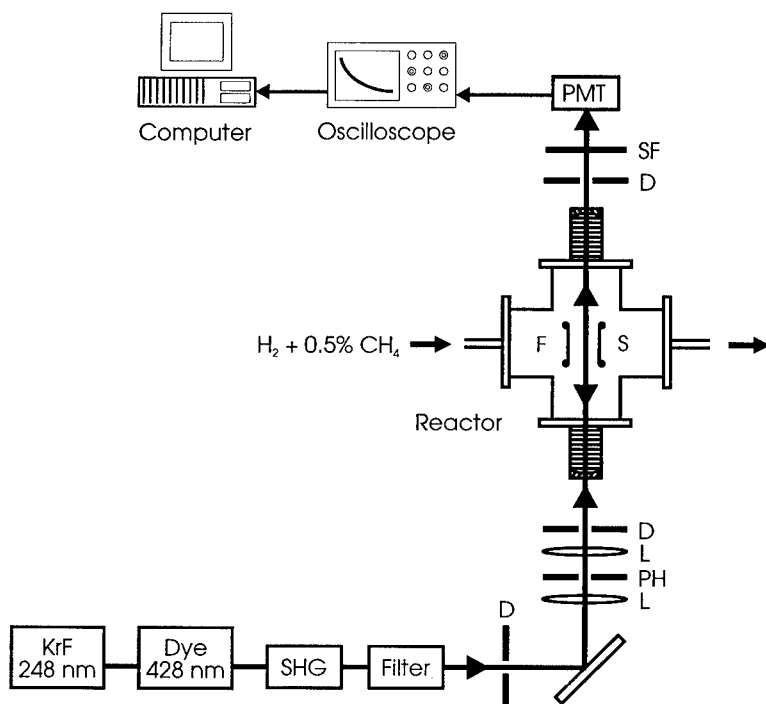


Figure 3.14 Schematic of the CRDS system / hot-filament reactor. D = iris diaphragm, L = lens, PH = 50  $\mu$ m pinhole, SF = spectral filter, F = Filament, and S = substrate.

determined directly by the ring-down time  $\tau_0$  of the empty cavity. The  $\text{TEM}_{00}$  cavity mode has approximately a cylindrical form with a waist of 0.5 mm in diameter.

The light transmitted through the back mirror of the cavity was collected by a photomultiplier (PMT) and the PMT signal as a function of time was recorded on an HP 54510A digitizing oscilloscope with 2 ns temporal resolution. The ring-down waveforms digitized on the oscilloscope were transferred to a PC computer, averaged, and the ring-down time  $\tau$  was obtained from a real-time computer fit. The  $\text{CH}_3$  absorbance is then obtained from the measured  $\tau$  and  $\tau_0$  via the relation  $\alpha l_s = \tau_r/2(1/\tau - 1/\tau_0)$ , where  $\tau_r$  is the cavity round-trip time, and  $l_s$  is the sample length.

Figure 3.15 shows spatial profiles of the  $\text{CH}_3$  number density (absorbance) within the hot-filament reactor at two different substrate temperatures. The filament temperature is held constant at 2300 K, the total pressure is 20 Torr, and the gas mixture is 0.5%  $\text{CH}_4$  in  $\text{H}_2$  flowing from left to right at a flowrate of 100 sccm. One can observe that the concentration of methyl radicals falls rapidly with increasing distance from the filament, and that the methyl radical concentration increases significantly at the higher substrate temperature. It is interesting to note that the methyl concentration well upstream of the filament is strongly influenced by the substrate temperature, possibly due to an overall increase in the reactor temperature field and hence methyl radical production. One can also observe that for the 900  $^\circ\text{C}$  substrate condition that the peak methyl concentration occurs at a distance away from the filament (approx. 2 mm). This peaked result agrees qualitatively with the behavior of the  $\text{CH}_3$  REMPI signal as a function of a distance from the filament reported by Ota and Fujimori,[39] but the peak  $\text{CH}_3$

The schematic of our CRDS setup is shown in Figure 3.14. An excimer-laser-pumped dye laser (Lambda-Physik) working with Coumarin 440 was used as the pulse source. The pulses were 15 ns long with 0.18  $\text{cm}^{-1}$  linewidth. After frequency doubling in a BBO crystal with an Inrad Autotracker, the 214 nm pulse was shaped with the system of pinholes and lenses to match approximately the  $\text{TEM}_{00}$  transverse mode of the optical cavity. The quasi-hemispherical optical cavity was 62 cm long with a flat entrance mirror and a 2 m curvature concave back mirror. The mirrors were coated by Lightning Optical Corp. and achieved 98.9 % reflectivity at 213.9 nm, as

The  $\text{TEM}_{00}$  cavity mode has



concentration we find is two orders of magnitude higher than their estimate. Goodwin, Glumac, and Corat[38] also measured spatial profiles of the  $\text{CH}_3$  REMPI signal in the hot-filament reactor; however, their data do not extend to positions close to the filament and cannot be directly compared with our observations.

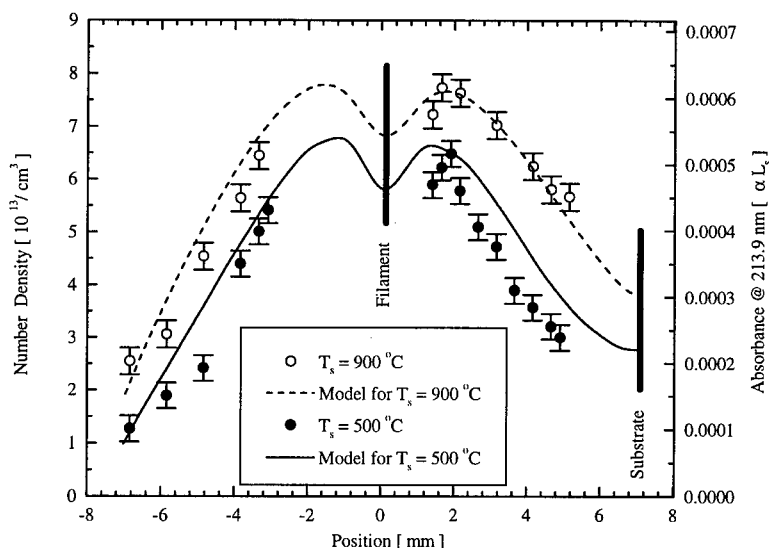


Figure 3.15 Spatial profiles of the measured  $\text{CH}_3$  number density (absorbance) within the hot-filament reactor at two different substrate temperatures along with the model predictions of Mankelevich. The filament temperature is 2300 K, the total pressure is 20 Torr, and the gas mixture is 0.5%  $\text{CH}_4$  in  $\text{H}_2$  flowing from left to right at a flowrate of 100 sccm.

Figure 3.15 also shows the methyl radical concentration profile predicted by the two-dimensional model of Mankelevich et al.[51, 52] for the same reactor conditions probed experimentally. In this two-dimensional model conservation equations for species, mass, momentum, and energy are solved including molecular and thermal diffusion, along with chemistry for 15 species via 38 reversible reactions. Temperature “slips” at the filament and substrate surface are prescribed from a separate Monte Carlo simulation. The largest uncertainty in this model is the production rate of atomic hydrogen at the filament surface. The results of the model prediction are in good agreement with the experimental measurements both in shape and relative magnitude for the two cases presented. Deviation of the model and experimental data near the substrate in the case of  $T_{\text{sub}}=500^\circ\text{C}$  is most likely due to the sensitivity of methyl radical production to the local gas temperature.

Methyl radical number density measurements were also taken very near the substrate surface (within  $\sim 0.5$  mm) as a function of both substrate and filament temperature. Results of those measurements are shown in Figures 3.16 and 3.17 respectively. In both cases the reactor pressure was 20 Torr with a mixture of 0.5%  $\text{CH}_4$  in  $\text{H}_2$  flowing at a rate of 100 sccm, and the substrate prepared by operating at diamond growth conditions of  $T_f = 2300$  K,  $T_s = 900^\circ\text{C}$  for approximately 12 hours. In Figure 3.16, the filament temperature was held at 2300 K while the substrate temperature was increased from  $600^\circ\text{C}$  to  $1200^\circ\text{C}$ . The power to the substrate was increased after each data point by increments of approximately  $50^\circ\text{C}$  and allowed to stabilize for 10 minutes before the next point was taken. One can see an approximately linear increase in the near surface methyl radical concentration with increasing substrate temperature. This is in qualitative agreement with the results of Corat and Goodwin[37] for the near surface region, although our data does not extend to high enough temperature to confirm their observed high temperature roll-off in methyl concentration. Our observed activation energy of the near surface radical concentration, based on substrate temperature, is  $4.2 \pm 0.2$  kcal/mol. This value agrees with the value reported by Corat and Goodwin.[37]

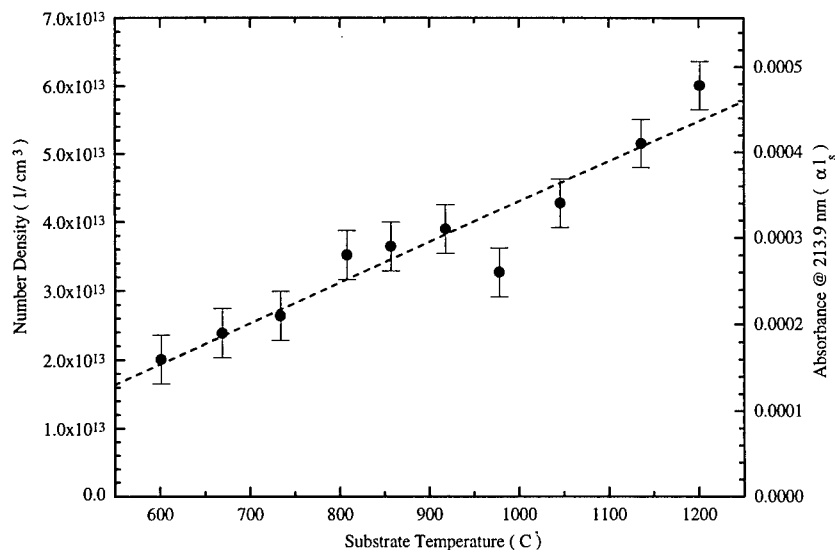


Figure 3.16 Variation of the  $\text{CH}_3$  number density (absorbance) near the substrate surface (within  $\sim 0.5$  mm) as a function of substrate temperature. The filament temperature is 2300 K, the reactor pressure is 20 Torr, and the gas mixture is 0.5%  $\text{CH}_4$  in  $\text{H}_2$  with a flowrate of 100 sccm.

In Figure 3.17, the substrate temperature was held at 900 °C while the filament temperature was increased from approximately 2000 K to approximately 2550 K. We observe the near surface methyl concentration to first increase strongly with increasing filament temperature, and then to saturate somewhat above 2400 K. This strong increase is in qualitative agreement with the REMPI measurements of Corat and Goodwin,[37] but we do not observe a decrease in methyl concentration above 2300 K as evident in their measurements. Our data trends do, however, compare favorably to the model predictions of Kondoh et al.[44]

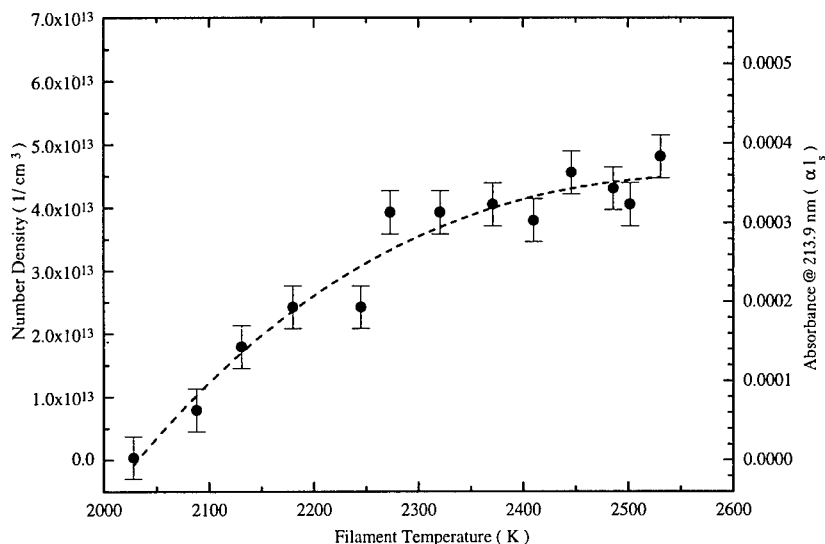


Figure 3.17 Variation of the  $\text{CH}_3$  number density (absorbance) near the substrate surface (within  $\sim 0.5$  mm) as a function of filament temperature. The substrate temperature is 900°C, the reactor pressure is 20 Torr, and the gas mixture is 0.5%  $\text{CH}_4$  in  $\text{H}_2$  with a flowrate of 100 sccm.

On the basis of our observations we conclude that the CRDS technique can be used for quantitative diagnostic of methyl radicals with high sensitivity. We have applied CRDS to the measurement of methyl radicals generated in a hot-filament reactor. We have observed a strong sensitivity of the methyl radical concentration throughout the reactor to the substrate temperature. At some operating conditions, we also observe the methyl radical concentration to peak at the location several mm from the filament surface. This behavior of  $\text{CH}_3$  with distance from filament is not predicted by current one-dimensional models of the reactor. This off-filament maximum concentration indicates that the methyl is not generated at the filament surface, but rather by gas-phase reactions. The near surface concentration of methyl is observed to increase linearly with increasing substrate temperature, and is found to increase and saturate with increasing filament temperature.

### 3.3.3 Two-photon Atomic Laser Induced Fluorescence (TALIF)

Atomic hydrogen plays an important role in the diamond synthesis environment by affecting both the quality and quantity of diamond films produced. With this in mind, the need to nonintrusively detect and monitor ground state atomic hydrogen, and probe its role in nonequilibrium chemistry becomes quite clear. Unfortunately, due to the large energy spacing between the ground state of atomic hydrogen and its first excited state (10.2 eV), single photon optical techniques would require wavelengths of 121.5 nm in the vacuum ultraviolet. This wavelength is strongly absorbed by most materials, and only propagates easily through vacuum. These drawbacks have led to the application of two photon laser based techniques such as two photon atomic laser induced fluorescence (TALIF).

The TALIF technique uses two photons of laser light to promote a ground state atom to one of its excited states, and monitors the resultant fluorescence (either to another excited state or to the ground state). In this manner, a laser of longer wavelength (243 nm for the Lyman  $\alpha$  transition) can be utilized, and is much easier to produce and propagate. We have carried out preliminary experiments to develop and use a TALIF technique to detect ground state atomic hydrogen in a hot-filament reactor. The TALIF technique we are using is shown schematically in Figure 3.18 below. In this technique, a ground state atomic hydrogen atom absorbs two photons from a 243 nm laser field, and is promoted from the  $1S$  state to the  $2S$  state. The  $2S$  state is collisionally coupled to the nearly iso-energy  $2P$  state and the two states rapidly equilibrate. The subsequent fluorescence from the  $2P$  state to the  $1S$  state (Lyman  $\alpha$  at 121.5 nm) is then be detected with a solar blind PMT whose photocathode is placed within the hot filament reactor. A sample spectra taken within the hot filament reactor is shown below in Figure 3.19. In this case, the reactor was filled with 20 Torr of  $\text{H}_2$ , and the spectra was measured 4.5 mm from the filament surface.

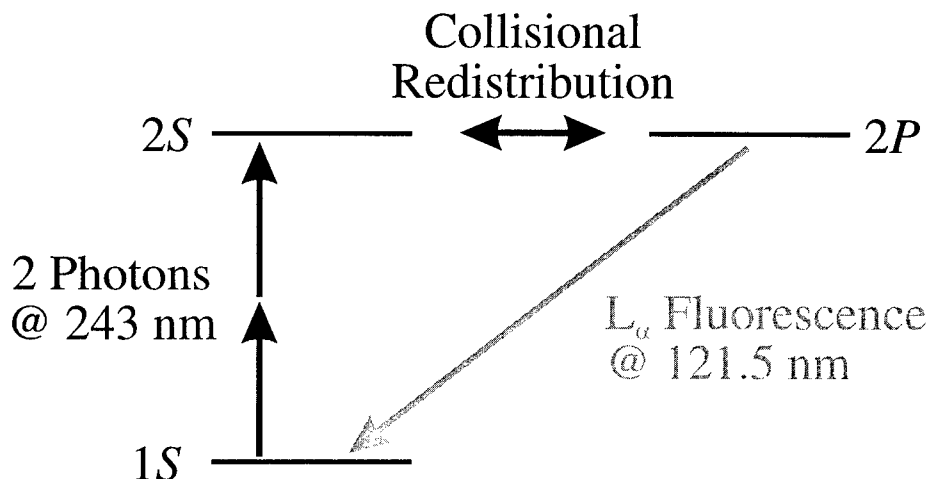


Figure 3.18 Schematic of the TALIF technique for atomic hydrogen detection.

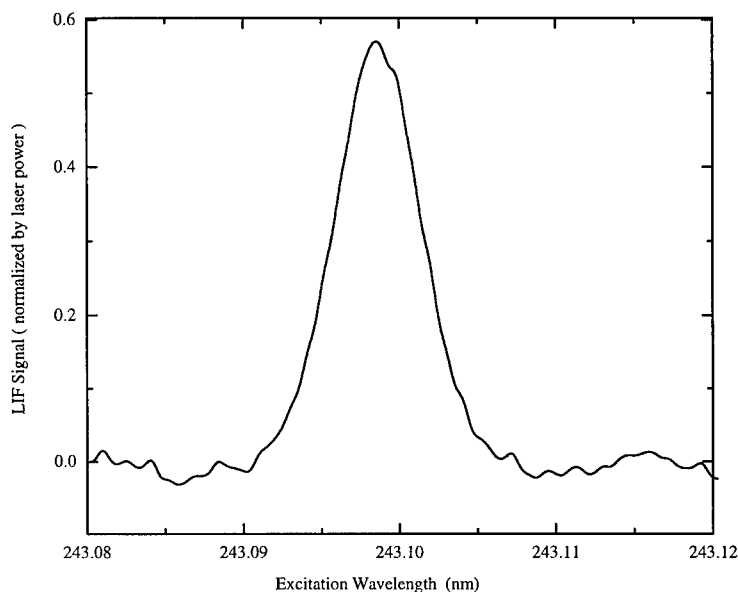


Figure 3.19 TALIF spectra of atomic hydrogen in a hot filament reactor.

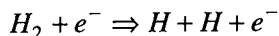
Using this TALIF technique, we are developing methods to determine both the concentration and temperature of ground state atomic hydrogen with the hot filament reactor. These measurements, in conjunction with CRDS measurements of the  $\text{CH}_3$  radical will yield an important database of experimental measurements to which models of the deposition environment may be compared.

### 3.4 Discharge Induced Nonequilibrium Plasma Chemistry

Several radical species in the diamond growth environment are thought to contribute to the deposition of the diamond thin-films. Of these, atomic hydrogen is believed to be particularly important.[53-55] Atomic hydrogen makes surface sites available to carbon containing species needed for the diamond growth process by abstraction of surface hydrogen. Atomic hydrogen also acts to incorporate adsorbed hydrocarbon radicals into the diamond lattice. Carbon containing radical fluxes factor directly into the diamond growth rate, as they are the source of carbon for continued diamond growth,[55] and are often strongly linked to the available atomic hydrogen concentration.

There are several ways to increase the radical concentration at the growth surface, leading to rapid growth of high-quality diamond. It has been shown[56, 57] that by increasing the plasma velocity, the boundary layer thickness above the deposition surface is thinned. This effect decreases the time available for recombination of radical species that are created in the freestream and the boundary layer as they approach the substrate. This can lead to higher fluxes of these species to the growth surface and higher growth rates of CVD diamond. A factor of 5 increase in growth rate has been observed when the plasma velocity was increased by an order of magnitude.[56] Additionally, recent analysis of scaling relations for convection-dominated reactors has found that the use of high pressure ( $\geq 1$  atm), sonic flow conditions will maximize the H atom concentration delivered to the deposition surface.[53, 54] A different approach to increase radical fluxes to the deposition surface involves actively driving the boundary layer chemistry to a greater degree of nonequilibrium by means of discharge induced plasma chemistry.[58-60] Matsumoto, et al. [60, 61] applied a positive potential to the deposition surface in a sub-atmospheric dc arcjet and found a twofold increase in diamond growth rate as compared with an unbiased case, although the deposited films had a low degree of uniformity across the deposition surface. They implied that an enhancement in gas phase dissociation near the substrate was the cause for the increased deposition rate.[61] Conversely, negative-biasing of the substrate has been used in low pressure, microwave reactors to enhance and control the nucleation of CVD diamond.[62, 63]

We have conducted preliminary experiments to address the secondary discharge method as a means of augmenting the deposition rate while maintaining a high degree of film quality. By biasing the deposition surface with respect to the plasma, the free electrons gain kinetic energy from the imposed electric field. These energetic electrons can promote super-equilibrium concentrations of radical species in the boundary layer via bond-breaking collisions with the molecular species. In particular these electrons can shift the balance of important dissociation reactions such as



to produce elevated concentrations of atomic hydrogen. Calculations[59] of flowing plasmas with elevated electron temperatures have shown that increased dissociation of hydrogen is possible with moderate discharge currents and voltages. In the case of a recombining plasma approaching a water cooled substrate, energetic electrons can decrease the recombination rate of radical species (specifically atomic hydrogen) which have shown to be important in the diamond CVD process.

Diamond deposition experiments were performed in the DC arcjet facility (Figure 2.2) over a range of substrate biasing conditions while all other reactor conditions were held nominally constant. A hot-pressed boron nitride insulator was used on the substrate assembly to confine the discharge current and the deposition area to the 1.25 cm<sup>2</sup> area of the molybdenum rod. The secondary discharge was produced by a bank power supplies, capable of delivering a biasing voltage of up to +400 V to the deposition surface. The substrate temperature was monitored with an infrared optical pyrometer. The flow rates of the feed-gases for these experiments were 450 slpm of argon, 4.25% hydrogen in argon, and 2.44% methane in hydrogen. In the cases reported here the substrate temperature was maintained at 1125°C±25°C, and all the deposition times were one hour. Highly uniform films were deposited, covering the full area of the substrate.

The deposited films were measured for cross-sectional film thickness using scanning electron microscopy. A summary of growth rate as a function of current density through the secondary discharge can be seen in Figure 3.20. A factor of seven increase in the growth rate was observed with a significant bias current (4.9 cm<sup>2</sup> at 170 V) compared with the floating substrate case for these conditions. There appears to be a threshold current of ~2.4 A/cm<sup>2</sup> that must be reached in the secondary discharge before an increase in growth rate is observed. This threshold may be related to the energy required to increase the electron temperature to a critical value. At this point electron catalyzed reactions such as the one described above may become an important factor in controlling the amount of atomic hydrogen in the boundary layer and at the deposition surface.

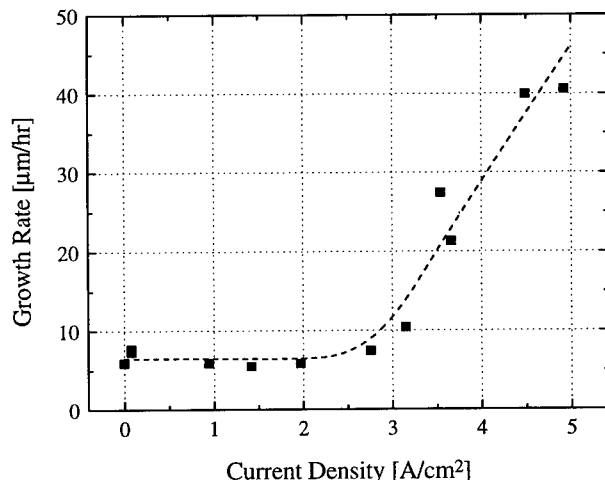


Figure 3.20 (♦) Growth rate of CVD diamond as a function of current density in the secondary discharge.  
(---) Approximate fit to the data.

Optical emission spectroscopy measurements have found that the electron temperature at the substrate is elevated above the freestream electron temperature when a potential is applied to the substrate. This indicates that the secondary discharge can be used to target the energy addition to the highly mobile free electrons in the plasma through joule heating.

Image processing was employed in this study to obtain a two-dimensional map of the emission from the first atomic hydrogen Balmer line ( $H_{\alpha}$ ).  $H_{\alpha}$  emission is a result of an H atom decaying from its third to its second electronic energy level. This process emits a photon at a wavelength of 656.3 nm. A charge-coupled device (CCD), a lens system and a narrow band-pass interference filter centered at 656.3 nm were used to obtain images with and without a potential applied to the substrate. A computer analysis package acquired and analyzed the data for different biasing conditions. Figure 3.21 shows the results of the  $H_{\alpha}$  imaging of the secondary discharge for a typical diamond growth experiment. The biasing conditions for this case were 5.1 A/cm<sup>2</sup> and 140 V across the secondary discharge. This image represents a 40 frame average with the potential applied to the growth surface after subtracting a 40 frame average without the potential applied. There is a large increase in  $H_{\alpha}$  emission, particularly within the boundary layer, with a strong potential applied to the growth surface. The intensity of the  $H_{\alpha}$  emission in this region was much brighter (by a factor of 5) than from the ~5000 K freestream. This may be an indication that the secondary discharge is significantly increasing the atomic hydrogen concentration in the boundary layer and flux to the substrate, leading to the higher growth rates observed.

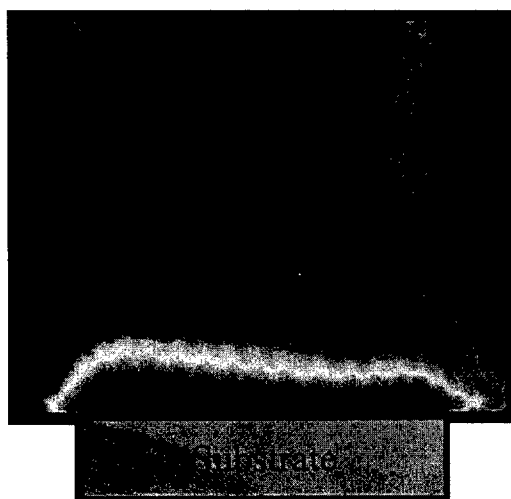


Figure 3.21 Two-dimensional image of the increase in the  $H_{\alpha}$  emission due to the secondary discharge.

Raman analysis of each of the samples indicates very high quality films were deposited over the range of biasing conditions. Each of the spectra consisted of a sharp peak near 1332 cm<sup>-1</sup> with little or no amorphous carbon Raman signal. Figure 3.22 shows the Raman spectra for a diamond film deposited under a highly biased substrate condition (100 V and 2.76 A/cm<sup>2</sup>). The inset to Figure 3.22 is a high resolution scan and displays splitting of the 1332 cm<sup>-1</sup> diamond line (split ~4.3 cm<sup>-1</sup> in this case). In all the cases reported here, a full-width half-maximum (FWHM) of no more than 4.0 cm<sup>-1</sup> for the unshifted diamond component was measured, indicating high quality films were deposited. This splitting phenomena was typical of all the samples grown in this study, and has been attributed to high quality, highly oriented films that were stressed perpendicular to the growth direction (in-plane stresses). [64, 65] These in-plane, or anisotropic, stresses can arise in CVD diamond films during the cool-down period after the deposition process, and are caused by the mismatch in the thermal expansion coefficients of CVD diamond and the substrate material. The anisotropic stress shifts the Raman signal associated with

the crystal planes that are perpendicular to the growth direction while leaving the signal associated with the crystal plane in the growth direction unshifted. In the spectra, the higher wavenumber peak is attributed to the singlet mode and the lower wavenumber peak to the doublet mode of the Raman diamond line. These modes are normally degenerate in the absence of stress.[65]

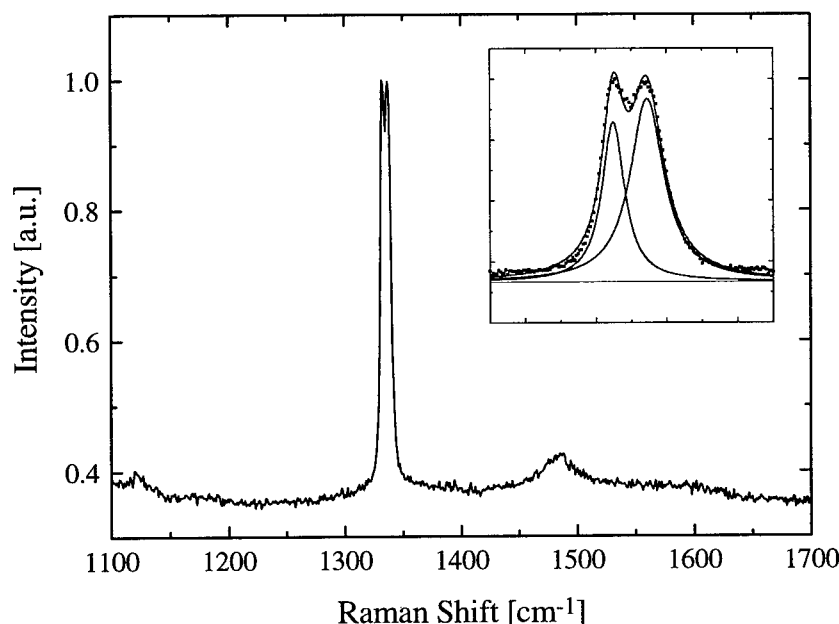


Figure 3.22 - Raman spectra of the deposited diamond film. Inset shows splitting of the 1332  $\text{cm}^{-1}$  diamond peak.

These experiments indicate that a significant increase in growth rate of CVD diamond is possible with a positive potential applied to the growth surface. We observed that the growth rate increased by a factor of 7 when the deposition surface was biased at 170 V and 4.9  $\text{A}/\text{cm}^2$  as compared with the floating substrate case. The increased growth rate may be attributed to an increased flux of atomic hydrogen to the growth surface resulting from an elevated electron temperature that increased the near surface dissociation fraction of hydrogen. Imaging of the flow field found a significant increase in the  $\text{H}_\alpha$  emission signal in the boundary layer over the deposition surface with a positive potential applied. Raman spectroscopy analysis indicated high quality films were deposited in all cases reported here. Splitting of the 1332  $\text{cm}^{-1}$  Raman diamond line indicates highly oriented films that have a high degree of in-plane stresses.

#### 4. CONCLUSIONS

Experimental investigations of atmospheric pressure plasma environments have demonstrated that the nonequilibrium behavior of these plasmas can be quite significant. The ability to understand nonequilibrium atmospheric pressure plasma systems and to apply them in plasma processing roles will rely on the accurate measurement of the plasma state and chemistry, and the ability to beneficially control the nonequilibrium state. Recent laser-based techniques have been demonstrated as powerful diagnostic tools, complimentary to traditional diagnostics of these environments, and initial experiments have shown great promise in the beneficial control of plasma chemical nonequilibrium for plasma CVD applications.

#### Acknowledgements

The authors would like to acknowledge the other members of our research group who have participated in these investigations: Dr. Scott Baldwin, Mr. Richard Gessman, Mr. Edward Wahl, and Mr. Maosheng Zhao. The authors would also like to acknowledge the organizations that have sponsored

the various research programs presented in this paper: the Department of Energy, Basic Energy Sciences (Grant #DE-FG03-88ER13957 under the direction of Dr. Oscar Manley), the Air Force Office of Scientific Research (Grant #F4962-94-1-0052 under the direction of Dr. Robert Barker), the Electric Power Research Institute (Grant #RP8042-05 under the direction of Dr. John Stringer), and the Engineering Research Center for Plasma-Aided Manufacturing (Grant #387P380 under the direction of Prof. J. Leon Shohet). The authors would also like to thank Prof. David G. Goodwin of Caltech for the use of his computational model.

### References

- [1] T. G. Owano, M. H. Gordon, and C. H. Kruger, *Physics of Fluids B (Plasma Physics)*, vol. 2, pp. 3184-90, 1990.
- [2] T. G. Owano and C. H. Kruger, "Electron-Ion Three Body Recombination Coefficient of Argon," presented at the AIAA 22nd Fluid Dynamics, Plasma Dynamics & Lasers Conference, Honolulu, HI, 1991.
- [3] M. H. Gordon and C. H. Kruger, *Physics of Fluids B (Plasma Physics)*, vol. 5, pp. 1014-23, 1993.
- [4] G. M. W. Kroesen, D. C. Schram, C. J. Timmermans, and J. C. M. de Haas, *IEEE Transactions on Plasma Science*, vol. 18, pp. 985-91, 1990.
- [5] R. J. Kee and J. A. Miller, "A structured approach to the computational modeling of chemical kinetics and molecular transport in flowing systems," Sandia National Laboratory, Livermore, CA Report SAND86-8841, 1986.
- [6] D. K. Bohme, J. B. Hasted, and P. P. Ong, *Journal of Physics B (Atomic and Molecular Physics)*, vol. 1, ser.2, pp. 879-92, 1968.
- [7] C. Park, *Nonequilibrium Hypersonic Aerothermodynamics*. New York: Wiley, 1989.
- [8] M. H. Gordon and C. H. Kruger, "Ultra-Violet Recombination Continuum Electron Temperature Measurements in a Nonequilibrium Atmospheric Argon Plasma," presented at the AIAA 22nd Fluid Dynamics, Plasma Dynamics & Lasers Conference, Honolulu, HI, 1991.
- [9] S. C. Snyder, L. D. Reynolds, C. B. Shaw, Jr., and R. J. Kearney, *Journal of Quantitative Spectroscopy and Radiative Transfer*, vol. 46, pp. 119-24, 1991.
- [10] D. S. Baer, "Plasma Diagnostics with Semiconductor Lasers Using Fluorescence and Absorption Spectroscopy," Ph.D. Thesis, Stanford University, (1993).
- [11] C. O. Laux, R. J. Gessman, and C. H. Kruger, *AIAA Journal*, vol. 34, pp. 1745-1747, 1996.
- [12] M. G. Dunn and S.-W. Kang, "Theoretical and Experimental Studies of Reentry Plasmas," NASA CR-2232, April 1973 1973.
- [13] R. N. Gupta, J. M. Yos, R. A. Thompson, and K.-P. Lee, "A Review of Reaction Rates and Thermodynamic and Transport Properties for an 11-Species Air Model for Chemical and Thermal Nonequilibrium Calculations to 30,000 K," NASA RP-1232, August 1990 1990.
- [14] C. Park, *Journal of Thermophysics and Heat Transfer*, vol. 7, pp. 385-398, 1993.
- [15] C. O. Laux, R. J. Gessman, and C. H. Kruger, "Modeling the UV and VUV Radiative Emission of High-Temperature Air," presented at the 28th AIAA Thermophysics Conference, Orlando, FL, AIAA 93-2802, 1993.
- [16] C. O. Laux, T. G. Owano, M. H. Gordon, and C. H. Kruger, "Measurements of the Volumetric Radiative Source Strength of Air for Temperatures Between 5,000 and 7,500K," presented at the AIAA 5th Thermophysics and Heat Transfer Conference, AIAA 90-1780, 1990.
- [17] C. Park, "Nonequilibrium Air Radiation (NEQAIR) Program: User's Manual," NASA-Ames Research Center, Moffett Field, CA NASA-TM86707, 1985.
- [18] C. O. Laux, R. J. Gessman, and C. H. Kruger, "Mechanisms of Ionizational Nonequilibrium in Air and Nitrogen Plasmas," presented at the 26th AIAA Plasmadynamics and Lasers Conference, San Diego, CA, AIAA 95-1989, 1995.
- [19] R. J. Kee, F. M. Rupley, and J. A. Miller, "Chemkin-II: A Fortran Chemical Kinetics Package for the Analysis of Gas Phase Chemical Kinetics," Sandia National Laboratories, Livermore, CA, Report SAND89-8009, 1989.



- [20] G. V. Candler, C. O. Laux, R. J. Gessman, and C. H. Kruger, "Numerical simulation of a nonequilibrium nitrogen plasma experiment," presented at the 28th AIAA Plasmadynamics and Lasers Conference, Atlanta, GA, AIAA 97-2365, 1997.
- [21] H. Partridge, S. R. Langhoff, and C. W. Bauschlicher, *Journal of Chemical Physics*, vol. 88, pp. 3174-3186, 1988.
- [22] D. A. Levin, G. V. Candler, R. J. Collins, P. Erdman, E. Zipf, P. Espy, and C. Howlett, *Journal of Thermophysics and Heat Transfer*, vol. 7, pp. 30-36, 1993.
- [23] R. J. Gessman, C. O. Laux, and C. H. Kruger, "Experimental study of kinetic mechanisms of recombining atmospheric pressure air plasmas," presented at the 28th AIAA Plasmadynamics and Lasers Conference, Atlanta, GA, AIAA 97-2364, 1997.
- [24] T. G. Owano, C. H. Kruger, D. S. Green, S. Williams, and R. N. Zare, *Diamond and Related Materials*, vol. 2, pp. 661-666, 1993.
- [25] D. S. Green, T. G. Owano, S. Williams, D. G. Goodwin, R. N. Zare, and C. H. Kruger, *Science*, vol. 259, pp. 1726-9, 1993.
- [26] T. G. Owano, D. S. Green, E. H. Wahl, C. H. Kruger, and R. N. Zare, "Degenerate Four-Wave Mixing as a Spectroscopic Probe of Atmospheric Pressure Reacting Plasmas," presented at the 11th International Symposium on Plasma Chemistry, Loughborough, Leicestershire, England, 1993.
- [27] S. Williams, D. S. Green, S. Sethuraman, and R. N. Zare, *Journal of the American Chemical Society*, vol. 114, pp. 9122, 1992.
- [28] T. G. Owano, E. H. Wahl, C. H. Kruger, and R. N. Zare, "Degenerate Four-Wave Mixing as a Spectroscopic Probe of Boundary Layer Chemistry in Thermal Plasma CVD," presented at the 26th AIAA Plasmadynamics & Lasers Conference, San Diego, CA, AIAA 95-1954, 1995.
- [29] C. H. Kruger, T. G. Owano, and M. H. Gordon, *Journal of Pure and Applied Chemistry*, vol. 64, pp. 637, 1992.
- [30] D. G. Goodwin and G. G. Gavillet, *Journal of Applied Physics*, vol. 68, pp. 6393-400, 1990.
- [31] S. J. Harris, *Applied Physics Letters*, vol. 56, pp. 2298-2300, 1990.
- [32] M. Frenklach, *Journal of Chemical Physics*, vol. 97, pp. 5794-802, 1992.
- [33] S. S. Lee, D. W. Minsek, D. J. Vestyck, and P. Chen, *Science*, vol. 263, pp. 1596-8, 1994.
- [34] F. G. Celii, P. E. Pehrsson, H. t. Wang, and J. E. Butler, *Applied Physics Letters*, vol. 52, pp. 2043-5, 1988.
- [35] E. Villa, J. A. Dagata, J. Horwitz, D. Squire, and M. C. Lin, *Journal of Vacuum Science & Technology A (Vacuum, Surfaces, and Films)*, vol. 8, pp. 3237-40, 1990.
- [36] F. G. Celii and J. E. Butler, *Journal of Applied Physics*, vol. 71, pp. 2877-83, 1992.
- [37] E. J. Corat and D. G. Goodwin, *Journal of Applied Physics*, vol. 74, pp. 2021-9, 1993.
- [38] D. G. Goodwin, N. G. Glumac, and E. J. Corat, "Optical detection of CH<sub>3</sub> during diamond chemical vapor deposition," presented at the SPIE conference on laser techniques for state-selected and state-to-state chemistry, Los Angeles, CA, 2124, 1994.
- [39] N. Ota and N. Fujimori, "In situ detection of methyl radicals in filament assisted diamond growth environment by resonance ionization spectroscopy," presented at the Advanced in New Diamond Science and Technology, MYU, Tokyo, Japan, 1994.
- [40] M. A. Childs, K. L. Menningen, P. Chevako, N. W. Spellmeyer, L. W. Anderson, and J. E. Lawler, *Physics Letters A*, vol. 171, pp. 87-9, 1992.
- [41] H. Toyoda, M. A. Childs, K. L. Menningen, L. W. Anderson, and J. E. Lawler, *Journal of Applied Physics*, vol. 75, pp. 3142-50, 1994.
- [42] W. L. Hsu, *Applied Physics Letters*, vol. 59, pp. 1427-9, 1991.
- [43] S. J. Harris and A. M. Weiner, *Journal of Applied Physics*, vol. 67, pp. 6520-6, 1990.
- [44] E. Kondoh, T. Ohta, T. Mitomo, and K. Ohtsuka, *Journal of Applied Physics*, vol. 72, pp. 705-11, 1992.
- [45] E. Kondoh, T. Ohta, T. Mitomo, and K. Ohtsuka, *Diamond and Related Materials*, vol. 3, pp. 270-6, 1994.
- [46] D. Romanini and K. K. Lehmann, *Journal of Chemical Physics*, vol. 99, pp. 6287-301, 1993.
- [47] P. Zalicki and R. N. Zare, *Journal of Chemical Physics*, vol. 102, pp. 2708-17, 1995.

- [48] A. O'Keefe, J. J. Scherer, A. L. Cooksy, R. Sheeks, J. Heath, and R. J. Saykally, *Chemical Physics Letters*, vol. 172, pp. 214-18, 1990.
- [49] T. Yu and M. C. Lin, *Journal of the American Chemical Society*, vol. 115, pp. 4371, 1993.
- [50] G. Meijer, M. G. H. Boogaarts, R. T. Jongma, D. H. Parker, and A. M. Wodtke, *Chemical Physics Letters*, vol. 217, pp. 112-16, 1994.
- [51] Y. A. Mankelevich, A. T. Rakhimov, and N. V. Suetin, *Diamond and Related Materials*, vol. 4, pp. 1065-8, 1995.
- [52] Y. A. Mankelevich, , 1996.
- [53] D. G. Goodwin, *Journal of Applied Physics*, vol. 74, pp. 6895-906, 1993.
- [54] D. G. Goodwin, *Journal of Applied Physics*, vol. 74, pp. 6888-94, 1993.
- [55] J. C. Angus and C. C. Hayman, *Science*, vol. 241, pp. 913-921, 1988.
- [56] S. K. Baldwin, Jr., T. G. Owano, and C. H. Kruger, *Plasma Chemistry and Plasma Processing*, vol. 14, pp. 383-406, 1994.
- [57] B. W. Yu and S. L. Girshick, *Journal of Applied Physics*, vol. 75, pp. 3914-23, 1994.
- [58] C. H. Kruger, "Nonequilibrium effects on thermal plasma chemistry," presented at the The 8th International Symposium on Plasma Chemistry, Tokyo, Japan, 1987.
- [59] C. H. Kruger, *Plasma Chemistry and Plasma Processing*, vol. 9, pp. 435-43, 1989.
- [60] S. Matsumoto, I. Hosoya, and T. Chounan, *Japanese Journal of Applied Physics*, vol. 29, pp. 2082-2086, 1990.
- [61] S. Matsumoto, I. Hosoya, Y. Manabe, and Y. Hibino, *Pure and Applied Chemistry*, vol. 64, pp. 751-758, 1992.
- [62] S. Yugo, T. Kanai, T. Kimura, and T. Muto, *Applied Physics Letters*, vol. 58, pp. 1036-1038, 1991.
- [63] B. R. Stoner, G. H. M. Ma, S. D. Wolter, and J. T. Glass, *Physical Review B*, vol. 45, pp. 11067-11084, 1992.
- [64] M. H. Loh, J. G. Liebeskind, and M. A. Cappelli, "Arcjet thrusters for the synthesis of diamond and cubic-boron nitride films," presented at the 30th AIAA/ASME/SAE/ASEE Joint Propulsion Conference, Indianapolis, IN, AIAA 94-3233, 1994.
- [65] S. A. Stuart, S. Praver, and P. S. Weiser, *Applied Physics Letters*, vol. 62, pp. 1227-1229, 1993.

## Ectons and their Role in Electrical Discharges in Vacuum and Gases

G.A. Mesyats

*Institute of Electrophysics of the Russian Academy of Sciences, 34 Komsomolskaya St.,  
Ekaterinburg 620049, Russia*

**Abstract.** The present paper deals with the short-term bursts – ectons of electrons appearing due to micro-explosions occurring at the cathode surface owing to the high specific energy and the strong overheating of the metal. Ectons play a fundamental role in vacuum arcs and sparks, in low-pressure discharges, in compressed and high-strength gases, etc. i.e., in cases where a high electric field exists at the cathode surface and a high density field emission current is emitted by the cathode or there exists a possibility to produce a high energy density ion a cathode microvolume.

### 1. INTRODUCTION

“Ectons” [1] is formed of the initial letters of the English wording “explosive center”. The discovery of ectons is based on the advances in the study of explosive electron emission [2-4]. The term “explosive electron emission” (EEE) refers to the emission of electron current from the surface of a conductor being a cathode as a result of an explosion of the cathode material in a microscopic volume at its surface. The most common way to initiate EEE is to rapidly heat microregions of the cathode by a high-density electric current. The simplest example is the current of field emission (FE) from cathode microprotrusions, whose density at rather high electric fields may reach  $10^9$  A/cm<sup>2</sup>. For a long time it was thought that EEE is initiated only by FE current. Now it is clear that other processes can also be responsible for the initiation of EEE. The electron emission in an ecton generally lasts  $10^{-9}$ – $10^{-8}$  s and then ceases by itself since the emission center is cooled through heat conduction, a decrease in current density, and ejection of heated metal. To excite an ecton, it is necessary that the specific energy in a cathode microvolume be higher than the sublimation energy (over  $10^4$  J/g) with the total energy being  $10^{-8}$  J.

### 2. ELECTRICAL EXPLOSION OF METAL AND ECTONS

#### 2.1 Electrical explosion of conductors

While on the subject of ectons, we suppose that the metal in a microvolume is subjected to essentially the same processes as in an electrical explosion of a conductor (EEC) [5]. Of greatest interest for us, from the viewpoint of the EEC physics, is the fast heating of the conductor (at a rate of over  $10^{13}$  K/s). This forms the basis for studying the physical properties of metals and their phase transformations as they rapidly go through all – from solid to plasma – states. These studies are important to elucidate the behavior of metals in the neighborhood of the critical point, the properties of nonideal plasmas, and the high-temperature metal–nonmetal phase transition [6].

The EEC process can be subdivided into two stages. The initial stage involves the heating of the metal in the solid state, its melting, and the heating of the liquid metal to the onset of vaporization. At this stage, the change in the density of the metal is not essential. This is followed by the stage of explosion where the conductor resistance increases abruptly ( $10^2$  or more times). This is due to the

expansion of the conductor and, hence, due to a decrease in its density. For the initial stage of EEC, the state of the metal can be characterized by only one thermodynamic variable such as temperature or specific energy. The resistivity of the conductor at this stage depends only on temperature or specific energy, i.e., the dependence  $\kappa(T)$  or  $\kappa(w)$  takes place.

The stage of the explosion, as such, is most complicated to study. At this stage, a number of phenomena develop that add complexity to the physical mechanism of EEC. Among these phenomena are instabilities, shunting discharges, stratification, and the like. A feature of this stage is that the resistance is not a single-valued function of energy density but depends on power density [5]. Besides experimentation, there are three other methods of attack for the EEC problems: numerical simulation, simplified calculations using models, and similarity techniques. In EEC calculations using similarity techniques, an important role is played by the specific integral of action (specific action) defined as

$$\bar{h} = \int_0^{t_d} j^2 dt, \quad (2.1)$$

where  $j$  is the current density and  $t_d$  is the time delay to explosion.

Table 1 presents experimental values of the specific action for various conductors with the initial temperature being room temperature and the highest energy density being  $10^8 \text{ A/cm}^2$  ( $\bar{h}_1$ ) and with the initial temperature equal to the melting temperature ( $\bar{h}_2$ ) [7]. The weak dependence of  $\bar{h}$  on  $t$  and  $j$  for  $j \leq 10^7 \text{ A/cm}^2$  has also been noted in other works. Some of them are reviewed in [8]. Sometimes, the specific action is roughly estimated in terms of a classical approach assuming that the explosion occurs within one stage as a certain critical temperature,  $T_{ex}$ , has been achieved. If we assume that the resistivity is given by  $\kappa = \kappa_0 T$ , and the heat capacity  $c$  is temperature independent, we obtain

$$\int_0^{t_d} j^2 dt = \frac{\rho c}{\kappa_0} \ln \frac{T_{ex}}{T_0} = \bar{h}, \quad (2.2)$$

where  $T_0$  is the initial temperature and  $\rho$  is the density of the conductor material.

Table 1.

Material	Al	Ag	Au	Cu	Ni	Fe	W
$\bar{h}_1, 10^9 \text{ A}^2 \cdot \text{s/cm}^4$	1.8	2.8	1.8	4.1	1.9	1.4	1.8
$\bar{h}_2, 10^9 \text{ A}^2 \cdot \text{s/cm}^4$	1.4	2.0	1.3	3.0	1.6	1.2	1.4

Attention must be given to the fact that the specific action  $\bar{h}$  depends on the initial temperature of the conductor  $T_0$ . Recall that the data in Table 1 have been obtained for the initial temperature being room temperature and for the melting temperature.

## 2.2 The simplest model of an ecton

The simplest ecton model is constructed based on the energy balance equation for a conical point. Therefore, formula (2.2) can be used. The heat conduction in the point is ignored since the process is short-term. It is assumed that the electron emission in the ecton ceases due to the cooling of the emission center. The center is considered cool when the Joule heating radius becomes equal to the heat conduction radius. Eventually, this has the results as follows [10]. The ecton operation time is given by

$$t_e = i^2 / (\pi^2 a^2 \bar{h} \theta^4). \quad (2.3)$$

where  $\theta$  is the cone angle,  $a$  is the diffusivity,  $i$  is the current. The mass of the metal removed in the process of explosion will be

$$m_e = 2\rho i^3 / [3\pi^2 (a\bar{h})^{3/2} \theta^4]. \quad (2.4)$$

The electron charge removed by the ecton will be

$$n_e = i^3 / \pi^2 a^2 \bar{h} e \theta^4, \quad (2.5)$$

where  $e$  is the charge of an electron. The mass per unit charge removed from the cathode will be given by

$$\gamma_m = \frac{2}{3} \rho \left( \frac{a}{\bar{h}} \right)^{1/2}. \quad (2.6)$$

It follows that in terms of this model, the specific mass removed from a cathode by explosion depends only on the properties of the cathode material. After explosion, the plasma produced starts expanding. We have proposed [4] a model for adiabatic plasma expansion. Let a specific energy  $w_0$  be introduced into a certain volume of a cathode. This energy, in the process of plasma expansion, converts to the kinetic energy of the plasma particles. For the plasma radius becoming much larger than the characteristic dimension of the initial volume, from the condition that the total energy is conserved in the particle volume it follows that the velocity of propagation of the leading layers of the plasma,  $v$ , is related to the specific energy  $w_0$  as

$$v = \left( \frac{4\gamma}{\gamma-1} w_0 \right)^{1/2}, \quad (2.7)$$

where  $\gamma$  is the adiabatic exponent. For an expanding plasma we have  $\gamma = 1.24$  [11]. The plasma expansion velocity is  $(1-2) \cdot 10^6$  cm/s for W, Mo, Cu, Al, Ni, Pb, and other metals. Therefore, the specific energy prior to a microexplosion is  $w_0 = (2-8) \cdot 10^4$  J/g. The same values  $w_0$  have been obtained from a numerical simulation of a cathode spot [12]. The plasma produced as a result of a microexplosion contains, depending on the metal type, singly, doubly, and even triply charged ions. These ions have rather high energies. For instance, singly charged ions of copper having a velocity of  $1.5 \cdot 10^6$  cm/s are accelerated to 70 eV. Let us discuss the reason for the current cutoff in an ecton. This problem is closely related to the mechanism for the electron emission from a metal. This emission seems to be thermal electron emission enhanced, through the Schottky effect, by the electric field at the metal-plasma interface. In terms of the classical heat model it can be assumed that the temperature may become much higher than the boiling temperature within a time of the order of  $10^{-9}$  s. If we believe that the Richardson-Schottky formula is valid for these conditions, we have

$$j = AT^2 \exp \left( -\frac{e\varphi - \alpha E^{1/2}}{kT} \right), \quad (2.8)$$

where  $j$  is the electron current density (A/cm<sup>2</sup>),  $A = 120.4$ ,  $T$  is the temperature of the cathode (K),  $\varphi$  is the work function ( $\varphi = 4.4$  eV for copper),  $\alpha = 3.79 \cdot 10^{-4}$ ,  $E$  is the electric field at the emitting surface (V/cm), and  $k$  is Boltzmann's constant.

A simulation of the processes occurring in an ecton has shown that the electric field  $E$  is not over  $10^5$  V/cm [5]. According to estimates for copper, for the input energy equivalent to  $10^4$  K, the current density will be of the order of  $10^8$  A/cm<sup>2</sup>, while for  $7 \cdot 10^3$  K it will be only  $5 \cdot 10^6$  A/cm<sup>2</sup>, i.e., as the ecton zone is cooled by 30 %, the current density decreases 20-fold. Thus, the qualitative pattern of the current cutoff in an ecton is as follows: Initially, as the ecton has been initiated, the current density is about  $10^9$  A/cm<sup>2</sup>. The cathode material in a microvolume is heated and then explodes, which gives rise to intense thermal electron emission. As the explosion is developing, there take place an increase in the size of the emission zone, heat removal by conduction, and heat removal through evaporation and ejection of the heated liquid metal. All this reduces the temperature in the ecton operation zone and the current density of the thermal electron emission. The decrease in emission current density results in a more rapid cooling of the emission zone due to the Joule heating becoming less intense.

### 3. ELECTRODE SURFACE CONDITION

In the initiation of an ecton, an important role is played by three types of imperfectness of the cathode surface: microprotrusions, adsorbed gases, and dielectric inclusions and films. The irregularities present on the cathode surface [13, 14] are due to various factors such as mechanical treatment, heating, the electric field present at the surface, electrical discharges, etc. (Fig. 1). The irregularities on the surface of a metal are especially large when threadlike crystals appear [15] whose height-to-radius ratio may be over  $10^3$ . Such crystals are formed on the surfaces of electrodes on condensation of oversaturated vapors. In

vacuum, the cathode microrelief is changed substantially by electrical discharges. The discharge current, through thermal processes, produces erosion of the electrodes, which is accompanied by the formation of craters and microprotrusions. To characterize the cathode surface quantitatively, the notion of electric field enhancement is introduced, and the field enhancement factor is denoted as  $\beta_E$ . This factor is the ratio of the true value of the electric field at the protrusion tip to its average macroscopic value. For  $\beta_E \geq 1$ , the relation  $\beta_E \approx h/r$  can be used [13].

A way of determining the field enhancement factor is measuring the field emission current in vacuum as a function of the electric field. The FE current from a point is described by the Fowler–

Nordheim equation

$$i = A \frac{\beta_E^2 E^2 S_{em}}{\varphi} \exp\left(-B \frac{\varphi^{3/2}}{\beta_E E}\right), \quad (3.1)$$



Fig. 1. Cathode surface microrelief [1].

where  $A$  and  $B$  are the constants entering the Fowler–Nordheim formula,  $E$  is the average electric field,  $S_{em}$  is the emission area, and  $\varphi$  is the work function. As follows

from Eq. (3.1), the plot of  $\log(i/E^2) = f(1/E)$  should be a straight line. So, for a known work function  $\varphi$ , we can estimate  $\beta_E$  from the slope of the straight line and  $S_{em}$  from the portion of the y-axis intercepted by the straight line. The field enhancement factor may vary over a wide range (from 10 to  $10^2$ ) [9]. Many researchers, however, believe that the values of the order of  $10^3$  are too high; nevertheless, points with these  $\beta_E$  values are actually observed on cathode surface. Therefore, additional investigations are needed to explain this contradiction. An important role in the initiation of ectons at a cathode is played by the gas adsorbed on its surface. The phenomenon of surface adsorption is the absorption of a gas or vapors by the surface of a solid. From the chemical viewpoint, an adsorbent has on its surface atoms with an unsaturated valency. This means that the surface of a solid body has some regions where chemical binding with adsorbed particles is provided. Particles in numbers sufficient for all surface bonds to be saturated form a monolayer. This corresponds to the density of adsorbed atoms of the order of  $10^{14} \text{ cm}^{-2}$  [16]. The binding between adsorbed particles in the monolayer is effected by chemical forces. Therefore, this type of adsorption is referred to as chemical adsorption or chemisorption. In chemical adsorption, the binding energy is rather high enough and reaches several electron-volts per particle.

In the environment of a gas capable to oxidize electrodes, the cathode surface turns out to be coated with an oxide film. Moreover, the cathode surface may contain contaminants and dielectric inclusions remained after polishing as well as dielectric inclusions having present in the cathode bulk and exposed on the surface on electrochemical polishing or ion etching [17]. At rather high electric fields induced by the electric charge of ions, breakdown may occur inside the dielectric film. If the resistivity of the dielectric film present on the cathode surface is high, its outer surface is charged by the flow of positive ions onto the cathode. As the breakdown electric field is achieved, the film is broken down and the cathode is damaged at the site of breakdown. Some models [18, 19] use as a criterion for breakdown the achievement of a certain critical FE current density at which a microprotrusion and the adjacent regions of the dielectric are heated and explode. The process under consideration is an act of excitation of an ecton at the surface of a metal.

#### 4. THE ROLE OF ECTONS IN VACUUM BREAKDOWN

##### 4.1 General considerations

Ectons play an important role in electrical discharges in vacuum. A vacuum discharge involves a vacuum breakdown, a vacuum spark, and a vacuum arc. Vacuum breakdown, i.e., failure of a vacuum insulation, ecton. A vacuum spark and a vacuum arc represent the behavior of ectons in non-steady-state conditions, such that the current in the gap is growing, and in steady-state conditions, reflects the mechanism for the

initiation of an respectively.

Figure 2 presents electro-optical photographs of the evolution of a glow in a gap in the process of a vacuum discharge [4]. They were taken for a pulse generator charged to a voltage  $V_0$  which was discharged through a resistor of resistance  $R$ . Three phases of the process can be distinguished: (1) There is no glow in the gap. This is the stage of breakdown during which energy concentration in a cathode microvolume takes place (Photo I). (2) A glow appears in the gap initially at the cathode and then at the anode. This is the spark stage (Photos from IIth to IXth). The cathode glow testifies to the appearance of an ecton, the ending of the breakdown phase, and the beginning of the spark stage. The number of microexplosions varies from photo to photo. The microexplosions have a random character. The cathode plasma propagates toward the anode with a velocity of  $\sim 2 \cdot 10^6$  cm/s. In Photo VI, the appearance of a glow at the anode is seen. This is the result of the heating of the anode by the current of explosive electron emission. (3) When the cathode and the anode plasmas close the gap, the discharge goes to the arc phase (Photo X). In the spark phase, the current grows to its peak value  $i_a = V_0/R$ .

So, we will believe that the processes occurring in breakdown lead to concentration of energy in a cathode microvolume, and this energy reaches values sufficient for the material in the microvolume to explode and for an ecton to appear. By a spark we will mean the process from the beginning of a microexplosion at the cathode to the instant the current reaches its highest value determined by the applied voltage and the circuit resistance. The following steady-state operation of the discharge will be referred to as an arc. With that, we suppose that the spark and the arc currents are high enough for the process to be self-sustaining.

#### 4.2 The vacuum breakdown

The processes occurring in a vacuum breakdown strongly depend on the surface condition of the electrodes and on the quality of the vacuum. With thoroughly cleaned electrode surfaces and a high-grade vacuum, breakdown occurs due to the current of the field emission proceeding from cathode microprotrusions, and to the Joule heating and further explosion of the microprotrusions. The evidence for this is as follows: The numerous experimental data reviewed in [4] show that for the above conditions, there are two criteria for the appearance of a spark: For the mode where a dc voltage is applied to the gap we have [4]

$$j = \text{const}_1 \quad (4.1)$$

and for the pulsed mode [3, 4]

$$\int_0^{t_d} j^2 dt = \text{const}_2, \quad (4.2)$$

where  $j$  is the FE current density at the tip of a microprotrusion,  $t_d$  is the time delay to explosion, and the constants characterize the cathode material and the shape of the microprotrusion. Relation (4.1) implies that the electric field at the surface of microprotrusions remains unchanged irrespectively of the gap spacing. This follows from the data reported in [20-22] and summarized in Fig. 3.

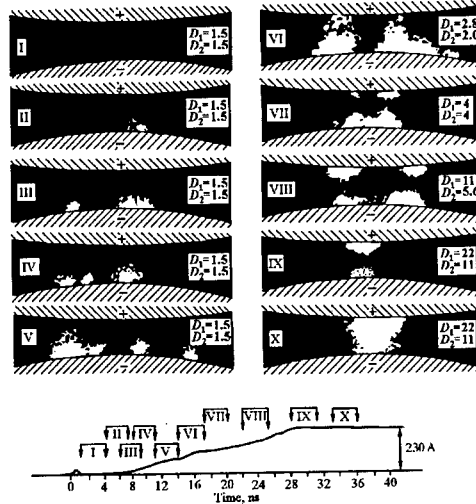


Fig. 2. Typical photographs of the glow in a copper electrode gap, corresponding to different stages of breakdown development ( $d = 0.35$  mm,  $V_0 = 35$  kV,  $D_1$  and  $D_2$ : lens apertures). The pictures are taken of different discharges.

A theoretical description of the initiation of an ecton by FE current has the goal to explain relations (4.1) and (4.2). It turns out that this is possible in terms of the Joule model of the heating of a microprotrusion. The heating of a cylindrical cathode microprotrusion by the FE current it carries in the steady state gives rise to a threshold current density and subsequent explosion provided that

$$j = \frac{1}{h} \sqrt{\frac{\lambda}{\kappa_0}}, \quad (4.3)$$

where  $h$  is the height of the protrusion and  $\lambda$  is the heat conductivity. Thus, for a protrusion of height 1  $\mu\text{m}$ , the current density  $j$  is  $2 \cdot 10^8$ ,  $0.5 \cdot 10^8$ , and  $0.25 \cdot 10^8$  A/cm<sup>2</sup> for copper, tungsten, and nickel, respectively. With short pulses, the threshold FE current density is higher than that for the steady-state case. If the pulse duration  $t_p$  is much shorter than the time required for a discharge to go to the steady state, the relation

$$t_p \ll \frac{h^2 \rho c}{\lambda} \quad (4.4)$$

is valid. For instance, if for tungsten we have  $h = 0.6 \mu\text{m}$ , relation (4.4) is satisfied even with  $t_p = 10$  ns. For condition (4.4) fulfilled, the temperature of a cylindrical emitter increases with time by an exponential law:

$$T = T_0 \exp \frac{\kappa_0 \int_0^{t_p} j^2 dt}{\rho c}. \quad (4.5)$$

Let the current density be invariable in time. If we assume by convention that a protrusion will explode as a certain critical temperature,  $T_{ex}$ , is reached, the time delay to explosion will be determined from relation (2.2), which is similar to relation (4.2). Thus, the simple Joule model for the heating of protrusions offers an adequate explanation of the principal experimental criteria given by Eqs. (4.1) and (4.2). It should be noted that these are criteria for the appearance of a spark rather than criteria for breakdown. These criteria yield the time  $t_d$  being the duration of the breakdown stage.

To pass from relations (4.1) and (4.2) to the dependence between the time  $t_d$  and the electric field  $E$ , we write an approximation of the Fowler–Nordheim formula:

$$j = A \frac{E^2}{\varphi} \exp \left( -B \frac{\varphi^{3/2}}{E} \right), \quad (4.6)$$

Here,  $j$  is the current density (A/cm<sup>2</sup>),  $A = 1.55 \cdot 10^{-6}$  (A),  $E$  is the electric field (V/cm),  $B = 6.85 \cdot 10^7$ , and  $\varphi$  is the work function of an electron outgoing from the metal. Formally, formula (4.6) suggests that the electron current density may reach  $10^{10}$  A/cm<sup>2</sup> and even more. However, even when the current density is as low as of the order of  $10^8$  A/cm<sup>2</sup>, the dependence  $j(E)$  shows a departure from the F–N theory which is reflected in a less intense rise of the emission current (Fig. 4) [23]. It turned out that this effect is inherent in all investigated metals such as W, Mo, Ta, Re, etc. The above departure is the greater, the higher is the current density and the lower the work function. This effect is due to the influence of the space charge of the emitted electrons. With high electric fields and current densities, the influence of the space charge on the character of the dependence  $j(E)$  is predominant. In this case, the dependence  $j(E)$  is governed by the

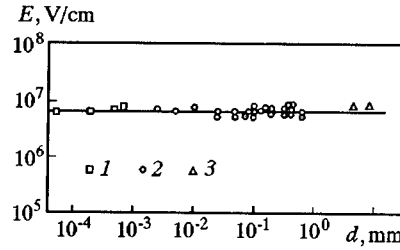


Fig. 3. Local breakdown field at cathode versus electrode separation for tungsten electrodes. Data from [20] (1), [22] (2), and [21] (3).

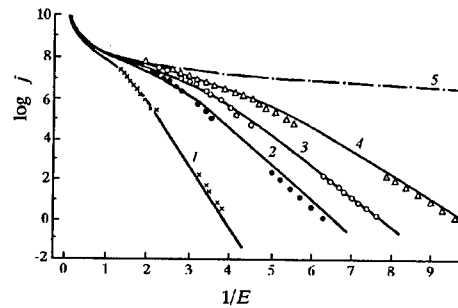


Fig. 4. Comparison of experimental data with predictions of an FE theory, taking account of space charge. Work function  $\varphi = 4.50$  (1), 3.19 (2), 2.80 (3), and 2.44 eV (4); (5) the Child–Langmuir curve [23].



Child-Langmuir law which is written as [24]

$$j = \frac{4}{9} \epsilon_0 \left( \frac{2e}{m} \right)^{1/2} E^{3/2} r_{em}^{-1/2}, \quad (4.7)$$

where  $\epsilon_0$  is the dielectric constant,  $e$  and  $m$  are the electron charge and mass, respectively, and  $r_{em}$  is the radius of the emitting surface. Dependence (4.7) is presented in Fig. 4 by curve 5. Investigations of many researchers have demonstrated that with voltage pulses of duration  $10^{-9}$ – $10^{-6}$  s applied to a tungsten emitter, one can achieve current densities of up to  $10^9$  A/cm<sup>2</sup> [4,25]. High current densities cause microemitters to explode. If  $j$  remains unchanged within the time  $t_d$  and the current density is determined by the F-N formula, we have

$$t_d = \frac{\hbar}{A^2 E^4 \phi^2} \exp\left(\frac{2B\phi^{3/2}}{E}\right), \quad (4.8)$$

where  $A$  and  $B$  are constants depending on the work function of the material and  $E$  is the electric field at the tip of the protrusion. Equation (4.8) demonstrates a strong dependence of  $t_d$  on  $E$ . This strong dependence takes place only at comparatively low fields at the protrusion surface when  $j \leq 10^8$  A/cm<sup>2</sup>.

At high values of the current density, the latter is limited by the electron space charge in the region adjacent to the protrusion. Therefore, we have  $t_d \propto E^3$ , which is confirmed experimentally (Fig. 5) [4]. Thus, measurements of  $t_d$  have confirmed that the delay to the appearance of EEE current is due to the delay of the onset of a microexplosion at the cathode and that the value of  $t_d$  depends only on the field  $E$ , which is confirmed experimentally [4]. For a liquid-metal cathode, its surface structure is destroyed under the action of electro-static forces. Tonks [26] considered the balance of the surface tension, gravity, and electrostatic forces. The condition that a horizontal liquid-metal surface is unstable has the form

$$\epsilon_0 \frac{E^2}{2} > \frac{\alpha}{r} + \rho g r, \quad (4.9)$$

where  $\rho$  is the density of the material,  $\alpha$  is the coefficient of surface tension,  $g$  is the gravitational acceleration, and  $r$  is the radius of the liquid surface. The lowest value of  $E$  at which the liquid surface is destroyed corresponds to an optimal value of  $r = r_0$ , such that inequality (4.9) becomes an equality. Thus, for mercury the electric field at which the surface starts destroying is 53 kV/cm and  $r_0$  is 0.37 cm [27]. When inequality (4.9) is fulfilled, a hump starts growing on the liquid-metal surface. The electric field at its surface increases, which leads to a larger extension of the liquid at this place. Initially, the hump has a nearly spherical segment shape (Fig. 6) and then it transforms to a cone. With that, the tip radius decreases. A protrusion like this can explode under the action of FE current. Thus, for the case of a liquid-metal cathode, the breakdown process involves extraction of a microprotrusion from the liquid metal. To summarize, under ideal conditions where only microprotrusions are present on the cathode surface and there are no contaminants and adsorbed gas, the appearance of the first electron results from the energy concentration in a cathode microvolume due to the Joule heating of the cathode microprotrusions. In this case, the principal processes in the breakdown are the passage of FE current and the heating of microprotrusions prior to explosion.

However, there is a great deal of experimental data which suggest that other breakdown mechanisms also exist [4, 28]. Let us take a brief look at them.

1. The FE electrons are accelerated in the vacuum gap and transfer their energy to a region of the anode surface causing its heating and vaporization and gas desorption from the anode. This leads to the appearance of a flow of plasma and ions from the anode to the cathode.

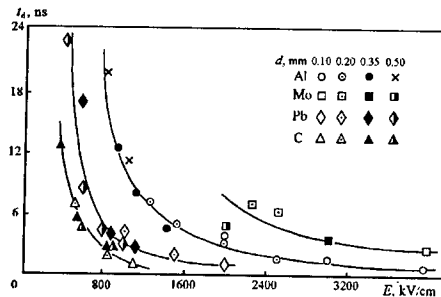


Fig. 5. Time delay to breakdown versus average electric field for electrodes made of various materials.

2. The metal and impurity particles weakly attached to the electrodes, under the action of the voltage applied to the gap, when hitting the opposite electrode, may create conditions for breakdown (heating and evaporation of the particles, deformation of the electrode surface, gas desorption, *etc.*)
3. Under the action of the ponderomotive forces of the electric field, changes of the electrode surfaces may occur, namely, formation of micropoints, breakoff of material pieces, deformation of the surface of liquid metals, *etc.* Thereafter, the first or the second mechanism comes into effect.
4. The nonmetal inclusions and films present on the cathode may become efficient emission centers because of the decrease in the work function of the cathode metal or of the breakdown of inclusions and films which plays the role of a trigger discharge.
5. Gas desorption from the electrode surfaces favors the appearance of a gas discharge initiating the breakdown of the vacuum gap.

In our opinion, all these mechanisms, forced initiation included, eventually lead to energy concentration in a cathode microvolume, explosion of the material in this microvolume, and formation of an ecton. Two criteria are necessary for the ecton process to be self-sustaining: the required energy density,  $w_0$ , and critical mass,  $m_0$ , formed as a result of the explosion. For some metals (Cu, Al, Ag) the criteria are approximately follows:

$$w_0 \approx 5 \cdot 10^4 \text{ J/g}; \quad m_0 \approx 10^{-13} \text{ g} \quad (4.10)$$

A fundamental role in the process of energy concentration is played by the plasma generated at the cathode. Let us consider this process in more detail.

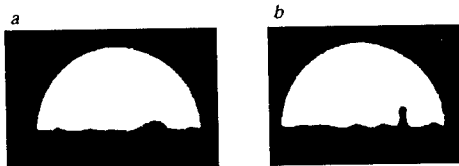


Fig. 6. Microprotrusions on a mercury surface grown at different electric fields between electrodes. The field in case (a) was lower than in case (b).

#### 4.3 Plasma initiation of breakdown

It is well known that a vacuum discharge can be initiated by supplying plasma to the cathode. This process strongly depends on the dielectric films and inclusion present on the cathode. The formation of ectons under the action of the plasma produced by a plasma gun is described in [4]. The plasma arrived at the nearly placed

cathode. Ectons appeared when dielectric contaminants were obviously present on the cathode surface. This testifies to the energy concentration in a cathode microvolume. The most probable appearance of an ecton was at a distance less than 100  $\mu\text{m}$ . The probability was the higher, the closer the plasma source was located. With that, the lowest plasma density was  $10^{16} \text{ cm}^{-3}$ . For thoroughly cleaned and degassed cathodes, the appearance of ectons was not observed. Ectons were observed to appear at a very short distance from the plasma source to the cathode (about 5  $\mu\text{m}$ ), when the cathode surface had been thoroughly cleaned from oxides and dielectric impurities [29]. In this zone, the plasma density was of the order of  $10^{20} \text{ cm}^{-3}$  and the ion current density at the cathode was of the order of  $10^7 \text{ A/cm}^2$ . The formation of new ectons at a short distance (of the order of several micrometers) was judged from the current waveform and by the appearance of microcraters. What are the reasons for these effects? When plasma is flowing over the surface of a cathode in the presence of an electric field, there takes place the effect of enhancement of the current density at the cathode microprotrusions.

Let us consider three configurations of a microprotrusion on a plane cathode: a cylinder, a cone, and a sphere (Fig. 7). If such a microprotrusion is flown up with plasma, an ion current  $i_i = j_i S$  (with  $j_i$  being the ion current density and  $S$  the surface area of the protrusion) will flow over the protrusion surface. When the current will enter the cathode, the area through which it will pass equals  $\pi r^2$  for all three microprotrusion geometries. So the current density at the cathode will be

$$j = j_i S / \pi r^2. \quad (4.11)$$

The area  $S$  will be  $2\pi r h$ ,  $\pi r l$ , and  $4\pi R^2$  for a cylinder, a cone, and a sphere, respectively (with  $l$  being the generatrix of the cone). With that, the current density enhancement factor,  $\beta_j$ , will be, respectively,  $2h/r$ ,

$l/r$ , and  $4R^2/r^2$ .

The effect of current density enhancement holds not only for an ion current but also for any current emitted or received by the cathode surface. For instance, if the cathode surface is heated to a high temperature, the surface of a cathode microprotrusion will emit a thermal field emission current whose density in the cathode region will be  $\beta_j$  times higher than the density averaged over the surface area. This conclusion is

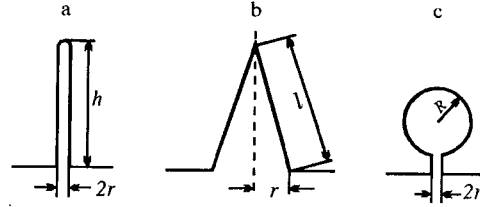


Fig. 7. Cathode microprotrusion geometries for definition of the coefficient of current density enhancement: cylinder (a), cone (b), and sphere (c).

also valid for the backward current of the plasma electrons flying toward the cathode. The above effect is important for the self-sustaining of microexplosive processes, i.e., for the appearance of secondary ectons. Moreover, if irregularities are in the close vicinity of an explosive center, the ion current density at them may be rather high, which, in view of the effect of its enhancement, leads to a microexplosion at the cathode surface. Actually, the ion current density is given by

$$j_i = q_i n_i v_i / 4, \quad (4.12)$$

where  $q_i$  is an average charge of the ions,  $n_i$  is their density, and  $v_i$  their velocity. Since the ion density decreases with distance  $x$  from the emission center as  $n_i \propto 1/x^2$ , one should expect that the effect of current density enhancement will be strong near the emission center [29].

The influence of the cathode plasma on the energy concentration in a cathode microvolume becomes much more pronounced when a dielectric film or a dielectric inclusion is present on the cathode surface. Let a dielectric film be present on the surface of a cathode with a metal microprotrusion located beneath the film. If this system is in an electric field and plasma arrives at the dielectric surface, the ions moving toward the dielectric film will charge it. The electric field in the film will be

$$E = j_i t / \epsilon \epsilon_0, \quad (4.13)$$

where  $\epsilon$  is the permittivity of the film and  $t$  is the time. As the electric field reaches a certain value, the film is broken down. The breakdown current will give rise to an ecton. Thus, we have shown that there are two ways of the plasma-assisted initiation of ectons. One of them is associated with the charging of dielectric films and inclusions on the cathode by the plasma ions and the other with the enhancement of the current density at cathode microprotrusions.

If we assume that an ecton is formed with the electric field inside the dielectric  $E > 10^6$  V/cm, then, in order that the dielectric film be charged and broken down within a time  $t < 10^{-9}$  s, the relation

$$n_i v_i > 10^{23} \text{ cm}^{-2} \text{ s}^{-1} \quad (4.14)$$

must be satisfied. For  $v_i \sim 10^6$  cm/s and  $n_i \sim 10^{17}$  cm<sup>-3</sup>, the appearance of ectons under the plasma arrived at the cathode can be expected. For the second way of the plasma-assisted initiation of ectons, with the current density being  $10^9$  A/cm<sup>2</sup>, the relation

$$n_i v_i > 10^{28} \beta_j^{-1}, \quad (4.15)$$

should be fulfilled. If we suppose that  $\beta_j \approx 10^2 - 10^3$ , then, in order that ectons be initiated, it is necessary that, provided that the ion density be the same, the plasma density should be two or three orders of magnitude higher [1]. This explains why an ecton can readily be initiated with a low-density plasma at a contaminated cathode, while at a cleaned cathode an ecton is initiated only with a high plasma density (of the order of  $10^{20}$  cm<sup>-3</sup>). Other methods for the initiation of breakdown are eventually reduced to the creation of plasma at the cathode. For instance, a general way is to focus laser radiation onto the cathode surface [13, 30, 31]. The appearance of plasma is observed when the radiation energy flux density is in the range 0.01–10 J/cm<sup>2</sup>. This energy is insufficient for the cathode metal to explode but sufficient for a plasma blob to appear at the cathode. This action causes a heating of the cathode surface, gas desorption, evaporation of the metal, and thermal electron emission. This leads to ionization of the vapor by hot

electrons. For instance, thermal electron emission from the surface of tungsten was observed when the intensity of irradiation was over  $2.5 \cdot 10^7$  W/cm<sup>2</sup> with the laser pulse duration 50 ns. The thermal electron current density was 0.5 A/cm<sup>2</sup>. The cathode plasma generated by laser radiation gives rise to an ecton and leads to vacuum breakdown. The adsorbed gas present on the cathode encourages the process of breakdown. The influence of the adsorbed gas on the initiation of ectons is twofold: On the one hand, this gas affects the work function of the metal and thus participates in the initiation of ectons by FE current and, on the other hand, after desorption and ionization, it acts on the metal like plasma. With electric fields  $E \geq 10^7$  V/cm, field desorption takes place.

In our view, ectons also appear when a microscopic material particle accelerated to a high velocity hits a cathode. With that, three options for the initiation of an ecton can be qualitatively distinguished. If the velocity of the particle is not very high, its impact on the cathode results in a heating of a cathode microregion, gas desorption and evaporation of the cathode material in this microregion and of the particle itself, ionization of the gas and the vapor, and appearance of an ecton due to the plasma-cathode interaction. At a high velocity, the particle may give rise to a microexplosion and to produce an ecton on its direct interaction with the cathode.

## 5. THE VACUUM SPARK

The vacuum spark most clearly shows up the properties of ectons and EEE under non-steady-state conditions. The role of EEE in a vacuum spark was identified based on the results of a three series of experiments performed using nanosecond high-voltage pulses [4]. First, the electron current at the initial stage of a vacuum spark was investigated. Second, the cathode and anode glows were observed using an electron-optical image converter with nanosecond exposure times and light amplification up to  $10^6$  times. Third, the character of the cathode and anode erosion was investigated and the mass of the material removed from their surfaces was measured. Let us discuss in detail the results obtained.

All experiments were performed with a nanosecond pulse generator. The current rise proceeds within a time interval which involves the time delay,  $t_d$ , and the closure time,  $t_c$  [4] (Fig. 8). The time  $t_c$  is generally taken as the time between the points where the current makes up 0.1 and 0.9 of its amplitude value,  $i_a$ , defined as  $V_0/R$ , where  $V_0$  is the voltage amplitude and  $R$  is the resistance of the discharge circuit. The time  $t_d$  is associated with the breakdown phase,  $t_c$  with the spark phase, and the subsequent time with an arc discharge. The electrodes used in the experiments were made of copper, aluminum, tungsten, molybdenum, steel, lead, and graphite; the gap spacing,  $d$ , was varied from 0.1 to 1 mm.

The conclusions made about the time  $t_c$  for plane electrodes are as follows: The closure time  $t_c$  increases linearly with gap spacing and does not depend on the amplitude of the applied voltage. The current rise rate  $di/dt$  decreases with increasing gap spacing and increases with voltage. The ratio  $d/t_c$  is of the order of  $10^6$  cm/s for all electrode materials investigated (Fig. 9). It is interesting that the regularities found for the closure time  $t_c$  are the same for pulsed and dc vacuum discharges.

The regularities found for the closure time  $t_c$  are accounted for by the expansion of the cathode plasma resulting from a microexplosion. Electron-optical records of the cathode glow (see Fig. 2) show plasma microblobs appearing a few nanoseconds after the application of voltage [4]. These microblobs, named cathode flares (CF), represent the plasma formed as a result of an explosion of the cathode material in surface microregions. Generally, a single or several CFs appear at the cathode, depending on the overvoltage across the gap. At a dc breakdown, only one CF appears. It has been shown [4] that the glow of the CF plasma is interrupted in character and for a copper cathode its periodicity is 3–5 ns. This may be an indication of disappearance of ectons and appearance of new ones at the cathode surface.

For copper, the velocity of motion of the cathode flare is about  $1.6 \cdot 10^6$  cm/s. An investigation of the regularity of the EEE current rise has shown that this rise is limited by the space charge of the electron current emitted by CF. In the general form, this regularity is written as

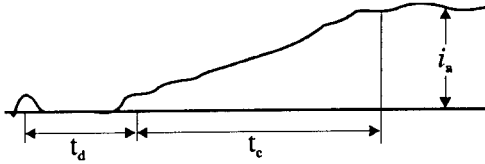


Fig. 8. Current waveform in vacuum discharge.

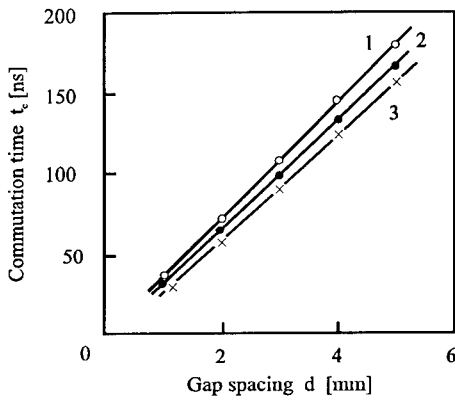


Fig. 9. Closure time versus vacuum gap spacing for electrodes made of aluminum (1), copper (2), and molybdenum (3).

Fig. 10. Current density burst at anode along the discharge axis.  $V = 30$  kV,  $d = 4$  mm.

obtained by investigating the local current density at the anode. If we make a hole in the anode and measure the electron current, we may observe intense current bursts on the background of a monotonically rising spark current [4]. This suggests that at local sites of the cathode new electron sources – ectons – appear. Figure 10 shows a current burst at the discharge axis for copper electrodes: a point cathode and a plane anode. The duration of this burst was  $\sim 10$  ns. Current bursts of the same duration were observed for a voltage of 20–200 kV and gap spacings of 1–17 mm [4].

Examination of the microcraters formed on the cathode has revealed two types of microcraters. First, there are many craters at one and the same place. Second, there are craters located at a certain distance from one another. Both types of craters may be produced by a single discharge (Fig. 11). Craters of the first type appear due to the fact that liquid-metal jets interacting with plasma explode and produce new craters at the same place. Craters of the second type may be formed for two reasons: by several simultaneous microexplosions initiated by simultaneous Joule heating of several micropoints (as can be seen in Fig. 2) and by a plasma-initiated microexplosion occurring due to charging and breakdown of dielectric inclusions on the cathode surface or due to the effect of current density enhancement at microprotrusions flown over with plasma (see Sec. 4). A detailed study of the craters has been made by B. Juttner *et al.* in a number of papers, which are generalized in a thesis [33].

We can estimate the existence time of EEE current, i.e., the existence time of an ecton,  $t_e$ , from the radius of a corresponding on the cathode surface crater ( $r_c \approx 2 \cdot 10^{-4}$  cm). If the crater radius is related to heat conduction, it is found from the formula:

$$r_c \approx 2(at_e)^{1/2}. \quad (5.3)$$

$$i = A_0 V^{3/2} \dot{F}(vt/d), \quad (5.1)$$

where  $A_0$  is a constant depending on the gap geometry,  $V$  is the voltage between the cathode and the anode,  $v$  is the velocity of expansion of the cathode plasma,  $d$  is the gap spacing, and  $t$  is the time. For a single CF at a cathode of radius  $r < vt$  with  $d \gg vt$  we have  $F(vt/d) \propto vt/d$ . For this case, the current rise rate at the initial stage of EEE is given by

$$\frac{di}{dt} \approx A_0 V_0^{3/2} \frac{v}{d} = A_0 V_0^{1/2} E_0 v, \quad (5.2)$$

where  $E_0$  is the initial field in the gap. For  $E_0 \approx 10^6$  V/cm,  $v = 2 \cdot 10^6$  cm/s,  $V_0 \approx 10^4$  V, and  $A_0 \approx 3.7 \cdot 10^{-5}$   $AV^{-3/2}$ ,  $di/dt$  will be on the order of  $10^{10}$  A/s, as obtained in experiment [4]. The linear rise of the closure time  $t_c$  on the gap spacing  $d$  follows immediately from formula (5.1), as for a fixed current we have  $vt_c/d = \text{const}$  and, hence,  $t_c$  proportional to  $d$ .

After a time, in addition to the CF, an anode flare (AF) appears, which is due to the heating of the anode surface by the EEE current (see Fig. 2). This fact together with the existence of intense X-radiation at the anode during the time the CF moves toward the anode and the reflection of the beam by the magnetic field perpendicular to the electric field are strong evidence for the electronic character of the current emitted by the cathode after the appearance of an ecton at the cathode surface. An important information about ectons can be

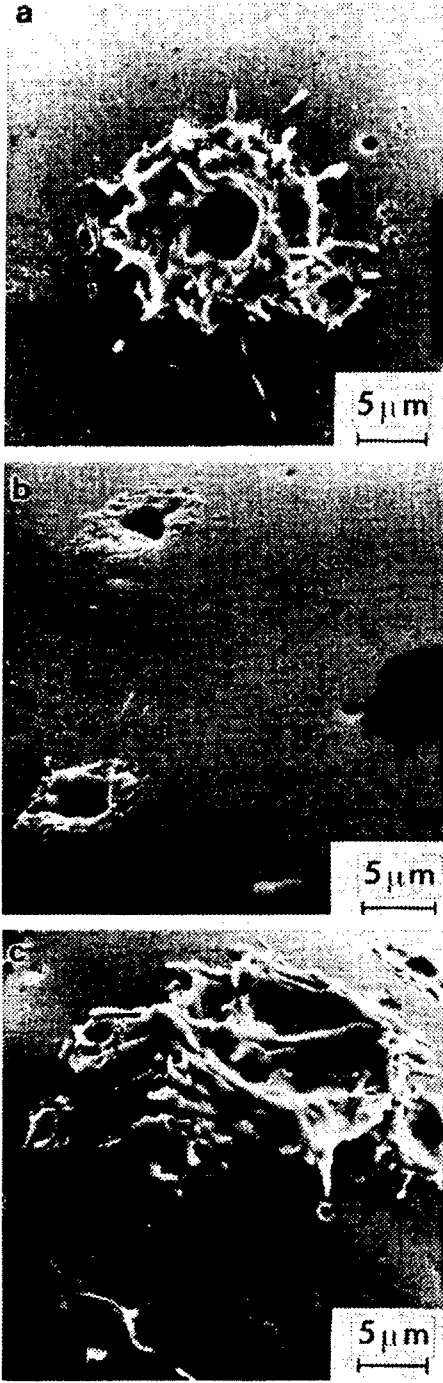


Fig. 11. Micrographs of the surface of a copper cathode after a single current pulse with  $t_p = 20$  (a), 50 (b), and 100 ns (c);  $d = 3$  mm,  $V = 30$  kV.

$\bar{h} \cong 3 \cdot 10^9 \text{ A}^2/\text{cm}^4$ , and  $\rho = 8.9 \text{ g/cm}^3$ , and so  $\gamma_m \cong 7.5 \cdot 10^{-5} \text{ C}^{-1}$ . Measurements of  $\gamma_m$  in a vacuum discharge with a cathode made of a cylindrical copper wire of diameter  $50 \mu\text{m}$  and with a current rise rate of  $(0.3\text{--}1.1) \cdot 10^9 \text{ A/s}$  have yielded in average  $\gamma_m \cong 4 \cdot 10^{-5} \text{ g/C}$  [4]. The difference between estimates and

We have  $a \approx 1.6 \text{ cm}^2/\text{s}$ , and so  $t_e \approx 6 \text{ ns}$ . About the same value of  $t_e$  can also be inferred from the micrograph given in Fig. 11. Here, three craters have been formed at the same place within 20 ns. Therefore, the lifetime of each of them was  $\sim 6\text{--}7 \text{ ns}$ . Important data about the spark stage of a discharge have been obtained in studying the ejection of drops from a cathode [4]. For a copper cathode, the reduced specific number of ejected drops has been obtained to be in average  $\gamma_d \approx 2 \cdot 10^7 \text{ C}^{-1}$ . The maximum of the drop diameter distribution for the pulse duration ranging from 30 to 300 ns remained fixed and corresponded to the drop diameter  $\sim 0.1 \mu\text{m}$ . This is strong evidence in support of the cyclic nature of the processes occurring at the cathode in a vacuum discharge (see Fig. 10). If we assume that the appearance of drops is an element of an ecton cycle, this means that the duration of an ecton process is shorter than 10 ns (Fig. 12). Thus, we have found that  $t_e \approx 5\text{--}10 \text{ ns}$ . From the foregoing, a model of a vacuum spark emerges as follows: After the appearance of a first ecton through spontaneous and secondary processes, new ectons appear whose number depends on the current and duration of the spark stage. If each ecton has a charge  $q_e$  and one drop corresponds to one ecton, the charge of one ecton will be

$$q_e = 1/\gamma_d. \quad (5.4)$$

For  $\gamma_d \approx 2 \cdot 10^7 \text{ C}^{-1}$  we have  $q_e \approx 5 \cdot 10^{-8} \text{ C}$ . Since  $q_e = i_e t_e$ , then for  $t_e = 5\text{--}10 \text{ ns}$  the ecton current will be  $\sim 5\text{--}10 \text{ A}$ . The number of ectons initiated during the spark stage,  $N_0$ , will be determined from the relation

$$N_0 \approx \int_0^{t_s} i dt / q_e = \gamma_d \int_0^{t_s} i dt, \quad (5.5)$$

where  $t_s \approx t_e$  is the duration of the spark stage. Since the total charge transferred during the spark stage can be found approximately as  $Q_s \approx t_s i_a$ , where  $i_a$  is the pulsed current amplitude, we have

$$N_0 \cong \gamma_d t_s i_a \approx \gamma_d i_a d / v_{ac}, \quad (5.6)$$

where  $v_{ac}$  is the velocity with which the cathode plasma approaches the anode plasma. From Eq. (5.4) it follows that the number of electrons in an ecton is  $\sim 3 \cdot 10^{11}$ .

For a current of 100 A,  $d = 1 \text{ cm}$ , and  $v_{ac} \cong 2 \cdot 10^6 \text{ cm/s}$ , the total number of ectons initiated during the spark stage will be, according to Eq. (5.6),  $N_0 \cong 10^3$ . Let us now estimate the reduced mass removed from the cathode in the spark stage of a vacuum discharge. According to Eq. (2.6), we have  $\gamma_m = (2\rho/3)(a/\bar{h})^{1/2}$ . The values of  $a$  and  $\bar{h}$  should be taken for molten metal. For copper we have  $a = 0.47 \text{ cm}^2/\text{s}$ ,

measurements is perhaps related to the error involved in the determination of the charge from current oscillograms and to the use of the  $\alpha$  and  $\bar{h}$  values corresponding to a solid-state metal for a liquid metal.

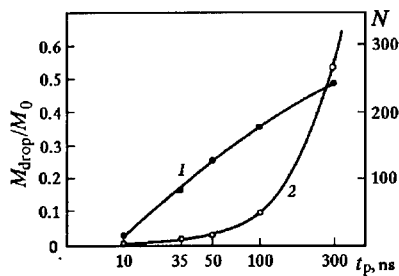


Fig. 12. Relative drop fraction mass (1) and number of drops (2) versus pulse duration for a copper cathode.

## 6. THE VACUUM ARC

The vacuum arc has some features making it different from other types of discharge. In its operation, there is a low potential difference which is localized in the cathode region and equals approximately the ionization potential of the cathode material. There is a threshold current at which an arc ceases to operate. The vacuum arc space between the cathode and the anode consists of three regions. One of them is at the cathode and looks like a bright luminous spot executing a fast random motion over the cathode surface. This region is called

a cathode spot. Another region takes most of the space between the cathode and the anode and has the appearance of a bright diffuse glow. This region is referred to as a positive column and plays the role of a plasma conductor between the cathode and the anode. It is characterized by a uniform electric field distribution and a comparatively low potential gradient. At the anode, a region exists which is named an anode region. The peculiarity of the phenomenon of a vacuum arc is in fact associated with the cathode spot. The problem of studying the vacuum arc is reduced to the study of its cathode spot which, as mentioned above, is characterized by a high current density and a high energy concentrated in a unit volume. To initiate an arc in a vacuum between metal electrodes, it is necessary to fulfil some conditions. First of all, a certain minimum potential difference should be maintained, which, for short arcs, approaches the cathode fall voltage  $V_c$ . Moreover, an arc will operate if only the discharge current is over a threshold value,  $i_{th}$ , depending on the electrode material.

The now available techniques for the initiation of a vacuum arc are as follows [32]: initiation of breakdown in the vacuum gap with a fixed electrode separation, approaching the electrodes to one another, breaking the circuit, passing a current through a semiconductor immersed in liquid metal, inducing the glow-to-arc transition, producing a plasma flowing over the cathode surface, *etc.* We will not consider these techniques in detail but only note that all them are eventually reduced to the concentration of energy in a cathode microvolume and to the initiation of a primary ecton.

A cathode spot is a small bright luminous region over the cathode surface through which the current transfer between the cathode and the arc column occurs. In the spot region, the cathode surface is heated to a temperature being much over the boiling point of the cathode material. A recent review of the cathode spot studies has been made by [13]. Cathode spots come in two types [33]. A first-type cathode spot consists of individual bright spots located at a certain distance from one another. For these spots, the mass of the cathode material removed per unit charge is not large (for copper  $\gamma_m = 5 \cdot 10^{-7}$  g/C). Spots like these appear due to the excitation of ectons on charging dielectric films and inclusions by the current of the plasma flowing over the cathode. This is so indeed since first-type spots do exist only at a cathode which has not been cleaned from contaminants. At a cathode thoroughly cleaned by heating, ion bombardment, or by other techniques, second-type spots appear which have large dimensions and consist of individual fragments. Furthermore, first-type spots, when operating for several hundreds of microseconds (with a current on the order of 100 A), change into spots of the second type. This can be accounted for by the fact that within this time the cathode surface is cleaned from adsorbed gases and dielectric inclusions and films. For second-type spots,  $\gamma_m$  is much greater (on the order of  $10^{-5}$ – $10^{-4}$  g/C).

Kesaev [32] has shown that a cathode spot contains individual cells which carry a current being not over than the doubled threshold current. When the current becomes higher than the doubled threshold current, it is observed that some cells cease to exist and new cells appear through division of the

remaining ones. The cathode spot ejects plasma, vapors, and drops of the cathode material. The appearance of a cell, its functioning and the following death make up an arc cycle.

We will proceed from the Kesaev's idea that a cathode spot consists of individual cells, each carrying a current equal to the doubled threshold arc currents:  $i_m = 2i_{th}$ . For copper we have  $i_{th} \approx 1.6$  A. In our opinion, the functioning of a cathode spot cell is a typical ecton process. An ecton is formed as a result of the interaction of a molten-metal jet with plasma. Such jets are ejected from the cathode surface due to a high pressure in the microexplosion zone, which may reach  $10^4$ – $10^5$  atm [4]. For a current exceeding the threshold arc current, a liquid-metal jet forms a drop which, still before its break-off, provides an enhancement of the ion current density at the jet-drop joint. This results in concentration of energy at the joint and in a microexplosion initiated by Joule heating of the joint [1].

In our view, an arc cycle involves two processes (Fig. 13). The first one, whose duration is  $t_e$ , is the operation of an ecton, and the second one, whose duration is  $t_i$ , is associated with the ion current flowing in the cathode region. In Fig. 10, the time  $t_e$  corresponds to the low-voltage stage and  $t_i$  to the stage with an increased voltage. Let us use the notation  $\alpha = t_i/t_e$ . Within the time  $t_e$ , the ecton current flows and the formation of a new liquid-metal jet is completed. Within the time  $t_i$ , a new ecton is induced. Thus the process becomes self-sustaining.

For an ecton produced as described above, i.e., on detachment of a drop or with a drop being a constituent of an ecton cycle, the criterion for the arc cycle to be self-sustaining is written as

$$\gamma_d t_c i_m \geq 1, \quad (6.1)$$

where  $\gamma_d$  is the number of drops produced per unit charge and  $t_c = t_e + t_i$  is the time of the arc cycle, where  $t_e$  is the electronic phase of the cycle and  $t_i$  is the ionic phase of the cycle. Assume that a liquid-metal jet has the shape of a cone [10, 34]. Then the ecton lifetime and the mass of the metal removed from the cathode will be determined from formulas (2.3) and (2.4) with  $i = 2i_{th}$ . For an arc, the reduced mass removed from the cathode is given by

$$\gamma_m = \frac{2}{3} \rho (1 - \alpha) \left( \frac{a}{\bar{h}} \right)^{1/2}. \quad (6.2)$$

For copper we have  $\alpha \approx 0.2$ ,  $a = 0.42$  cm<sup>2</sup>/s,  $\bar{h} \approx 3 \cdot 10^9$  A<sup>2</sup>·s/cm<sup>4</sup> [10, 34] and, hence,  $\gamma_m \approx 0.6 \cdot 10^{-4}$  g/C. Daalder [35] in his experiments obtained  $\gamma_m \approx 0.4 \cdot 10^{-4}$  g/C. Studies of the vacuum discharge have shown that the explosion of micropoints on the cathode is accompanied by ejection of cathode plasma



Fig. 13. Arc cathode potential oscillations for a copper cathode with a current of 4 A.

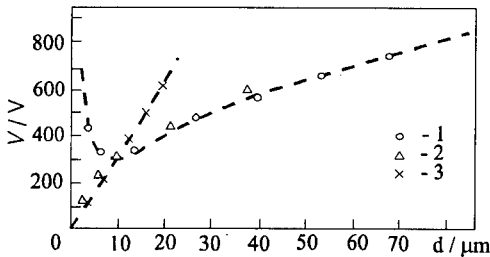


Fig. 14. The right branch of the Paschen curve  $V = f(pd)$  for air (1) and hydrogen (2) [45].

which propagates toward the anode with a velocity  $v > 10^6$  cm/s [4]. This results in the appearance of a positive ion current flowing toward the anode,  $i_i$ , (anode erosion) whose fraction in the total arc current is

$$i_i/i = \gamma_m q Z e / m_a, \quad (6.3)$$

where  $i$  is the arc current,  $q$  is an average ion charge,  $Z$  is the degree of ionization of the plasma,  $m_a$  is the atomic mass, and  $e$  is the charge of an electron. According to the data of Kimblin [36],  $Z = 0.55$  and the average charge  $q = 1.5$  [37] or 1.85 [38]. We take an averaged value:  $q = 1.7$ . Substitution of  $\gamma_m$  determined from Eq. (6.2) into Eq. (6.3) yields  $i_i \approx 0.08i$ , which agrees with the experimental data of Kimblin [36]. For further estimates it is necessary to know the cone angle  $\theta$ . For known  $\alpha$  and  $t_e$  we can find  $t_e$  and determine  $\theta$  from Eq. (2.3). For our case we have  $\theta \approx 0.53$ . The cone angle can also be found knowing the reduced number of drops  $\gamma_d$  ejected by the vacuum arc cathode spot. For instance, for silver we have  $\gamma_d \approx 1.4 \cdot 10^7$  C<sup>-1</sup> [39]. According to Eq. (6.2), for  $i_{th} = 1.6$  A we obtain the time of the cycle  $t_c \approx 22$  ns, which is close to the value measured from potential oscillations. For the general case, substituting



(6.1) into (2.3), we obtain

$$\theta^4 \approx \frac{1}{\pi^2(1-\alpha)} \frac{i_m^3 \gamma_d}{a^2 \bar{h}}. \quad (6.4)$$

From Eq. (6.4) it follows that  $\theta = 0.54$ . Now we dwell on the estimation of the arc current density. It is different for different points in time. The current density at the instant an ecton is initiated will be found from the relation  $j^2 t_d = \bar{h}$ . Since we have  $\bar{h} \approx 10^9 \text{ A}^2/\text{cm}^4$ , the time delay to explosion is  $t_d \approx 10^{-9} \text{ s}$ . For the instant the ecton ceases to operate, the current density will be determined from the formula

$$j_e = \pi a \bar{h} \theta^2 / i_m. \quad (6.5)$$

For copper it will be  $2.2 \cdot 10^8 \text{ A/cm}^2$ . However, the current density is commonly estimated from the measured radius of the crater,  $r_c$ , on the cathode surface and from the arc current. Estimation of the crater radius by the formula  $r_c = 2(at_c)^{1/2}$  yields  $r_c \approx 2 \cdot 10^{-4} \text{ cm}$ , which is close to the data of [40] for arc currents  $i < 10 \text{ A}$ . For this case, the apparent current density defined as  $j_c = i_m/(\pi r_c^2)$  will be  $2.7 \cdot 10^7 \text{ A/cm}^2$ . This is close to the measured value for copper [40]. Based on the ecton mechanism of a vacuum arc, the Tanberg effect [41] can be explained. This effect is that during the operation of an arc, a force acts on the cathode that seeks to increase the distance between the cathode and the anode. The Tanberg effect is characterized by a parameter,  $f$ , which is the force per unit current:

$$f = m_e v / (2 t_e i_m), \quad (6.6)$$

Here,  $v$  is the velocity of the cathode plasma. According to Tanberg [41], for copper this velocity is  $\sim 10^6 \text{ cm/s}$ . The number two in Eq. (6.6) accounts for the anisotropy of the plasma expansion. In view of the relation  $m_e/(t_e i_m) = \gamma_m$ , we have

$$f = \frac{\rho v}{3} \left( \frac{a}{\bar{h}} \right)^{1/2}. \quad (6.7)$$

For copper we obtain  $f \approx 30 \text{ dyn/A}$ . The experimental data of Tanberg yield  $20 \text{ dyn/A}$  for the reduced force. The above results show that the ecton mechanism offers a satisfactory explanation to the operation of the cathode spot of a vacuum arc. The threshold current, the cathode fall potential, the plasma jet velocity, and other parameters of the arc phenomena are explained in terms of the ecton mechanism in our works [1, 4, 34]. Interesting evidence for the existence of cyclic processes in an arc is also provided in [42].

## 7. ECTONS IN A GAS DISCHARGE

### 7.1 Departure from the Paschen law

We think ectons play an important part in many types of electrical discharge in gases. The appearance of ectons has the result that the classical discharge mechanisms are violated. The reasons for the appearance of ectons at the cathode are the same for gas and vacuum discharges. They are the explosion of cathode microprotrusions caused by the high FE current resulting from a high electric field at the cathode and the breakdown of dielectric films and inclusions present on the cathode surface due to their charging by ions from the discharge plasma. On the one hand, the gas present in the discharge gap facilitates the initiation of ectons owing to the existence of the gas discharge plasma and the dielectric films formed as a result of the interaction of the gas and the metal. On the other hand, a microexplosion at the cathode surface is not necessarily accompanied by a fast rise of the current because present an obstacle to the current rise the atoms and molecules met by the ecton electrons in their motion. A manifestation of the ecton processes is the violation of similarity laws, in particular, in the Paschen law. The latter relates the statistical breakdown voltage,  $V$ , to the gas pressure,  $p$ , and the gap spacing,  $d$ , as  $V = f(pd)$ .

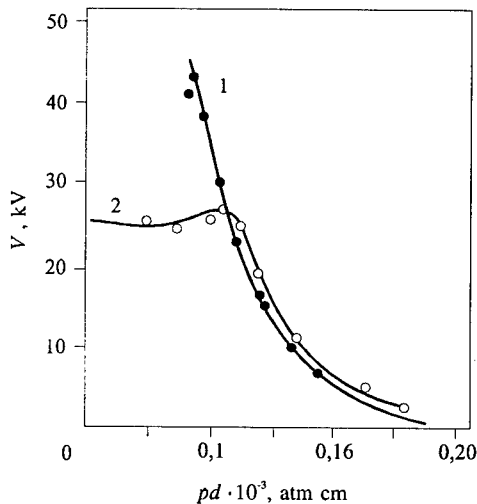


Fig. 15. The left branch of the Paschen curve: (1) classical dependence and (2) dependence in the presence of an ecton [43].

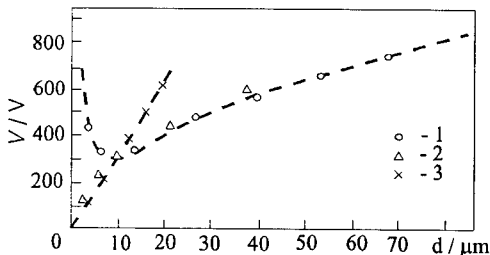


Fig. 16. Neighborhood of the minimum of the Paschen curve: (1) points on the Paschen curve; (2) points of deviation from the Paschen curve, and (3) points corresponding to the average electric field  $3 \cdot 10^5$  V/cm [43].

of an ecton by FE current or by breakdown of the dielectric film present on the cathode surface. In view of the fact that discharges of all mentioned types constrict in the same manner, we consider this effect for a glow discharge as an example.

Characteristic features of a glow discharge are the spatial character of the current flow and the presence of a cathode fall potential layer owing to which electrons from the near-cathode regions come uniformly into the discharge column. The potential fall across the near-cathode regions is typically equal to several hundreds of volts and the size of the near-cathode region is established such that conditions for the discharge to be self-sustaining are provided through ionization processes in the gas and through secondary processes at the cathode.

The secondary electrons appear at the cathode on its bombardment by positive ions, due to photoeffect, and on bombardment of the cathode by fast neutral atoms resulting from charge exchange and other processes. These processes provide, as a rule, a uniform current density of secondary electrons at the cathode and, correspondingly, a homogeneous structure of the cathode layer. For a normal glow discharge, the current density remains constant, while the total current increases due to the increase in the area taken by the discharge at the cathode. Once the discharge has taken the entire surface, further increase in the total current in the circuit results in an increase in its density and in discharge operating voltage. The glow discharge in this case is said to operate in an abnormal mode. As a certain current density is achieved in an abnormal discharge, this results in a jumpwise glow-to-arc transition.

A departure from the Paschen law is generally observed for three portions of the Paschen curve: the right branch corresponding to high pressures, the left branch corresponding to low pressures, and the region of the minimum. For all these portions, the average electric field in the gap is high enough (on the order of  $10^6$  V/cm and more) for FE to occur from individual cathode microprotrusions. The emitted electrons ionize the gas and the resulting ions move toward the cathode. With that, FE is enhanced by the ion space charge, which further increases the FE current density. Eventually, all this leads to the formation of ectons. As can be seen from Figs. 14, 15, and 16, any departure from the Paschen curve results in a decrease in breakdown voltage compared to the breakdown voltage determined by the Paschen law.

## 7.2 Constriction of a volume discharge

Another manifestation of the ecton processes in a gas discharge is the constriction of the discharge, i.e., its transition from spatial to channel operation [43]. Examples of space discharges are the low-pressure glow discharge, the self-sustained pulsed space discharge operating at both low and high pressures (1 atm and more), and, finally, the non-self-sustained discharge with intense external ionization, e.g., by an electron beam [44].

For space discharges, the discharge constriction begins directly at the cathode because of the initiation

The glow-to-arc transition is accompanied by redistribution of the current in the discharge column (column constriction) and of the current at the cathode (current localization in the cathode spot region). There are two viewpoints on the mechanism of the glow-to-arc transition.

One viewpoint implies that the discharge constriction is due to the instabilities appearing in the discharge column. For instance, for a glow discharge operating in a long tube, the column may constrict owing to the fact that more energy is released at the axis than in the peripheral regions. This results in heating of the gas and in a decrease in the density of neutrals. The decrease in neutral density in turn leads to more intense power dissipation at the discharge axis [46, 47].

However, another approach also exists which is based on experimental data on the instabilities developing in the near-electrode regions (more often in the cathode region) and causing the discharge to constrict [43]. It is believed that these instabilities are responsible for the instability of the discharge column. This viewpoint is less represented in the literature. Even in early experiments, both the radial constriction of the column of a glow discharge, with the cathode layer parameters being unchanged, was observed as the current reached its critical value [48] and arcing induced by the instabilities having developed in the cathode region was detected [49]. With that, the second mechanism was realized over a wide range of experimental conditions, at high and at low gas pressures.

In accordance with the concept being developed in this review, one type of instability may occur in the cathode region if the electric field at the cathode is high enough for FE to be initiated at separate regions of the surface. The FE current is then enhanced by the space charge of positive ions which leads to further increase in current density, explosion of micropoints, and formation of ectons.

### 7.3 The corona discharge

A corona discharge is generally realized with a point-plane electrode geometry. A high electric field (over  $10^5$  V/cm) takes place at the point tip at which the corona starts developing. Depending on the polarity of the electrode with a small radius of curvature, the corona discharge may be either positive or negative. The electric field at the point tip is defined as  $E \approx V/r$ , where  $r$  is the radius of curvature of the point tip and  $V$  is the potential at the point. At a high field near the point, the gas is intensely ionized since the coefficient of impact ionization strongly depends on electric field. From the data reported elsewhere [45] it can be concluded that some effects observed in a negative corona may be treated as ectons. First, at the cathode of a negative corona, bright cathode spots are observed. Second, Meek and Craggs [45] paid attention to holes appeared on the negative point with coronas operating in nitrogen and hydrogen. In the experiment described in [45], positive ions that reached the cathode had energies not over 1 eV; therefore, the appearance of "craterlike holes" seemed very strange. This phenomenon was observed for tungsten, platinum, copper, and lead electrodes. Now this effect can be interpreted through the appearance of ectons.

The initiation of ectons at the stage of the formation of a corona discharge in air was observed by Gamdlin [48]. His experiments were performed in the main with an electrode gap of spacing 0.6 cm to which strictly single rectangular pulses of controllable duration were applied. The initial voltage was 25 kV and the voltage risetime was  $10^{-9}$  s. The radius of the point tip was 1 mm and more. The opposite electrode was a hemisphere of radius 0.3 cm. After breakdown, the point surface was examined in a scanning electron microscope. Moreover, the state of the test points was judged by viewing them through a shadow electron microscope. With a pulse of duration 3 ns, a crater appeared regardless of the polarity of the voltage applied to the point. However, for points of larger radius, a spot was initiated if only the point was a cathode. With that, erosion marks having the form of microcraters were observed on the cathode. The initiation of ectons at a cathode is accounted for by the development of a cathode instability. This is confirmed by the unlike character of the surface damage for the cathode and the anode. The cathode surface damage looks like grouped molten balls 1–2  $\mu\text{m}$  in diameter which more often are

closely packed within a region of size 20–30  $\mu\text{m}$ . This means that, like in a vacuum discharge, ectons are initiated at microirregularities of the cathode surface, appearing at the edges of the craters produced by preceding breakdowns. For a point whose polarity is negative, a cathode spot is initiated within a time  $t < 3$  ns. The current density at the anode increases with pressure and for a pulse duration of 20 ns and a pressure of 76, 152, and 228 mm/Hg it is equal to  $1.3 \cdot 10^4$ ,  $2.6 \cdot 10^4$ , and  $5 \cdot 10^4$  A/cm<sup>2</sup>, respectively. Putting for the electron drift velocity  $v = 10^7$  cm/s, we obtain that the electron density in the widest part of the diffuse channel near the anode is on the order of  $10^{16}$  cm<sup>-3</sup>.

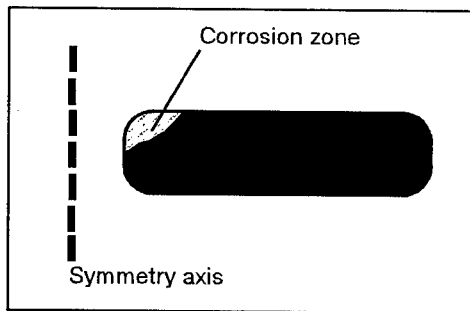


Fig. 17. Schematic view of a molybdenum cathode after  $5 \cdot 10^6$  breakdowns for a discharge of duration 90 ns and current 20 kA [52].

#### 7.4 The pseudospark discharge

In the recent decade, the pseudospark, a variety of the high-current space discharge, has been studied extensively [50]. This is a discharge with a hollow cathode and a hollow anode. It is initiated in high-current switches, which outperform thyatrons, and in electron sources. Of particular interest for this type of discharge is the emission mechanism that provides an average current density of  $10^4$  A/cm<sup>2</sup>. The principal characteristics of pseudosparks are as follows: the gas pressure in the spark gap is typically  $p \approx 0.1$  mm Hg, the gap spacing  $d \approx 0.1$ –1 cm, and the free path of an electron in the gap between the electrode  $\lambda_e > d$ . Once a discharge has been initiated in the hollow cathode, the plasma produced enters the zone of the hole, and an electron beam is formed whose current reaches 10–100 A. At this stage, the gas present on the cathode surface is desorbed and then ionized, and the plasma density in the region of the hole reaches of the order of  $10^{16}$  cm<sup>-3</sup>. The diameter of the luminous channel is approximately equal to the diameter of the hole [50]. A high-current discharge with a current density of  $10^4$  A/cm<sup>2</sup> is formed when the plasma glow expanding in radius with a velocity of  $10^8$  cm/s [50] fills the electrode gap to a size equal to five or six point diameters. The voltage across the discharge falls to several hundreds of volts. This voltage is localized across a layer of thickness  $10^{-4}$  cm and induces the field at the cathode  $E = (1\text{--}5) \cdot 10^6$  V/cm [50]. Thermal electron emission is generally assumed as the most probable emission mechanism. To produce the current density  $j = 10^4$  A/cm<sup>2</sup> at the electric field  $E = (2\text{--}5) \cdot 10^6$  V/cm, the cathode temperature  $T$  should be over 3500 K. For this temperature to be achieved for a molybdenum cathode within a time  $t < 50$  ns (the formative time of a high-current discharge), the power density at the cathode should be  $(3\text{--}4) \cdot 10^7$  W/cm<sup>2</sup>. However, the most optimistic predictions yield the energy flux intensity not over  $10^6$  W/cm<sup>2</sup>, which is evidently insufficient to heat the cathode to the melting point. The cathode microrelief after the operation of a pseudospark looks like the relief formed as a result of the action of an arc discharge [50]. The cathode material mass removed per unit charge for molybdenum is  $(5\text{--}8) \cdot 10^{-5}$  g/C, which is typical of an ecton process. The metal erosion is most intense at those places where the electric field is high, i.e., at the cathode edge (Fig. 17). In view of the character of the cathode damage, there are strong grounds for believing that the high average current density in pseudosparks is provided by ectons.

The study of the physical processes involved in the initiation and development of vacuum breakdown and the mechanisms for the emission in the cathode spot of a vacuum arc and in a space gas discharge has made it possible to establish some regularities proving that the mechanism for the emission in a pseudospark is conditioned by ectons [51]. We will proceed from the fact that the average current density on the order of  $10^4$  A/cm<sup>2</sup> in a pseudospark can be provided by  $10^3$  ectons, each carrying a current

of 10 A. The current density in an ecton may reach  $10^8$  A/cm<sup>2</sup>. The appearance of ectons within the time  $t_d$  takes place provided that  $j^2 t_d = \text{const}$ . For an initial current density of  $10^9$  A/cm<sup>2</sup>, the time  $t_d$  is in the nanosecond range. It has been shown [4] that for a molybdenum cathode conditioned in high vacuum with the average electric field at the cathode  $E > 2 \cdot 10^6$  V/cm, we have  $t_d \sim 1$  ns. The field produced by a space discharge at the initial stage of the formation of a pseudospark is of the same order of magnitude, and, hence, there exist prerequisites for the formation of an ecton within a time  $t < 10$  ns.

## 8. CONCLUSION

The present paper shows that in a number of electric gas and vacuum discharges, a fundamental role attaches to ectons. These are short-term electron avalanches emitted by the cathode for  $10^{-9}$ – $10^{-8}$  s. Ectons arise from the overheating and explosion of microvolumes near the surface of the cathode, owing to Joule heating or other effects (laser beam, the impact of a microparticle, the action of the plasma, etc.). After a primary ecton has been initiated, secondary ectons may appear if the current exceeds the threshold current. Secondary ectons emerge from the explosion of jets of liquid metal as they interact with the plasma produced by the preceding ecton. We have provided conclusive evidence for the role of ectons in a vacuum discharge (breakdown, spark, arc). As regards the gas discharge, especially at a high gas pressure, our statement here is a hypothesis. An ecton theory is currently difficult to create because as an ecton is produced the cathode material in a volume  $10^{-12}$  cm<sup>3</sup> passes from the solid to the liquid, vapor and plasma entity in no more than  $10^{-8}$  s. The semiclassical estimates that we have made by invoking the quantity "specific action" give a fairly good fit to experimental data. We hope that our paper will give an impetus to studying a phenomenon such as the ecton and its role in electric discharges.

## References

- [1] Mesyats G.A., *Pisma Zh. Eksper. Teor. Fiz.* **57** (1993) 88-92.
- [2] Mesyats G.A. and Proskurovsky D.I., *Pisma Zh. Eksper. Teor. Fiz.* **13** (1971) 7-10.
- [3] Mesyats G.A., "The role of fast processes in vacuum breakdown", X Int. Conf. on Phenomena in Ionized Gases, Inv. Pap., (Oxford, 1971) p. 333.
- [4] Mesyats G.A. and Proskurovsky D.I., *Pulsed Electrical Discharge in Vacuum* (Springer-Verlag, Berlin-Heidelberg, 1989).
- [5] Burtsev V.A., Kalinin N.V., and Luchinsky A.V., *Electrical Explosion of Conductors*, (Energoatomizdat, Moscow, 1990).
- [6] Fortov V.E. and Yakubov I.T., *Nonideal Plasmas* (Energoatomizdat, Moscow, 1994).
- [7] Sedoi V.S., Chemezova L.I., Chernov A.A., *Megagauss Fields and Pulsed Power Systems* (Nova Science, New York, 1990).
- [8] Vitkovitsky I.M., *High Power Switching* (Van Nostrand Reinhold Comp., New York, 1987).
- [9] Juttner B., Puchkarev V.F., Rohrbeck W. "Behavior of Micropoints During High Voltage Vacuum Discharges", VII Int. Symp. on Discharges and Electrical Insul. in Vacuum (ISDEIV) (Novosibirsk, 1976) p. 189.
- [10] Mesyats G.A., *IEEE Trans. on Plasma Science* **23** (1995) 879.
- [11] Zel'dovich Ya.B. and Raizer Yu.P., *Physics of Shock Waves and High-Temperature Hydrodynamic Phenomena* (Nauka, Moscow, 1966).
- [12] Vogel N. and Skvortsov V., "Plasma Parameters within the Cathode Spot of Laser-Induced Vacuum Arcs: Experimental and Theoretical Investigations", XVII ISDEIV (Berkeley, 1996) pp.89-98.
- [13] *Handbook of Vacuum Arc Science and Technology*, Ed. by R.L. Boxman, P.J. Martin, and D.M. Sanders (Noyes Publications, New York, 1995).

- [14] Little R.P. and Whitney W.T., *J. Appl. Phys.* **34** (1963) 2430-2432.
- [15] Nadgorny E.M., Osip'yan Yu.A., Perkas M.D., *Usp. Fiz. Nauk* **67** (1959) 625-662.
- [16] McDaniel E.W., *Collision Phenomena in Ionized Gases* (John Wiley & Song Inc., 1964).
- [17] Cox B.M., *J. Phys. D* **8** (1975) 2065-2073.
- [18] Gopra K.L., *Electrical Phenomena in Thin Films* (Mir, Moscow, 1972).
- [19] Vorobjov G.A. and Mukhachev V.A., *Breakdown of Thin Dielectric Films* (Sov. Radio, Moscow, 1977).
- [20] Boyle N.S., Kisliuk K.P., and Germer L.H., *J. Appl. Phys.* **26** (1955) 730.
- [21] Dyke W.P., Trolan J.K., Martin E.E., *Phys. Rev.* **91** (1953) 1043.
- [22] Alpert D., Lee D.A., Lyman E.A., *J. Vacuum Sci. and Technol.* **1** (1964) 35.
- [23] Elinson M.I. and Vasiliev V.G., *Field Emission* (GIFML, Moscow, 1958).
- [24] Dyke W.P., Trolan J.K., Martin E.E., *Phys. Rev.* **5** (1951) 1054.
- [25] Fursei G.N., Doctoral (Phys. & Math.) Thesis (Inst. of Semiconductor Physics, Novosibirsk, 1973).
- [26] Tonks L., *Phys. Rev.* **48** (1935) 562.
- [27] Pranevicius L., Serzentas S., and Bartasius J., "Liquid cathodes to study high voltage breakdown", VII ISDEIV (Novosibirsk, 1976) p. 234.
- [28] *High Voltage Vacuum Insulation*, ed. by R. Latham (Academic Press, New York – Tokyo, 1995).
- [29] Juttner B., *Plasma Sci*, **PS-15 5** (1987) 474.
- [30] Shwizke F., Taylor R. *J. Nucl. Mat.* **93-94** (1980) 780.
- [31] Seikov I.N., *High-Voltage Processes in Vacuum* (Energoatomizdat, Moscow, 1986).
- [32] Kesaev I.G., *Cathode Processes in Electric Arcs* (Nauka, Moscow, 1968).
- [33] Juttner B., *Katodenprozesse Elektrischer Enladung in Vakuum* (Berlin, ZIE, 1981).
- [34] Mesyats G.A., *Pisma Zh. Tekh. Fiz.* **60** (1994) 514-517.
- [35] Daalder J.E., *J. Phys. D* **8** (1975) 1647-1659.
- [36] Kimblin C.W., *J. Appl. Phys.* **44** (1973) 3074-3081.
- [37] Davis W.D. and Miller H.C., *J. Appl. Phys.* **40** (1969) 2212.
- [38] Plyutto A.A., Ryzhkov V.N., and Kapin A.T., *Zh. Eksper. Teor. Fiz.* **47** (1964) 494-507.
- [39] Utsumi T. and English J.H., *J. Appl. Phys.* **46** (1975) 126-131.
- [40] Daalder J.E., *IEEE Trans. Pow. Suppl. Syst.* **93** (1974) 1747-1757.
- [41] Tanberg R., *Phys. Rev.* **35** (1930) 1080.
- [42] Juttner B., *J. Phys. D* **30** (1997) 221.
- [43] Korolev Y.D. and Mesyats G.A., *Physics of Pulsed Breakdown in Gas* (Nauka, Moscow, 1991).
- [44] Bychkov Yu.I., Korolev Yu.D. and Mesyats G.A., *Usp. Fiz. Nauk* **126** (1978) 451.
- [45] Meek J.M. and Craggs J.D., *Electrical Breakdown of Gases* (Clarendon Press, Oxford, 1953).
- [46] Ecker G., Kroll W., and Zoller O., *Phys. Fluids* **7** (1964) 2001.
- [47] Jacob J. and Mani S.A., *Appl. Phys. Lett.* **26** (1975) 53.
- [48] Gamdlin W.A. and Edels H., *Nature* **177** (1956) 1090.
- [49] Boyle W.S. and Haworth F.E., *Phys. Rev.* **101** (1956) 935.
- [50] Gundersen M.A. and Schaefer G., *Physics and Application of Pseudosparks*, NATO ASI, Ser. B, (Plenum, New York, 1989).
- [51] Mesyats G.A. and Puchkarev V.F., "On mechanism of emission in pseudosparks", XV ISDEIV (Darmstadt, 1992) p. 488.

## The Birkeland Terrella Experiments and their Importance for the Modern Synergy of Laboratory and Space Plasma Physics

K. Rypdal and T. Brundtland

*Department of Physics, University of Tromsø, 9037 Tromsø, Norway*

**Abstract.** A study of the evolution of Kristian Birkeland's theories of cosmical physics is presented, with special reference to his laboratory gas-discharge experiments. It is found that his most important thoughts were molded from an intense cross-fertilization between laboratory experiments, geophysical observations and mathematical modelling. Occasionally, original ideas of fundamental importance in the cosmic context emerged from unexpected laboratory results. Possible implications for a sound cross-disciplinary approach to modern plasma science are discussed.

### 1. INTRODUCTION

Although plasma physics emerged as an independent physical discipline as late as in the 1950's, the roots can be traced back to the nineteenth century, even to the time before the electron was discovered by J. J. Thomson in 1897. At that time one did not have a clear conception of the fourth state of matter, but a few great scientists developed through laboratory experiments in discharge tubes and geophysical observations fundamentally correct ideas about the plasma nature of the sun, the interplanetary space, and the solar terrestrial interaction. A giant among these visionaries was the Norwegian physicist and inventor Kristian Birkeland (1867–1917), whose outstanding scientific work has received increasing recognition throughout the last two decades of active space exploration.

Even though modern space science continues to rediscover the deep truth of many of Birkeland's ideas, an even more interesting aspect of his work may be his interdisciplinary approach to scientific exploration. Birkeland acquired and processed information from a number of research disciplines which today are virtually non-interacting, and by bold inferences and analogies he proposed hypotheses which were not generally accepted until more than half a century after his death. Among these disciplines were electromagnetic theory, electrical engineering, laboratory gas discharges, geophysics and astrophysics. During the first decades after the end of World War II plasma science emerged as a new field that unifies the fundamental disciplines of electromagnetic theory, statistical mechanics, kinetic theory with astrophysics, space physics and materials science. However, in the last twenty years there seems to have been a decline of consciousness about plasma science as an independent, but unifying, scientific discipline. There has been a tendency towards fragmentation of plasma science into specialities like fusion plasmas, space plasmas, weakly ionized laboratory plasmas and industrial plasma processing, and many plasma physicists find it easier to market themselves to the funding agencies as fusion scientists, space physicists, and so on. This, in turn, leads to reduced emphasis on basic plasma physics, to more specialized journals and conferences, and to reduced interdisciplinary interaction. The main lesson we can learn from Birkeland and the other great founders of plasma science is to regain faith in the unity and basic nature of our science, and to strive to tear down the walls that are erected between specialized areas.

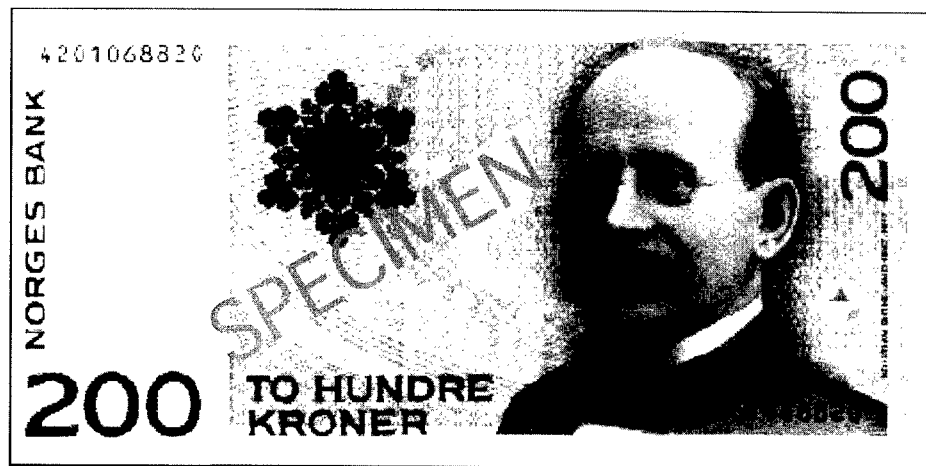


Figure 1: The 200 kr banknote issued in 1996 in celebration of the centennial anniversary of the auroral hypothesis. To the immediate left of Birkeland's portrait one can see an auroral arc from below, rising towards the polar star. One also observes several stellar constellations. The snow crystal symbolizes the winter, when aurora is most frequently observed. To the very left is a drawing of the last and largest terrella-chamber. This chamber is now restored and at display for the public at the University of Tromsø.

## 2. A BRIEF BIOGRAPHY

Kristian Olaf Bernhard Birkeland was born in Christiania (now Oslo) in Norway on December 13th, 1867. He studied physics at University of Christiania 1885–90, and in the years 1890–93 he worked as a research assistant at the University with experimental and theoretical studies on electromagnetic wave propagation. In 1893 he went abroad to continue his studies in Paris, Geneva, Bonn and Leipzig. In Paris he worked with H. Poincaré, P. Appell and E. Picard, and did his first experiments on cathode rays in a monopole magnetic field. In Switzerland he collaborated with geophysicist like E. Sarasin, and it was probably here Birkeland got his strong passion for the study of geomagnetism and polar aurora. In Bonn he worked in Heinrich Hertz' radio-laboratory. He did not obtain a fruitful collaboration with Hertz, who was ill and died shortly after, but worked for some time with P. Lénard.

Birkeland returned to a position at the University of Christiania in 1895 and immediately started to do experiments on gas discharges and cathode rays. In 1896 he performed experiments where cathode rays were attracted by a magnetic pole, and he could produce a glowing light in the vicinity of this pole reminiscent of the northern light (polar aurora) [1]. This observation made him state his auroral hypothesis — the aurora must be produced by cathode rays attracted by the earth's magnetic poles, and in some way or another the energy must be derived from the sun. The formulation of this hypothesis initiated an extensive experimental, observational and theoretical programme to unveil Nature's secrets about the origin of auroras, geomagnetic storms, the nature of solar activity, comets, planetary rings and even the origin of the solar system itself. In 1996, at the centennial anniversary of Birkeland's auroral hypothesis, a bank note was issued by the Bank of Norway (Fig. 1). In addition to the portrait of Birkeland it contains a number of details related to auroral research. In particular, one can see a drawing of the last and largest of his terrella experiments.

In the period 1897–1903 Birkeland organized three expeditions to the Arctic to make geomagnetic and other geophysical measurements. During the latest of these expeditions, "The Norwegian Aurora Polaris Expedition 1902–1903", four observatories were set up at different locations in the Arctic,



collecting geophysical data for a period of approximately a year. These data were combined with data from a large number of geomagnetic observatories around the globe and with results from laboratory terrella-experiments, and made the foundation for far-reaching theories about the cause of magnetic storms and terrestrial magnetism. This work was summarized in an 800 page treatise. The first part was published in 1908 and the second in 1913 [2].

The first series of terrella experiments were performed in glass tubes of variable shape and size in the period 1900–1908. They were conducted in between and after the arctic expeditions, and were obviously a very useful tool for Birkeland when he was striving with making sense out of the extensive mass of geophysical data acquired. During the work with the second part of his treatise he felt constrained by certain limitations of the small glass tube experiments, and started to build a series of box-shaped chambers with flat glass walls. Experiments with four different box-chambers of increasing size were conducted in the period 1908–1913, and the results were published in the second part of his treatise.

In 1903 Birkeland started a collaboration with the Norwegian mathematician and auroral physicist Carl Størmer. Henri Poincaré had already learnt about Birkeland's early cathode ray experiments from 1896, and immediately presented a solution of the equation of motion for a charged particle in a magnetic monopole field [3]. Birkeland elaborated further on this problem in an experimental and theoretical paper from 1898 [4]. The monopole problem is integrable, but the corresponding dipole problem is not, and it was this problem Birkeland wanted the gifted young Størmer to solve. For Størmer this task became a lifelong enterprise, and his calculations became a cornerstone in Birkeland's theories [5].

During his entire career Birkeland spent a lot of time on practical, industrial research and technical inventions. Among his most famous inventions are his electromagnetic gun and the development of a plasma furnace for oxidation of the air's nitrogen, which soon was developed into one of Norway's most profitable industries. Birkeland got 59 patents, and made a considerable fortune on some of them. This money was spent primarily to fund his own research. Not all of his ideas came to immediate practical application. As early as in 1906 he was searching for funds to start a project on developing methods for the release of atomic energy.

Towards the end of his short life, Birkeland's health was gradually reduced. He moved permanently to Egypt in 1913, and hoped the warm climate would do him well. Here he could also study one of his latest passions — the zodiacal light. However, his physical and mental health did not get better. In March 1917 he decided to go back to Norway, not through the war-ridden Europe, but by sea to Japan and then by rail through Siberia. He wanted to stay a few months in Japan, but on the 15th of June he was found dead in his hotel room with a handgun and a small bag of veronal on his table.<sup>1</sup>

### 3. ORIGIN AND SIGNIFICANCE OF THE AURORAL HYPOTHESIS

When Birkeland came back to Norway in summer 1895 he had become very interested in gas discharges, which was a popular field of research at that time. He obtained a position at the university, at an age of 28, and during a few hectic months in the fall 1895 he established a laboratory for gas discharge research. He also began to prepare a course in "gas discharges and experiments" with a planned start in February 1896. In January 1896 newspapers all around the world wrote about the new rays discovered by W. C. Röntgen in Germany [9]. In Christiania, Birkeland commented on this news with articles in the newspapers [10]. Less than one month after Röntgen made his first public demonstration, Birkeland demonstrated X-rays for a group of engineers, physicists and physicians. On March 23, he gave a public performance, where he could also demonstrate artificial northern

<sup>1</sup>For a more complete biography we refer to A. Egeland and E. Leer, "Professor Kr. Birkeland: His Life and Work" [6], to A. Egeland, "Kristian Birkeland, the Man and the Scientist" [7], and to A. Egeland, "Kristian Birkeland, mennesket og forskeren" [8].

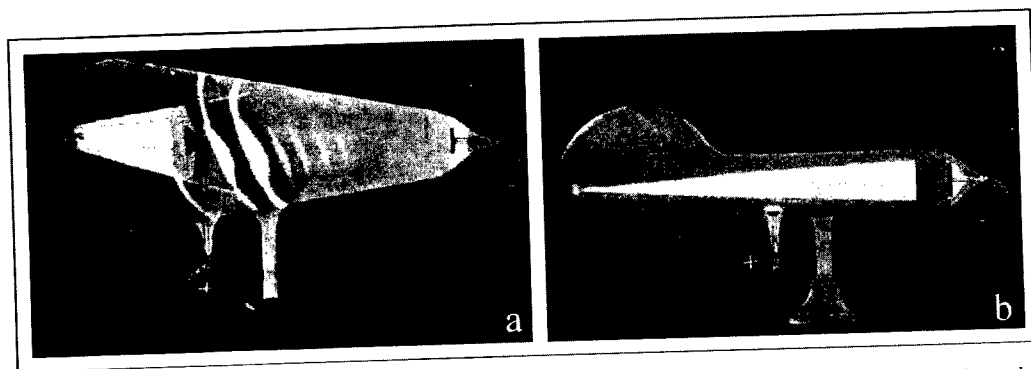


Figure 2: (a) The first production of artificial aurora in March 1896. (b) The set-up Birkeland used for writing his initials onto glass by means of cathode rays.

light in a gas discharge tube by letting "air glow in stripes as the Aurora, by magnetic influence on cathode rays". He also suggested to send photographic plates, only sensitive for cathode rays, up to high altitudes with balloons, to investigate the relationship between aurora and cathode rays.

In April 1896 he published an article [11], where he described several different experiments with gas discharges. The paper dealt with magnetic lenses, magnetic spectra and discharges that have a remarkable resemblance to the Aurora Borealis. In one experiment he was able to focus the cathode rays by external magnets, to the size of a needle point on the inner side of the glass wall. The action of such a beam was so intense and hot that if it was allowed to travel over the surface of the glass by moving the magnets, it left the mark of its track by splitting off glass particles from the wall. In this way, writings could be etched on the glass. Birkeland was easily able to write his initials, Kr. B. on the inside. The discharge tubes used for these experiments are shown in Fig. 2.

These were very important results in themselves, but the most far reaching consequences of this experimental work is contained in the inferences drawn in the last paragraph:

...Several times phenomena have been described, which show that cathode rays are drawn towards a magnetic pole. This observation is considered to be of interest in the connection with the theory of the Aurora Borealis. Paulsen, the Danish meteorologist, considers that the Aurora Borealis is due to the phosphorescence of the air by cathode rays in the highest strata of the atmosphere. The greatest difficulty in this theory has been to explain why these displays are confined to a zone surrounding the magnetic pole of the earth, and from whence the energy comes which gives rise to these rays. After what has been said above, it may be assumed that the rays are attracted by the earth's magnetic pole, and that in some way or other the energy is derived from the sun. The latter hypothesis is at least supported by the fact of the diurnal variations of the northern lights, and the cyclic changes which correspond with the 11 year periods of maximum solar activity.

The hypothesis stated above was not entirely new, although it was competing with a wealth of other colorful ideas about the origin of the aurora. About 1878 H. Becquerel suggested that particles were shot off from sunspots and were guided by the Earth magnetic field to the auroral zone. A similar idea was proposed by E. Goldstein. What distinguished Birkeland's hypothesis from the others is that he was guided by controlled experiments. This made his idea more than a suggested explanation of a phenomenon, it was a hypothesis formulated for immediate experimental test, and for two decades to come it guided him through what perhaps was the most extensive experimental and observational programme in the world to that date.

In the first years after the auroral hypothesis was formulated Birkeland conducted more laboratory work on cathode rays and magnetism. He had several publications on this subject, but he was also

studying sunspots and cosmic phenomena. Birkelands later wrote proudly and with great satisfaction that J. J. Thomson, in his classic paper on the nature of the cathode rays from 1897 [12], had taken some of his discoveries from this period as a starting point when proving that the atom is not the smallest unit of matter.

Birkeland, who became professor in September 1898, campaigned for getting an observatory for auroral studies established on the mountain of Haldde, near Alta in northern Norway. The Norwegian government provided funds, and Birkeland and an assistant stayed in an observation hut at the mountain top during the winter of 1899–1900. The results from this expedition are described in the book “Expedition Norvegienne 1899–1900” [13]. This book, published in 1901, also has a chapter on experiments with gas discharges performed in the laboratory in Christiania. One of the many experiments described in this book is a discharge set-up that showed spectacular phenomena due to electrostatic actions. He was able to guide the visible discharges towards the glass wall by putting his finger at the outside, not unlike modern “plasma balls” made for decorations.

He also described experiments with a spherical discharge tube placed on top of a big electromagnet, and with the anode located at the center of the tube. With this arrangement he was able to create some discharges of ravishing beauty, playing and dancing like the merry dancers of the auroral bands. He concluded this experiment with the following phrase:

The produced bands present then such an analogy with the auroral bands, that when witnessing this experiment, no doubt is possible, we see the evidence that the two phenomena are strongly related.

With this successful experiment a period in Birkeland’s laboratory activity was over. After four years of hard work with classical gas discharge tubes, studying X-rays, influence on cathode rays by magnets and discharges which resemble the Aurora Borealis, he now turned to a new class of experiments. During the hibernation at the mountain top in the North he had got greater ideas.

#### 4. EVOLUTION OF EXPERIMENTS AND IDEAS

In October 1900, the Norwegian electrical engineering journal, “Elektroteknisk Tidsskrift”, had a note called “The Auroral Expedition.” It contained a short description of Birkeland’s second expedition to the Arctic. Birkeland was now back in Christiania and had already done some new experiments with a “spherical electromagnet”. He would like to test some details of his auroral theory, based on recent observations during the expedition. In two gas discharge set-ups, he produced results which he interpreted as current whirls around a metallic sphere painted with phosphorescent material, with an electromagnet inside. The spheres in each case simulated the Earth with its magnetic field. The currents were created by a cold cathode discharge between electrodes in the tube, and were seen on the terrella as illuminations of the phosphorescent paint and as wedges of light with embedded rays in the rarefied gas. He could see two narrow rings of light around the poles of the sphere which was interpreted as aurora in miniature. The observations in the Arctic combined with these successful experiments were for Birkeland a great step towards a verification of his auroral hypothesis.

In the book from the expedition [13], which was published the next spring, he had a chapter describing in detail these experiments. Later he named the spherical electromagnet a *terrella* (little Earth) after the small magnets or loadstones used as Earth models back in the sixteenth century by William Gilbert (1540–1603), and described in the book “De Magnete” [14].

The idea of using a magnetizable sphere in a gas discharge opened up a new and great field of research for Birkeland. Almost all his future laboratory physics would be focused on this miniature Earth. In the hectic years 1900–1913 he used many terrellas for different purposes, varying in size and construction. In addition to studying artificial aurora he also used the terrellas for simulating solar phenomena, comets and the rings of Saturn. Ten different terrellas are described with diameters from

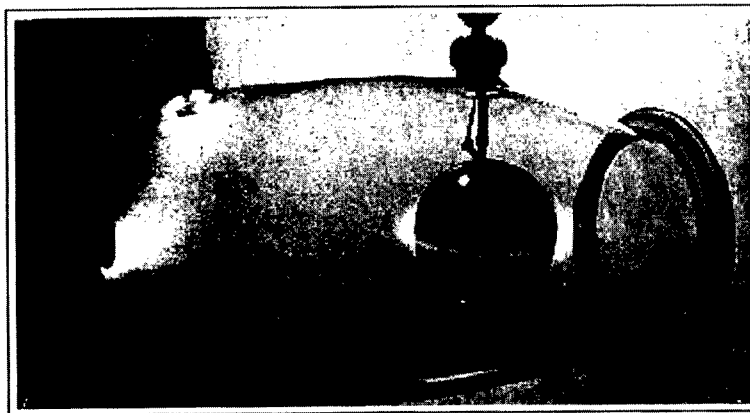


Figure 3: This simulation of “Equatorial Rings of Light” was performed in the first 12 liter glass tube with a 10 cm terrella. It was excited by an induction machine giving 6000 V, and with 10 A terrella magnetizing current. In this experiment, he ran the discharge between a cathode (left) and a separate anode (top left). Since no circuit diagram is given, the potential of the terrella surface is not known.

2.5 to 36 cm. In the first experiments, performed in the autumn of 1900, Birkeland used two terrellas, 5.0 and 7.5 cm in diameter. The electromagnets with core and windings were shaped as spheres and surrounded with a thin crust of brass covered with a coat of barium platinocyanide. Birkeland was well aware that he could not achieve quantitative similarity to natural magnetic conditions. With a terrella diameter of 7.5 cm and thereby  $1.7 \times 10^8$  times smaller than the Earth diameter, it would require an analogous magnetic field surrounding the sphere  $1.7 \times 10^8$  times stronger than the intensity of the geomagnetic field, certainly impossible to achieve in practice. Fortunately he observed that the luminous phenomena did not vary too much with the magnetic force of the terrella, provided that the force already had reached a considerable value.

All the other terrella experiments of Birkeland were described in the treatise from the third arctic expedition [2], which covers his lab work from 1901–1913. Many of the experiments were performed with terrellas where the coil and thus the magnetic axis were tilted relative to the vertical axis. During the experiments he was able to rotate the terrellas around the vertical axis, and in this way he studied the effect of the eccentricity of the Earth’s magnetic poles on the aurora.

When first starting systematic terrella experiments he used cylindrical tubes, with a volume of approximately 12 liters, as shown in Fig. 3. Experiments in this tube were also used for comparison with the orbit calculations of Carl Størmer. For direct comparison with experiments wire models were made for visualization of the trajectories in space, as shown in Fig. 4.

When simulating the aurora in the laboratory Birkeland had to give the terrella some sort of atmosphere. This problem was solved in various ways. In the early weak discharges the surface of the terrella was covered with a phosphorescent paint that produced visible light when hit by the rays. Later he described another method that made it easier to observe rays in the surrounding space. By running a high current through the magnetizing coil, the terrella surface became hot and gave off gas. He then reduced the magnetic field to the desired value, ignited the discharge, and took pictures. A third method was to cover the surface with a thin layer of pump oil, which evaporated during the discharge.

In Fig. 4 is shown a terrella with a large vertical screen. With low intensity discharges it was only possible to see where the cathode rays hit the terrellas by the phosphorescence of the surface. In order to be able to see the trajectories of the rays before they hit the terrella, it was supplied with plates (called screens by Birkeland), which were also painted with phosphorescent material. There were vertical and horizontal screens, screens with holes and slits, sets of as many as eight screens

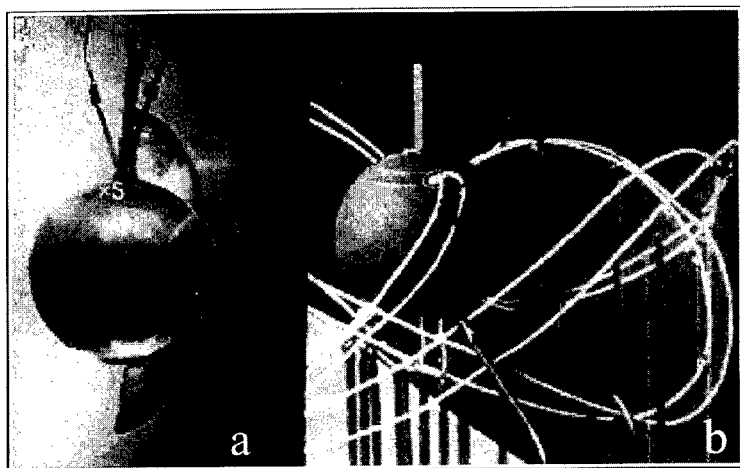


Figure 4: A comparison between a terrella experiment (left) and a model showing professor Størmer's calculated trajectories for that experiment. This experiment was performed in July 1907 in the first 12-liter glass tube, and shows illuminated regions along "the auroral zone". The calculated trajectories are for particles starting out in slightly different directions at a position corresponding to the cathode and with energies corresponding to the discharge voltage.

on one terrella, screens with pins, combinations of screens and pins pointing out from the terrella surface, and so on. The pins created shadows which provided information on the ray paths.

From 1895 to 1908 all his lab experiments, including auroral studies, were performed in fragile glass tubes where refraction of light through the curved glass walls tended to give distorted spatial information on the photographs. Guided by these shortcomings Birkeland now designed a new experimental chamber as a box, with top and bottom made of metal plates, and glass windows on the four sides. The total volume of this new box was 22 liters, the glass plates or windows had an area of approximately  $20 \times 45$  and  $20 \times 25$  cm and a thickness of 2.0 cm. They were cemented together with "Cementium" and the entire chamber was finished on the outside with picein, a tar-like, black sealing agent. With this improved construction he continued to study discharges with the purpose to gain a clear idea of the course of the rays around magnetized terrellas. One reason for continued experimental research on this problem was his scepticism to idealized mathematical models. As long as the mathematical models were not perfect, the usefulness of such calculations were limited, he claimed, with address to Størmer.

At this time, in the winter 1910–1911, Birkeland's laboratory interest turned from the aurora borealis to solar and cosmic phenomena. He started up with some quite new experiments in the 22-liter chamber, now simulating the Sun, Saturn and comet tails.

In several of his auroral experiments Birkeland had come upon phenomena which could serve as a starting point for an explanation of the zodiacal light. This light is a glow which appears in the western sky after sunset, and in the eastern sky before sunrise, at lower latitudes. He believed that this light also was due to discharges, as the aurora, and tried to simulate it in his laboratory. This experimental set-up was very similar to the one for the aurora, but the polarity of the discharge was changed. The terrella, which was without phosphorescent coating, was now negative and served as the cathode, simulating the Sun. He used one or two aluminium discs for anodes.

As far as can be ascertained from the text, this was his usual way of connecting the apparatus when doing experiments simulating zodiacal light, sunspots and the rings of Saturn. He also experimented with using the metal parts of the chambers as an electrode. His explanation of the zodiacal light was that clouds of "atomic dust" originating from the Sun were spread out in a very thin layer in the Sun's

equatorial plane, and were illuminated by a some sort of cosmic discharge. He demonstrated this for the first time by running discharges with an 8 cm terrella. With the terrella highly magnetized, and with a low discharge current he could create a flat, thin, luminous discharge in the equatorial plane of the terrella. Under ideal conditions, he could produce plane rings sharply intercepting the glass windows. He wrote that if he had been in possession of sufficient quantities of pure radium bromide, he would have coated the equator of the most highly magnetized terrella and observed whether rings of  $\alpha$ - and  $\beta$ -rays would develop in addition to the rings of cathode-rays. This comment reflects the prevailing conception at the time of matter as composed of neutral atoms and the three known types of corpuscular rays. Later, however, Birkeland expressed ideas about interplanetary matter which were much closer to the modern concept of *dusty plasmas*.

In 1910, during the passing of Halley's comet, Birkeland formulated an explanation on the formation of the comet's tail. He suggested that as the comets approach the Sun, they are charged to a high negative potential by cathode-rays emanating from areas around the sunspots. An anode-cathode relationship is set up and a visible discharge takes place in the outstreaming gas from the comet core. Also this theory was tested in the laboratory. It was believed that the comet cores were carbonaceous, and he performed numerous discharge experiments with carbon in different forms over a metallic cathode in the vacuum container. The rapid disintegration and light emission from the carbon confirmed Birkeland's idea that the visible tail is formed by the outstreaming gas "ignited" by a discharge. He also simulated the comet by a very thin, hollow silver needle penetrating into the vacuum chamber from the outside. With the pumps in action, and blowing a weak stream of  $\text{CO}_2$  through the needle into "space", he managed to set up a discharge between the needle and the anode, the needle acting as a cathode. By carefully adjusting the gas flow and the discharge voltage he could get thin pencils of light shooting out from the "comet".

In the description of his first terrella experiment from 1900 Birkeland mentioned that he in some experiments had seen three luminous rings around the terrella. In addition to the rings in the polar regions he had sometimes been able to observe a third one, that encircled the Earth model almost like the rings of Saturn. Later, during his systematic studies of laboratory aurora, he now and then described this phenomenon, which was rather difficult to produce under his standard experimental conditions. Ten years later he started up with systematic simulations of the Saturnian rings. He had discovered that they were easily formed by changing the polarity of the discharge. In fact, this was the same set-up he used for simulating the zodiacal light, but the discharge parameters were different. In a new 70 liter box he created discharges consisting of three and sometimes as much as five equatorial rings around the terrella. His explanation of these rings was similar to that of the zodiacal light. A constant *electric radiation* from the planet is accompanied by an ejection of tiny material particles he called *electric evaporation*, and these particles form the rings. The laboratory analogy to this evaporation is what today is called *sputtering*. Terrella-experiments simulating zodiacal light and rings of Saturn are shown in Fig. 5

For studies of the sputtering phenomenon Birkeland performed several experiments in an evacuated bell jar placed in a strong magnetic field. He investigated the disintegration of palladium cathodes in a powerful discharge, and the deposition of the palladium on the glass walls. In other words, he demonstrated that material can be thrown off from an active cathode and guided by a magnetic field. Also from a magnetic globe, when acting as a cathode in the vacuum chamber, material was thrown off in the equatorial plane. This he deduced from the blackening of glass sheets located near the terrella. He concluded this study by stating that he believed Saturn throws off tons of matter every day in the plane of the rings, and that the rings are constantly replenished. He also speculated that the moons of the planet could have been formed from such ejected matter. Under the influence of gravitational forces, the dust in Saturn's rings would clump together, forming more moons, and at last the dust rings would disappear. Also the planets in the solar system could have been formed by electrically ejected matter from the Sun.

The experiments simulating the zodiacal light and Saturn's rings guided Birkeland to discoveries that appeared to be of great importance. In the years to follow he developed a great theory on the

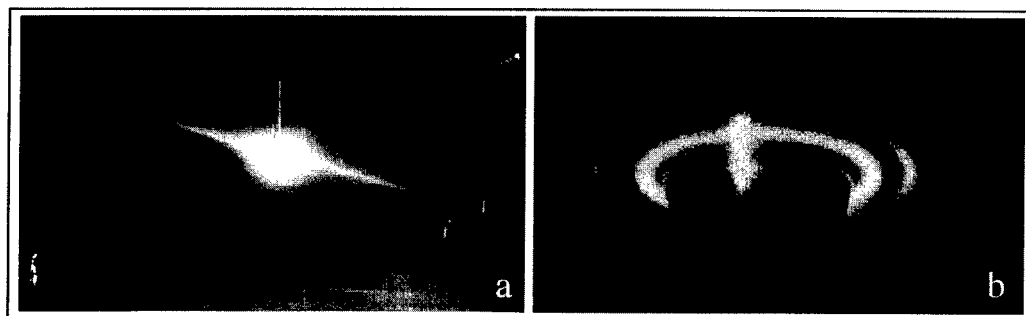


Figure 5: (a) Zodiacal light. In the middle of the picture we have the smallest terrella, 2.5 cm in diameter, as the Sun. The terrella is covered with a glow, the solar corona, and the zodiacal light is seen end on as a thin disc of light in the equatorial plane of the terrella. (b) Rings of Saturn. This experiment was performed in the third chamber of 320 liter volume and with the 24 cm terrella. The terrella acted as a cathode and was strongly magnetized.

origin of the solar system [15]. He believed that the sunspots were foot-points of huge disruptive electric discharges from the sun into space, which again were the source of aurora borealis, the zodiacal light and even the planets. During earlier experiments he had seen that disruptive discharges could radiate from points on the cathodic terrella surface. With a low gas pressure, a very high discharge current and with no magnetic field around the terrella, he could create arcs from points on the surface to the anode disc and chamber walls. This was again the same discharge configuration that produced the zodiacal light and Saturnian rings, but with different parameters.

These point discharges, which were spread all around the surface of the terrella, were interpreted by Birkeland as small sunspot models. He observed that the spots were easier to make when the surface was rough. When introducing magnetic field on the terrella, he observed that the spots were grouped in two zones at a certain northern and southern magnetic latitude. By increasing the field the zones moved closer to the equator of the sphere. At increasing magnetic field the sunspots turned into luminous bands which coalesced at the equator.

After running discharges, he took out the terrella and studied it in a microscope, and observed small craters where the spot discharges had been. This observation supported his hypothesis that mass is thrown out from the Sun during solar flares. Some of this *atomic dust*, falls back to the surface of the Sun, some disappears into Space, and some will end up orbiting the Sun, and slowly clump together and form planets. He considered the asteroid belt as masses halfway in the process from solar dust to planets.

With an increased gas pressure the pencils of rays were no longer emitted radially from the globe surface, but formed star-like shapes or vortices around the eruptive spots. He considered this phenomenon as being very important, and tried to photograph them. His vacuum chambers, however, did not work to his expectations, and consequently a new 320 liter chamber was built in which he continued his simulations of the sunspots, now using a 24 cm terrella. It turned out not to be easier to produce sunspots in this chamber in the conventional way, but he could easily produce spot-like discharges by changing the polarity. With the globe as the anode, and the rough and unpolished top and bottom plates of the chamber as the cathode, he could set up "fireworks" of point discharges with the footpoints on the plates.

In one set-up with low pressure, no terrella field, and low discharge current he got phenomena where the entire terrella was covered by the cathode glow. This was described by Birkeland as "a light that resembles the sun's corona". In this 320 liter chamber he performed experiments on the zodiacal light, Saturnian rings, sunspots, the Sun's corona and space propulsion by cathode rays.

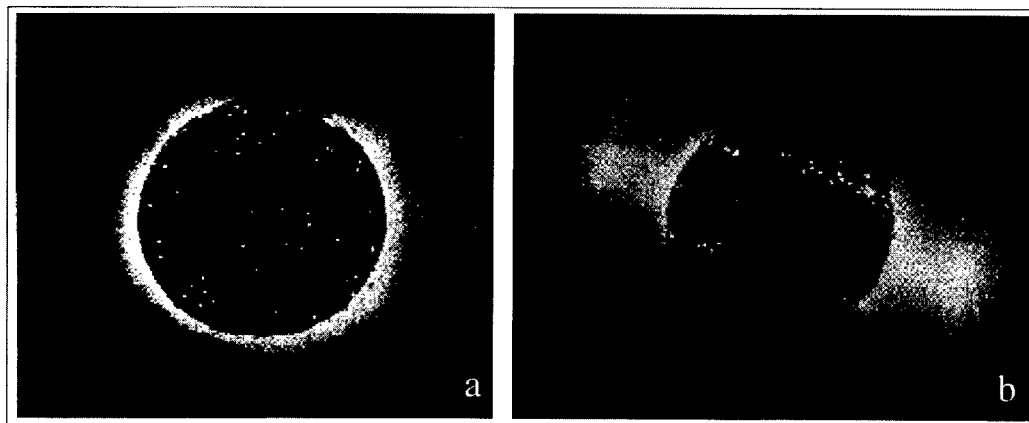


Figure 6: The photos show “sunspots” on one of the smaller terrellas. The spots are hot-spots on a rough cathode surface (the terrella) in a high current discharge. With no magnetic field the spots spread all over the terrella (left), while with a magnetic field present the spots are concentrated in two belts (right).

However, as the experiments became more refined, it turned to be a disadvantage to have the floor and ceiling made from magnetizable steel plates, in particular with big terrellas. Many phenomena were influenced by the magnetism of these plates, and the problem could only be solved by using a different alloy and by further increase in chamber dimension. His next chamber had a volume of 1000 liters, with a 36 cm terrella. This time floor and ceiling would be made of bronze, and thickness of glass plates for the windows was designed to be 5.0 cm.

Birkeland expressed satisfaction and joy over the simplicity and also the beauty of the experiments in this vacuum chamber. He noted that the experiments became increasingly interesting as the scale was increased. A glance could now be enough to show the occurrence of phenomena that earlier, only with much trouble, could be deduced from a long series of experiments. The one and only auroral simulation in this chamber was described as “remarkably beautiful”.

The studies of simulated solar and cosmic phenomena were not performed in the same systematic way as the lab aurora. Data from the experiments became more scarce, and were almost totally absent in his last experiment in the largest chamber. One gets the impression that he now considered the displays behind the glass walls and their resemblance to natural phenomena as sufficient confirmation of his theories. He came closer to his starting point from 1896, using the experiments as a *generator of ideas*, being well aware that he could not simultaneously model all aspects of a cosmic phenomenon in a glass box. His great speculations about the “origin of the worlds” were undoubtedly inspired by the terrella-experiments, but he certainly had no means by which he could simulate the formation of the solar system and the planets in his laboratory.

From the descriptions of his last experiments one gets the impression that he no longer had the patience and self-discipline to perform series of accurate and systematic laboratory work, in spite of the great advances he had accomplished in experimental techniques during the preceding decade. It is not unlikely that this development was related to his change of interest towards more cosmological problems, which were impossible to investigate in detail in the laboratory. It is also possible, however, that it was a reflection of his reduced physical and mental capacity, which was becoming quite apparent around 1913.

Diagnostics of the terrella-discharges were limited to visual inspection and photography, and is of course due to the fact that more refined diagnostics were non-existent until I. Langmuir developed the electrostatic plasma probe in 1923. It was Langmuir who first coined the word *plasma* to characterize an ionized gas, and thus pointed out the necessity of a selfconsistent treatment of particles and field and the importance of collective effects. Birkeland was well aware of the shortcomings of particle



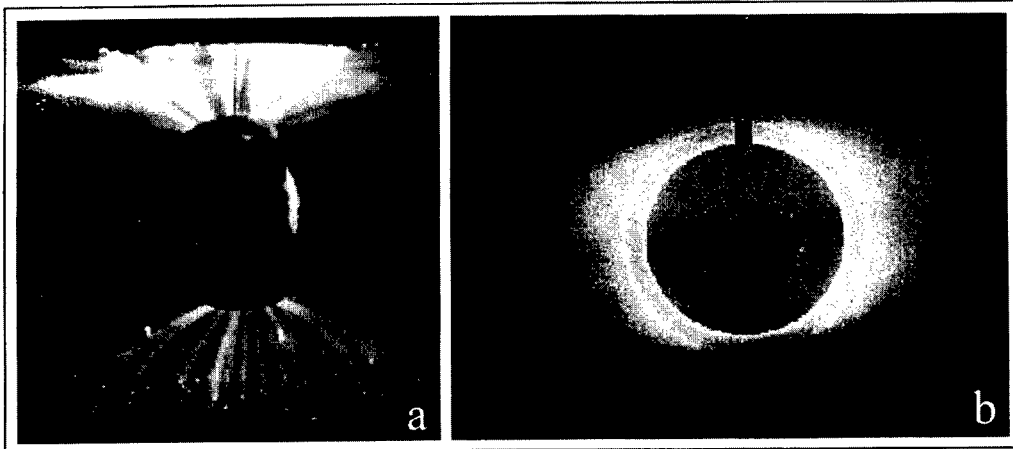


Figure 7: (a) Point discharges done in the 320 liter chamber with the top and bottom surfaces as cathode and the 24 cm terrella as the anode. (b) Simulation of the Sun's corona performed with the 24 cm terrella and a very low magnetic field.

tracing in given fields, and in his work on the solar system he struggled with the development of the new concept of a medium consisting of positively and negatively charged particles and dust, governed by electric and magnetic forces. He used a varying terminology for describing the medium filling his discharge chambers and the interplanetary space. Expressions like *luminous* or *rarefied gas*, *radiant matter*, and *the fourth state of matter* were used at different occasions, where a modern writer would have used the word *plasma*.

## 5. RELATING LABORATORY RESULTS TO GEOPHYSICAL OBSERVATIONS

On April 5., 1741 O. P. Hiorter in Uppsala discovered that auroral displays seemed to agitate a magnetic needle, and in 1826 H. C. Ørsted explained this as an electric discharge along the auroral arc. In 1770 J. C. Wilcke noted that auroral rays extend upwards along the magnetic field. Thus, at Birkeland's time geophysicists were well aware of the intimate connection between aurora and geomagnetic field perturbations. In the period 1825–1850 H. Schwabe made systematic sunspot registrations, and in 1844 he discovered the solar sunspot cycle. It was soon realized that the auroral occurrence was strongly related to this cycle, and in 1851 E. Sabine showed that the intensity of the geomagnetic disturbances also varied in concert with the sunspot cycle. During the first half of the 19<sup>th</sup> century there was developed a global network of widely spaced magnetometers, which were spread to all the British colonies, and one got methods to separate contributions to the geomagnetic field from currents inside the earth and those arising high in the atmosphere.

After stating his auroral hypothesis Birkeland realized that a closer study of magnetic perturbations would be a key to the understanding of the solar-terrestrial interaction. One problem, however, was that all magnetic observatories were located on lower and middle latitudes, while the most interesting perturbations were taking place in the polar regions. He organized an expedition to northern Norway in February and March 1897, but this venture was a complete failure, since they were not prepared for the very rough winter conditions in these regions. However, practical experience from this expedition was very useful when he organized the second, and very successful, expedition in 1899–1900. His observations on the two mountain tops, Haldetop and Talviktop during that winter made it clear that auroral precipitation had to be connected with strong currents in the upper at-

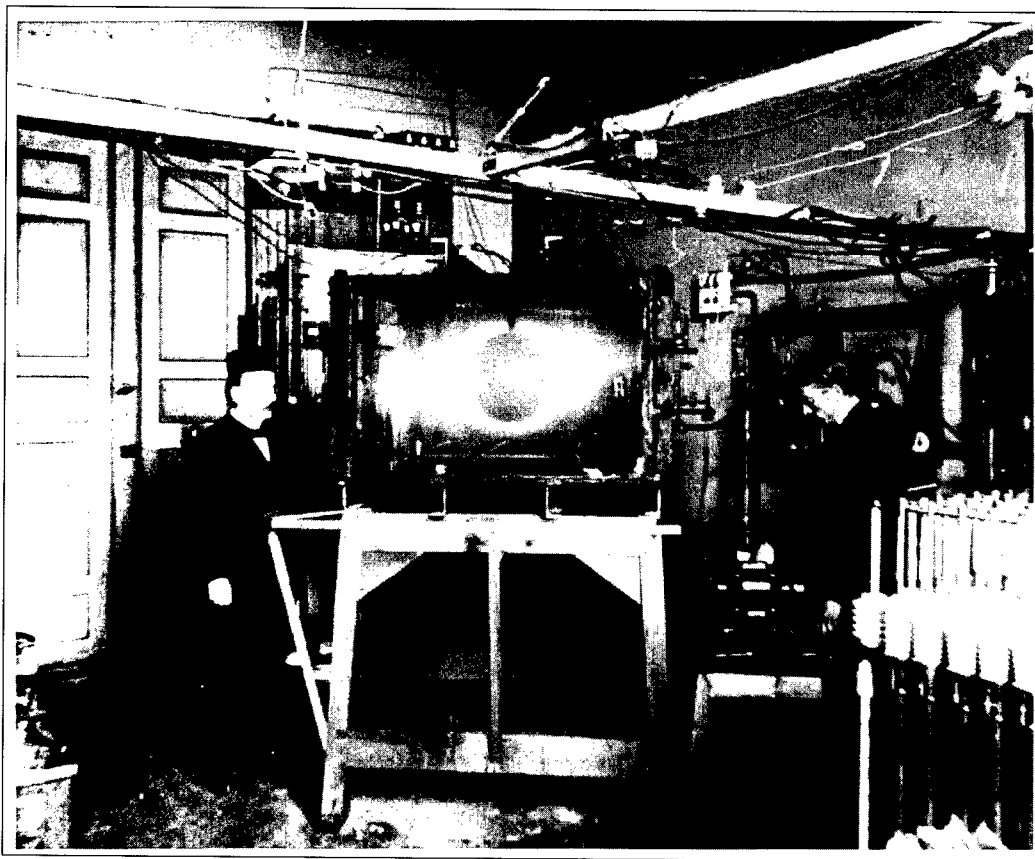


Figure 8: Birkeland and his assistant Olav Devik with the 1000 liter chamber and the 36 cm terrella (1913). The drawing on the banknote (Fig. 1) was made from this picture.

mosphere, and in his report from the expedition he concludes that the same particles that produce the aurora also produce the electric currents that give rise to the magnetic perturbations. This may seem obvious today, but one should keep in mind that this was only a few years after the discovery of the electron, and it was not generally agreed that all electric currents are carried by subatomic electrically charged particles.

The pattern of magnetic perturbations turned out to be extremely complex, however, and Birkeland felt that further progress required observations of a global network of stations, including the polar region. This was the basis for his third expedition in 1902–1903, where he erected four widely spaced observatories in the Arctic. At these stations he performed magnetic and auroral registrations, measurements of atmospheric electricity and earth currents, and meteorological observations. The registrations from these stations were combined with data he gathered from magnetic observatories around the world, and this made him able to create global maps of magnetic perturbations and current patterns. From meticulous analysis of these current patterns he divided the geomagnetic perturbations into three main categories, the equatorial perturbations, the polar elementary storms, and the cyclo-median storms.

The equatorial perturbations correspond to what now is called geomagnetic storms, and are caused by eastward or westward current perturbations close to the equatorial plane. The existence of such currents can be deduced from Størmer's trajectory calculations, and in modern language they are associated with variations in the westward ring-current caused by energetic particles trapped in

the Earth's radiation belts.

Birkeland performed terrella-experiments which demonstrated the existence of the radiation belts. In Fig. 3 we observe a luminous ring, which Birkeland attributed to electrons spiralling eastward near the equatorial plane, constituting a ring current. However, the equatorial perturbations were of two kinds, positive and negative, corresponding to eastward and westward current perturbations respectively, whereas the ring current itself is directed towards the west. In his discussion of this problem he wrote:

If, on the other hand, we assumed the permanent existence of such a ring, we might imagine the (positive) perturbation to be explained by a diminution in the strength of this current. This explanation is very improbable and unnecessary.

This is what is believed today to be the correct explanation, but Birkeland abandons it. The reason seems to be observations he did with the terrella equipped with a vertical screen. An eastward drift of trapped electrons should give illumination of the west side of the screen. The experiment, however, shows the opposite result, as shown in Fig. 9a. Birkeland could explain this result with a particular class of Størmer-trajectories, but these particles were not trapped, and could not contribute to a permanently existing ring current. His alternative explanation was very vague, and he admitted that he was far from the final solution. This is an example where the terrella experiments led him astray, and there are certainly many other examples. The important thing, however, is that he pinpointed the problem, leaving the final solution for later investigation.

The polar storms, now called magnetic substorms, represented a more serious challenge, since the magnetic field perturbations seemed very difficult to explain by a horizontal current system alone. After very tedious analysis of a vast amount of data Birkeland concluded that these perturbations were associated with a downward current at one longitude and an upward current at another longitude, connected by a horizontal current segment through the upper atmosphere at a height of a few hundred kilometers. Current patterns like these could to some extent be supported by Størmer's calculated orbits (Fig. 10a), and he also found support in the terrella-experiments in the form of strong luminous bands on a vertical screen along the magnetic field in the late night and early morning sector at high latitudes as shown in Fig. 9b. These bands were interpreted as due to field aligned currents, which were connected via an east-west current across the night-time sector. But he also discussed mechanisms that were beyond the non-selfconsistent orbit calculations:

In this descent of electric corpuscles, some will occasionally come so near the earth that they will be partially absorbed by its atmosphere, and will then eventually give rise to aurora. If the earth were able to retain an electric charge, we should have approximately horizontal currents, which would be necessary for the production of electrical equilibrium. But secondary electric radiation ought also to begin, and then, as it is still influenced by terrestrial magnetism, give rise to vertical ray-currents. ... Starting from physical considerations, we are thus naturally led to seek to explain the field by a system, which in its average effects, has the character of two vertical currents in opposite directions, connected by a horizontal part.

Thus, it appears that he realized that the auroral particles will ionize the atmosphere, and that horizontal currents may flow across the magnetic field in response to an electric field in this conducting medium. He then assumed that secondary electrons will be accelerated upwards along the magnetic field due to the electric field created by the accumulating space charge from the incoming electrons, and thus closing the electric circuit. This explanation is very close to the modern theories, except for the cause of the incoming flux of particles. According to these theories a potential drop across the earth's magnetotail is induced by the solar wind flow, and this potential difference is projected down onto the ionosphere. During a magnetic substorm, the normal current pattern far out in the magnetosphere is interrupted and short-circuited through the conducting ionosphere, qualitatively

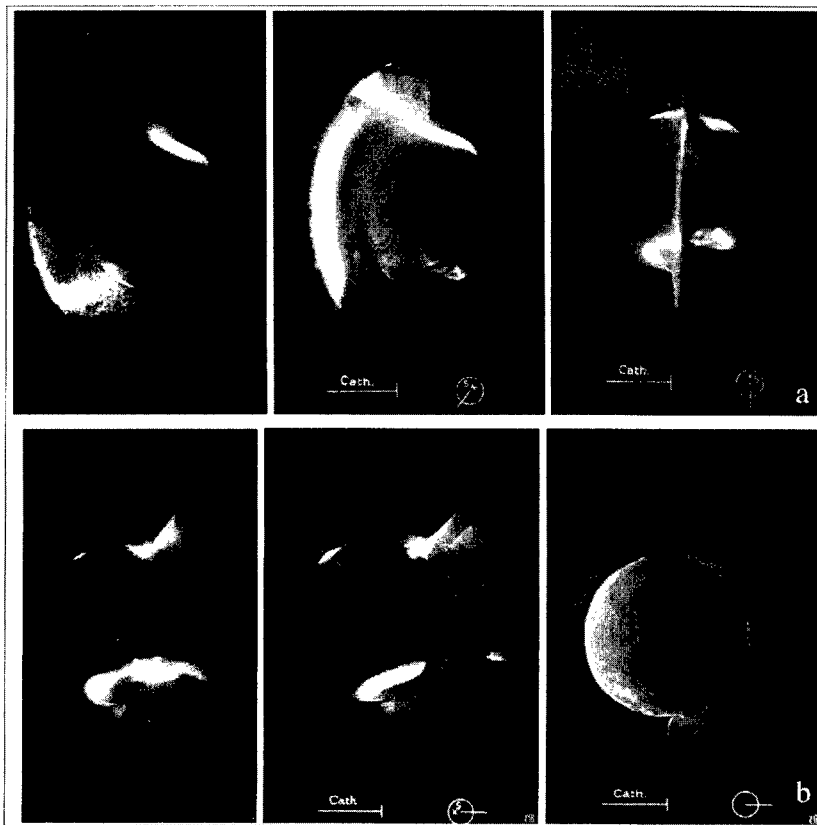


Figure 9: (a) Experiment on ring current effects with vertical screen. Note that the east side of the screen is illuminated, while a current of trapped electrons would illuminate the west side (see discussion in text). (b) The bright illuminations on the screen along the magnetic field were interpreted as due to field aligned currents.

in the same way as described by Birkeland. This theory has far-reaching consequences, since it underscores that the electric current systems in the Earth's atmosphere are directly coupled to current systems in the interplanetary space. Moreover, the quotation above shows that Birkeland realized that an ionosphere exists, at least in connection with aurora. The ionosphere was discovered by E. V. Appleton in 1925.

In support of this interpretation Birkeland calculated the magnetic field perturbations from various current patterns of this kind, and obtained very convincing agreement with observed patterns. Unfortunately, these results were overlooked by the space physics community for more than half a century, with the result that incorrect theories of ionospheric currents and magnetic storms prevailed until results from satellites confirmed the existence of currents along the magnetic field in 1973 [16]. These currents are now generally called "Birkeland currents".

The cyclo-median storms appear as a large current vortex with the center on relatively low latitudes. Today they are attributed to high energy photons from solar flares causing currents due to changes in ionospheric conductivity due to increased ionization. Birkeland observed similar current structures with very high energy cathode rays in his terrella-experiments, and Størmer was able to explain these results by calculating the orbits of such particles (Fig. 11).

As for many of the orbit calculations, the energy of the trajectories calculated were very much

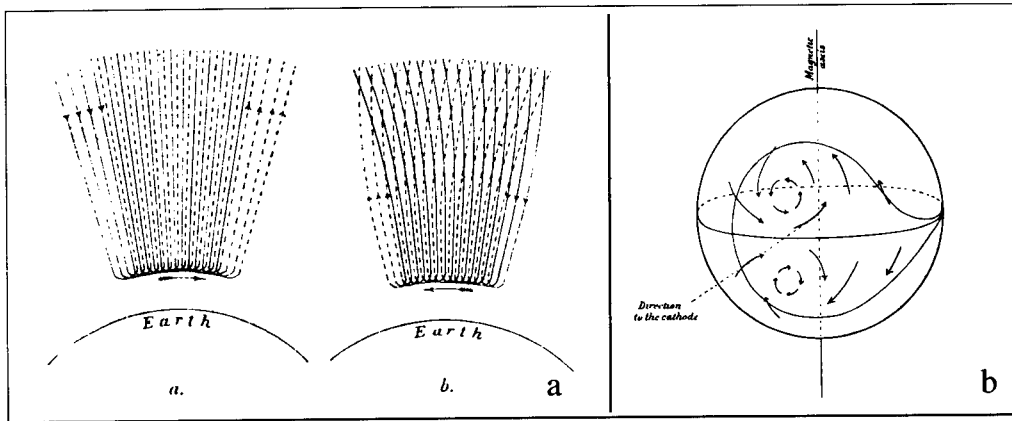


Figure 10: (a) Birkeland's own illustration of the currents during a polar elementary storm. The current pattern yielding the westward horizontal current (left) corresponds to one possible class of Størmer orbits, and the pattern yielding the eastward current (right) to another. In both cases a sheath or curtain of precipitating and returning particles has the net effect of descending currents at one longitude and ascending currents at another, connected by a horizontal current. The wedge shaped pattern agrees with the modern view, but the detailed explanation is different. (b) Birkeland's own illustration of the current pattern associated with cyclo-median storms.

higher than the typical energy for solar wind- and magnetospheric particles (the exception is the radiation belt particles). This means that theories directly based on the orbit calculations have to be modified, and today we know that field and particles will have to be treated selfconsistently. Birkeland was obviously very impressed with Størmer's calculations, but there are also instances where he criticized this approach as being too idealized and ignoring experimental facts. Størmer's theory certainly is more adequate for the terrella-experiments than for the solar-terrestrial system, since the early terrella-experiments did not involve a flowing plasma (solar wind).

Geomagnetic observations were not the only registrations made during Birkeland's polar expeditions. Among the many observations done routinely were recordings of auroral forms and occurrence. It was well known at the time that the aurora had a maximum occurrence zone close to  $23^\circ$  from the magnetic poles, but the exact shape of the auroral oval was not known. The diurnal variation of the

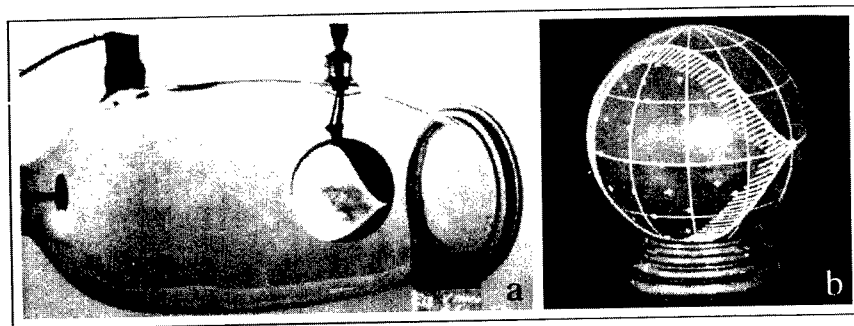


Figure 11: (a) Terrella-experiment showing the region of illumination from high-energy cathode rays. (b) Results of Størmer's calculations for the same case. Compare to Birkeland's drawing in Fig. 10b.

auroral zone at given location on Earth could be attributed to a deviation of the oval from a circle, but also to the deviation of the magnetic poles from the geographic poles.

In 1907 or 1908 Birkeland performed an elegant experiment to investigate how his artificial aurora behaved when he simulated conditions corresponding to various seasons on the Earth. He made a geometric arrangement where he could position the Earth corresponding to any season and any time of the day (at the magnetic south pole). In this experiment he used the second glass tube of 12 liter volume. It was supported in one end by a hinge which made it possible to incline the tube  $23.5^\circ$  above and below the horizontal plane. The terrella had a tilted magnetic core and was suspended at the geographical north pole by a universal joint. In this way it always maintained its north-south axis vertical when the tube was inclined. The terrella could be rotated, and since the magnetic axis was different to the geographic axis, he could put the magnetic pole into positions corresponding to different hours of the day and night. The cathode, which represented the Sun, was located in one end of the tube, near the hinge. The terrella was mounted in the other end, near the flat glass plate. With this construction he could simulate variations of the angle between the cathode rays from the Sun and the rotational axis of the Earth by tilting the tube, and thus simulate the seasonal variations. By rotating the terrella around a vertical axis he got the diurnal revolution of the Earth and thus the diurnal movement of the magnetic pole. The arrangement has been reconstructed in Fig. 12.

Fig. 13 shows 8 photos taken at different angles during winter solstice, with the magnetic south pole in the dawn position.

Birkeland considered the spiral shape of the auroral oval as a very significant finding, and made attempts to explain observations of diurnal wandering of auroral arcs from these experiments. These interpretations are mostly obsolete today, but again the investigations pinpointed an important problem for further study.

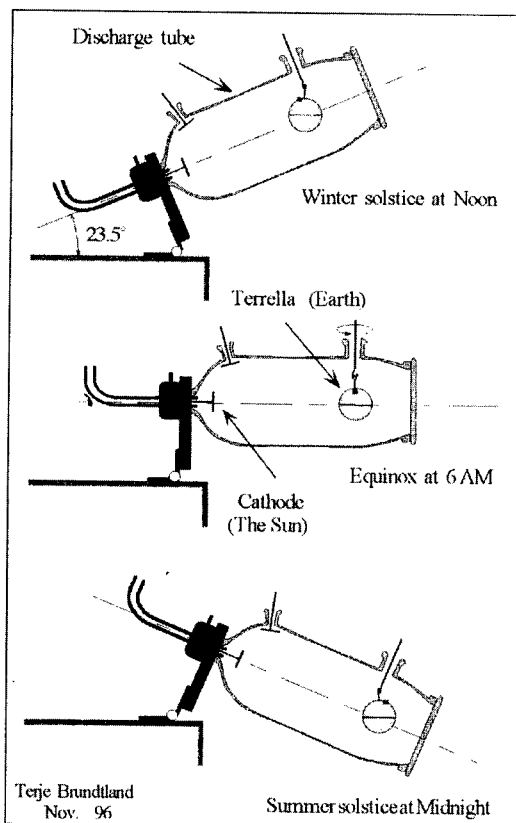


Figure 12: Geometric arrangement for studying seasonal and diurnal variations of the auroral oval.

## 6. THE BIRKELAND – STØRMER LEGACY

It is an unfortunate fact that Birkeland's work on gas discharges and solar-terrestrial physics was ignored by the plasma- and space-physics communities for more than half a century. After satellite observations began to confirm many of Birkeland's most controversial ideas, the attitude among space physicists changed to one of admiration and almost total acceptance. Plasma physicists, on the other hand, date the birth of their discipline to the 1920's, and are usually ignorant about Birkeland's work. However, the recent Birkeland laudation, based on the realization that many of his ideas have proven to be essentially correct, does not by itself serve the progress of science. In fact, it can be even more important to study the development of incorrect ideas and dead ends, because the right ideas often develop through struggle with competing lines of thought. In one sense, Birkeland's work was

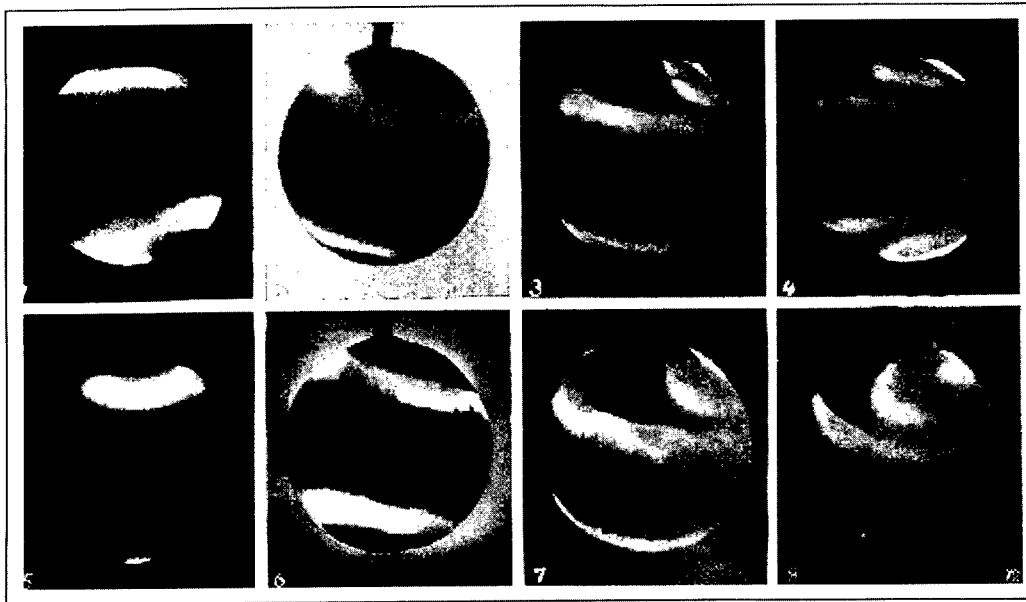


Figure 13: Photos of terrella taken from different camera angles with the tube in the position corresponding to winter solstice and magnetic south pole in the 6 AM position.

doomed to failure, because it was too far ahead of his time. He wanted to develop a grand theory corresponding to H. Alfvén's *Plasma Universe* [17], but did not have to his disposal the concepts and theoretical methods of plasma physics. He wanted to investigate and understand in depth discharge phenomena in ionized gases, but did not have the diagnostic tools that were necessary. However, by applying all scientific knowledge and methods available at the time, he was able to formulate comprehensive and consistent theories ready for tests against future advances in physics and technology. The tragedy was, however, that only a handful of scientists accepted the challenge of dealing with the explosive power of Birkeland's theories after his untimely death. One of the few that went against the mainstream was Carl Størmer, another was Hannes Alfvén (1908-1995).

In his opening address to the Birkeland Symposium on Aurora and Magnetic Storms arranged by IAGA in Norway in 1967 Sydney Chapman (1888-1970) had the following comment to the Birkeland - Størmer collaboration [18]:

The apparently unshakable hold, on Birkeland's mind, of his basic but invalid conception of intense electron beams mingled error inextricably with truth in the interpretation of his ideas and experiments on auroras and magnetic storms. As regards to aurora, somewhat the same may be said about Størmer's theoretical work.

Chapman was perhaps the most influential scientist in the field of cosmical geophysics in the period 1920-1960, and was the creator of a mathematically elegant theory for ionospheric current systems and magnetic storms [19]. According to this theory all geomagnetic field perturbations could be explained from a system of currents flowing horizontally in a spherical shell surrounding the Earth, and there was no place for Birkeland's field-aligned currents. Chapman also developed a kinetic theory of ionized gases, found in the last chapter of his famous book with T. G. Cowling [20]. In many respects this theory was obsolete before the first edition was published in 1939, since it could not describe the collective effects in plasmas which were observed by Langmuir and others [21] a decade earlier.

If Birkeland and Størmer were to be evaluated as contemporaries to ourselves, Chapman's judgement would certainly be in place. But such judgements create blindness to the weaknesses in our own conceptions, which was exactly what happened to Chapman. By criticizing Birkeland as if he were a contemporary adversary, he missed a golden opportunity to use the old giant's ideas as a stepping stone for further advances. Alfvén did not miss this opportunity, however. Many of Alfvén's basic ideas can be traced back to Birkeland, and this was emphasized by Alfvén himself. In 1987, Alfvén gave the first lecture in a series called "The Kristian Birkeland Lecture" at the University of Oslo, and from the paper based on his oral presentation one clearly observes the strong similarities in their scientific approach. Concerning Chapman's rôle, Alfvén wrote [22]:

Since Chapman considered his theory of magnetic storms and aurora to be one of his most important achievements, he was anxious to suppress any knowledge of Birkeland's theory. Being a respected member of the proud English tradition in science, and attending – if not organizing – all important conferences in this field, it was easy for Chapman to do so. The conferences soon became ritualized. They were opened by Chapman presenting his theory of magnetic storms, followed by long lectures by his close associates who confirmed what he had said. If finally there happened to be some time left for discussion, objections were either not answered or dismissed by a reference to an article by Chapman. To mention Birkeland was like swearing in the church.

The bitter undertone in this strong statement certainly reflects Alfvén's sentiments associated with his own struggle to achieve recognition for his theories, which usually gained acceptance decades after their publication. But he also attempted to find a rational explanation of this resistance to radical ideas, and attributed this tendency to the increasing specialization of science.

This specialization has also affected the advancement of the ideas of Birkeland and Størmer. Due to the strong influence of the Chapman school, the mathematical achievements of Størmer did not get the attention they deserve. Rather recently, it has been realized that Størmer's problem, the motion of a charged particle in a magnetic dipole-field, is an example of a chaotic Hamiltonian system. Størmer proved that the system has two integrals of motion, and can be reduced to a two-dimensional Hamiltonian, which is integrable only for a particular value of the energy integral. In 1970 it was shown that the KAM-theorem applies for small perturbations of this energy, and hence phase-space consists of Cantor-sets of chaotic and regular orbits [23]. This is, in fact, quite apparent just from inspection of the two-dimensional potential corresponding to the reduced Hamiltonian, which consists of three potential "hills" grouped around a saddle point. The problem is structurally similar to the much studied "3-disk problem", where a billiard ball collides with three cylinders placed in the corners of a triangle. One of the most impressive achievements of Størmer and his assistants was their numerical calculations of particle trajectories without electronic computers. More than 18000 working hours were spent on such calculations, and from the drawings and wire-models of these trajectories one gets a clear idea about how sensitive some trajectories are with respect to small changes in the initial conditions. This sensitivity, and its connection to chaos was first discovered in connection with other dynamical systems after it became common to solve such systems on computers. It is interesting to speculate, however, whether chaos-theory would have developed earlier if Størmer's calculations, which probably were the first numerical calculations of chaotic orbits, had been more widely known.

Better known than the intrinsic chaos in unperturbed Størmer orbits is the chaos that may arise from perturbations due to waves or other collective effects. Such effects may be very important for how particles escape from the radiation belts. Recently a very interesting terrella-experiment has been set up at Columbia University, where the purpose is to study this radial particle transport in an artificial radiation belt. This experiment is a direct continuation of the work by Birkeland and Størmer, and is highly relevant to the actual geophysical problem [24].

The Columbia University Terrella (CTX) is an example of a class of laboratory experiments where the purpose is to study in detail micro-processes that are assumed to be essential for the



global dynamics of the solar-terrestrial system. Birkeland's experiments attempted to model the global system itself, but theoretical discussions and a series of terrella-experiments performed at the Royal Institute of Technology in Stockholm in the 50's and 60's have shown that it is impossible to scale all relevant physical parameters down to laboratory dimensions [25]. The scaling problem is being used by many space physicists as an argument for abandoning laboratory experiments as a tool in space physics, which claim that large scale numerical simulations are more valuable than experiments. This argument is certainly valid for global laboratory simulations, but it does not hold for the experimental investigation of micro-processes. An example is large three-dimensional MHD-simulation of the magnetospheric cavity, which have proven to be of limited value because ideal MHD is insufficient to describe the global dynamics. MHD breaks down in critical boundary regions like the bow shock and reconnection regions in the magnetopause and the magnetotail. In fact, virtually all the interesting physics that shapes the magnetic topology, energizes auroral particles and so on, occur in such regions. This micro-physics will have to be included in the global models, and this is where laboratory experiment has an important rôle to play.

There is also a widespread reluctance among laboratory physicists against dealing with space-related plasma problems. Presumably this is partly due to lack of funding for such type of work, but is probably also due to general ignorance about the wealth of interesting problems space physics can offer the creative laboratory plasma scientist.

A small, but growing, group of scientists from the two communities have sensed this problem, and since 1991 this group has organized four bi-annual workshops entitled "Interrelationship between Plasma Experiments in Laboratory and Space" (IPELS). This workshop, very much in the spirit of Kristian Birkeland, signals a hope for increased awareness of the necessity of an interdisciplinary approach to all sciences that deal with matter in the ionized state.

### Acknowledgments

The authors are grateful to A. Br kke, A. Egeland, H. P cseli, M. Mauel and B. Bingham for interesting discussions. A special thanks to the staff of the Norwegian Museum of Science and Technology for assistance during the study of old apparatus and written sources.

### References

- [1] Birkeland, K., *Archives des sciences physiques et naturelles* 3 me periode **T.33** (1896) 297-309.
- [2] Birkeland, K., *The Norwegian Aurora Polaris Expedition 1902-1903*, Vol. 1, (H. Aschehoug & co., Christiania 1908 and 1913).
- [3] Poincar , H., *C/ R. Acad. Sci., Paris*, **123** (1896) 930.
- [4] Birkeland, K., *Archives des sciences physiques et naturelles* 4 me periode **T.6** (1898) 205-228.
- [5] St rmer, C., *The Polar Aurora* (Clarendon Press, Oxford, 1955).
- [6] Egeland, A. and Leer E., *IEEE Trans. on Plasma Science* **Ps-14** (1986)
- [7] Egeland, A., "Kristian Birkeland, The Man and the Scientist", *Magnetospheric Currents*, AGU Geophys. Monograph 28, T. A. Potemra, Ed. (Amer. Geophys. Union, Washington D.C., 1984) pp. 1-16.
- [8] Egeland, A., *Kristian Birkeland, mennesket og forskeren* (Norges Banks Seddeltrykkeri, Oslo, 1994) ISBN 82-7553-017-7

- [9] Röntgen, W. C., "Ueber eine neue Art von Strahlen" (Würtzburger Physik-Med Gesellschaft, Würtzburg, 1895).
- [10] Birkeland, K., "De Røntgenske Straaler", (Aftenposten January 22, 1896).
- [11] Birkeland, K., *Archives des Sciences physiques et naturelles* 4ème période **T.1** (1896) 497-512.
- [12] Thomson, J.J., *Phil. Mag.* No. CCXIX, October (1897).
- [13] Birkeland, K., Expedition Norvegienne 1899-1900 (Videnskabselskabets Skrifter I. Mat-Nat Klasse 1901. no 1, Christiania, 1901).
- [14] Gilbert, W., De Magnete (Dover Publications, Inc., New York, 1958).
- [15] Birkeland, K., *Archives de sciences physiques et naturelles*, 4ème période, **T.35** (1913) 529-564.
- [16] A McPherron, R. L., Russel C. T. and Aubry M., *J. Geophys. Res.* **78**, (1973) 3131-3149.
- [17] Alfvén, H., *Physics Today*, September (1986), pp. 22, and *IEEE Transaction of Plasma Science* **PS-14** (1986) 629-639.
- [18] Chapman, S., "Historical Introduction to Aurora and Magnetic Storms", Proceedings from The Birkeland Symposium on Aurora and Magnetic Storms, Egeland, A. and J. A. Holtet Eds. (Centre Nat. de la Rech. Sci., Paris, 1967).
- [19] Chapman, S. and Bartels J., *Geomagnetism*, vol 1. (Oxford, Clarendon Press, 1962).
- [20] Chapman, S. and Cowling T. G., *The Mathematical Theory of Nonuniform Gases* (Cambridge University Press, London, 1939).
- [21] Langmuir, I. *Phys. Rev.* **33** (1929) 954.
- [22] Alfvén, H. and Egeland A., "Auroral Research in Scandinavia", The Kristian Birkeland Lecture 1. (The Norwegian Academy of Science and Letters, 1987).
- [23] Braun, M., *J. Differential Equations* **8** (1970) 294.
- [24] Mauel, M., "Laboratory observations of wave induced radial transport within an artificial radiation belt", Topical invited lecture this conference.
- [25] Block, L. P., *Planet. Space Sci.* **15** (1967) 1479-1487.

## Gas Discharges Studies in Japan and some of my Own Researches

S. Takeda

*1-12-19 Gakunanchou, Okayama 700, Japan*

**Abstract.** The charge distribution on an insulating sheet induced by a surface discharge can be directly observed by "Dust figure". "Discharge chamber" is a sensitive high energy particle detector with a luminous trajectory. The high frequency breakdown voltage as a function of  $p$  and  $f$  is an extension of Paschen's law in dc discharge. The recombination loss predominant to attachment one was found in an afterglow of water vapour with the high electron density of plasmas by the phase angle of the reflection coefficient of a wave. The ripple of the electron temperature of high frequency produced plasma was measured as function of frequency for various pressures. An improvement of a laser interferometer to eliminate the fluctuation of the detected signal induced by the mechanical vibration of the system is developed.

### 1. DISCHARGE STUDIES IN JAPAN

The earliest studies of gas discharges in Japan, related to the high voltage engineering and insulation problems in the atmosphere, started more than seventy years ago. In associating with the industrial people and their support, basic researches were also carried out.

A few examples of interest for me will be mentioned here. The first one is "dust figure" technique developed by Prof. Toriyama [1], as shown in Fig.1. A needle electrode is in contact with an insulating sheet put on a metal plate. If the sheet is replaced by a photographic film, the "Lichtenberg" figure is recorded. After a pulse voltage is applied to the electrode, two kinds of colours powder are scattered on the sheet. Then each powder accumulates on positive and negative charges distributed on the sheet along the streamer produced by the surface discharge. Thus the distribution of each charge can be clearly observed.

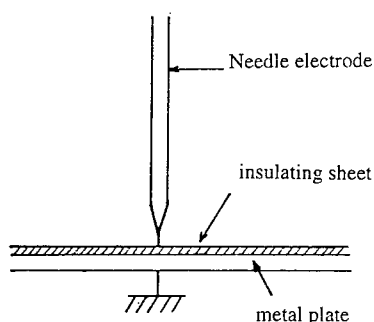


Figure 1 : Arrangement of dust figure

The second example is "discharge chamber" for a high energy particle detector invented by Prof. Fukui [2], as shown in Fig.2. The chamber consists of the glass box filled with Ar or Ne-Ar mixture at atmospheric pressure. When a pulsed voltage is applied to the electrodes immediately after the passage of the ionizing particle, the luminous discharge shown in left corner in Fig.2

appears along the trajectory. The pulsed voltage is triggered by the output signal from a G.M. counter. I heard that the chamber was widely used through out the world.

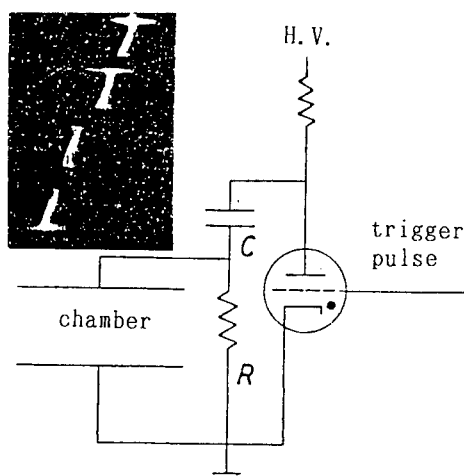


Figure 2 : Arrangement of discharge chamber

The low pressure discharges were also studied. The third example for interest for me is the back-fire, which sometimes appeared in the arc of the Hg rectifier. It supplies the dc power to the electric train to drive its motor. Although the problem was extensively studied, the investigation stopped before a perfect understanding of the mechanism was reached, since the rectifier was replaced by the solid state devices.

Recently, high frequency plasmas found wide use in plasma processings and other discharge applications. Since such new topics are extensively discussed in the respective conferences, I am not going to dwell on these problems.

Following are some of my own researches.

## 2. HIGH FREQUENCY BREAKDOWN

During the second war, a triode tube for a long wave length was used in the radar system. When an aircraft carried the device and flew in high altitude with decreased pressure, frequent high frequency breakdown troubles between the electrodes outside the vacuum tube were reported. At that time the sufficient data of high frequency breakdown were not available.

After the war, I attend to investigate the breakdown in broad ranges of frequencies and pressures. Using a simple theoretical consideration and numerous experimental data, I classified various ranges in a (pl-fl)-plane and made empirical formulae of the breakdown voltages  $V_s$  in each range as function of pl and fl. This is an extension of Paschen's law in dc discharge.

The various range are shown in Fig.3 [3]. When  $f$  is low,  $V_s$  goes to dc values [range (1)]. When  $f$  increases, the oscillating ions are trapped between the plane electrodes and deform the electric field, resulting the increase of the  $\gamma$ -action of ions. Then  $V_s$  somewhat decreases [range (2)]. When  $f$  is higher, the electrons are trapped between the electrodes and  $V_s$  again decreases by the enhanced ionization efficiency due to their long life time. The decrease is quite sharp in low pressures [range (3)]. When  $f$  is further increased, the movement of trapped electrons become less active for ionization and  $V_s$  increases [range (4)]. When the electron mean path is longer than 1, the vacuum discharge appears and  $V_s$  is quite high [range (5-6)]. For high fl,  $V_s$  is low and increases [range (7)]. Fig.4 shows the contour lines of  $V_s$  in the (pl-fl)-plane, much like isohyps on a map. Fig.5 shows a solid model of  $V_s$  as a function of pl and fl. Since the computer graphic techniques were not available at that time, the model was handmade of clay. The figure in the right is the model seen from the reverse side. If a plane of constant fl cuts the model, the dependence of  $V_s$  on pl is obtained. And if a plane of constant pl cuts it, the dependence of  $V_s$  on fl is obtained.

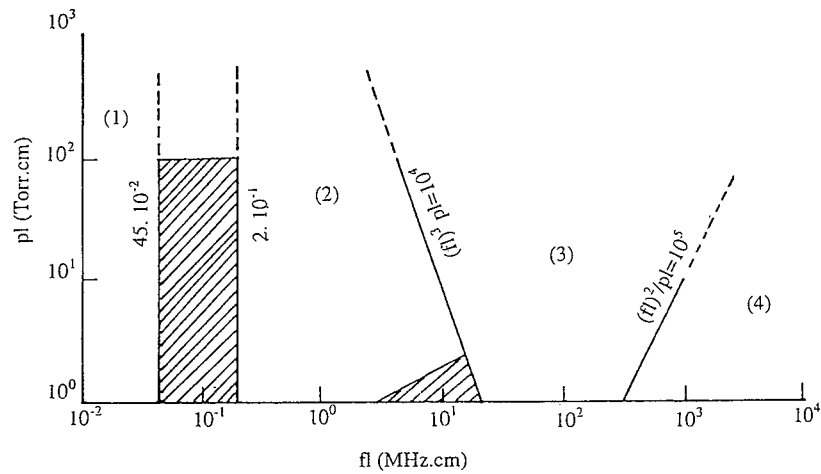


Figure 3 : Ranges of Vs in (pl-fl)-plane

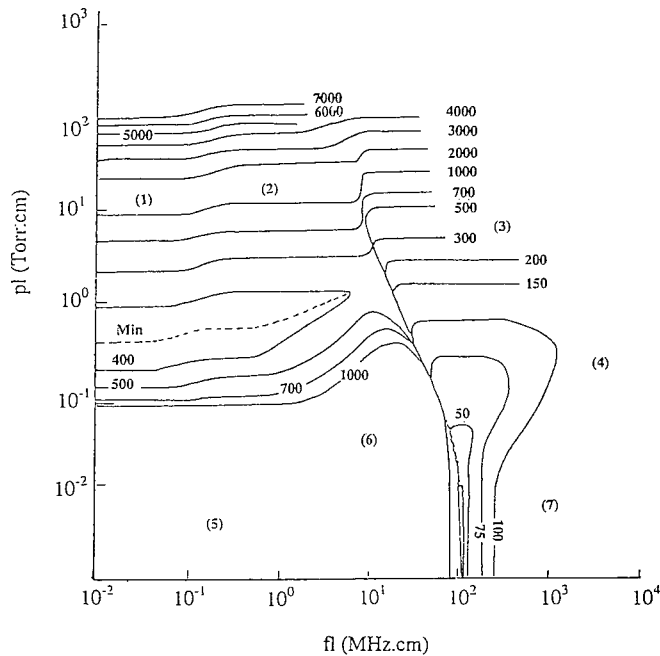


Figure 4 : Contour lines of Vs in (pl-fl)-plane

Almost at the same time, Prof. Brown [4] of MIT published a paper, which showed  $E/p$  as a function of  $p$  and  $p\lambda$  ( $\lambda$  is the wave length) and included a corresponding theory of microwave frequency domain. Prof. Honda [5] in our country also independently published a theory with the same idea but with a different final expression.

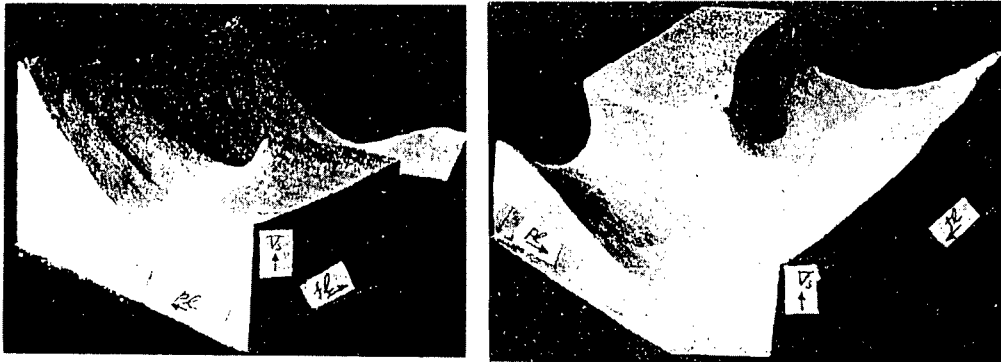


Figure 5 : Solid model of Vs

### 3. AFTERGLOW IN WATER VAPOUR

Being stimulated by afterglow studies of Prof. Brown, I was eager to start the research. However, since the elaborate microwave equipments were not available and the vacuum system in my laboratory was poor, I joined a group at the University of Illinois directed by Prof. Goldstein and Prof. Dougal.

They used the wave of 9000 MHz, which propagated through a long discharge tube installed in a waveguide. By measuring the wave characteristics, they determined the electron density  $n$  and the collision frequency  $\nu$ . Contrary to the 3000 MHz wave in a cavity at MIT, the electron density of  $10^{11} \text{ cm}^{-3}$ , which is one order of magnitude higher than that at MIT, could be measured. Thus they had already succeeded in detecting the electron-ion collision frequency in a weakly ionized plasma of high density and the low electron temperature.

The theme that I proposed was afterglow in water vapour. Discharge tube filled with argon mixed with water vapour was used in the radar system for separating the transmitting and receiving signals. It was assumed at that time that the water vapour helps to decrease the de-ionization time by its attachment process to find an object in a short distance. After my careful experiment, I found that the recombination loss surpassed the attachment one in plasmas of high electron density and low electron temperature. In addition, the collision probability, which is proportional to the collision cross section of electrons with molecules was determined as a function of the electron energy. When I presented the result at Gaseous Electronic Conference held in 1958, Dr Hull also reported the similar result with somewhat different value. Both data are shown with the theoretical line in Fig.6 [6].

### 4. MEASUREMENTS OF HIGH ELECTRON DENSITIES

After I was back to my country, I developed [7] a method to measure the high electron density for high values of the ratio  $\omega_p^2/\omega^2 = \eta$ , which is proportional to the electron density. When a wave reflects at a sharp boundary of a plasma, the reflection coefficient  $|R|e^{i\theta}$  is calculated as a function of  $\eta$ . Fig.7 shows the absolute value  $|R|$ . It increases toward unity at  $\eta=1$  and remains constant beyond  $\eta=1$ . However, the phase angle  $\theta$  changes from zero at  $\eta=1$  to  $180^\circ$  for the extremely high  $\eta$ s which correspond to a perfect conductor. Thus, the local electron density can be determined by measuring  $\theta$ . The electron density from  $10^{13}$  to  $10^{16} \text{ cm}^{-3}$  are measurable by using an 8 mm wave.

By inserting a waveguide into a plasma, the standing wave in the guide is represented by a real line, shifted from that for a perfect conductor (dotted line), as shown in Fig.8. The dotted line is realized by closing the end of the waveguide by a metal plate. For the plasma measurement the end of the waveguide is covered by a thin mica sheet to keep the plasma from penetrating into the waveguide filled with air. When the phase difference between  $180^\circ$  and  $\theta$  is measured,  $n$  can be determined. Moreover, the standing wave ratio changes by the loss due to the collisions. Thus  $n$  and

$v$  can be determined from  $h_1$  and  $h_2$  at the positions of a half and a quarter wave length distances from the end. If  $h_3$  and  $h_4$  are used, more accurate values for the smaller phase shifts can be measured.

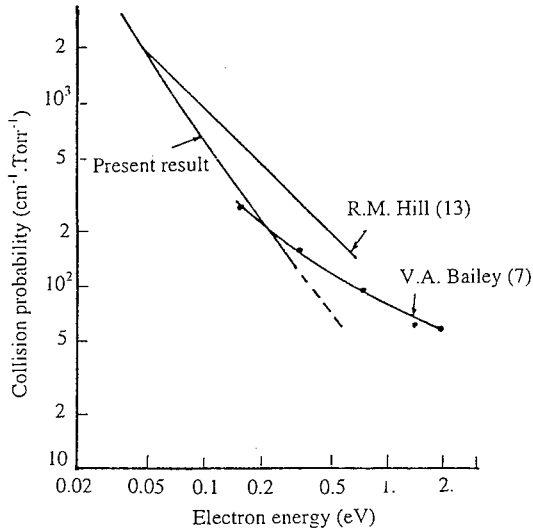


Figure 6 : Collision probability versus electron energy

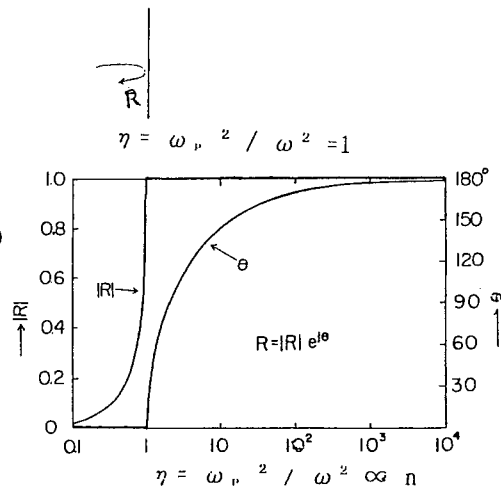


Figure 7 :  $|R|$  and  $\theta$  versus  $\eta$

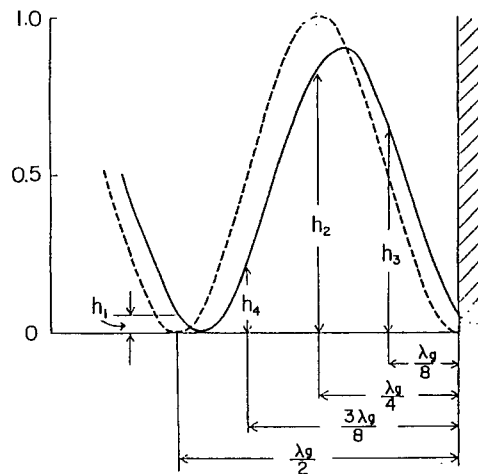


Figure 8 : Standing waves for a perfect conductor and a plasma

Since the skin depth penetrating into the plasma just after the reflection is much longer than the sheath width, its non-uniform electron density can be perfectly neglected for the calculation. I tried to measure the electron densities of  $10^{14}$ - $10^{15}$  cm $^{-3}$  by this technique in a shock-wave produced plasma. The values were in a fairly good agreement with those obtained by the spectroscopic methods, namely, Stark broadening.

Here I add that Prof. Simonet [8] developed a method of measuring the position of cutoff or  $\eta=1$  from the phase angle of the reflection coefficient and determined the density profile by using a swept-frequency oscillator.

### 5. RIPPLE OF ELECTRON TEMPERATURE

Recently, high frequency produced plasmas are widely used for processings. I studied the ripple of the electron temperature of such a plasma. The measured ripples, defined as the ratio of the amplitude to the mean value, were plotted in Fig.9 [9], as a function of a frequency, for various pressures. Since the density fluctuation was neglected in the range of parameters studied, the ripple could be deduced from the observed emitted-light intensity. The result agreed well with the theoretical calculation which predicts that the ripple is inversely proportional to the frequency.

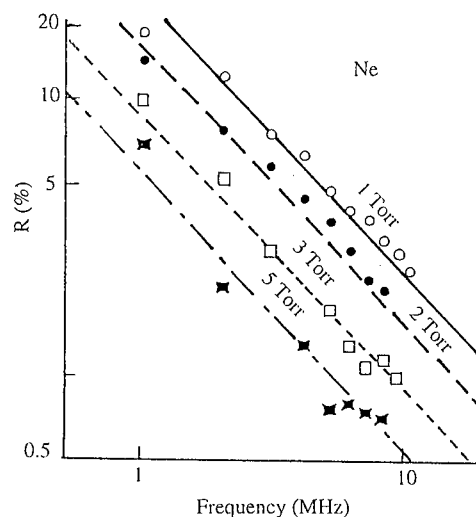


Figure 9 : Ripple of electron temperature

### 6. IMPROVEMENT OF LASER INTERFEROMETRY

Recently, the laser interferometer became widely used to measure high electron densities of plasmas. When the wave length is comparable to the amplitude of the mechanical vibration of the system, a careful arrangement is required to eliminate the effect. An improvement by Prof. Yasuda [10] was developed for this purpose. Fig.10 shows the total system. Two Ne-He lasers, with wave lengths of  $0.63\mu\text{m}$  and  $3.39\mu\text{m}$  respectively are used as sources of light which passes through a Michelson interferometer. A mirror at the right corner is driven by a magnetic coil of a loud speaker. The detected signal from  $\text{PD}_1$  is fed back to the moving coil after being reversed and amplified. Then the mirror can compensate the varying signals induced by fluctuation of the light path due to the mechanical vibration. Another wave of  $3.39\mu\text{m}$  is used as the usual way of the interferometry. This is an automatic stabilization technique. Fig.11 shows the fringe pattern from  $\text{PD}_1$  without and with stabilization. To confirm the principle, Prof. Yasuda measured the refractive index of air with variable pressures. The values agreed well with the theoretical ones.

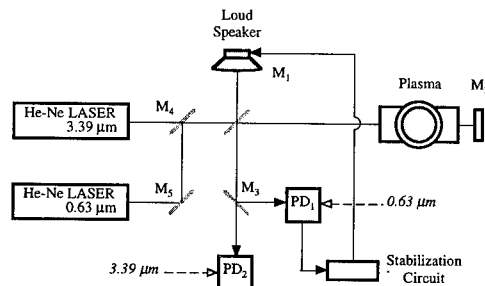


Figure 10 : Stabilization system of a laser interferometer



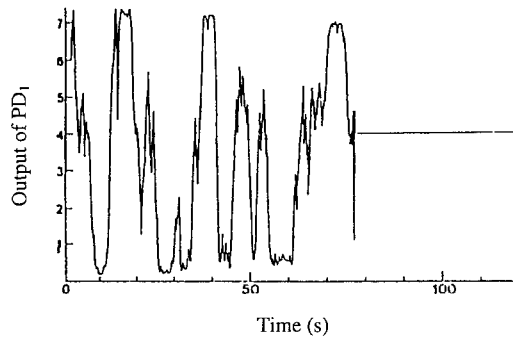


Figure 11 : Signal of  $PD_1$  without and with the stabilization

#### Acknowledgements

Finally I would like to thank the International Scientific Committee members for awarding me Penning prize. .

#### References

- [1] Toryyama Y., Arch. Elektrotech, 28(1934) 105
  - [2] Fukui S. and Miyamoto S., Nuovo Cimento, 11(1959) 113
  - [3] Takeda S., Japan I.E.E.72 (1952) 753
  - [4] Herlin M.A. and Brown S.C., Phys. Rev. 74(1948) 291
  - [5] Honda K., Japan I.E.E.68 (1948) 92
  - [6] Takeda S. and Dougal A.A., J. Appl. Phys. 31(1960) 412
  - [7] Takeda S., J. Phys. Soc. Japan, 16(1961) 95
  - [8] Simonet F., Rev. Sci. Instrum. 56(1985) 664
  - [9] Takeda S. et al., J. Phys. Soc. Japan, 57(1988) 3036
  - [10] Yasuda A. et al., Rev. Sci. Instrum. 51(1980) 1652
- Takeda S. and Yasuda A., Rev. Sci. Instrum. 42(1971) 394

**Topical**

## Nonlocal Electron Kinetics in DC Discharges

L.L. Alves, G. Gousset\* and C.M. Ferreira

*Centro de Física dos Plasmas, Instituto Superior Técnico, 1096 Lisboa codex, Portugal*

*\* Laboratoire de Physique des Gaz et des Plasmas, Université de Paris-Sud, 91405 Orsay cedex, France*

**Abstract:** The self-consistent modeling of a DC discharge must consider the spatial dependences introduced by the inhomogeneous structure of the radial field and the density gradient. To start tackling the problem, we develop a *self-contained formulation* to solve the steady-state spatially inhomogeneous electron Boltzmann equation in a plasma positive column. The problem is solved in cylindrical geometry using the classical *two-term approximation*, with appropriate boundary conditions for the electron velocity distribution function, especially at the tube wall. The present formulation is *self-contained* in the sense that the relationship between the applied maintaining field and the gas pressure, termed the *discharge characteristic*, is obtained as an *eigenvalue solution* to the problem. A progress report on the *self-consistent solution* to this nonlocal kinetic problem is also presented.

### 1. INTRODUCTION

The complete modeling of gas discharges constitutes a very complex research program, as it must include Maxwell's equations and the macroscopic transport equations (particle balance and motion) for the existing charged/neutral species, in order to calculate self-consistently the spatial distributions (and, eventually, the temporal evolution) of the electromagnetic fields, the particle densities, and the macroscopic fluxes. Further, when the electron characteristic lengths for the different discharge processes are of the same order of magnitude as the typical dimensions of the discharge container, a space dependent microscopic description of the electron kinetics is recommended.

In recent years there has been an increasing interest devoted to the problem of the spatial description of the electron kinetics in various discharges and/or discharge configurations, which led to the development of various nonequilibrium discharge models and, in many cases, to the introduction of new numerical tools in order to solve the problem in an efficient, accurate way. In general, these models have adopted either a *statistical approach*, using Particle-in-Cell and/or Monte-Carlo simulations, or a *kinetic equation approach*, by solving the electron Boltzmann equation (EBE) written under different approximations.

Because the *statistical approach* is based on first principles, involving no *a priori* approximations, it can be considered as more rigorous than the *kinetic equation approach*. However, to produce reliable statistical results, these calculation programs must use a very high number of test particles, which in practical terms leads to very long computation times. This is why the numerical integration of the EBE is still considered as a valid interesting approach, especially in those situations where we can use approximations well adapted to the description of the physical systems under study.

Two examples of very well-known approximations are the *two-term approximation* [1, 2, 3], valid when the discharge anisotropies are small, and the *dc effective field approximation* [1, 2, 4], valid when the discharges are produced by hf applied electric fields of sufficiently high frequencies. These

particular approximations were adopted by many authors to solve the spatially dependent EBE, using a variety of numerical techniques in order to speed up the calculations [5, 6, 7, 8]. Other authors have solved the EBE by adopting the so-called *total energy formulation*, in which the *total energy* (kinetic plus potential) of the electrons replaces the kinetic energy as an independent variable [9, 10, 11, 12].

The contribution of these models was decisive to construct an overall picture of the electron kinetics in inhomogeneous situations. However, the formulations adopted so far to solve this nonlocal kinetic problem still require some improvements in order to achieve a *self-consistent description*.

The reasons are threefold. First, the nonlocal electron kinetics is strongly dependent on the phenomena occurring at the plasma-sheath boundary, near the discharge wall, where the anisotropies are expected to increase. To gain further physical insight into this problem one has to derive a correct **wall boundary condition** from **theoretical considerations**, instead of assuming any arbitrary law at the wall [6, 7, 11, 12]. Second, a *self-contained steady-state solution* to the EBE must verify the electron particle balance equation. This requirement yields a relationship between the discharge maintaining field and the pressure, termed the *discharge characteristic*, which has to be **simultaneously** obtained as an *eigenvalue solution* to the problem. Such a formulation constitutes the sole correct approach for solving this problem, as it does not resort to experimental (or parametric) *discharge characteristics* as input data [10, 11]. Third, a *self-consistent solution* to this nonlocal problem requires a simultaneous description of the electron and the ion kinetics. In the case of a DC discharge, for example, this can only be achieved through a kinetic-fluid hybrid model, that couples the Boltzmann equation for the electrons with the fluid-type equations for the ions and Poisson's equation for the space-charge field.

The main purpose of this paper is to present a *self-contained formulation* to numerically solve the spatially inhomogeneous EBE in a plasma positive column [8, 13], including the spatial gradient and the space-charge field terms in the equation for the isotropic component. The problem is solved in cylindrical geometry, with appropriate boundary conditions for the electron velocity distribution function, in particular at the tube wall. The last section of the paper reports the first progresses made on the *self-consistent solution* to this nonlocal kinetic problem, obtained by calculating the space-charge field that gives a match between the macroscopic radial flux of electrons and ions.

## 2. GENERAL FORMULATION

### 2.1 Radially dependent electron Boltzmann equation

The system under analysis is a DC positive column of radius  $R$ , under the action of a total electric field of the form  $\vec{E}(r) = E_r(r)\vec{e}_r + E_z\vec{e}_z$ , where the radial component  $E_r(r) = -\nabla_r\phi$  is the space-charge field ( $\phi$  represents the space-charge potential), and the axial one is the applied electric field, assumed uniform.

The distribution of electrons in the discharge can be described by the electron distribution function (EDF)  $F(r, \vec{v})$ , obtained by solving the corresponding Boltzmann equation with the normalization condition  $\int F(r, \vec{v})d^3v = n_e(r)$ , where  $n_e(r)$  is the electron density.

In the present situation, we consider the existence of a total anisotropy with an axial component due to the applied field, and a radial component due to the space-charge field and the density gradient. In order to solve the EBE we adopt the *two-term approximation* [1, 2], that is, we represent the EDF by the first two terms of its expansion in spherical harmonics around the total anisotropy direction  $\vec{e}_{\text{anisotropy}}$ , along which we assume  $F$  to be cylindrically symmetric,

$$F(r, v, \theta) = \sum_{l=0}^{\infty} F^l(r, v) P_l(\cos \theta) \quad (1a)$$

$$\simeq F^0(r, v) + F^1(r, v) \cos \theta = F^0(r, v) + \frac{\vec{v}}{v} \cdot \vec{F}^1(r, v) \quad (1b)$$

In these equations,  $P_l(\cos \theta)$  denotes the  $l$ -Legendre polynomial, where  $\theta$  is the spherical polar angle in velocity space, and  $\vec{F}^1 \equiv F^1 \vec{e}_{\text{anisotropy}}$  is the *first-anisotropy vector*.

With this approximation, the EDF is decoupled into an isotropic component  $F^0(r, v)$ , an axial anisotropic component  $F_z^1(r, v)$ , and a radial anisotropic component  $F_r^1(r, v)$ . Introducing the expansion (1b) into the EBE yields a scalar equation for the isotropic component of the EDF, and a vector equation for its anisotropic components. After the renormalization

$$\frac{F^0(r, v)}{n_{e0}} 4\pi v^2 dv \equiv f(r, u) \sqrt{u} du \quad ; \quad \frac{F^1(r, v)}{n_{e0}} 4\pi v^2 dv \equiv f^1(r, u) \sqrt{u} du \quad ,$$

where  $n_{e0}$  is the electron density at the tube axis, so that

$$\int_0^\infty f(r, u) \sqrt{u} du = \frac{n_e(r)}{n_{e0}} \Rightarrow \int_0^\infty f(0, u) \sqrt{u} du = 1 \quad , \quad (2)$$

one obtains [1, 2]

$$\frac{\partial G(r, u)}{\partial u} + \sqrt{\frac{2e}{m_e}} \frac{u}{3} \vec{\nabla}_r \cdot \vec{f}^1(r, u) \simeq \sqrt{u} [J(r, u) + I(r, u)] \quad (3)$$

$$f_z^1(r, u) \simeq \frac{1}{N\sigma_i(u)} E_z \frac{\partial f(r, u)}{\partial u} \quad (4a)$$

$$f_r^1(r, u) \simeq \frac{1}{N\sigma_i(u)} \left[ E_r(r) \frac{\partial f(r, u)}{\partial u} - \nabla_r f(r, u) \right] \quad . \quad (4b)$$

Herein,  $G = G_E + G_c$  is the *total upflux* in energy space due to the total field and the elastic collisions given by, respectively,

$$G_E(r, u) \equiv G_{E_z}(r, u) + G_{E_r}(r, u) \equiv -\sqrt{\frac{2e}{m_e}} \frac{u}{3} [E_z f_z^1(r, u) + E_r(r) f_r^1(r, u)] \quad (5a)$$

$$G_c(r, u) \equiv -\sqrt{\frac{2e}{m_e}} \frac{2m_e}{M + m_e} N u^2 \sigma_c(u) \left[ f(r, u) + \frac{k_B T_g}{e} \frac{\partial f(r, u)}{\partial u} \right] \quad . \quad (5b)$$

In these equations,  $u = m_e v^2 / 2e$  is the electron energy in eV, where  $e$  and  $m_e$  are the electron charge and mass, respectively;  $M$  is the atom mass;  $N$  is the gas density;  $T_g$  is the gas temperature;  $\sigma_i(u) = \sigma_c(u) + \sum_i \sigma_0^i(u) + \sigma_0^I(u)$  is the total electron-neutral momentum transfer cross-section;  $\sigma_c(u)$  is the elastic momentum transfer cross-section;  $\sigma_0^i(u)$  is the direct electron excitation cross-section for the  $i$ -th state; and  $\sigma_0^I(u)$  is the direct electron ionization cross-section (all inelastic collisional processes are assumed to be isotropic). The quantities  $J(r, u)$  and  $I(r, u)$  represent electron operators for the collisional processes here considered, i.e., ground state excitations and ionization, taking into account the production of secondary electrons.

Substituting Eqs. (4a)-(4b) and (5a)-(5b) into Eq. (3) yields a second-order partial differential equation for  $f(r, u)$ , in the energy and configuration spaces; this equation is to be solved subject to appropriate boundary conditions.

## 2.2 Boundary conditions

The solution of Eq. (3) requires the knowledge of two boundary conditions in energy space and two boundary conditions in configuration space.

In energy space we impose [2]

$$G(r, 0) = G(r, \infty) = 0 \quad , \quad (6)$$

corresponding to the *total upflux* conservation, whereas in configuration space, at  $r = 0$ , symmetry considerations lead to

$$\frac{\partial f(r, u)}{\partial r} \Big|_{r=0} = 0 \quad . \quad (7)$$

In order to deduce a *meaningful* physical boundary condition at  $r = R$ , we first obtain the *net (microscopic) radial flux of electrons with velocity between  $v$  and  $v + dv$* ,  $\gamma_r(r, v)$ , by integrating the product  $F(r, \vec{v}) v_r$  over all angles in velocity space

$$\gamma_r(r, v) \equiv \int \int_{\Omega} F(r, \vec{v}) v_r d\Omega \quad . \quad (8)$$

In Eq. (8), at  $r = R$ , it is convenient to separate the integration over the polar angle in its forward and backward hemispheres, yielding

$$\begin{aligned} \gamma_r(R, v) &\equiv \gamma_r^+(R, v) - \gamma_r^-(R, v) \\ &= 2\pi \int_{\theta=0}^{\pi/2} F(R, \vec{v}) (v \cos \theta) \sin \theta d\theta - 2\pi \int_{\theta=\pi}^{\pi/2} F(R, \vec{v}) (v \cos \theta) \sin \theta d\theta \quad , \end{aligned} \quad (9)$$

where  $\gamma_r^+(R, v)$  [ $\gamma_r^-(R, v)$ ] is the *forward (backward) microscopic radial electron flux at  $r = R$* , that is, the total number of electrons, with velocity between  $v$  and  $v + dv$ , reaching (reflected by) the wall per unit area and unit time.

For the case of a perfectly absorbing wall, the boundary condition at  $r = R$  can be expressed by

$$\gamma_r^-(R, v) = 0 \quad , \quad (10)$$

which corresponds, after calculations, to

$$f_r^1(R, u) = \frac{3}{2} f(R, u) \quad , \quad (11)$$

where we have assumed that the EDF can be well represented by the two-term expansion in spherical harmonics (1b), and we have used the usual energy renormalization (cf. Sec. 2.1).

Equation (11) can be obtained from the general wall boundary condition deduced in [13], in the particular case of an infinitely thin *boundary layer* and, for consistency, a potential drop  $\Delta\phi = 0$ .

Note that the wall boundary condition given by Eq. (11) implies that  $f_r^1(R, u) > 0$ , which means that the radial anisotropy always points toward the wall at  $r = R$ . Further note that, as shown in [8], the wall boundary condition (11) reproduces well the results obtained from other theories, in some limiting cases.

Equation (11) was directly obtained from transport considerations, which constitutes the correct procedure to derive a wall boundary condition, without resorting to any arbitrary law for the EDF or the electron density at  $r = R$  [6, 7, 11, 12]. In any case, numerical tests show that, for a given  $E_r(r)$ , the solution to the EBE is not too sensitive to modifications in the wall boundary condition. The EDF's so obtained only differ near  $r = R$ . In spite of this, the expression of the wall boundary condition does play a major role in the *self-consistent* resolution of this kinetic problem, as it directly defines the radial electron flux at  $r = R$ , which is to be equated to the corresponding radial ion flux in order to yield the correct space-charge field.

### 3. INTEGRATION OF THE EBE. MACROSCOPIC EQUATIONS

#### 3.1 Electron particle balance equation

The electron particle balance equation is obtained by integrating Eq. (3) over all energies, taking into account Eq. (6) for the boundary conditions in energy space. The resulting equation is [8]

$$\vec{\nabla}_r \cdot \vec{\Gamma}_{r_e}(r) = \nu_I(r) n_e(r) \quad , \quad (12)$$

where  $\nu_I(r)$  is the direct ionization collision frequency ( $\nu_I(r)/N$  is the corresponding rate coefficient), and  $\Gamma_{r_e}(r) \equiv n_e(r)v_{de}(r)$  is the radial electron flux ( $v_{de}(r)$  is the electron radial velocity), obtained by an appropriate integration of Eq. (4b) over all energies

$$\frac{\Gamma_{r_e}(r)}{n_{e0}} = \frac{1}{3} \left( \frac{2e}{m_e} \right)^{1/2} \int_0^\infty f_r^1(r, u) u du \quad (13)$$

A *self-contained solution* to the isotropic EBE [Eq. (3)] **automatically verifies** Eq. (12), yielding an ionization rate that exactly compensates for the loss rate to the wall. Assuming that  $E_r(r)/N$  is known *ab initio*, this condition yields a relationship of  $E_z/N$  vs.  $NR$ , termed the *discharge characteristic* for the maintaining field, which has to be **simultaneously** obtained as an *eigenvalue solution* to the problem.

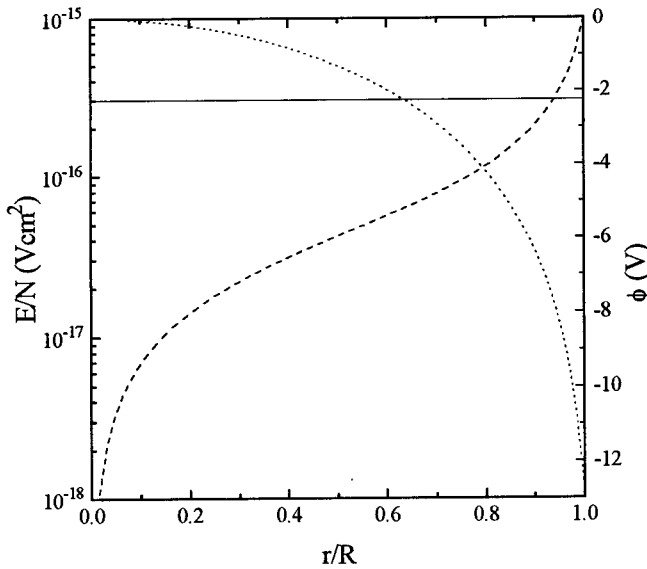


**Figure 1:** Radial profiles of  $E_z/N$  (solid curve),  $E_r/N$  (dashed), and  $\phi$  (dotted).

### 3.2 Electron power balance equation

The electron power balance equation is obtained by multiplying Eq. (3) by the electron energy  $u$ , and then integrating over all energies (taking into account Eq. (6) for the boundary conditions in energy space). The resulting equation can be written as

$$\Theta(r) \equiv \Theta_{\text{transp}}(r) + \Theta_{\text{coll}}(r) \quad (14a)$$

with

$$\Theta_{\text{transp}}(r) \equiv P_{E_r}(r) + P_{\text{conv}}(r) \quad (14b)$$

$$\Theta_{\text{coll}}(r) \equiv P_{\text{el}}(r) + P_{\text{exc}}(r) + P_{\text{ion}}(r) \quad (14c)$$

The l.h.s. term of Eq. (14a) represents the mean power absorbed from the applied field per electron, while the r.h.s. terms represent the power lost by the electrons due to the radial transport across the discharge,  $\Theta_{\text{transp}}$ , and collisional processes,  $\Theta_{\text{coll}}$ . According to Eqs. (14b)-(14c), the quantity  $\Theta_{\text{transp}}$  includes the power lost in flowing against the space-charge field,  $P_{E_r}$ , and the net power lost

due to convection in configuration space,  $P_{\text{conv}}$ , whereas  $\Theta_{\text{coll}}$  accounts for the power lost in elastic collisions,  $P_{\text{el}}$ , excitation,  $P_{\text{exc}}$ , and ionization,  $P_{\text{ion}}$ . Explicit expressions for these terms can be found in [8].

#### 4. NONLOCAL ELECTRON KINETICS. SOLUTION TO THE EBE

##### 4.1 Input parameters and numerical resolution

The simulations presented in this work were made for helium, adopting the set of electron cross-sections derived in [14, 15]. In this section, dedicated only to the study of the nonlocal electron kinetics, a given radial profile for the space-charge field is assumed. Figure 1 represents the field distributions here used, corresponding to  $E_z/N = 3 \times 10^{-16} \text{ Vcm}^2$ ,  $NR = 1.3 \times 10^{17} \text{ cm}^{-2}$  (*eigenvalue solution*), and a reduced space-charge field that follows a Bessel-type law

$$\frac{E_r(r)}{N} = 2.4 \frac{u_s}{NR} \frac{J_1(2.4r/R)}{J_0(2.4r/R)}, \quad (15)$$

where we have imposed  $u_s \simeq 0.5u_k(0)$  ( $u_k(r)$  is the electron characteristic energy [8]). Note that Eq. (15) gives for  $E_r(r)$  a more realistic profile than the one assumed in [8, 13].

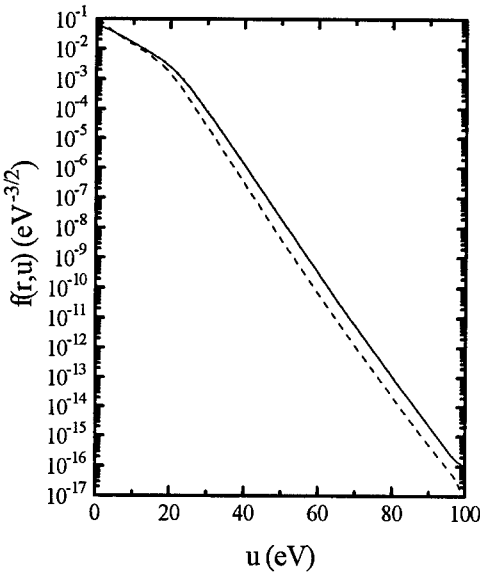


**Figure 2(a):** Isotropic component of the EDF as a function of  $u$ . Solutions to the inhomogeneous EBE at the following  $r/R$  positions: solid curve, 0; dashed curve, 1. The dotted curve is for the solution to the homogeneous EBE. All curves are renormalized to 1.

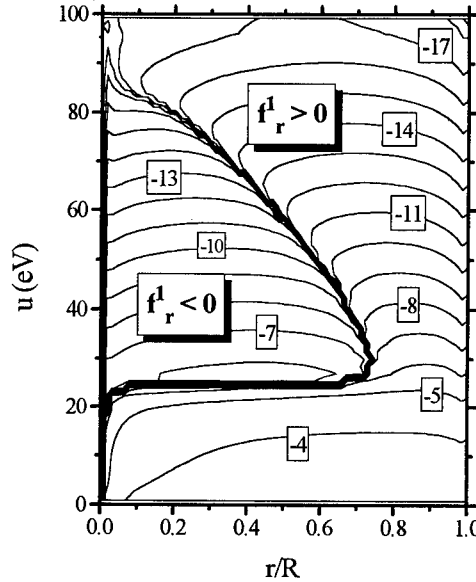


**Figure 2(b):** Countour plot of  $\log_{10} |f_r^1|$  as a function of  $r/R$  and  $u$ .

The numerical method employed to solve Eq. (3) [after substitution of Eqs. (4a)-(5b)], with the boundary conditions (6), (7), and (11), is based on its conversion into a set of  $N_T$ -coupled algebraic equations by second-order, fixed-step finite differencing in the energy and configuration spaces.

The resulting matrix system is solved using a *multigrid method* [16], whose algorithm exactly includes all boundary conditions and allows for the calculation of an *eigenvalue*. The system convergence test is applied to the solution  $f(r, u)$  and to the electron macroscopic equations (particle and power balance equations), checking for relative errors less than  $10^{-6}$  and  $10^{-10}$ , respectively.



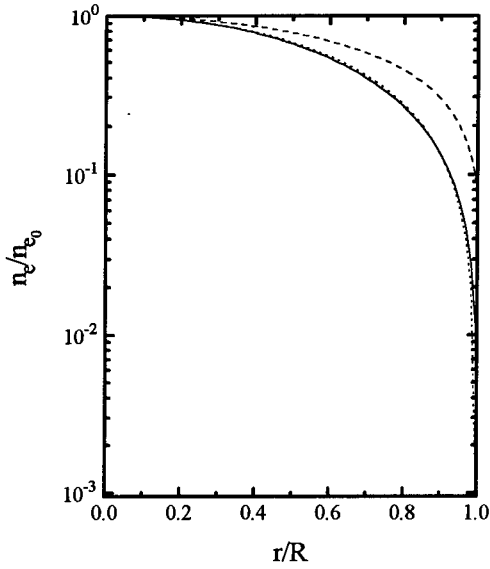


**Figure 3(a):** Electron density radial distribution. Solid curve: solution to the inhomogeneous EBE. Dashed curve: calculation assuming Boltzmann equilibrium in the space-charge potential. Dotted curve: Bessel distribution with  $n_e(R) = 0$ .

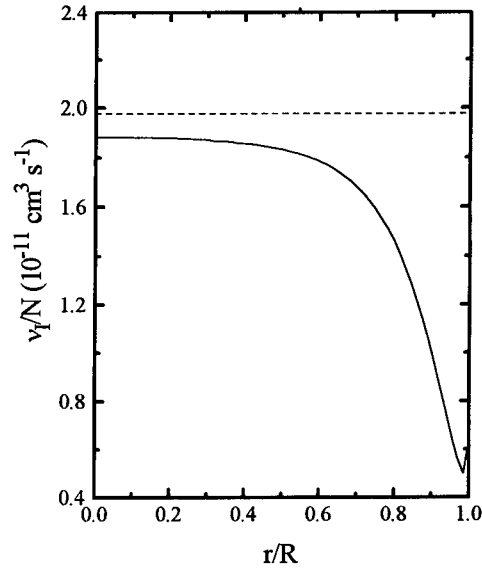


**Figure 3(b):** Electron ionization rate coefficient as a function of  $r/R$ . Solid curve: solution to the inhomogeneous EBE. Dashed curve: solution to the homogeneous EBE.

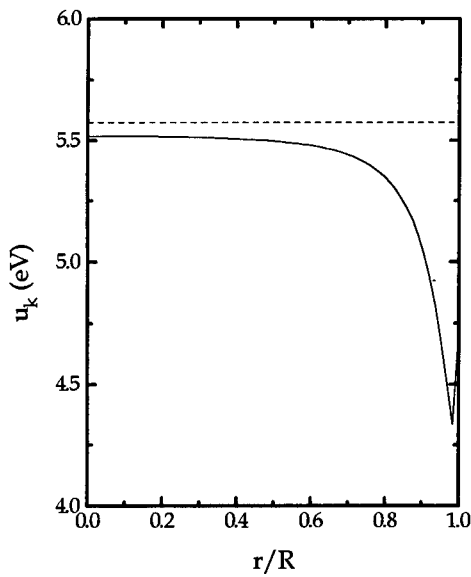


**Figure 3(c):** Electron characteristic energy as a function of  $r/R$ . Solid curve: solution to the inhomogeneous EBE. Dashed curve: solution to the homogeneous EBE.

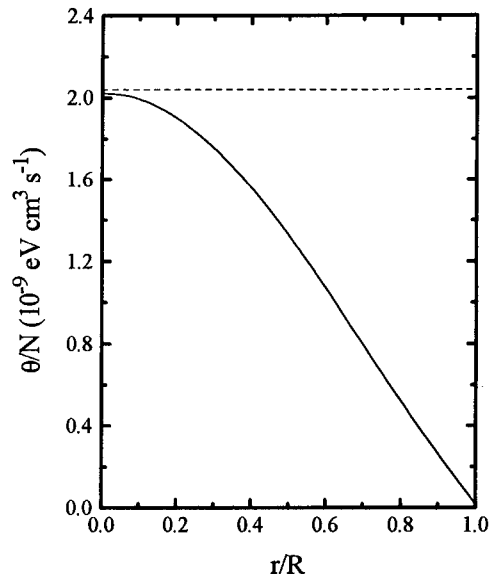


**Figure 3(d):** Mean power absorbed from the applied field per electron at unit gas density as a function of  $r/R$ . Solid curve: solution to the inhomogeneous EBE. Dashed curve: solution to the homogeneous EBE.

## 4.2 Results and discussion

Figure 2(a) represents, for the working conditions considered, the isotropic component of the EDF  $f(r, u)$ , as a function of  $u$  for different radial positions, together with the distribution  $f(u)$  for the corresponding homogeneous situation. For the purposes of comparison, all functions are renormalized to 1, that is,  $\int_0^\infty f(r, u) \sqrt{u} du = 1$ . This figure clearly shows the depletion of the isotropic EDF as the boundary at  $r = R$  is approached, due to the electron drain to the wall.

Figure 2(b) represents a countour-plot of  $\log_{10} |f_r^1(r, u)|$  vs.  $(r/R, u)$ . Note that the radial anisotropy **normally points toward the wall** ( $|\nabla_r f(r, u)| > E_r(r) |\partial f(r, u) / \partial u|$ ) [cf. Eq. (4b)], which means that the **electrons do flow toward the wall against the space-charge field**. However, an exception to this occurs for an intermediate kinetic energy range, where  $f_r^1$  becomes negative. This behaviour is observed in a region beyond an energy around the inelastic thresholds, and it can be explained by the strong depletion of the electron energy distribution in that region [8].

As we can see from Fig. 2(b), the radial anisotropy **always points toward the wall** at  $r = R$  due to the strong electron drain occurring in this region, as a direct consequence of the wall boundary condition deduced here (cf. Sec. 2.2).

The radial electron density distribution,  $n_e(r)/n_{e0}$ , is represented in Fig. 3(a). For comparison, we have also plotted on this figure the density distributions assuming Boltzmann equilibrium in the space-charge potential,  $n_e(r)/n_{e0} = \exp(\phi(r)/\bar{T}_e)$  ( $\bar{T}_e$  is the radially averaged electron temperature, with  $T_e \equiv (2/3)\langle u \rangle$ ), and the typical Bessel distribution with  $n_e(R) = 0$ .

The electron ionization rate coefficient,  $\nu_I/N$ , the electron characteristic energy,  $u_k$ , and the mean power absorbed from the applied field per electron at unit gas density,  $\theta/N$ , are shown in Figs. 3(b), 3(c), and 3(d), respectively, as a function of  $r/R$ . On these figures, we have also represented the values of these quantities as calculated for the homogeneous situation.

We note that the values calculated using the spatially dependent EDF are quite different from those corresponding to the homogeneous situation, although the electron density distribution closely follows the typical Bessel profile. This is a clear indication of a nonlocal behaviour, which is associated to the impossibility of performing a separation of variables in the energy and configuration spaces.

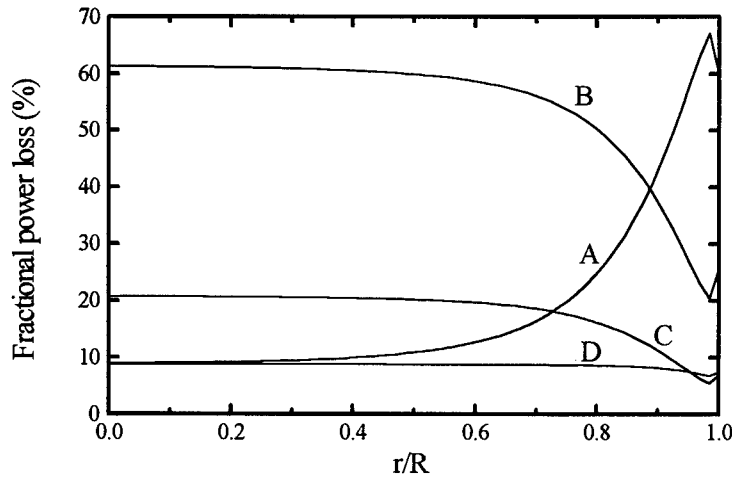


**Figure 4:** Average fractional power lost by the electrons vs.  $r/R$ . The labels are for the following power loss channels: A, radial transport in the discharge (diffusion against the space-charge field + convection flow in configuration space); B, excitation; C, ionization; D, elastic collisions.

The distribution of the fractional power lost by the electrons is shown in Fig. 4 as a function of  $r/R$ . The curves plotted in this figure correspond to the different terms in the electron power balance equation [cf. Eqs. (14a)-(14c)]: the fractional power lost by the electrons due to the radial transport in

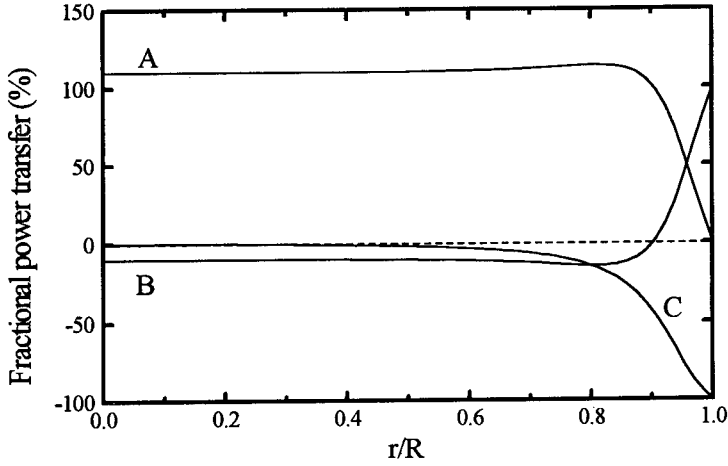


**Figure 5:** Average fractional power gained/lost by the electrons vs.  $r/R$ . The labels are for the following power transfer channels: A, acceleration by the applied field; B, diffusion against the space-charge field; C, convection flow in configuration space. The positive (negative) values indicate a power gain (loss) by the electrons. Percentages were calculated relative to the net power gain from the A+C mechanisms.

the discharge,  $\Theta_{\text{transp}}/\Theta$ , in elastic collisions  $P_{\text{el}}/\Theta$ , in excitations,  $P_{\text{exc}}/\Theta$ , and in ionizations,  $P_{\text{ion}}/\Theta$ . As expected, the main electron power loss channel is associated with excitations, throughout most of the discharge cross-section, but the losses due to the radial transport become dominant near the wall.

The two components of  $\Theta_{\text{transp}}/\Theta$  can be unfolded into the power lost by the electrons in flowing against the space-charge field,  $P_{E_r}$ , and that due to the radial flux in configuration space,  $P_{\text{conv}}$ .

Figure 5 represents  $\Theta/(\Theta - P_{\text{conv}})$ ,  $-P_{E_r}/(\Theta - P_{\text{conv}})$ , and  $-P_{\text{conv}}/(\Theta - P_{\text{conv}})$ , as a function of  $r/R$ . Note that the positive (negative) values on this figure indicate an electron power gain (loss). Further, note that the percentages are now calculated relative to the *net power gain*,  $\Theta - P_{\text{conv}}$ , because the quantity  $P_{\text{conv}}$  can represent either a loss or a gain of power. As seen from Fig. 5, the term  $-P_{\text{conv}}$  becomes positive close to the wall, which means that the divergence of the power flow due to convection is negative. Physically, this corresponds to a gain of power in this region due to heat convection. Such a gain is necessary to overcome the increased losses associated with the rapid variation in the space-charge field near the wall (note that  $P_{E_r} \gtrsim |P_{\text{conv}}|$  near the wall).

## 5. PROGRESS REPORT ON SELF-CONSISTENT CALCULATIONS

The *self-consistent modeling* of a DC discharge requires the simultaneous description of the electron and the ion kinetics. This can only be achieved through a kinetic-fluid hybrid model, that couples the EBE (3)-(5b), the ion particle balance equation

$$\vec{\nabla}_r \cdot \vec{\Gamma}_i(r) = \nu_I(r)n_e(r) \quad , \quad (16)$$

the ion transport equation [17] (written in the case of small discharge anisotropies)

$$v_{d_i}(r) \frac{dv_{d_i}(r)}{dr} = \frac{e}{m_i} E_r(r) - \frac{1}{n_i(r)} \frac{d}{dr} \frac{k_B T_i(r)}{m_i} n_i(r) - \frac{\nu_{c_i} + \frac{n_e(r)}{n_i(r)} \nu_I(r)}{\nu_{c_i}} v_{d_i}(r) \quad , \quad (17)$$

and Poisson's equation

$$\vec{\nabla}_r \cdot \vec{E}_r(r) = \frac{e}{\epsilon_0} (n_i(r) - n_e(r)) \quad . \quad (18)$$

In these equations,  $n_i(r)$  is the ion density;  $v_{di}(r)$  is the ion radial velocity;  $\Gamma_{ri}(r) \equiv n_i(r)v_{di}(r)$  is the ion radial flux;  $T_i(r)$  and  $m_i$  are the ion temperature and mass, respectively; and  $\nu_{ci}$  is the ion-neutral momentum transfer collision frequency.

Note that the particle balance equations for the electrons (12) and the ions (16) can be solved together, yielding the charged particle radial flux conservation

$$\Gamma_{re}(r) = \Gamma_{ri}(r) \quad . \quad (19)$$

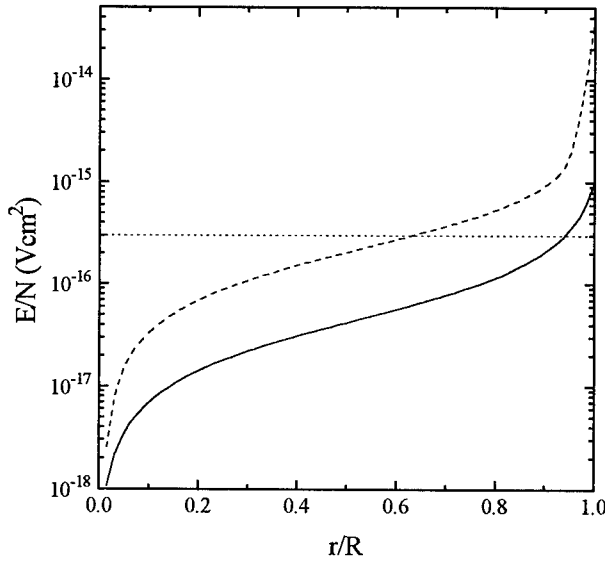


**Figure 6:** Radial profiles of the reduced fields. Solid curve:  $E_r/N$  as calculated from Eq. (15). Dashed curve:  $E_r/N$  after 5 iterations over the flux conservation condition [cf. Eq. (21)]. Dotted curve:  $E_z/N$ .

The complete resolution of this system of equations constitutes a very complex task, to be accomplished in future works. In the present paper, we will start to tackle this problem, by introducing the following hypothesis for simplification purposes:

- the quasi-neutrality [that replaces Poisson's equation (18)]:

$$n_i(r) \simeq n_e(r) \quad ; \quad (20a)$$

- the field drift approximation (that simplifies the ion transport equation (17), by assuming that the radial motion of the ions is exclusively due to a drift under the action of the space-charge field):

$$v_{di} \simeq \frac{e}{m_i \nu_{ci}} E_r(r) = \mu_i E_r(r) \quad , \quad (20b)$$

where  $\mu_i$  represents the ion mobility.

Equation (20b) can now be worked, subject to the conditions (19) and (20a), to give an expression for the self-consistent space-charge field

$$E_r(r) \simeq \frac{v_{di}(r)}{\mu_i} \quad . \quad (21)$$

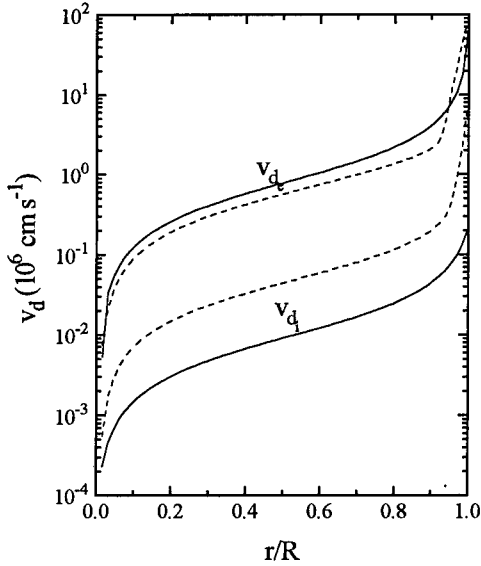


**Figure 7(a):** Radial velocities for electrons ( $v_{de}$ ) and ions ( $v_{di}$ ) as a function of  $r/R$ . Solid curves: results obtained with  $E_r/N$  as calculated from Eq. (15). Dashed curves: results obtained with  $E_r/N$  as calculated after 5 iterations over the flux conservation condition [cf. Eq. (21)].

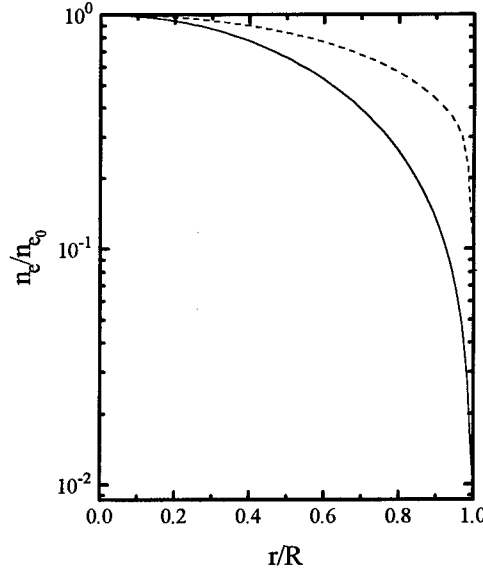


**Figure 7(b):** Electron density radial distribution. Solid curve: results obtained with  $E_r/N$  as calculated from Eq. (15). Dashed curve: results obtained with  $E_r/N$  as calculated after 5 iterations over the flux conservation condition [cf. Eq. (21)].

Note that Eq. (21) clearly shows the very strong nonlinear behaviour of the system, by expressing the space-charge field as a function of the electron radial velocity, which already is a function of  $E_r(r)$  [cf. Eq. (13)].

From the results presented in Sec. 4.2, obtained with the space-charge field given by equation (15), and by adopting a reduced ion mobility of  $\mu_i N \simeq 2 \times 10^{20} \text{ cm}^{-1} \text{ V}^{-1} \text{ s}^{-1}$ , it is possible to calculate the charged particle radial fluxes, by using Eqs. (13) and (20b). The result is that  $\Gamma_{re}(r)/\Gamma_{ri}(r) \simeq 100$  across the discharge radius, which clearly reveals that the condition for the charged particle flux conservation is not verified in our calculations.

In order to start correcting this lack of consistency we have solved the EBE (3)-(5b) coupled with Eq. (21), allowing for the self-consistent calculation of the space-charged field in order to obtain a match between the radial flux of electrons and ions. This was done after appropriate modifications in the numerical algorithm presented in Sec. 4.1, which was carefully redesigned in order to meet the requirements introduced by the very strong nonlinear features of the problem.

Work is still in progress in order to achieve a completely converged solution to the system, and so we will present here only intermediate calculation results.

Figure 6 shows the modification in the space-charge field profile, after **5 iterations over the flux conservation condition**. On this figure, and for the purposes of comparison, we have also plotted the value for the  $E_z$  field. Note that the space-charge field has roughly increase one order of magnitude, which makes that it now overpasses the applied field at  $r/R \simeq 0.6$ .

From the solution to the EBE, obtained with the *new* space-charge field profile, we have calculate the radial velocities for electrons and ions (represented in Fig. 7(a) as a function of  $r/R$ ), and the electron density radial distribution [represented in Fig. 7(b)]. On these figures, and for the purposes of comparison, we have also plotted the radial distribution of these quantities obtained with the *initial* profile of the space-charge field. An observation of these figures reveals that the ratio

$\Gamma_{r_e}(r)/\Gamma_{r_i}(r)$  has already been reduced by a factor 10, after 5 iterations over the flux conservation condition. Furthermore, the radial distribution  $n_e(r)/n_{e0}$  was upwardly deviated from the Bessel profile initially obtained, as a direct consequence of the  $E_r(r)$  increase and the  $\Gamma_{r_e}(r)$  decrease.

A final important consequence of this *self-consistent* procedure is the fact that the  $NR$  value was reduced to  $1.6 \times 10^{16} \text{ cm}^{-2}$ , after 5 iterations over the flux conservation condition. This modification, of about one order of magnitude in the *eigenvalue solution*, clearly shows the influence of the space-charge field on the results and justifies the need for a complete resolution of this problem. This should include a **simultaneous** calculation of the *discharge characteristic*,  $E_z/N$  vs.  $NR$ , and the radial field,  $E_r(r)$ , instead of using experimental (or parametric) values for some of these quantities, as input data [11].

## 6. FINAL REMARKS

We developed a *self-contained formulation* to solve the steady-state spatially inhomogeneous EBE taking into account the spatial gradient and the space-charge field terms. The present formulation is *self-contained* in the sense that the relationship between the applied maintaining field and the gas density, termed the *discharge characteristic*, is obtained as an *eigenvalue solution* to the problem. We also reported the first progresses made on the *self-consistent solution* to this nonlocal kinetic problem, obtained by calculating the space-charge field that gives a match between the macroscopic radial flux of electrons and ions. The complete resolution of this problem can only be achieved through a kinetic-fluid hybrid model, by coupling the Boltzmann equation for the electrons with the fluid-type equations for the ions and Poisson's equation for the space-charge field. Work is in progress in this direction.

## Acknowledgments

This work was supported by the *PRAXIS XXI* Programme, partly funded by the EC FEDER, under Contract No. Fis/377/94.

## References

- [1] T. Holstein, Phys. Rev. **70**, 367 (1946).
- [2] W. P. Allis, *Handbuch der Physik* (ed. S. Flügge, Springer, Berlin, 1956), Vol. 21, p. 383.
- [3] L. C. Pitchford, S. V. O'Neil, and J. R. J. Rumble, Phys. Rev. A **23**, 294 (1981).
- [4] R. Winkler, H. Deutsch, J. Wilhelm, and C. Wilke, Beitr. Plasmaphys. **24**, 285 (1984).
- [5] V. A. Feoktistov *et al.*, IEEE Trans. Plasma Sci. **19**, 163 (1991).
- [6] P. M. Meijer, W. J. Goedheer, and J. D. P. Passchier, Phys. Rev. A **45**, 1098 (1992).
- [7] M. J. Hartig and M. J. Kushner, J. Appl. Phys. **73**, 1080 (1993).
- [8] L. L. Alves, G. Gousset, and C. M. Ferreira, Phys. Rev. E **55**, 1 (1997).
- [9] F. Sigeneger and R. Winkler, Phys. Rev. E **52**, 3281 (1995).
- [10] C. Busch and U. Kortshagen, Phys. Rev. E **51**, 280 (1995).
- [11] D. Uhrlandt and R. Winkler, J. Phys. D **29**, 115 (1996).
- [12] Yu. B. Golubovskii *et al.*, in *Proc. XXIII International Conference on Phenomena in Ionized Gases* (Université Paul Sabatier, Toulouse, 1997), Vol. 2, p. 4.
- [13] L. L. Alves, G. Gousset, and C. M. Ferreira, in *Proc. 3<sup>rd</sup> International Workshop on Microwave Discharges: Fundamentals and Applications*, J. Physique, (in press, 1997).
- [14] L. L. Alves and C. M. Ferreira, J. Phys. D **24**, 581 (1991).
- [15] G. D. Alkhazov, Zh. Tekh. Fiz. **40**, 97 (1970), [Sov. Phys. Tech. Phys. **15**, 66 (1970)].
- [16] W. Hackbush, *Multi-Grid Methods and Applications* (Springer-Verlag, Berlin, 1985).
- [17] V. E. Golant, A. P. Zhilinsky, and I. E. Sakharov, *Fundamentals of Plasma Physics* (ed. S. C. Brown, John Wiley & Sons, New York, 1980).

## **Crystal and Fluid-Like Assemblies in Plasma Sheaths**

B.M. Annaratone

*Department of Engineering Science, University of Oxford, Parks Road, Oxford OX1 3PJ, U.K.*

**Abstract.** The broad topic of the dust-dust interaction phenomenology in the plasma and in the plasma sheath is here analysed with reference to the work of the Oxford team. The theory includes preliminary consideration on the dust charge in the plasma sheath region, in a crystal environment and in the case of fast-moving particles. Among other experimental observations the dust-laser interaction and the motion of the particulate in non uniform electric fields are shown in some detail.

### **1. INTRODUCTION**

Dust-plasma interaction is a relatively young area. In the last few years it has grown substantially due to the increase in interest worldwide. Three separate communities: space physics, plasma processing and basic plasma physics are now interacting to understand, jointly, the complex behaviour of small objects in plasma and space charge environments. The dynamical equilibrium charge of these objects is easily modified by any fluctuation of plasma parameters, particle or light beams, interaction with other grains, electric fields, etc., making the theoretical speculations extremely complex. For this reason the experimental results cannot be overestimated: they can orient the theoretical research and also find quickly their way into applications.

In fact the physics of dust is undergoing important development in many areas. The most well known is contamination control in microelectronic fabrication processes, etc. [1]. Dust control allows higher yields in semiconductor nanotechnology but dust caused defects are still one of the major causes of discarding. Another new development is the control of industrial processes by the change in the light scattered by the dispersed particles. The dust in the mesopause, and its influence in radar back-scatter, is an issue of primary importance to communications.

One focus of interest is the interaction between planetary rings, in particular the distributed fine grains and the planetary magnetospheric field and the formation of protoplanetary disks. Other effects of importance for planetary rings are stability, perturbations, structure and dynamics.

The dust crystal experiment in RF sheaths [2,3] has still to be fully investigated. Interacting sheaths, multifluid treatments, particle codes, perturbations and diagnostics will explain the properties of such a novel state of the matter. The planned microgravity experiments

open new prospectives to basic plasma physics research[4].

There are also expectations that dust-plasma physics could become important for environmental monitoring, pollution in the mesosphere, optical communications, in the manufacture of new "nanodot" materials with quantal effects [5], and many other applications.

### 1.1 Charge of Isolated Particle in Plasma and Plasma-sheath

Extensive theoretical work has now dealt with charge of dust in uniform plasma [6,7]. These theories, which lead to different results for the floating potential, and the grain charge, need to be compared with experiments. In gravity only very fine particles are suspended in the weak fields of the plasma [8]. These small particles will present statistical fluctuation of the floating potential because the continuous approximation for ion and electron current is not longer valid.

Other considerations are needed in gravity for dust grains above 100nm diameter (density of the order of  $10^3 \text{ Kg m}^{-3}$ ). Particles are suspended in the sheath, and not in plasma, where gravitational and "ion drag" forces are balanced by electric forces. The charge of the isolated dust in the sheath is still unexplored. The only attempt found in the literature uses the orbital motion theory which is clearly applicable only in a very weak non-central force field [9].

The behaviour of grains in a DC or RF sheath can be quite different. This is because the non-linearity of the I-V characteristic of the electrode sheath, averaged over the radiofrequency period, would increase the average electron current, an effect which is counterbalanced by the electrode becoming more negative with respect to plasma. These considerations do not apply for the sheath created at the grain surface as no RF current can flow. In a collisionless electrode sheath the ion energy (due to the electrode RF sheath) is high in comparison to the grain-local space voltage difference (DC sheath). Ions are hardly deflected and the ion-dust cross section tends to the geometrical cross section. In a collisional sheath the slow ions will give a higher contribution to the ion current to the grain than in the collision-free case. Experiments have so far been reported only for RF, driven electrodes, collisional sheaths and in "special" DC cases as striations.

The above considerations on the charging have to be modified when the dust grain in the sheath is surrounded by other grains, as in the crystal or liquid dust assembly.

## 2. EXPERIMENTS

A dust crystal was formed in a 13.56 MHz capacitively-coupled RF plasma of argon maintained within the  $10^{-1}$  Torr range, with a power of about 5W and electrode voltage of about 100V. Different kinds of powder were introduced through a sieved hole in the upper, grounded electrode. The suspended powder was illuminated from a side with a laser beam made planar through an arrangement of lens, and observed using a video camera, fitted with a macroscopic lens, see fig.1 and ref.[10]. The analysis of successive frames allows us to view the detailed evolution of particle distributions over time.

### 2.1 Dust Settling

Particles of the same charge over mass ratio are confined to thin layers of the sheath. They interact with each other, forming molecules or aggregates which could become a crystal when the ratio of the thermal to the electrostatic forces is small. For the parameters of the discharge stated above, distinct dust-clouds form within or near plasma-sheath boundaries. If the kinetic energy of dust is low, a condition achieved in the higher pressure and low power range, the mutual interaction between particles leads to the formation of organised structures of dust in the



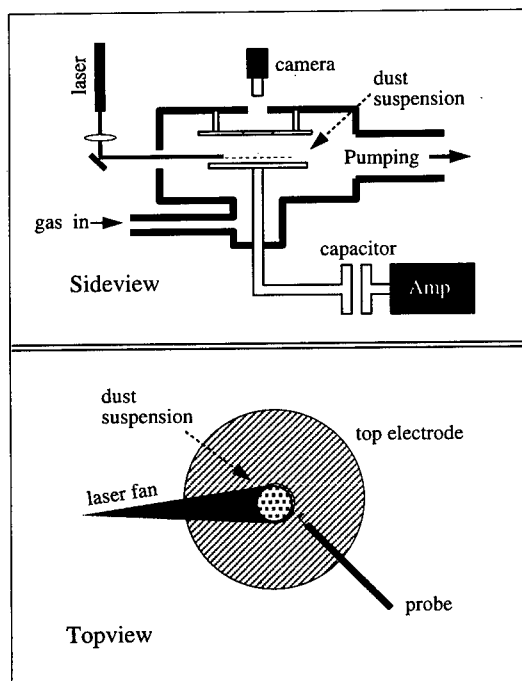


Fig. 1 Schematic representation of the experimental apparatus.

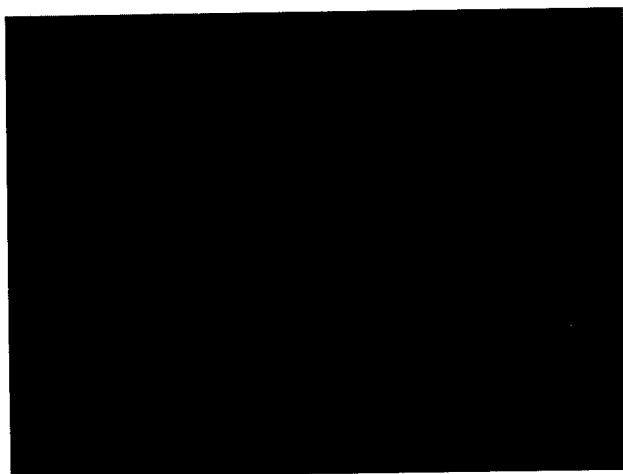


Fig. 2 A single video frame of the dust crystal as seen from above. The crystal is composed of spherical melamine-formaldehyde particles,  $\phi = 15 \mu\text{m}$ .

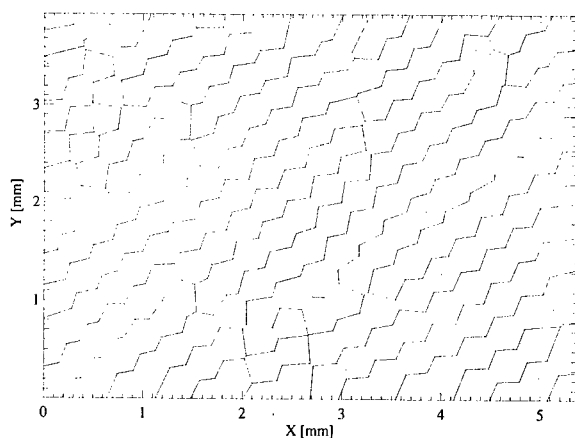


Fig. 3 The same frame as in fig. 2, computer enhanced, with marked Wigner-Seitz cells.

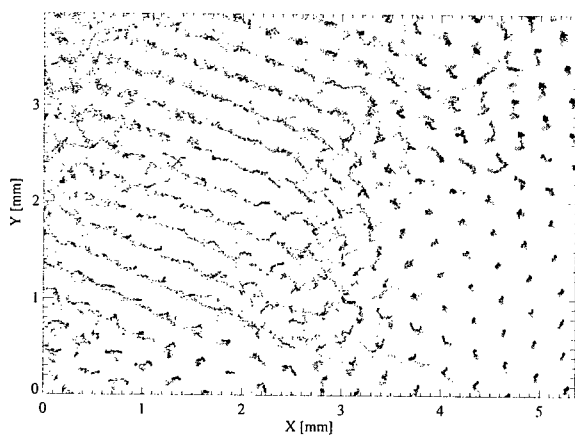


Fig. 4 View of fig 2 with 750 overlapping crystal frames (30s) indicating the movement of dust particles.

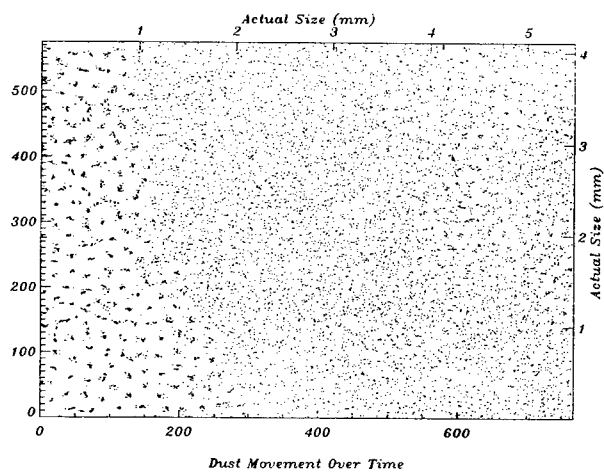


Fig. 5. A semicrystalline region of dust which goes continuously to a region of fast grain motion, 12 overlapping frames (0.5s).

cloud, now commonly referred to as a plasma crystal. In other cases a more liquid-like, or gas (plasma) structure is observed. The status of the dust assembly depends on the size, the dispersion and shape of the powder as well as on the plasma density and electron temperature.

Observation of the isogonal lattice, figs. 2 and 3, would suggest a kind of two dimensional structure due to the repulsion of the negative charges of the grains. This is somehow in contradiction with the space physics community study of dust clouds and our evidence. The sharp edges observed would suggest a surface tension due to attraction. The negative charge of the grains interacts somehow with the positive sheath space charge. The slow motion of the crystal shown in fig. 2 can be seen in fig. 4 where 30s (750 frames) are overlapped. Fig. 5 shows the dust assembly going continuously from 'solid' to a fast moving 'gas' state. Here the electric field varies in strength. If in the solid state the flux of ions follows precise patterns around the negative charge of the grains, in the gas (or plasma) state the ions fall from plasma uniformly. The melting of the crystal is sometimes abrupt.

In the space charge sheath ions acquire a directional velocity and form a continuous stream towards the electrode. A dust particle suspended in this stream will create a wake downstream and in this wake other particles, with different mass accommodate. In fact a chain of about 20 grains, all in a row, with separations 150-250 $\mu$ m, has been observed in the vertical direction when a highly dispersed graphite powder  $\phi = 0.3 - 30\mu$  was inserted. The charging mechanism is clearly perturbed with respect to the single grain in plasma or plasma sheath. Theoretical and experimental work is needed.

## 2.2 Dust Assembly and Laser Interaction

It was found that coherent laser-beams interact strongly with dust-crystals, in a sense, fracturing them and clearing a path along the axis of the beams in which particles accelerate if caught, fig. 6. In some cases, particles trapped in the crystal are set to rotate, which then precess, spin, and in some cases, hop from bound state to bound state along the direction of the beam, see fig. 7. The phenomenon of crystal fracturing with lasers has previously only been observed with megawatt lasers and their interaction with glass. Ours is a 10-16mW HeNe laser.

Mention should be made here to the widely diffuse belief that the interaction of light and grains produce an acceleration which is intrinsically thermal. The illuminated side will be hotter and release more energetic particles than the dark side. This effect makes the black and white vanes to rotate. But in the vanes there is a very good thermal insulator between the white and the black side. This is impossible in small objects. The characteristic time for the diffusion of heat in a grain of radius  $r_0$  is given by:  $t = \rho \sigma r_0^2 / K$ , where  $\rho$  is the density,  $\sigma$  is the specific heat and  $K$  is the thermal conductivity. For micron size grain the diffusion of heat is of the order of  $10^{-6}$ - $10^{-3}$ s depending on the insulating properties of the material. A gradient of temperature cannot possibly be held to cause acceleration. Ponderomotive forces, in the plasma physics usual meaning, also should be excluded. They are ignorable in magnitude and the direction would push the particles outside the beam. Instead the pressure of a 10mW radiation will impart to a 30 $\mu$  grain an acceleration of 1mm/s<sup>2</sup>.

The laser is applied to a system of grains levitated at the edge of the Argon RF plasma. Varying the power of the laser beam by the use of neutral filters, i.e. varying the rate of flow of the momentum transferred to the grains, we could identify the force necessary to break the bond of the crystal, see fig. 8. The experiment was repeated in different plasma-sheath conditions and for different grain sizes and materials [11], the results are summarised in the table I. In this table the four underlined dust crystals have been demonstrated to fracture at full laser power. It is assumed that the crystals of the remainder of the powders would also fracture with stronger lasers. In all four of the fracture cases the explanation can be found in terms of weak electrostatic

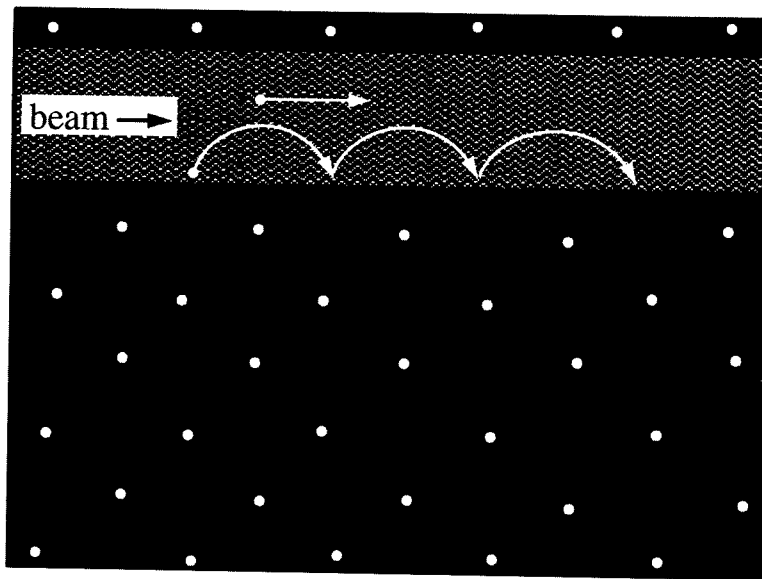


Fig. 6 Schematic representation of a hopping particle.

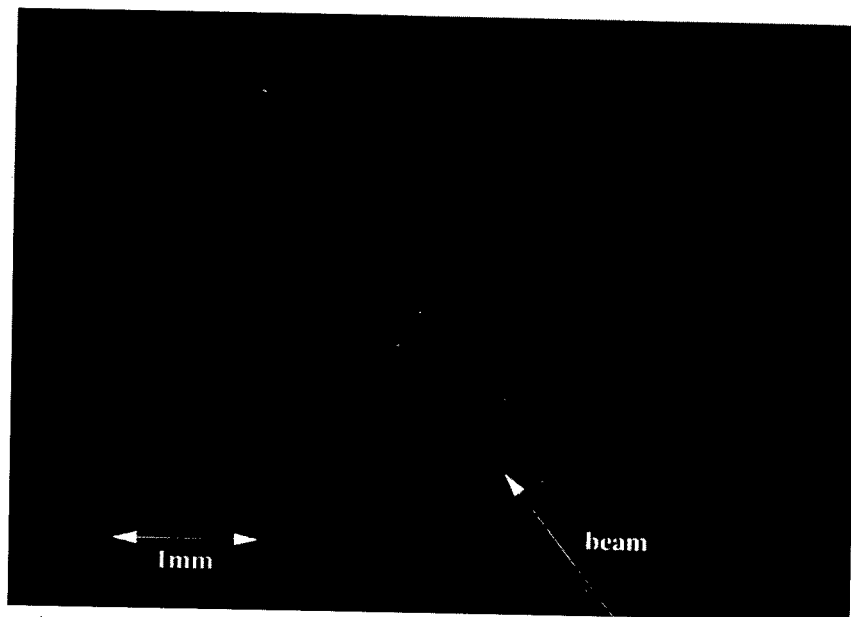


Fig. 7 Particles being pushed along the path of a laser beam, used to fracture the crystal lattice.

Powder	Size Distribution	Density g/cc	Mass x10 <sup>-10</sup> g	Work Function eV	Thermal Conductivity W/m K	Force* per grain x 10 <sup>-13</sup> Kg m/s <sup>2</sup>	Acceleration of unbounded grain* mm/s <sup>2</sup>
MF Polymer	15 micron diameter	1.5	27		-0.2	1.33	52
MF Polymer	7 micron diameter	1.5	2.7		-0.2	0.29	103
MF Polymer	2 micron diameter	1.5	0.063		-0.2	0.022	350
MF Polymer	1 micron diameter	1.5	0.0075		-0.2	0.0059	800
Tungsten	1 to 5 micron diameter	19.3	0.097 to 13	4.5	190	0.006 to 0.15	62 to 11.3
Tungsten	100 micron max. diameter	19.3	1x10 <sup>5</sup>	4.5	190	59	0.59
Carbon	2 to 20 micron diameter	2.25	0.095 to 95	4.7	0.24	0.023 to 2.3	242 to 24

\* Calculations for radiation pressure of a 16mW red HeNe laser (632.8nm) with a focused beam diameter of 300 um on a single isolated dust grain. Energy of a photon is 2eV. Dust crystals fractured in experiment are underlined.

Table 1: Properties of the dust used and calculations of the radiation pressure on an unbound dust grain

attractive forces [12]. The negative charge of the grain controls the vertical position in the non uniform electric field and, the environment being overall positively charged, is responsible for the attractive forces in the horizontal direction, see fig. 9 and explains the hopping of particles shown in fig. 6.

Melamine dust crystal can only be broken for the lower sizes. While the density of surface charge, at least for isolated grains in plasma, increases at smaller sizes [6,7], the total grain charge is smaller for small grains. This reduces both attractive and repulsive forces.

For the same range of sizes Tungsten crystals can be broken and Alumina or Melamine crystals cannot. The Tungsten crystal sets itself in a lower plane, where the field is stronger to counterbalance the higher weight. The charge in all these particles might not be much different and so the horizontal attractive forces. We should mention here that metal grains will reflect the laser light gaining a higher momentum with respect to the insulating ones.

Toner particles (polymerised graphite) crystals also can be easily destroyed. This is attributable to the high dispersion, see fig 10. Charge distributions are not uniform in the grains and in the space in between the grains. When one particle, say one with high cross-section for the laser light, is removed the local crystal equilibrium is modified and the beginning of the creation of the empty channel is established.

Additional experiments revealed that strong visible and ultraviolet light interacts significantly with the dust particles, sometimes modifying the grain charge.

### 2.3 Dust Assembly in a Two Dimensional Varying Electric Field

A Langmuir probe above the electrode space charge region, where the dust crystal is located, influences the dust structure in a most peculiar way. In this experiment the probe was located about 20mm above the driven electrode, the visible emission being confined at about 10mm away from the electrode and the upper layer of the crystal being at 8-9mm, see also refs. [13,14].

The crystal below the probe shows a perfect stationary almost circular area, of a diameter comparable to the length of the probe. The crystal around the circular region streams continuously towards this stationary crystal and interpenetrates for 1-2 intergrain distances, see fig 10. The increased density resulting from the streaming along the radii leads to a lower intergrain distance and below a critical minimum distance some grain rows fall to lower planes. This fact indicates that for small distances the charge balance on each grain is not enough to levitate the grain in the local electric field. When the constant stream enters the stationary crystal, a similar effect happens, the arriving grains fall to lower layers where a new crystal is reconstructed. The gradient in density causes the lower layers to counter stream and close a loop far from the probe disturbance, see fig. 11. In this figure we can also see a second loop of particles counter streaming below the main loop. The intergrain distance between the two layers streaming in opposite directions is much larger than layers streaming in the same direction. We could deduce the presence of a kind of surface tension and hence attractive forces.

The disturbance caused by the probe can be described as a modification of the local potential. With the probe positive with respect to the local plasma potential, the electric field below the probe is higher than in the unperturbed case. We suppose also that most of the electrons, intercepted by the probe, do not enter the sheaths and that the ion bombardment on the grains is modified. The equilibrium charge of the grains near the probe is hence different from that of the grains far away. In this situation the fact that the upper surface of the dust assembly is, in most of the cases, flat and horizontal can only be explained by a tension along the streamlines due to attractive, as well as repulsive forces between neighbouring grains<sup>11</sup>.

A similar circulation is noticed in the case of discontinuities on the electrode surface, as the gasket shown in fig. 1. In fact the same curvature in the electric field caused by a positive

## Attractive Forces

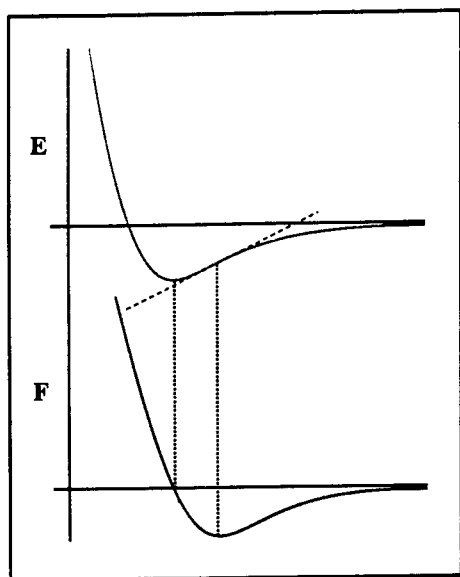


Fig. 8 Schematic representation of energy and force as a function of distance.

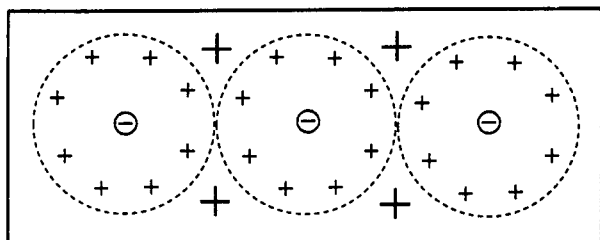


Fig. 9 Schematic representation of the excess of positive charge around the negatively charged grains in the plasma sheath.

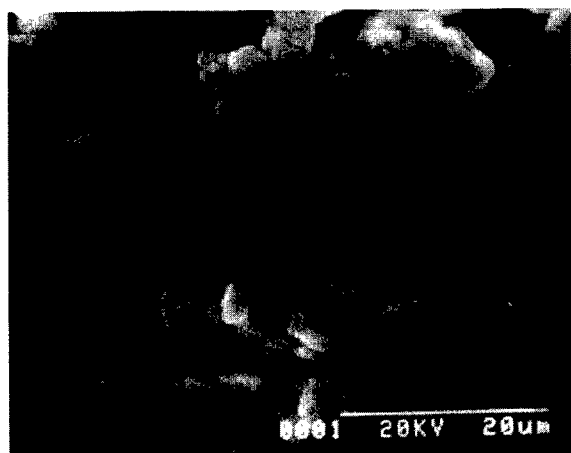


Fig. 10 SEM photograph of the toner powder.

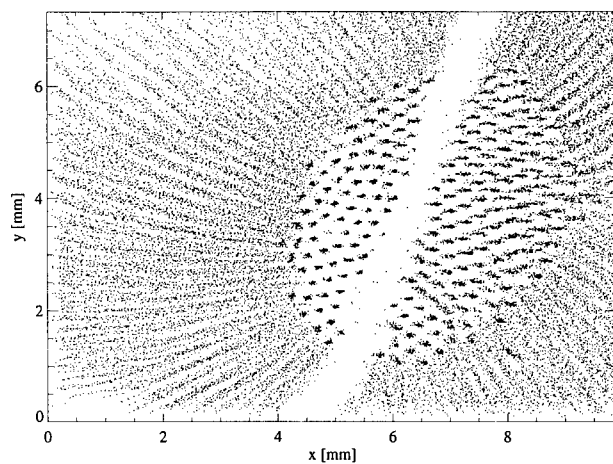


Fig. 11 Interpenetrating crystals  
seen from top.

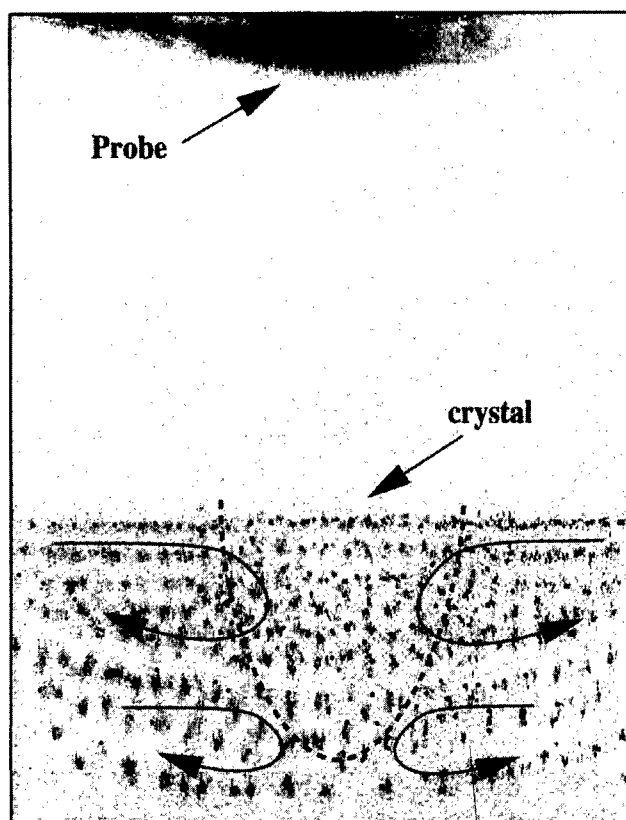


Fig. 12 Interpenetrating crystals  
seen from side.



probe in the plasma above the sheath can be obtained inserting a negative protrusion at the electrode. The full understanding of the dust motion in non uniform sheaths will require more experiments and modelling.

### Acknowledgments

The collaboration of Prof. J. E. Allen, D. A. Law, W. H. Steel and all the "Plasma Group" is gratefully acknowledged. The work has been financed by E.P.S.R.C.

### References

- 1) G. S. Selwyn, 1991, J. Vac. Sci. Tech. **A9**, 2817
- 2) J. H. Chu and I. Lin, 1994, Phys. Rev. Lett., **72**, 25, 4009-4012.
- 3) H. Thomas, *et al.* 1994, Phys. Rev. Lett., **73**, 652
- 4) G.E. Morfill *et al.* private communication.
- 5) A. D. Yoffe, 1993, Advances in Physics, **42**, 173-266
- 6) C.M. Nairn, B.M. Annaratone and J.E. Allen, 1997, Plasma Sources, Sci.Tech., in press.
- 7) J. E. Allen, B. M. Annaratone, R. D.Daryanani, U. de Angelis, to be sent to: J. Plasma Physics,
- 8) J.L. Dorier, C. Hollenstein, A. A. Howling, C. Courteille, W. Schwarzenbach, A. Merad and J. P. Boeuf, 1996, IEEE Transactions on Plasma Science, **24**, 1, 101
- 9) T. Nitter, 1996, Plasma Sources, Sci.Tech., **5**, 1, 93.
- 10) D.A. Law 1996, Proc. XIII ESCAMPIG, Poprad, Slovakia, Eur. Phys. Abstracts, **20E**, 187.
- 11) W. H. Steel, D. A. Law, B. M. Annaratone and J. E. Allen, 1997, XXIII International Conf. on Phenomena in Ionized Gases, Toulouse, France, **1**, 194.
- 12) B. M. Annaratone, J. E. Allen, W. H. Steel and D. A. Law, to be published.
- 13) D. A. Law, W. H. Steel, B. M. Annaratone and J. E. Allen, 1997, XXIII International Conf. on Phenomena in Ionized Gases, Toulouse, France, **1**, 192.
- 14) D. A. Law, W. H. Steel, B. M. Annaratone and J. E. Allen, submitted to Phys. Rev. Lett.

## **Modelling of the Parametric Behaviour of a Self-Heated Copper Vapour Laser: Issues Governing the Thermal Runaway Behaviour of the Plasma Tube Wall Temperature**

R.J. Carman

*Centre for Lasers and Applications, Macquarie University, North Ryde, Sydney, NSW 2109, Australia*

**Abstract.** A computer model has been used to simulate the discharge kinetics and parametric behaviour of a self-heated copper vapour laser for a wide range of optimum and non-optimum conditions. The results indicate that the ground state copper density and the peak electron temperature are the two most important parameters that affect laser performance. The results also confirm the existence of a threshold wall temperature (or threshold copper density) above which the plasma tube becomes thermally unstable with respect to the deposited electrical power, the wall temperature and the copper density, ultimately leading to thermal runaway. At low pulse repetition frequency ( $\text{prf} < 8\text{kHz}$ ), the thermal instability restricts the copper density (and laser output power) to values well below optimum.

### **1. INTRODUCTION**

In the class of high average-power pulsed metal-vapour lasers (eg. Sr-He, 430.5nm & 416.2nm; Ba-Ne, 1.5 $\mu\text{m}$ , 2.55 $\mu\text{m}$ ; Ca-He, 370.6nm & 373.7nm), the copper laser (Cu-Ne, 510.6nm & 578.2nm) is probably the most successful and universally recognised source of high-power radiation (typically up to 100W) at kHz repetition frequencies and with good wallplug efficiencies (~1-2%). Topical applications of copper vapour lasers (CVLs) include pumping solid-state media for frequency conversion to the ultraviolet[1] and infrared[2], laser guidestars[3], and industrial materials processing[4][5]. As part of the ongoing development of these devices, numerical modelling has been used to unravel the complex plasma kinetics of the pulsed glow discharge in the Cu-Ne mixture comprising the laser active medium[6][7]. However, modelling studies of the parametric behaviour of CVLs, including analysis on both optimum and non-optimum operating conditions, remain scarce in the literature[8]. This is undoubtedly largely due to the substantial computing time required to perform detailed calculations for a wide-range of operating conditions. However, the results from such a study could be used to clarify a number general issues concerning the plasma kinetics and the observed behaviour of CVLs, particularly relating to processes that ultimately limit the laser output power. The aim of the present study is to use an existing computer model[9] to generate a body of results describing the parametric behaviour of a single CVL device, and to compare these results with experimental data[10][11]. The results from such a study indicate that the laser output power is limited by thermal instability of the plasma tube wall temperature, particularly at low pulse repetition frequencies. This instability is caused by positive feedback between the electrical power deposition, the wall temperature, and the copper vapour density.

### **2. THE MODEL**

The computer model used to generate the results in this paper has been described in detail elsewhere [9]. It is based on a spatially and time dependent rate-equation analysis of the plasma kinetics, including the external circuit, integrated over many excitation/afterglow cycles to yield temporally self-consistent results. A total of 15 atomic and ionic species of copper and neon are considered in addition to two intracavity laser flux intensities, a gas temperature, and around 70 electron collisional, heavy-body and radiative processes. A two-temperature (bi-Maxwellian) electron energy distribution function is used throughout to calculate the electron collision rates and plasma conductivity. The equations of continuity, energy conservation and momentum conservation are solved simultaneously for the electrons, ions and

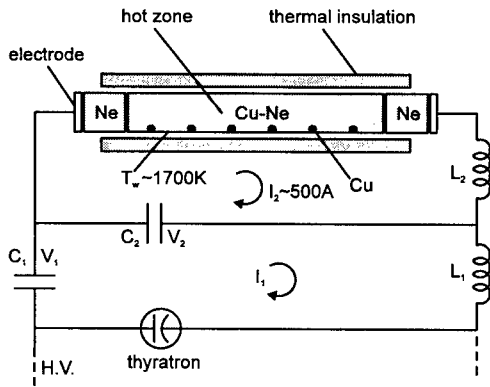


Figure 1: Schematic diagram of the copper laser and external pulse forming network.

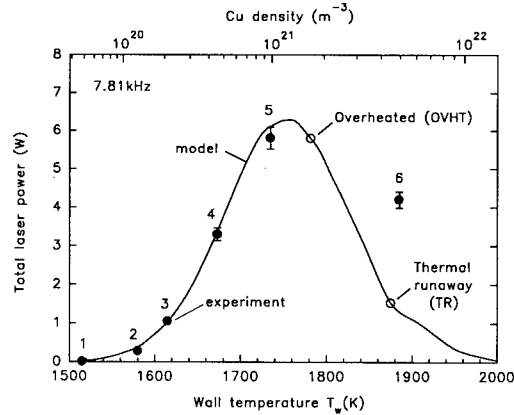


Figure 2: Calculated laser output power (solid line) as a function of wall temperature for a fixed prf=7.81kHz compared with experimental data [14] (filled circles). Specific operating conditions are represented by the legend (1)-(6), OVHT (overheated) and TR (thermal runaway).

neutrals as a function of time and radial position assuming axial homogeneity and radial symmetry for the Cu-Ne "hot zone" (fig 1). The behaviour of the pure neon plasma in the two "cold-zone" regions extending beyond the thermal insulation layers is modelled in a similar manner. The plasma skin effect relating to the temporal evolution of the electric field across the tube radius is taken into account for the Cu-Ne zone. The temperature of the plasma tube wall  $T_w$  (controlling the copper density) is evaluated from the calculated total power deposited in the discharge plasma. The model has also been adapted to include a kinetics scheme for an additional 10 hydrogen species ( $H_2$ ,  $H$ ,  $H^+$ ,  $H_2(v)$ ,  $H^*$ ,  $H^+$ ) to investigate the known performance enhancement of CVLs using  $H_2$  admixtures [12]. Results from the model have been compared with experimental data from a small bore CVL (see table I), including spatially and temporally resolved "hook" population measurements. The calculations have been carried out using a CRAY Y-MP/EL and Microvax 3100 using a standard IMSL package [13] to solve the set of first-order coupled differential equations based on the backward differentiation or GEAR method for "stiff" equations. Self-consistent results for around 950 different operating conditions have been generated requiring ~2500 CPU hours use on the CRAY.

Table I

Cu-Ne hot-zone length	75cm
Neon cold-zone length (total)	18cm
Plasma tube diameter	1.8cm
Neon pressure	40mb
Storage/Peak capacitance $C_1/C_2$	6/2nF
Circuit Inductances $L_1/L_2$	1.0/0.5 $\mu$ H
Mirror reflectivities	0.04/1.0
Optical cavity length	175cm

### 3. RESULTS AND DISCUSSION

The total laser output power (510.6nm + 578.2nm) calculated by the model as a function of the wall temperature  $T_w$  for a fixed pulse repetition frequency (prf) is shown in fig 2. In the model as in actual experiments, changes in  $T_w$  occur as a result of varying the storage capacitor voltage  $V_1$  (and thus the

deposited power) whilst keeping the capacitance  $C_1$  and prf constant. Experimental points are plotted for six distinct operating conditions, and are in close agreement with the model data for  $T_w < 1750\text{K}$ . In the region where the output power is falling with increasing wall temperature ( $T_w > 1750\text{K}$ ), the plasma tube was observed (experimentally) to exhibit the well known thermal runaway behaviour[14]. Under these conditions, the laser output slowly diminishes (turning yellow) over a period of a few minutes as the wall temperature steadily climbs by tens of degrees, despite the fact that the charging voltage  $V_1$  is kept constant. Throughout the remainder of this paper, two distinct operating points are used for this unstable regime as depicted in fig.2; to represent a slightly overheated (OVHT) wall temperature ( $T_w = 1781\text{K}$ ), and conditions of thermal runaway (TR) ( $T_w = 1875\text{K}$ ). The temporal evolution of the axial  $\text{Cu } ^2\text{P}_{3/2}$  population density, the upper level for the 510.6 laser transition, is shown in fig.3 and compared with experimental hook measurements for specific operating conditions in fig.1. Once again the agreement is good for the data sets denoting different operating conditions and wall temperatures, notably for the experimental data and the model results for the OVHT condition with  $T_w = 1781\text{K}$  (fig.2).

Insight into the cause of the observed thermal runaway behaviour of the plasma tube can be gained by calculating the fractional energy deposition in the Cu-Ne zone, based on the initial energy in the storage capacitor ( $\frac{1}{2}C_1V_1^2$ ), as shown in fig.4. For wall temperatures corresponding to the leading edge of the output power curve in fig.1 ( $T_w < 1740\text{K}$ ), this fraction decreases slightly with increasing  $T_w$  due to an overall fall in the plasma resistance (increased plasma conductivity) as the copper density rises. For a given point on the curve in this region characterised by a fixed input power (or fixed  $V_1$ ), any small perturbation of the copper density in the Cu-Ne zone (caused by a hot-spot on the wall for example) will produce a change in the fractional power deposition. The ensuing change in the wall temperature will occur in the opposite sense, tending to restore the copper density to the original value, thus ensuring thermally stable operation through negative feedback. For higher temperatures beyond the local minimum of the curve ( $T_w > 1740\text{K}$ ), the fractional power deposition increases with rising  $T_w$ , due to an overall increase of the plasma resistance or lowering of plasma conductivity. Any small perturbation of the copper density (at fixed  $V_1$ ) will result in an increase in the fractional power deposition and a rise in  $T_w$ , leading to a further increase of the copper vapour density establishing a positive feedback mechanism. Under such conditions, the plasma tube will eventually exhibit the well-known thermal runaway behaviour. Experimentally, it is known that in the unstable regime before thermal runaway occurs, the wall temperature becomes very sensitive to small changes in the charging voltage  $V_1$ . In the model for calculations in the temperature range  $T_w > 1800\text{K}$ , the wall temperature calculated from the deposited power is also extremely sensitive to small increases in  $V_1$  beyond 9.2kV as shown in fig.4. Indeed

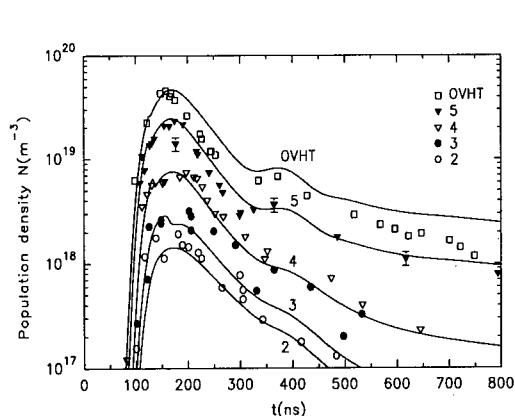


Figure 3. Calculated temporal evolution of the axial population density of the  $^2\text{P}_{3/2}$  upper laser level during the excitation phase for different operating conditions at prf=7.81kHz compared with hook measurements [14]. The legend (2)-(5) and OVHT is the same as in fig. 2.

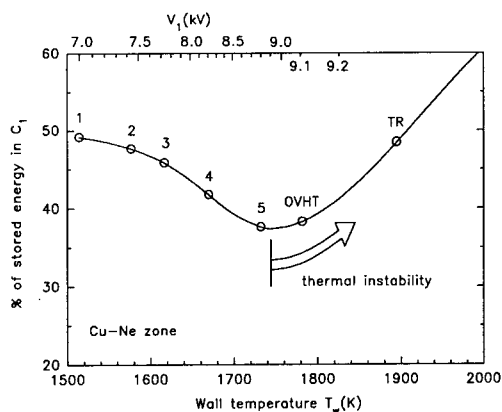


Figure 4. Calculated fractional power deposition in the Cu-Ne hot zone as a function of the wall temperature at prf=7.81kHz. The legend (1)-(5), OVHT and TR is the same as

for  $T_w > 1850\text{K}$ , the self-consistent results asymptotically converge to a small but consistent pulse-to-pulse increase of the wall temperature ( $\Delta T_w \sim 0.1\text{K}-1.0\text{K}$ ) at fixed  $V_i$ . It was not possible to follow the plasma evolution over a large number of cycles ( $>100$ ) (to simulate thermal runaway) due to limitations in computing power.

The fractional power deposition in the Cu-Ne zone is directly related to the plasma resistance or the equivalent plasma conductivity  $\sigma$ :

$$\sigma = \frac{N_e e^2}{3kT_e} \left\langle \frac{v_e}{\sum_j N_j \sigma_{mj}} \right\rangle \quad (1)$$

where  $\sigma_{mj}$  is the electron momentum transfer cross-section with the species  $N_j$ ,  $v_e$  is the electron velocity, and  $k$  is the Boltzmann constant. At low  $T_w$  ( $<1740\text{K}$ ) corresponding to the regime of thermal stability, the conductivity decreases with rising  $T_w$  because there is a gradual drop in the peak electron temperature  $T_e$  and a rise in the pre-pulse electron density. The drop in the peak  $T_e$  occurs as a result of the increasing importance of inelastic collisions with copper atoms which have relatively large impact cross-sections compared with the neon buffer gas. At maximum output power (at  $T_w = 1760\text{K}$ ), the peak axial  $T_e$  is around  $3.3\text{eV}$ , in agreement with semi-empirical calculations reported elsewhere (peak  $T_e \sim 2.9\text{eV}$ ) for a CVL with a similar size bore[15]. At high  $T_w$  ( $>1740\text{K}$ ) in the regime of thermal instability, the plasma conductivity begins to fall again due mainly to the increasing importance of e-Cu momentum transfer collisions, and partly to a drop in the pre-pulse electron density. The fall in output power at high  $T_w$  ( $>1800\text{K}$ ) is due to a fall in the electron temperature rather than a build-up of population in the metastable lower levels since the density ratios with respect to the ground state (eg.  $^2D_{5/2}/^2S_{1/2}$ ) decrease with increasing  $T_w$ . As a further illustration of the influence of the copper atoms on the plasma conductivity, the ratio  $\sigma/N_e$  (on axis) is plotted in fig.5 for the seven specific operating conditions defined in fig.2. At low  $T_w$  corresponding to conditions (1)-(4), the curves are practically identical because the momentum transfer collision frequency is dominated by collisions with neon atoms. However, the peak electron temperatures are lower due to e-Cu inelastic collisions as more copper is introduced into the plasma (higher  $T_w$ ), so the  $\sigma/N_e$  values are higher on average. For condition (5) close to maximum output power,  $\sigma/N_e$  values are slightly lower, particularly at low  $T_e$ . This follows from the e-Cu momentum transfer cross-section which is peaked around  $E=0.5\text{eV}$  and thereafter falls rapidly (fig 5, inset) whereas the same

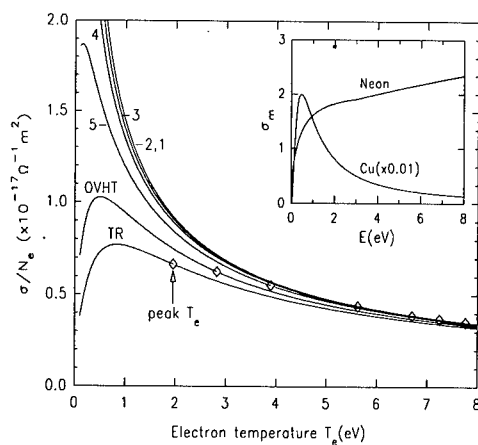


Figure 5. Calculated plasma conductivity parameter  $\sigma/N_e$  as a function of the electron temperature  $T_e$  for different operating conditions (1)-(5), OVHT and TR (prf=7.81kHz). The energy dependence of the momentum transfer cross-section for e-Ne and e-Cu collisions is shown inset (units are  $10^{-20} \text{m}^2$ ).

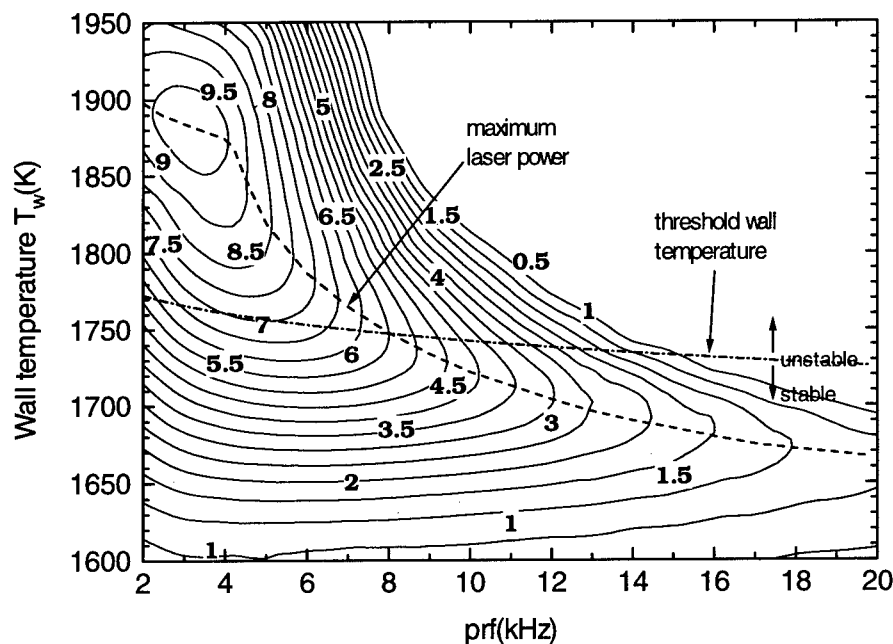


Figure 6. Calculated total laser power (shown in watts on each contour) as a function of prf and wall temperature (buffer gas pressure is 40mb,  $C_1/C_2 = 6/2nF$ ).

cross-section for neon climbs more gradually to reach a peak around  $E=30\text{eV}$ . For conditions (OVHT) and (TR) in the unstable regime ( $T_w > 1740\text{K}$ ),  $\sigma/N_e$  values are strongly dependent on the copper density at low  $T_e$  ( $< 2\text{eV}$ ), although less so at higher  $T_e$ . Thus, the e-Cu momentum transfer collisions cause a reduction in the overall plasma conductivity giving rise to a larger fractional power deposition (fig.4), with the reduction in the peak  $T_e$  acting as a compounding factor. To delay the onset of thermal instability towards higher wall temperatures and larger copper densities, it is therefore necessary to increase the density of neon atoms and/or increase the peak  $T_e$  to diminish the influence of the e-Cu momentum transfer collisions in determining the  $\sigma/N_e$  values.

A detailed parametric study of the CVL performance has also been carried out with the total output power calculated as a function of both  $T_w$  and prf as shown in fig.6. The results indicate that the maximum attainable output power should be around 10W in the prf range 2-4kHz, diminishing slowly as the prf increases. Furthermore, the optimum wall temperature for maximum output power is lower at higher prfs, consistent with the smaller excitation pulse energies at higher prfs. A "threshold" wall temperature can be defined as that corresponding to the lowest point of the curve in fig.4 marking the transition between thermally stable and unstable modes of operation. As shown in fig.6, this threshold temperature exhibits a relatively weak dependence on the prf over the range 2-20kHz, in the range 1725K-1775K. Consequently, the copper density at the tube wall will be limited to a similarly narrow range ( $9 \times 10^{20}$ - $1.6 \times 10^{21} \text{m}^{-3}$ ). These results suggest that CVL operation for wall temperatures above the threshold, would not be possible in reality owing to thermal instability of the plasma tube, leading to thermal runaway.

The calculated maximum output powers for CVL operation within the stable regime are shown in fig.7a together with those at low prf (2-8kHz) that fall in within the unstable regime. Experimentally, laser output powers are found to optimise around 6W for prfs 5-8kHz (fig.7a), in agreement with the calculated values for operation within the stable regime. These results are consistent with the hypothesis that the

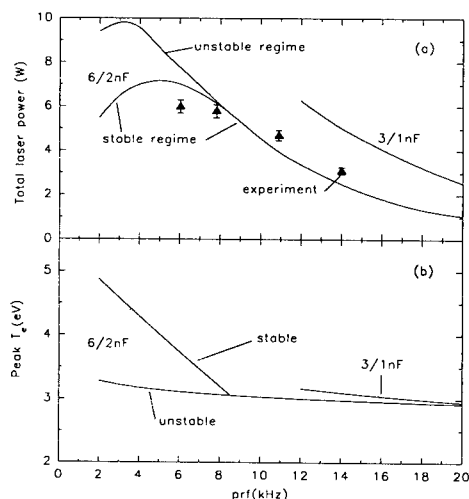


Figure 7. (a) Calculated maximum laser output power as a function of prf for operation in the stable and unstable regimes compared with experimental data [11] (triangles). (b) calculated peak electron temperature as a function of prf.

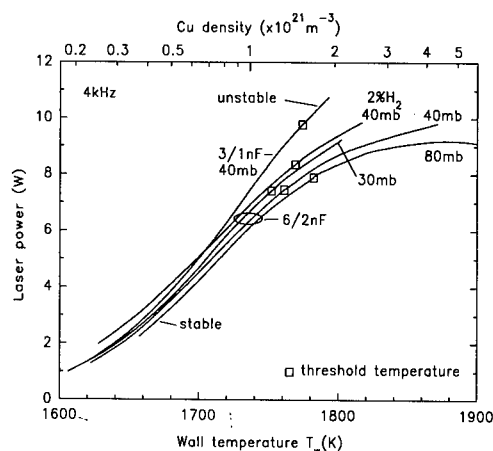


Figure 8. Calculated total laser power as a function of wall temperature at 4kHz for different neon pressures, capacitance values, and with a 2%  $H_2$  admixture.

laser output powers for  $prf < 8kHz$  are indeed limited by thermal instability which sets an operating limit on the wall temperature and copper density.

Another important result is that the calculated peak electron temperature, at the radial position giving maximum laser pulse energy, is almost constant ( $T_e = 2.9-3.1eV$ ) at high prf ( $>8kHz$ ) as shown in fig.7b. For  $prf < 8kHz$ , the peak  $T_e$  rises linearly to 5eV with decreasing prf when in the stable regime, but would remain around 3eV if it were possible to operate in the unstable regime at the maximum power level. The model results suggest that fundamentally, there is an optimum peak electron temperature around 3eV for maximising the laser output power. In the absence of thermal instability effects, maximum output power is achieved by matching the copper density to the available excitation pulse energy to maintain the peak  $T_e$  at  $\sim 3eV$ . Additional calculations have also been performed using smaller values of circuit capacitance ( $3/1nF$ ) as usually employed experimentally to enhance laser output powers at high prfs (fig 7). Although the output powers at high prf are nearly doubled, the peak  $T_e$  remains at the optimum around 3eV.

Changes in the predicted laser output power for slightly different operating conditions than were standard (40mb,  $C_1/C_2 = 6/2nF$ ) have been calculated for a prf of 4kHz (fig.8) to investigate the influence on the threshold wall temperature which limits the attainable copper density at this prf. There appears to be little difference in the output power for gas pressures in the range 30-80mb, although operation at 80mb enables the threshold wall temperature to rise by 20K (a 20% increase in copper density) before instability sets in. It is interesting to note that the overall laser output power is slightly higher at 80mb than at 40mb (+0.4W) because the small drop in output power at fixed  $T_w$  is more than offset by the increased threshold wall temperature. By using smaller capacitance values ( $C_1/C_2 = 3/1nF$ ) and higher charging voltages ( $V_1$ ), the output power at fixed  $T_w$  is significantly increased, and the threshold temperature also rises by 13K (a 12% increase in copper density). Such changes are consistent with an increase in the peak  $T_e$  resulting from the higher charge voltages  $V_1$  (and subsequently the applied tube voltage  $V_2$ ). The addition of a 2% admixture of hydrogen to the buffer gas also increases the laser output power and threshold wall temperature (+7K) at 4kHz compared with the standard case. In this case, the hydrogen improves the interpulse plasma relaxation rate giving rise to a higher tube voltage  $V_2$  (and peak  $T_e$ ).

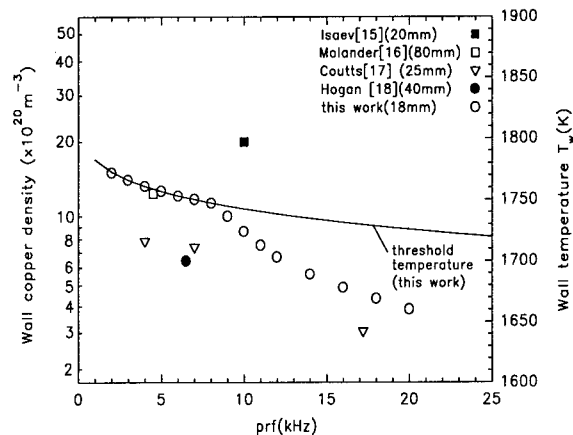


Figure 9. Copper density at the plasma tube wall as a function of the prf for different copper lasers.

As discussed above, the results shown in fig 6 suggest that the wall temperature at the threshold of thermal instability (and associated copper density) falls within the narrow range  $T_w = 1725\text{K} - 1775\text{K}$  ( $Cu_{\text{wall}} = 9 \times 10^{20} - 1.6 \times 10^{21} \text{m}^{-3}$ ) for the prfs investigated (2-20kHz). It is interesting to note that direct measurements of the copper density at the wall in elemental CVLs from different laboratories [15-18] do not exceed these limits, in the majority of cases, as shown in fig.9. This is despite the fact that the devices differ greatly in the bore size, in their electrical power loading and in the design of the thermal insulation. (In reality, each CVL device will have its own characteristic range of threshold wall temperatures marking stable/unstable operation depending on the specific operating parameters of the laser). One exception is the CVL of Isaev[15] where a relatively high copper density ( $Cu_{\text{wall}} = 20 \times 10^{20} \text{m}^{-3}$ ) was reported. The stable operation of the laser at this high copper density is undoubtedly related to the very high neon gas pressure employed (300mb) in their device which would delay the onset of thermal runaway until higher wall temperatures are reached (see fig 8).

#### 4. SUMMARY

A self-consistent model has been used to map the parametric behaviour of an elemental copper vapour laser for optimum and non-optimum operating conditions. The results show that the two most important plasma parameters affecting laser performance are the ground state copper density, and the peak electron temperature. Fundamentally, there appears to be an optimum peak electron temperature of  $\sim 3\text{eV}$  at any given point in the plasma for maximising the laser power. The results also confirm the existence of a threshold wall temperature (and copper density) above which the plasma tube exhibits a thermal runaway behaviour due to a positive feedback mechanism between the deposited electrical power, the wall temperature and the copper density. This phenomenon occurs when the copper atom density is high enough to directly influence the plasma conductivity through e-Cu momentum transfer collisions. The threshold wall temperature falls within a narrow range  $1725\text{K} < T_w < 1775\text{K}$  for the prf range 2-20kHz, corresponding to a copper density of  $9 \times 10^{20} - 1.6 \times 10^{21} \text{m}^{-3}$ . At low prf values ( $< 8\text{kHz}$ ), thermal runaway limits the attainable copper density (and laser output power) to values below optimum with respect to the peak electron temperature. It is shown that the threshold wall temperature can be increased allowing operation at elevated copper densities (leading to increased laser output power) by increasing the neon buffer gas density and/or by increasing the peak  $T_e$  through the use of hydrogen admixtures and low circuit capacitances/high charge voltages.



### Acknowledgments

The author thanks D.J.W. Brown (Macquarie University) for generously providing unpublished experimental data and K.F. Scheibner (Lawrence Livermore National Laboratory) for providing unpublished cross-sections for e-Cu inelastic collisions. I am also indebted to Prof. M.A. Morrison (University of Oklahoma) for providing a detailed set of cross-sections for electronic excitation/de-excitation of the ro-vibrational states of H<sub>2</sub>. This work was supported by the Australian Research Council in the form of an Australian Research Fellowship (1994-1998).

### References

- [1] Coutts D.W. and Brown D.J.W. IEEE J.Sel.Topics Quantum Electron., **3**, (1995).
- [2] Knowles M.H. and Webb C.E. Opt. Lett. **18** (1993) 607.
- [3] Kapitan D., Booth H., Murray G.J., Hogan G.P. and Webb C.E. Proc. SPIE **3092** (1997) 732.
- [4] Glover A.C.J., Illy E.K. and Piper J.A. IEEE J.Sel.Topics Quantum Electron. **1** (1995) 830.
- [5] Kupfer R., Bergmann H. and Lingenauer M. Proc. SPIE **1598** (1991) 46.
- [6] Kushner M.J. and Warner B.E. J.Appl.Phys. **54** (1983) 2970.
- [7] Borovich B.L. and Yurnchenko N.I., Sov. J.Quantum Electron. **14** (1985) 1391.
- [8] Kushner M.J., IEEE J. Quantum Electron. **QE-17** (1981) 1555.
- [9] Carman R.J., Brown D.J.W and Piper J.A. IEEE J. Quantum Electron. **QE-30** (1993) 1876.
- [10] Brown D.J.W., Kunemeyer R. and McIntosh A.I. IEEE J. Quantum Electron. **QE-26** (1990) 1609.
- [11] Brown. D.J.W. (unpublished data).
- [12] Carman R.J. (to be published)
- [13] IMSL Library of Fortran subroutines, "DGEAR differential equation solver" IMSL Inc. (1985).
- [14] Brown D.J.W., PhD dissertation, University of New England, Armidale, Australia, (1988).
- [15] Isaev A.A. and Petrash G.G. Proc. SPIE **2110** (1993) 2.
- [16] Molander W.A. Proc. SPIE **1041** (1989) 11.
- [17] Copper ground state densities have been inferred from comparisons of the performance of an existing laser device and modelled results for that device. See Coutts D.W., PhD dissertation, Macquarie University, Australia (1993).
- [18] Hogan G.P. PhD Dissertation, University of Oxford, England, (1994).

## Application of Non-Linear Optical Methods to Plasma Diagnostics

U. Czarnetzki

*Institut für Laser- und Plasmaphysik, Universität GH Essen, 45117 Essen, Germany*

**Abstract.** The application of non-linear optical methods nowadays allows the measurement of an increasing number of specific plasma quantities which were previously not amenable to diagnostics. Among those are state resolved measurements of molecular density distributions, sensitive measurement of light atomic radical densities, electric field measurements, and determination of quenching rates. In this paper an overview of the available techniques and trends is given. Some selected topics are discussed in more detail.

### 1 INTRODUCTION

Since the early days of plasma physics the emission of light from the discharge has always been a very valuable tool for the study of basic phenomena. This is still true today where emission spectroscopy is finding wide application not only in research but also in process monitoring in industrial applications [1,2,3]. The sensitivity of the spectra to changes of the discharge conditions and the relatively modest experimental requirements have contributed to this development. However, to obtain an unambiguous picture of the physical conditions that lead to the measured spectra turns out to be often very difficult and one has to be very careful when drawing conclusions. This is partly due to the complexity of the problem and partly to the lack of reliable atomic and molecular cross-sections [4].

Laser spectroscopy often allows a more direct interpretation of the measured data and in addition can be a more sensitive probe with, at the same time, better spatial and temporal resolution. Although for most laser techniques the experimental requirements are more demanding, many methods have become standard in plasma diagnostics. Examples are the determination of electron and ion distributions and densities by Thomson scattering, laser induced fluorescence spectroscopy for the measurement of neutral particle densities and ion drift velocities, and IR-absorption spectroscopy by laser diodes for the measurement of molecular populations in the ground states [5-10]. These techniques have in common that the generated signal is proportional to the laser intensity and to the number of particles involved as long as saturation is avoided. Therefore they are called linear laser spectroscopy. For practical applications it might also be important that only a single laser system is required. Although these techniques are very powerful diagnostic tools, there are certain technical and basic physical limitations, e.g. available laser wavelengths or powers, selection rules for dipole transitions or absorption of gases in the VUV.

Nonlinear laser spectroscopy techniques allow some of these constraints to be overcome. In addition to serving as a diagnostic tool nonlinear optical techniques can also be applied to the generation of radiation necessary for linear as well as nonlinear spectroscopy. It is the aim of this paper to give an overview of the available techniques and to discuss briefly some examples of their applications to plasma diagnostics. However, in this frame it is not the intention to give a complete review of experiments and applications of nonlinear optics in plasma physics or to discuss all variants and aspects of a particular technique.

In the following a brief introduction to nonlinear spectroscopy will be given that leads to the classification of the basic phenomena into certain groups. For every group examples of application to plasma diagnostics will then be discussed in more detail.

## 2 SOME BASIC PRINCIPLES OF NONLINEAR LASER SPECTROSCOPY IN PLASMAS

Nonlinear optical phenomena in the plasma itself (free electrons), like e.g. harmonic generation, parametric amplification, and phase conjugation, have been the subject of intense research especially in connection with laser induced plasmas and laser fusion [11-16]. However, in the framework of this paper nonlinear phenomena are defined to be connected to the interaction of the laser beams with neutral particles, i.e. with bound electrons. It is further assumed that no strong gradients are present and that the medium can be considered as isotropic. This assumption is justified in most cases of low as well as high temperature plasma applications.

The interaction of radiation with matter is described by Maxwell's equations together with the susceptibility tensor [17-18]. The susceptibility times the electric fields acts as the source term in the wave equations. This means that the electric fields of the laser beams are inducing a polarization in the medium and that this polarization generates a wave at the sum or difference of the frequencies of the incoming waves. As a consequence of the isotropy only nonlinear optical phenomena of third or higher odd order in the susceptibility are possible. Phenomena well known from optical crystals like frequency doubling are not possible in a plasma. With increasing order of the nonlinear effect the interaction efficiency is drastically reduced and therefore only third order effects or combinations of third and first order techniques have found application in plasma spectroscopy so far.

In general four groups of nonlinear phenomena can be distinguished. As in linear spectroscopy the real and imaginary part of the susceptibility describe the refractive index and the absorption of radiation, respectively. Although nonlinear in the intensity they are still linear with respect to the particle density. The most important example is two-photon absorption. Nonlinear dispersion as an isolated phenomenon is of no importance for plasma diagnostics. While absorption and dispersion are still similar to what is known from linear spectroscopy the following group has no such counterparts and a more detailed introduction will be given.

The third group comprises phenomena based on the square of the absolute value of the susceptibility. These spectroscopic techniques are called four-wave mixing and they depend quadratically on the particle density. Probably the best known example is coherent anti-Stokes Raman scattering (CARS). No energy is dissipated in the medium but it acts like a "catalyst" for the generation of radiation, i.e. the sum of the photon energy of the incoming laser beams and the generated signal wave is conserved. Therefore the frequency of the signal wave can be only the sum or difference of the generating laser frequencies.

The generated signal wave is highly directed with a low divergence like a laser beam and makes application especially favorable in cases of high radiation background. The reason for this directionality is the conservation of momentum. Since the atoms or molecules do not absorb photons the momentum of the photons has also to be conserved. In other words the sum of the  $k$ -vectors of the four waves involved has to be zero. Since the  $k$ -vector times the interaction length gives the phase of a wave this condition is called phase-matching. As a consequence propagation of the signal wave is only possible in a certain direction defined by the directions of the laser beams. Dispersion in the medium can change the value of the  $k$ -vectors and therefore for given frequencies this can restrict propagation to certain directions. This is especially pronounced in the VUV and close to atomic or molecular one-photon resonances where dispersion is strong and is an important effect for the generation of VUV radiation by frequency mixing or high-order anti-Stokes Raman scattering.

However, atomic and molecular resonances also greatly enhance the efficiency of four-wave mixing. For example the CARS technique is taking advantage of two-photon resonances to selectively probe vibrational and rotational levels. Since four-wave mixing generates radiation, it has found application as a direct diagnostic technique as well as a method for the efficient conversion of tunable laser radiation to frequencies that can not be generated otherwise. This radiation can then be again applied to linear or non-linear plasma spectroscopy.

As a fourth group one may consider applications that are a combination of linear and nonlinear techniques like e.g. laser induced fluorescence among excited states after a previous two-photon excitation of the atom.

Nonlinear spectroscopic techniques in plasma diagnostics are therefore either based on nonlinear absorption, four-wave mixing, or a combination of linear and nonlinear methods. Examples for these groups will be given in the following. In addition to be a spectroscopic technique, four-wave mixing is also applied to the generation of VUV radiation for linear spectroscopy.

### 3 APPLICATIONS TO THE GENERATION OF RADIATION FOR LINEAR SPECTROSCOPY

Without going into the details of the nonlinear processes two examples from high and low temperature plasmas should be mentioned. Here the radiation is generated by nonlinear optics but the spectroscopy is still linear. The selected examples show applications of the two most common methods for generation of laser radiation in the vacuum ultraviolet (VUV).

For the detection of atomic hydrogen in the boundary layers of the tokamak experiment TEXTOR Bogen and Mertens developed a frequency tripling cell for the generation of coherent radiation at Lyman- $\alpha$  [19, 20]. The frequency tripling cell filled with a mixture of krypton and argon converts radiation at 364.68 nm coming from a dye laser down to the third harmonic at 121.56 nm. The generated radiation is used for the measurement of atomic hydrogen densities by laser induced fluorescence spectroscopy. With particles at room temperature densities of the order of less than  $10^8 \text{ cm}^{-3}$  could be detected.

The population of the vibrational and rotational states of molecular hydrogen and deuterium in the electronic ground state is of great importance for the understanding of the formation of negative ions in magnetic multi-cusp sources. These populations can be measured with high sensitivity by absorption spectroscopy. However, tunable radiation in the VUV in the spectral range between 120 nm and 140 nm is required. This radiation has been generated in an experiment performed by Wagner and Döbele by stimulated anti-Stokes Raman scattering [21]. Population of vibrational levels between  $v = 2$  and  $v = 6$  could be investigated. In this case a cell filled with molecular hydrogen converts the pump radiation coming from a dye laser to a series of anti-Stokes orders spectrally displaced from the pump frequency by an integer number of the Raman-transition frequency of  $4155 \text{ cm}^{-1}$ . Up to 15 anti-Stokes orders have been reported in the literature [22,23].

Recently the generation of very high anti-Stokes orders at short VUV wavelengths between 120 nm and 140 nm has been greatly improved by the combination of two Raman-cells (Fig. 1) [24,25]. Tunable dye-laser radiation around 370 nm is first passing through a high pressure Raman-cell filled with hydrogen. There a small amount of radiation at the wavelength of the first Stokes-order is generated. The

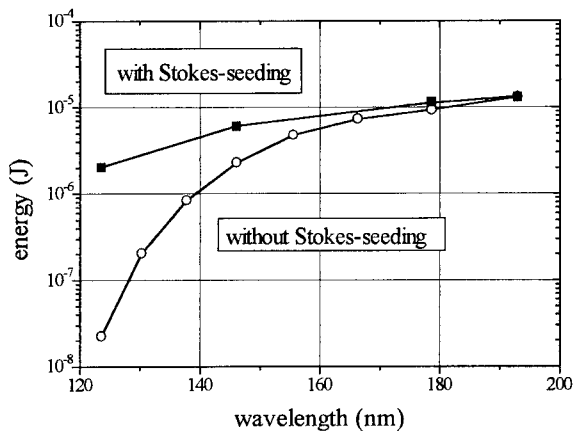


Figure 1: Energies of various anti-Stokes orders with and without Stokes-seeding.

combined beams are then focused into a subsequent Raman-cell at normal pressure where the high anti-Stokes orders are generated. This method is called "Stokes-seeding".

For the four-wave mixing process that generates high anti-Stokes orders the presence of the first Stokes component is essential. With a single Raman-cell the first Stokes-component builds up from quantum noise. Therefore the entire process can be improved essentially if a small portion of Stokes radiation is already present initially. The spectral region in the VUV is especially interesting for laser induced fluorescence spectroscopy in atomic hydrogen (121 nm) and oxygen (130 nm).

#### 4 APPLICATIONS BASED ON NONLINEAR ABSORPTION

Two-photon absorption laser induced fluorescence spectroscopy (TALIF) is one of the most widely applied methods of nonlinear optics in plasma diagnostics [26,27,28]. Although already predicted by Maria Göppert-Mayer in 1931 [29] it was not until the development of the laser that this phenomenon could be observed in the optical region. The reason for this is obvious when one looks at the required intensities. While in one-photon laser induced fluorescence spectroscopy usually intensities of the order of  $100 \text{ Wcm}^{-2}$  are sufficient for the saturation of a transition, two-photon excitation requires intensities of typically  $10^9 \text{ Wcm}^{-2}$  to reach a similar population in the excited state [30]. However, modern pulsed laser systems can easily deliver such intensities when the laser beam is focused. For instance 1 mJ in a 10 ns pulse focused to a spot diameter of 0.1 mm gives an intensity of  $10^9 \text{ Wcm}^{-2}$ . Although the required intensities can easily be reached, problems can arise in complex molecular media where one has to avoid photo-dissociation. Excitation wavelengths are usually in the UV and therefore photo-dissociation can be very efficient [31, 32]. Another limiting factor is photo-ionisation by a third photon. This gives rise to saturation of the excitation efficiency at typically a few percent of the ground state population [30]. As long as saturation can be neglected the number of excited atoms scales with the square of the laser intensity.

But there are some more differences to the one-photon case. Because of the selection rules two-photon excitation and one-photon excitation are exclusive to each other: Two states that can be coupled by a one-photon dipole transition can not be coupled by a two-photon transition and vice versa. The emission of fluorescence light from the excited state is always at a wavelength different from the exciting radiation if no intermediate resonance is involved, which is usually not the case. Since the transition energy is twice that of a single photon large interatomic energy gaps can be spanned without the need of having radiation in the VUV - a great advantage especially for light radicals like e.g. H, O, or N.

A further improvement of two-photon excitation can be made by Doppler-free excitation by two counterpropagating beams. Atoms can absorb one photon from one beam and another from the beam traveling in the opposite direction. If the atom is moving at a certain velocity it will see one beam Doppler-shifted to the red and the other beam shifted to the blue by exactly the same amount. Therefore in the sum the Doppler-shift cancels out and independent of their individual velocities all atoms are equally excited. This Doppler-free technique offers high excitation efficiency and high spectral resolution at the same time [26,33]. However, it requires a laser bandwidth much smaller than the Doppler-width, a requirement often difficult to match with pulsed lasers.

Another problem connected with TALIF is the calibration in order to measure not only relative but absolute densities. A method often applied is the generation of the species under investigation at a known amount in a so called "flow-tube reactor" [34,35]. The reactor can usually be externally attached to the discharge chamber. In a microwave discharge the atomic species are generated by dissociation. The atoms are then carried through a tube to the laser focus in the experimental chamber. Therefore the excitation and detection set-up remains unchanged. By adding a certain gas at a known rate the atomic species is then destroyed in a chemical titration reaction. From the slope of the decrease of the fluorescence signal as a function of the flow of the added titration gas together with the total flow and pressure one can deduce the total particle density at the beginning of the titration. This finally gives the calibration constant.

Tab. 1: Two-photon excitation and fluorescence emission wavelengths for some atoms.

Atom	2-photon transition wavelength (nm)	Fluorescence wavelength (nm)
H	205	656
N	211	871
C	287	166
O	225	845
Cl	210	904

A list of two-photon excitation wavelengths for various light atoms is given in table 1. Atomic hydrogen is an interesting example since it allows various alternative excitation schemes as shown in Fig. 2 [30]. An example of a density profile measured by Doppler-free two-photon excitation at 205 nm in a capacitively coupled RF-discharge in the GEC-reference cell is shown in Fig. 3. Comparison is made with emission spectroscopy at Balmer- $\alpha$ . Due to the gain in sensitivity by the Doppler-free technique an unfocused laser beam of 5 mm diameter is used in this experiment and detection is by a CCD camera perpendicular to the laser beam. This allows instantaneous spatial resolution along the radial direction of the discharge [36].

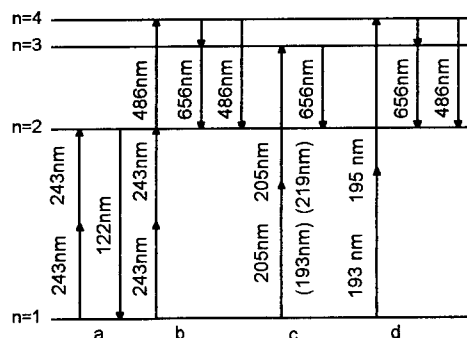


Figure 2: Various alternative two-photon excitation schemes in atomic hydrogen.

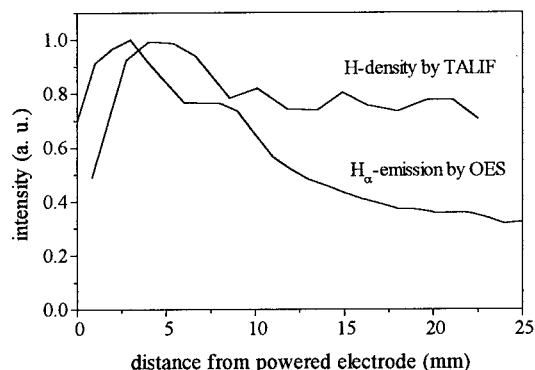


Figure 3 : Axial density distribution of atomic hydrogen atoms measured by two-photon absorption laser induced fluorescence spectroscopy (TALIF) and intensity distribution of plasma induced optical emission at H $_{\alpha}$  (OES) in a hydrogen capacitively coupled RF-discharge in the GEC-reference cell.

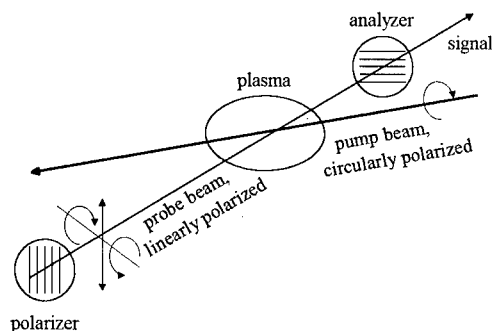


Figure 4: Scheme for two-photon polarization spectroscopy.

A problem connected with spectroscopy in general is quenching of the upper state by collisions with other neutrals or ions and electrons [37,38]. Although less sensitive than LIF, absorption spectroscopy avoids this problem and probes directly the ground state population. Grützmacher et al. [39] have developed a nonlinear Doppler-free absorption technique called "two-photon polarization spectroscopy" that depends on both, the squares of the real and the imaginary part of the nonlinear susceptibility and takes advantage of the selection rules for two-photon transitions.

Two laser beams are counter-propagating and intercept over a certain region within the plasma (Fig. 4). One beam is circularly polarized, e.g. clock wise, this is the pump beam, and the other beam is linearly polarized, e.g. in the x-direction, this is the probe beam. Both beams have slightly different wavelengths, 248.5 nm and 237.8 nm, so that only the combination of the two is in resonance with the two-photon transition between the 1s and 2s states in atomic hydrogen. The linearly polarized probe beam can be considered as a superposition of two circularly beams with opposite helicity. Since the angular momentum in the atom is not changing in the absorption process only the clock wise circularly polarized part of the probe beam will be absorbed. This gives rise to the appearance of a component in the probe beam that is polarized perpendicular to the initial direction. This component is measured behind a polarizer and scales with the squares of density, interaction length, and nonlinear susceptibility. Actually a more rigorous treatment shows that the generation of the perpendicular component can also be understood as a four-wave mixing process.

Since the effect is very small this technique can be applied only at relatively high densities in the excess of  $10^{13} \text{ cm}^{-3}$ . However, this is also the region where quenching usually has an effect that this technique avoids in an elegant way. The authors have demonstrated their method in an electrical arc plasma at 10 kPa.

The knowledge of quenching rates is also of great importance for emission spectroscopy. A widely applied emission technique, especially in thin film diamond deposition, is actinometry with argon. In order to obtain the quenching rate of the argon 750.4 nm line time resolved TALIF was applied [40]. The necessary radiation for two-photon excitation at 184 nm was generated by stimulated anti-Stokes Raman scattering in hydrogen. Starting with dye-laser radiation at 396 nm the 7th anti-Stokes component is at the desired wavelength. The quenching rates are deduced from the change in the decay of the fluorescence light with increasing gas pressure. An example with acetylene is shown in Fig. 5. Here nonlinear optical methods have been applied to the generation of the radiation as well as for the diagnostic method itself.

## 5 APPLICATIONS BASED ON FOUR-WAVE MIXING

Probably the most prominent of the four-wave mixing techniques is coherent anti-Stokes Raman scattering (CARS) [41-46]. It is a technique that can measure the rotational and vibrational population of molecules in the ground state, e.g.  $\text{H}_2$ ,  $\text{N}_2$ ,  $\text{CO}_2$ ,  $\text{C}_2\text{H}_2$ ,  $\text{CH}_4$ . Due to the selection rules for optical transition in

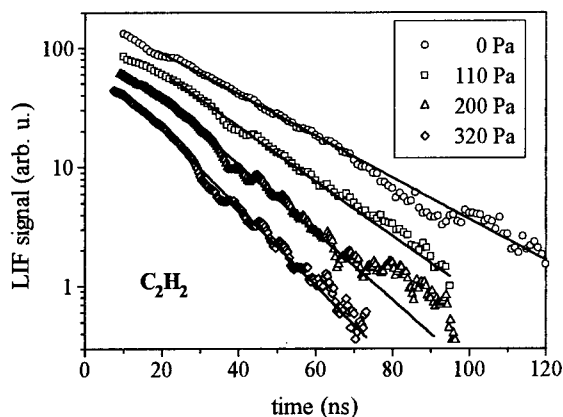


Figure 5: Decay of argon 750.4 nm fluorescence emission after two-photon excitation at various pressures of acetylene. The argon pressure is kept constant at 50 Pa.

molecules Raman and infra-red absorption transitions are exclusive. Therefore the two techniques complement one another.

Like in all four-wave mixing techniques three incoming laser beams are generating a fourth beam that is emitted into a direction that is defined by the phase matching condition and the direction of the incoming beams. The amplitude of the signal is proportional to the square of the density, the interaction length, and the nonlinear susceptibility and depends linearly on the intensities of the three incoming beams. An energy level diagram for CARS is shown in Fig. 6. A pump beam at  $\omega_p$  and a Stokes-beam at  $\omega_s$  are at a two-photon resonance between the initial state (*i*) and a state (*s*). Both states are rovibronic states of the electronic ground state of the molecule. The third beam, which is also at  $\omega_p$  then generates an anti-Stokes wave at  $\omega_{as}$  by a two-photon resonant transition back to the initial state. If the laser at  $\omega_s$  is detuned off the resonance between the states (*i*) and (*s*) the anti-Stokes generation will terminate. Therefore by tuning the Stokes frequency the various molecular resonances can be probed and the population in these states can be measured. From these data rotational and vibrational temperatures can be directly derived. The selectivity and high spectral resolution and the directionality of the signal beam are great advantages of the CARS method.

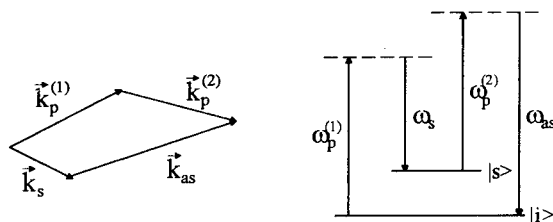


Figure 6: Simplified scheme for coherent anti-Stokes Raman scattering (CARS).

In order to measure absolute densities a calibration procedure is necessary. Often a reference cell with a known concentration of the species to be measured is used. It should be noted that the analysis of the CARS spectra usually requires a detailed knowledge of the molecular constants and processes and is carried out by comparing them with theoretical simulations. An example of a comparison between a measured and a calculated CARS spectrum in acetylene is given in Fig. 7 [47]. The minimal detectable particle density per state is typically of the order of  $10^{11} \text{ cm}^{-3}$  or above.

A very interesting variant of the CARS technique has been presented by Ochkin et al [48]. Actually the four waves present in the CARS process must not necessarily all be waves. If one replaces the second pump beam at  $\omega_p$  by a static electric field there will still be a generated signal wave, now with a frequency corresponding to the energy gap between the two levels involved. The amplitude of this signal wave is



then proportional to the square of the static electric field. Ochkin et al. applied this novel technique of electric field measurement to a corona discharge. With hydrogen at atmospheric pressure their sensitivity was about 25 V/cm. This technique is especially suited for high pressure discharges.

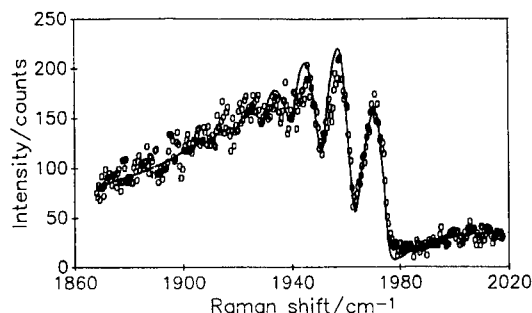


Figure 7: Comparison of measured and calculated CARS-spectrum in acetylene.

Another recent development in CARS diagnostics in plasmas is the so called resonant CARS (RE-CARS) [41,49]. The difference between the two methods is the following: As shown in Fig. 6 two two-photon steps are involved in the CARS process. For these two-photon transitions the excited electronic states of the molecule serve as the intermediate states and they are all far from resonance in the ordinary CARS process. However, if one or both of the pump lasers get in resonance with these states the efficiency of the CARS process is greatly enhanced. RE-CARS has been applied to the detection of e.g. CH in an Ar/CH<sub>4</sub> microwave discharge.

A double-resonant four-wave mixing scheme has been proposed for the detection of atomic hydrogen [50](Fig. 8). Here two beams at 205 nm are in resonance with the two-photon transition between the ground state and  $n=3$ . The third beam is close to the resonance at Balmer- $\alpha$  and generates a signal wave close to Lyman- $\alpha$ . Like in the CARS-scheme this signal wave is highly directed and allows the efficient suppression of background radiation by spatial filtering. In a first experiment this novel technique was tested on atomic hydrogen generated by dissociation at a hot filament [51]. At elevated energies of the visible laser with the laser tuned on resonance the process gets saturated. In the saturated case the dependence of the signal on the particle density changes from quadratic to linear. This is shown in Fig. 9. The particle density was about  $10^{13} \text{ cm}^{-3}$ . Theoretical calculations predict a possible detection threshold of the order of  $10^9 \text{ cm}^{-3}$ .

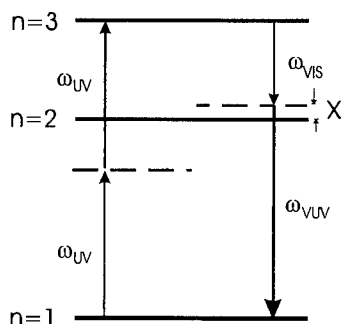


Figure 8: Scheme for double-resonant four-wave mixing (DORFWM).

So far the four waves involved had different frequencies. However, four-wave mixing is also possible when all four waves have identical frequencies. This is called degenerate four-wave mixing (DFWM) [52, 53]. Two different schemes can be distinguished: DFWM with a two-photon resonance and with a one-photon resonance. Both schemes can be understood in terms of transient spatial gratings. Two strong pump beams form a spatial interference pattern where the grating constant depends on the angle

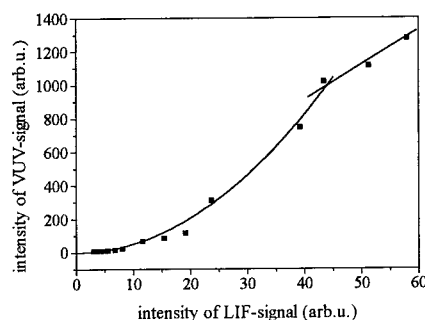


Figure 9: Saturation behavior of the DORFWM-signal as a function of the particle density.

between the two beams. This interference pattern is then reflected in the spatial excitation distribution that forms a similar grating. A probe beam is then scattered at this grating and a signal beam is generated. With counterpropagating beams this scheme is Doppler-free and offers a high spectral resolution. Since DFWM does not depend on the emission of fluorescence light the effect of quenching is greatly reduced. In the case of DFWM with one-photon resonances the signal scales with an exponent between 8 and 2 of the transition dipole moment, depending on the degree of saturation [54]. This makes absolute concentration measurements difficult and also often limits the application to relatively high densities.

DFWM has been applied to the detection of molecular and atomic species like e.g.  $H_2$ ,  $CH$ ,  $OH$ ,  $NH$ ,  $NO_2$ ,  $C_2$ ,  $He$ ,  $Hg$ ,  $Na$  [55-57]. An example for the application of the one-photon scheme are electric field measurements in helium [58, 59]. Electric fields of the order of 500 V/cm have been measured in the sheath of a glow discharge. The experimental set-up is shown in Fig. 10. The grating is formed by the forward beam together with the reflected beam from the mirror. A small fraction of the probe beam is scattered backwards at the grating and detected by a photomultiplier. By tuning the frequency of the laser the Stark-splitting of Rydberg-states is measured and from this splitting the electric field is deduced.

A two-color six-wave mixing scheme, which is actually a process of 5th order in the nonlinear susceptibility, has been demonstrated by Gray et al. [60] for the detection of atomic hydrogen. They report a detection threshold at about  $10^{13} \text{ cm}^{-3}$ . The experiment was performed in a flame, however, it might also find application in plasma diagnostics in the future.

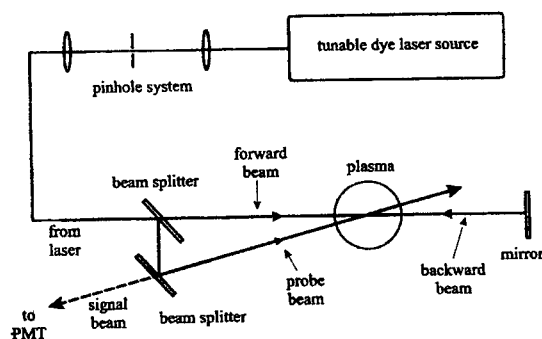


Figure 10: Experimental setup for electric field measurements in helium by degenerate four-wave mixing (DFWM).

## 6 COMBINED TECHNIQUES

In this chapter two examples will be given where nonlinear and linear spectroscopic methods have been combined to measure electric field distributions in atomic hydrogen. Electric fields can be measured by probing the Stark splitting of Rydberg states where the splitting scales with the principle quantum

number like  $n(n-1)$ . Since atomic hydrogen can not be excited directly from the ground state due to the large excitation energy a multi-photon scheme has to be applied.

Booth et al. [61] therefore used a two-photon excitation at 243 nm for excitation to the  $n=2$  level. With a third photon at 410 nm they then further excited the atom to the  $n=6$  state. The laser at 243 nm was fixed on resonance while the laser at 410 nm was tuned over the Stark split  $n=6$  state. Fluorescence light after collisional population transfer to  $n=3$  was observed at the Balmer- $\alpha$  transition. Electric fields were measured in the cathodic layer of a 30 kHz discharge in hydrogen with a sensitivity as low as 20 V/cm.

With increasing quantum number of the Rydberg state the electric field sensitivity is increasing, however, at the same time the signal amplitude is drastically decreasing. This is due to the long life time of the Rydberg states and the unfavorable branching ratio. Recently we developed a novel technique in hydrogen that can overcome these limitations [62]. In our scheme we excite the atom in a two-photon step at 205 nm to the  $n=3$  state (Fig. 11). This excitation is Doppler-free and the laser beams are unfocused, therefore allowing instantaneous spatial resolution. Fluorescence light at 656 nm is observed. A second laser is now tuned to the resonance between  $n=3$  and a Rydberg state. Whenever this laser is in resonance with one of the Stark-split components of this state, population is transferred from  $n=3$  to the Rydberg state. This is noticed in a decrease of the fluorescence signal at Balmer- $\alpha$ . Since this does not depend on the lifetime of the Rydberg state or on the branching ratio or on the collisional transfer almost any Rydberg state can be probed. The limiting factor for the Rydberg-state quantum number is the energy necessary to transfer a noticeable amount of population from  $n=3$  to the Rydberg state. This energy is increasing with increasing principle quantum number. Nevertheless, high Rydberg-states up  $n=26$  or even higher should be accessible. This could also prove to be an alternative method for the determination of electron densities.

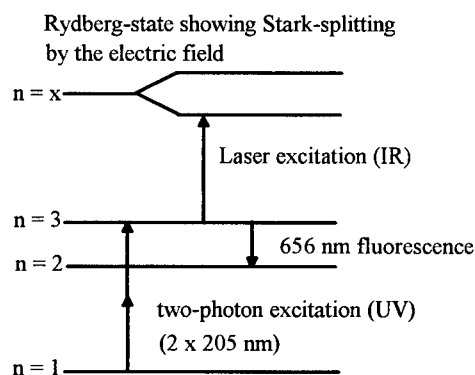


Figure 11: Scheme for optical double-resonance spectroscopy in hydrogen.

In a first experiment up to  $n=19$  could be probed in the sheath of an RF-discharge in hydrogen. An example at  $n=16$  and about 1060 V/cm is shown in Fig. 12. At high field strengths the Stark-

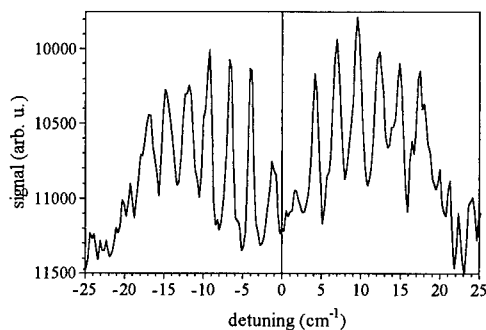


Figure 12: Stark-splitting of H-atom,  $n=16$  at 1060 V/cm.

components are all well resolved. However, for the determination of the electric field strength it is sufficient to measure the width of the spectrum which is possible also at much lower values. Therefore this method seems to be a very promising candidate for the measurement of very low electric fields of the order of 10 V/cm or less in e.g. the positive column of glow discharges or in inductively coupled RF-discharges.

## 7 SUMMARY

Nonlinear laser spectroscopy techniques have proved to be a very powerful tool for plasma diagnostics. They are not a substitute for, but complementary to conventional techniques. Recent improvements in laser systems and detector techniques have opened new fields of application. Novel techniques have been developed and established techniques from other fields of laser spectroscopy have found new applications to problems in plasma physics. This has opened windows to areas that have been previously inaccessible. In addition knowledge gained from nonlinear laser spectroscopy can also turn out to be very valuable for the further development and improvement of more conventional diagnostic techniques.

## References

- [1] Hans R. Griem, *Plasma Spectroscopy* (McGraw-Hill, 1964)
- [2] H.-J. Kunze: In J. M. Proud and L.H. Luessen, eds.: *Radiative Processes in Discharge Plasmas* (Plenum Press, New York, 1986)
- [3] Z. Quing, D.K. Otorbaev, G.J.H. Brussaard, M.C.M. van de Sanden, and D.C. Schram, *J. Appl. Phys.* **80**, 1312 (1996)
- [4] V. Schulz-von der Gathen and H.F. Döbele, *Plasma Chemistry and Plasma Processing* **16**, 461 (1996)
- [5] H.-J. Wesseling and B. Kronast, *J. Phys. D.* **29**, 1035 (1996)
- [6] K. Muraoka and M. Maeda, *Plasma Phys. and Contr. Fus.* **35/6**, 633-656 (1993)
- [7] E.A. Den Hartog, H. Persing, and R.C. Woods, *Appl. Phys. Lett.* **57**, 661 (1990)
- [8] K. Niemax, H. Groll, and C. Schnürer-Patschan, *Spectrochimica Acta Rev.* **15**, 349 (1993)
- [9] M. Ikeda, K. Aiso, M. Hori, and T. Goto, *Jpn. J. Appl. Phys.* **34**, 3273 (1995)
- [10] G. Bachet, L. Chérigier, M. Carrère, and F. Doveil, *Phys. Fluids B* **5**, 3097 (1993)
- [11] A. Lal and C. Joshi, *J. Opt. Soc. Am. B* **8**, 2148, (1991)
- [12] D. Steel and J. Lam, *Opt. Lett.* **4**, 363, (1979)
- [13] J. Federici and D.K. Mansfield, *J. Opt. Soc. Am. B* **3**, 1586 (1986)
- [14] Y. Kitagawa, R. Savage, and C. Joshi, *Phys. Rev. Lett.* **62**, 151, (1989)
- [15] I. Nebenzahl, A. Ron, and N. Rostoker, *Phys. Rev. Lett.* **60**, 1030 (1988)
- [16] M. V. Goldman and E. A. Williams, *Phys. Fluids B* **3**, 751, (1991)
- [17] Y. R. Shen, *The Principles of Nonlinear Optics* (John Wiley & Sons, 1984)
- [18] A. Yariv, *Quantum Electronics* (John Wiley & Sons, 1975)
- [19] Ph. Mertens and P. Bogen, *J. Nucl. Mat.* **128 & 129**, 551 (1984)
- [20] Ph. Mertens and P. Bogen, *Appl. Phys. A* **43**, 197 (1987)
- [21] D. Wagner and H.F. Döbele, to be published
- [22] V. Schultz-von der Gathen, T. Bornemann, V. Kornas, and H.F. Döbele, *IEEE J. Quant. Electr.* **26** (4), (1990)
- [23] U. Czarnetzki, H.F. Döbele, M. Hörl, M. Röwekamp, B. Reimann, V. Schultz von der Gathen, *J. Nucl. Mat* **86**
- [24] M. Spaan, A. Goehlich, V. Schultz-von der Gathen, and H.F. Döbele, *Appl. Opt.* **33**, 3865 (1994)
- [25] A. Wolf, M. Thomson, U. Czarnetzki, and H.F. Döbele, to be published
- [26] K. Grützmacher, M.I. de la Rosa, A. Steiger, W. Bohmeyer, H. Grote and E. Parsch, *P7.4 in Verhandl. DPG* **30**, 176 (1995)

- [27] A. D. Tserepi and T.A. Miller, J. Appl. Phys. **77**, 505 (1995)
- [28] J.E.M. Goldsmith, J. Opt. Soc. Am. B **11**, 1979 (1989)
- [29] M. Göppert-Mayer, Ann. Phys. **9**, 273 (1931)
- [30] U. Czarnetzki, K. Miyazaki, T. Kajiware, and K. Muraoka, J. Opt. Soc. Am. B **11**, 2155 (1994)
- [31] K. Miyazaki, T. Kajiware, K. Uchino, and K. Muraoka, J. Vac. Sci. Technol. A **14**, 125 (1996)
- [32] J.E.M. Goldsmith, Appl. Optics **28** (6), (1989)
- [33] W. Demtröder, *Laser Spectroscopy* (Springer-Verlag Berlin Heidelberg New York, 1981)
- [34] D. W. Setser, *Reactive Intermediates in the Gas Phase* (Academic, New York, 1979)
- [35] U. Meier, K. Kohse-Höinghaus, L. Schäfer, and C.-P. Klages, Appl. Opt. **29**, 4993 (1990)
- [36] L. Cherigier, D. Luggenhölscher, U. Czarnetzki, and H. F. Döbele, to be published
- [37] J. Bittner, K. Kohse-Höinghaus, U. Meier, and Th. Just, Chem. Phys. Lett. **143**, 571 (1988)
- [38] B. L. Preppernau, K. Pearce, A. Tserepi, E. Wurzburg, and T. A. Miller, Chem. Phys. **196**, 371 (1995)
- [39] R. Dux, K. Grützmacher, M. I. de la Rosa, B. Wende, Phys. Rev. E **51**, 1416 (1995)
- [40] A. Francis, N. Sadeghi, U. Czarnetzki, and H.F. Döbele, submitted to Appl. Phys. Lett. (1997)
- [41] S. A. J. Druet and J.-P. Taran, Prog. Quant. Electr. **7**, 1-77 (1981)
- [42] T. Doerk, J. Ehlbeck, P. Jauernick, J. Stanco, J. Uhlenbusch, T. Wottka, J. Phys. D: Appl. Phys. **26**, 1015 (1993)
- [43] D. A. Greenhalgh, in, *Advances in Nonlinear Spectroscopy*, R.J.H. Clark, R.E. Hester, eds., Wiley, London (1988)
- [44] D. Maker and R.W. Terhune, Phys. Rev. **137** (1965) A 801- A818
- [45] J.W. Nibler, G.V. Knighton, in, *Raman Spectroscopy of Gases and Liquids*, Ed. A. Weber, Springer Verlag, Berlin 1979
- [46] M.D. Levenson, *Introduction to nonlinear Laser Spectroscopy*, Academic Press, New York 1982
- [47] V. Kornas, A. Roth, H.F. Döbele, and G. Proß, Plasma Chemistry and Plasma Processing **15**, 71 (1995)
- [48] O.A. Evsin, E.B. Kupuyanov, V.N. Ochkin, S.Y. Savinov, and S. N. Tsakhai, Quantum Electr. **22**, 295 (1995)
- [49] T. Doerk, P. Jauernik, S. Hädrich, B. Pfelzer, and J. Uhlenbusch, Opt. Commun. **118**, 637 (1995)
- [50] U. Czarnetzki and H.F. Döbele, Rev. Sci. Instrum. **66**, 587 (1995)
- [51] M. Thomson, U. Czarnetzki, and H.F. Döbele, to be published
- [52] H.J. Eichler, P. Günter, and D.W. Pohl, *Laser Induced Dynamic Gratings*, (Springer, Berlin 1986)
- [53] R.A. Fisher, ed., *Optical Phase Conjugation* (Academic Press, New York 1993)
- [54] R.L. Farrow, D. Rakestaw, and T. Dreier, J. Opt. Soc. Am. B, **9** (19), 1770 (1992)
- [55] G. Meijer and D.W. Chandler, Chem. Phys. Lett. **192**, 1 (1992)
- [56] S. Williams, D. S. Green, S. Sethuraman, and R. Zare, J. Am. Chem. Soc. **114**, 9122 (1992)
- [57] M. Versluis, G. Meijer, and D. W. Chandler, Appl. Optics **33** (15), 3289 (1994)
- [58] Marc Bowden, in, *Proceedings of the 7th international Symposium on Laser-Aided Plasma Diagnostics*, Fukuoka, Japan 1995
- [59] Marc Bowden, private communication
- [60] J.A. Gray, J.E.M. Goldsmith, and R. Trebino, Optics Letters, **18** (6), 444 (1993)
- [61] J. P. Booth, M. Fadlallah, J. Derouard, and N. Sadeghi, Appl. Phys. Lett. **65**, 819, (1994)
- [62] U. Czarnetzki, D. Luggenhölscher, and H.F. Döbele, to be published

## Transient Phenomena in Plasma Torches and in Plasma Sprayed Coating Generation

P. Fauchais, J.F. Coudert and M. Vardelle

*Université de Limoges, Faculté des Sciences, Laboratoire de Matériaux Céramiques et Traitements de Surface, UPRES A 6015, 123 avenue Albert Thomas, 87060 Limoges cedex, France*

**Abstract.** D.C. plasma torches are more and more widely used for different applications among which cutting, welding and spraying are probably the most developed. For a long period it is mainly their static characteristics which have been considered and their applications were studied on a macroscopic scale.

However many transient phenomena occur, the systematic study of which has started only a few years ago. To limit the discussion we present only the case of plasma spraying with :

- the transient phenomena, at the anode, and their evolution with the torch working parameters and the electrodes erosion,
- the consequences of these fluctuations on plasma jet temperature and velocity fields as well as mean electric field in the arc column,
- the characterization of the molten particles flattening and resulting splat cooling and consequences on coating properties.

### 1. INTRODUCTION

Plasma spraying is now a versatile technology that has been successful as a reliable cost-effective solution for many industrial problems. It allows the spraying of a wide range of high performance materials, from superalloys and refractory intermetallic compounds to ceramics with continuously increasing commercial applications[1]. In most cases (99%) plasma spraying is achieved by using d.c. plasma torches which will be described summarily in section 2. The solid particles, with diameters ranging between 20 and 60  $\mu\text{m}$ , are injected orthogonally to the plasma jet, either upstream or downstream of the nozzle exit with the help of a carrier gas which is mainly argon[2-3]. Their flow rate is between 2 and 6 kg/h. The coating is built by layering of splats resulting from the flattening of particles in a molten state upon a substrate disposed at a distance, which for atmospheric plasma spraying (APS), is between 80 and 120 mm. The flattening time is in the 1 to 1.8  $\mu\text{s}$  range and, on a smooth surface (mean roughness  $R_a < 0.1 \mu\text{m}$ ), the resulting splat which diameter, assuming a disk shape, is 3 to 6 times that of the impacting particle solidifies in times between a few  $\mu\text{s}$  to 20  $\mu\text{s}$ [4,5]. Unmolten particles rebound from the substrate or coating and finally the deposition efficiency is in the range 40 to 70%. Especially in industrial conditions, process parameters to produce sound coatings are specified in terms of stationary controllable parameters associated with the spray equipment, e.g. arc current, plasma gas composition and flow rate, stand-off distance, particle carrier gas flow rate, particle injector position, particle mass flow rate... They are typically established based on experiment or experience.

If they were known[6] 25 years ago, transient phenomena taking place in plasma torches were rediscovered by scientists about 5 years ago but are still ignored by industry. This rediscovery is due to the recent availability of investigation means such as fast numerical oscilloscopes and powerful software for signal treatment.

In the eighties McPherson[7] has underlined that contact between the layered splats was far from being perfect and conditioned the resulting coating thermomechanical properties[7-8]. The only way to understand which parameters control the contact between the layered splats is, for an impacting particle with a given velocity, diameter and temperature, to follow the evolution of its temperature and diameter during flattening and of the corresponding splat temperature upon cooling. Such studies require fast micro-pyrometers (50-100 ns response time) that became available only a few years ago[9].

This presentation will be devoted to an overview of our actual knowledge of :

- the transient phenomena especially at the anode and their consequences on plasma jet temperature and velocity fields, as well as arc column mean electric field,

- the measurement of molten particles flattening and the resulting splat cooling. Finally it will be shown how these microscopic results correlate with coating macroscopic properties.

## 2. TRANSIENT PHENOMENA IN D.C. PLASMA TORCHES

### 2.1. Used plasma torches

The most common configuration is a stick type thoriated (2 wt%) tungsten cathode associated with a nozzle shaped anode serving also as a constrictor. Fig. 1 shows a typical configuration. In most cases the nozzle has a conical shape followed by a cylindrical duct.

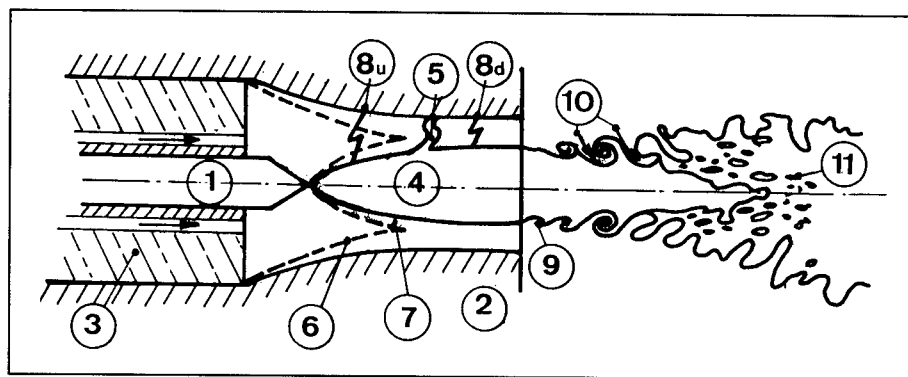


**Figure 1 :** Plasma spray torch operation at atmospheric pressure showing (1) stick type cathode with a conical tip, (2) anode, (3) insulating material with axial injection, (4) plasma column, (5) arc column attachment to the anode wall, (6) cold boundary layer, (7) hot boundary layer, (8) short circuits upstream (u) and downstream (d) of the arc root, (9) vortex ring coalescence, (10) cold gas engulfment, (11) entrained cold gas bubbles. The injected plasma forming gas is indicated with the arrows along the cathode.

The plasma forming gas is injected either axially (as shown in fig. 1) or as a vortex around the cathode or along its conical tip... The used plasma gases are Ar-H<sub>2</sub> (5 to 25 vol%), N<sub>2</sub>-H<sub>2</sub> (5 to 20 vol%) and Ar-He (40 to 80 vol%). The first gas (Ar or N<sub>2</sub>) gives the jet momentum and the second (H<sub>2</sub> or He) improves its thermal conductivity.

The plasma column develops between the cathode and the anode where an electrically conducting gas at  $T > 8000$  K and  $10^5$  Pa (for the considered plasma gases) can be found. The radius of the plasma column, also termed the electrical radius  $r_e$ , depends on the plasma gas flow rate and composition, cooling conditions at its fringes and arc current.

The arc root strikes at the nozzle wall when the cold boundary layer close to the anode wall is sufficiently heated to reduce the arc column constriction. This configuration is called "the free arc length". The voltage depends on the arc length linked to arc current, nozzle diameter, gas composition and flow rate.

Typical operation conditions are : anode-nozzle internal diameter (i.d.)  $D$  between 5 and 8 mm, total gas flow rates between 35 and 120 standard liters per minute (slm) and power levels between 20 and 60 kW with arc currents generally below 700 A.

### 2.2. Transient phenomena at the anode

In this plasma torch configuration, if the arc geometry is rather simple in the vicinity of the cathode tip, where the arc column shows a cylindrical symmetry, the arc exhibits a complex and changing shape in the arc-anode attachment region, under the influence of gas dynamic and magnetic body forces.

The modifications of the morphology of the arc are associated with typical features of the recorded voltage which gives a sawtooth shaped waveform with quasi-linear increasing ramps followed by negative voltage jumps (fig. 2). In all the experiments performed the arc current varies very little when the voltage jumps to lower values : small peaks show up which amplitude is less than 2.5% of the regulated mean arc current. The slope of the ramps indicates the rate at which the arc and the imbedded current lines

are stretched and lengthened by the flow. Each of the lengthening phases is limited by an electrical breakdown through the cold and electrically insulating gas layer surrounding the arc. Each breakdown initiates a short circuit, together with a new arc attachment at the nozzle wall, and is associated with a negative jump of the voltage. This situation corresponds to the so called "restrike mode"[6] and has been reported in the past by different experimental investigators[10-12].

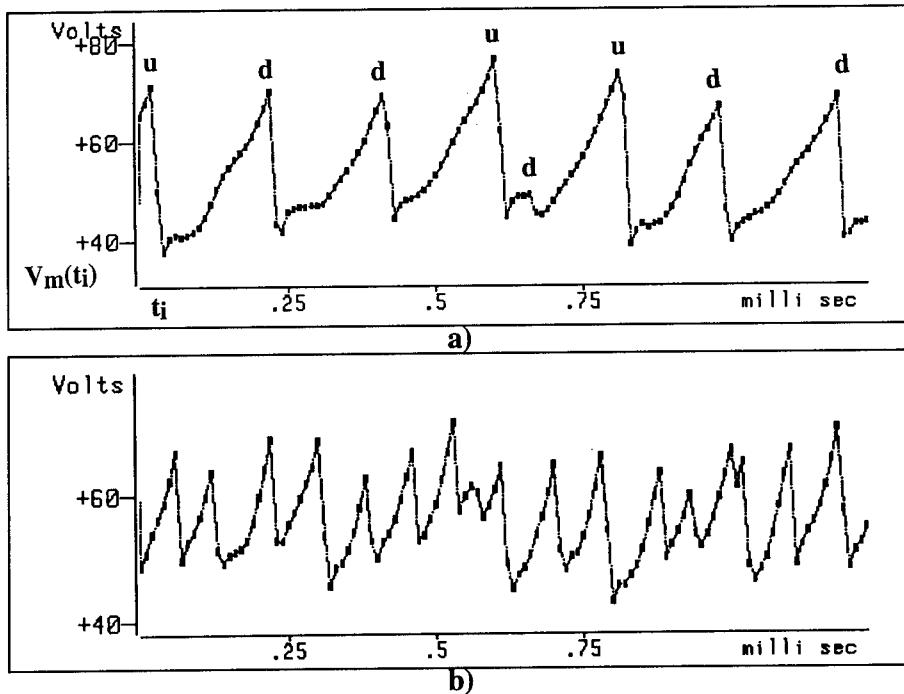


**Figure 2 :** Typical voltage signals obtained with a 8 mm i.d. nozzle with Ar-H<sub>2</sub> (25 vol%) 60 slm for two different arc currents : a) 209 A ; b) 604 A.

Such transient phenomena can be studied with the help of a Fast Fourier Transform (FFT) algorithm[13,14] or a statistical study of the tendencies shown by the characteristics of the arc voltage fluctuating components[15,16,17]. With FFT, characteristic frequencies  $f$  can be isolated and their variations with torch working parameters : arc current  $I$  (A), gas flow rate  $m_g$  (kg/s), gas composition, anode-nozzle internal diameter  $D$  (mm), plasma forming gas injection mode can be studied. With the statistical study of the voltage signals (see fig. 2) the minimum voltages  $V_m$  (local minimum value of the arc voltage immediately after breakdown) the slopes of the voltage ramps, the life times of the arc root  $\tau_i$  ( $\tau_i = t_{i+1} - t_i$ ), the voltage jumps  $\Delta V$ , the "upstream" (u) breakdowns ( $V_m(t_i) < V_m(t_{i-1})$ ) and the "downstream" (d) breakdowns ( $V_m(t_i) > V_m(t_{i-1})$ ) (see fig. 2.a) can also be linked to the arc working parameters. The obtained results[13-18] for Ar-H<sub>2</sub>, Ar-N<sub>2</sub>, N<sub>2</sub> and Ar-He plasmas show that the restrike mode is mainly governed by the thickness and stability of the "cold" gas layer surrounding the plasma column. The thicker will be this layer the higher will be the voltage jumps  $\Delta V$ , the lower the characteristic frequency and the arc root lifetime  $\tau$ .

This is illustrated in fig. 3 showing the evolutions of  $\Delta V$  and  $\tau$  with the arc current  $I$  (the electrical radius  $r_e$  increases with  $I$ [19]).



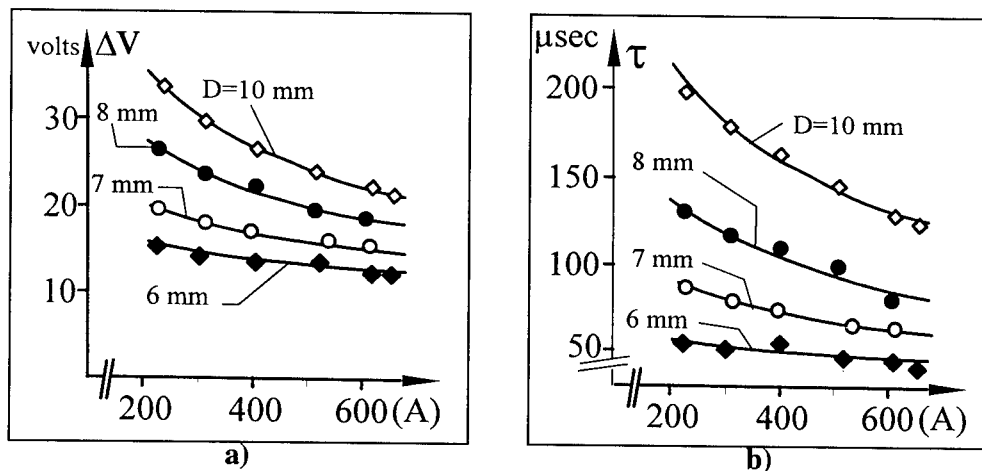


Figure 3 : Evolution of a) voltage jump  $\Delta V$  and b) arc root life times with arc current for four anode nozzle i.ds. for an Ar-H<sub>2</sub> plasma : 45 slm Ar, 15 slm H<sub>2</sub> gas injection along the cathode tip.

In fact when representing the arc root lifetime with the corresponding voltage minima two distributions are obtained as shown in fig. 4 corresponding respectively to the upstream and downstream restriking (see fig. 2.a). The highest lifetimes are obtained for the high voltage minima which means that the erosion is enhanced in these regions as confirmed by the wear of the anode material.

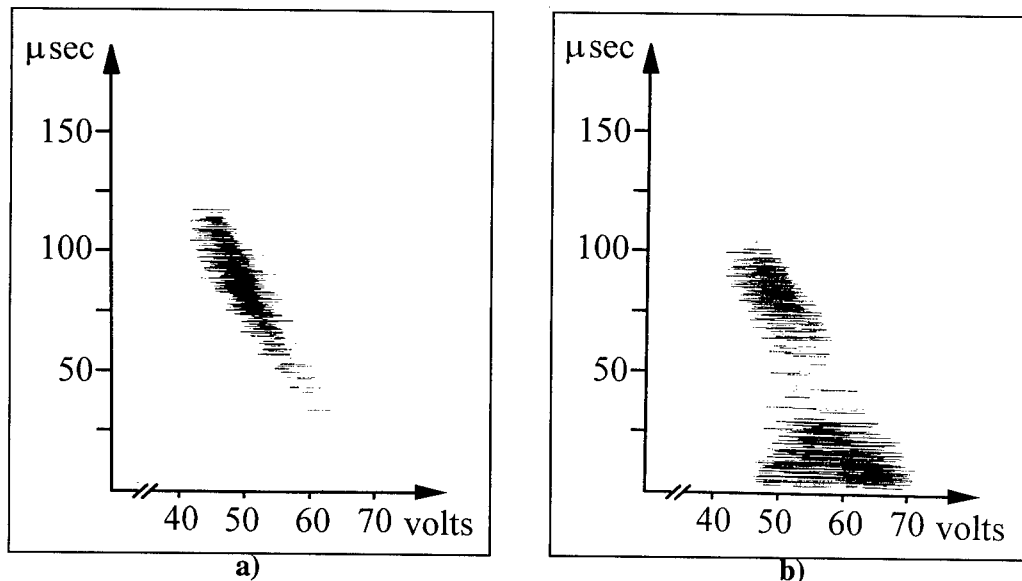


Figure 4 : Individual arc root lifetimes evolution with their corresponding voltage minima : a) downstream jumps ; b) upstream jumps.  $d = 7$  mm, 45 slm Ar, 15 slm H<sub>2</sub>,  $I = 600$  A.

Semi-empirical correlations, obtained through dimensionless analysis[20,18], allow to relate the working parameters ( $I$ ,  $d$ ,  $m_g^\circ$ ) to arc root lifetimes, ramp slopes and voltage jumps for a given gas mixture. They are of the type :

$$\bar{\tau}_u = K_u \times m_g^\circ^{-0.32} \times I^{-0.69} \cdot D^{2.0}$$

where  $K_u = 14.6$  for Ar-H<sub>2</sub> (25 vol%) and 12.7 for N<sub>2</sub>.

A similar relationship is obtained for the downstream lifetimes  $\bar{\tau}_d$ . With correlations better than 0.95 they show that the approach of the phenomena is good.

The values of the characteristic frequencies deduced from the FFT are somewhat lower, especially for high arc currents, than those calculated from arc root mean lifetimes. This is due probably to the fact that FFT favors the higher amplitudes of the voltage signal while the statistical analysis takes into account

all the peaks. As it can be observed in fig. 2.b that, at 600 A the voltage jump amplitudes are more irregular than those obtained at lower arc current (see fig. 2.b).

The way the plasma forming gas is injected has a great importance on  $f$ ,  $\tau$ ,  $\Delta V$ [14]... When the gas is injected axially or along the cathode tip the arc column expands closer to anode-nozzle wall and the cold gas layer around the arc determines the restrike as explained in the previously described results. The higher is arc gas flow rate, the thicker the boundary layer and the lower the restrike frequency (see fig. 5.a). With vortex injection the influence of the gas flow rate is the opposite. For higher gas flow rate the frequency peak increases with increasing gas flow rate (see fig. 5.b). Two opposing effects are present in

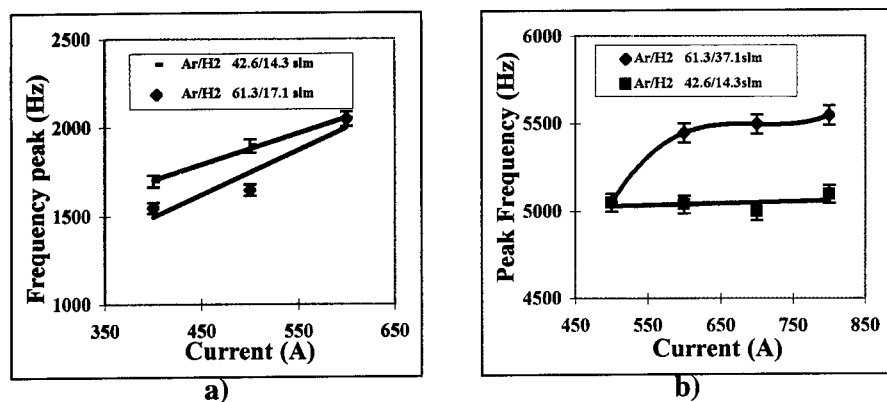


**Figure 5 :** Evolution with arc current of the characteristic FTT frequency for two different types of plasma forming gas injectors : a) axial injection ; b) vortex injection, anode  $D = 7.2$  mm, with two gas flow rates 42.6 slm Ar and 143 slm  $H_2$  and 61.3 slm Ar and 17.1 slm  $H_2$  respectively.

this case. First increasing  $m_g^\circ$  induces a constriction of the arc column which can be verified by the increase of the arc mean voltage. The consequence is reduced restrike probability and longer anode attachment. On the other hand, increasing the gas flow rate leads to higher flow velocity especially in the cold boundary layer. Because of this the connection between the arc column and the anode surface is pushed downstream faster, yielding faster and more frequent breakdowns.

The last parameter is of course the gas composition. Diatomic gases either pure ( $N_2$ ) or added to Argon ( $H_2$  or  $N_2$ ) constrict drastically the plasma column due to their high thermal conductivity[20] and with them the restrike mode is well defined. On the contrary in case of Ar-He mixtures the mean voltage is less than 40 V, the voltage fluctuations have very small amplitudes and the restrike does not obviously appear on the time resolved signals which lead to a "noisy" power spectrum. This is due to the poor constriction of the column with these gases.

### 2.3. Electrode erosion

#### a) Anode

In their experiments with flat anodes with a smooth surface ( $Ra < 0.5 \mu m$ ) Wutzke et al[6] have shown that it was the arc root itself which was sliding on the anode surface before a new spot was created by a short circuit shortening the arc. Later on Zhukov et al[11], by using real plasma torches with a cylindrical anode equipped with observation windows, have demonstrated that the arc root once it was created by a short circuit did not move at all. It was the connecting column between the arc root and the main plasma column which was stretched downstream as long as a short circuit did not create a new arc root. It is worth to note that in both cases, moving arc root or stretching connecting column result in the same saw-tooth shape of the arc voltage. A recent experiment was performed at the laboratory[22] with the arc transferred to a flat anode orthogonal to the cathode axis, arc stabilized by gas injection along the conical tip of the cathode and working in the anode jet dominated mode in order to simulate a behavior identical to that of the plasma torch where an anode jet always exists at the anode[19]. It has been shown that when moving the cathode parallel to the anode with a new smooth ( $Ra < 0.1 \mu m$ ) copper anode surface the arc moves as a whole. As soon as the surface is oxidized or roughened by the arc and, depending on cathode-anode relative velocity, the arc root does not move anymore and a small connecting column between the arc root and the arc main column is stretched. When the voltage drop in it becomes too high a short circuit occurs between the anode and the main plasma column and a new connecting

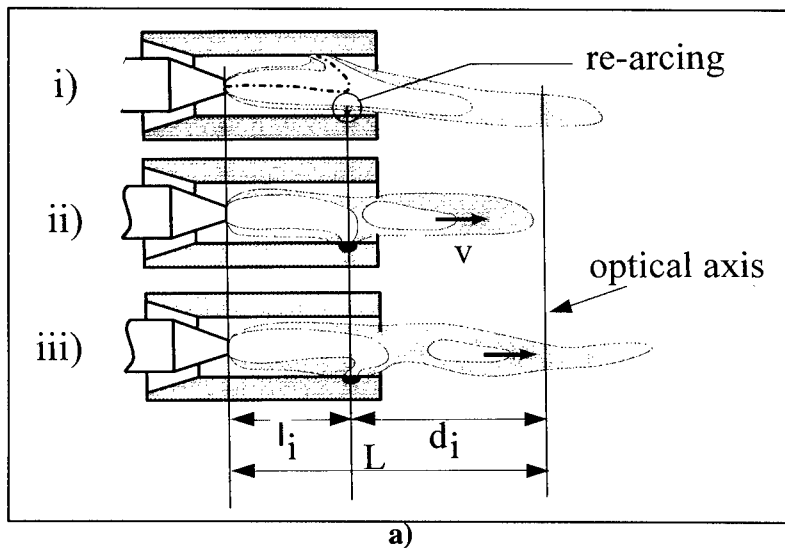
column is formed in about  $1 \mu\text{s}$ . The voltage signal shape is exactly the same as that shown in fig. 2. This is probably what happens in the d.c. torch. At the beginning during the first working hour the arc root moves at the surface and the distributions  $\tau = f(V_{\text{min}})$  are very dispersed with relatively low values of  $\tau$ . The observation of the anode shows a clean surface with a well distributed slight erosion. Later on, for example after 10 h, the distribution is well defined as that shown in fig. 4 and the electrode erosion is distributed along an area which length is about  $1.5 \times D$ . The depth of the eroded zone is about 0.2-0.5 mm. When time increases  $\tau$  increases too while the amplitude of  $\Delta V$  increases and the depth of the eroded area increases drastically (a few mm after 20 to 50 h depending on working conditions).

#### b) Cathode

The high temperatures ( $T > 3800 \text{ K}$ ) observed at the thoriated (2 wt%) tungsten cathode tip<sup>[23-25]</sup> promotes the dopant diffusion and evaporation<sup>[24-27]</sup>. After less than about 1 h the temperature of the cathode tip is that of pure tungsten (almost 1000 K higher than that with the dopant) and its erosion increases drastically. Of course it depends on electrode diameter and tip shape controlling the heat withdrawal and temperature gradients and on gas composition, diatomic gases enhancing the constriction of the arc root and thus the erosion. The erosion that occurs is a neck erosion below the tip which falls off after a while<sup>[26]</sup>. Thus, starting with a sharp tip, after a few hours working the cathode shape is that of a truncated cone, the extremity diameter of which increases with time.

### 2.4. Consequences of fluctuations and erosion

Each time a new arc root is created, a plasma bubble, the volume in which the electrical conductivity is high enough, begins to grow (see fig. 6<sup>[15,28]</sup>). This plasma bubble is then pushed downstream by the plasma flow partly due to the gas feeding and partly by thermal expansion and M.H.D. forces. During the growth of the plasma bubble, the current lines are lengthened (voltage ramps in fig. 2). When a new arc root is created, the arc is shunted and voltage drops and the bubble partly disconnected from the plasma giving rise to a flying puff travelling with the flow. The shape of the puff, even though not clearly defined, is gradually modified by dissipative phenomena. Thus the generated plasma flow may be thought of as a rather inhomogeneous medium made up of puffs of hot gas surrounded by colder layers.



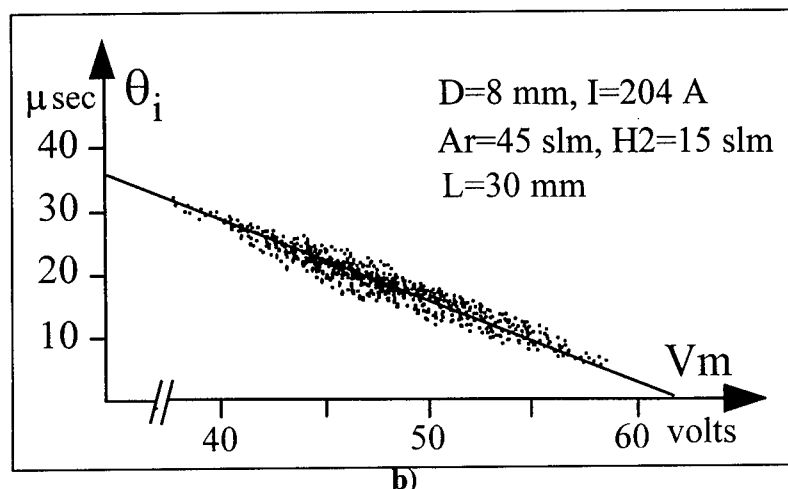


Figure 6 : a) Scheme of plasma bubble generation : i) just before rearing, ii) just after rearing and iii) lengthening phase ; b) Plot of time delay  $\Theta$  versus the minimum voltage.

In the set-up developed by Coudert et al<sup>[28]</sup> the image of the jet was split and focused with a known magnification, in two planes where the wavelength integrated light was sampled by two optical fibers. The distance between the two fibers was known with a precision of 2/100 mm. When a bright puff of plasma crossed the optical system line of sight it generated a peak clearly associated with a ramp of voltage variation. The observation of the fluctuating optical signal generated suggested that only slowly varying details were preserved and that the useful information was kept in low frequency band pass. After careful signals treatment it was shown that the low-band-pass filtered signals were cross-correlated giving rise to a function exhibiting a rather well marked and shifted maximum. A mean value of the velocity was determined as well as its fluctuating components, limited to a 500 Hz band pass due to the specificity of the method, fig. 7<sup>[29]</sup> shows two axial velocity distributions measured at the nozzle exit.

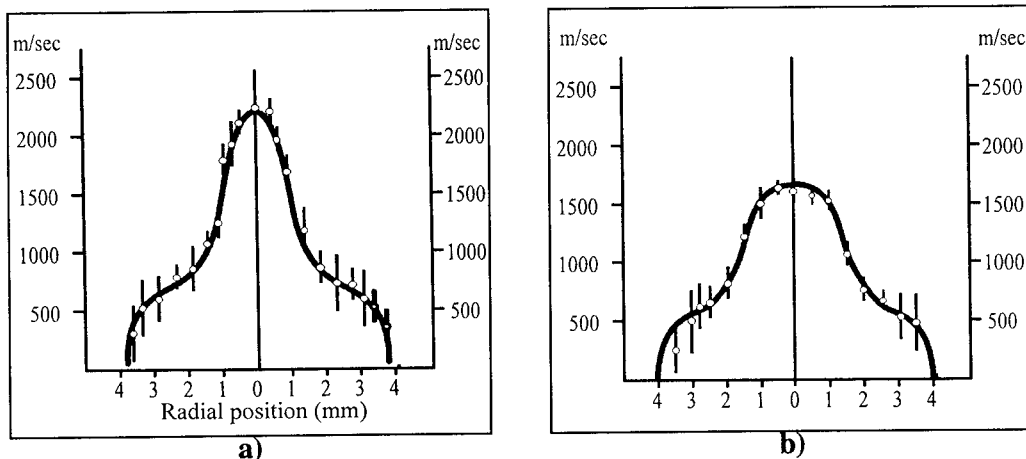


Figure 7 : Radial velocity profile of a d.c. plasma torch (45 slm Ar, 15 slm H<sub>2</sub>, I = 600 A, D = 7 mm) for two working times of the torch : a) t = 1 h, b) t = 12 h.

Three remarks can be made :

- i) With the Ar-H<sub>2</sub> (25 vol%) mixture used at 14000 K axial temperature at the nozzle exit the sound velocity  $a = 2900$  m/s<sup>[30]</sup> and thus the measured velocities are subsonic.
- ii) The short time scale fluctuations, represented by the height of the bars show an almost constant value in the central part of the jet and increases in its fringes due to turbulences. It is the same for measurement along the axis z of the torch. For  $z \geq 30$  mm corresponding to the plasma core tip (in the

working conditions of fig. 7) the fluctuations increase drastically due to instabilities generated by the engulfment of cold surrounding gas<sup>[31]</sup>.

iii) The cathode erosion reduces the plasma jet maximum velocity and broadens its radial distribution. This erosion has a stabilizing effect after a few hours.

Voltage fluctuations have also an important influence on temperature distributions measured by emission spectroscopy : mean value of an exponential term does not give the mean value of the exponent! Thus the signal has also to be treated<sup>[32,17]</sup> to get stationary and fluctuating components of the temperature, the stationary temperature component being smaller than temperature value deduced from a time averaged light intensity signal. Contrarily to what happens for velocity, temperature profiles seem to be unaffected by the electrode erosion<sup>[29]</sup>.

At last by comparing the voltage and light fluctuations signals it is possible to determine the mean electric field within the arc column as well as the mean position of the erosion inside the anode-nozzle<sup>[33]</sup>.

The time delay between light and voltage signals is given by :

$$\Theta = d_i/v$$

where  $v$  is the velocity of the plasma bubble and  $d_i = L - \ell_i$  (see fig. 6) where  $L$  is the distance between the cathode tip and the optical axis and  $\ell_i$  is the instantaneous arc root position.

For the minimum voltage :

$$V_m = \bar{E} \times \ell_i + V_A + V_K$$

where  $\bar{E}$  is the mean electrical field within the arc column,  $V_A$  and  $V_K$  the anodic and cathodic voltage drops respectively. In these conditions the measured values of  $\Theta$  are related to  $\bar{E}$  by :

$$\Theta = \frac{L}{v} - \frac{V_m - V_A - V_K}{v \cdot \bar{E}}$$

A plot of  $\Theta$  as a function of  $V_m$  (see fig. 6.b) gives a straight line which at its intercepts with  $\Theta$  axis gives  $L/v$  thus  $v$  and which slope gives  $\bar{E}$ .

### 3. SPRAYED PARTICLES FLATTENING AND SPLAT COOLING

#### 3.1. Measuring techniques

As emphasized in the introduction, plasma sprayed coating properties depend strongly upon the contact between the layered lamellae<sup>[7,8]</sup>. Study this layering is not a simple problem due to the particle trajectory distribution<sup>[4]</sup> and their small size. For example when spraying alumina particles 30  $\mu\text{m}$  in diameter at a rate of 3 kg/h their injection rate is  $2.10^7$  part/s ! and they impact on the substrate with velocities between 150 and 300 m/s. For now 5 years many efforts have been devoted to the development of fast pyrometers ( $\sim 50$ -100 ns) to follow temperature and surface evolution during particle flattening and the resulting splat cooling together with flattening and cooling models<sup>[5,34]</sup>.

a) First techniques were developed to collect the particles within the spray cone without overlapping and without<sup>[35]</sup> or with<sup>[36]</sup> substrate temperature control.

By optical or scanning electron microscopy coupled with image analysis the splats diameter and shape factor distributions can be determined all over the spray cone.

b) The first pyrometer to study particle flattening was developed in 1992<sup>[37]</sup> at CNRC Boucherville Canada and then improved regularly<sup>[38-40]</sup>. The last system consists of a Phase Doppler Particle Analyser (PDPA) and a pyrometer as shown in fig. 8.a.

The PDPA system make it possible to measure the velocity and size of a single particle before its impact.

The size and velocity of a particle in-flight are determined from the light scattered by the particle passing through an interference fringe pattern generated by the intersection of two coherent laser beams whose wavelength was 514.5 nm. The velocity is deduced from the frequency of the Doppler burst generated by the particle crossing the fringe pattern (see fig. 8.b). The size is computed from the phase shift between the light signals collected by two sensors looking at the probe volume from two different angles. This phase shift is linearly related to the particle size. In the PDPA system used in this work, the two sensors are avalanche diodes. After amplification, the signals from the diodes are recorded using a digital oscilloscope. Algorithms based on a cross spectral density method are used to obtain the frequency and the phase shift of signals. The probe volume is limited using a spatial filter placed before the photodetectors. It corresponds to a cylinder (1.5 mm long and 0.4 mm in diameter) whose axis is orthogonal to plasma jet axis. Velocities between 50 m/s and 500 m/s can be measured for particles which diameters are between 5  $\mu\text{m}$  and 100  $\mu\text{m}$ .

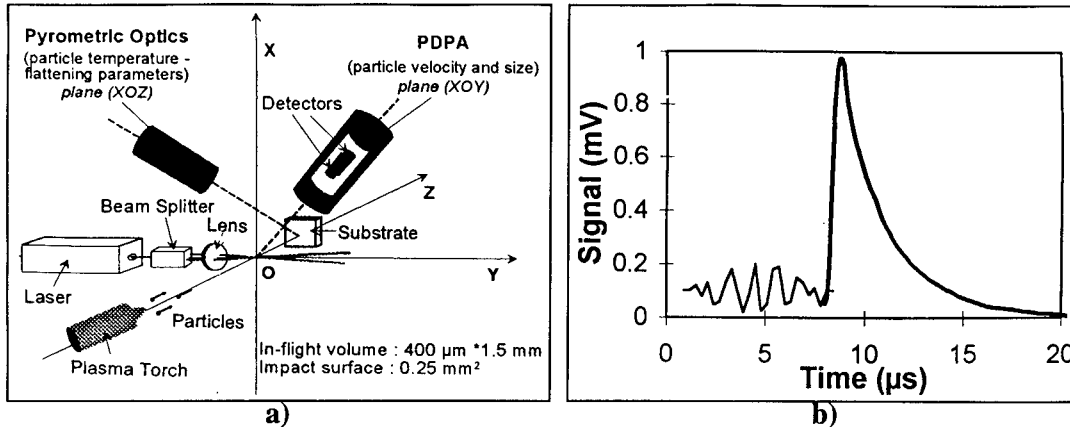


**Figure 8 :** a) Schematic view of the experimental set-up for the monitoring of particles impinging on a surface<sup>[40]</sup>, b) typical signals.

The temperature of the particle before its impact, the time-temperature evolution of the resulting splat and the flattening parameters (flattening time and flattening degree) are determined from the thermal radiation emitted by the particle in flight and at impact<sup>[40]</sup> (see fig. 7.b). This radiation is collected by a pyrometer head focused onto the substrate. The monitored area on the substrate surface was about 0.5 mm<sup>2</sup>. The temperature range of the set up is between 2000 K and 4000 K.

The flattening time is deduced from the rise time of the signals upon impact. The temperature of a particle just before its impact and that of the resulting splat are derived, after calibration, from the ratio of the photodetector outputs of the pyrometer, by assuming that the material behaved as a grey body. As the signal is proportional to the cross section of the emitted area, the flattening degree is estimated from the square root of the ratio signals just before and upon impact after a correction for temperature effect. When significant cooling takes place during the flattening processes, the collected signal is diminished. However, in that case it is possible to determine the flattening degree for the resulting collected disk-shaped splats by measuring their thickness and diameter.

The mean cooling rate of the splat after the spreading process is complete, is estimated from the time-temperature evolution of the lamella.

c) The collected splats, coming from impacting particles whose history of temperature, velocity and diameter is known, are examined by Atomic Force Microscopy (AFM) which allows to determine the size of the columnar structure (see fig. 9.a), the area of poor contact (see fig. 9.b), the columns coalescence<sup>[41]</sup>.

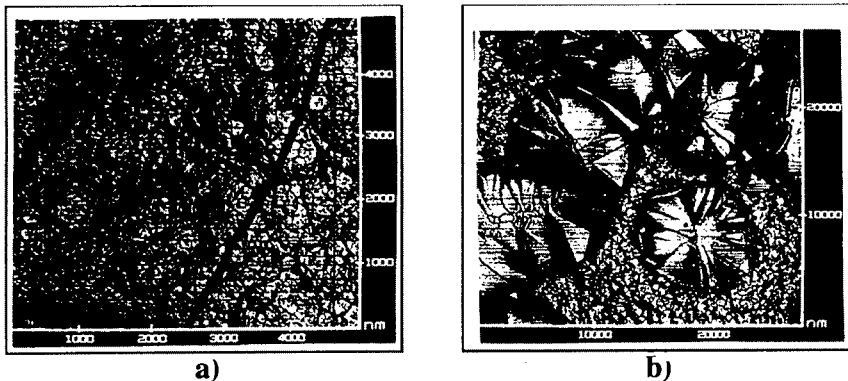


**Figure 9 :** AFM view of an alumina splat sprayed with a d.c. torch (7 mm) : a) on previously deposited alumina, b) on stainless steel 304L (the "big crystals" correspond to a poor contact area)<sup>[41]</sup>.

### 3.2. Characteristic results for zirconia

For given spraying conditions resulting in fully molten particles upon impact such measurements have shown the drastic influence of substrate material, roughness, preheating temperature and oxidation stage[5,36,39,42,43]. The main results are the following :

#### a) Single splat

A critical temperature  $T_c$  of the substrate exists. For zirconia it corresponds to 200°C. Below  $T_c$  on smooth ( $R_a < 0.1 \mu m$ ) substrates the splats are extensively fingered with a shape factor ( $SF = 4.\Pi.S/P^2$  where  $P$  is the splat perimeter and  $S$  its surface area) below 0.6 while for  $T > T_c$  they have almost a perfect disk shape ( $SF > 0.9$ ). For  $T > T_c$  the mean diameter of the splats all over the spray cone is about 40% higher than for  $T < T_c$  where material splashing during particle flattening reduces drastically the splat surface. The cooling rates are also one order of magnitude lower when  $T < T_c$  (see fig. 10 showing the measured cooling rate evolution with impacting particle fig. 10.a and velocity 10.b). A 1D model[5] allows to calculate the splat cooling (assuming a disk shape) which depends on the splat

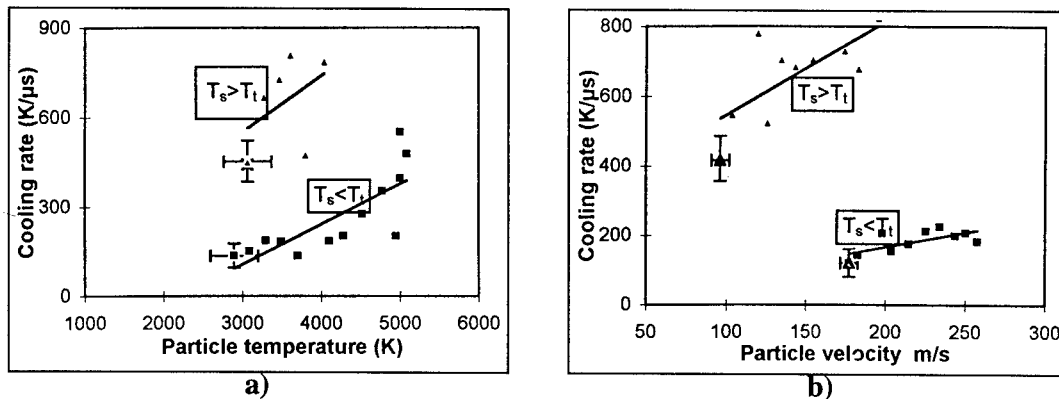


Figure 10 : Evolution of the splat cooling rate with zirconia impacting particle : a) temperature and b) velocity for two substrate preheating temperatures.

thickness (decreasing with increasing impact velocity) and on thermal contact resistance  $R_{th}$  between the splat and substrate or previously deposited layers. By comparing the measured and calculated cooling rates for  $T > T_c$ , knowing the splat thickness, it allows to determine  $R_{th}$  which in this case is of the order of  $10^{-7} - 10^{-8} m^2.K/W$  (almost a perfect contact). The explanation for  $T_c$  has been given by A. Vardelle et al[44]. If the substrate surface temperature  $T_i$  (resulting from preheating and flattening particle heat transfer) is higher than the hypercooling temperature  $T_H$  of the impacting particle, solidification occurs only at the end of the flattening stage and develops all over the splat surface resulting in an homogeneous columnar growth. If  $T_i < T_H$  solidification starts at a few area before flattening is completed and the flowing liquid material, blocked by this solidified area, splashes away. Preheating at  $T_c$  allows to obtain or not the case  $T_i > T_H$ .

The cooling rate of the splat is closely linked to  $T_c$  and splat thickness. The size of the splat columns increases when the cooling rate decreases.

On rough surfaces, as the flowing liquid material of the impacting particle is blocked by the surface asperities it results in thicker splats. Here again the influence of  $T_c$  is drastic the cooling rates being higher for  $T > T_c$ .

The way substrate oxidation modifies the splat shape even for  $T > T_c$  is not yet clearly understood but works are in progress[45].

#### b) Layered splats

In classical spraying conditions where a pass corresponds to 3 to 10  $\mu m$  (about 3 to 10 layered splats) and where temperature between successive passes is in the range of 500-600°C the results obtained for  $T_c$  have been confirmed. With a preheating temperature over  $T_c$  the adhesion/cohesion of the coatings is more than doubled[41,46]. When increasing the preheating temperature over  $T_c$  and the pass thickness, temperatures in the range of 900-1000°C within the coating are reached and the new impacting particle starts to nucleate only at the end of the flattening stage. Thus the columnar structure of the previously

deposited and solidified splat acts as a nucleation site and it results in a columnar structure growing through the whole pass and between passes<sup>[47]</sup>. However a compromise has to be found with the increase of the stresses<sup>[40]</sup> and work is in progress in this field.

#### 4. CONCLUSION

Arc root restrike mode in d.c. plasma torches has a great influence on their working conditions especially for plasma spraying. It results in :

- important power fluctuations (up to 50%), due to voltage variations, at frequencies between a few kHz and 20 kHz. This frequency depends strongly on the hot boundary layer formation around the arc column. If its correlation with the torch working parameters is now well understood for axial gas injection, the effect of gas vortex injection requires more studies.
- a discontinuous behavior of the plasma which can be described by a succession of hot puffs travelling with the flow and surrounded by colder layers.
- the possibility to use these transient phenomena to measure the plasma flow velocity by analyzing the light signals recorded at two points which distance is known. This requires an appropriate signal treatment, the useful information being kept in the low frequency band pass.
- to determine the mean electric field of the column by comparing the light and voltage signals.
- the necessity to extract the stationary component of the volumetric emission coefficient in order to determine spectroscopically the plasma jet temperature, the classical measurements based on time averaging being incorrect.

However a lot of work has still to be done to :

- extract information from the high frequency (a few kHz) voltage signal<sup>[33]</sup>.
- determine the contribution of this piston flow (succession of puffs) on the plasma flow modelling including the engulfment process of the surrounding air entrainment<sup>[48]</sup>.

If the transient phenomena in d.c. plasma torches start to be well understood their consequences on the injected particles treatment has not yet been studied and work is in progress to :

- evaluate the influence of these puffs and their frequency on the sprayed particles heating by the plasma jet, the first measurements<sup>[49]</sup> showing that the flux emitted by the hot particles fluctuates too.
- find a way to determine statistically the particles treatment within the jet and how it can affect the splats formation and their layering.

If in the eighties many studies were focused on the measurement of particle surface temperature, velocity and diameter distribution, during their flight within the plasma jet, it is only for about 5 years that the study of their flattening and the resulting splat cooling has been developed. Fast pyrometers (< 100 ns) associated with laser scattering measurements have allowed to determine for a single particle its temperature, velocity and diameter prior to its impact, its flattening degree and time (~ 1  $\mu$ s) as well as the resulting splat temperature evolution. Such measurements have allowed to understand better the drastic influence of the substrate temperature, roughness and oxidation stage on splats adhesion and work is in progress to study their layering in order to achieve coatings with better thermomechanical properties.

#### References

- [1] P. Fauchais and M. Vardelle, *Pure and Applied Chemistry*, **66** (1994) 1247-1258.
- [2] *Thermal Spraying* (Pub.) American Welding Soc. Miami, FL, USA (1985), 180 p.
- [3] L. Pawlowski, *The science and engineering of thermal spray coatings* (Pub.) J. Wiley and sons, NY, USA (1995), 286 p.
- [4] M. Vardelle, A. Vardelle and P. Fauchais, *J. of Thermal Spray Technology*, **2** (1) (1993) 79-92.
- [5] M. Vardelle, A. Vardelle, A.C. Leger, P. Fauchais and D. Gobin, *J. Thermal Spray Technology*, **4** (1) (1995) 50-58.
- [6] S.A. Wutzke, E. Pfender and E.R.G. Eckert, *AIAA Journal*, **5** (4) (1967).
- [7] R. McPherson, *Thin Solid Films*, **83** (1981) 297-310.
- [8] R. McPherson, *Surf. Coating Technol.*, **39/40** (1989) 173-181.
- [9] C. Moreau, P. Cielo, M. Lamontagne, S. Dallaire and M. Vardelle, *Meas. Sci. Technology*, **1** (1990) 807-817.
- [10] W. Neumann, *Beitr. Plasma Physik*, **16** (1976) 97-109.
- [11] M.F. Zhukov et al, *Electric arc gas heaters (plasma torches)* (Pub.) Nauka, Moscow (1973) 232 p (in Russian).
- [12] M.F. Zhukov, in *Thermal Plasma and New Materials Technology*, (eds.) O.P. Solonenko and M.F. Zhukov, (Pub.) Cambridge Interscience (1994) 9-43.
- [13] J.F. Brilhac, B. Pateyron, G. Delluc, J.F. Coudert and P. Fauchais, *Plasma Chemistry, Plasma Proc.*, **15** (1) (1995) 231-255.



- [14] M.P. Planche, Z. Duan, O. Lagnoux, J. Heberlein, J.F. Coudert, E. Pfender, Study of arc fluctuations with different plasma spray torch configurations, to be published in proc. of ISPC 13, (ed.) Prof. W.K. Wu, Beijing, Aug. (1997).
- [15] J.F. Coudert, M.P. Planche and P. Fauchais, High Temp. Chem. Processes 3 (1994) 639-651.
- [16] J.F. Coudert, M.P. Planche and P. Fauchais, in Heat and Mass Transfer under Plasma Conditions (ed.) P. Fauchais, (Pub.) Begell House, N.Y., USA (1994) 253-264.
- [17] J.F. Coudert, M.P. Planche and P. Fauchais, Time resolved measurements of arc voltage, temperature and velocity in a d.c. plasma torch, in Proc. ISPC12 (ed.) Prof. J. Heberlein, Univ. of Minnesota MN, USA 3 (1995) 1619-1626.
- [18] M.P. Planche, Contribution à l'étude des fluctuations dans une torche à plasma, Application à la dynamique de l'arc et aux mesures de vitesse de l'écoulement, Ph.D. Thesis, Univ. of Limoges, France (1995).
- [19] E. Pfender, Electric Arcs and Arc Gas Heaters, in Gaseous Electronics (eds.) M.N. Hirsch and H.J. Oskam (Pub.) Academic Press 1 (1978) 291-345.
- [20] O.I. Yas'ko, Brit. J. Appl. Phys. 2 (2) (1969) 733-741.
- [21] M. Boulos, P. Fauchais and E. Pfender, Thermal Plasma, Vol. 1 Fundamental phenomena, (Pub.) Plenum Press (1995) 452 p.
- [22] J.M. Sobrino, J.F. Coudert and P. Fauchais, Anodic arc root behavior of a transferred arc moving orthogonally to a plume surface, in proc. of ISPC 12 (ed.) J. Heberlein, Univ. of Minnesota 3 (1995) 1455-1460.
- [23] X. Zhou and J. Heberlein, Plasma Sources Sci. Technol. 3 (1994) 564-574.
- [24] X. Zhou and J. Heberlein, in Proc. of Symp. on heat and mass transfer under plasma conditions (ed.) P. Fauchais, (Pub.) Begell House Inc., NY, USA (1995) 237-243.
- [25] X. Zhou and J. Heberlein, Plasma Chem. Plasma Proc. (1996) 229S-244S.
- [26] X. Zhou, B. Ding and J. Heberlein, IEEE Trans. Components Pkg. and Mfg. Tech. 19 (3) (1996) 320-328.
- [27] M. Ushio, K. Tanaka and M. Tanaka, see [23] (1995) 265-272.
- [28] J.F. Coudert, M.P. Planche and P. Fauchais, Plasma Chem. Plasma Proc. 15 (1) (1995) 47-70.
- [29] M.P. Planche, J.F. Coudert and P. Fauchais, see [21] 3 (1995) 1475-1480.
- [30] B. Pateyron, M.F. Elchinger, G. Delluc and P. Fauchais, Plasma Chemistry Plasma Processing 16 (1) (1996) 39-57.
- [31] E. Pfender, J. Fincke and R. Spores, Plasma Chem. Plasma Process, 11 (4) (1991) 529-544.
- [32] J.F. Coudert and P. Fauchais, J. of High Temp. Chem. Processes 3 (1) (1992) 443S-453S.
- [33] J.F. Coudert, M.P. Planche and P. Fauchais, Plasma Chem. Plasma Process. 16 (1) (1996) 211S-228S.
- [34] P. Fauchais, A.C. Leger, M. Vardelle and A. Vardelle, Formation of plasma sprayed oxide coatings, in Proc. of J. Szekely Memorial Symposium (Oct. 1997) to be published by TSM.
- [35] K.A. Roberts and T.W. Clyne, Surface and Coating Technology 41 (1990) 103-115.
- [36] L. Bianchi, A. Grimaud, F. Blein, P. Lucchese and P. Fauchais, J. Thermal Spray Technology 4 (1) (1995) 59-66.
- [37] C. Moreau, P. Cielo and M. Lamontagne, J. of Thermal Spray Technology 1 (3) (1992) 317-323.
- [38] M. Vardelle, A. Vardelle, C. Moreau and P. Fauchais, Meas. Sci. Technol. 5 (1994) 205-212.
- [39] S. Fantassi, M. Vardelle, P. Fauchais and C. Moreau, J. Thermal Spray Technol. 2 (4) (1993) 379-384.
- [40] A.C. Leger, Contribution to experimental study of zirconia splat formation, splats layering and coating residual stresses, Ph.D. Thesis, Univ. of Limoges, March (1997).
- [41] L. Bianchi, A. Denoirjean, F. Blein and P. Fauchais, accepted in Thin Solid Films (1997).
- [42] L. Bianchi, A.C. Leger, M. Vardelle, A. Vardelle and P. Fauchais, accepted in Thin Solid Films.
- [43] C. Moreau, P. Gougeon and M. Lamontagne, J. Thermal Spray Technol. 4 (1) (1995) 25-33.
- [44] A. Vardelle, N.J. Themlis, B. Dussoubs, M. Vardelle and P. Fauchais, Transport and Chemical rate phenomena in plasma sprays, accepted in J. of High Temp. Material Proc. 3 (1997).
- [45] A. Denoirjean, L. Bianchi and P. Fauchais, Study of oxide layers obtained on 304L substrates heated by a d.c. plasma jet plume, to be published in Proc. of UTSC 97 (Pub.) ASM Int. OH USA.
- [46] P. Fauchais, M. Vardelle, A. Vardelle, L. Bianchi and A.C. Leger, Plasma Chem. Plasma Process. 16 (1) (1996) 99S-126S.
- [47] A. Haddadi, A.C. Leger, A. Grimaud, P. Fauchais and F. Nardou, Influence of substrate and coating temperature on columnar growth in Proc. of UTSC 97 (Pub.) ASM Int. OH, USA.
- [48] E. Pfender, J. of Thermal Spray Technology 6 (2) (1997) 126-128.
- [49] K.I. Li, M. Vardelle and P. Fauchais, in Advances in Thermal Spray Science and Technology (eds.) C.C. Berndt and S. Sampath (Pub.) ASM Int. OH, USA (1995) 45-50.

## Grafting of Chemical Groups onto Polymers by Means of RF Plasma Treatments: a Technology for Biomedical Applications

P. Favia, R. d'Agostino and F. Palumbo

*Dipartimento di Chimica, Università di Bari, Centro di Studio per la Chimica dei Plasmi, CNR,  
via Orabona 4, 70126 Bari, Italy*

**Abstract.** A brief review on plasma-processes used in biomedical applications is presented, along with results obtained by our group on the plasma-grafting of chemical functionalities onto polymers. RF Glow Discharges in  $\text{NH}_3/\text{H}_2$  and  $\text{O}_2/\text{H}_2\text{O}/\text{H}_2$  feeds have been utilized for grafting nitrogen- (*e.g.*  $-\text{NH}_2$ ) and oxygen-containing (*e.g.*  $-\text{OH}$ ,  $-\text{COOH}$ ) functionalities onto polymers in a reproducible, controlled, selective fashion. Efficiency and selectivity of the grafting can, in principle, be tuned by optimizing the treatments with a proper, combined use of Actinometry and derivatization-aided Electron Spectroscopy for Chemical Analysis. Grafted  $-\text{COOH}$  groups have been used as "anchor sites" for immobilizing heparin and highly-sulphated hyaluronic acid in an active, anti-thrombotic form onto polyethylene.

### 1. INTRODUCTION

According to many reviews [1-4], low-pressure, non-equilibrium plasma-processes allow to alter the surface of polymeric biomaterials (see refs. [5-8] for proper definitions of the words *biomaterial* and *biocompatibility*) in a number of attractive ways for improving their compatibility with blood, soft tissues, bones, cells and biomolecules in biomedical applications.

Plasma Enhanced Chemical Vapor Deposition (PE-CVD) and Plasma Treatments (PT) are the favourite plasma-techniques for changing surface properties such as wettability, lubricity, adhesion to other materials, cell growth, leach of additives and protein adsorption in biomedical devices. Vascular grafts, heart valves, catheters and other devices used in contact with human blood, for example, can take advantage of blood-compatible plasma-deposited coatings [2, 9-11] as well as of anti-thrombotic molecules immobilized onto plasma-treated surfaces [1, 7, 12-16]. Plasma Treatments, *i.e.* plasma-processes performed with non-depositing reactive ( $\text{NH}_3$ ,  $\text{O}_2$ ,  $\text{N}_2$ , etc.) or inert (Ar, He) gas feeds, are used for altering only the topmost layer of a polymer surface by grafting chemical functionalities and/or by cross-linking the polymer chains through positive-ion bombardment. Radio Frequency (RF, 13.56 MHz) Glow Discharges are the most popular plasma sources for PE-CVD and PT processes.

Table 1 lists classes of surfaces that can be engineered on biomedical devices and prostheses by means of PE-CVD and PT. This contribution is designed to show how Plasma Treatments can be driven for grafting, somewhat in a selective fashion, chemical polar groups onto the surface of polymers, and how Actinometry [17-19] and Electron Spectroscopy for Chemical Analysis can be utilized for investigating the process. This approach can be utilized for engineering polymer surfaces with a dosed density of proper functionalities to be utilized for immobilizing biomolecules onto polymers.

TABLE 1. Deliverables of PE-CVD and PT processes of interest in biomedical applications

<b>Blood-compatible surfaces</b>
PE-CVD of coatings with blood-compatible properties.
Anti-thrombotic biomolecules immobilized onto plasma-treated polymers.
<b>Non-fouling surfaces</b>
PE-CVD of coatings where proteins, cells, bacteria, biofilms, etc. don't adhere.
<b>Surfaces with tailored hydrophilic-hydrophobic character</b>
PE-CVD of coatings with tailored surface energy.
Grafting of polar (e.g. -OH, -COOH, N-groups) or non polar (e.g. -F, -CF <sub>x</sub> ) functionalities by means of Plasma Treatments.
<b>Sterilization and cleaning</b>
Plasma Treatments with oxidizing (e.g. O <sub>2</sub> ) ashing feeds.
<b>Barrier coatings</b>
PE-CVD of barrier coatings for: drug-release systems, gas-exchange membranes, device protection, reduction of leaches (ions, additives, catalyst) from materials.

## 2. ON THE USE OF DIAGNOSTIC TECHNIQUES IN THE BIOMATERIAL FIELD

Process control is usually performed in the biomaterial community at the end of the plasma-process, by means of surface analysis techniques such as: Electron Spectroscopy for Chemical Analysis (ESCA), static Secondary Ion Mass Spectroscopy (s-SIMS), Scanning Electron Microscopy (SEM), Attenuated Total Reflectance FTIR (ATR-FTIR) spectroscopy and Contact Angle (CA) measurements [20, 21]. Recently, ESCA analysis of hydrated-frozen surfaces has been developed [22, 23] and derivatization techniques introduced [24] for investigating in deeper detail polymer surfaces of biological interest. More advanced techniques such as Near Edge X-ray Absorption Fine Structure (NEXAFS) [25, 26] and scanning probe methods such as Atomic Force Microscopy (AFM) [27] have been utilized too.

The great attention dedicated to the study of plasma-processed surfaces, as well as to the interactions of such surfaces with blood, tissues, cells, proteins and other biological systems, is not counterbalanced, in the field of biomaterials, by the diagnostic analysis of what happens in the plasma gas-phase; further, low to none care is paid to reactor engineering and very simple reactor configurations are used. The density of the *active species* in the plasma, the bias of the surfaces and other *internal parameters* [19, 28-31] that, at

the end, drive surface modifications at a chemical level in glow discharges, apparently are not a concern in the biomaterial community, as it comes evident from the literature of the field. This lack of process control, common also for applications in other areas (food packaging, corrosion protection, etc.) where non-equilibrium plasmas are used, is responsible of a trial-and-error, *black box* approach to plasma-processing, which has contributed to generate problems of reproducibility and difficulties of technological transfers and scale-up of processes. Process control is possible, instead, because well established reactor-engineering criteria and a large number of plasma-diagnostic techniques [17-19, 28, 29, 32-34] are available from the scientific background of microelectronics. Plasma diagnostics such as Optical Emission Spectroscopy (OES), Laser Induced Fluorescence (LIF), Mass Spectrometry (MS), Langmuir Electrostatic Probes (LEP), IR and UV Adsorption Spectroscopy (IR-AS, UV-AS), particularly when applied *in situ* and supported by surface analysis, have contributed to fully understand, optimize and control at submicron level plasma-etching and PE-CVD processes devoted to the production of highly integrated electronic circuits. This approach has led to the booming development of the microelectronic technology led by plasma-processes.

This picture of the situation reflects the point of view of the authors. We are convinced that coupling surface and plasma diagnostic techniques would allow to fully exploit plasma-processes also in biomaterial science, where their potential as surface modification techniques is already recognized and appreciated, but only partially exploited.

### 3. GRAFTING OF CHEMICAL FUNCTIONALITIES ONTO POLYMERS BY MEANS OF PLASMA TREATMENTS

Plasma Treatments can graft proper chemical groups onto polymers and consequently increase (*e.g.* with  $\text{NH}_3$ ,  $\text{O}_2$ ,  $\text{N}_2$  plasma feeds) or lower (*e.g.* with  $\text{CF}_4$ ) their surface energy and hydrophilic-hydrophobic character, two related properties that drive the interactions with biological systems. Plasma-grafting oxygen- or nitrogen-containing polar groups, as an example, can improve adhesion and growth of cells on polymers [1-3, 35, 36] utilized in prostheses and biomedical devices, while plasma-fluorination can work in the opposite way [37].

Selected plasma-grafted chemical functionalities such as  $-\text{NH}_2$ ,  $-\text{OH}$ ,  $-\text{COOH}$  are also utilized as anchor sites for covalently immobilizing biomolecules able to confer their biological properties (molecule recognition, anti-thrombogenicity and blood-compatibility, wear resistance, non fouling character) to the surface where they are tied [1, 7, 38]. Immobilization procedures always start with plasma-processing of the polymer substrate, then continue with wet reactions. A spacer molecule with proper functional groups on both ends is immobilized on the grafted surface with one side, then bound to the biomolecule on the other side. The spacer can be essential for ensuring to the biomolecule full conformational movement, thus biological activity; direct coupling to polymer surfaces, in fact, can lead to inactivation and denaturation [39, 40]. Also PE-CVD can provide layers with proper functional groups. With this approach heparin has been immobilized onto materials such as polyethylene (PE), pyrolytic carbon and others [12-16], collegene has been immobilized onto polytetrafluoroethylene [41] and glucose oxidase (GOx) onto polyurethane [42].

Ageing of the plasma-treated surfaces (*i.e.* rearrangements, mobility of groups and polymer chains, reactions of groups with atmospheric oxygen, contaminations, loss of volatile or soluble compounds [35, 43, 44]) is always a concern for the applications, since the recovery of the surface properties (*e.g.* wettability) toward the values of the untreated surface usually happens with time. The *shelf life* of a plasma-treated surface should always be evaluated, and the timing of conventional processes to be applied on such surface carefully planned, in order to have each reaction (*i.e.* molecule immobilization) or procedure (*i.e.* cell growth, protein adhesion) to be lately practiced fully effective.

### 3.1 Grafting of nitrogen-containing functionalities, with particular reference to -NH<sub>2</sub>

Polymer substrates have been modified in a tubular quartz reactor by means of NH<sub>3</sub>/H<sub>2</sub> RF Glow Discharges. External parameters such as the NH<sub>3</sub>/H<sub>2</sub> feed ratio and the RF power input, that can be conveniently tuned for changing the distribution of species in the plasma, as well as the position of the substrate in the plasma reactor (glow *vs.* afterglow) and the treatment time have been changed, in order to explore their influence on the grafting process [45, 46].

ESCA analysis of treated polymers allows to measure their surface N/C surface ratio, which has been taken as a measure of the *efficiency* of the treatment in grafting all kinds of N-groups. 4-trifluoromethyl-benzaldehyde (TFMBA) vapors have been utilized for titrating -NH<sub>2</sub> groups grafted onto PE and polystyrene in a well-characterized and selective derivatization procedure [45]. The fluorine density of the derivatized surfaces, proportional to the density of grafted -NH<sub>2</sub> groups, allows to express the *selectivity* of the treatment (NH<sub>2</sub>/N surface ratio) in grafting -NH<sub>2</sub> rather than other N-groups. Actinometric Optical Emission Spectroscopy (AOES), simply known as Actinometry, has been used for investigating the distribution of species formed in the discharges. It allows to monitor, in a semi-quantitative fashion, the relative density of emitting species in the plasma-phase as a function of external parameters such as pressure, feed gas composition and flow rate, power, etc., provided certain conditions are satisfied [17-19, 30]. He and Ar have to be added in small and constant quantity to the feed in order to compare their emission with those of the other emitting species. Table 2 shows the species detected in NH<sub>3</sub>/H<sub>2</sub> RF Glow Discharges, along with their spectral features.

TABLE 2. Emission lines and bands observed  
by AOES in NH<sub>3</sub>/H<sub>2</sub> RF Glow Discharges

Species	System	Spectral feature (Å)
NH	A <sup>3</sup> Π - X <sup>3</sup> S <sup>-</sup>	3360
	C <sup>1</sup> Π - a <sup>1</sup> Δ	3240
N <sub>2</sub>	c <sup>3</sup> Π <sub>u</sub> - B <sup>3</sup> Π <sub>g</sub>	3159
H	2p <sup>2</sup> P <sup>0</sup> <sub>3/2</sub> - 3d <sup>2</sup> D <sub>3/2</sub>	6563 (Hα)
Ar	4s <sup>1</sup> [1/2] <sup>0</sup> - 4p <sup>1</sup> [1/2]	7503
He	2s <sup>3</sup> S - 3p <sup>3</sup> P <sup>0</sup>	3889

Correlating the relative density of the species detected by AOES with the efficiency and selectivity of the grafting performed in various conditions has allowed to draw the chemical mechanism of the process. Figure 1A shows how the N/C surface ratio of treated PE correlates with the actinometric density of excited  $N_2$ , NH and H species determined at different  $H_2$  feed content. The N/C ratio increases with the relative density of the N-species in the plasma-phase, while it is negatively correlated with that of H-atoms. Opposite trends have been recorded as a function of the *selectivity* ( $NH_2/N$ ) of the process, as shown in figure 1B. Other species related to those mentioned above, *e.g.* N atoms, likely present in the plasma and involved in surface processes, have not been detected.

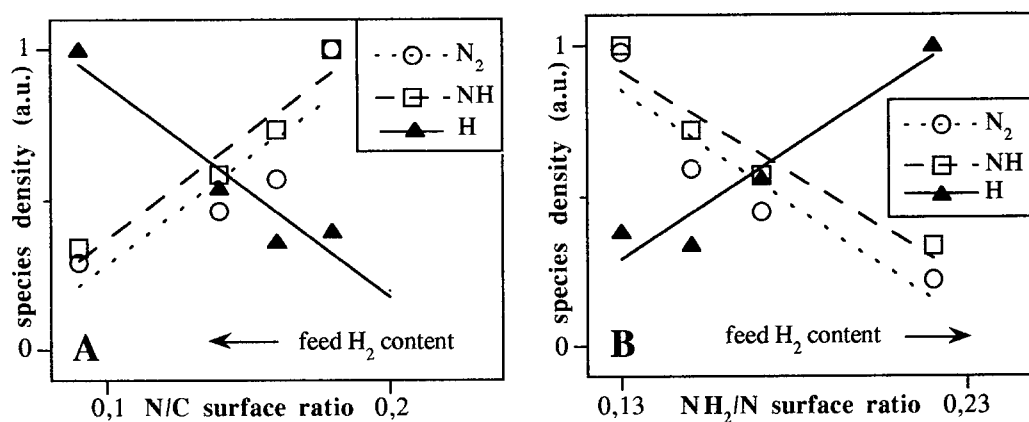


FIGURE 1. Relative species densities in RF Glow Discharges fed with different  $NH_3/H_2$  flow ratios as a function of: A) the surface N/C ratio B) the surface  $NH_2/N$  ratio of PE substrates directly exposed to the plasma (11 sccm total flow rate, glow position, 10 W, 500 mtorr, 5 min).

The correlations with the N/C and  $NH_2/N$  ratios holds also in other experimental conditions, and allow to elucidate the role of each class of species in plasma-surface interactions, as well as to identify the best conditions for obtaining a pre-determined surface chemistry. The chemical mechanisms of the treatment can be described as follows [45, 46]:

- a -  $NH_3$  and  $H_2$  are fragmented in the glow and give origin to excited species, NH,  $N_2$  and H among them, whose relative density can be tuned with the  $NH_3/H_2$  feed ratio and the RF power.
- b - Heterogeneous processes due to the N-species graft N-containing organic groups (*e.g.* amine, imine, cyano, etc.) at the surface of the polymer. The grafting process occurs, with different efficiency and selectivity, for substrates exposed directly to the plasma or placed in the afterglow zone of the reactor.
- c - H-atoms produce  $-NH_2$  groups on the polymer through the reduction of the other N-functionalities. This role of the H-atoms has been elucidated through afterglow and direct-glow  $H_2$  Plasma Treatments of substrates previously  $NH_3$  plasma-treated. The reduction process can be continued, in certain conditions, until no more nitrogen is detected on the polymer.

Low RF power values, a low  $H_2$  (H-atoms) content in the feed and long ( $\geq 5$  min) treatment times allow to obtain high grafting N/C efficiency. On the other hand, high RF power values, a low  $H_2$  (H-atoms) feed content, short (seconds) treatment times and, particularly, treatments with the substrate in the afterglow zone of the reactor, drive the process toward high  $NH_2/N$  selectivity. Afterglow treatments show this effect most likely for the different life-times of the active species produced in the plasma, for their lower density respect to the glow zone and for the absence of positive-ion bombardment on the afterglow surfaces.

Efficiency and selectivity of  $NH_3/H_2$  Plasma-Treatments follow always opposite trends as a function of the same parameter [45, 46]; as a consequence, it is difficult to obtain surfaces characterized by an high absolute density of  $-NH_2$  groups in one step only. In order to bypass this situation and to test the effective ability of H-atoms in reducing N-groups to  $-NH_2$ , different treatments in sequence have been experimented with success. A treatment in high grafting efficiency conditions is to be performed first, followed by a second one in the afterglow zone of an  $H_2$  discharge. The reduction of the N-groups grafted in the first process takes place during the second, thus allowing high yields of  $-NH_2$  groups.

### 3.2 Grafting of oxygen-containing functionalities, with particular reference to $-COOH$ utilized for immobilizing heparin and highly-sulphated hyaluronic acid

Heparin and highly-sulphated hyaluronic acid ( $HyalS_x$ ,  $x = 3.5$ ) have been immobilized onto polyethylene previously plasma-grafted with oxygen-containing groups,  $-COOH$  among them [14, 47]. Heparin- and  $HyalS_{3.5}$ -immobilized samples show higher anti-coagulant character respect to the unmodified polymer. Due to its anti-thrombotic anticoagulant character, heparin is widely used in the treatment of cardiovascular diseases, surgery and extracorporeal blood circulation systems, and a large effort is being profused for obtaining heparin-like molecules like  $HyalS_x$ , as well as for immobilizing such molecules onto blood-contacting devices.

PE substrates have been grafted with O-groups in a quartz tubular reactor [45, 46] by means of RF Glow Discharges fed with  $O_2/H_2O/H_2$  mixtures (Ar and He were added in small quantity for performing Actinometry [14]). Different RF power values, treatment times and the role of the position of the substrate (glow vs. afterglow) have been investigated. The species listed in Table 3 have been detected and their actinometric density profiles obtained as a function of the feed composition, as shown in Figure 2 for an  $O_2/H_2$  discharge.

Differently from  $NH_3$ -based plasmas,  $O_2/H_2O/H_2$  discharges lead to the etching of organic polymers, as attested by C-containing species (CO, CH) detected in the plasma. As a consequence, the formation of Low Molecular Weight Oxidized Materials (LMWOM) [48, 49] on the substrates has been noted. Such compounds form a weak, water-soluble boundary layer on the surface of the treated polymer, that makes difficult reproducing surface analysis.

ESCA analysis of PE treated in  $O_2/H_2O/H_2$  RF Glow Discharges, then rinsed in distilled water and dried, has been performed, and the presence of  $-COOH$  groups available for the wet immobilization reactions attested on the final surface by means of derivatization with trifluoroethanol vapors according to [14, 24]. Studies are in progress in our laboratory [50] aimed to find correlations between the relative

density of the plasma species and the chemistry of the treated surface, similarly to those shown in 3.1. The scope of the investigation is to understand the chemical mechanism of the grafting-etching process, and to optimize plasma-parameters to the optimal density of -COOH groups needed for obtaining the best anti-throbogenic surfaces.

TABLE 3. Emission lines and bands observed by AOES in  $\text{H}_2\text{O}/\text{O}_2/\text{H}_2$  RF Glow Discharges

Species	System	Spectral feature ( $\text{\AA}$ )
$\text{CO}^*$	$\text{B}^1\Sigma - \text{A}^1\Pi$	4511, 4835, 5198, 5610
$\text{OH}$	$\text{A}^2\Sigma^+ - \text{X}^2\Pi$	3064
$\text{CH}^{**}$	$\text{A}^2\Delta - \text{X}^2\Pi$	4314
$\text{O}$	$3s^3S^0 - 3p^3P$	8446
$\text{H}$	$2p^2P^0_{3/2} - 3d^2D_{3/2}$	6563 ( $\text{H}\alpha$ )
$\text{Ar}$	$4s^1 [1/2]^0 - 4p^1 [1/2]$	7503
$\text{He}$	$2s^3S - 3p^3P^0$	3889

\* Produced by the etching of the polymer substrate

\*\* Produced by the etching of the polymer substrate when  $\text{H}_2$  is added to the feed

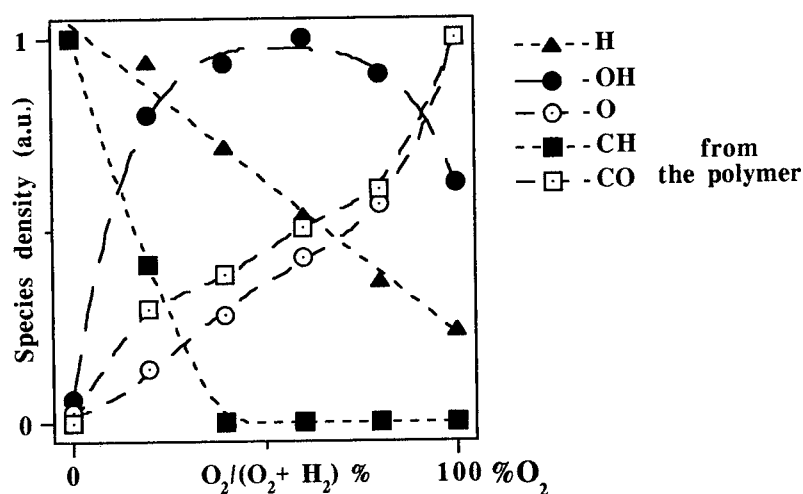


FIGURE 2. Relative species densities in RF Glow Discharges fed with different  $\text{O}_2/\text{H}_2$  flow ratios as a function of the  $\text{O}_2$  percent in the feed. PE substrates are directly exposed to the plasma (11 sccm total flow rate, glow position, 10 W, 500 mtorr, 5 min).

O,O' bis (2-aminopropyl)polyethyleneglycol 500 (Fluka, avgd. m.w. 600 a.u.,  $n = 9-11$ , PEG<sub>500</sub>) has been utilized as spacer-arm molecule to immobilize heparin (Roche) and HyalS<sub>3.5</sub> (synthesized from



hyaluronic acid [51]) onto plasma-modified PE. The detailed procedure, adapted from the literature [15] is reported elsewhere [14, 47]. Each immobilization step, *i.e.* the immobilization of the spacer and that of the biomolecule, deals with the formation of amide covalent bonds between -COOH groups, grafted on PE and present on the biomolecules, and -NH<sub>2</sub> functionalities present on both side of PEG<sub>500</sub>.

After each reaction step the substrates have been rinsed with deionized water and the presence of either the diamine spacer or that of heparin (or HyalS<sub>3,5</sub>) revealed on the surface by detecting N and S atoms with ESCA, respectively. Both heparin and HyalS<sub>3,5</sub>, in fact, contain sulphur. Derivatization with TFMBA has been utilized for tracking the -NH<sub>2</sub> groups of the immobilized PEG<sub>500</sub> molecule on the substrates, thus confirming its presence for the next immobilization step. Best-fitting procedures of the N1s signals have been utilized in order to evaluate that PEG<sub>500</sub> and other diamines utilized in the experiments were coupled to the surface by one amine side only, thus leaving the other available to react.

At the end of the modification steps heparin- and HyalS<sub>3,5</sub>-immobilized PE samples have been obtained, whose surface structure could be represented as in Figure 3. Blood-contact (thrombin time) and platelet-activation tests reveal for such samples an higher surface anti-coagulant character respect to unmodified PE, hence attesting that heparin and HyalS<sub>3,5</sub> have been immobilized in active form.

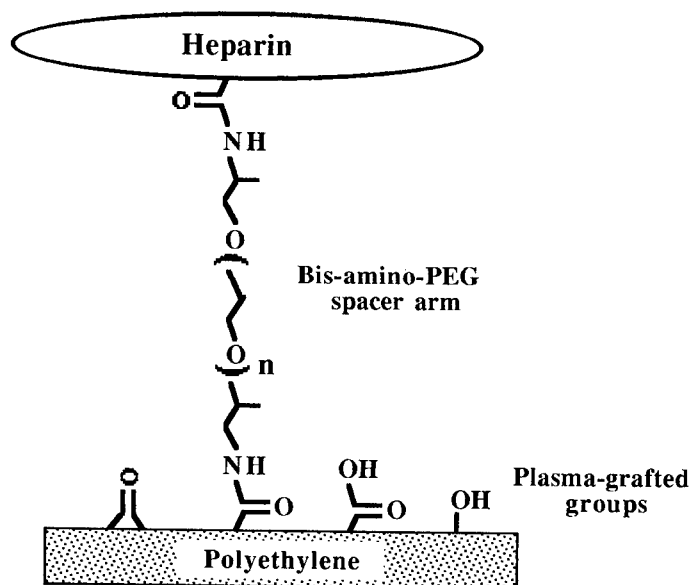


FIGURE 3. Sketch of heparin immobilized onto polyethylene by means of our procedure.

### Acknowledgements

Prof. Rolando Barbucci, Dr. Agnese Magnani and Dr. Stefania Lamponi (Department of Science and Chemical Technologies of Biosystems, University of Siena, Italy) are gratefully acknowledged for providing heparin and HyalS<sub>3,5</sub> molecules, as well as for important issues triggered by discussions and suggestions.

## REFERENCES

- 1 Gombotz W.R., Hoffman A.S., *CRC Crit. Rev. Biocomp.* **4**(1) (1987) 1-42.
- 2 Ratner B.D., Chilkoti A., Lopez G.P. in: *Plasma Deposition, Treatment and Etching of Polymers*, d'Agostino R. ed., Plasma-Materials Interaction serie, Academic Press (1990) 463-516.
- 3 Ratner B.D. in: *Plasma-Processing of Polymers*, d'Agostino R., Favia P., Fracassi F. eds., Kluwer (1997), in press.
- 4 Yasuda H., Gazicki. M., *Biomaterials* **3**(2) (1982) 68-77.
- 5 Williams D.F. ed., *Progress in Biomedical Engineering* **4** (1987).
- 6 Peppas N.A., Langer R., *Science* **263** (1994) 1715-1720.
- 7 Ratner B.D., Hoffman A.S., Lemons J.E., Schoen F.J. eds., *Biomaterials Science - An introduction to materials in Medicine*, Academic Press, New York, (1996).
- 8 Williams D.F., *J. Mater. Sci.* **22** (1987) 3421-3445.
- 9 Kiaei D., Hoffman A.S., Ratner B.D., Horbett A.T., Reynolds L.O., *J. Appl. Pol. Sci.: Polym. Symp.* **42** (1988) 269-283.
- 10 Garfinkle A.M., Hoffman A.S., Ratner B.D., Reynolds L.O., Hanson S.R., *Trans. Am. Soc. Art. Int. Org.* **30** (1984) 432-439.
- 11 Kiaei D., Hoffman A.S., Horbett A.T., *J. Biomat. Sci.: Polym. Ed.* **4** (1992) 35-44.
- 12 Yuan S., Cai W., Szakalas-Gratzl G., Marchant K.K., Tweden K., Marchant R.E., *J. Appl. Biomat.* **6** (1995) 259-266.
- 13 Yuan S., Szakalas-Gratzl G., Ziats N.P., Jacobsen D.W., Marchant K.K., Marchant R.E., *J. Biomed. Mat. Res.* **27** (1993) 811-819.
- 14 Favia P., Palumbo F., d'Agostino R., Lamponi S., Magnani A., Barbucci R., submitted.
- 15 Kyu Kang I., Hyeong Kwon O., Moo Lee Y., Kiel Sung Y., *Biomaterials* **17** (1996) 841-847.
- 16 Pallassana V.N., *J. Biomat. Sci. Pol. Ed.* **6**(2), (1994) 181-193.
- 17 Coburn J.W., Chen M.J., *App. Phys.* **51** (1980) 3134-3136.
- 18 d'Agostino R., Cramarossa F., De Benedictis S., Ferraro G., *J. Appl. Phys.* **52** (1981) 1259-1265.
- 19 d'Agostino R., Cramarossa F., Fracassi F., Illuzzi F. in: *Plasma Deposition, Treatment and Etching of Polymers*, d'Agostino R. ed., Plasma-Materials Interaction serie, Academic Press (1990) 95-162.
- 20 Ratner B.D. in: *Plasma-Processing of Polymers*, d'Agostino R., Favia P., Fracassi F. eds., Kluwer (1997), in press.
- 21 Ratner B.D., *Cardiovasc. Pathol.* **2**(3) supp. (1993) 87S-100S.
- 22 Ratner B.D., Castner D.G., *Coll. Int. B: Bioint.* **2** (1994) 333-346
- 23 Yasuda H., Charlson E.J., Charlson E.M., Yasuda T., Miyama M., Okuno T., *Langmuir* **7**(10) (1991) 2394-2400.
- 24 Chilkoti A., Ratner B.D. in: *Surface Characterization of Advanced Polymers*, Sabbatini L., Zambonin P.G. eds., VCH (1993).
- 25 Castner D.G., Lewis Jr. K.B., Fischer D.A., Ratner B.D., Gland J.L., *Langmuir* **9** (1993) 537-542.
- 26 Castner D.G., Favia P., Ratner B.D. in: *Surface Modifications of Polymeric Biomaterials*, Castner D.G., Ratner B.D. eds., Plenum Press, New York (1996).
- 27 Klemberg-Sapieha J. in: *Plasma-Processing of Polymers*, d'Agostino R., Favia P., Fracassi F. eds., Kluwer (1997), in press.
- 28 Morosoff N. in: *Plasma Deposition, Treatment and Etching of Polymers*, d'Agostino R. ed., Plasma-Materials Interaction serie, Academic Press (1990) 1-93.
- 29 Kay E., Coburn J.W., Dilks A. in: *Topics in Current Chemistry* **94**, Veprek S., Venugopalan M. eds., Springer Verlag, Berlin, (1980) 1.
- 30 d'Agostino R. in: *Plasma-Processing of Polymers*, d'Agostino R., Favia P., Fracassi F. eds., Kluwer (1997), in press.
- 31 Favia P. in: *Plasma-Processing of Polymers*, d'Agostino R., Favia P., Fracassi F. eds., Kluwer (1997), in press.
- 32 Donnelly V.M. in: *Plasma Diagnostics I*, Auciello O., Flamm D.L. eds., Academic Press, New York (1989) 1-46.

- 33 Hershkowitz N. in: *Plasma Diagnostics I*, Auciello O., Flamm D.L. eds., Academic Press, New York (1989) 113-183.
- 34 Dreyfus R.W., Jasinski J.M., Walkup R.E., Selwyn G.S., *Pure & Appl. Chem.* **57**(9) (1985) 1265-1276.
- 35 Griesser H.J., Chatelier R.C., Gegenbach T.R., Johnson G., Steele J.G., *J. Biomat. Sci. Pol. Ed.* **5**(6) (1994) 531-554.
- 36 Lee J.H., Park J.W., Lee H.B., *Biomaterials* **12** (1991) 443-448.
- 37 Eloy R., Parrat D., Duc M.T., Legeay D., Bechetoille A., *J. Cataract Ref. Surg.* **19** (1993) 364-370.
- 38 Hoffman A.S., *Clin. Mat.* **11** (1992) 61-66.
- 39 Kiaei D., Hoffman A.S., Horbett T.A., Lew K.R., *J. Biomed. Mat. Res.* **29** (1995) 729-739.
- 40 Safranj A., Kiaei D., Hoffman A., *Biotechnol. Prog.* **7** (1991) 173-177.
- 41 Tran N.B.C., Walt D.R., *J. Coll. Int.* **132**(2) (1989) 373-381.
- 42 Danilich M.J., Marchant K.K., Anderson J.M., Marchant R.E., *J. Biomat. Sci. Pol. Ed.* **3**(3) (1992) 195-216.
- 43 Xie X., Gegenbach T.R., Griesser H.J., *J. Adh. Sci. Tech.* **6**(12) (1992) 1411-1431.
- 44 Youxian D., Griesser H.J., Mau A.W.H., Schmidt R., Liesegang J., *Polymer* **32**(6) (1991) 1126-1130.
- 45 Favia P., Stendardo M.V., d'Agostino R., *Plasmas and Polymers* **1**(2) (1996) 91-112.
- 46 Favia P., Palumbo F., Stendardo M.V., d'Agostino R. in: *Surface Modifications of Polymeric Biomaterials*, Castner D.G., Ratner B.D. eds., Plenum Press, New York (1996).
- 47 Favia P., Palumbo F., d'Agostino R., 213th ACS National Meeting, S. Francisco, USA, April 1997, *Polymer Preprints* **38**(1) (1997) 1039-1040.
- 48 Foerch R., Beamson G., Briggs D., *Surf. Int. Anal.* **17** (1991) 842-846.
- 49 Wertheimer M.R., Bartnikas R. in: *Plasma-Processing of Polymers*, d'Agostino R., Favia P., Fracassi F. eds., Kluwer (1997), in press.
- 50 Palumbo F., Rinaldi A., Favia P., d'Agostino R., unpublished results.
- 51 Barbucci R., Magnani A., G. Cialdi G., Italian Patent PD 94A000054.

## **Time Resolved Spectroscopy of RF Plasmas: A Comparison of Hydrogen and Deuterium Plasmas**

W.G. Graham and C.M.O. Mahony

*Department of Pure and Applied Physics, The Queen's University of Belfast, Belfast BT7 1NN,  
Northern Ireland*

**Abstract.** Spatio-temporal resolved emission is a powerful technique for exploring the neutral, ionic and electron characteristics of rf driven plasmas. Here this is illustrated by measurements of emission from capacitively coupled H<sub>2</sub> and D<sub>2</sub> rf driven plasmas. These exhibit two pronounced emission regions, one associated with the normal sheath edge and the other near the driven electrode. Time-resolved electrode and plasma potential measurements show this near-electrode emission is associated with field reversal in the electrode sheath. The close similarity of the emission structure in the two isotopes, and the general lack of such structure in He plasmas indicates that the structure and hence field reversal are not solely due to ion mass effects but may also involve the details of the electron collisionality of the gas.

### **1. INTRODUCTION**

Visual observation of a typical rf plasma provides the most obvious plasma diagnostic tool. For example, from an observation of change of the colour or the spatial variation in intensity experienced operators can diagnose a vacuum leak or a change in the character of a surface. Often such colour or intensity changes occur immediately after ignition or after a change of operating conditions or substrate. However the emission of light is a complex process depending on the detailed chemical and physical nature of the plasma and so can reveal much more detailed information. The abundance of atomic and molecular species in the ambient gas and its plasma products in the ground and excited states influence the emission. Most emission occurs as a result of collisions of the atom or molecule with an electron, so the electron density and energy distributions are important. Carefully designed experiments can therefore provide detailed information about these plasma species and parameters. Here the emphasis will be on the observation of plasma emission to study the behaviour of plasma electrons.

By observing only light at a wavelength specific to a particular constituent species and under conditions where it can be assumed that the density of that species is spatially and temporally uniform, the emission is indicative of the behaviour of the electrons exciting that species. In rf driven plasmas the electrons may be modulated with the frequency of the electrode voltage. In most technological plasmas this frequency is 13.56 MHz i.e. a period of 73.7 ns. Fast photon counting techniques allow emission intensity variation measurements with a resolution in the nanosecond region, permitting a study of the high energy portion of the electron energy distribution through the rf cycle. There have been many previous studies of spatio-temporal resolved measurements of emission from such plasmas [1-12]. We have exploited the fast gating (< 2 ns) capabilities of recently available ICCD detectors to study emission. Since the plasma can be imaged onto the detector array, this greatly facilitates spatially resolved measurements. In our previously reported measurements we have compared and contrasted spatio-temporal emission of H<sub>2</sub>, He and Ar atoms [13,14]. The most obvious difference in the excitation data from the three gases was the prominent double emission structure observed in H<sub>2</sub>. Such emission structure has previously been reported in H<sub>2</sub> and H<sub>2</sub>-containing gas mixtures [6,7,10,12-17].

A number of mechanisms to explain the inner near-electrode emission layer have been advanced. These include electrons propagating from the electrode [10] and electric field reversal for a portion of the rf cycle [15]. The latter involves the presence of structure in the sheath electric field i.e. a change in electric field direction over a certain region. Several authors [18-20] have reported measurements of field reversal within rf sheaths in Ar and He but not specifically associated with double emission layers. Many rf sheath models predict a change in electric field direction when the sheath is contracting [18, 21-25]. While in general little attention has been given to these features they were recently seen as evidence of sheath reversal and subsequent plasma heating during sheath contraction in an rf driven nitrogen plasma [24]. Therefore we additionally measured the time dependence of the electrode-plasma potential difference correlated with the time dependence of excitation through the rf cycle [13,14]. These measurements showed that, in contrast to He and Ar, in  $H_2$  the electrode goes positive with respect to the plasma i.e. there is a period during the rf cycle when electrons are accelerated towards the electrode. This electric field reversal is at that phase of the rf cycle where the near electrode emission in  $H_2$  occurs.

The physical process that leads to this electric field reversal is not yet clear. We felt our measurements supported a postulate that it arose from the relatively high electron collision rate in hydrogen, others have associated this effect with the lighter ion mass of hydrogen or the presence of negative ions. In preliminary ion mass studies we noted almost identical behaviour in  $H_2$  and  $D_2$  [13]. In an attempt to throw further light on this issue here we report a more detailed study of plasmas with the two hydrogen isotopes.

## 2. EXPERIMENTAL DETAILS

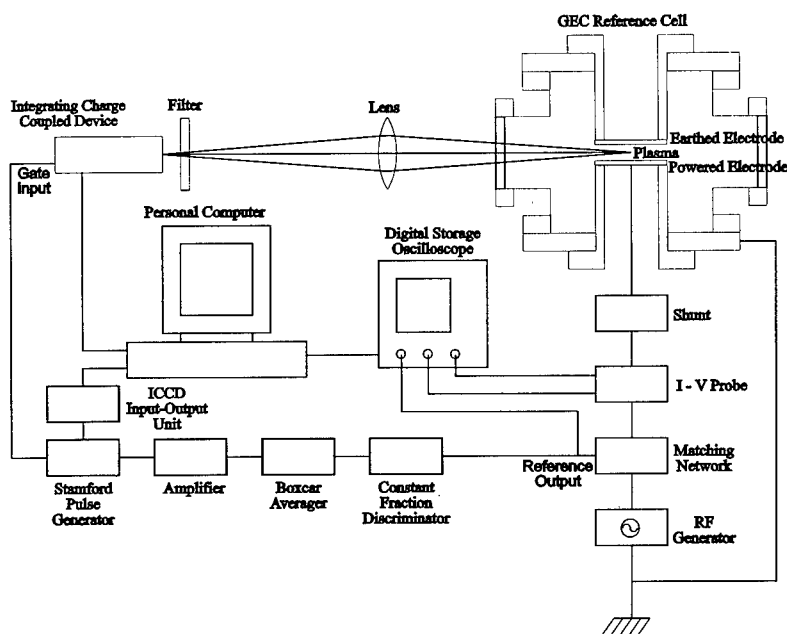


Figure 1: A schematic diagram of the apparatus

A schematic diagram of the plasma and optical emission systems are shown in Fig. 1. The present measurements were made in the UK GEC (Gaseous Electronics Conference) rf reference reactor [26]. This is a parallel plate device with two 102 mm diameter electrodes separated by 25.4 mm. The upper, aluminium electrode and the stainless steel vacuum vessel were grounded. The plasma was created by capacitively coupling rf voltages at 13.56 MHz, to the lower, stainless steel electrode. In the present

measurements peak-to-peak rf voltages of up to 1200 V were applied producing plasma input powers of up to 150 W and discharge currents of up to 3 A. The operating pressures, ranging from 33 to 133 Pa (250 to 1000 mTorr), were measured using a capacitance manometer.

Time resolved light emission measurements were obtained by imaging the central plasma onto an Oriel Instruments Instaspec V fast-gated integrating charge coupled device (ICCD). A lens with a focal length of 200 mm and aperture  $f/4.5$ , placed 250 mm from the ICCD and 1.1 m from the plasma centre was used. This imaged a vertical section of the plasma region, which included both the electrodes, and a horizontal section which extended  $\sim 15$  mm either side of the central axis. A 657 nm filter with a HWHM bandpass of 11 nm was used to select the 656 nm Balmer- $\alpha$  line of  $H_2$  and  $D_2$ .

The depth of field of the image represented 18 mm of the central plasma region. Vignetting of the image by the electrodes was a small effect in the present measurements. The collection angle of the lens was effectively constant except within 0.5 mm of either electrode, dropping linearly to about 80% of the central value at the electrode. The spatial resolution was  $0.5 \pm 0.1$  mm, determined by comparison with a test image.

The ICCD gate was triggered by the output of a delayed pulse generator which was triggered by a pulse derived from a reference waveform from the matching unit. Software automatically incremented the pulse delay by 2 ns to record data for the next gating step, and the process was repeated until 75 delay steps (150 ns) had been completed, i.e. two complete rf cycles. The time and space resolved images were accumulated within 120 s. The accuracy of the gating pulse with respect to the phase of the matching network reference signal was determined to be  $\pm 0.3$  ns.

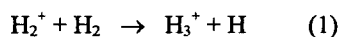
The time variation of the light emission intensity  $I(t)$  was measured but it is the time dependence of the excitation  $E(t)$  which reflects the time-dependent behaviour of the electrons,  $I(t)$  is related to  $E(t)$  via a convolution integral [2]. Here the measured emission signal  $I(t)$  is deconvoluted with the radiative lifetime of the excited state (15 ns) to give the excitation  $E(t)$ . In hydrogen we neglect quenching which introduces at most an uncertainty of 1 ns in timing [10, 16]. The self quenching rate for deuterium will be slower.

The time varying electrode potential relative to the plasma was obtained from dc and ac measurements of the electrode and the plasma potentials [13]. The time-averaged and ac components of plasma potential were measured using a passively compensated Langmuir probe and a capacitive probe respectively. The Langmuir probe was also used to measure time-averaged plasma parameters such as electron density and temperature. The dc component of the electrode potential was recorded directly from the rf matching unit. We used a derivative probe and shunt to determine time resolved electrode potentials (time resolved plasma currents were also recorded by this technique).

To reduce noise our instruments employ averaging over a number of cycles for these optical and electrical measurement techniques so cycle to cycle variation would not be apparent. Never the less single shot measurements of the ac component of electrode current and potential shows only random cycle to cycle variation of  $\sim 1\%$  with no significant contribution from sub harmonics.

### 3. RESULTS AND DISCUSSION

The Langmuir probe measurements indicate that the electron density in  $H_2$  plasmas varied from  $2 \times 10^9$  to  $3 \times 10^{10} \text{ cm}^{-3}$  for the present pressure and power conditions. The measured electron densities in  $D_2$  were generally about 50% lower. The kinetics of hydrogen plasmas are complicated and no self-consistent numerical model exists for rf plasmas. For example the plasma contains three types of positive ions  $H^+$ ,  $H_2^+$  and  $H_3^+$  but their relative concentration has, to our knowledge, not been measured or calculated. While  $H_2^+$  is created directly by electron impact ionisation of the  $H_2$  molecules they can be rapidly converted to  $H_3^+$  by



which has a very large cross section for low energy  $H_2^+$  ( $> 3 \times 10^{-15} \text{ cm}^2$  for  $E < 0.1 \text{ eV}$  [27]). Since the dissociation fraction in capacitively coupled plasmas is relatively low  $\sim 0.005$  [28] and protons are produced mainly from the direct ionisation of atoms they are probably the minority ionic species. The densities of the three ionic species are strongly coupled and will vary with plasma conditions and with

isotope. Models of  $H_2$  glow discharges have to date assumed a single  $H_2^+$  species [12]. This lack of information makes it difficult to accurately determine the ion response to the rf fields. Using the measured electron densities and assuming the diatomic ion is dominant then the ion plasma frequency is expected to vary from 9 MHz to 33 MHz in  $H_2$  and from 4 MHz to 16 MHz in  $D_2$ . If the triatomic ion is dominant then the values are 5 MHz to 20 MHz in  $H_2$  and from 3.5 MHz to 13 MHz in  $D_2$ .

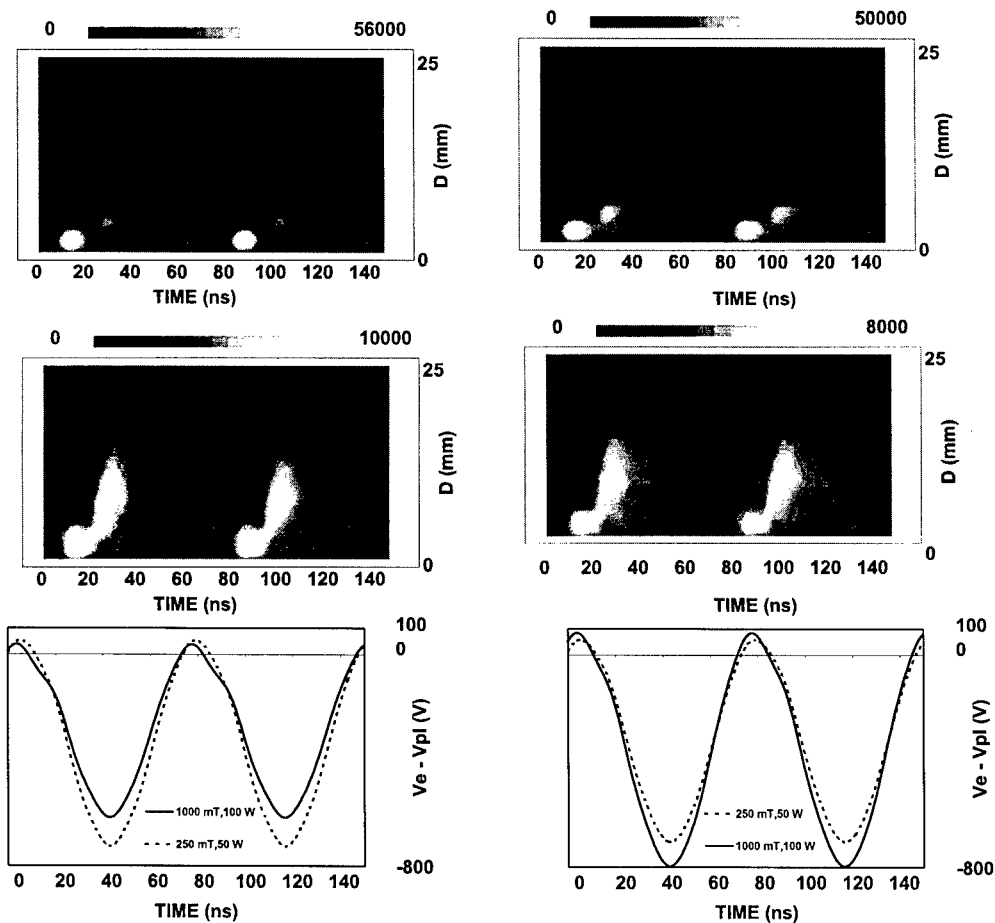


Figure 2. Spatially and temporally resolved Balmer alpha excitation from a hydrogen plasma operating with a forward directed rf power of 50 W and gas pressure 250 mTorr (top) and 100 W and 1000 mTorr (middle). The temporal dependence of the driven electrode potential relative to the plasma under the same conditions (bottom).

Figure 3. Spatially and temporally resolved Balmer alpha excitation from a deuterium plasma operating with a forward directed rf power of 50 W and gas pressure 250 mTorr (top) and 100 W and 1000 mTorr (middle). The temporal dependence of the driven electrode potential relative to the plasma under the same conditions (bottom).

The space and time resolved excitation data for Balmer-alpha excitation typical of those obtained in  $H_2$  and  $D_2$  are shown in Figs 2 and 3 respectively. The threshold energy for exciting this state from the  $H_2$  ground state is 16.6 eV. This is probably the dominant mechanism since the dissociation fraction is low.

The results for both  $H_2$  and  $D_2$  are very similar. While the potentials are slightly different the near electrode excitation is seen to occur after the electrode is at its least negative with respect to the plasma. The strong positive peaks in the electrode current waveforms occur at this time. In both cases the electrode is positive with respect to the plasma, indicating a sheath collapse. This is a period during the rf cycle when electrons are accelerated towards the electrode, causing excitation of, and subsequent emission from, gas atoms in the near electrode region. This is an important observation since it appears to invalidate the argument that the near-electrode emission is an ion mass effect. The ion mass effect has been studied in fluid and PIC-MC models[12]. These correctly predicted the emission structure in hydrogen, using  $H_2^+$  as the dominant ion. No calculations have to date been made for  $D_2$ . Helium would have the same or intermediate ionic mass to  $D_2$  depending on which ion state is dominant. The models shows no evidence of near-electrode emission which is largely consistent with our measurements in He[14]. In our helium measurements the only indications of near-electrode emission are at lower pressures and highest powers where associated sheath collapsed is also observed in our potential measurements.

The close similarity of the two emission region structure in the  $H_2$  and  $D_2$ , and general lack of such structure in He plasmas indicates that the structure and hence field reversal are not solely due to ion mass effects but also involves the details of the atomic structure of the gas.

#### Acknowledgements

This work was supported by the UK Engineering and Physical Science Research Council.

#### References

- [1] Barnes R. M. and Winslow R. J., J. Phys. Chem., **82** (1978) 1869.
- [2] de Rosny V., Mosburg E.R., Abelson J.R., Devaud G. and Kerns R.C., J. Appl. Phys. **54** (1983) 2272.
- [3] Donnelly V.M., Flamm D.L. and Bruce R.H., J. Appl. Phys. **58** (1985) 2135.
- [4] Bletzing P. and de Joseph Jnr C. A., IEEE Trans. Plasma Sci. **PS-14** (1986)124.
- [5] Flamm D.L. and Donnelly V.M., J. Appl. Phys. **59** (1986) 1052.
- [6] Tochikubo F., Suzuki A., Kakuta S., Terazono Y. and Makabe T., J. Appl. Phys. **68** (1990) 5532.
- [7] Tochikubo F., Kokubo T., Kakuta S., Suzuki A. and Makabe T., J. Phys. D, **23** (1990) 1184.
- [8] Koehler W.E., Seeboeck R. J. and Rebentrost F., J. Phys. D: Appl. Phys. **24** (1991) 252.
- [9] Shimozuma M., Tochitani G. and Tagashira H., J. Appl. Phys. **70** (1991) 645.
- [10] Tochikubo F., Makabe T., Kakuta S. and Suzuki A., J. Appl. Phys. **71** (1992) 2143.
- [11] Djurovic S., Roberts J.R., Sobolewski M.A. and Olthoff J.K., J. Res. Natl. Inst. Stand. Technol. **98** (1993) 159 .
- [12] Leroy O., Stratil P., Perrin J., Jolly J. and Belenguer P., J. Phys. D: Appl. Phys., **28** (1995) 500 .
- [13] Mahony C.M.O., Al Wazzan R. and Graham W.G., Appl. Phys. Lett. **71** (1997) 608.
- [14] Graham W.G. and Mahony C.M.O., "Experimental studies of rf sheaths." Proc. NATO ARW on Kinetic modelling of rf discharges (Plenum Publishing. to be published).
- [15] Mutsukara N., Koyabashi K. and Machi Y., J. Appl. Phys. **66** (1989) 468.
- [16] Kakuta S., Kitajima T., Okabe Y. and Makabe T., Jpn. J. Appl. Phys., **33** (1994) 4335.
- [17] Radovanov S.B., Dzierzega K., Roberts J.R. and Olthoff J.K., Appl. Phys. Lett., **66** (1995) 263.
- [18] Sato A. and Lieberman M.A., J. Appl. Phys., **68** (1990) 6117.
- [19] Ruzik D.N. and Wilson J.L., J. Vac. Sci. & Technol., **A8** (1990) 3746.
- [20] Okuno Y. and Fujita H.J., Appl. Phys., **70** (1991) 642 .
- [21] Sommerer T.J., Hitchon W.N.G. and Lawler J.E., Phys. Rev. Lett., **63** (1989) 2361.
- [22] Sommerer T.J., Hitchon W.N.G., Harvey R.E.P. and Lawler J.E., Phys. Rev. A., **43** (1991) 4552.
- [23] Surendra M. and Graves D.B., Phys. Rev. Lett., **66**, 1469 (1991) and IEEE Trans. Plasma Sci., **19** (1991) 144 .



- [24] Turner M.M. and Hopkins M.B., Phys. Rev. Lett., **69** (1992) 3511.
- [25] Vender D. and Boswell R.W., J. Vac. Sci. Technol., **A10** (1992) 331.
- [26] Hargis Jr. P.J., Greenberg K.E., Miller P.A., Gerardo J.B., Torczymski J.R., Roley M.E., Hebner G.A., Roberts J.R., Olthoff J.K., Whetstone J.R., Van Brunt R.J., Sobolewski M.M., Anderson H.M., Splichal M.P., Mock J.L. Bletzinger P., Garscadden A., Gottscho R.A., Selwyn G., Dalvie M., Heidenreich J.E., Bitterbaugh J. W., Brake M.L., Passov M. L., Pender J., Lujan A., Elta M.E., Graves D.B., Sawin H.H., Kushner M.J., Verdeyen. T., Horwath R. and Turner T.R. , Rev. Sci. Instrum. **65** (1994) 140.
- [27] Neynaber R.H. and Trujillo S.M., Phys. Rev. **167** (1968) 63.
- [28] Tserepi A.D., Dunlop J.R., Preppernau B.L. and Miller T.A., J. Appl. Phys. **72** (1992) 2838.

## Interaction of Grains in Dusty Plasmas

A.M. Ignatov

*General Physics Institute, 38 Vavilova Str., Moscow 117942, Russia*

**Abstract.** Plasma absorption by dust grains results in anisotropy of plasma distribution function. This yields the effective attractive interaction between grains. Here a brief review of physical properties of this interaction is given. First we demonstrate that there is the attracting force between two grains obeying the inverse square law. Then a set of kinetic equations taking into account both attracting and repulsing forces is proposed. We study a simple model of a dust cloud consisting of finite number of grains. It is shown that even within gaseous approximation a dust cloud is a compact object with a sharp boundary. Finally, we discuss recent experiments aimed to detecting the attractive force between massive bodies

## 1 Introduction

Both space and laboratory low-temperature plasmas are often polluted with a certain number of dust grains. The size of these grains varies over a very wide range from nanometers to micrometers. Since a dust grain can carry additional electric charge, sometimes as high as  $10^4$  elementary charges, whose amount depends on the state of surrounding plasma, relatively low dust concentration can crucially change the plasma properties. This medium composed of several species of particles with fixed charge (electrons and ions) and variable charge (dust grains), which is referred to as a dusty plasma, exhibits many specific properties.

During the recent decade a great number of studies on dusty plasmas were performed. The review of these studies may be found, e.g., in Refs. [1,2]. Also, many original works on dusty plasma were presented at the ICPIG meetings. In the present paper, we focus on the following specific problem. If the dust grain is relatively large (more than several micrometers under typical laboratory conditions), it behaves like a floating Langmuir probe. A grain absorbs plasma particles hitting its surface and tunes its charge and electric potential in such a way that the net electric current is zero. As a result, the net charge of an individual grain is always negative. However, the dust often forms various patterns, like crystals, clusters or clouds. Obviously, to maintain the stability of the ensemble of likely charged particles some additional, either external or attracting intrinsic forces are required.

Although under laboratory conditions external forces like the external electrostatic field or the gravitational field of the Earth are extremely important, there is question of general interest: If there are any attracting forces between likely charged particles in a medium? Generally, there are numerous examples of the so-called overscreening, but in application to dusty plasma a first attempt to answer this question, to my knowledge, was made only three years ago by Tsytovich [3]. He showed that the electrostatic interaction energy of two grains decreases as the distance between them decreases to the values less than the Debye length, and this is a hint at the electrostatic attraction of some kind. Another possibility discussed in the literature is that the static dielectric permittivity in nonequilibrium plasmas often changes its sign, that results in the oscillatory interparticle potential.

For example, this may arise due to the ion flow past the dust grains [4,5]. Of interest also is the nonlinear Debye screening discussed in application to colloidal plasmas [6]. This process resembles the formation of the hydrogen bond in electrolytes: two particulates (macroions) each carrying sufficiently large negative charge can form a stable complex collecting a cloud of positive charges between them.

All mentioned processes can provide the attraction of grains at relatively small distance, of the order of the Debye length. In the present paper we focus on another mechanism giving rise to the attraction at much larger distances [7,8]. It originates from a mechanistic theory of the universal gravitation proposed in the 18-th century by G.L. Lesage and may be outlined as follows [9]. He was an adept of the ancient atomistics and it was evident for him that the ether consists of tiny atoms moving in random directions. Lesage's main hypothesis was that an ether atom hitting a massive body loses a small part of its vital force. If there are two bodies, then the ether flux coming through the first body is smaller in the direction of the second body, hence, the effective attracting force must arise. The reduction of the ether flux and, consequently, the force acting upon the first body are proportional to the solid angle, at which the second body is visible, and the latter is proportional to the inverse distance squared.

Although this ingenuous theory has many obvious drawbacks and, to tell the truth, even two hundred years ago very few accepted it seriously, it is evident that a similar process may be relevant in a plasma. Since the interaction of plasma particles with the solid surface is practically always inelastic, we can apply Lesage's theory to a plasma merely replacing in his reasoning the words "vital force" by the more habitual "momentum". Moreover, a plasma may be even a more favourable medium for providing the attraction of this kind because a massive body often absorbs plasma particles. In other words, a massive body in a plasma, e.g., a floating probe, creates a converging plasma flow, and evidently there should arise some drag force acting upon any other object in its vicinity [7,8].

The existence of this force was confirmed in computer experiments by Khodataev et al. [10]. Recently two attempts were made to measure the force between massive bodies in a plasma which we briefly describe below.

This paper is organised as follows. In section 2 the essence of the Lesage gravity is illustrated using a simple model of two grains with absorbing surface. Then we formulate the kinetic equations for dusty plasma taking into account absorption of plasma by dust grains (Sec. 3). In section 4 a simple model of a dust cloud sustained by the Lesage gravity is discussed. We briefly describe the preliminary results of two known experiments aimed to detect this interaction in Sec. 5.

## 2 Attraction of two dust grains

### 2.1 Large grains

We start with the case of relatively large dust grains with radiuses,  $a_i$ , exceeding the Debye length,  $\lambda_D$ , of the surrounding plasma. Let us first consider the dynamics of ions. Since the electric potential is nonzero in the thin layer around the grain only, we ignore the influence of the electric field in the bulk of the plasma. So it is natural to assume that the only way the grain influences the ionic distribution is the absorption of ions hitting its surface.

The trajectories of plasma particles deviate from straight lines at the nearest vicinity of dust grains, that is, the ionic distribution function is zero if a straight line coming from infinity to the observation point  $\mathbf{r}$  intersects one of the grains. With a set of spherical dust grains placed at  $\mathbf{r} = \mathbf{R}_i$ , this distribution may be written as

$$f^{(i)}(\mathbf{r}, \mathbf{v}) = f_0^{(i)}(\mathbf{v}) \prod_i g\left(\mathbf{v}, \frac{\mathbf{r} - \mathbf{R}_i}{a_i}\right), \quad (1)$$

where  $g(\mathbf{v}, \mathbf{x}) = \theta(\mathbf{v}\sqrt{\mathbf{x}^2 - 1} - \mathbf{v}\mathbf{x})$  and  $f_0^{(i)}(\mathbf{v})$  is the distribution function at infinity. This distribution function is zero inside a certain number of cones in the velocity space and it is equal to the unperturbed distribution otherwise.

The force upon a grain is the momentum flux through its surface. It was evaluated using the distribution (1) and the force between two grains was found to be [8]

$$F = \frac{3\pi}{4} n_0^{(i)} T_i \frac{a_1^2 a_2^2}{R^2} \quad (2)$$

where  $n_0^{(i)}$  is the density,  $T_i$  is the ion temperature and  $R$  is the distance between the centres of the grains. Since in performing these calculations we have just improved the Lesage's reasoning in a little more advanced fashion, in what follows this mechanism of attraction is called the Lesage gravity. Of interest is that this model reproduces the well-known feature of the Newtonian gravitation: two spherical bodies interact as point masses.

The force (2) is independent of the ion mass, and the same expression, at first sight, should be valid for electrons also. However, in assuming the total absorption, the current density of electrons and ions entering the grain within this model is by the order of magnitude the random current,  $n_0^\alpha \sqrt{T_\alpha/m_\alpha}$  ( $\alpha = e, i$ ), while in equilibrium the electron current must be equal to the ion current. This means that only a small part of electrons ( $\sqrt{m_e/m_i}$  if  $T_e \approx T_i$ ) is actually absorbed, and the remaining part is scattered by the Debye shield. Since  $a \gg \lambda_D$ , the scattering results in mirror reflection for the bulk of electrons.

Evidently, for the Lesage gravity to exist some energy absorption in particle-dust collisions is required. The mirror reflection gives no rise to the anisotropy and the electron distribution function remains nearly Maxwellian. Thus the electron component of the attracting force is at least  $\sqrt{m_e/m_i}$  times less than the ion force (2) and, therefore, is negligible.

It is of importance that, unlike the genuine gravitation, the Lesage gravity is a non-pairwise interaction. Moreover, with other types of boundary conditions at the grains, Newton's third law may no longer hold. Generally, such concepts as a field or a potential are inapplicable to this force [8].

## 2.2 Small grains

Let us estimate now how the Lesage gravity is modified if the grains' radii are much smaller than the Debye length. Suppose there is a single dust grain with the radius  $a_1$ . Let us denote the ion current entering the grain as  $eJ_i$ ; by the order of magnitude  $J_i = a_1^2 n_0^{(i)} \sqrt{T_i/m_i}$ . Due to the conservation of the number of ions in a plasma, there is a constant flow converging to the grain with the velocity

$$v_r(r) = -\frac{1}{4\pi r^2} \frac{J_i}{n^{(i)}(r)}. \quad (3)$$

At the distance exceeding few Debye lengths we can neglect the deviation of ion density from its equilibrium value,  $n^{(i)}(r) \approx n_0^{(i)}$ . It should be noted that since Eq. (3) is a solution of the continuity equation, it is insensitive to all types of collisions conserving the number of particles.

Suppose that there is some object, say, another grain with radius  $a_2$ . Since the second grain is immersed into the plasma flow, there should be the drag force acting upon it. Evidently, the direction of the drag corresponds to the effective attraction of the grains, and if  $v_r(r)$  is small compared to the ion thermal velocity, the force has to be proportional to  $v_r(r)$ .

The ion drag force acting upon a dust grain was evaluated in [12]. Generally, there are two processes: the drag provided by ions collected by the grain, which is an analogue of the discussed above Lesage force, and the momentum transfer by ions scattered in the electric field of the grain, which was discarded in the previous discussion. (Again, the electron drag force is negligible.) If

$a \ll \lambda_D$ , then both these forces are of the same order of magnitude and the total force may be estimated as  $F \approx a_2^2 \sqrt{T_i m_i n_i} v_r(r)$ . Combining the latter with Eq.(3) results in

$$F \approx n_0^{(i)} T_i \frac{a_1^2 a_2^2}{R^2} \quad (4)$$

Comparing this with Eq.(2) we conclude that the dependence of the attracting force on the ratio  $a/\lambda_D$  is rather weak and is introduced by a coefficient of order unity.

### 3 Kinetic equations

Due to the mentioned peculiarities of the Lasage gravity we cannot use a pairwise potential of any kind to describe the interaction of grains in a large ensemble. The only way to take into account this attracting force is simultaneous solution of kinetic equations for plasma and dust. Unfortunately, the problem of consistent derivation of kinetic equations for a dusty plasma, to my knowledge, is far from satisfactory solution, and we have no other choice but to guess these equations. Here the following set of kinetic equations describing a large number of dust grains immersed in a plasma is used [11]:

$$\frac{\partial f_\alpha(t, \mathbf{r}, \mathbf{p})}{\partial t} + \frac{\mathbf{p}}{m_\alpha} \frac{\partial f_\alpha(t, \mathbf{r}, \mathbf{p})}{\partial \mathbf{r}} + e_\alpha \mathbf{E}(\mathbf{r}) \frac{\partial f_\alpha(t, \mathbf{r}, \mathbf{p})}{\partial \mathbf{p}} = I_\alpha^{(a)} + I_\alpha^{(c)} \quad (5)$$

$$\frac{\partial f_d(t, \mathbf{r}, \mathbf{p}, Q)}{\partial t} + \frac{\mathbf{p}}{m_d} \frac{\partial f_d(t, \mathbf{r}, \mathbf{p}, Q)}{\partial \mathbf{r}} - Q \mathbf{E} \frac{\partial f_d(t, \mathbf{r}, \mathbf{p}, Q)}{\partial \mathbf{p}} = I_d^{(a)} + I_d^{(c)}, \quad (6)$$

$$\nabla \mathbf{E} = 4\pi \int d\mathbf{p} \left( \sum_\alpha e_\alpha f_\alpha(\mathbf{r}, \mathbf{p}) - \int dQ Q f_d(\mathbf{r}, \mathbf{p}, Q) \right) \quad (7)$$

Electron and ion variables here are distinguished with the lower index  $\alpha = e, i$ , the charge of the dust is  $-Q < 0$ , other notation is standard. Since the charge of each grain is determined by the state of the surrounding plasma, in using the kinetic approach it should be treated as an additional intrinsic variable of the dust component, i.e., the dust distribution function,  $f_d$ , besides the coordinate and the momentum depends on the grain charge,  $Q$ .

Generally, there are many various collisional processes in a dusty plasma. For simplicity only two of them are taken into account: (i) inelastic collisions of plasma particles with dust grains resulting in absorption of electrons and ions, and (ii) elastic scattering of plasma particles in the electric field of a grain. The collision terms in the right-hand sides of Eqs. (5,6) are obtained considering the probabilities of corresponding processes [11]. Assuming that all dust grains are of the same size,  $a$ , small compared to the Debye length and  $m_\alpha \ll m_d$ , the terms corresponding to the absorption of a plasma by dust grains look like:

$$I_\alpha^{(a)}(\mathbf{r}, \mathbf{p}) = - \int dQ v_\alpha \sigma(v_\alpha, Q) n_d(\mathbf{r}, Q) f_\alpha(\mathbf{r}, \mathbf{p}); \quad \alpha = e, i \quad (8)$$

$$I_d^{(a)}(\mathbf{r}, \mathbf{p}, Q) = - \frac{\partial}{\partial \mathbf{p}} \left( \mathbf{A}^{(a)}(\mathbf{r}) f_d(\mathbf{r}, \mathbf{p}, Q) \right) - \frac{\partial}{\partial Q} \left( J(\mathbf{r}, Q) f_d(\mathbf{r}, \mathbf{p}, Q) \right), \quad (9)$$

where  $v_\alpha = p/m_\alpha$ ,

$$\begin{aligned} n_d(\mathbf{r}, Q) &= \int d\mathbf{p} f_d(\mathbf{r}, \mathbf{p}, Q) \\ J(\mathbf{r}, Q) &= \sum_{\alpha=e,i} e_\alpha \int d\mathbf{p} v_\alpha \sigma_\alpha(v_\alpha, Q) f_\alpha(\mathbf{r}, \mathbf{p}) \\ \mathbf{A}^{(a)}(\mathbf{r}) &= \sum_{\alpha=e,i} \int d\mathbf{p} \mathbf{p} v_\alpha \sigma_\alpha(v_\alpha, Q) f_\alpha(\mathbf{r}, \mathbf{p}). \end{aligned} \quad (10)$$

The physical meaning of these quantities is evident:  $J(\mathbf{r}, Q)$  is the net electric current at a dust grain with the charge  $Q$  situated at the point  $\mathbf{r}$ , while  $\mathbf{A}^{(a)}(\mathbf{r})$  is the drag force due to plasma absorption acting upon it, that is, the Lesage force. The absorption cross-section,  $\sigma_\alpha$ , is usually obtained assuming that a grain traps all particles coming at the distance smaller than its radius from the point charge  $-Q$  with the Coulomb potential:

$$\sigma_\alpha(v, Q) = \pi a^2 \theta \left( 1 + \frac{2Qe_\alpha}{am_\alpha v^2} \right). \quad (11)$$

Electrons are repulsed from a grain ( $e_e < 0$ ) and this cross-section is nonzero for rather large  $v$ , normally exceeding several thermal velocities. As for ions, the expression (11) is divergent for small values of velocity, that is, all slow ions are collected by a single grain. To avoid this evidently non-physical divergence some kind of cut-off is needed, which is discussed below.

Coulomb scattering is introduced by collision terms in Eqs. (5,6) marked with the upper index (c). As a simplest approximation we use Landau's collision integral resulting in additional Coulomb drag force

$$I_d^{(c)}(\mathbf{r}, \mathbf{p}, Q) = -\frac{\partial}{\partial \mathbf{p}} \left( \mathbf{A}^{(c)}(\mathbf{r}) f_d(\mathbf{r}, \mathbf{p}, Q) \right), \quad (12)$$

where

$$\mathbf{A}^{(c)}(\mathbf{r}) = \sum_\alpha 4\pi e^2 Q^2 L m_\alpha \int d\mathbf{p} \frac{\mathbf{p}}{p^3} f_\alpha(\mathbf{r}, \mathbf{p}). \quad (13)$$

and  $L = \ln(\lambda_D/a)$ . Coulombian collision term for the plasma component in Eq. (5) is given by the Landau integral.

Kinetic equations (5, 6) combined with collision terms (8, 9, 12) and the Poisson equation (7) form a complete set. This set guarantees the conservation of the total charge and momentum of the plasma-dust system, but the energy and the number of plasma particles are no longer conserved. It is evident that to describe a steady state of a dusty plasma within this model one should take into account external plasma sources of some kind. In what follows we consider a compact dust pattern consisting of finite number of grains and assume that these sources are removed to infinity where the plasma distribution function is Maxwellian.

It should be noted the kinetic equations written above obviously describe nonstationary grain charging. The equation for the average grain charge is easily obtained integrating Eq. (6) over  $\mathbf{p}$  and  $Q$ . However, it generally differs from that proposed in [13] where the dispersion over the grain charge was neglected.

## 4 Dust cloud

### 4.1 Basic equations

In this section we discuss the simplest model of a rarefied compact dust cloud. Let us consider an ensemble of  $N$  ( $N \gg 1$ ) immobile dust grains randomly distributed in space. Assuming that the plasma is steady, *i.e.*, all time derivatives are zero, the first two momenta of Eq. (6) are written as

$$J(\mathbf{r}, Q) n_d(\mathbf{r}, Q) = 0, \quad (14)$$

$$(Q\mathbf{E}(\mathbf{r}) - \mathbf{A}(\mathbf{r})) n_d(\mathbf{r}, Q) = 0, \quad (15)$$

where  $\mathbf{A} = \mathbf{A}^{(a)} + \mathbf{A}^{(c)}$  is the total drag force acting upon the dust component. Eq. (14) guarantees the absence of the net electric current in the equilibrium state. Its only solution is  $n_d(\mathbf{r}, Q) = n_d(\mathbf{r}) \delta(Q - Q_0(\mathbf{r}))$ , where  $Q_0(\mathbf{r})$  is the self-consistent charge of the dust component obeying the

relation  $J(\mathbf{r}, Q_0(\mathbf{r})) = 0$ . The value of the grain charge is estimated as  $Q \approx aT_e/e$ . It is determined mainly by the electron temperature and its dependence on other plasma parameters is fairly weak. In what follows we ignore the spatial variation of the grain charge.

The structure of the dust cloud is described by the equation of the momentum balance (15). Evidently, in the absence of external forces the cloud is spherically symmetric. To evaluate the Lesage force we have to solve the kinetic equations (5) with some dust distribution  $n_d(r)$ . This solution was obtained in powers of the dust density and the linear term of expansion was found to be [11]

$$f_\alpha(\mathbf{p}, \mathbf{r}) = f_{0\alpha}(p) \left( 1 - \sigma_\alpha(v_\alpha) \lambda(r, \mathbf{v}_\alpha) - \frac{e_\alpha}{T_\alpha} \phi(r) \right), \quad (16)$$

where  $\mathbf{E} = -\nabla\phi$ ,

$$\lambda(r, \mathbf{v}) = \int_{R_0}^{\infty} \frac{r' dr'}{\sqrt{r'^2 - R_0^2}} n_d(r') + \text{sign}(v_r) \int_{R_0}^r \frac{r' dr'}{\sqrt{r'^2 - R_0^2}} n_d(r') \quad (17)$$

and  $R_0 = |\mathbf{r} \times \mathbf{v}|/v$ . The deviation of the distribution function (16) from its equilibrium value is provided, first, by the electric potential,  $\phi(r)$ , and second, by the plasma absorption. The latter contribution is introduced by the non-local dependence on the dust density because the probability of absorbing a plasma particle depends on a path it reaches the observation point.

Straightforward integration of Eq. (16) results in expressions for the plasma density and the Lesage force acting upon the dust component. The density deviation is caused by the self-consistent electric potential and the plasma absorption

$$n_\alpha(r) = n_0 \left( 1 - \frac{e_\alpha}{T_\alpha} \phi(r) - \kappa_\alpha(r) \right), \quad (18)$$

where

$$\kappa_\alpha(r) = \frac{1}{2n_0} \int_0^\infty v^2 dv \sigma_\alpha(v) f_{0\alpha}(v) \int_0^\infty \frac{r' dr'}{r} \ln \left| \frac{r+r'}{r-r'} \right| n_d(r') \quad (19)$$

The drag force,  $\mathbf{A}$ , is independent of the electric field and determined by the dust density only:

$$A_r = -\beta \frac{1}{r^2} \int_0^r r'^2 dr' n_d(r') \quad (20)$$

where

$$\beta = 4\pi \sum_\alpha \int_0^\infty dv f_{0\alpha}(v) \left\{ m_\alpha v^4 \sigma_\alpha(v)^2 + \frac{4\pi e^2 Q^2 L}{m_\alpha} \sigma_\alpha(v) \right\}. \quad (21)$$

Regardless the above mentioned singularity of the absorption cross-section (11), the integrals for the plasma density (19) and for the net electric current (10) are convergent. At the same time, the second term in the integrand of Eq. (21) diverges for small  $v$ . This divergence is provided by multiplication of two factors. On one hand, dust absorbs mostly slow ions, and, on the other hand, the Coulombian drag force given by Eq. (13) is very sensitive to the details of the distribution in a range of small ion velocities. (It is evident that the influence of the electrons is negligible.) Of importance is that the integrand in (21) behaves like  $1/v^2$ , that is, introducing any kind of cut-off one can hope for qualitative result only.

There are two ways to get rid of this divergence. First, one should take into account the nonlinear corrections to the distribution function (16). It is a complicated task which I managed to solve in the absence of the electric field only [12]. In this case the ionic distribution roughly behaves as

$\exp(-v_1^2/v^2)$ , where  $v_1 \approx v_{Ti} a N^{1/2}/R_0$  with  $R_0$  being the characteristic size of the dust cloud. Second, the cross-section (11) presumably cannot exceed  $\pi\lambda_D^2$  that results in another cut-off velocity  $v_2 \approx v_{Ti} a/\lambda_D$ . In the following estimations the second cut-off velocity is used — this mechanism prevails if the total number of grains is not too large, namely,  $N \ll R_0^2/\lambda_D^2$ . In this case the integral (21) is estimated as  $\beta \approx n_0 a^3 \lambda_D T_i$ .

## 4.2 Force balance

The steady state of a dust cloud is described by the condition of the momentum balance (15) with the drag force given by (20) combined with the Poisson equation

$$\Delta\phi - \frac{1}{r_D^2}\phi = 4\pi \left( Qn_d(r) - n_0 \sum_{\alpha} e_{\alpha} \kappa_{\alpha}(r) \right). \quad (22)$$

Consider first the force balance far from the cloud. Since the total number of particles is finite, the dust density should decrease at large distances,  $n_d(r) < 1/r^3$ . This means that the drag force (20) behaves like  $A_r \approx \beta N/4\pi r^2$ . As it follows from the integral (19),  $\kappa_{\alpha}(r) \propto 1/r^2$  at  $r \rightarrow \infty$ , that is the potential  $\phi(r) \propto 1/r^2$  and the electric field  $E_r \propto 1/r^3$ . Therefore, the force attracting grains at large distance always exceeds the repulsing electric force.

In this situation, the only way to satisfy the momentum balance equation (15) is to put  $n_d(r) = 0$ . However, the dust density is not identically zero, that is, there should exist some limiting radius,  $R_0$ , such that  $n_d(r) = 0$ ,  $QE_r < A_r$  for  $r > R_0$ , and  $n_d(r) \neq 0$ ,  $QE_r = A_r$  for  $r < R_0$ . In other words, the plasma-dust cloud is not a diffuse object with smooth density profile, but it is a compact formation with a sharp boundary. It should be stressed that the asymptotic behaviour of attracting and repulsing forces is of geometrical origin, that is, this conclusion is independent of the problems with evaluating the drag coefficient (21).

To determine the radius of the dust cloud let us consider the force balance inside it. Assuming the  $R_0 \gg \lambda_D$ , we implement Eq. (20) and the plasma neutrality condition  $\sum_{\alpha} e_{\alpha} n_{\alpha} - Qn_d = 0$  to rewrite the force balance equation as

$$\frac{1}{r^2} \frac{d}{dr} r^2 \frac{d}{dr} \left( n_d(r) + \frac{n_0}{Q} \sum_{\alpha} e_{\alpha} \kappa_{\alpha}(r) \right) = -\frac{n_d(r)}{b^2}, \quad (23)$$

where

$$b^2 = \frac{4\pi Q^2 \lambda_D^2}{\beta} \quad (24)$$

fixes the spatial scale of the cloud, that is,  $R_0 \propto b$ . According to the estimations written above,  $b^2 \approx \lambda_D^3/a$ . The second term in the left-hand side of Eq. (23) arises due to the absorption of plasma. It is estimated as  $n_d a/\lambda_D$ , therefore, evaluating the electric field inside the cloud we can neglect the absorption. Eq. (23) is now easily solved resulting in

$$n_d(r) = C \frac{\sin(r/b)}{r}; \quad r < R_0 \quad (25)$$

where  $C$  is a normalising coefficient. Since the expression (25) changes its sign as  $r$  exceeds  $\pi b$ , the cloud radius must be smaller than  $\pi b$ . On the other hand, any stepwise discontinuity of dust density would result in high electric field at the edge of the cloud, and it is impossible to counterbalance the strong repulsing force by the attracting drag force. Thus, the only way to maintain the force balance is to put  $R_0 = \pi b$ . In this case, the dust density at the edge of the cloud is zero, and no high electric field arises. The normalising coefficient,  $C$ , is now easily expressed in terms of the number of dust grains:

$$C = \frac{N}{4\pi^2 b^2}. \quad (26)$$



The range of validity of the expansion in powers of the dust density may now be written as  $N \ll \lambda_D/a$ . With larger number of dust grains, the absorption of slow ions becomes significant.

It should be noted that although all equations we have solved are linear, the problem in general is nonlinear — the condition of force balance (15) is quadratic in  $n_d$ . In a sense, the obtained solution may be regarded as a standing shock wave bounding a dust cloud.

## 5 Experiments

The Lesage force should act between any massive bodies immersed in a plasma. Although one can hardly perform direct measurement of the forces between small dust grains, recently two attempts were made to detect the force between larger objects immersed in a plasma.

Sergeichev and Sychoy [15] used two pieces of optical fiber 300  $\mu m$  in diameter and about 20 cm long fixed horizontally in the rf discharge. They observed some attraction of these strings with a microscope, but since it was very small, less than the diameter, no detailed measurements were performed.

Another attempt was made by the group from Arzamas-16 [11]. They have studied the attraction of massive bodies in the glow discharge in air (0.01 – 0.1 Torr). First, two glass threads about 100  $\mu m$  in diameter and 45 cm long were freely hung along the direction of the discharge current. The distance between threads was 6 mm. Observed with an unaided eye, the approach of their ends was roughly proportional to the discharge current. However, when the direction of the discharge current was perpendicular to the threads no approach was observed. It was supposed that in this situation the attraction is provided by the Ampere force in the current-carrying plasma.

In the second series of experiments they used two thin (10  $\mu m$ ) mylar ribbons ( $8 \times 100$  mm) 5 mm distant from each other hanging down across the discharge current. With the growing current, the attraction between ribbons increased, so they could even clap. Seemingly, with this geometry of the experiment, the Ampere force is excluded, while due to the difference in surface areas of ribbons and threads all surface effects should be strongly enhanced. That is why one can assume that the attraction between ribbons is provided by the discussed above Lesage force.

## Acknowledgments

I am grateful to Yu. Klimontovich, A. Rukhadze and S. Trigger for many helpful remarks, and to K. Sergeichev and I. Sychev for discussions of their unfinished experiments.

This work has been supported by the Russian Foundation for Basic Research, projects # 93-02-03357, # 96-02-16456.

## References

- [1] Dusty and Dirty Plasmas, Noise and Chaos in Space and in the Laboratory, Kikuchi H., Ed., N.-Y.: Plenum, 1994
- [2] Tsytovich V.N., Uspekhi fiz. nauk, **167**, 57 (1997).
- [3] Tsytovich V.N., Comm. Plasma Phys., **15**, 349 (1994).
- [4] Vladimirov S.V. Nambu M., Phys.Rev. E, **52**, R2172 (1995)
- [5] Melanso F. Goree J. , J. Vac. Sci. Technol. A., **14**, 511(1996).
- [6] Allakhyarov E.A., Podlubny L.I., Schram P., Trigger S.A. Physica A., **220**, 349(1995)
- [7] Ignatov A.M., Bull. Lebedev Physics Inst. # 1-2, 58 (1995).

- [8] Ignatov A.M., Fizika plasmy (Plasma Physics Reports), **22**, 648 (1996).
- [9] Rosenberger F., Die Geschichte der Physik, Dritter Teil, Braunschweig (1887)
- [10] Khodataev Ya., Bingham R., Tarakanov V., Tsytovich V., Fizika plasmy (Plasma Physics Reports) **22**, 1028 (1996).
- [11] Ignatov A.M., Fizika plasmy (Plasma Physics Reports), to be published.
- [12] Barnes M.S., Keller J.H., O'Neil J.A., Coultas D.H., Phys. Rev. Lett., **68**, 313 (1992).
- [13] Sitenko A.G., Zagorodny A.G., Chutov Yu.I., Schram P., Tsytovich V.N., Plasma Phys. Control. Fusion, **38**, A105 (1996).
- [14] Sergeichev K.F., Sychev I.A. , private communication.
- [15] Dubinov A.E., Zhdanov V.S., Ignatov A.M., Kornilov S.Yu., Sadovoi S.A., Selemir V.D., Bull. Lebedev Physics Inst. # 7-8 ( 1997), to be published

## The Switching Dynamics of the Plasma Addressed Liquid Crystal Display

K.J. Ilcisin, T.S. Buzak and G.J. Parker\*

*Technical Visions Inc., M/S 46-944, 14000 S.W. Karl Braun Dr., Beaverton, OR 97077, U.S.A.*

*\* Lawrence Livermore National Laboratory, P.O. Box 808, L-418, Livermore, CA 94551, U.S.A.*

**Abstract:** The plasma addressed liquid crystal display (PALC) is a flat, large area, full-colour television and monitor technology made possible through the unique application of the properties of an ionized gas. Liquid crystal displays require an active switching element at the location of each pixel. The PALC display uses a plasma switch to address each of the display pixels, replacing typically used semiconductor devices. The use of the plasma switch permits the manufacture, in very large sizes, of a display possessing excellent image quality. The performance of the PALC display is intrinsically related to the behaviour of the plasma used as the switching element. This paper reviews the trends that led to the development of the PALC display, describes the operating principals, and examines, in detail, one of the many areas of ongoing plasma physics research. The successful development of a model, which agrees with the measured decay behaviour of the plasma, contributed to a significant improvement in the performance of the PALC display.

### 1. INTRODUCTION

For decades, "Hang on the wall" TVs have been conjured up in the minds of display researchers and science fiction writers alike. The writers have recently been infuriated by the limits being placed on their imaginations as display researchers have been successful in developing flat panel displays (FPD). Several display technologies have been invented by groups intent on replacing the CRT. These devices are found in a multitude of applications from calculators to lap-top computer monitors. Most of these technologies, however, are limited in maximum diagonal size to less than 65 cm and are not suitable for use as TVs or desktop monitors. Even the ubiquitous Thin Film Transistor (TFT) active matrix liquid crystal display (AMLCD)—the performance leader in FPDs used in the majority of the world's lap-top computers—becomes exceedingly difficult to manufacture in sizes approaching 50 cm. This size limitation rises from the use of semiconductor devices and their related manufacturing constraints. Wafer scale integration on substrates with surface areas exceeding 1,000 cm<sup>2</sup> is a tremendously difficult task.

Two alternative display technologies have emerged as the replacement for the CRT in large sizes. Both of these technologies have in common their use of a plasma, and are referred to as plasma addressed displays. The first is the plasma addressed liquid crystal display or PALC, the other is the plasma addressed phosphor display or PDP. The difference between these two technologies is the reliance on different plasma phenomena for their operation. PDP panels utilize the UV emission from a plasma to excite phosphor[1]. In contrast, the PALC display uses the electrical properties of a glow discharge to act as a high performance, and easily manufactured, switching device[2]. PALC technology, invented in 1990, permits the manufacture of a very large AMLCDs. The PALC display embodies the performance characteristics of current AMLCDs—high contrast, high brightness, full motion video and full gray scale fidelity—but without the size limitation. As a testament to the ease of scalability for the PALC display technology, it is edifying to compare the recent advances in the size of the PALC display. In 1990 a 15 cm display was introduced, a 40 cm PALC monitor was demonstrated in 1993[3], a 64 cm wide format TV was developed in 1996[4], and most recently, plans were announced for the demonstration of an over 100 cm PALC display in early 1998. For comparison, size increases for semiconductor devices have averaged about 2 cm a year during the past two decades.

We organized this paper as follows. In Section 2, we detail the operating principles of a PALC display. In Section 3, we describe the computational model used to investigate the dynamics of the plasma switch. Finally, in Section 4, we illustrate how the knowledge gained from the computations and measurements resulted in a significant improvement in the performance of the PALC display.

## 2. PLASMA ADDRESSING OF LIQUID CRYSTAL DISPLAYS

The quality of the visual image of an AMLCD is influenced by the performance and properties of the active matrix switch. For TFT AMLCDs, which rely on semiconductor switches, the physics of the device is reasonably well understood. In contrast, the switch in the PALC display represents a relatively new regime of study, as the physical geometries, time scales of interest, and operating conditions differ significantly from typical experimental devices. The following sections illustrate how a glow discharge functions as an active matrix switch and how the properties of this switch influence display performance.

### 2.1 The Glow Discharge Tube as a Three Terminal Switch

The plasma addressing technique relies on the properties of a confined, ionized gas and is embodied in a structure that can be used as an electrical switch. It is well known, from probe measurements, that the plasma potential of a cylindrically symmetric discharge tube is very near the anode potential for most of the tube volume, except near the cathode region where one measures the profile of the cathode fall. This effect, allows one to construct a hypothetical three terminal switch using a discharge tube and a voltage probe as illustrated in Figure 1.

The cathode connection can be thought of as a control or "gate" electrode. When the cathode voltage is switched on and the gas is ionized, the probe electrode appears electrically connected to the anode, here shown at ground potential. This would permit charging of the sampling capacitor. When the control electrode voltage is reduced below the plasma sustaining voltage, the plasma is extinguished and the probe electrode is no longer connected to the grounded anode. The charge stored on the sampling capacitor would remain fixed. The device sketched in Figure 1 behaves like a simple sample-and-hold circuit.

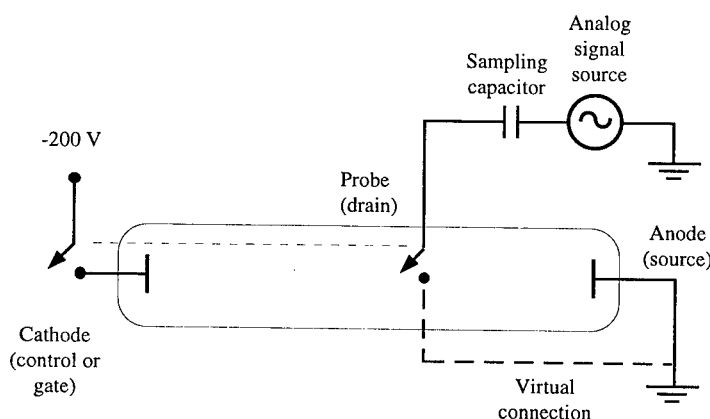


**Figure 1:** A sketch of a discharge tube configured as a sample-and-hold circuit using the tube as a three terminal switch.

The circuit would work equally well if the plasma switch were replaced by a conventional silicon field-effect transistor (FET). When compared to a FET switch, the plasma cathode electrode plays a role similar to a transistor gate electrode; the anode and probe electrodes take on roles similar to the transistor source and drain electrodes; and the plasma sustain voltage is analogous to the gate-source threshold voltage.

## 2.2 Plasma Addressing of a Liquid Crystal Display

A description of how a display device can be developed utilizing the switching device described in the previous section can be accomplished with the aid of Figure 2 which illustrates a partial cross-section of a PALC display. An electro-optic layer—a twisted nematic liquid crystal layer—and a protective dielectric layer are contained between two sheets of glass. The top sheet is patterned with transparent indium-tin-oxide (ITO) conductive stripes; the bottom sheet has in its surface parallel grooves or channels. Each channel contains two parallel electrodes that run the entire channel length. The anodes are shown as grounded. The cathodes are partially hidden by the channel walls and electrically connected to the strobe drivers. The function of the “probe connection” is achieved by the storage of charge on the bottom surface of the dielectric which acts as the “bottom” of the pixel capacitor.

Active matrix displays update images by writing each horizontal line of an image frame sequentially. During one horizontal line time, analog data corresponding to a single line of video appears on the data outputs and the transparent conductors. Except for the one row where the gas is ionized, the analog voltage has no effect on light transmissivity of the liquid crystal since there is no electrical connection or conductor on the bottom side of the liquid crystal. Along the line above the ionized channel, however, the pixel capacitance can charge to the value determined by the data voltage. In effect, the plasma completes the electrical circuit between the data electrodes and the grounded channel anode.

For each pixel along a channel, the gas discharge functions as an electrical switch that changes between a conducting (plasma) state and a nonconducting (de-ionized) state in response to the applied data strobe signal. Analog data values are sampled and held in a row-by-row basis, sequentially addressing an entire image field of the liquid crystal layer. It is important to note that this is not an emissive plasma display: there is no image in the barely visible plasma glow. Power consumption is low: only one line of plasma is on at any given time, and then on only for a fraction of a horizontal line time.

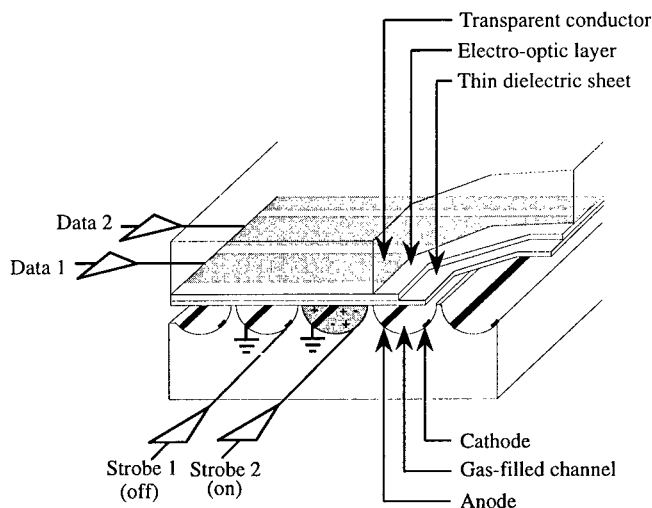


**Figure 2:** A partial cross-section of a PALC panel showing several channels and data electrodes. Channel 2 has a strobe voltage applied, filling that channel with conductive ions and electrons. Voltages from the data electrodes are captured at the intersections where the data electrodes cross channel 2.

## 2.3 Addressability, Data Capture, and Switching Speed Requirements

The addressability of a display—the number of lines that can be addressed in a single frame time—depends upon the speed with which any single line can be addressed. A modern high information content display, like a computer display or a high definition television display, requires an addressability of at least 1,000 lines with 60 Hz frame rates. This implies a minimum line time of approximately 16.6 $\mu$ s for progressively scanned displays, and 33.3  $\mu$ s for interlaced displays.

For a PALC display, line time is determined by the sum of the plasma initiation, data capture, and plasma decay times. Figure 3 illustrates this relationship.

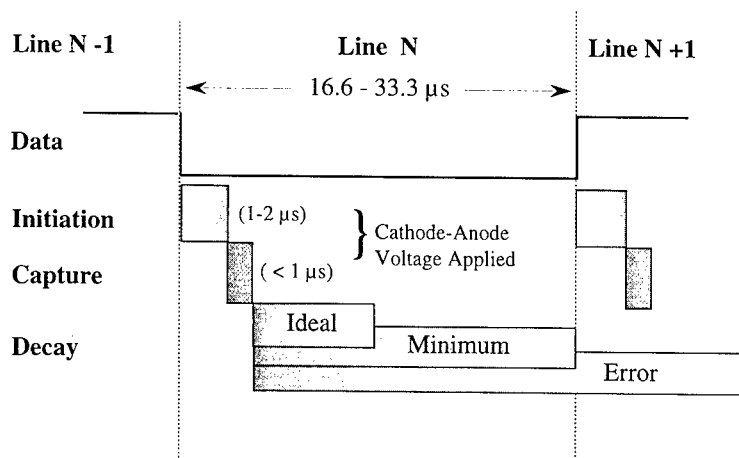


**Figure 3:** Horizontal line time requirements. One horizontal line time contains time segments for plasma initiation, data capture, and plasma decay.

The initiation time is the time it takes to turn the plasma on. This time is typically one to two microseconds. Although the initiation time can be established before the beginning of line time, the savings of time is minimal given the short time required for initiation.

The data capture time is the time for plasma to reach a steady state condition which is referred to as the active phase of the discharge. During this time, the pixel capacitance is charged to the value nominally close to that of the data voltage. Because of the low value of the pixel capacitance, data capture is very fast and can usually be held to less than one microsecond.

The most important time segment in a line time is the plasma decay time. The plasma must decay to a high resistivity before the image data can be changed to the values required for the next line. If the data is changed before the plasma has had an opportunity to decay, data from the subsequent line will be incorrectly captured. This is shown schematically in Figure 4, where for simplicity, the sheath layer present at the end of the active discharge was ignored.

Figure 4a) shows the conditions that exist just after the cathode voltage has been removed. A large density of charged particles exists in the gas volume, but there is nominally no net charge except at the surfaces. Correspondingly, the electric field exists predominately across the LC and dielectric layers and terminates near the bottom surface of the dielectric where a net negative surface charge layer is present for an applied positive data voltage. The voltage across the LC and dielectric layers is much larger than the applied voltage  $V_1$  at  $t = 0$ . This is due to the fact that the initial charge distribution reflects the cathode potential during the active phase. If the data voltage remains constant, then all of the free charge will diffuse to a surface or recombine. If no changes to the data voltage are made, the situation at  $t = \infty$  is shown in Figure 4b). A surface charge layer at the bottom of the dielectric surface produces an electric field across the LC layer corresponding to the applied data voltage  $V_1$ . The gas volume is essentially field free.

In Figure 4c), we examine the situation where at an intermediate time  $T_h$  the data voltage  $V_1$  is switched to a smaller value  $V_2$ . At  $T_h$  the surface charge layer is similar to that at  $t = \infty$ , and an electric field is impressed in the discharge volume. Although the net charge density is nominally zero, there can still be a large charged particle density. These charges are created through processes such as metastable-metastable collisions in the afterglow and will move in response to this applied field. In Figure 4d) we see that a change in applied voltage results in a different charge density and electric field at  $t = \infty$ . However, the final surface charge density, field and potential across the LC and dielectric layers is not equal to  $V_2$  but to some admixture of  $V_1$  and  $V_2$ . Thus, if the plasma has not completely decayed before the data voltage is changed for the subsequent horizontal line, an error occurs in the stored charge. Under these conditions, incorrect data capture can only be avoided by extending the line time, resulting in lower addressability.

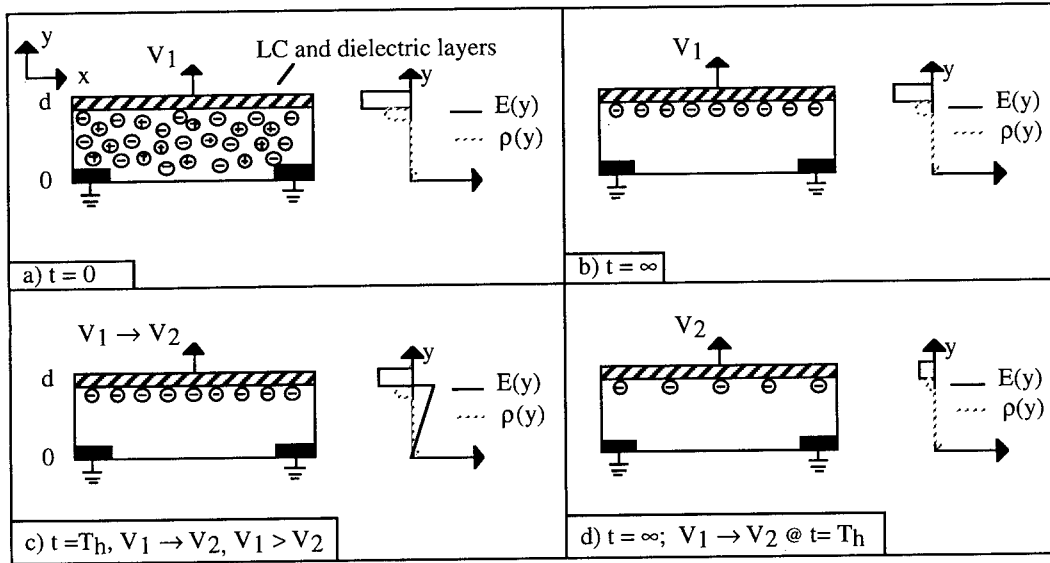


**Figure 4:** Figures a) and b) sketch the evolution of the charge and field profiles when the applied data voltage remains constant during the plasma decay period. Figures c) and d) illustrate the changes that occur when the data voltage is switched during the decay phase.

### 3. PLASMA COMPUTATIONAL MODEL

Due to the size and structure of the plasma channel in a typical PALC display, many experimental measurements are difficult, if not impossible. Accordingly, an efficient computational model of the PALC display was developed to further the fundamental understanding of the device characteristics and possible approaches to improving the performance. In this section, we first outline the computational method used to simulate the plasma and then describe some of the results from the model.

#### 3.1 Computational Model

The computational approach used in simulation of the plasma channel is a formidable task. During the 'active' or 'on' state of the plasma channel, large variations of the electric field occur inside a small plasma region. The typical approach of using hydrodynamic equations with the local field approximation (where the electron collision rates depend only on the ratio of the electric field and neutral number density) would lead to large errors in collision rates spatially, temporally, and in magnitude. In addition, during the 'afterglow' or 'off' state of the plasma channel high energy electrons are produced from metastable-metastable atom ionization thus making the electron energy distribution function non-Maxwellian which is what is usually assumed in such schemes. In contrast, a completely kinetic approach where the Boltzmann equation is solved for each particle species would be completely computationally unfeasible at the large neutral densities due to the extreme range in time scales: electron collision ( $\sim 10^{-12}$ s) to neutral diffusion ( $\sim 10^{-4}$ s) times. To overcome these computational obstacles, a hybrid approach was used. In this scheme, the hydrodynamic equations along with Poisson's equation are solved semi-implicitly. Instead of assuming an electron energy distribution function, which is needed to close the system of equations, it is calculated periodically according to the instantaneous field and particle density profiles. Once computed, various moments are computed and used to complete the hydrodynamic transport equations.

The model used to solve the hydrodynamic equations along with Poisson's equation has been discussed elsewhere[6] and so we only outline the basic equations here. For each charge species, the continuity equation is solved:

$$\frac{\partial n}{\partial t} = -\vec{\nabla} \cdot n\vec{v} + R \quad (1)$$

where  $n$  is the species number density,  $\vec{v}$  is the drift velocity and  $R$  is the net production rate per unit volume. Neutral species are assumed to be described by the diffusion equation:

$$\frac{\partial n}{\partial t} - \nabla D \cdot \nabla n = R \quad (2)$$

where  $D$  is the diffusion coefficient. The electron drift velocity is assumed to be described by the drift/diffusion approximation, while the ion drift velocities are solved via solution of the momentum equation:

$$\frac{\partial n\vec{v}}{\partial t} = -\vec{\nabla} \cdot (n\vec{v}\vec{v}) + \frac{nq\vec{E}}{m} - \frac{1}{m} \vec{\nabla} n k T_i - \sum_j n\vec{v}v_j \quad (3)$$

where  $q$  (m) is the charge (mass) of the ion,  $E$  is the electric field,  $v_j$  is the collision frequency of  $j$ 'th ion-neutral collision and  $T_i$  is the ion temperature, which is assumed to be constant and uniform. Due to fierce ion-neutral collisions, this approximation is valid and therefore the ion energy equation does not need to be solved. In addition, the electron energy equation is redundant since we will be calculating the actual electron energy distribution function directly.

Ion and metastable impact onto the electrodes and dielectric surfaces can result in electron emission and this is simply characterized by a number,  $\gamma$ , which is the probability that an electron will be emitted for each ion and/or metastable impinging on a surface element. Obviously, different surfaces and species combinations have different values of gamma.

Finally, Poisson's equation,

$$\vec{\nabla} \cdot \epsilon \vec{\nabla} \Phi = -\vec{\nabla} \cdot \epsilon \vec{E} = \sum_k q_k n_k \quad (4)$$

where  $\Phi$  is the electrostatic potential and  $\epsilon$  is the permittivity of free space, is solved subject to the boundary conditions. To avoid tight numerical constraints on the time step, Poisson's equation along with the electron continuity equations are solved simultaneously[6]. As mentioned previously, the electron energy distribution function (EEDF) is calculated periodically according to the instantaneous electric field and particle density profile. From this EEDF, the electron collision frequencies and temperature profiles are computed and used to advance the hydrodynamic equations until the fields and/or particle density profiles change significantly so that a new EEDF is needed. The method chosen to calculate the EEDF is by use of a Monte Carlo[7] technique which uses a fourth order Runge-Kutta integrator[8] for advancing the electron trajectory and uses a null-collision technique[7,9] for collisions. However, to increase the computational efficiency of the Monte Carlo technique, electrons are split into two groups. The first group is unconfined electrons which are defined to be electrons whose total energy (kinetic plus potential) is greater than the minimum confining potential. The second group consists of all other electrons. If there is no confining potential, then the number of electrons in the second group is zero. Unconfined electrons, by definition, have a finite lifetime in the plasma region—either they escape to a surface or they lose sufficient kinetic energy to become confined. Unconfined electrons are initially produced from electrons emitted off surfaces from ion and/or metastable impact or from heavy particle collisions in the plasma bulk which lead to ionization. A large number of unconfined electrons (~1000s) are launched according to the emission and heavy particle ionization collision profiles. The EEDF and total time are tracked until they either leave the discharge or become confined electrons. Any electrons produced in electron-impact ionization are also followed. A smaller number (~100s) of confined electrons are then followed which are initially launched according to the newly confined electron profile and the previously saved confined EEDF from the last iteration. These electrons are followed, tracking their EEDF and total time, until either they leave the discharge (either by having a superelastic or Coulomb collision which transfers the needed kinetic energy), become attached, or the total time followed reaches the time between calls to the Monte Carlo routine. The computational advantage is that the confined electrons are low energy electrons which do not participate in the plasma chemistry and are expensive because they must be followed for a long time. Following only a few of the confined electrons thus represents a large savings in computational time. After following each group of electrons, we have determined two EEDFs: confined and unconfined electrons. However, we scale the confined EEDF before adding it together with the unconfined EEDF to get the full EEDF. This combined function is then used to compute the electron temperature and collision frequency profiles. This scaling is found by using the hydrodynamic electron density. From the instantaneous electron number density profile, the total number of electrons in the discharge is computed by a simple volume integral. This number must be equal to the number of unconfined electrons plus the number of confined electrons. The number of unconfined electrons is simply the rate (number/s) they are being created (surface emission plus



volume heavy particle ionization collisions) times the average lifetime of these electrons (and their progeny) in the discharge. The difference between these two numbers must be the number of confined electrons and is how the scaling of the confined EEDF is found.

### 3.2 Results of Computational Model

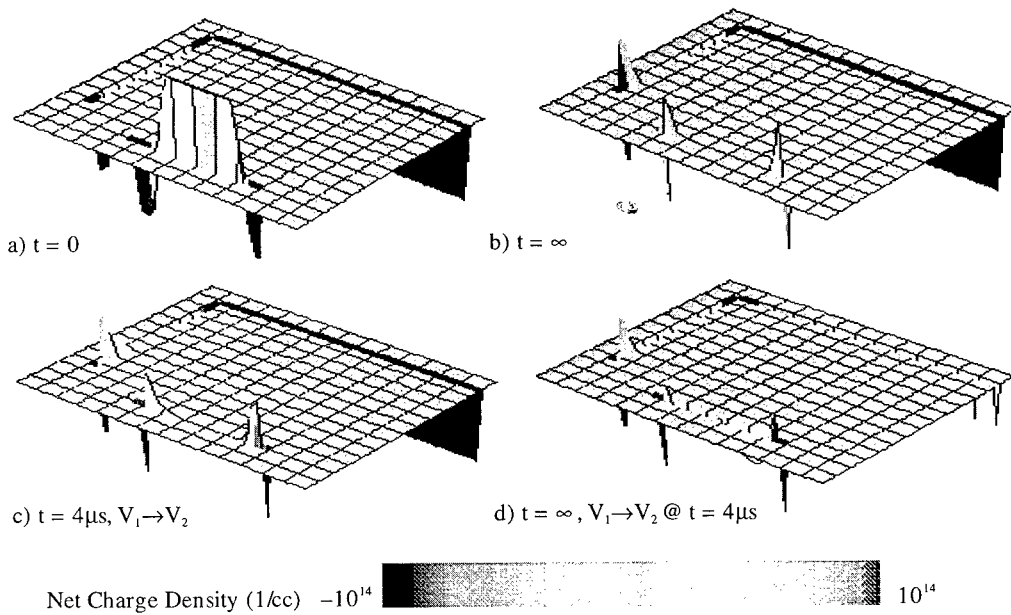


**Figure 5:** Figures 5 a) and b) illustrate the charge density at  $t=0$  and  $t=\infty$  for a fixed data voltage.. Figures 5 c) and d) show the profiles at  $t=4\mu s$  when the data voltage changes from  $V_1$  to  $V_2$  and the resultant profiles at  $t=\infty$ .

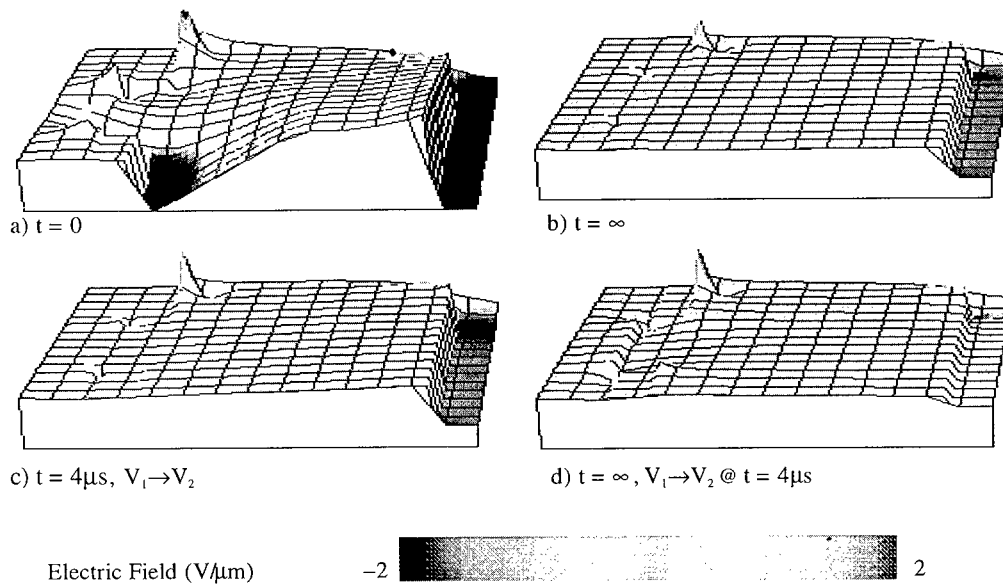


**Figure 6:** Figures 6 a) and b) illustrate the electric field profile at  $t=0$  and  $t=\infty$  for a fixed data voltage.. Figures 6 c) and d) show the profiles at  $t=4\mu s$  when the data voltage changes from  $V_1$  to  $V_2$  and the resultant profiles at  $t=\infty$ .

In this section we present some of the results of the computational model which was presented above. The model was used for both the 'active' and 'afterglow' discharge. Results from the afterglow period are presented here. The simulation starts by specifying the voltage on the electrodes and the voltage on the address electrode. Once steady state solution is achieved corresponding to the end of the data capture phase in Figure 3, the applied sustaining voltage across the electrodes is removed and the plasma is allowed to decay. Figure 5 shows the charge density when the sustain voltage is first turned off ( $t=0$ ) and the final profile at long time ( $t=\infty$ ) when the address voltage is kept constant. Also shown is the charge density when the address voltage is changed to a lower voltage  $4\text{ }\mu\text{s}$  after the sustain voltage is turned off and again at long times. Figure 6 shows the corresponding electric field perpendicular to the address electrode for the same cases.

#### 4. PERFORMANCE IMPROVEMENTS IN THE PALC DISPLAY

The results of these types of calculations give an indication of the length of the decay period and are used to determine the maximum addressability for a particular architecture and gas mixture. Measurements and modeling indicated that the typical decay time for pure He was  $20\text{ }\mu\text{s}$  which is sufficient for NTSC or VGA addressability (480 lines), but not for high addressability monitors or HDTV ( $>1,000$  lines). The calculations indicated that it is ionization from the metastable atoms which affect the charge density on the dielectric at long times. This is seen with the aid of Figure 7 in which we plot the density evolution for the ions, electrons and metastable particles in the afterglow. In Figure 7, the differences in the particle densities from the case when the data voltage is switched at  $4\text{ }\mu\text{s}$  are compared. The stairstep in the electron density profile is due to the acceleration technique which does not follow the true electron density once it falls below a level where it no longer affects the rest of the plasma. In the absence of these metastables, the ion and electron densities would decrease in a few microseconds. Thus to reduce the decay time, it is necessary to reduce the metastable density in the afterglow. This can be done by decreasing the diffusion time of metastables (geometry changes and or neutral pressure changes) or by creating a more efficient means of metastable ionization through Penning ionization. Recent experimental results with He- $\text{H}_2$  mixtures have produced a display system with a decay time of less than  $3\text{ }\mu\text{s}$  which is equivalent to over 3,000 lines addressability at 60 Hz frame rates[10]. This performance improvement has made the PALC display the only technology suitable for a direct view HDTV monitor with full motion and full gray-scale capability, without the use of dual scan electronics or other cost prohibitive techniques.

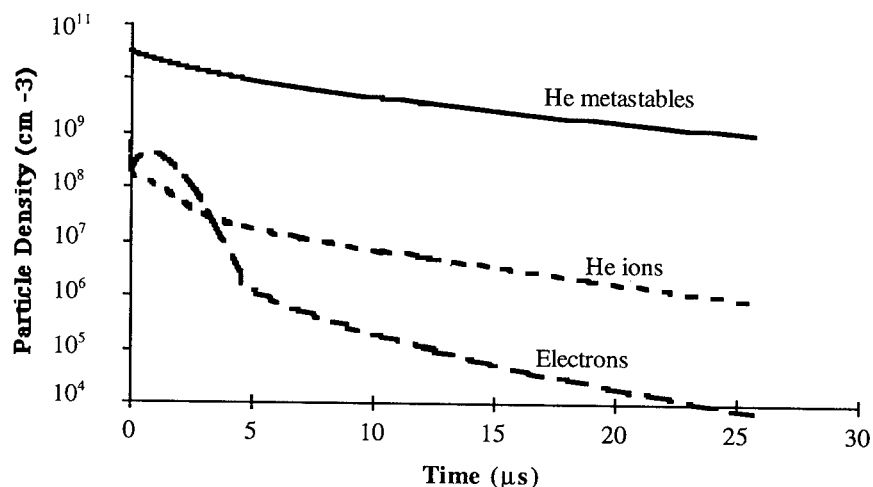


Figure 7: Density evolution of the particles in the afterglow. The symbols show the change in the density evolution when the data voltage is switched to 0 Volts at  $t=4\text{ }\mu\text{s}$ .

## 5. SUMMARY

The plasma addressed liquid crystal display is a new application for the properties of a glow discharge. By replacing a semiconductor switch with a three terminal plasma equivalent, a display technology that can be manufactured in large sizes was invented. Subsequent study of the properties of the plasma in these devices, a regime that has not previously seen a significant amount of attention has provided pathways to performance enhancements. The successful development of a model of the active discharge and afterglow provided insight into the underlying phenomena that were constraining the displays addressability. With a improved understanding, these limitations were removed. The result is a technology that is destined to replace the CRT in a size and format not previously thought possible.

## Acknowledgments

The authors would like to acknowledge the efforts of both the process engineering and device physics groups at Technical Visions and several contributors at Lawrence Livermore National Laboratories. Several discussions with J. Moore, N. Bardsley, R. Hinchliffe, and M. Roberson have been particularly elucidating. The authors would also like to thank L. Taylor for help in the preparation of this manuscript.

## References

- [1] Weber L., Plasma Displays in Flat-Panel Displays and CRTs, L. Tanns Ed. (Van Nostrand Reinhold, 1985) pp. 332-407.
- [2] Buzak T. "A New Active-Matrix Technique Using Plasma Addressing", Digest of Technical Papers, 1990 SID International Symposium, (Society for Information Display, 1990), pp. 420-423.
- [3] Buzak T., Green P., Guthrie S., Hartley S., Hillen K., Lamer G., Martin P., Nishida D., O'Neal T., Stein W., Stinger K. and Wagner M., "A 16-inch Full-Color Plasma Addressed Active-Matrix LCD," Digest of Technical Papers, 1993 SID International Symposium, (Society for Information Display, 1993), pp. 883-886.
- [4] Kakizaki T., Tanamachi S., Hayashi M., "Development of 25-in. Active-Matrix LCD Using Plasma Addressing for Video Rate High quality Displays", Digest of Technical Papers, 1995 SID International Symposium, (Society for Information Display, 1995), pp. 915-918.
- [5] "Sony and Sharp Agree to Develop Jointly Big-Screen Displays" (Wall Street Journal, Sept. 20, 1996).
- [6] Bubkowski J., Graves D. and Vitello P., *J. Appl. Phys.*, in press (1996).
- [7] Boeuf J. and Marode E., *J. Phys. D*, 15, pp. 2169 (1982).
- [8] Press W., Teukolsky S., Vetterling W., Flannery B., Numerical Recipes in FORTRAN, second edition, (Cambridge University Press 1992).
- [9] Kortshagen U., Parker G. and Lawler J., *Phys. Rev. E*, 54, pp. 6746 (1996).
- [10] Ilcisin K., Buzak T., Hinchliffe R., Martin P., Roberson M., Kakizaki T., Tanamachi S., Hayashi M., Morita T., "Breakthrough Gas Mixtures for HDTV Performance in Plasma Addressed Displays," Eurodisplay '96, Proceedings of the 16th Annual International Display Research Conference, (Society for Information Display, 1996), pp. 595-599.

## Production of Large Diameter ECR Plasma

Y. Kawai and Y. Ueda

*Interdisciplinary Graduate School of Engineering Sciences, Kyushu University, Kasuga, Fukuoka 816, Japan*

**Abstract.** The production of a large diameter ECR plasma with microwaves of frequency 2.45 GHz is reviewed, including our experimental results with a multi-slot antenna and a  $TE_{01}$  mode microwave converter. It is pointed out that the electromagnetic waves play an important role in plasma uniformity as well as plasma production. Furthermore, it is found that the X wave contributes to plasma uniformity for electron density of  $(1-2) \times 10^{17} \text{ m}^{-3}$  which almost corresponds to the L cutoff.

### 1. INTRODUCTION

Recently the development of a large diameter plasma source has become one of the most important subjects in plasma processing such as etching and CVD. Above all, there has been great interest in an electron cyclotron resonance (ECR) plasma [1-3] because of the high density plasma at low pressure ( $<5 \text{ mTorr}$ ) and quite low ion energy (tens of eV) at the wafer, compared with the RF plasma. Usually the principal mode in waveguides,  $TE_{10}$  or  $TE_{11}$  mode, is adopted to produce an ECR plasma [1-3]. In this case, the wavelength of microwaves in vacuum is about 120 mm at 2.45 GHz so that it is hard to produce an ECR plasma whose diameter is more than 120 mm without any ideas. Now, a large diameter plasma with the diameter more than 200 mm has been required for etching and CVD from industry. Thus, the production of an ECR plasma whose diameter is more than 200 mm has become interesting topic in plasma processing.

Many attempts [4-11] to produce an ECR plasma of 200 mm in diameter were made and interesting results were reported. We also developed two types of ECR plasma sources using a multi-slot antenna [5-6] and a circular  $TE_{01}$  mode microwave [7-8]. A multi-slot antenna has an advantage that the diameter of the antenna can be chosen independently of the microwave frequency so that the production of a large diameter ECR plasma is expected. In fact, a large diameter uniform plasma 200 mm in diameter was produced with a multi-slot antenna 280 mm in diameter [6,9]. Furthermore, it was found [9] by measuring wave patterns that both the whistler wave (R wave) and the L wave (Left-handed wave) [12] exist in the plasma.

A high plasma density such as  $10^{18} \text{ m}^{-3}$  is necessary for higher speed etching or deposition. In order to realize a uniform and dense ECR plasma, we developed a new type of ECR plasma source [7] using a circular  $TE_{01}$  microwave mode which is converted from the principal rectangular mode  $TE_{10}$ . The ion saturation current density of  $360 \text{ A/m}^2$  was achieved for the input microwave power of 3 kW at nitrogen pressure of  $5 \times 10^{-4} \text{ Torr}$ . The uniformity of the ion saturation current density was within  $\pm 3\%$  over 200 mm in diameter. It was also confirmed that when the electron density is higher than  $10^{17} \text{ m}^{-3}$ , the whistler wave (R wave) propagates, while when the electron density is lower than  $10^{17} \text{ m}^{-3}$ , both the R wave and L wave propagate [8].

Above mentioned results suggest that the electromagnetic waves such as the R wave and L wave play an

important role in plasma production. Aydil et al [13] investigated how the radial profile of the ion saturation current depends on input microwave powers and discussed the relationship between the radial profile and the L wave. However, it is still not clear what the dominant mechanisms are in ECR plasma uniformity. In order to clarify the physical mechanism of ECR plasma uniformity, we have performed the experiments on the propagation of the electromagnetic waves in the radial direction as well as in the axial direction, where an ECR plasma was produced with a conventional TE<sub>11</sub> mode. Recently, it was found [14] that the extraordinary wave (X wave) mainly contributes to plasma uniformity around the electron density of  $10^{17} \text{ m}^{-3}$ , which corresponds to the cutoff density of the X wave (L cutoff) [12]. This result will be useful for producing a 300 mm diameter ECR plasma which has been required as a next generation plasma source from industry.

In this paper, we describe some attempts of producing a large diameter ECR plasma, including our experiments, and point out that the X wave as well as the R wave contributes to plasma uniformity.

## 2. ATTEMPTS OF PRODUCING A LARGE DIAMETER ECR PLASMA

### 2.1 Typical results on the production of a 200 mm diameter ECR plasma

Matsuo et al [3] developed an ECR plasma source for plasma processing using a divergent magnetic field configuration. Microwave powers (frequency 2.45 GHz, TE<sub>11</sub> mode) were introduced into the plasma chamber through a waveguide and a quartz window. Then, a highly activated plasma was produced at low gas pressures in the range from  $10^{-5}$  to  $10^{-3}$  Torr. The plasma parameters were:  $n_e = 10^{16} - 10^{18} \text{ m}^{-3}$ ,  $T_e = 5 - 10$  eV and plasma potential  $V_p = 15 - 20$  V. Now this ECR plasma system has been widely used for etching and CVD. However, this conventional ECR plasma source does not provide a uniform plasma because a divergent magnetic field distribution is used as a magnetic field configuration.

Samukawa et al. [4] succeeded in the production of a large diameter ECR plasma of 200 mm in diameter by optimizing both the size of the discharge chamber and the gradient of the magnetic field. In this case, note that the 875 gauss equimagnetic field plane was located on the substrate holder, that is, uniform magnetic fields were adopted instead of divergent magnetic fields. They obtained the ion saturation current density of  $160 \text{ A/m}^2$  at nitrogen gas pressure of  $5 \times 10^{-4}$  Torr, where the uniformity of  $\pm 5\%$  was achieved. Furthermore, they carried out the etching using their system and obtained a lot of interesting results [4].

There were many attempts [5-11] to produce an ECR plasma whose diameter is larger than 6 inches with other methods. Plasma sources employing multi-pole magnetic fields are compact and less expensive. Furthermore, magnetic field coils to confine plasmas are not necessary. Sato et al [10-11] tried to produce a large diameter plasma with a plane multi-slot antenna and obtained the uniformity within  $\pm 3\%$  for a diameter of 200 mm. A microwave of 2.45 GHz traveling through a rectangular waveguide was converted into a coaxial mode. The plane antenna consisted of a back-plate with permanent magnets behind and a slotted plate connected to the inner electrode of the coaxial waveguide. The antenna surface was covered with a glass plate of 1 mm thickness to prevent direct contact with plasma particles. The ECR condition was satisfied in a limited region within 10 mm from the magnet surface. The density and temperature of electrons were about  $2 \times 10^{16} \text{ m}^{-3}$  and 3 eV, respectively, at the microwave power of 50 W under the argon pressure of  $10^{-4}$  Torr. The plasma density was almost proportional to the microwave power. They succeeded in producing a uniform ECR plasma of 400-450 mm (16-18 inches) in diameter with a plane slot antenna. However, the physical mechanism of plasma uniformity has not been clarified, so far.

### 2.2 Production of a large diameter ECR plasma with a multi-slot antenna

We have succeeded in producing a uniform and large diameter ECR plasma using a large diameter multi-slot antenna (MSA). The MSA has an advantage that the plasma diameter does not depend on the frequency of the incident microwave [5-6]. So far, the MSA has been regarded to be an assembly of a lot

of thin-slot antennas distributed uniformly on the surface of a cylinder [5]. A uniform plasma (8 inches,  $\pm 5\%$ ) was realized [9] by the MSA under the optimized conditions of microwave power, pressure and magnetic field configuration. Especially, the uniformity of the radial profile of the ion saturation current density depended greatly on magnetic field configurations. It was also found that the ion saturation current density axially increased after the resonance point under the certain magnetic field profiles. Usually, an ECR plasma has been produced by two methods: resonant acceleration of electrons by microwave electric fields, and resonant interaction between the whistler wave and electrons. The mechanism of the production of an ECR plasma using a multi-slot antenna has been considered as the former. The above mentioned results suggest that there may exist normal modes relating to the plasma production. Thus, we examined the effect of the magnetic field configuration on the uniformity of the ion saturation current density in order to clarify the mechanism of the ECR plasma production using the MSA. Furthermore, it was examined by measuring the dispersion relation of electromagnetic waves whether normal modes in the plasma exist or not.

A schematic diagram of the experimental apparatus is shown in Fig. 1(a). The vacuum chamber is made of stainless steel with 290mm in inner diameter and 1200mm in length. An ECR plasma was produced with a multi slot antenna which is made of stainless steel of 280 mm in diameter, as seen in Fig. 1(b). The length and width of slots are 70 mm and 2 mm, respectively. The magnetic coil assembly consisted of six coils; some coils to make uniform magnetic fields, while, the other to form the magnetic mirror and control the current for magnetic mirror. The gas used was He, and the typical pressure was  $2 \times 10^{-4}$  Torr. In this experiment, the substrate which is at floating was placed at 800 mm from the multi-slot antenna ( $Z = 1000$  mm). In discussing a large diameter plasma, it is important whether or not a substrate is placed in the chamber, because the plasma is disturbed by the substrate. Here we examined the uniformity of plasma in the presence of a substrate of 8 inches in diameter. The ion saturation current density,  $I_{is}$ , in the absence of the substrate were two times larger than in the presence of it. Plasma parameters were measured with a cylindrical Langmuir probe in front of the substrate. Electromagnetic waves in the plasma were measured with a loop antenna movable along z axis and the wave patterns were obtained by the interferometer method [15] as usual.

It was achieved under the gas pressure  $2 \times 10^{-4}$  Torr,  $2 \times 10^{-3}$  Torr and microwave power 470W, 1000W that the radial uniformity of the ion saturation current density is within 5% over 200 mm in diameter, as seen in Fig. 2(a). The electron density and the electron temperature of the uniform plasma in front of the substrate were  $7 \times 10^{16}/\text{m}^3$  and 6eV, respectively. The radial profile of the floating potential,  $V_f$ , in the case of 470W where the plasma is uniform is shown in Fig. 2(b), which indicates that the profile of  $V_f$  is uniform,  $\pm 0.75\text{V}$  over 200 mm. The value of  $V_f$  are slightly positive although  $V_f$  in the case where the radial profiles are not uniform were in the range from  $-5\text{V} \sim -20\text{V}$ , which means that there are little high energy electrons under the condition of the uniform plasma.

It has been pointed out [13,16] that the whistler wave (or R wave) plays an important role in the production of a large diameter ECR plasma. As already mentioned, it seems that a multi-slot antenna can excite normal modes in the plasma. Thus, electromagnetic waves in the plasma were measured [9] with a small loop antenna in order to clarify the dependence of the radial profiles of  $I_{is}$  on the magnetic field configurations from the point of view of plasma production. Figure 3(a) is a typical interferometric wave pattern of  $B_x$  in the uniform plasma. As seen in Fig. 3(b), the wave pattern was decomposed graphically into two traces assuming that it consisted of two waves with different wave numbers. Figures 4(a) and 4(b) show the dispersion relations before the ECR point and after the ECR point where the solid line is the theoretical dispersion curve. Here, the local wave numbers were estimated from the wave patterns in the regions between the MSA and ECR point and after ECR point. Figure 4 shows that both the R-wave and the L-wave propagate in the region between the MSA and ECR point, and the only L-wave propagates after the ECR point, which is the same results as those obtained with a conventional ECR plasma source [15].

Thus, it is concluded from above results that the MSA is regarded a sort of microwave antennas with higher order modes.

### 2.3 Production of a high density-large diameter ECR plasma with $TE_{01}$ mode

It is a little hard to produce a plasma whose density is higher than  $10^{17} \text{ m}^{-3}$  with a multi-slot antenna. On the other hand, higher density plasma will be required from industry, in particular for plasma CVD or sputtering. We have developed a new ECR plasma source using a circular  $TE_{01}$  mode and succeeded in the production of a uniform high density ECR plasma. A microwave source of 2.45 GHz frequency was used to generate an ECR plasma. Microwaves generated by the magnetron propagate into an ECR plasma through the waveguides. There are many waveguide modes of microwaves, such as TE mode and TM mode. In the case of a conventional ECR plasma source, microwaves are introduced into cylindrical chambers as the circular  $TE_{11}$  mode converted from the rectangular  $TE_{10}$  mode. In the case of the  $TE_{11}$  mode, the electric field has a strong peak at the center of the waveguide, which causes the peaking of the plasma density at the central region. On the other hand, in the case of the  $TE_{01}$  mode, the electric field near the wall is stronger than that at the center of the waveguide. This strong electric field near the wall may compensate the density decrease near the chamber wall. Furthermore, as for the  $TE_{01}$  mode, the electric field distribution along the circumferential ( $\theta$ ) direction is uniform at the same radial position. Conversely, the  $TE_{11}$  mode has a different electric field strength for different  $\theta$  values. Consequently the  $TE_{01}$  mode will be more convenient in generating a uniform ECR plasma.

Figure 5 shows the experimental apparatus. The microwave power of 2.45 GHz could be varied up to 5 kW. The rectangular  $TE_{10}$  mode was converted to the circular  $TE_{01}$  mode and introduced into the ECR plasma source. The diameter and length of the ECR plasma source are 300 mm and 620 mm, respectively. The distance between the magnetic coils and the substrate is variable along the z axis. The magnetic field profile was controlled by changing the coil current and the coil locations. The base pressure was kept less than  $1 \times 10^{-7}$  Torr. The ion saturation current density and the plasma potential were measured by a plane Langmuir probe 1 mm in diameter.

Actually we measured the electric field distribution of the microwave emitted from both the  $TE_{01}$  and  $TE_{11}$  mode converter. Figure 6 is typical profiles of the measured electric field distributions. Because of the interference by the probing microwave antenna, the distributions are not always symmetric. It is obvious that the electric field intensity from the  $TE_{01}$  mode converter has a couple of peaks around  $R = \pm 65$  mm and is almost zero at  $R = 0$  mm. As predicted, the electric field of the  $TE_{11}$  mode converter peaks at  $R = 0$  mm.

Figure 7 shows the dependence of the ion saturation current density on the input microwave power. The nitrogen gas pressure is  $5 \times 10^{-4}$  Torr and the ion saturation current density is measured at  $Z = 350$  mm and  $R = 0$  mm. As seen in Fig. 7, the ion saturation current density increases nearly in proportion to the input microwave power. In order to examine the uniformity of the ECR plasma, the radial distribution of the ion saturation current density was measured with a movable Langmuir probe. The result is shown in Fig. 8 for different microwave modes. In this case, the input microwave power was 3 kW and the nitrogen gas pressure was  $5 \times 10^{-4}$  Torr. In Fig. 8(a), note that the ion saturation current density is uniform within  $\pm 3\%$  over 200 mm in diameter and  $360 \text{ A/m}^2$  is achieved with the  $TE_{01}$  mode. The measured electron temperature ( $T_e$ ) and the plasma density ( $N_e$ ) were 6 eV and  $6 \times 10^{17} \text{ m}^{-3}$ , respectively.

On the other hand, the ion saturation current density distribution with the  $TE_{11}$  mode is less uniform. Note here that all external parameters were the same except for the microwave mode. Thus, it is obvious that the  $TE_{01}$  mode is better than the  $TE_{11}$  mode from the standpoint of obtaining a radially uniform plasma.

To clarify the production mechanism of a large diameter uniform ECR plasma generated by a circular  $TE_{01}$  mode microwave experimentally, wave propagation characteristics in the plasmas were measured, as

in the case of a multi-slot antenna. It was found [8] that a microwave introduced into the chamber is transformed mainly into the electron cyclotron wave (R-wave) and then absorbed around the resonant point.

In conclusion, it was found that an ECR plasma source with a circular  $TE_{01}$  mode is very convenient for achieving a high and uniform ion current density. The ion saturation current density was uniform within  $\pm 3\%$  over 200 mm in diameter and  $360 \text{ A/m}^2$  was achieved.

### 3. MECHANISM OF PLASMA UNIFORMITY

As described in Sec.2, an ECR plasma of 200 mm in diameter came to be realized experimentally with a multi-slot antenna and a  $TE_{01}$  mode converter. However, the conditions where such a uniform ECR plasma is produced strongly depended on the external conditions such as magnetic field distribution, pressure, input microwave power and so on. In addition, it seems that the electromagnetic waves play an important role in ECR plasma uniformity. Stevens and Cecchi [15] pointed out that the R wave contributes to plasma uniformity by calculating the ray trace of the R wave. Aydil et al [13] and Carl et al [18] found a uniform profile of the ion saturation current and tried to explain it by the L wave although electromagnetic waves were not measured. Thus, we have performed the experiments on electromagnetic wave measurements in order to clarify the physical mechanism of plasma uniformity. It was found that the extraordinary wave (X wave) radially propagates and contributes to plasma uniformity.

Figure 9 shows the experimental apparatus which is the same apparatus as that of Sec.2.2 except for the introduction of the microwaves. In this case, the  $TE_{11}$  mode was adopted in order to compare with the experimental results [13,15,18] reported so far. The microwave power could be varied up to 5 kW. The used gas was  $N_2$  and the pressure was ranged from 0.5 to 5 mTorr. An electron cyclotron resonance point was set at  $Z=230$  mm. The plasma parameters were measured with a 1 mm-diam Langmuir probe. The electric fields were picked up with a movable loop antenna connected to a crystal diode or a mixer and the wave patterns were observed by the interferometer method [8-9,15] to obtain the dispersion relation of electromagnetic waves. In this experiment, a phase shifter was used to measure whether waves propagate or not.

The radial profile of the ion saturation current density  $I_{is}$  was examined as a function of input microwave power. It was found that as the input microwave power was increased, the radial profile of  $I_{is}$  became initially convex, wavy, concave, uniform and finally convex, which is the same tendency as observed so far [13,18]. Whenever the radial profile of  $I_{is}$  was uniform around the center, it had a peak near the chamber, as shown below. In order to clarify such behavior, we measured the radial propagation of electromagnetic waves using a radially movable loop antenna which was installed at  $Z=450$  mm. Figure 10 and Fig.11 show the interferometric wave patterns for different input microwave powers  $P_{in}$ , where the wave patterns of electromagnetic waves were taken by changing the phase of the reference signal with the phase shifter. These figures indicate that there are radially propagating waves. Note that as seen in Fig.11(a), the wavelength of the waves is very short near the chamber wall, while it is long around the center. Furthermore, Fig.11(b) shows that the output of the crystal diode which is proportional to the electric field intensity of waves peaks near the chamber wall. On the other hand, Fig.12 shows that the radial profile of  $I_{is}$  peaks near the chamber wall. Thus, it turns out that the peak of  $I_{is}$  corresponds to that of the electric field. When the input microwave power was increased further and the electron density exceeded about  $2 \times 10^{17} \text{ m}^{-3}$ , the radially propagating waves disappeared. In this case, the L wave propagating along the axial direction was not excited and only the R wave propagated to the electron cyclotron resonance point.

In order to identify what kind of electromagnetic waves were excited, the dispersion relation was plotted for different electron densities. Here the wavelength was estimated from the wave patterns of Fig.10 and Fig.11. The obtained dispersion relation agrees with the theoretical one of the X wave, as seen in Fig.13 where  $\omega_{ce}$  and  $k_x$  are the electron cyclotron frequency and wavenumber of the X wave. According to the



linear theory[12], when the wavelength of the X wave becomes short, upper hybrid resonance takes place. Thus, a peak of the ion saturation current density near the chamber wall is considered to be caused by upper hybrid resonance. The observed cutoff density,  $2 \times 10^{17} \text{ m}^{-3}$ , at which the X wave disappeared corresponds to the L cutoff [12]. In conclusion, the X wave contributes to ECR plasma uniformity around the cutoff density of the X wave and the L wave does not play a dominant role in plasma uniformity.

#### 4. CONCLUSION

We reviewed the production of an ECR plasma whose diameter is 200 mm with microwaves of frequency of 2.45 GHz and pointed out that the R wave plays an important role in the plasma production. Furthermore, it was found the X wave contributes to ECR plasma uniformity for the electron density around the L cutoff,  $(1-2) \times 10^{17} \text{ m}^{-3}$ , which will be useful for designing larger diameter ECR plasma sources. Recently, it seems that Watanabe et al at Hitachi [19] succeeded in producing a 300 mm diameter ECR plasma with  $\text{TE}_{01}$  mode [7]. An ECR plasma with the electron density higher than the L cutoff will be necessary for CVD to increase the deposition rate, which is one of future problems concerning ECR plasma sources.

#### References

- [1] SAKUDO N., TOKIGUCHI K., KOIKE H. and KANOMATA I., *Rev. Sci. Instrum.*, **48** (1977) 762-766.
- [2] SUZUKU K., OKUDAIRA S., SAKUDO N. and KANOMATA I., *Jpn. J. Appl. Phys.*, **16** (1977) 1979-1984.
- [3] MATSUO S. and KIUCHI M., *Jpn. J. Appl. Phys.*, **22** (1983) L210-L212.
- [4] SAMUKAWA S., *J. Vac. Sci. Technol.*, **B8** (1990) 1192-1198.
- [5] YONESU A., TAKEUCHI Y., KOMORI A. and KAWAI Y., *Jpn. J. Appl. Phys.*, **27** (1988) L1746-L1749.
- [6] UEDA Y., TANAKA M., SHINOHARA S. and KAWAI Y., *Surface and Coating Technology*, **74-75** (1995) 503-507.
- [7] HIDAKA R., YAMAGUCHI T., HIROTSU N., OHSHIMA T., KOGA R., TANAKA M. and Kawai Y., *Jpn. J. Appl. Phys.*, **32** (1993) 174-178.
- [8] HIROTSU N., YAMAGUCHI T., HIDAKA R., TANAKA M. and KAWAI Y., *Jpn. J. Appl. Phys.*, **33** (1994) 2712-2717.
- [9] UEDA Y., TANAKA M., SHINIHARA S. and KAWAI Y., *Rev. Sci. Instrum.* **66** (1995) 5423-5427.
- [10] IIZUKA S. and SATO N., *Jpn. J. Appl. Phys.*, **33** (1994) 4221-422.
- [11] ISHIDA T., NAKAGAWA Y., ONO T., IIZUKA S. and SATO N., *Jpn. J. Appl. Phys.*, **33** (1994) 4236-4238.
- [12] CHEN F.F. *Introduction To Plasma Physics* (Plenum Press, New York and London, 1974), Chap.4.
- [13] AYDIL E.S., GREGUS J.A. and GOTTSCHO R.A., *Rev. Sci. Instrum.*, **64** (1993) 3572-3584.
- [14] UEDA Y. and KAWAI Y., to be published in *Proc. of ICPIG* (Toulouse, July, 1997).
- [15] STEVENS J.E. and CECCHI J.L. *Jpn. J. Appl. Phys.*, **32** (1993) 3007-3012.
- [16] SAMUKAWA S., *J. Vac. Sci. Technol.*, **A11** (1993) 2572-2576.
- [17] UEDA Y. and KAWAI Y., to be published in *Appl. Phys. Lett.* (1997).

[18] CARL D.A., WILLIAMSON M.C., LIEBERMAN M.A. and LICHTENBERG A.J., *J. Vac. Sci. Technol.*, **B9** (1991) 339-347.

[19] WATANABE S. et al., to be published in *Jpn. J. Appl. Phys.* (1997).

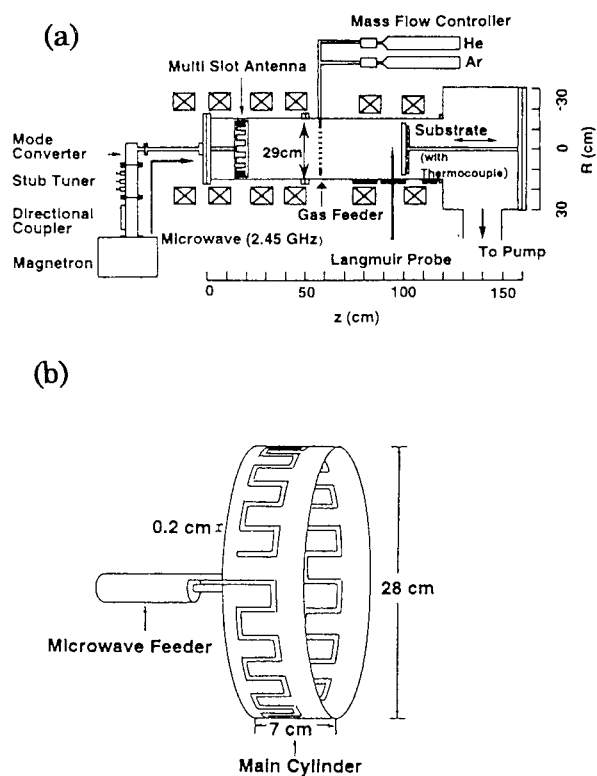


Fig. 1. Schematic diagram of (a) the experimental apparatus and (b) the multi-slot antenna.

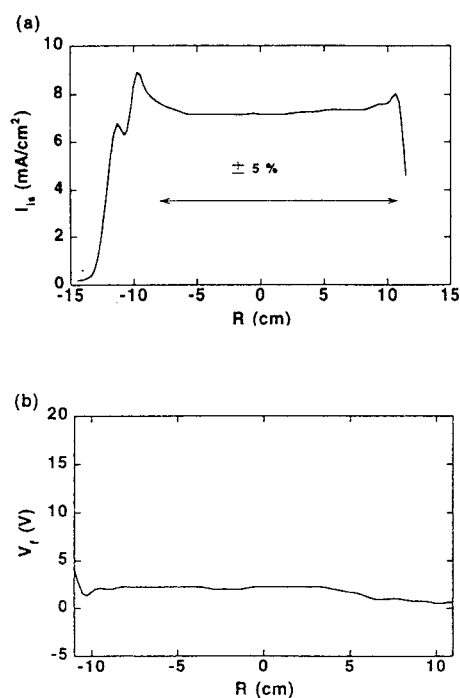


Fig. 2. Radial profile of (a) the ion saturation current density and (b) the floating potential for the uniform plasma. The input microwave power and gas pressure were 470 W and 2 mmTorr, respectively.

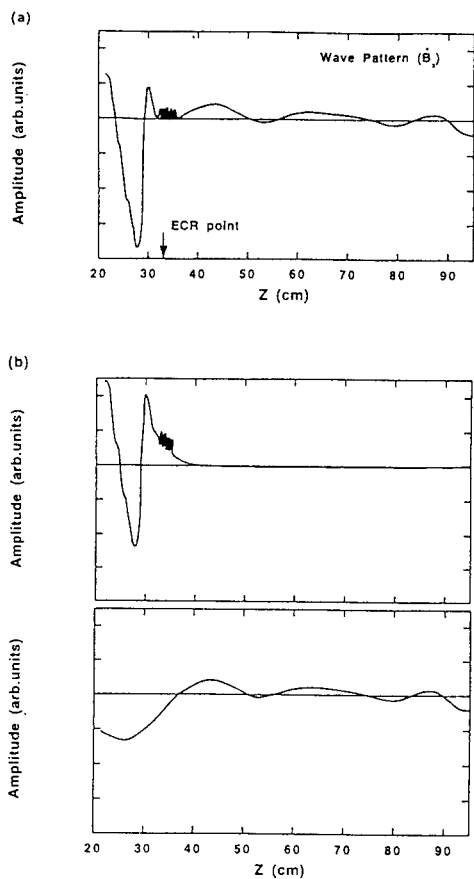


Fig. 3. (a) Wave pattern of  $B_x$  and the axial profile of the output of the power meter in the case of the uniform plasma. (b) Wave patterns decomposed graphically from  $B_x$ .

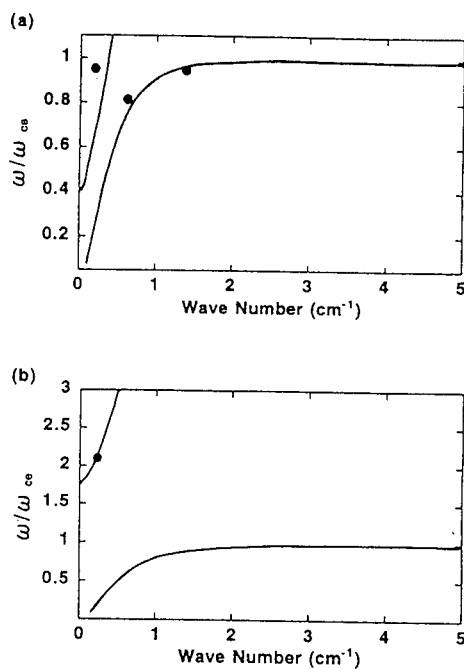


Fig. 4. Dispersion curves (a) before the ECR point and (b) after the ECR point, where solid lines are the theoretical dispersion curves.

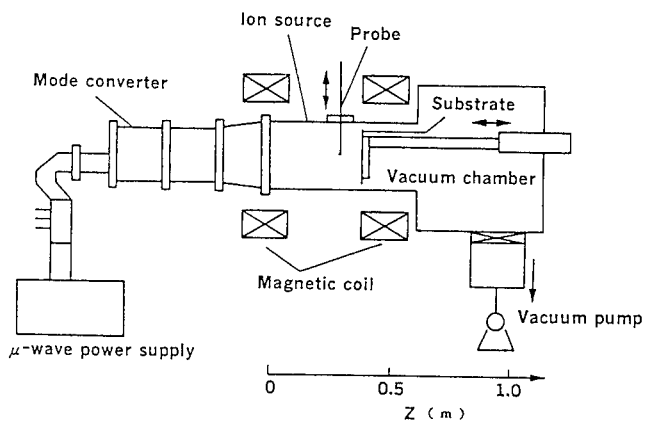


Fig. 5. Schematic diagram of the experimental apparatus.

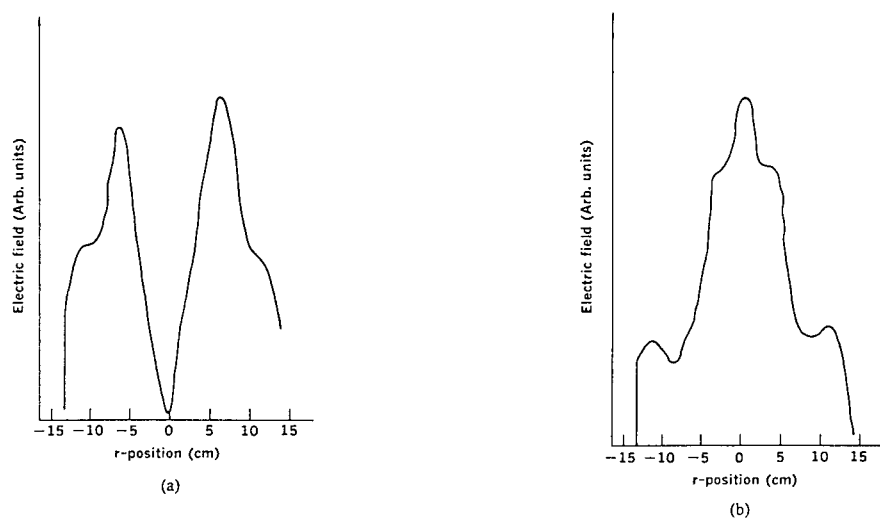


Fig. 6. Measured electric field distributions of the microwave emitted from (a) TE<sub>01</sub> and (b) TE<sub>11</sub> mode.

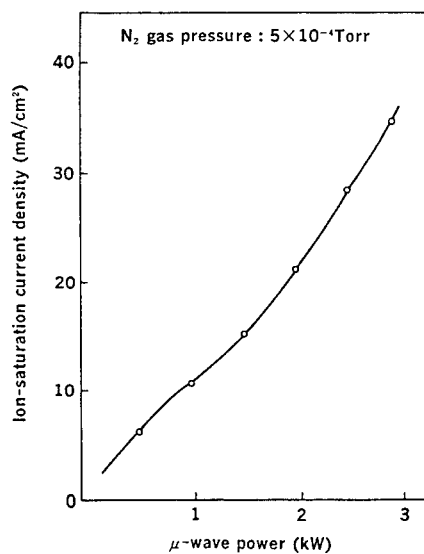


Fig. 7. Dependence of the ion saturation current density on the input microwave power, where the nitrogen gas pressure is  $5 \times 10^{-4}$  Torr.

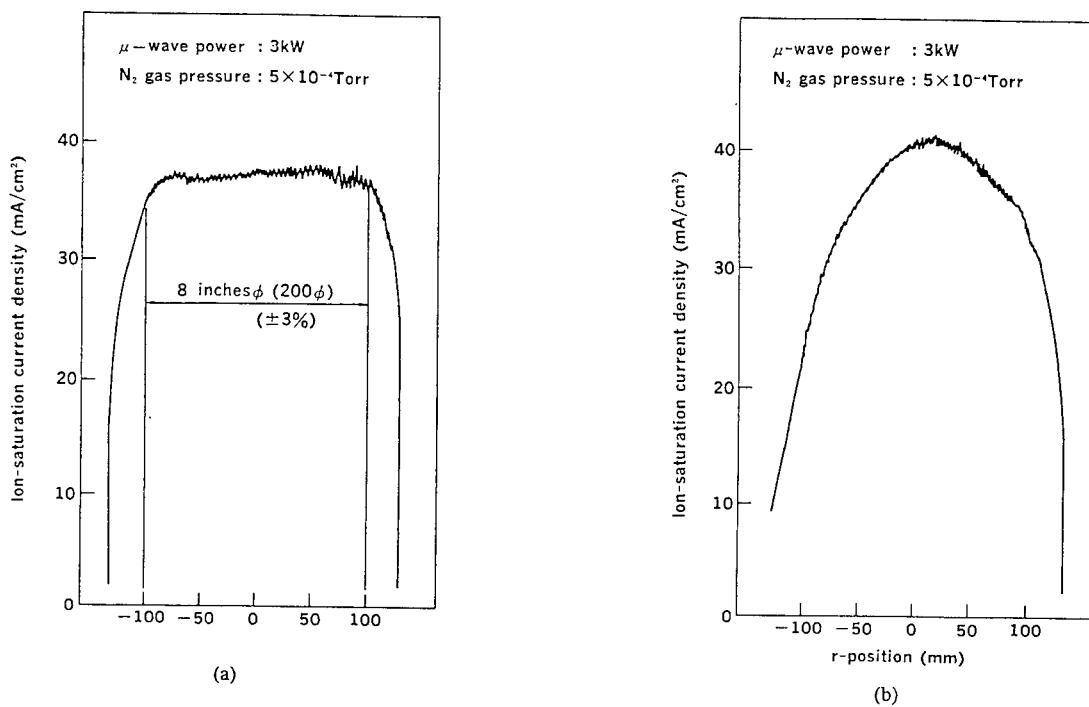


Fig. 8. Radial distributions of the ion saturation current density in the case of the (a)  $TE_{01}$  and (b)  $TE_{11}$  mode, where the input microwave power is 3 kW.

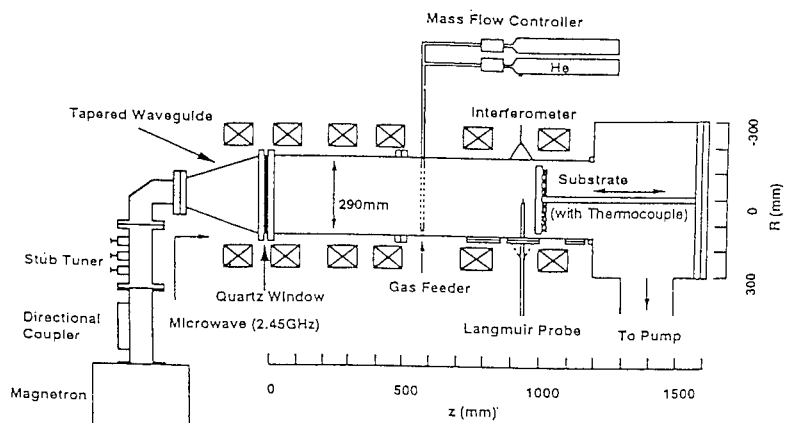


Fig. 9. Schematic diagram of the experimental apparatus.

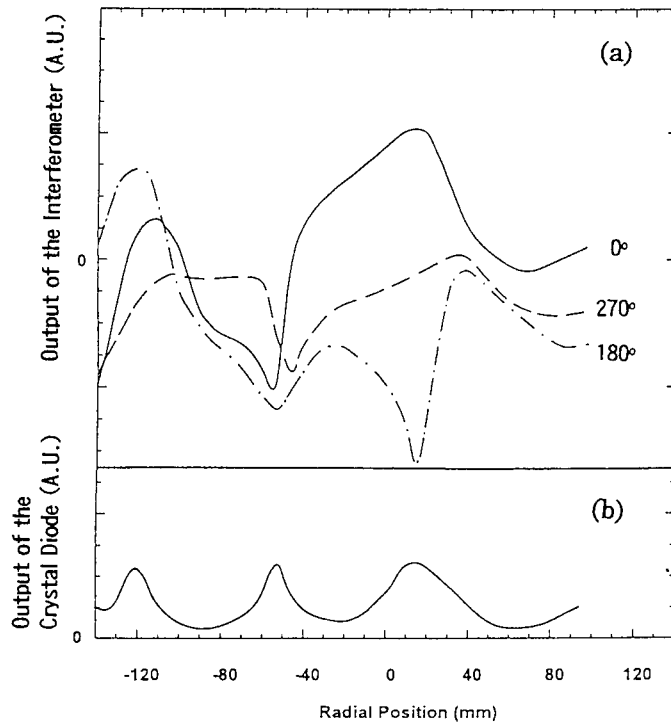


Fig. 10. (a) Radial wave patterns for different phases and (b) the output of the crystal diode, where the input microwave power is 0.8 kW and the pressure is 2 mTorr. The electron temperature is 5.3 eV.

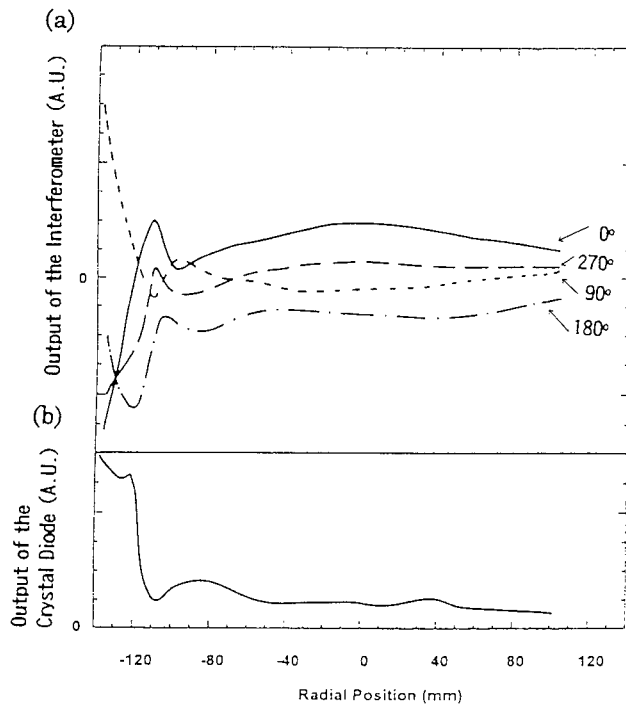


Fig. 11. (a) Radial wave patterns for different phases and (b) the output of the crystal diode, where the input microwave power is 1.5 kW and the pressure is 2 mTorr. The temperature and density of electrons are 8.5 eV and  $(1-2) \times 10^{17} \text{ m}^{-3}$ , respectively.

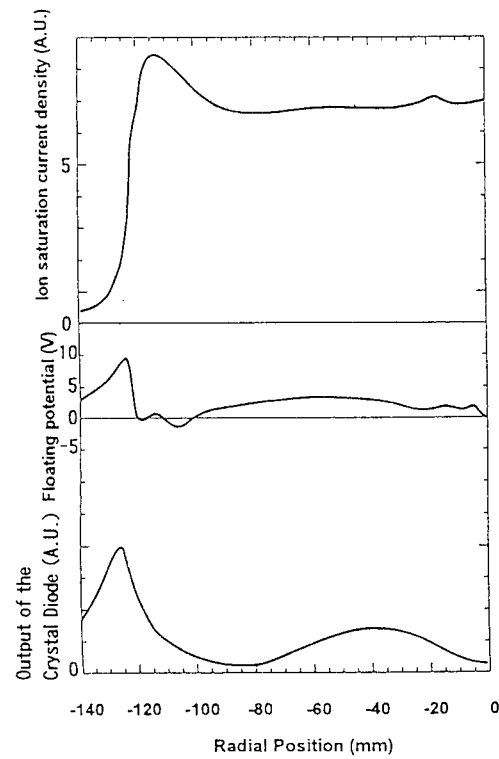


Fig. 12. The radial profiles of the ion saturation current density, floating potential, output of the crystal diode where the electric field is large near the chamber wall.

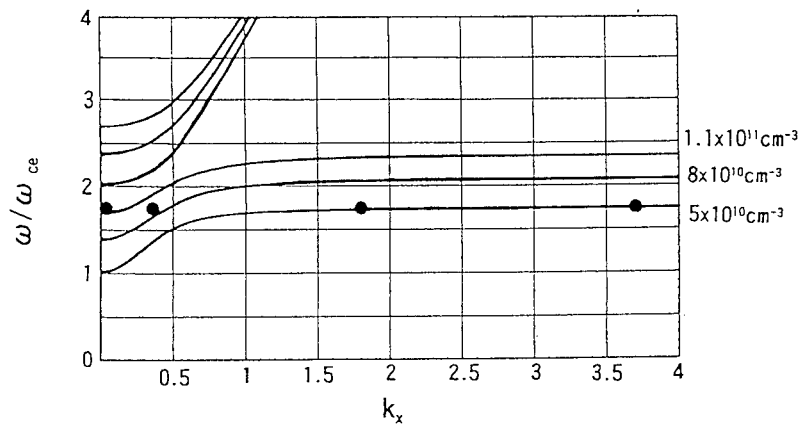


Fig. 13. The dispersion relations of the X wave for different electron densities. The closed circles and the solid lines correspond to the experimental values estimated from Fig. 10 and Fig. 11 and the theoretical dispersion relation of the X wave, respectively.

## Emission Spectroscopy of the Cathode Fall Region of an Analytical Glow Discharge

N. Konjević, I.R. Videnović and M.M. Kuraica

*Faculty of Physics, University of Belgrade, P.O. Box 368, 11001 Belgrade, Yugoslavia*

**Abstract.** Stark spectroscopy of hydrogen Balmer lines and neutral helium lines with forbidden components is used for the study of an analytical glow discharge.

Splitting of the hydrogen  $H_\beta$  and  $H_\gamma$  lines is applied for simultaneous determination of local electric field and temperature of excited H atoms in pure hydrogen and in argon-hydrogen mixture. Temperature measurements showed that, in pure hydrogen discharge, at least two groups of excited atoms exist: "slow", with average energies in the range from 3.4 eV to 8.2 eV and "fast", ranging between 80 eV and 190 eV. In argon-hydrogen discharge, excited hydrogen neutrals with average energies between 32 eV and 43 eV are detected only. The origin of these energetic neutrals is related to the presence of  $H^+$  and  $H_3^+$  ions in pure hydrogen, and to the dominant role of  $H_3^+$  ion in argon-hydrogen mixture. For both gases, in the negative glow region, the increase of the excited hydrogen atoms temperature is detected and explanation suggested.

For the electric field measurements in pure helium and helium-hydrogen mixture, the Stark splitting and shifting of the neutral helium 492.19 nm, 447.15 nm and 406.62 nm with respect to their forbidden counterparts is used. Good agreement between electric field measurements from these three helium lines is obtained.

### 1. INTRODUCTION

A glow discharge source (GDS) with a flat cathode and cylindrical hollow anode, first described by Grimm [1], is a well established excitation source for the analysis of conducting solid samples by optical emission spectroscopy [2,3], see also [4]. Owing to sample ablation by cathodic sputtering, matrix effects resulting from selective volatilization are absent. Because of the layer by layer ablation of the sample surface, the Grimm GDS is used for in-depth profiling analysis [5,6]. Similar advantages are realized when atomic absorption spectrometry is performed with a Grimm GDS [7,8]. In the last several years various types of GDSs were also used as ion sources for mass spectrometry [9]. For solids analysis, direct current (DC) GDSs have been successfully complemented by the radio-frequency (RF) discharges. Namely, the use of DC discharges is limited to metals, whereas the RF discharges are applicable for non-conducting materials also (see [10] and references therein). A comprehensive list of publications dealing with GDSs and their applications is given in [11-13].

However, if one scans the literature dealing with Grimm GDS, see e.g. [11,12], it is evident that most of the papers are devoted to various applications. Only few report results of the discharge parameter measurements and they are mainly concentrated on volt-ampere characteristics, cathode surface studies and measurements of relative line intensities for different discharge conditions. This observation may be generalized to all analytic GDSs. In order to supply new reliable data, several years ago, we set up in our laboratory an experiment to measure plasma parameters of a modified Grimm GDS. First results of negative glow plasma diagnostics (electron density and temperature, excitation temperatures and gas temperature) are obtained in argon with a small admixture (3%) of hydrogen [14]. Unexpected intensive spectral line broadening of the wings of all hydrogen Balmer lines was detected and studied in detail [15,16].

In this paper we resume results of the experimental studies [17-19] of the cathode fall region (CFR) of the Grimm GDS. The study of the physical processes in this part of the discharge is of importance for understanding the operation of the GDS and the sputtering processes at the cathode surface which are both



of primary interest for analytical applications. Here we use Stark spectroscopy of hydrogen Balmer lines for spatial distribution measurements of the electric field intensity and the temperature of excited hydrogen atoms in the CFR of pure hydrogen and argon-hydrogen mixture discharges. In pure helium and helium-hydrogen mixture, we applied Stark splitting and shifting of the neutral helium 492.19 nm ( $2p^1P^0 - 4d^1D$ ), 447.15 nm ( $2p^3P^0 - 4d^3D$ ) and 402.62 nm ( $2p^3P^0 - 5d^3D$ ) lines with respect to their forbidden counterparts ( $2p^1P^0 - 4f^1F$ ), ( $2p^3P^0 - 4f^3F^0$ ) and ( $2p^3P^0 - 5f^3F^0$ ), respectively, for electric field spatial distribution measurements in the cathode fall region of the Grimm GDS.

## 2. EXPERIMENTAL APPARATUS AND PROCEDURE

Since we describe here two sets of measurements, one in pure hydrogen and in an argon-hydrogen mixture, and the other one in pure helium and in a helium-hydrogen mixture, common details of both experiments will be outlined first. Their specific details will be given separately. The latter experiment, in pure helium and in the helium-hydrogen mixture, is considerably improved and therefore its setup is schematically presented in Fig. 1.

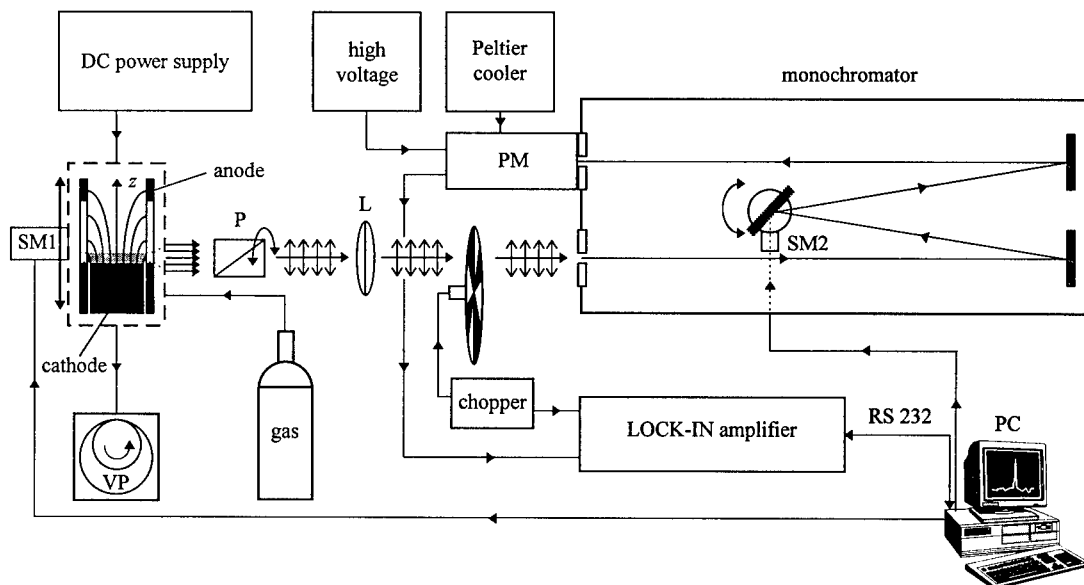


**Fig. 1.** Schematic diagram of the central part of the Grimm GDS and experimental setup for side-on observations in the helium-based experiments. Symbols: VP - vacuum pump, SM - stepping motors; P - polarizer; L - lens; PM - photomultiplier.

### 2.1 Common details

Our discharge source, a modified Grimm GDS, is laboratory made after Ferreira *et al.* [20] and described in detail elsewhere [14]. Here, for completeness, only minimum information will be given. The hollow anode, 30 mm long with inner and outside diameters 8.00 and 13 mm, has a longitudinal slot (15 mm long and 1 mm wide) for side-on observations along the discharge axis. The water cooled cathode holder has an exchangeable iron electrode, 18 mm long and 7.60 mm in diameter, which screws tightly onto its holder to ensure good cooling. Unlike the original Grimm design, the cathode is mounted inside the hollow anode. A gas flow was sustained at a selected pressure by means of a needle valve and a two-stage mechanical vacuum pump. In order to prevent backstreaming of oil vapors, the zeolite trap is mounted between discharge vessel and vacuum pump. To run the discharge, a 0 - 2 kV and 0 - 100 mA current stabilized power supply (Kepco BHK 2000-01 M) is used. A ballast resistor of 10 k $\Omega$  is placed in series with the discharge and power supply.

After polarization with the Glan-Thomson prism or plastic polarizer, the radiation from the discharge source is focused with unity magnification onto the entrance slit of the scanning monochromator-photomultiplier system, see Fig. 1. For electric field intensity axial distribution measurements, the discharge tube is moved in about 0.1 mm steps along the discharge axis, so the discharge image obtained through the observation slot is shifted in the plane of the entrance slit of the monochromator, see Fig. 1. The photomultiplier signals were A/D converted, collected and processed by a PC.

## 2.2 Specific details

### 2.2.1 Experiment in pure hydrogen and in the argon-hydrogen mixture (97% Ar : 3% H<sub>2</sub>):

gas flow: 300 - 500 cm<sup>3</sup>/min (at room temperature and atmospheric pressure);  
 pressure: 195-250 Pa (pure H<sub>2</sub>) and 240-425 Pa (Ar-H<sub>2</sub>);  
 spatial resolution: 0.02 mm (pure H<sub>2</sub>) and 0.01 mm (Ar-H<sub>2</sub>), along the discharge axis;  
 monochromator: 2m PGS-2 Carl Zeiss Jena (Ebert type), 640 mm<sup>-1</sup> reflection grating, 0.74 nm/mm inverse linear dispersion in the first order;  
 slit width: same entrance and exit slits of 15  $\mu$ m and 30  $\mu$ m for the H $\beta$  and H $\gamma$  spectra recordings, respectively, and 15  $\mu$ m entrance and 50  $\mu$ m exit slits for the integral Fe I, Ar I and Ar II line intensities measurements;  
 instrumental halfwidth: 0.014 nm with 15  $\mu$ m entrance and exit slits (Gaussian form);  
 radiation detection: photomultiplier EMI 9789QB.

### 2.2.2 Experiment in pure helium (99.95%) and in the helium-hydrogen mixture (95% He : 5% H<sub>2</sub>):

gas flow: 300 cm<sup>3</sup>/min (at room temperature and atmospheric pressure);  
 pressure: 120-200 Pa;  
 spatial resolution: 0.01 mm along the discharge axis, by a PC-controlled stepping motor;  
 monochromator: 4m Hilger and Watts (Ebert type), 1200 mm<sup>-1</sup> reflection grating, 0.242 nm/mm inverse linear dispersion in the first order, equipped with a PC-controlled stepping motor enabling wavelength changes in steps of 0.0028 nm;  
 slit width: 30  $\mu$ m both entrance and exit;  
 instrumental halfwidth: 0.022 nm (Gaussian form);  
 radiation detection: Peltier-cooled photomultiplier, lock-in amplifier (SR 510 Stanford Research) with radiation chopper (SR 540 Stanford Research) operating at 83.3 Hz.

## 3. THEORY

### 3.1 Theoretical basis for electric field and excited hydrogen temperature measurements using Stark splitting of hydrogen Balmer lines

The splitting of energy levels of the hydrogen and hydrogen-like emitter in an external electric field is successfully described both by semiclassical and quantum mechanical theory of the linear Stark effect (see e.g. [21,22]). Both theories yield the same result: an energy level with principal quantum number  $n$  is splitted into  $2n-1$  equidistant sub-levels determined by quantum numbers  $k$  ( $|k| < n$ ). Therefore, the spectral line emitted as a transition between energy levels 1 and 2 of the hydrogen atom consists of numerous components which are polarized either linearly, parallel to the vector of external field  $E$  ( $\Delta m = 0$ , or  $\pi$ -components), or circularly, in the plane perpendicular to  $E$  ( $\Delta m = \pm 1$ , or  $\sigma$ -components). Stark components are wavelength shifted from the line center by the value

$$(n_1 k_1 - n_2 k_2) \Delta \lambda_0, \quad (1)$$

where  $\Delta \lambda_0$  is the smallest shift determined by the local field intensity [22]:

$$\begin{aligned}\Delta\lambda_0 [\text{nm}] &= 1.52 \cdot 10^{-3} E [\text{kV/cm}] - \text{for the } H_\beta \text{ line,} \\ \Delta\lambda_0 [\text{nm}] &= 1.21 \cdot 10^{-3} E [\text{kV/cm}] - \text{for the } H_\gamma \text{ line.}\end{aligned}\quad (2)$$

With the polarizer axis set parallel or perpendicular to the electric field, the appropriate ( $\pi$  or  $\sigma$ ) overall profile is formed. In order to create overall  $\pi$  and  $\sigma$  Stark profiles we assumed that plasma broadening effects in the cathode fall region may be neglected; calculations of Bogaerts *et al.* [23] show that electron densities in the cathode dark space of an analytical glow discharge at 1000 V and 100 Pa do not exceed  $10^7 \text{ cm}^{-3}$ . Thus, to each Stark component we have assigned a Gauss function only. The full halfwidth  $\Delta\lambda_G$  of each Gaussian results from Doppler,  $\Delta\lambda_D$ , and instrumental,  $\Delta\lambda_I$ , halfwidths:

$$\Delta\lambda_G = \sqrt{\Delta\lambda_D^2 + \Delta\lambda_I^2}. \quad (3)$$

For hydrogen, the Doppler halfwidth can be calculated from

$$\Delta\lambda_D = 7.16 \cdot 10^{-7} \lambda_0 \sqrt{T}, \quad (4)$$

where  $\lambda_0$  is the central wavelength of the line and  $T$  is the temperature of the excited H atoms. The overall profile is calculated as the superposition of all components:

$$I(\lambda, E, T) = \sum_{i=1}^N I_{0i} \exp \left\{ - \left[ \frac{\lambda - (n_1 k_1 - n_2 k_2)_i \Delta\lambda_0}{\Delta\lambda_G / 2\sqrt{\ln 2}} \right]^2 \right\}, \quad (5)$$

where  $I_{0i}$  are relative intensities [21] and  $N$  is the total number of components (10 - for the both  $H_\beta$   $\pi$  and  $\sigma$  profiles, 14 and 13 - for the  $H_\gamma$   $\pi$  and  $\sigma$  profiles, respectively). The theoretical profiles (5) are fitted to the experimental recordings, by varying the electric field intensity  $E$  and the temperature  $T$  of excited hydrogen atoms. In the negative glow region, the difference between  $\pi$  and  $\sigma$  profiles disappears ( $E \approx 0$ ), and the fitting procedure is reduced to variation of  $T$  only. A detailed explanation of the theoretical basis of these measurements, fitting procedure and discussion of the influence of the fine structure splitting on the shape of  $\pi$  and  $\sigma$  profiles one can find in [17].

### 3.2 Theoretical basis for electric field measurements from Stark splitting and shifting of helium lines and their forbidden components

To measure electric field strengths in the CFR of pure helium and helium-hydrogen mixture discharges, we used the perturbation theory for the evaluation of the displacements of helium energy sub-levels in the external electric field, see e.g. [22]. Following the classical work by Foster [24], we calculated the displacements of the Stark sub-levels of the He I 492.19 nm ( $2p^1P^0 - 4d^1D$ ), 447.15 nm ( $2p^3P^0 - 4d^3D$ ) and 402.62 nm ( $2p^3P^0 - 5d^3D$ ) lines and their forbidden components ( $2p^1P^0 - 4f^1F$ ), ( $2p^3P^0 - 4f^3F^0$ ) and ( $2p^3P^0 - 5f^3F^0$ ), respectively, in the electric field ranging from 0 to 20 kV/cm. For these calculations, helium energy levels are taken from Martin [25]. As an example, the results for the 447.15 nm line (in wavelength units) are given in Fig. 2. For further analysis we concentrate here to the  $\pi$  ( $\Delta m = 0$ ) components which are usually stronger and easier to measure than  $\sigma$  ( $\Delta m = \pm 1$ ) components. The mutual wavelength separation  $\Delta\lambda_{AF}$  of  $\pi$  components of allowed and forbidden line is calculated in 1 kV steps and the results (see Fig. 3) are fitted by polynomial best fits with correlation factors better than 0.9999. Here, for an electric field ranging from 0 to 20 kV/cm, we neglected splitting of the common lower energy level for all three lines and their forbidden components. From Figs. 2 and 3 (see data for the 402.62 nm line) it is clear that, within the investigated range of electric field strengths, Stark components arising from transitions between sub-levels with magnetic quantum numbers  $m = 0$  and  $m = 1$  of both allowed and forbidden lines are practically unresolvable with our spectral resolution. Therefore with the polarizer mounted with its axis parallel to the external field only one allowed and one forbidden  $\pi$  component are detected. Thus, to evaluate the separation  $\Delta\lambda_{AF}$  (in nm) between corresponding lines we have taken an average value for the  $m_{upper} = 0 \rightarrow m_{lower} = 0$  and  $m_{upper} = 1 \rightarrow m_{lower} = 1$  displacements. The obtained results are fitted with following polynomials (see Fig. 3):

3<sup>rd</sup> order for the He I 492.19 nm line:

$$\Delta\lambda_{AF} = -1.87(9) \cdot 10^{-5} \cdot E^3 + 8.8(3) \cdot 10^{-4} \cdot E^2 + 1.4(2) \cdot 10^{-3} \cdot E + 0.1316(5), \quad (6)$$

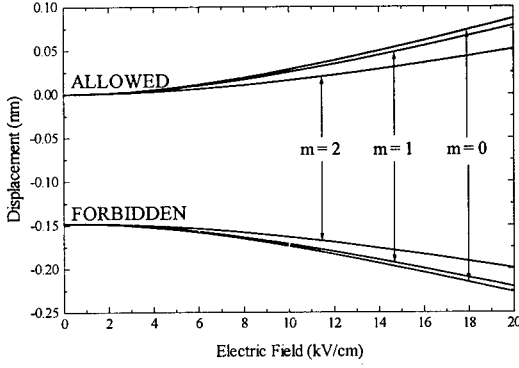


Fig. 2. The calculated sub-level displacements (in wavelength units) of  $4d\ ^3D$  and  $4f\ ^3F$  helium energy levels, which are the upper levels of the He I 447.15 nm allowed and its forbidden line, respectively.

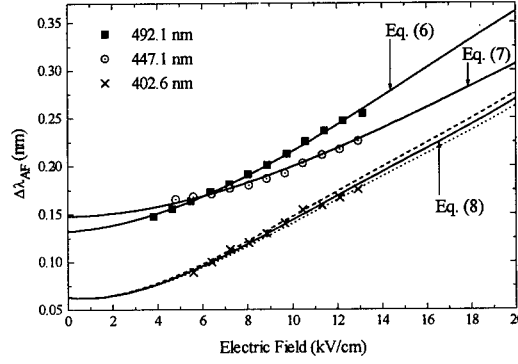


Fig. 3. The polynomial best fits of the calculated wavelength separation  $\Delta\lambda_{AF}$  of  $\pi$  components of the 402.62 nm line and its forbidden line:  $m_{upper} = 0 \rightarrow m_{lower} = 0$  transition (dashed line),  $m_{upper} = 1 \rightarrow m_{lower} = 1$  transition (dotted line) and average between  $m = 0$  and  $m = 1$  displacements, Eq. (8) (solid line). For the 492.19 nm and 447.15 nm lines only

average values (solid lines, Eqs. (6) and (7) respectively) are given. The results (scattered graphs) of the experimental testing of Eqs. (6-8), obtained by measuring  $\Delta\lambda_{AF}$  for all three He I lines vs. electric field strength determined from the  $\pi$  shape of  $H_\beta$  profile in helium-hydrogen mixture, are also given.

3<sup>rd</sup> order for the He I 447.15 nm line:

$$\Delta\lambda_{AF} = -1.06(3) \cdot 10^{-5} \cdot E^3 + 5.95(8) \cdot 10^{-4} \cdot E^2 + 2.5(7) \cdot 10^{-4} \cdot E + 0.1479(2), \quad (7)$$

4<sup>th</sup> order for the He I 402.62 nm line:

$$\Delta\lambda_{AF} = 1.9(2) \cdot 10^{-6} \cdot E^4 - 9.8(7) \cdot 10^{-5} \cdot E^3 + 1.86(9) \cdot 10^{-3} \cdot E^2 - 2.6(4) \cdot 10^{-3} \cdot E + 0.0638(6), \quad (8)$$

where  $E$  is the electric field strength in kV/cm. In addition, this averaging can be justified by the fact that  $m_{upper} = 0 \rightarrow m_{lower} = 0$  and  $m_{upper} = 1 \rightarrow m_{lower} = 1$  components of both allowed and forbidden lines are approximately of the same intensity [24].

In order to test Eqs. (6-8), we performed an experiment in a helium-hydrogen mixture where electric field strengths are independently determined from the shape of  $H_\beta(\pi)$  profile (see Eq. (14) in [17]) at various positions along the CFR of our discharge. At the same positions (same electric field strengths)  $\Delta\lambda_{AF}$  for the He I lines are determined and the results are given in Fig. 3. If one takes into account errors of both sets of measurements, the agreement with Eqs. (6-8) is very good.

## 4. RESULTS AND DISCUSSION

### 4.1 Pure hydrogen discharge

The examples of experimental recordings, best fits and the results of electric field intensities at various distances from the cathode derived from the  $H_\beta$  and  $H_\gamma$  lines are given in Figs. 4 and 5, respectively. Here it should be pointed out that, in the pure hydrogen discharge, best fits of experimental profiles are obtained assuming that two groups of excited hydrogen atoms exist: one with temperatures around 5 eV (so called "slow" neutrals) and another group with temperatures around 100 eV ("fast" neutrals). In the negative glow region, a third central narrow profile is observed, with a width determined by the Stark and Doppler ( $T_g \approx 1000$  K, see [14]) effects in the plasma as well as instrumental broadening [14], see Figs. 4 and 5. It is important to mention also, that by fitting a single experimental profile with a theoretical one (5), results of local electric field, temperatures of "slow"  $T_s$  and "fast"  $T_f$  excited hydrogen atoms and their relative concentrations are obtained simultaneously, see [17].

The comparison of experimentally determined electric fields from  $\pi$  and  $\sigma$  profiles, see Figs. 4 and 5, shows systematic discrepancies, with the field measured from  $\sigma$  being always smaller. These discrepancies have been discussed in detail in [17]. To determine the electric field intensity distribution in

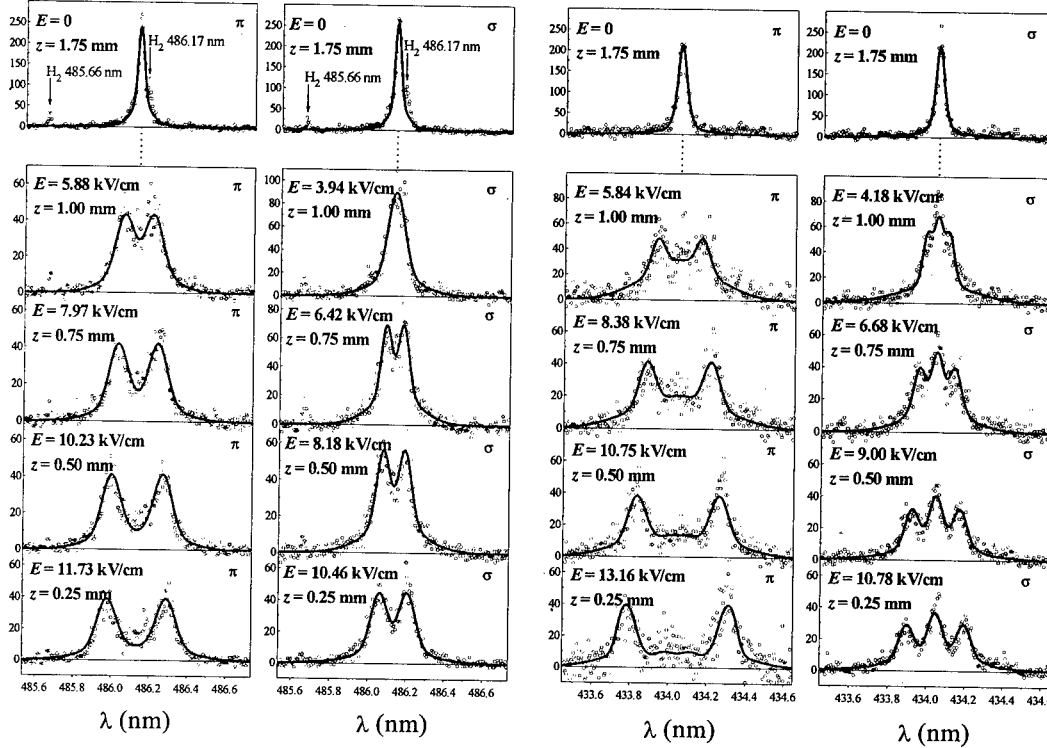


Fig. 4. Measured Balmer  $H_\beta$  Stark profiles and their best fits (solid lines) at several distances from the cathode. Intensities are given in arbitrary units. Discharge conditions: pure hydrogen at 228 Pa, 30 mA, 920 V.

Fig. 5. As in Fig. 4, but for the  $H_\gamma$  line.

the cathode fall region of the Grimm GDS, for the local field strength we used an average value determined from  $\pi$  and  $\sigma$  profiles, see [17]. The obtained data are used to calculate the cathode fall potential  $U_c = \int_0^L E dz$ , which is compared with the measured cathode-anode potential  $U_0$ . If one takes into account the uncertainties in electric field measurements, one may conclude that the agreement within  $\pm 10\%$  between electric field measurements from the  $H_\beta$  and  $H_\gamma$  line profiles is satisfactory, see [17]. The agreement between the measured cathode-anode voltage  $U_0$  and the potential fall derived from the electric field measurements indicates that, for the present experimental conditions, the whole potential applied to the electrodes is consumed in the cathode fall region.

Typical results of electric field axial distribution, obtained by fitting  $\pi$  and  $\sigma$  profiles of both  $H_\beta$  and  $H_\gamma$  lines through the cathode fall region, are presented in Fig. 6. The usual linear fit of the electric field intensity in the CFR is applied and shown in Fig. 6 also.

The origin of two groups of excited hydrogen atoms may be related to the presence of  $H^+$ ,  $H_2^+$  and  $H_3^+$  ions which are accelerated in the cathode fall region. Striking the cathode, these ions are neutralized, fragmented into atoms and reflected back towards the negative glow region. After the reflection from the cathode, neutrals collide mainly with  $H_2$  and excite, see e.g. [16]. We have shown [17] that only two groups of hydrogen atoms, originated from  $H^+$  and  $H_3^+$  ions, have enough energy to exceed threshold for Balmer lines excitation. "Slow" H atoms, whose average temperatures in different experimental conditions vary in our case from 3.4 - 8.2 eV are, most likely, excited in collisions of hydrogen atoms from  $H_3^+$  with  $H_2$ . On the other hand, the origin of "fast" excited H atoms, with average temperatures between 80 eV and 190 eV, may be related to energetic  $H^+$  ions only, see [17]. The typical axial distributions of both "slow" and "fast" excited hydrogen atoms temperature are shown in Fig. 7. The temperature distributions show a decrease with the distance from the cathode, which corresponds well

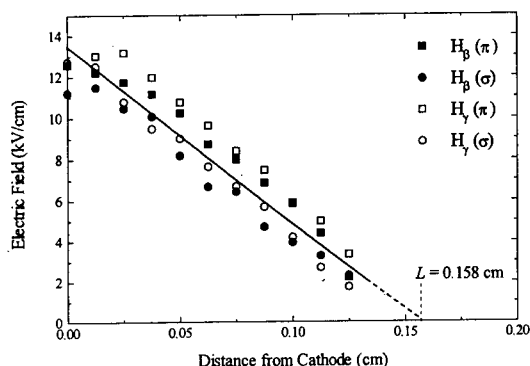


Fig. 6. Electric field distribution in the cathode fall region of the Grimm GDS, operating in pure hydrogen at 228 Pa, 30 mA, 920 V. Solid line corresponds to the usual linear fit.

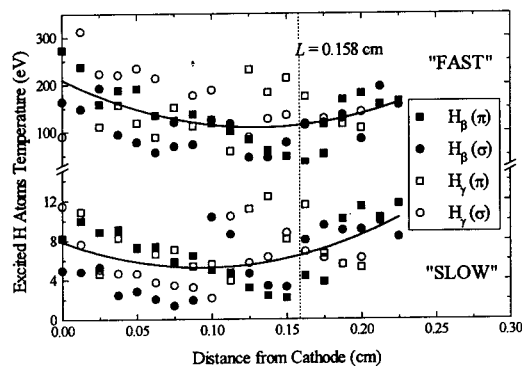


Fig. 7. Axial distribution of "slow" and "fast" excited hydrogen atoms temperature in the cathode fall region of the Grimm GDS, operating in pure hydrogen at 228 Pa, 30 mA, 920 V.

with decreasing energy of the reflected atoms. An unexpected rise of the temperature in the negative glow region, see Fig. 7, could be related to the additional collision processes with electrons, whose concentration is rather large ( $\approx 10^{14} \text{ cm}^{-3}$ , see [14]). Here, most likely, one has a superposition of profiles originating from two different excitation processes: one resulting from collisions with heavy particles, and another - collisions of fast neutrals with electrons. Assuming an exponential decrease of the number of reflected energetic atoms due to collisions with the matrix gas, a simple calculation using total cross section data [26] for collisions of neutral hydrogen atoms at 133.4 eV with  $\text{H}_2$  at  $p = 228 \text{ Pa}$ ,  $T_g = 1000 \text{ K}$  and  $L = 0.158 \text{ cm}$  shows that about 18% of the reflected "fast" H atoms arrive at the negative glow without a collision. In this region they collide with both electrons and matrix gas which results in two groups of excited atoms with different temperatures. Since electrons change the internal atom energy only, the group with larger temperature is the one from atom-electron collisions. Therefore, the resulting profile is broader than in the cathode fall region. Unfortunately, the spectral resolution does not allow us to separate these two profiles, and the results for average temperatures in the negative glow region in Fig. 7 represent some kind of an average value. In addition, the axial intensity distributions of the Balmer lines in hydrogen, see Fig. 8, show a second maximum in the beginning of the negative glow region, which could be another indication of the described fast atom - electron excitation.

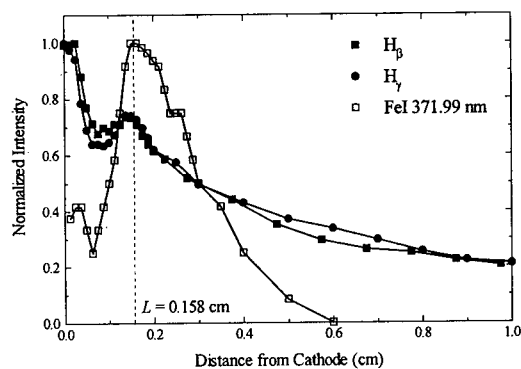


Fig. 8. Normalized axial intensity distributions of the hydrogen  $\text{H}_\beta$  and  $\text{H}_\gamma$  Balmer lines and neutral iron line.  $L$  is the length of the cathode fall region. Discharge conditions:  $\text{H}_2$  at 228 Pa, 30 mA, 920 V.

From the spatial distribution of the emission of hydrogen and sputtered material, shown in Fig. 8, one can see that the mechanism of hydrogen excitation is different from the mechanism of excitation of the metal atoms. Hydrogen atoms are excited in collisions with  $\text{H}_2$ , while Fe atoms are excited in collisions with electrons. The intensities of H lines are the largest close to the cathode surface where the energy and concentration of fast H atoms are the largest. The intensity of the iron line however, increases gradually from the cathode and this behavior may be related to the gradual increase of electron energy which reaches the optimum for excitation at the beginning of the negative glow region.

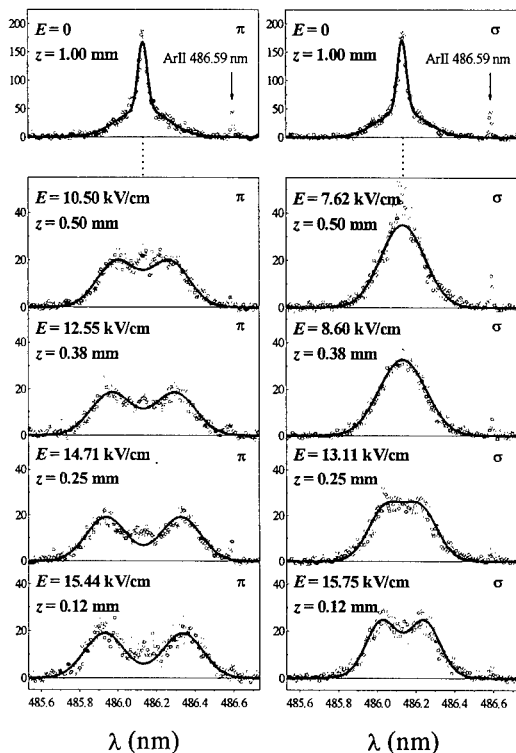


Fig. 9. As in Fig. 4, but in the Ar+3% $H_2$  mixture. Discharge conditions: 320 Pa, 30 mA, 820 V.

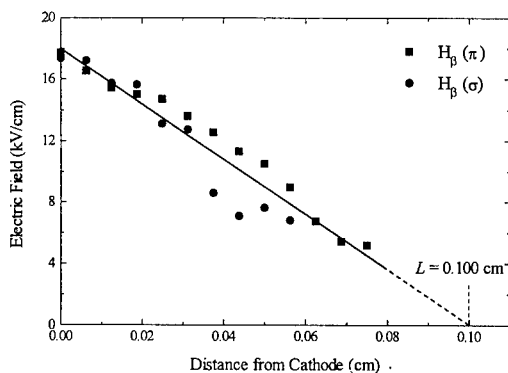
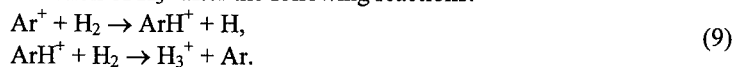


Fig. 10. Electric field distribution in the cathode fall of the Grimm GDS, operating in the Ar+3% $H_2$  mixture at 320 Pa, 30 mA, 820 V.

It is very interesting to note that hydrogen lines in the argon-hydrogen mixture exhibit much stronger wings of the lower part of profile, see Figs. 4 and 9, while the temperatures of excited hydrogen atoms are between those of "slow" and "fast" atoms in pure hydrogen, see [17]. In the gas mixture the role of argon is important for the very efficient production of  $H_3^+$  after the following reactions:



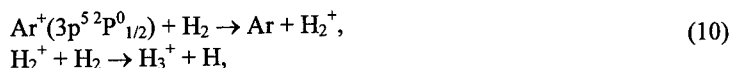
Another two reactions contribute considerably to the increase of  $H_3^+$  concentration in argon-hydrogen mixture:

## 4.2 Discharge in an argon-hydrogen mixture

In comparison to pure hydrogen, the discharges in an argon-hydrogen mixture are located closer to the cathode, with smaller lengths of the cathode fall region, so the gradients of electric field in the radial direction are larger. Due to the interference of the Ar I and Ar II lines with the hydrogen  $H_\gamma$  line in argon-hydrogen mixture, the electric field measurements are performed using  $\pi$  and  $\sigma$  profiles of the  $H_\beta$  only. Typical examples of the  $H_\beta$  Stark profile recordings, best fits and results of electric field measurements are given in Fig. 9. A small central peak superimposed on the  $\pi$  and  $\sigma$  profiles even close to the cathode arises out of the part of the discharge which is inevitably protruding through the observation slot into the field-free space. Again, differences between results of electric field measurements from  $\pi$  and  $\sigma$  profiles are detected, and they are also discussed in [17].

Typical results of the electric field distribution in the cathode fall region of the discharge operating in an argon-hydrogen mixture are presented in Fig. 10. As a consequence of the smaller cathode fall region, in comparison with pure hydrogen, see Fig. 6, the electric field intensities at the cathode surface are larger, as well as electric field gradients. Again, experimental electric field distributions are fitted by usual linear fit, presented by the solid line in Fig. 10.

Contrary to pure hydrogen, here one cannot distinguish several groups of excited hydrogen atoms with different velocities in the procedure of  $H_\beta$   $\pi$  and  $\sigma$  profiles fitting. Namely, only excited H atoms with energies in the range 32 - 43 eV exist, see [17]. The overall profiles are smooth, without distinct characteristic peaks induced by "slow" excited atoms, see Fig. 4, which helped us measure the electric field in hydrogen accurately. As a consequence, two typical peaks of  $H_\beta$  ( $\sigma$ ) - profiles can be resolved only in the first few observation positions from the cathode. This certainly affects the accuracy of our measurements.



see [16]. A large concentration of  $\text{H}_3^+$  ions increases the intensities of the hydrogen line wings. Therefore,  $\text{H}_3^+$  is now the dominating hydrogen ion and backscattered H atoms from the cathode originate mainly from this ion. In comparison with the pure hydrogen discharge, where “fast” H atoms originate from reflection of  $\text{H}^+$ , and “slow” from reflection of  $\text{H}_3^+$  ions, here we have excited atoms formed in reflection of  $\text{H}_3^+$  ions only. However  $\text{H}_3^+$  ions gain more energy in the cathode fall region due to the higher transparency of argon (mass ratio 3:40) than the hydrogen matrix (3:2). Typical axial distribution of the excited hydrogen atoms temperature in the argon-hydrogen mixture discharge is shown in Fig. 11.

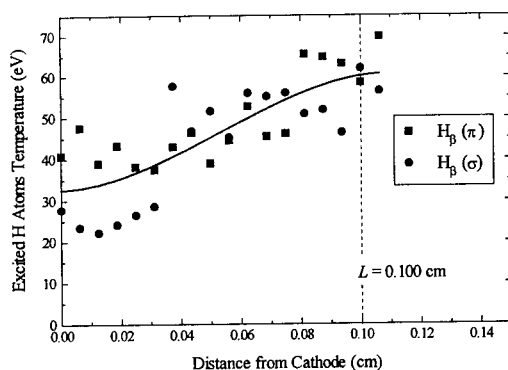


Fig. 11. Axial distribution of the excited hydrogen atoms temperature in the cathode fall region of the Grimm GDS, operating in the argon-hydrogen mixture at 320 Pa, 30 mA, 820 V.

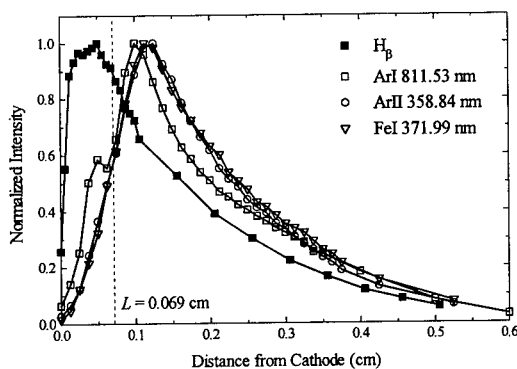


Fig. 12. Normalized axial line intensity distributions of the hydrogen  $\text{H}_\beta$ , neutral and ionized argon, and neutral iron line.  $L$  is the length of the cathode fall region. Discharge conditions:  $\text{Ar}+3\%\text{H}_2$  at 320 Pa, 20 mA, 490 V.

From Fig. 11 one can see that the effect of the excited hydrogen atoms temperature increasing towards the negative glow region is even more pronounced in the argon-hydrogen mixture than in pure hydrogen, see Fig. 7. The similar explanation could be drawn: in addition to the excitation of back-reflected hydrogen atoms by collisions with matrix gas, they are excited in collisions with electrons. Once again, assuming an exponential decrease of the number of reflected energetic atoms due to collisions with matrix gas, a simple calculation using total cross section data [27] for collisions of H atoms at 75 eV with argon at a pressure of 320 Pa and gas temperature ( $T_g$ ) of 1000 K, shows that, for a cathode fall length of 0.1 cm, as many as 66% of the reflected neutrals reach the negative glow region without any collision. Their higher concentration in comparison with pure hydrogen, makes this effect more pronounced in the argon-hydrogen discharge.

The axial distributions of the Ar I, Ar II, Fe I and  $\text{H}_\beta$  line intensities are given in Fig. 12. Again the maximum of intensity of the  $\text{H}_\beta$  line is close to the cathode surface. However, contrary to pure hydrogen, where the maximum of intensity is at the cathode surface, see Fig. 8, steep rise of the  $\text{H}_\beta$  intensity in argon-hydrogen mixture is detected. This difference may be explained by a more efficient collisional energy transfer between reflected energetic hydrogen atoms and  $\text{H}_2$  molecules (mass ratio 1:2) than in case of argon (1:40). The second maximum in the  $\text{H}_\beta$  line intensity axial distribution, clearly observed in pure hydrogen, see Fig. 8, is partially covered here by the first maximum, which is slightly shifted away from the cathode surface towards the negative glow, see Fig. 12.

#### 4.3 Discharge in pure helium and in a helium-hydrogen mixture

To obtain local electric field strengths in pure helium and in helium-hydrogen mixture discharges, we used polarization-dependent Stark splitting and shifting of helium lines, as described in Section 3.2. As an illustration of the influence of the electric field strength on the wavelength position of the He I 492.1 nm and He I 447.1 nm allowed and their forbidden lines, the typical  $\pi$  polarized spectra, recorded at several



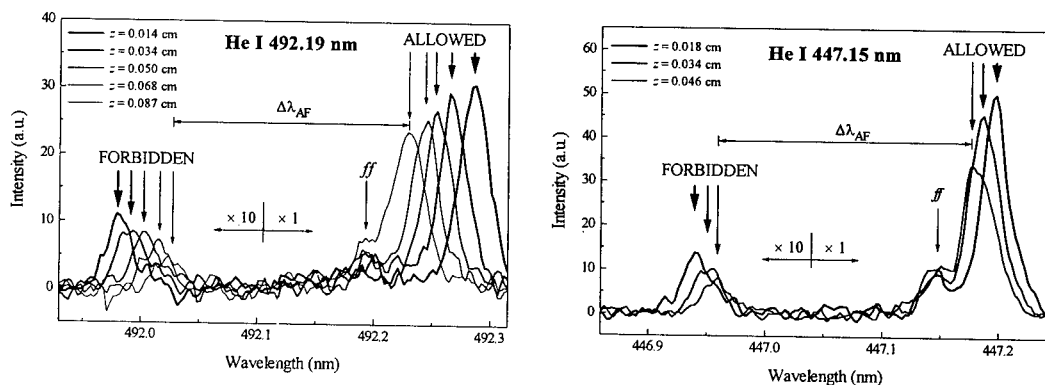


Fig. 13. Typical  $\pi$  polarized spectra of the He I 492.19 nm and He I 447.1 nm lines and their forbidden counterparts, recorded at several distances from the cathode surface of the Grimm GDS operating in pure helium. Discharge parameters: 128 Pa, 20 mA, 1500 V. Unshifted peaks denoted by *ff* (field-free) are emitted from the plasma protruding through the observation slot. The forbidden lines are recorded with 10 times larger detection sensitivity.

distances from the cathode of the Grimm GDS, are given in Fig. 13. The unshifted maxima in these figures originate from the discharge protruding through the observation slot into the field-free space. To facilitate mutual agreement of the results obtained from three He I lines for the same experimental conditions, we have measured the electric field distribution in the CFR of our glow discharge and the results are given in Fig. 14.

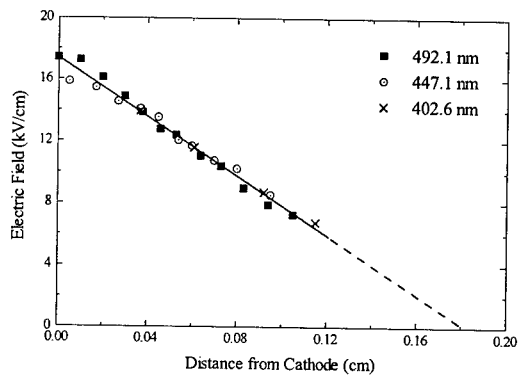


Fig. 14. The axial distribution of the electric field determined from  $\Delta\lambda_{AF}$  for all three He I lines in the CFR of the Grimm GDS. Experimental conditions as in Fig. 13.

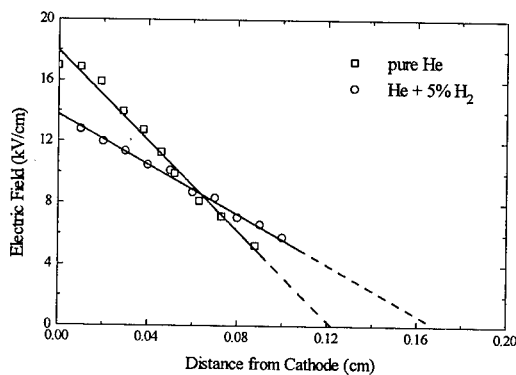


Fig. 15. The axial distribution of the electric field strength in pure helium and in the helium-hydrogen mixture for the same discharge conditions: 202 Pa, 20 mA, 1050 V.

To compare the results in pure helium and in the helium-hydrogen mixture, we had to establish the same discharge conditions (pressure, current and voltage) in both gases. This is achieved by changing the gas flow ratio in two vacuuming branches of our Grimm GDS lamp, see [19]. The typical results of electric field axial distribution, measured using the He I 492.19 nm line, are given in Fig. 15. It is important to notice that even a small amount (5%) of hydrogen decreases the electric field intensity at the cathode surface by  $\approx 25\%$  and extends the length of the CFR by  $\approx 30\%$ .

In pure helium, the measurements are performed using the He I 492.19 nm line, for a 20 mA discharge current at three different pressures (128, 145 and 202 Pa). It is interesting that for all pressures the maximum electric field at the cathode surface remains the same, and only the length of the CFR changes, see Fig. 16. This result suggests that, in this range of discharge conditions, the electric field strength at the cathode surface does not depend upon the applied voltage and the pressure. To check our experimental results of the local electric field intensity, the cathode fall potential  $U_i = \int_0^L E dz$  is calculated and compared with the measured anode-cathode voltage  $U_0$ . As in our above described measurements in pure hydrogen and the argon-hydrogen mixture [17],  $U_i$  is approximately equal to the total anode-cathode

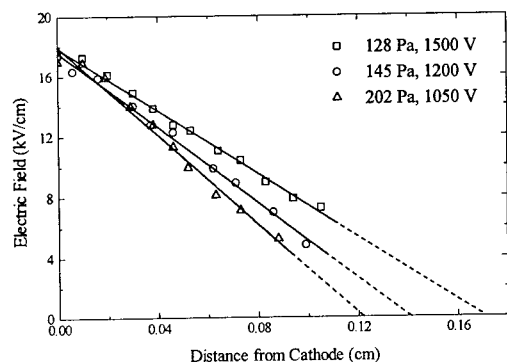


Fig. 16. The results of the electric field axial distribution measurements in pure helium at three different pressures.

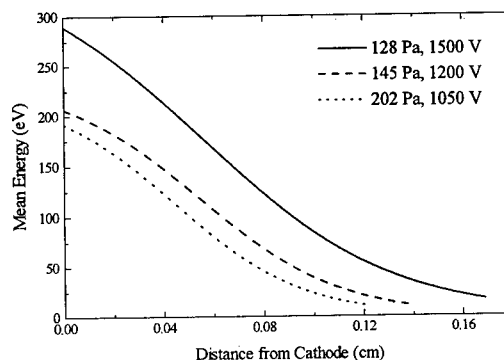


Fig. 17. Spatial distributions of  $\text{He}^+$  ion mean energies in the CFR of the Grimm GDS in pure helium.

voltage  $U_0$ , indicating that most of the applied voltage is consumed in the CFR of the Grimm GDS. The obtained axial distributions of the electric field strength in pure helium are used to calculate the mean free paths of the  $\text{He}^+$  ions generated in symmetrical charge exchange processes and their mean energy distributions in the CFR. For this purpose, the theory of Wronski [28] is applied, the basics of which are given in detail in [17,19]. The results of these calculations, i.e. spatial distributions of the  $\text{He}^+$  ion mean energies for three investigated pressures of pure helium, are given in Fig. 17. It is interesting to notice that the maximum mean ion energy at the cathode surface (190 - 290 eV) represents approximately 20% of the anode-cathode voltage, see Fig 17. The same correlation is found between the mean free path and the length of cathode fall region, see [19].

## 5. CONCLUSIONS

In this paper we presented results of the experimental study of the cathode fall region of a Grimm-type glow discharge in pure hydrogen, an argon-hydrogen mixture, pure helium and a helium-hydrogen mixture. First, the details of the experimental setup are given, with the emphasis on the improvements in the helium-based experiment. This is followed by the short reviews of the theoretical basis of our measurements: Stark splitting of the hydrogen Balmer  $H_\beta$  and  $H_\gamma$  lines in an external electric field, and Stark splitting and shifting of the neutral helium 492.19 nm, 447.15 nm and 406.62 nm lines with respect to their forbidden counterparts.

In the pure hydrogen discharge, the results of electric field strength axial distributions obtained from the  $H_\beta$  and  $H_\gamma$  lines show good mutual agreement, see Figs. 4 - 6. Doppler spectroscopy of the same Balmer lines showed that at least two groups of excited hydrogen atoms with considerably different velocities exist in the discharge. The origin of "slow" neutrals, with average energies in the range 3.4 - 8.2 eV is related to the existence of  $\text{H}_3^+$  ions which are accelerated in the CFR, neutralized and fragmented into atoms at the cathode surface, and back-reflected towards the negative glow region. The other group of "fast" hydrogen atoms, with average energies ranging between 80 and 190 eV, most likely originate from the neutralization and reflection of energetic  $\text{H}^+$  ions. These back-reflected atoms, on their way to the negative glow region, collide mostly with  $\text{H}_2$  and excite. Approaching the negative glow region, the increase of both "slow" and "fast" hydrogen atoms temperature is detected, see Fig. 7, and related to the additional excitation in collisions with electrons.

The discharge in the argon-hydrogen mixture is located closer to the cathode and, therefore, higher electric fields at the cathode surface as well as higher field gradients are detected, see Fig 9. Due to the shorter CFR and the absence of "slow" hydrogen atoms, the electric field measurements are less accurate, see Fig 10. Namely, in the argon-hydrogen mixture only one group of excited hydrogen atoms is detected, with average energies in the range 32 - 43 eV. Their origin is related to the dominant role of  $\text{H}_3^+$  ions in the discharge. The temperature increase towards the negative glow region is even more pronounced than in pure hydrogen, see Fig. 11, due to the higher number of energetic neutrals which reach the negative

glow without any collision. In both gases, the axial intensity distributions of hydrogen Balmer lines and lines of sputtered material and matrix gas, see Figs. 8 and 12, confirm the different excitation mechanism of hydrogen lines in comparison with all others. Balmer lines are excited in collisions with heavy particles, while the excitation of lines of other species results from the collisions with electrons.

Finally, in pure helium and helium-hydrogen discharges, the method of electric field measurements using Stark splitting and shifting of neutral helium allowed and forbidden lines is demonstrated. Good mutual agreement between electric field measurements from three helium lines is obtained, see Fig. 14. It is detected that even a small amount of hydrogen considerably changes ( $\approx 25\%$ ) the electric field intensity at the cathode surface and the length of CFR, see Fig. 15. In pure helium, for all three investigated pressures, the electric field at the cathode surface remains constant (around 17 kV/cm), and the length of CFR changes only, see Fig. 16. By applying the theory of Wronski [28], the spatial distributions of  $\text{He}^+$  ion mean energies in the CFR of pure helium discharge are obtained, see Fig. 17. At the cathode surface, maximum mean ion energies range from 190 - 290 eV at the present discharge conditions, see Fig. 17.

#### Acknowledgments

The loan of a 4 m spectrometer from the Paris Observatory - Meudon is gratefully acknowledged. This work is supported by the Ministry of Science and Technology of the Republic of Serbia.

#### References

- [1] Grimm W., *Spectrochim. Acta Part B* **23** (1968) 443-454.
- [2] Dogan M., Laqua K., Maßmann H., *Spectrochim. Acta Part B* **26** (1971) 631-649.
- [3] Dogan M., Laqua K., Maßmann H., *Spectrochim. Acta Part B* **27** (1972) 65-88.
- [4] Broekaert J.A.C., *J. Anal. At. Spectrom.* **2** (1987) 537-545.
- [5] Berneron R., *Spectrochim. Acta Part B* **33** (1978) 665-673.
- [6] Koch K.H., Kretschmer M., Grunenberg D., *Microchim. Acta II* (1985) 1-25.
- [7] Gough D.S., *Anal. Chem.* **48** (1976) 1926-1931.
- [8] Ohls K., *Fresenius' Z. Anal. Chem.* **327** (1987) 111-118.
- [9] Harrison W.W., Bentz B.L., *Prog. Anal. Spectrosc.* **11** (1988) 53-59.
- [10] Parker M., Marcus R.K., *Appl. Spectrosc.* **48** (1994) 623-631.
- [11] Boumans P.W.J.M., *Spectrochim. Acta Part B* **46** (1991) 711-739.
- [12] Broekaert J.A.C., *Appl. Spectrosc.* **49** (1995) 12A-19A.
- [13] Boumans P.W.J.M., Broekaert J.A.C., Marcus R.K.,  
Eds. *Spectrochim. Acta Part B* **46** (2) (1991) 111-313; **46** (4) (1991) 457-546.
- [14] Kuraica M., Konjević N., Platiša M., Pantelić D., *Spectrochim. Acta Part B* **47** (1992) 1173-1186.
- [15] Kuraica M., Konjević N., *Phys. Rev. A* **46** (1992) 4479-4482.
- [16] Kuraica M., Konjević N., *Phys. Scripta* **50** (1994) 487-492.
- [17] Videnović I.R., Konjević N., Kuraica M.M., *Spectrochim. Acta Part B* **51** (1996) 1707-1731.
- [18] Kuraica M.M., Konjević N., *Appl. Phys. Lett.* **70** (1997) 1521-1523.
- [19] Kuraica M.M., Konjević N., Videnović I.R., *Spectrochim. Acta Part B* **52** (1997) 745-753.
- [20] Ferreira N.P., Human H.G.C., Butler L.R.P., *Spectrochim. Acta Part B* **35** (1980) 287-295.
- [21] Condon E.U., Shortley G.H., *The Theory of Atomic Spectra*, (University Press, Cambridge, 1977).
- [22] Ryde N., *Atoms and Molecules in Electric Fields*,  
(Almqvist & Wiksell International, Stockholm, 1976).
- [23] Bogaerts A., van Straaten M., Gijbels R., *Spectrochim. Acta Part B* **50** (1995) 179-196.
- [24] Foster J.S., *Proc. R. Soc. London A* **117** (1927) 137-163.
- [25] Martin W.C., *J. Phys. Chem. Ref. Data* **2** (1973) 257-265.
- [26] Phelps A.V., *J. Phys. Chem. Ref. Data* **19** (1990) 653-675.
- [27] Phelps A.V., *J. Phys. Chem. Ref. Data* **21** (1992) 883-897.
- [28] Wronski Z., *Vacuum* **40** (1990) 387-394.

## Triggering of Negative Corona

M. Laan, P. Paris and V. Repän

*University of Tartu, Institute of Experimental Physics and Technology, Tartu Tähe Str. 4, EE2400 Estonia*

**Abstract.** The parameters of both low-current and high-current modes of DC negative corona discharge are described. The experiments were carried out in point-plane gaps in stagnant media of pure nitrogen, nitrogen, ambient air and in a dust-free air flow. A number of different types of point electrodes were used, including points covered by layers of  $\text{TiO}_2$  and  $\text{HfO}_2$  of controlled thickness. An overview of different methods of the triggering of the high-current mode is given. Discharges were initiated using x-ray radiation, laser radiation, UV radiation from different sources, and flux of positive ions. The correspondence of the model of dielectric switching mechanism as the triggering mechanism of high-current mode to the experimental results is discussed. Besides, the possible mechanisms limiting the repetition rate of Trichel pulses at its lower values ( $< 10^4 \text{ s}^{-1}$ ) are analysed.

### 1. INTRODUCTION

There are two modes of DC negative corona: the low-current (LCM) and the high-current (HCM) ones. These modes are observed in electronegative as well as in non-attaching gases ([1], [2]). Near the onset potential in electronegative gases the HCM exists in a pulsed manner and the parameters of the pulses are determined by the processes in the discharge gap. In non-attaching-gases the HCM is controlled by the outer circuit: the discharge may be a steady-state one [1] or relaxation-type oscillations may occur [3]. The processes leading to the oscillations are not treated here; i.e. we assume that the outer circuit ensures the establishment of a steady-state discharge of the HCM.

The study of the triggering of negative corona has a long-term history: the first systematical studies of pulsed corona (Trichel pulses) in air were carried out in a point-plane gap by Loeb et al [4]. Their most important findings were:

- The onset potential of repetitive Trichel pulses is badly reproducible, it has a strong dependence on the point prehistory.
- The onset potential of pulses does not depend on point material.
- The stable triggering of Trichel pulses was achieved when the points were covered by the specks of some insulating material. It was concluded that the Malter effect has a crucial role for the triggering of the pulses.
- Measurements of initiation of Trichel pulses by UV light gave contradictory results. Radiation of higher intensity suppressed the pulses, at lower intensities the pulses were well triggered.

We had two important reasons to carry out a cycle of studies of the triggering of the HCM of negative corona. Firstly, as was shown by experiments [1], during the first tens of nanoseconds of the LCM-HCM transition neither the spatio-temporal development of the light emitted by discharge nor the temporal changes of the current depend on gas composition. So, very likely the mechanisms of the triggering processes are similar. Furthermore, there is a striking similarity between the LCM-HCM transition and the development of instabilities in high pressure bulk discharges in a homogeneous field [5]. For this reason the study of the triggering of the HCM of negative corona might serve as a model of the rise of near-cathode ionisation instabilities in the case of bulk discharges. Secondly, the negative corona proved to be a very sensitive detector of electronegative trace gases: recording the repetition rate of corona pulses as a

function of the mean current of corona, it is possible to determine ppm-level concentrations of  $\text{SF}_6$  in argon [6] from the slope of the dependence. Unfortunately the effect of ageing interferes: in a stagnant medium at a certain gas composition the slope of the dependence altered with time [7]; i.e. the probability of the rise of a Trichel pulse changes with time. Whether the effect was caused by the changes of the gas composition or the point emissivity was not clarified.

As the field strength at the cathode surface ( $\sim 10^5$  V/cm) is close to that of vacuum breakdown, it was suggested [8] that the triggering mechanisms should not differ much and so the HCM of corona is triggered by the Fowler-Nordheim type burst-like emission of electrons. The studies of two research groups strongly influenced the set-up of this assumption:

- The similarities between the triggering mechanisms of vacuum breakdown and that of high pressure discharges have been emphasised and experimentally studied by Latham et al [9]. According to a detailed model developed (e.g. [10]), the emission starts from the site of the cathode covered by a dielectric inclusion. This 'dielectric switching mechanism' is supported by the measured energy distribution function of emitted electrons.
- In a number of publications Mesyats et al (e.g. [11]) have dealt with the viewpoint of the common nature of the triggering mechanisms of vacuum breakdown and gas discharges. They explain that in a wide range of discharge types (inc. corona) any discharge starts due to the formation of explosive centres - 'ectons'.

The purpose of the present paper is to give an overview of the different methods used for the initiation of negative corona, the experimental results, and to discuss the correspondence of the results with the model proposed.

## 2. EXPERIMENTAL

### 2.1. Discharge gaps and gas media

All the experiments were made in point-plane gaps. In most of the cases (if not mentioned otherwise) the gap spacing was 4 cm and the point electrode was stressed. The point electrodes were hemispherically capped wires of diameter 1 mm. The point electrodes were made of platinum (Pt), aluminium (Al), copper (Cu), molybdenum (Mo) and graphite (C). Their curvature radius differed from 0.5 mm not more than 10  $\mu\text{m}$ . Both previously non-oxidised Cu and Mo electrodes and the ones oxidised in hot air were used. A number of Mo and Cu points were covered by layers of  $\text{TiO}_2$  and  $\text{HfO}_2$  of different thickness (1-100 nm) [12]. The morphological changes caused by discharge at the point surface and the microprobe x-ray spectra of different sites at the point surface were recorded with the help of scanning electron microscope.

The experiments were made in four different media: stagnant media of pure nitrogen, nitrogen, ambient air, and in a dust-free air flow.

Pure nitrogen: the discharge chamber was evacuated to  $5 \cdot 10^{-8}$  Torr and warmed up to 100 °C, the duration of a pumping was at least 10h. The chamber was filled with pure nitrogen (nitrogen 4.6).

Nitrogen: the discharge chamber was evacuated to  $< 10^{-5}$  Torr and was filled with the nitrogen of the same purity as in the first medium.

Ambient air: the measurements were made with laboratory air.

Dust-free air flow: before the entering in a discharge chamber the air flow passed a high efficiency fibre filter; only the particles of less than 10 nm were recorded and their concentration was  $< 10^3$  1/cm<sup>3</sup>.

### 2.2. Common regularities of LCM-HCM transition

A sketch of a typical current pulse corresponding to the transition is presented in figure 1. Depending on the gas medium, its pressure and point material, a step  $i_s$  at the leading edge of the current pulse is more or less pronounced. In nitrogen a well-pronounced step is recorded in the case of C point in a wide range of pressures (up to atmospheric) while for Mo point a step is observable only in the limits of 100-150 Torr

[8]. If the other experimental conditions (pressure, point type etc.) are maintained the same, the leading edge does not depend remarkably on the gas composition used.

In contrast, the decay of a pulse has a strong dependence on medium. At atmospheric pressure in pure nitrogen and also in un-used nitrogen the current peak  $i_{max}$  is followed by a slow decay and after  $1.5 \mu s$  a steady-state HCM is established [1, 13]. After the discharge running some time in nitrogen, the steady HCM is replaced by a pulsed discharge (figure 1). The pulse duration  $\tau$  diminishes gradually with the increasing running time of discharge. In ambient air and air flow only a pulse form of the HCM exists and at the atmospheric pressure the typical decay time of the current is  $\sim 100$  ns.

### 2.3. LCM in stagnant media

The LCM in stagnant media are self-sustained ones, i. e. they exist without external irradiation.

The curve ABCDEF presented in figure 2 belongs to the discharge in pure nitrogen at near-atmospheric pressure [1]. The part AB is the  $i$ - $U$  characteristic for the LCM. The current of LCM is time-dependent: at a certain voltage the current diminishes with time, the decay-time has the range of tens of minutes. In [2] a similar curve of LCM was recorded in pure nitrogen at higher pressures. At the point B the transition BCDE to the HCM starts. If the protective resistor is small enough, the current pulse corresponding to the transition is very close to the one presented in figure 1. The part EF belongs to the HCM, the current is determined by a protective resistor.

It should be pointed that the point electrode was used for a long time and its surface was covered by craters.

In ambient air [1] the  $i$ - $U$  curve of the LCM ( $A'B'$  in figure 2) is more erratic, the dependence both on the point type and the sample was observed; e.g. for an oxidised Al point the current  $> 10^{-12}$  A was recorded only at voltages  $U > 7$  kV. At the point B' the discharge transits to the HCM; i.e. to the regime of repetitive Trichel pulses. The voltage  $U_0$  corresponding to B' is the onset potential.

### 2.4. Dependence of repetition rate of Trichel pulses on point properties

As it is described in sections 2.2 and 2.3, the LCM-HCM transition as well as the LCM are dependent on the point properties. In [14] the influence of the point properties on the parameters of the HCM (i.e. on the repetition rate and the mean current of Trichel pulses) in ambient air is described. Cu points oxidised in hot air (thickness of an oxide layer is  $> 250$  nm) and those covered by  $TiO_2$  layers of 5 nm and 100 nm thickness were tested. In the case of thick layers (250 and 100 nm) there is a huge difference between the repetition rate (RR) - voltage ( $U$ ) dependencies for a virgin point and for a point influenced by discharge

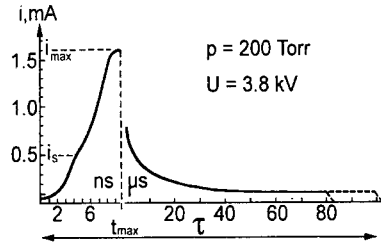


Figure 1: Typical current pulse in nitrogen, Al point;  $i_s$  - current step;  $i_{max}$  - current peak;  $\tau$  - pulse duration.

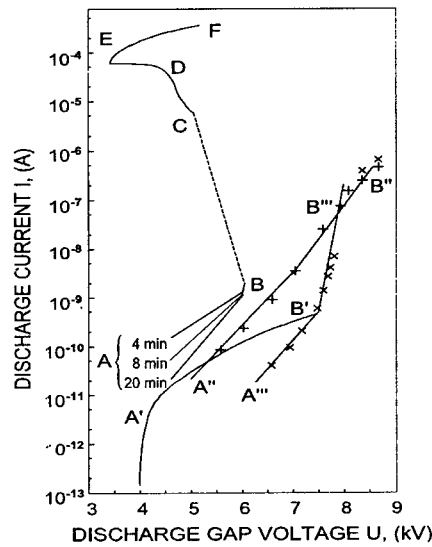


Figure 2:  $i$ - $U$  characteristics for negative coronas, Pt point; ABCDEF - pure nitrogen, stagnant medium, self-sustained discharge; A'B' - ambient air, self-sustained discharge; A''B'', A'''B''' - air flow, two different intensities of UV light, non-self-sustained discharge.

for a longer time. The curves presented in figure 3 belong to one and the same point and are recorded in a similar manner: firstly the voltage is increased by a 0.2 kV step (8.0 kV  $\rightarrow$  8.2 kV  $\rightarrow$  etc.) and then decreased (as 8.5 kV  $\rightarrow$  8.3 kV  $\rightarrow$  ). In the case of a virgin point a memory effect is observed: at every voltage the RR depends on its value at the previous voltage and not on the voltage established. At a certain voltage the RR is time-dependent: it gradually increases with time. This change lasts for several minutes and its duration depends on voltage. After this process the point becomes conditioned and the RR- $U$  dependence is nearly a linear one.

For the points covered by thin layers there are no remarkable differences between linear RR- $U$  dependencies for virgin and used points.

The observations with a scanning electron microscope indicated that due to the surface-discharge interaction a number of micrometer-size craters appeared at the surface of the points covered by thick layers while in the case of thin layers the craters were badly observable or they were missing at all.

The linear dependence of the RR on the mean current of corona seems independent of the point properties.

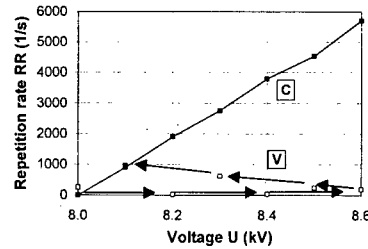


**Figure 3:** Repetition rate as a function of voltage, oxidised Cu point; V - dependence for virgin point; C - dependence for conditioned point.

## 2.5. Initiation of LCM-HCM transition in stagnant media

During the LCM-HCM transition occurring at a certain voltage the current suddenly increases by several orders of magnitude. To understand the nature of these huge changes it is not enough to study only the self-excited (spontaneous) corona pulses. The external triggering gives much more information on the processes leading to the transition.

### 2.5.1. X-ray initiation

In ambient air a flash of x-ray radiation of 5 keV mean quantum energy and of 50 ns half-width was directed through an aperture in anode to the discharge gap [1]. The repetition rate of flashes was  $10 \text{ s}^{-1}$ . To minimise the influence of spontaneous pulses the measurements were carried out at voltages close to the onset  $U_0$ . The distributions of delay times of Trichel pulses from the beginning of x-ray pulse were measured for different points. The distribution function varies with the point sample and voltage but always the highest probability of the rise of a Trichel pulse is in the limits 30-40 ns. When a Pt point is covered by a layer of transformer oil the current of the LCM is practically absent and the onset of spontaneous pulses rises remarkably (up to 1 kV) compared with  $U_0$  for non-covered points. Nevertheless the initiated ones start at voltage  $U_0$ . At higher voltages an x-ray flash initiates a series of Trichel pulses.

### 2.5.2. Laser initiation

In nitrogen where the onset  $U_0 \approx 9 \text{ kV}$  is considerably higher than in ambient air the corona pulses were triggered using the radiation of a pulsed XeCl laser ( $\lambda = 308 \text{ nm}$ , pulse duration  $\approx 60 \text{ ns}$ ) [13]. The radiation was directed to the gap through an aperture in the central part of the plane electrode and it was focused near the point surface. The maximum intensity  $\sim 10^7 \text{ W/cm}^2$  is much lower from that needed for the optical breakdown. It is possible to record laser-triggered current pulses starting from the voltage  $U \approx 3 \text{ kV}$  and starting from  $U \approx 7 \text{ kV}$  the waveform of a current pulse becomes similar to that of spontaneous pulses in nitrogen (figure 1) with its typical long tail. Decreasing the intensity of radiation by an order of magnitude the time interval between the beginning of a laser pulse and the beginning of current pulse changes from 5 to 90 ns. Very likely the triggering in this case is caused by the heating of the point surface up to the temperatures where the thermionic emission becomes effective. It is proved by the linear dependence of  $\ln(i_{\max})$  on  $\sqrt{U}$  for a number of different radiation intensities.

The main disadvantage of this way of initiation is that due to the high temperature of the point a large amount of impurities is liberated and the gas composition changes during a short time interval.

### 2.5.3. Laser-formed plasma initiation

Although the initiation of corona pulses by laser radiation described in the previous section is an efficient one, it is hardly possible that such thermal mechanism takes place in the case of spontaneous corona pulses. For that reason another laser-based triggering method was developed [15]. In ambient air the radiation of a pulsed XeCl excimer laser (pulse of  $\approx 50$  mJ energy, repetition rate  $10\text{ s}^{-1}$ ) was focused on the Pb target at the anode surface. The plasma formed at the target radiates in a wide range of spectra: we recorded a quasicontinuous spectrum in the limits of 200-600 nm. A pulse of plasma radiation has the rise-time of 5 ns followed by an exponential decay. The pulse duration is  $\approx 40$  ns. The method used allows to trigger corona pulses both below and above the onset potential  $U_0$ . The minimum voltage where the triggering is achieved depends to some degree on point type. The delay time changes from 30 ns at the minimum voltage to 10 ns at the onset  $U_0$ ; at higher voltages the delay time remains nearly constant. Slow but systematic changes of the delay time take place with running time of pulses. Very likely they are caused by the fine dust particles emitted from the target: as detected with an Auger spectrometer there were specks of Pb at the point surface.

### 2.6. Device for the study in dust-free air flow

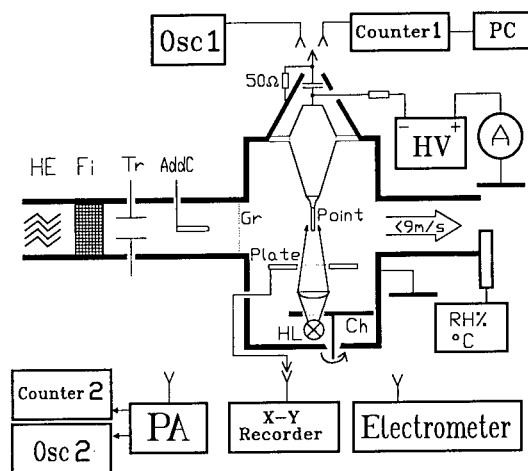


**Figure 4:** Device for studies in dust-free air flow; Osc1, Osc2 - oscilloscopes; A - ammeter; PC personal computer; HE - heat exchanger; Fi - fibre filter; Tr - ion trap; AddC - source of additional corona; Gr - calibrated grids; HL - hydrogen lamp; Ch - chopper; RH%, °C - hygrometer; PA - preamplifier.

On the point shape of AddC the ion flux was a steady state or pulsed ( $>10^4$  1/s) one. The flux was changed by the grids Gr. The mean current of ions was recorded with the ammeter A.

To radiate the point with UV light ( $\lambda > 200$  nm) a hydrogen lamp HL (20 W) was used. The intensity of light was changed by calibrated slits. For temporal studies a chopper Ch with variable apertures was used.

A high voltage supply HV allowed to change the voltage with the smallest step of 10 V. Mean currents were measured with the ammeter A and an electrometer. The waveforms of Trichel pulses were recorded with an oscilloscope Osc1 and the repetition rates with a counter 1 and a personal computer PC. The counter 1 was also used for the measurements of time intervals between light pulses and the Trichel

During experiments in a stagnant medium a number of accumulation processes may occur: fine dust particles created by discharge accumulate; gas composition changes due to plasma-chemical reactions; the heating of gas takes place. All these factors may influence the ionisation processes in gas as well as the emissivity of the cathode. Experiments in moving media give a possibility to diminish the number of uncontrolled parameters. A detailed description of the device presented in figure 4 is given in [12] and [16].

The rate of the air flow was changed from 10 to 45 l/s. With the help of a heat exchanger HE it was possible to fix the temperature in the limits 15-30 °C. The dust and ions in the entering ambient air were removed by the filter Fi and the ion trap Tr, respectively. The temperature, relative humidity and pressure were recorded.

It was possible to direct a flux of positive ions into the discharge chamber using a source of additional positive corona AddC. Depending on



ones. Slow ( $> 1$  s) temporal changes were recorded by an X-Y recorder. For the detection of faster processes of the LCM a preamplifier PA, an oscilloscope Osc2 and a counter 2 were used.

## 2.7. LCM in air flow

If the gap is not influenced externally, in an air flow at voltages less than  $U_0$  (onset in a stagnant air) a self-sustained LCM is missing ( $i < 10^{-12}$  A). The discharge current appears only when the UV radiation is directed to the point. At the same gas density, voltage and the intensity of the UV light the current recorded depends on the prehistory of the point: for how long the air flow has been switched on; whether before the recording the point has been illuminated and whether the discharge has been running. At an applied voltage  $U < U_0$ , after switching-on the air flow and the light the current increases gradually and it takes tens of minutes before a more or less stable current value is established.

### 2.7.1. Static characteristics

For the reasons described above, before the recording of the mean current  $i$  of the LCM as a function of voltage  $U$  every point passed a conditioning procedure described in [12]. After the conditioning a good day-to-day as well as sample-to-sample (for a certain point type) reproducibility was achieved. In figure 5 (for Pt point see also figure 2) a set of  $i$ - $U$  curves registered at a constant light intensity  $I$  is presented. The recording of a curve was stopped at the voltage where the first Trichel pulses appeared. The  $i$ - $U$  characteristics for different point types have the same typical parts: at lower voltages the slope of the dependence is nearly constant and does not depend on point type; at higher voltages an upcurving of the dependence takes place. At every voltage the current has a strong dependence on the insulating film which covers the point surface as well as on its thickness; the maximum difference of currents is more than three orders of magnitude. The current is determined by the insulator layer and not by the substrate material; in figure 6 the  $i$ - $U$  curves

for two different substrate material coincide. Another finding follows from this figure: at a certain voltage the relation of currents  $i_2/i_1$  is not equal to that of light intensities  $I_2/I_1 \approx 50$ . At every voltage the current  $i$  is a non-linear function of intensity  $I$ , as is demonstrated by the curve in figure 7. It should be emphasised that the dependence is nearly the same for all the curves although the difference between  $i_{max}$  is up to two orders of magnitude.

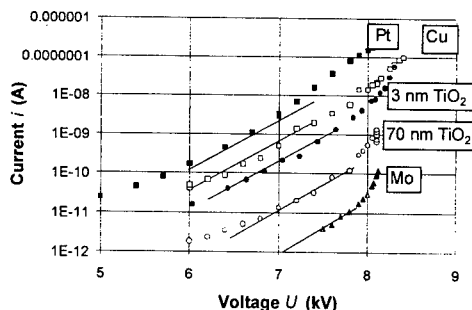


Figure 5:  $i$ - $U$  curves of LCM;  $\text{TiO}_2$  layers are on Mo substrate; Cu point is a previously oxidised one.

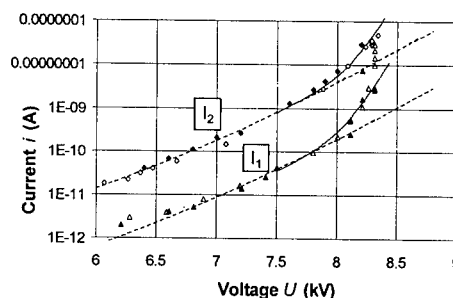


Figure 6:  $i$ - $U$  curves for points covered by 3 nm layer of  $\text{TiO}_2$ ; open and filled symbols - Cu and Mo substrate, respectively; relationship of light intensities  $I_2/I_1 \approx 50$ .

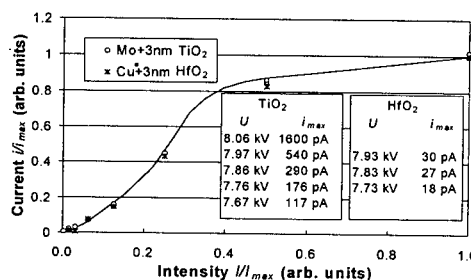


Figure 7: normalised current of LCM as a function of intensity for two point types;  $i_{max}$  corresponds to the maximum intensity used.

### 2.7.2. Temporal dependencies

The results presented in this section are our very recent ones [16]. The temporal changes of the LCM were recorded using a preamplifier of 1 MHz bandwidth. The noise level allowed to record signals starting from 5 nA. A chopper Ch was used to form light pulses (pulse duration of 1.8 ms, rise-time of 50  $\mu$ s and repetition rate of 50 s<sup>-1</sup>). Typical recordings of the current of LCM are presented in figure 8: on a steady level of a current pulse (which duration equals to that of the initiating light pulse) there is a number of sharp current spikes of varying amplitude. The noise level allowed to record spikes not more than 150 V below the voltage where the Trichel pulses started.

The distribution of spikes of different amplitudes during a light pulse is non-random; overlapping a number of recordings presented in figure 8A a certain regularity appear: spikes of larger amplitudes start preferably at the initial part of the light pulse. The probability of the rise of another large spike during the same light pulse is very low.

The amplitude distributions of the spikes for Pt point were measured as functions of voltage and light intensity. At a constant intensity the increasing of the voltage by 150 V causes a 10-fold rise in the number of spikes whose peaks exceed a certain value while no changes of the distribution function (figure 9) was found. At a fixed voltage the light intensity influences both the steady level of the current and the total number  $N$  of spikes. The lowering of the intensity from its maximum value to 1/64 of it reduces the steady component from tens of nanoamperes to a non-detectable level. The dependence of the total number of spikes  $N$  on intensity is a non-linear one having a trend of saturation. The amplitude distribution of spikes remains unchanged.

The number of spikes depends strongly on temperature: its alteration by only a few degrees causes remarkable changes in the number of spikes. At the temperatures < 30 °C and the RH < 40% there are no spikes between light pulses. At higher humidities the number of spontaneous spikes increases drastically.

The spikes recorded were integrated ones. To estimate the actual waveform of them a faster but less sensitive preamplifier was used: the rise-time of spikes is less than 10 ns and the halfwidth of a pulse has a 100 ns order of magnitude. Only the largest spikes were recorded this way and their peak value is  $\approx 10^{-6}$  A. No changes of the halfwidth of the spikes were noticed.

## 2.8. Triggering of Trichel pulses in an air flow

As a rule in an air flow the spontaneous Trichel pulses do not start at voltage  $U_0 \approx 8$  kV corresponding to the onset in stagnant air; for that considerably higher voltages (up to 9 kV) are needed. The voltage where the spontaneous pulses start is determined by the point sample: the less dust specks and/or protrusions are observed at the point surface the higher the voltage is. For external triggering experiments the samples having the highest mentioned voltage were selected from every point type.

### 2.8.1. Triggering by an ion flux

'Dielectric switching mechanism' [10] as well as Malter-like emission [4] assume the presence of insulating inclusions at the cathode. Indeed, as it was proved in our studies even in the case of previously

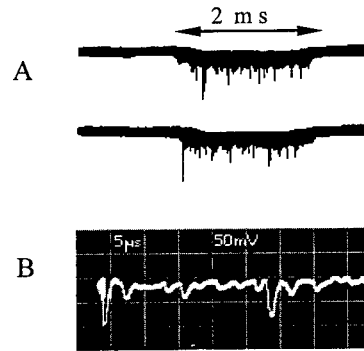


Figure 8: Recordings of spikes; duration of initiating light pulse is 1.8 ms.

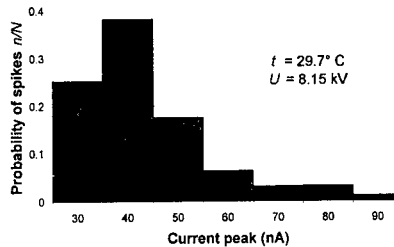


Figure 9: Amplitude distribution of spikes; number at category (X) axis is the lower limit of the column.

non-covered Pt point Trichel pulses start from a site where insulating inclusions are present. So there are sites at the point where the accumulation of the charge is possible and it may trigger Trichel pulses. To test it, a flux of externally created positive ions was directed to the point: the experimental procedure is described in [12]. The triggering becomes possible already at voltages below  $U_0$ . A set of dependencies typical for every point type is presented in figure 10. It is remarkable that there is an onset flux of ions starting from which the triggering becomes possible. Unlike the  $i$ - $U$  characteristics of the LCM it was not possible for the RR to fix clearly a dependence on point type.

Using triggering by a pulsed flux of ions the dependencies of the RR on the mean current of ions were similar to those in figure 10. The only difference is that the fluctuations of the RR are somewhat larger than those for a steady flux.

### 2.8.2. Triggering by steady radiation of integral UV light

A hydrogen lamp like that in section 2.7 was used. A very stable triggering was achieved starting from very low values of the RR as it is demonstrated in figure 11. Already a very faint radiation (e.g. light scattered from the walls of the chamber) triggers Trichel pulses. Higher intensities of radiation suppress Trichel pulses. The latter effect depends on the point type and it is especially remarkable for the Pt point (figure 2, curves A''B'', A'''B'''): 50 times higher intensity increases the starting potential of the initiated Trichel pulses by  $\approx 500$  V.

The RR as a function of intensity is presented in figure 12: the point used did not pass the preliminary training procedure (section 2.7.1.) and so its current of the LCM is small compared with that achieved after training; the RR saturates already at low intensities of light.

### 2.8.3. Triggering by monochromatic light

In these experiments the gap spacing was 1.3 cm. For triggering the light from a Xe lamp (1 kW) which passed a monochromator [16] or that of an excimer source ( $\lambda = 308$  nm) [17] was used.

The spectral intensity at the point plane as a function of wavelength (figure 13) was determined by measuring the spectral power and estimating the radiated area.

The RR depends on wavelength (figure 13) and the dependence is different for different point types. The dependencies of the RR on intensity recorded for two different wavelengths (figure 14) have the same trend of saturation as in the case of the measurements with integral light (figure 12). The difference between the values of the

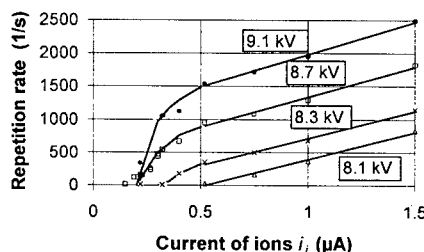


Figure 10: RR as a function of current of ions  $i_i$ ; previously oxidised Cu point.

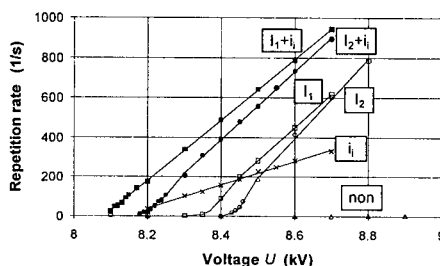


Figure 11: RR as a function of voltage; triggering both by UV light and flux of ions; relationship of intensities of UV light  $I_2/I_1 \approx 50$ ; current of ions  $i_i = 0.77 \mu\text{A}$ ; non -RR of spontaneous pulses.

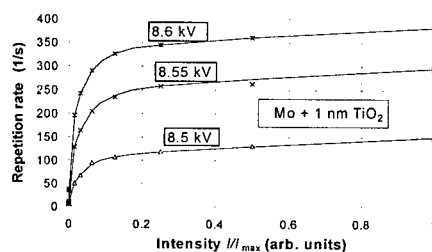


Figure 12: RR as a function of intensity; the point is not conditioned.

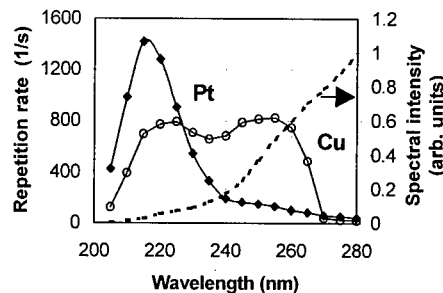


Figure 13: RR as a function of wavelength; gap spacing - 1.3 cm; dashed line- intensity at the point surface.

RR where the saturation is achieved is remarkable. Furthermore, for the Trichel pulses initiated using an excimer source [17] the saturation occurs at the  $RR \sim 10^4 \text{ s}^{-1}$ .

Again (see section 2.7.2.) the temperature changes had a huge influence on the discharge parameters. Temperature seems to be an independent parameter, as concluded from reducing the experimental results to the same gas density. The influence of temperature are demonstrated also by experiments with infrared ( $\lambda = 1\text{--}3 \mu\text{m}$ ) radiation of a 50 W halogen lamp [17]. In an air flow of the rate 20 l/s and temperature of  $28^\circ\text{C}$  the radiation of excimer lamp initiates  $10^3$  Trichel pulses per second. During a 70 s action of infrared radiation the RR increases to  $> 5000 \text{ s}^{-1}$ . In the mentioned experimental conditions radiation warms up only the point surface and maybe a very thin gas layer near it.

#### 2.8.4. Temporal characteristics of triggering

Trichel pulses were triggered by light pulses similar to those described in section 2.7.2. The limits of voltage were chosen so that the number of Trichel pulses created during a light pulse was close to one [16]. At a certain voltage the delay time (the time interval between the beginning of the light pulse and beginning of a Trichel pulse) as a function of light intensity was recorded. Delay time distribution (figure 15) becomes narrower with the increasing intensity. The same trend takes place while recording the distribution as a function of voltage at a constant light intensity.

Both formative and statistical time lags were determined from Laue plots. In the limits of the intensities and voltages used the formative time lags are  $< 50 \mu\text{s}$ ; i.e. close to the rise-time of the light pulse. Statistical time lags determined from the initial linear parts of Laue curves in figure 16 for light intensities  $I$ ,  $I/4$ ,  $I/8$  are  $82 \mu\text{s}$ ,  $149 \mu\text{s}$  and  $350 \mu\text{s}$ , respectively.

### 3. DISCUSSION

#### 3.1. Triggering mechanism

As it is modelled by Morrow [18], at lower pressures only few electrons are needed for triggering and an avalanche series supported by a cathode feedback  $\gamma$  mechanism leads to the rise of a Trichel pulse. At atmospheric pressures the onset potential is independent on point material. This effect may be caused by gas layers absorbed at the point surface thus making the actual  $\gamma$  insensitive to the point material [4]. In contrast to this assumption, in an air flow the current of the LCM caused by UV light is very sensitive to the cathode type (figure 5). In spite of this the voltages starting from which the triggering becomes

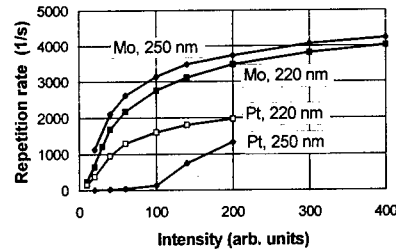


Figure 14: RR as a function of UV intensity for two different wavelength;  $U = 6.9 \text{ kV}$ .

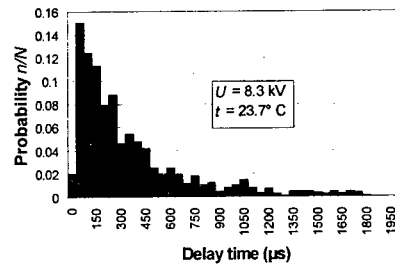


Figure 15: Delay time distribution of Trichel pulses.

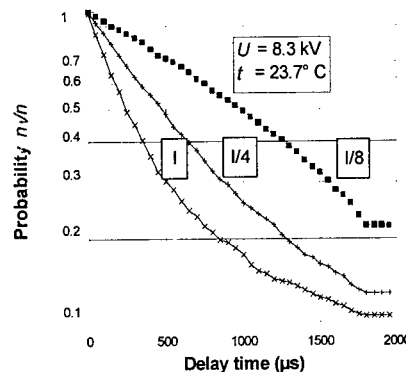


Figure 16: Laue curves of delay time distribution of Trichel pulses for three intensities of UV light.

possible for different point types lie within narrow limits ( $\approx 200$  V, figure 5). So it is unlikely that the avalanche series of  $\gamma_{ph}$  feedback lead to the rise of Trichel pulses. The other possibility that the avalanche series are caused by ion feedback  $\gamma_i$  is invalid as well: the number of Trichel pulses created by a pulsed flux of ions depends on the mean value of the current of ions (section 2.8.1.) and not on the peak value which is three orders of magnitude higher. Consequently, the ordinary cathode feedback mechanisms are not responsible for the processes leading to the triggering of corona pulses.

For triggering at atmospheric pressures it is not enough to liberate few electrons from the cathode: although during an initiating light pulse (section 2.7.2.) there is always a steady component of the current, the temporal distribution of the probability of the rise of Trichel pulses (figure 15) corresponds to the temporal distribution of the current spikes of the LCM having large amplitudes (figure 8A). So it is natural to suppose that a Trichel pulse is triggered by a larger current spike. A correspondence between the time intervals between larger current spikes (figure 8B) and the statistical time lags of Trichel pulses (section 2.8.4.) supports this assumption. The spikes recorded are not the fluctuations of the photoassisted current caused by the avalanche statistics; already the non-random distribution of spikes during a light pulse (figure 8) proves it. Consequently, the 'particles' which trigger Trichel pulses are current spikes of the LCM.

So the problem of the triggering of negative corona is reduced to the mechanism of the rise of the current spikes of the LCM. It is likely that spikes are caused by the switch-on of an extra emission mechanism. As a Trichel pulse always arises from a site where an insulator inclusion is present [12], let us analyse the nature of the initial currents from the viewpoint of a metal-insulator-gas (MIG) system like it is done for metal-insulator-vacuum systems [10].

A sketch in figure 17 corresponds to the situation where an emissive site is switched on; i.e. both traps and surface states are filled, the metal-insulator barrier is thin enough for tunnelling, and the barrier of the insulator-gas interface is lowered to the level which allows the emission of thermoelectrons [10]. As in our conditions the current is not recorded without UV radiation (section 2.7.), the voltage drop across the MIG system is too low for stable tunnelling. Another difference from the sketch presented is that in our case the layers of  $\text{TiO}_2$  and  $\text{HfO}_2$  were very thin ones and so the linear parts at the sketch belonging to the bulk of the insulator may be absent.

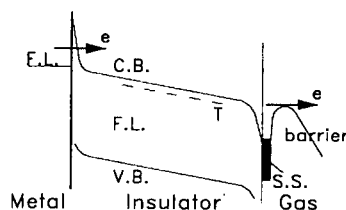


Figure 17: Configuration of energy gaps; F.L. - Fermi level; C.B. - conduction band; V.B. - valence band; T - traps; S.S. - surface states.

So without external assistance both the surface states and traps are empty and the emission current is absent. Under the influence of UV radiation the electrons are transferred from the valence band to the conduction band. These electrons may be emitted thermionically (thus causing the steady component of the LCM current) or captured by empty traps and surface states. The higher the UV intensity is the more surface states are filled. The electrons filling the surface states will screen the bulk of the insulator from the applied field. This is a probable reason for a non-linear dependence of the mean current of the LCM on UV intensity (figure 7). UV radiation not only causes the emission but also changes the band configuration. Due to the UV action the traps and surface states are more-or-less filled the increasing of the applied voltage makes the tunnelling possible and a burst of electrons is injected to the insulator. A part of them is thermionically emitted, another part is captured by surface states, thus interrupting the emission. Of course the similar burst-like emission may be caused not only by UV light but also by ions accumulating at the insulator and thus increasing the voltage drop over the MIG system (section 2.8.1.) or by the heating of the point due to the laser radiation (section 2.5.2.).

The burst of electrons emitted is amplified due to gas amplification and is recorded as a current spike. The higher the voltage is the larger the spikes are and the shorter is the time interval between spikes. The experimental findings described in this paper (including long-term changes of emissivity during the conditioning) are qualitatively explainable on the basis of the model proposed.

Besides, some speculations on the influence of the gas composition on the triggering characteristics are possible. Depending on the gas absorbed at the electrode it may cause upward as well as downward

bending of energy zones near the insulator-gas interface, thus changing the efficiency of emission. Oxygen and water vapour are bending the zones downward; maybe that is a reason why in humid air spontaneous spikes (and so Trichel pulses) arise more frequently (section 2.7.2.) and the onset of negative corona in nitrogen (section 2.5.2.) is considerably higher than in air.

### 3.2. Repetition rate

At a certain voltage and under conditions where spontaneous corona pulses are practically missing the RR is controlled by a flux of ions and/or by some kind of radiation (e.g. figures 10, 12). Whether the control of these triggers is caused by their action to the gas or to the cathode is not obvious.

The radiation may cause the detachment of electrons from negative ions existing in the gap, thus diminishing the influence of negative space charge. As a result Trichel pulses may arise more frequently. The same effect may be caused by a flux of positive ions - the concentration of negative ions may diminish due to the ion-ion recombination. The experiments with monochromatic light contradict the described explanations: the dependencies in figure 13 give the basis to confirm firmly that the repetition rate is determined by the emission of the point as there is a strong dependence of the RR on the point type.

The RR as a function of the intensity of initiating particles/radiation has always a trend of saturation. First of all the limitation of the rise of the RR may be caused by the space charge of negative ions created by the Trichel pulses. Calculations based on literature data for field distribution [19] and the mobility of negative ions [20] give drift times  $T_d = (2.2-2.6)$  ms for 4 cm gap and voltages used (figures 10, 11, 12) and  $T_d \approx 0.25$  ms for 1.3 cm gap (figure 14). It means that starting from  $RR > 1/T_d$  the negative space charge created by Trichel pulses accumulates in the gap thus reducing the field (and also field-dependent emission) at the point surface. Indeed, the saturation of the dependencies recorded starts at the values of the RR close to the calculated.

For 4 cm gap at close voltages the level of saturation of the RR differs for different point types 10 times (figures 10, 12); so there must be another reason for the creation of limiting space charge: it may be created by the steady component of the current existing between Trichel pulses. This steady component should be different for different point types like in the case of the LCM (figure 5) and for this reason the value of the RR at which the saturation is achieved is different for different point types. The limitation of the RR by the steady component is also the probable reason why higher intensities of UV light prevent the rise of larger current spikes and so at higher UV intensities Trichel pulses start at higher voltages (figure 2).

A number of different methods were used for the triggering of negative corona. Once triggered a corona pulse becomes independent on the way of its creation; i.e. its parameters are determined by the gas composition. For this reason in a gas flow where the discharge does not change the gas composition, a linear dependence of the RR on the mean current of corona has the same slope in spite of the fact that spontaneous or in some way initiated pulses are recorded. This statement based on a number of experiments in a dust-free air flow. So the slope of the RR-mean current dependence in a gas flow may be used as an indicator of the gas composition.

### CONCLUSIONS

- Study in a dust-free air flow allows to record the parameters of negative corona with a good reproducibility.
- Even at atmospheric pressures in air the current of the LCM is very sensitive to the surface properties.
- Negative corona is triggered by a short-duration burst-like emission of electrons.
- The dielectric switching mechanism explains a number of experimental findings without any contradictions.
- The common nature of the processes leading to the breakdown both in vacuum and in gases have found its further verification.

- Study of current spikes of the low current mode is an easy way to collect information about the processes preceding the switch-on of emissive sites.

### Acknowledgements

A common analysis of the processes which determine the repetition rate of Trichel pulses carried out by R.S. Sigmond and especially his contra-arguments to our different interpretations essentially helped us. The studies were supported by Estonian Scientific Foundation (grants No 88 and No 1328).

### References

- [1] Korge H., Laan M., Paris P., *J. Phys. D: Appl. Phys.* **26** (1993) 231-236.
- [2] Hernandez-Avila J.L., Nur M., Bonifaci N., Denat A., "D.C. Negative corona discharge characteristics in high density nitrogen in point-plane configuration", XXII ICPIG Hoboken, N.J. USA 31.7-5.8.1995, Contr. Papers 2 pp. 129-130.
- [3] Sigmond R.S., "Corona physics and diagnostics", XXII ICPIG, Hoboken N.J. USA 31.7-5.8.1995, Invited Papers pp. 332-344.
- [4] Loeb L.B., Electrical coronas (Berkeley & Los Angeles 1965), ch. 4.
- [5] Laan M., Paris P., "Formation of corona pulses", 9<sup>th</sup> Symp. on El. Processes and Chemical Reactions in Low Temperature Plasma, Small Carpathy, Slovakia 1992, Invited Lectures pp. 201-216.
- [6] Sigmond R.S., Goldman A., Goldman M., Laan M., Bjones B., Olsen I.-H., "Detection of electro-negative trace gases by corona discharges", 11<sup>th</sup> Int. Symp. on Plasma Chemistry Loughborough, UK 1993, **4**, pp.1315-1320.
- [7] Bjones B., Olsen I.-H., Corona discharges in air and argon with added trace gases, Diploma thesis (Trondheim, Norwegian Institute of Technology, Norway 1992), 179 p.
- [8] Laan M., Perelygin V., "The dependence of negative corona on electrode surface properties", XX ICPIG Pisa, Italy 1991, Contr. Papers 4, pp. 929-930.
- [9] Latham R.V., Bayliss K.H., Cox B.M., *J. Phys. D: Appl. Phys.* **19** (1986) 219-231.
- [10] Bayliss K.H., Latham R.V., *Proc. R. Soc. Lond. A* **403** (1986) 285-311.
- [11] Mesyats G. A., Ectons (UIF "Nauka", Yekaterinburg 1993) vol. 1, 2 (in Russian).
- [12] Laan M., Repän V., Aarik J., Sammelselg V., *J. Phys. D: Appl. Phys.* (1997), submitted.
- [13] Laan M., Paris P., Perelygin V., *Acta phys. Slov.* **42** (1992) No2, 91-97
- [14] Laan M., Repän V., Roos H., "Repetition rate of Trichel pulses and conditioning", 10<sup>th</sup> Symp. on El. Processes and Chemical Reactions in Low Temperature Plasma, Slovakia, High Tatras, 1994, *Acta Physica Univ. Comenianae* **35** 175-179.
- [15] Laan M., Paris P., Repän V., Uustare T., "Laser triggered negative corona", 12<sup>th</sup> ESCAMPIG - European Sect. Conf. on the Atomic and Molecular Physics of Ionized Gases (Noordwijkerhout, The Netherlands 1994), Inv. Lectures and Contr. Papers pp. 358-359.
- [16] Laan M., Paris P., Repän V., to be published.
- [17] Paris P., Laan M., Tiirik A., "UV light controlled repetition rate of Trichel pulses", XXIII ICPIG, Toulouse, France 1997 Contrib. Papers.
- [18] Morrow R., *Phys. Rev. A*, **32** (1985) 1799-1809.
- [19] Coelho R., Debeau J. *J. Phys. D: Appl. Phys.* **4** (1971) 1266-1280
- [20] Badaloni S., Gallimberti I. Basic data of air discharges (Italy, 1972) Report Upee-72/05, 91 p.

## The Coupling of PIC/MCC Models of Discharge Plasmas with Vibrational and Electronic Kinetics

S. Longo, M. Capitelli and K. Hassouni\*

*Dipartimento di Chimica dell'Università di Bari, Centro di Studio per la Chimica dei Plasmi del CNR,  
via Orabona 4, 70126 Bari, Italy*

*\* LIMHP, CNRS, Université de Paris Nord, avenue J.B. Clément, 93430 Villetaneuse, France*

**Abstract:** A 1D in position and 2D in velocity Particle in Cell with Monte Carlo Collision model of a low-pressure nitrogen discharge plasma has been coupled to a 1D reaction-diffusion kinetics for the whole vibrational ladder of the  $N_2(X)$  state, for the vibrationally lumped  $N_2(A)$ ,  $N_2(B)$ ,  $N_2(C)$ ,  $N_2(a')$  states as well as for N atoms. The model includes several electron-molecule as well as molecule-molecule processes. The effect of the self-consistent coupling of the two models on the results in the case of a parallel-plate RF discharge is discussed for two different values of the RF frequency.

### 1. INTRODUCTION

Most non-equilibrium plasmas of interest are characterized by a large number of electrons in the Debye sphere: in these conditions the interaction between charged particles can be approximated by a particle-space charge field interaction. This point of view is assumed in the so-called Particle-in-Cell, or PIC approach [1-5]. The advantage of particle methods such as the PIC over macroscopic 'fluid' approaches is the possibility of calculating the electron energy distribution function, or eedf,  $f(\epsilon)$ . This function is defined in such a way that the fraction of electrons with kinetic energy between  $\epsilon$  and  $\epsilon+d\epsilon$  is given by  $\epsilon^{1/2} f(\epsilon) d\epsilon$ . It gives an information on the electron kinetics that cannot be summarised by any single macroscopic parameter in the non-equilibrium case, differently from the near-equilibrium one, where the translational energy is distributed according to the Maxwell-Boltzmann law, which is completely characterized by the translational temperature  $T$ . Despite the impressive power and success of PIC/MCC approach, in order to apply it to the free electrons in low temperature plasmas it is necessary to include the interaction between the gas chemistry and the electron dynamics in the non-equilibrium case, that is, including state-to-state chemical kinetics with all the relevant electron-molecule collisions. The most important effect of the interaction between vibro-electronics kinetics and free electron kinetics is due to the effect of the super-elastic, or second kind collisions of electrons with excited molecules in the discharge plasma, leading to a change in shape of the eedf and thereby influencing the values of the rate coefficients for the state-specific kinetics [6]. In the following the present status of a comprehensive coupled particle (1Dr2Dv) / continuum (1D) model for discharge plasmas in pure Nitrogen realized in the last two years will be described.

### 2. DESCRIPTION OF THE MODEL

In the PIC approach the Newton equations for a large ensemble ( $10^4$  -  $10^5$  particles) of electrons and positive ions are solved taking into account the local electric field as it results from local interpolation within a cell of a mathematical mesh (from what follows the name 'Particle in Cell'). After any calculation step of the motion equations, the electric charge in any cell of the mesh is determined from the number of electrons and positive ions found in the cell itself. Known the electric charge density, the electric potential and field are determined by solving the Poisson Equation on the same mesh. Symbolically



$$\begin{aligned}
\Delta\phi(\mathbf{r}) &= -\rho(\mathbf{r}) / \epsilon_0 \\
\mathbf{E}(\mathbf{r}) &= -\nabla\phi(\mathbf{r}) \\
\frac{d^2}{dt^2} \mathbf{r}_i(t) &= (q/m)_i \mathbf{E}(\mathbf{r}) \\
(\mathbf{r}_i, q_i)_{\text{all particles}} &\rightarrow \rho(\mathbf{r})
\end{aligned} \tag{1}$$

Any simulated particle is really a 'superparticle', characterized by a 'weight'  $w$  which must be taken into account when sampling particles to deduce the charge density  $\rho$  but does not affect the  $q/m$  ratio. Therefore 'superparticles' follow the same equation of motions of the physical electrons or ions but they contribute  $wq$  to the space charge.

In the following we will consider a 1D model in space, with two limiting surfaces at  $x=0$  and  $x=L$ . The mesh used for space charge and the Poisson equation consist on  $n+1$  equispaced points at the positions  $jh$ , with  $j=0,1,\dots,n$ , and  $h = L/n$  is the grid spacing.

To sample the particles in space we use the so-called *CIC* (Cloud-in-Cell) sampling which assigns the (super)particle charge  $wq$  to the two neighbouring grid points (one on the right and one on the left of the particle) in two fractions depending on the particle position,

$$\begin{aligned}
&\text{for any particle } i: \\
&jh \leq x_i \leq (j+1)h \\
&Q(j+1) \leftarrow Q(j+1) + wq_i \frac{x_i - jh}{h} \\
&Q(j) \leftarrow Q(j) + wq_i \frac{(j+1)h - x_i}{h}
\end{aligned} \tag{2}$$

where the index  $j$  labels the mesh cells while  $i$  runs over particles. The mesh-interpolated space charge is calculated from the quantities  $Q(j)$  as

$$\rho(j) = (hS)^{-1} Q(j) \tag{3}$$

where  $S$  is the plasma cross section, which can be put equal to 1 (actually in a 1D system superparticles are infinitely thin 'sheaths' of charge, and the relevant charge density is a line density, measured in coulomb  $m^{-1}$ ). The factor  $S$  disappears when calculating  $E$  from  $\rho$ ). The same formulas must be used to weight (interpolate) the electric field acting on any particle, otherwise non-physical self-forces appear.

The Newton equations are solved using a simple scheme with interlaced grids for velocity and position, the so-called Leapfrog method:

$$\begin{aligned}
\mathbf{v}'_i &= \mathbf{v}_i + (q_i / m_i) \mathbf{E}(\mathbf{r}, t) \Delta t \\
\mathbf{r}'_i &= \mathbf{r}_i + \mathbf{v}'_i \Delta t
\end{aligned} \tag{4}$$

Note that the difference with respect to the explicit Euler method is just the substitution of  $v$  with  $v'$  in the second equation. This simple method is excellent for PIC provided it operates within its stability domain  $\pi v_{pe} \Delta t < 1$ , where  $v_{pe}$  is the electron plasma frequency. The Poisson equation, is solved numerically. The grid spacing  $h$  selected must be not too much higher than the electron Debye length and possibly smaller, and at the same time sufficiently large to avoid average-speed electrons travelling more than  $h$  in a single timestep. In order to apply the PIC method to collisional discharge plasmas, the electron (ion) / neutral collisions must be included. The inclusion is realized by the test-particle, null-collision

Monte Carlo method. The overall simulation technique is called PIC/MCC, where MCC stands for Monte Carlo Collisions. PIC/MCC simulation of plasmas produced by high-frequency electric discharge has given results in remarkable agreement with experiments for what regards the electron dynamic quantities, in particular the eedf [7].

The cross section for the electron-null species collision is chosen to obtain a constant total collisions frequency  $\nu_{\text{tot}}$ , given by

$$\nu_{\text{tot}} = \max_A \left( \sqrt{\frac{2\varepsilon}{m_e}} \sum_p n_p(x) \sigma_p(\varepsilon) \right) \quad (5)$$

where the sum runs over collision process,  $\sigma_p(\varepsilon)$  is the cross section and  $n_p(x)$  the number density of the collision partner. The A range is defined as  $0 < x < L$  and  $\varepsilon < \varepsilon_{\text{lim}}$ , where  $\varepsilon_{\text{lim}}$  is the limit of the scale of kinetic energy used to interpolate the cross sections. It is exential to maximize the frequency in space as well as in energy to calculate  $\nu_{\text{tot}}$ , since the gas composition is a function of position in the model. In this case the collision times are in fact distributed according to the law of free (flight) times

$$f(t) = \nu_{\text{tot}} \exp(-\nu_{\text{tot}} t) \quad (6)$$

and the time to the next collision can be calculated by

$$t_c = -\nu_{\text{tot}}^{-1} \ln \eta \quad (7)$$

where  $\eta$  is an element of a set of random numbers uniformly distributed between the values 0 and 1. The kind of collision process (including the *null* one) which occurs after the free flight is also randomly selected according to the related collision frequencies. After any collision, the new electron energy and the scattering angle is easily determined depending on the nature of the collision itself. The new charged particle speed is calculated according to the energy loss (or gain, for an exothermic 'super-elastic' or 'second-kind' collision). Elastic collisions also contribute to the energy loss (gain) because a superthermal particle transfers an energy fraction about  $2m/M$  to the neutral, while subthermal particles are heated by elastic collisions with neutrals at the gas temperature T: this is important for ions in the bulk region of the RF discharge. 'Superelastic' collision cross sections are calculated from the corresponding inelastic one in order to guarantee a Maxweel eedf in the equilibrium case, by

$$g\varepsilon\sigma_{\text{sup}}(\varepsilon) = g^*(\varepsilon + \Delta\varepsilon)\sigma_{\text{in}}(\varepsilon + \Delta\varepsilon) \quad (8)$$

where  $g$  and  $g^*$  are the intrinsic statistical weight of the target molecule for the two processes.

Treatment of scattering is very simple if isotropic scattering is assumed:

$$\begin{aligned} \cos \vartheta &= 1 - 2\eta \\ \sin \vartheta &= \sqrt{1 - \cos^2 \vartheta} \end{aligned} \quad (9)$$

where  $\eta$  is again a real random numbers in the (0,1) range, but in this case the elastic collision frequency must be calculated using the momentum transfer cross section in order to match the drift and diffusion coefficients in the energy space. In order to fit the Monte Carlo random collision times and the PIC timestep, the particle timestep flow-chart must be modified in order to allow collisions to take place at any intermediate time within the timestep, even more than once within a single PIC timestep [1]. The alternative method to treat collision events exactly at the end of the PIC timestep [3] is faster but can be used only for very low gas pressure (on the order of the mtorr). The code described in this paper as well

as in ref. [4,5] is based on the modified timestep cycle: any particle is represented by the set of numbers  $\{i, \mathbf{r}(i), \mathbf{v}(i), t_c(i), f(i)\}$ . Here  $i$  identifies the  $i$ -th simulated particle,  $\mathbf{r}$  and  $\mathbf{v}$  are the position and velocity vectors assigned to the particle,  $t_c$  is the time left to the next Monte Carlo collision event, and  $f$  is a flag representing the nature of the particle (electron or ion,  $f=0$  is used for particles to be deleted from the simulation at subsequent steps).

Let us now describe the coupling of the code described above with the reaction-diffusion kinetics of neutrals (fig.1)

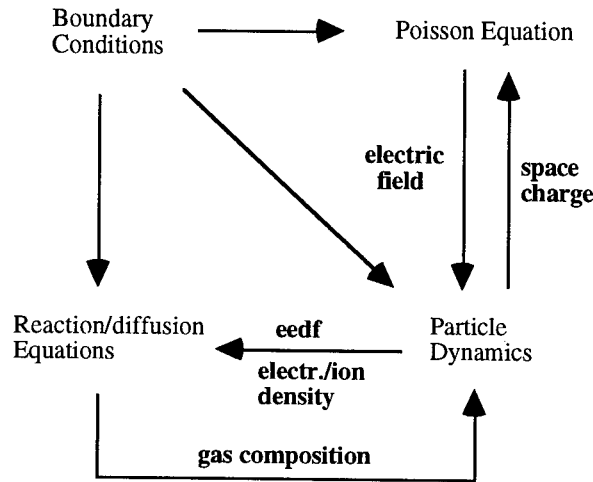
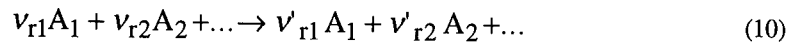


Figure 1: model scheme

During the calculations, the densities of different species subjected to several chemical reactions



must be updated by solving the equations for their reaction and diffusion kinetics, taking into account that the parameters entering these equations will not be constant, but on the contrary they will result by applying some linear functionals to the local electron energy distribution function  $f(\epsilon, x, t)$ , this last is sampled on the kinetic grid from the PIC-MCC simulation. The grid used for the chemical kinetics is not the same as the one used for the Poisson equations. It consist of  $N$  grid points located at  $x_j = (j-1/2)H$ , with  $j=1, \dots, N$ , where  $H=L/N$  is the grid spacing. Particles are assigned to the grid by the NGP (Nearest Grid Point) sampling:

for any particle  $i$ :

$$(j-1)H \leq x_i \leq jH$$

$$(k-1)\Delta\epsilon \leq \epsilon_i \leq k\Delta\epsilon \quad (11)$$

$$F_{j,k} \leftarrow F_{j,k} + w$$

where  $\Delta\epsilon$  is the energy grid spacing, and  $\epsilon_i$  the kinetic energy of the electron. The local eedf, particle density and mean energy are calculated from the function  $F_{j,k}$ .

$$f(j, k) = \frac{F_{j,k}}{\Delta \epsilon \sqrt{(k - \frac{1}{2})} \Delta \epsilon \sum_k F_{j,k}} \quad (12)$$

$$n_e(j) = H^{-1} \sum_k F_{j,k} \quad (13)$$

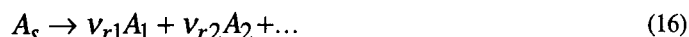
$$\bar{\epsilon}(j) = \sum_k (k - \frac{1}{2})^{3/2} \Delta \epsilon^{5/2} f(j, k) \quad (14)$$

The treatment of ions is exactly the same.

In reacting plasmas usually the relaxation times of the chemical kinetics are by far higher than the corresponding ones for the electron kinetics, therefore an adiabatic approach to the solution for the steady state can be applied. Our method consists in solving the vibration and diffusion kinetics up to the steady state at different times  $\{t_n\}$  during the PIC-MCC simulation (which is by far more computationally expensive). At each  $t_n$  the space-dependent values of rate coefficients and electron density are obtained from the PIC-MCC, time-averaged over the period  $t_n - t_{n-1}$ . The solution of the chemical and diffusion kinetics gives a new state-to-state composition and related electron-molecule collision frequencies for the PIC-MCC. The state-to-state gas composition is obtained differently for charged and neutral particles. Charged particle densities are in fact obtained by the PIC/MCC simulations. As for neutral densities, they are obtained by finding a stationary solution for the following set of non-linear, one-dimensional reaction and diffusion equations

$$\frac{\partial n_s}{\partial t} = D_s \frac{\partial^2 n_s}{\partial x^2} + \sum_r (v_{rs} - v_{rs}) k_r \prod_{s'} n_{s'}^{v_{rs'}} \quad (15)$$

which holds if the reactions (14) are elementary; otherwise the proper kinetic laws must be included. Here  $n_s$  is the particle density and  $D_s$  is the diffusion coefficient of the given species, while  $k_r$  is the rate coefficient of the  $r$ -th reaction and the product is extended to reactants only. The chemistry of gas molecules interacting with the reactor walls is connected with boundary conditions of the system. Let us consider only first order or pseudo first order reactions



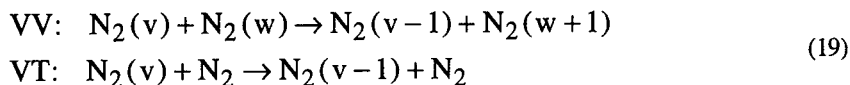
taking place on surface, with probability  $p_{rs}$ . The catalytic boundary conditions are:

$$-D_s \left. \frac{\partial n_s}{\partial x} \right|_{x=0} = D_s \left. \frac{\partial n_s}{\partial x} \right|_{x=L} = - \sum_{rs} p_{rs} \phi_s + \sum_{r's's'} p_{r's'} v_{r's'} \phi_{s'} \quad (17)$$

where  $\phi_s$  is the thermal diffusion flux of  $A_s$  particles to the wall surface, given by

$$\phi_s = (KT / 2\pi m_s)^{1/2} n_s(x=0) \quad (18)$$

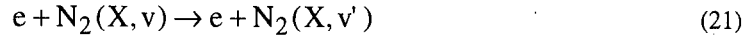
for  $x=0$ , and analogously for  $x=L$ . Let us now consider some examples of chemical reactions included in the model. A typical example is the so-called mono-quantum VV or VT relaxation process



These processes have rate coefficients which depends on the vibrational status of the colliding molecules as well as on the translational temperature.

$$\begin{aligned} k_{VV} &= f(T, v, w) \\ k_{VT} &= f(T, v) \end{aligned} \quad (20)$$

The explicit expression of  $k$  is calculated fitting by the SSH theory the results of molecular dynamics calculations, as in [8]. Another important class of chemical processes in plasmas is the eV one, i.e. the transition between two different states of a molecular species due to electron impact, for example:



The rate coefficient of the process in this case has a more complex expression because of the strongly non-Maxwellian shape of the electron energy distribution in typical cold plasmas. It depends on the whole cedf and cannot be written a function of macroscopic parameters, say the electron 'temperature'

$$k = \sqrt{\frac{2}{m_e}} \int_0^\infty \epsilon f(\epsilon) \sigma(\epsilon) d\epsilon \quad (22)$$

where  $f$  is the electron energy distribution,  $m_e$  the electron mass and  $\sigma(\epsilon)$  the cross section of the elementary process.

In the model described, the 1D reaction-diffusion equations after introducing the mesh is solved for the steady state by a partially-linearized Gauss-Seidel relaxation method [5].

### 3. CASE STUDY: RF DISCHARGE IN NITROGEN

The model was applied to a discharge in pure Nitrogen, produced into a parallel-plate high frequency reactor within the two plane electrodes. One of the plates (the so called 'grounded electrode') is constantly kept at zero voltage, while the other one (the 'powered electrode') is driven by an external generator, not explicitly simulated, to an oscillating voltage. This approximate treatment neglects the circuit as well the surface charge effects.

**Table I:** simulation parameters

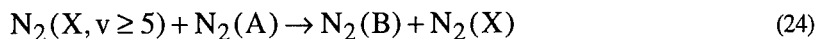
RF voltage	500
RF frequency (MHz)	13.5 (case a)
" "	27 (case b)
discharge gap (cm)	4
pressure (torr)	0.1
simulated particles	15000 (case a)
" "	36000 (case b)
timestep (s.)	$10^{-10}$
simulation time (s.)	$3 \cdot 10^{-4}$
PIC grid spacing (cm.)	0.01
kinetic grid spacing (cm.)	0.1
secondary emiss. coeff.	0
particle reflection coefficient	0
accomod. coeff. (vibrational)	$10^{-3}$
accomod. coeff. (electronic)	1

The boundary conditions are accordingly

$$\begin{aligned}\varphi(0, t) &= 0 \\ \varphi(L, t) &= V_{rf} \cos 2\pi ft\end{aligned}\quad (23)$$

where  $f$  is the RF frequency. Only electrons and  $N_2^+$  ions are moved as particles. The choice of the prevalent ion is discussed in [4]. Numerous electron-molecule collision processes are included, while for the ion/neutral we have included the elastic and charge transfer  $N_2^+/N_2$  processes. Details are in [4,5]. As regards the simulation conditions, they are reported on table I. Concerning the vibrational kinetics, the model includes 46 vibrational levels of  $N_2$  and a 47th pseudo-level to take into account dissociation by the 'ladder-climbing' mechanism [6]. The e-V excitation processes of  $N_2$  molecules have been included by using the formula (22) with scaled e-V cross section from the literature in order to cover the whole vibrational ladder. Details in ref. [5].

A simplified electronic kinetics of nitrogen molecules has also been included in the reaction/transport code. We considered the following electronic states:  $X^1\Sigma_g$  (ground state),  $A^3\Sigma$  (6.17 eV),  $B^3\Pi$  (7.35 eV),  $a'^1\Sigma$  (8.40 eV),  $C^3\Pi$  (11.03 eV). The excited states are primarily produced in discharge conditions through electron-impact excitation processes. At the same time, bimolecular processes involving heavy particles collisions have been considered using the kinetic scheme of Garscadden and Nagpal [9], but taking into account the threshold of internal energy for the X partner in the  $A+X \rightarrow B+X$  reaction channel, i.e. we wrote



as shown experimentally by Piper [10]. This last point is very important because vibrational kinetics affects the electronic kinetics also through the strong dependence of the rate coefficient of reaction above on the vibrational temperature. Let us examine the results. Figure 2 shows the time-averaged electron and ion density at the steady state, while fig.3 shows the result for the particle mean energy. The known phenomenological characteristics of the RF parallel plate discharge are displayed by the model results. High energy electrons are produced in the sheath region when they enter a 'contracted' sheath region and are consequently subjected to strong electric fields during the sheath expansion stage (' $\alpha$  regime RF' discharge).

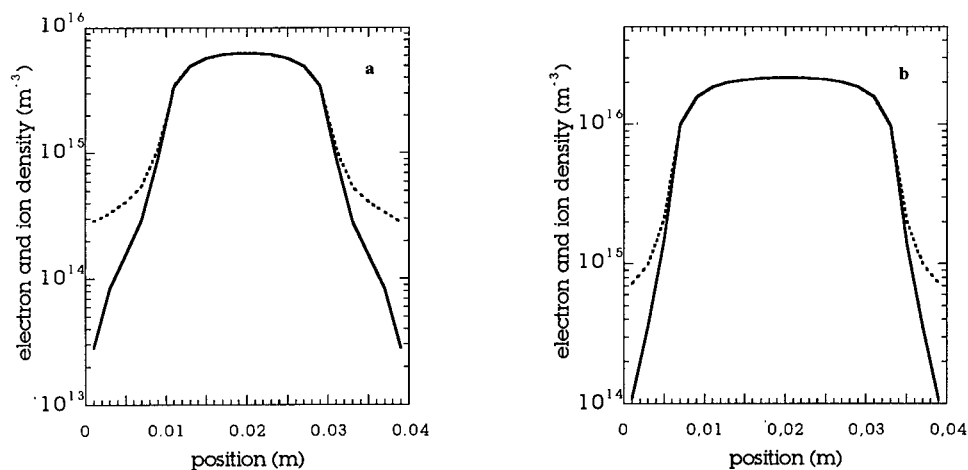
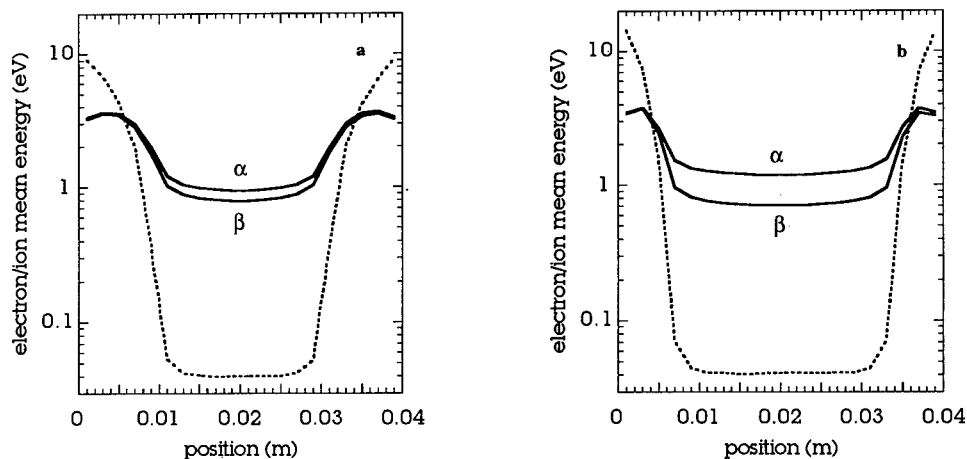
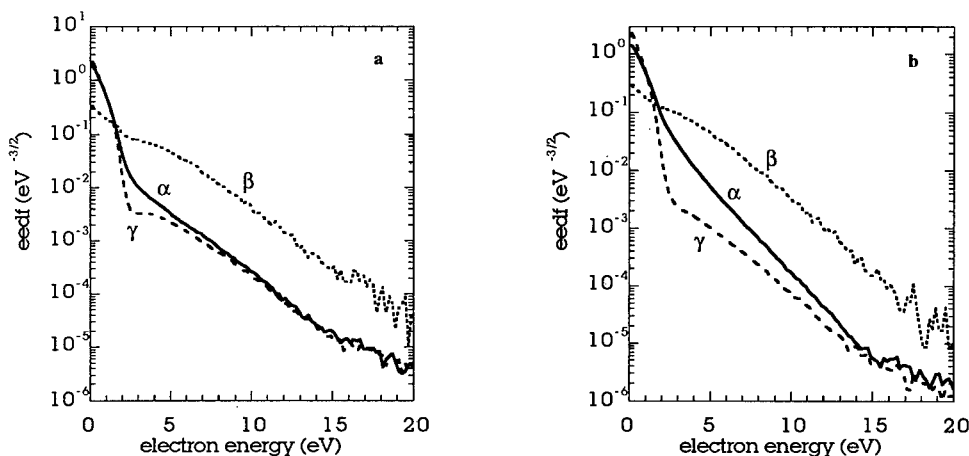


Figure 2: electron (full line) and ion (dashed line) density calculated at (a) 13.5 MHz and (b) 27 MHz



**Figure 3:** electron (full line) and ion (dashed line) mean energy calculated at (a) 13.5 MHz and (b) 27 MHz.  $\alpha$ : full model,  $\beta$ : neglecting the change of gas composition on the PIC/MCC

The fast electrons diffuse in the bulk, and as a result the mean electron energy in the bulk plasma is by far higher than the one which could be calculated by solving the quasi-isotropic, uniform Boltzmann Equation according to the bulk effective electric field ('non local' electron kinetics). At the same time, positive ions in the bulk plasma are at room temperature because of the effective energy exchange with neutrals, while they are accelerated up to quite high values of the mean energy close to the electrode surfaces. Furthermore, it can be observed the effect on the results of increasing the RF frequency. In a pure  $\alpha$  regime as the one shown here the RF frequency  $f$  is expected to have a strong effect on the discharge characteristics, since the sheath expansion frequency is equal to  $f$  and the peak sheath expansion speed is an increasing function of  $f$ . It can be seen that, due to the larger energy depositions, the



**Figure 4:** electron energy distribution functions calculated at (a) 13.5 MHz and (b) 27 MHz.  $\alpha$ : bulk plasma,  $\beta$ : close to the left electrode ( $x=0.8$  cm),  $\gamma$ : bulk plasma, but neglecting the change of gas composition on the PIC/MCC

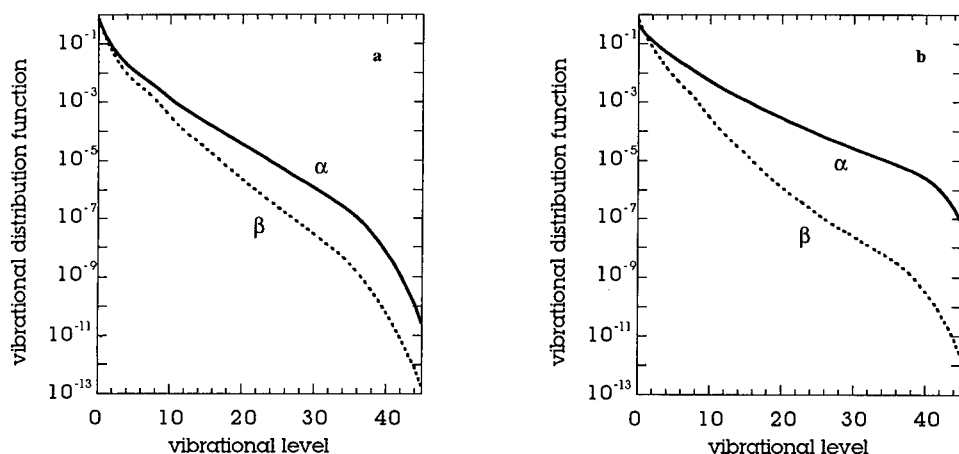


Figure 5: vibrational distribution function in the bulk plasma calculated at (a) 13.5 MHz and (b) 27 MHz.  $\alpha$ : full model,  $\beta$ : neglecting the change of gas composition on the PIC/MCC

bulk ionisation degree is larger. The ionisation degree is higher also in the sheath region, and consequently the peak sheath region extension is reduced: this kind of 'buffering' effect reduces the energy transfer to the bulk discharge, but the overall effect of increasing the RF frequency is by far higher pumping. In fig.4 it is shown time/averaged, steady state eedf calculated in two different positions in the discharge gap. As can be seen, the eedf near the electrode surface has a very long tail, which can be retraced in the high energy tail of the bulk plasma eedf, again confirming the strongly nonlocal conditions. In the same figure it is also shown the effect of the coupling of the PIC/MCC with the vibro-electronic kinetics, by comparison with a bulk plasma eedf calculated for a 'cold' gas in the same conditions.

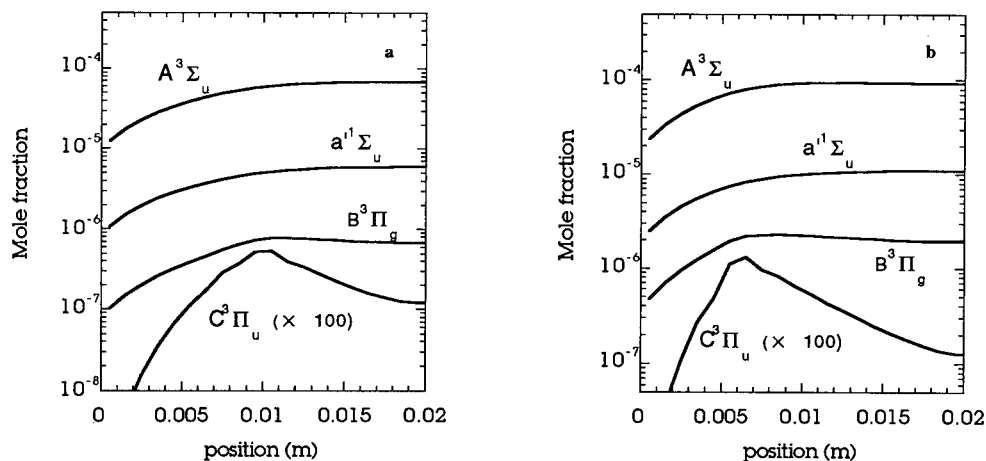
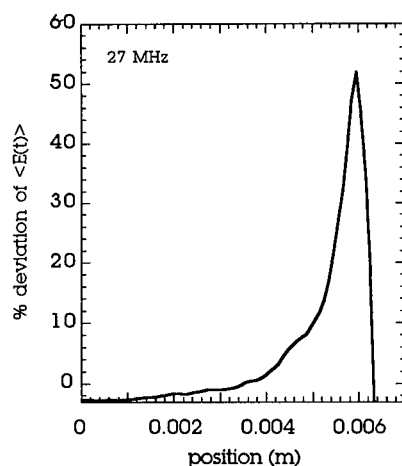


Figure 6: density of selected electronic states of  $N_2$  molecules calculated at (a) 13.5 MHz and (b) 27 MHz





**Figure 7:** relative difference between the time averaged electric field near the left electrode calculated with the full model and neglecting the change of gas composition on the PIC/MCC

It can be observed that the eedf in the bulk plasma is strongly influenced by the coupling with the chemical kinetics in the energy range of vibrational excitation processes in both cases, while at the higher frequency the eedf is also influenced in the energy range for electronic excitation processes, due to electronic super-elastic collisions, specially  $e/N_2(a')$ . In fig. 5 one can observe that the change in shape of the eedf is able to influence strongly the shape of the vdf, by increasing the energy input through e-V inelastic processes to be redistributed by VV processes (and quenched by VT one on the very tail of the vdf, as can be seen from the figure). Finally fig 6 shows the calculated space dependent densities of the selected electronic states of Nitrogen molecules. For these calculations an accommodation on the wall equal to 1 was selected, and the result is a strong gradient of concentration at the boundary: the value of the accommodation coefficient is however not an essential parameter here, since electronic states are mainly destroyed by volume processes (collisional and radiative).

The effect of the vibro-electronic kinetics on the PIC/MCC particle dynamics is reflected in turn on the electric field itself, as it is shown in fig.7, showing the relative difference between the time averaged value of the local electric field with and without self-consistent coupling.

**Table II:** simulation results for the bulk plasma

	13.56 MHz (full model)	13.56 MHz (decoupled)	27 MHz (full model)	27 MHz (decoupled)
electr. density ( $\text{cm}^{-3}$ )	$6.2 \cdot 10^9$	$6.4 \cdot 10^9$	$2.1 \cdot 10^{10}$	$2.5 \cdot 10^{10}$
electr. m. energy (eV)	0.94	0.80	1.22	0.71
T01 (K)	2800	2200	4600	2700

The combined effect of chemical kinetics and discharge frequency is better observed by inspecting table II, which also reports the T01 'bulk vibrational temperature' defined according to the 'Boltzmann' relation for the ratio  $vdf(1)/vdf(0)$ . As can be shown, the effect of the super-elastic collisions on the PIC/MCC kinetics is an increasing of the electron mean energy and a slight *reduction* of the

plasma density. This last point may sound strange compared to the phenomenology of 0D plasmas, but it can be understood for an RF discharge: the most of the low-energy electron are in fact trapped by the rather shallow ambipolar potential well. Super-elastic collisions raise the mean energy of the bulk electrons allowing them to reach the oscillating sheath regions, thereby increasing the energy deposition in the vibrational excitation channel but with no significant effect on the tail of the eedf. At the same time, charged particle loss takes place by ambipolar diffusion as the ions enter the pre-sheath region at Bohm velocity  $v_B = (KT_e/m_i)$ , and this dynamics is automatically reproduced by the PIC/MCC: therefore the increasing of the electron mean energy due to super-elastic collisions also increase the ambipolar diffusion losses.

#### 4. CONCLUSIONS

A 1Dr2Dv PIC/MCC model for bounded Nitrogen plasmas has been coupled self-consistently to a 1D vibrational, electronic and diffusion kinetics for molecules. The coupling produces effects on macroscopic plasma parameters and on the vibrational kinetics through a complex interplay of plasma dynamics and heavy particle kinetics which has no analogues in the uniform plasma models. Results confirm the necessity of full self-consistent modelling of chemical plasmas for 1D (and presumably 2D) RF discharge studies, specially at the higher frequencies.

#### Acknowledgements

This work has been partially supported by MURST and by "Progetto Strategico Applicazioni Industriali dei Plasmi" of CNR.

#### References

- [1] Hockney R.W. and Eastwood J.W., *Computer Simulation Using Particles*, (Adam Hilger, Bristol, 1991)
- [2] Birdsall C.K. and Langdon A.B., *Plasma Physics via Computer Simulation*, New York: Mc. Graw-Hill (1985)
- [3] Birdsall C.K. 'Particle in Cell Charged Particle Simulation, Plus Monte Carlo Collisions with Neutral Atoms, PIC-MCC', IEEE Trans. Plasma. Sci. **19**, (1991) 68-85
- [4] Longo S., Hassouni K., Iasillo D., and Capitelli M.: Coupled electron and molecular vibrational kinetics in a 1D Particle-in-Cell model of a low pressure, high frequency electric discharge in nitrogen, J.Phys.III **7** (1997) 707-718
- [5] Longo S., Hassouni K. and Capitelli M.: Non equilibrium vibrational distributions of N<sub>2</sub> in RF parallel plate reactors: a self consistent approach, 28th AIAA Plasma Dynamics and Laser Conference, Atlanta, GA, USA, 23-25 June 1997, AIAA Paper 97-2363
- [6] Capitelli M. (Editor), *Nonequilibrium Vibrational Kinetics*, Topics in Current Physics vol.39, Springer Verlag (1986)
- [7] Turner M.M. and Hopkins M.B. 'Anomalous Sheath Heating in a Low Pressure rf Discharge in Nitrogen', Phys.Rev.Lett. **69**, (1992) 3511-3514
- [8] Billing G., 'Vibration-Vibration and Vibration-translation energy transfer, including multiquantum transitions in atom-diatom and diatom-diatom collisions', in ref. [6], (1986) 85-112
- [9] Garscadden A. and Nagpal R., 'Non-equilibrium electronic and vibrational kinetics in H<sub>2</sub>-N<sub>2</sub> and H<sub>2</sub> discharges', Plasma Surces Sci. Technol. **4** (1995) 268-280
- [10] Piper L.G., 'The excitation of N<sub>2</sub>(B<sup>3</sup>Π<sub>g</sub>, v=1-12) in the reaction between N<sub>2</sub>(A<sup>3</sup>Σ<sub>u</sub><sup>+</sup>) and N<sub>2</sub>(X, v>=5)', J.Chem.Phys. **91**, 864-873 (1989)

## A Unified Theory of Arcs and their Electrodes

J.J. Lowke

CSIRO Telecommunications and Industrial Physics, Box 218, Lindfield, Sydney, NSW 2070, Australia

**Abstract.** For arcs at atmospheric pressure which have cathodes that are thermionic emitters, it is possible to calculate the major properties of the arc and the electrodes as a function of current, by accounting for electrode shape and the heat transfer processes occurring at the surface of the electrodes. Such processes occur due to electron and ion emission and absorption and also from radiation emission and absorption. Electrical resistance of the plasma near the electrodes is calculated either by taking account of ambipolar diffusion or simply using the local plasma value, with mesh sizes sufficiently large to account for ambipolar diffusion. Derived temperature profiles are in fair agreement with experiment. Results of electrode temperatures and arc melting effects, including such phenomena as the transition from globular to spray modes in arc welding, are also in good agreement with experiment. Prediction of properties for non-thermionic cathodes still constitute a major problem. Approximate calculations indicate that electrons at the surface of the non-thermionic cathodes may be produced by photo ionisation of neutral atoms rather than by field emission.

### 1. INTRODUCTION

Properties of electric arcs at atmospheric pressure depend not only on the arc plasma medium, but also on the electrodes. In particular they depend on the electrode shape and whether or not the cathode is a thermionic emitter. With the availability of modern high speed computers, it has recently become possible to make detailed predictions of properties of electric arcs from basic material properties, provided the arcs have thermionically emitting cathodes. Thus, given the electrode shape and the material properties of the plasma and the electrodes, it is possible to calculate the maximum temperature of the arc, the diameter of the arc, whether the electrodes will melt and the velocity profiles of the plasma flow within the arc, for any given arc current.

To make this type of prediction, we need to understand the physical processes that are occurring. We also need to know which of these processes are dominant, so that we can make adequate approximations to be able to make computations in a reasonable computation time. It is often the case that we understand the many atomic processes very well, but even with the enormous improvements in the speed and availability of computers, we still are unable to make economic computations in a reasonable time. The art of making valid approximations is then all important.

The major requirement is to include an account of the electrode shape [1] and the heat transfer processes that are occurring at the surface of the electrodes. For thermionic cathodes, the non equilibrium electrical conductivity of the plasma near the cathode surface can be obtained by calculating charge densities taking into account ambipolar diffusion [2]. Calculations indicate that for arcs with thermionic cathodes, the regions where positive and negative charges are unequal are small and can be neglected [3].

The calculation of detailed properties of arcs with non thermionic cathodes represents a major unsolved problem. Experimental evidence indicates that there is a sheath at the surface of cathodes with a voltage drop of 15-20 V, which has a remarkably small dependence on cathode material, plasma composition or arc current ; Kesaev [4], Matsumura *et al* [5]. There must be some mechanism for the production of the electrons for the arc current, at, or in front of the cathode. For vacuum arcs, the electron emission is generally accepted as being due to field emission caused by a high field produced by a sheath of positive ions in front of the cathode [6]. For high pressure arcs there is another possibility - photo-ionisation in the cathode sheath of neutral atoms in front of the cathode by ultra-violet photons from ions in the plasma.

We discuss the arc column in section 2, the cathode and cathode sheath for thermionic cathodes in Section 3, the anode and anode sheath in Section 4, and the cathode and cathode sheath for non-thermionic cathodes in Section 5. Finally, in Section 6, we present specific predictions compared with experiment of (a) the tips of sharp tungsten cathodes melting off at high current, (b) the effect on arc and electrode properties of adding hydrogen to argon, (c) the change from globular to spray transfer of molten metal in "Gas Metal Arc Welding (GMAW)" for arcs in argon, and (d) the different properties of electrode melting for arcs in carbon dioxide.

## 2. ARC COLUMN

It has been known for a long time that the column of electric arcs can be well represented as a plasma in local thermodynamic equilibrium; Finkenburg and Maecker [7]. The basic equations defining the temperature are conceptually simple, namely the equations for conservation of mass, energy, momentum and current. The equation for conservation of mass is

$$\frac{\partial \rho}{\partial t} + \frac{1}{r} \frac{\partial}{\partial r} (r \rho u_r) + \frac{\partial}{\partial z} (\rho u_z) = 0; \quad (1)$$

$\rho$  is the density, and  $u_r$  and  $u_z$  are the radial and axial velocities in the  $r$  and  $z$  directions. The equation for conservation of energy is

$$\frac{\partial(\rho h)}{\partial t} + \frac{1}{r} \frac{\partial}{\partial r} (r \rho u_r h) + \frac{\partial}{\partial z} (\rho u_z h) = \frac{1}{r} \frac{\partial}{\partial r} \left( \frac{rk}{c_p} \frac{\partial h}{\partial r} \right) + \frac{\partial}{\partial z} \left( \frac{k}{c_p} \frac{\partial h}{\partial z} \right) + \frac{j_r^2 + j_z^2}{\sigma} - U; \quad (2)$$

$h$  is the enthalpy,  $k$  is the thermal conductivity,  $U$  the radiation emission coefficient,  $c_p$  the specific heat,  $\sigma$  the electrical conductivity, and  $j_r$  and  $j_z$  the radial and axial current densities. The equations for the conservation of radial and axial momentum are

$$\begin{aligned} \frac{\partial(\rho u_r)}{\partial t} + \frac{1}{r} \frac{\partial}{\partial r} (r \rho u_r^2) + \frac{\partial}{\partial z} (\rho u_r u_z) &= -\frac{\partial P}{\partial r} - j_z B_\theta + \frac{1}{r} \frac{\partial}{\partial r} \left( 2r\mu \frac{\partial u_r}{\partial r} \right) \\ &+ \frac{\partial}{\partial z} \left( \frac{\mu \partial u_z}{\partial r} + \frac{\mu \partial u_r}{\partial z} \right) - 2\mu \frac{u_r}{r^2} \end{aligned} \quad (3)$$

and

$$\begin{aligned} \frac{\partial(\rho u_z)}{\partial t} + \frac{1}{r} \frac{\partial}{\partial r} (r \rho u_z u_r) + \frac{\partial}{\partial z} (\rho u_z^2) &= -\frac{\partial P}{\partial z} + j_r B_\theta + \frac{\partial}{\partial z} \left( 2\mu \frac{\partial u_z}{\partial z} \right) \\ &+ \frac{1}{r} \frac{\partial}{\partial r} \left( \frac{r \mu \partial u_z}{\partial r} + \frac{r \mu \partial u_r}{\partial z} \right) + \rho g; \end{aligned} \quad (4)$$

$P$  is the pressure,  $\mu$  is the viscosity,  $g$  the gravitational acceleration and  $B_\theta$  the azimuthal magnetic field.  $B_\theta$  is determined from Maxwell's equation

$$\frac{1}{r} \frac{\partial}{\partial r} (r B_\theta) = \mu_0 j_z; \quad (5)$$

where  $\mu_0$  is the permeability of free space;  $\mathbf{j} = \sigma \mathbf{E}$ , where  $\mathbf{E} = -\nabla V$  and  $V$  is the potential. The current continuity equation is

$$\frac{1}{r} \frac{\partial}{\partial r} \left( r \sigma \frac{\partial V}{\partial r} \right) + \frac{\partial}{\partial z} \left( \sigma \frac{\partial V}{\partial z} \right) = 0 \quad (6)$$

The above conservation equations also apply to the solid electrodes, and the molten metal, if the electrodes are molten, as is the case for welding arcs, discussed later in Section 6.3 and 6.4. Then the boundaries of these three phases need to be specified on the grid system and the material functions at each grid point chosen appropriate to each phase and the local temperature.

### 3. THERMIONIC CATHODES AND CATHODE SHEATHS

#### 3.1 Electrode Heat Exchange Processes

Calculations at points on the electrode surface need to include the heat transfer processes occurring at the surfaces. Additional to the usual energy fluxes by thermal conduction are energy losses by thermal radiation from the hot electrode, cooling or heating by the electrons leaving or entering the solid and heating by ion bombardment. Heating of the electrodes by radiation from the arc is neglected. For the cathode, the additional energy flux,  $F$ , is

$$F = -\epsilon a T^4 - |j_e| \phi + |j_i| V_i \quad (7)$$

$\epsilon$  is the emissivity of the surface,  $T$  is the surface temperature,  $\phi$  is the work function,  $j_e$  and  $j_i$  are the electron and ion current density,  $a$  is the Stefan Boltzmann constant, and  $V_i$  is the ionisation potential of the plasma. The term in  $\phi$  represents the loss in energy from electrons leaving the cathode and overcoming the work function potential. The ion current density,  $j_i$ , is taken to be  $j - j_R$  at the cathode surface, where  $j$  is the cathode surface current density from the current continuity equation (6) and  $j_R$  is the theoretical electron current due to thermionic emission obtained from  $j_R = AT^2 \exp(-\phi e/kT)$ ;  $e$  is the electronic charge,  $k$  is Boltzmann's constant and  $A$  is the thermionic emission constant for the surface of the cathode. If  $j_R$  is greater than  $j$  we take  $j_i$  to be zero. The assumption that heating of the cathode is given by  $|j_i| V_i$  is supported by the experimental results of Winters *et al* [8]. These experiments suggest that the full ionisation potential  $V_i$  is delivered to the cathode, there being no reduction in  $V_i$  by  $\phi$ , presumably because the electron for neutralisation of the ion is provided within the cathode surface.

#### 3.2 Cathode-Arc Sheath Resistance

There is a major problem associated with electrode effects. We need to decide how to calculate the electrical resistance of the plasma near the electrodes, where the plasma temperatures are relatively low. If we assume local thermodynamic equilibrium and a collision dominated sheath, the electron density would be effectively zero at the melting temperature of the electrodes, so that then the equilibrium electrical conductivity would be zero. For finite electrical conduction, there must be some mechanism such as thermionic emission or ambipolar diffusion to make these regions highly conducting. To account for ambipolar diffusion an effective electrical conductivity has been calculated for mesh intervals at the cathode surfaces [2,9-11].

First, the electron continuity equation is solved for the electrode sheath mesh interval ie

$$\nabla \cdot (D_A \nabla n_e) + S - \gamma n_e^2 = 0; \quad (8)$$

$D_A$  is the ambipolar diffusion coefficient [10] for the local temperature given by  $2kT\mu_i/e$ ;  $\mu_i$  is the ion mobility,  $n_e$  is the electron number density and  $\gamma$  is the electron-on recombination coefficient. A source term,  $S$ , representing the production of electrons and ions by thermal ionisation, is defined as  $S = \gamma n_{eq}^2$ , where  $n_{eq}$  is the equilibrium plasma value of electron density for the local plasma temperature. Then solutions for  $n_e$  in the sheath will be the equilibrium values if there is no diffusion. For the solution of equation (8), boundary conditions are needed for  $n_e$ . On the plasma side of the mesh interval the equilibrium plasma value is used. On the electrode side we take  $n_e = j_R/ev_t$ , where the thermal velocity  $v_t$  is obtained from  $mv_t^2/2 = 2kT$ ;  $m$  is electron mass.

Second, using the values of electron density as a function of distance within the sheath, the effective electrical conductivity of the sheath,  $\sigma_{eff}$ , is derived. A generalised form of Ohm's Law [9] is used:

$$j = \frac{n_e e}{\{n_0/n_T \mu_e E + 2e n_e n_{eq}(T)/n_T \sigma E\}} ; \quad (9)$$

$n_0$  is the equilibrium neutral particle density,  $\mu_e$  is the electron mobility and  $n_T = n_0 + 2n_e$  is the total particle density. This expression reduces to  $j = \sigma E$  in the plasma where  $n_0 = 0$  and to  $j = n_e e \mu_e E$  in a cold gas where  $n_0 \sim n_T$  and  $n_{eq} \sim 0$ . Equation (9) is used to derive  $E$  as a function of position within the sheath for a given  $j$  and thus, by integration, the potential drop,  $V_s$ , across the mesh interval is obtained.

Then  $\sigma_{eff} = js/V_s$  where  $s$  is the mesh thickness.

Equation (9) is a general approximation that can be derived for a partially ionised plasma. We take  $j \sim j_e$ , where the electron current density is given by  $j_e = n_e e W$ , where the drift velocity,  $W$ , of the electrons in a mixture of neutrals and charged particles can be represented to a good approximation by  $W = Ee/mv$  [12]. The total collision frequency,  $\nu$ , is given by  $\nu = \nu_n + \nu_c$ , the sum of the electron collision frequencies,  $\nu_n$ , with neutral particles and  $\nu_c$ , with charged particles. Using  $W_n = Ee/m\nu_n$ , it follows that  $\nu_n$  is given by  $e n_0 / m \mu_e n_T$ , where  $W_n = \mu_e E$  is the drift velocity of electrons in neutral atoms, and we have weighted this collision frequency with the proportion of neutral atoms,  $n_0/n_T$ . Similarly,  $\nu_c$  is given by  $n_e e^2 2n_{eq}/m\sigma n_T$ , where we have used (a) the relationship between the drift velocity,  $W_c$ , of electrons in an equilibrium plasma and  $\sigma$ , of  $n_e e W_c = \sigma E$ , (b)  $W_c = Ee/m\nu_c$  and (c) a weighting factor of  $2n_{eq}/n_T$  for the proportion of charged particles.

Figure 1 shows an example of a numerical solution of equation (8) for a region of the plasma at the tip of the cathode for a 200 A arc. The charge densities near the cathode, indicated by open circles, are orders of magnitude above the equilibrium values, labelled LTE, due to the influence of ambipolar diffusion. It is seen that in the main plasma the influence of diffusion is small, but that there is a region of significant non-equilibrium near the cathode surface which extends over a distance of about 0.005 cm. To obtain solutions of equation (8), values of  $\gamma$  are required as a function of temperature and charge density. We have used the classical formula  $\gamma = 1.1 \times 10^{-12} n_e T^{-4.5} \text{ cm}^3 \text{ s}^{-1}$  of Hinnov and Hirschberg [13], discussed by Mitchner and Kruger [14]. Other values are given by Biberman *et al* [15] and Hoffert and Lien [16].

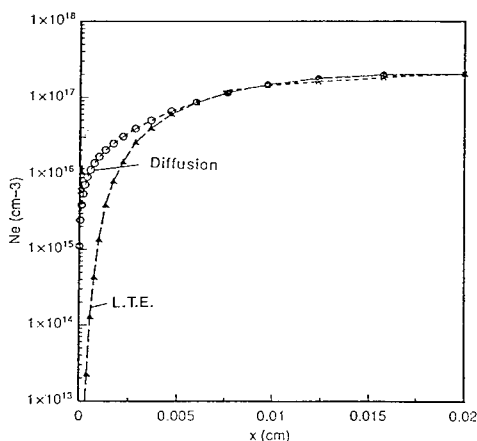


Fig. 1 Non-equilibrium charge densities at cathode for 200 A [11].

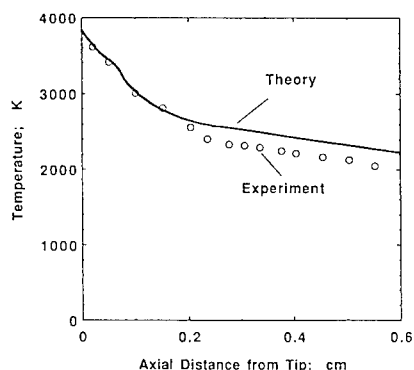


Fig. 3 Calculated [11] and experimental [18] cathode surface temperatures.

Equations (1-6) can be solved for any given arc current [2,10,11] to obtain  $h$ ,  $P$ ,  $u_r$ ,  $u_z$ ,  $B_\theta$  and  $V$  as a function of  $r$  and  $z$ . Temperature is obtained through the temperature dependence of  $h$ . The material

functions  $\rho$ ,  $c_p$ ,  $k$ ,  $\sigma$ ,  $U$ ,  $\epsilon$ ,  $\phi$ ,  $V_i$ ,  $n_{eq}$ ,  $n_0$ , and  $\gamma$  are required input as a function of temperature, from, for example, Murphy and Arundell [17]. For  $\rho$ ,  $c_p$ ,  $k$  and  $\sigma$ , values are required for the plasma and the electrodes, for both the solid and liquid state.

Figure 2 shows predicted temperature contours for a 200 A arc in argon with a thoriated tungsten cathode of 60 degree angle, separated from an anode of copper by 5 mm [10,11]. The bottom face of the copper is water cooled to maintain it at room temperature, assumed to be 300 K. Experimental values of the arc temperature from Haddad and Farmer [18] are shown as points. Figure 3 shows theoretical values of temperature of the surface of the tungsten cathode taken from Figure 2, as a function of distance from the cathode tip. Also shown are experimental values of surface temperature, taken spectroscopically, and shown as points [19]. For both figures the agreement between theory and experiment is very satisfactory. Results are largely independent of mesh size for mesh sizes varying from 0.003 to 0.02 cm [11].

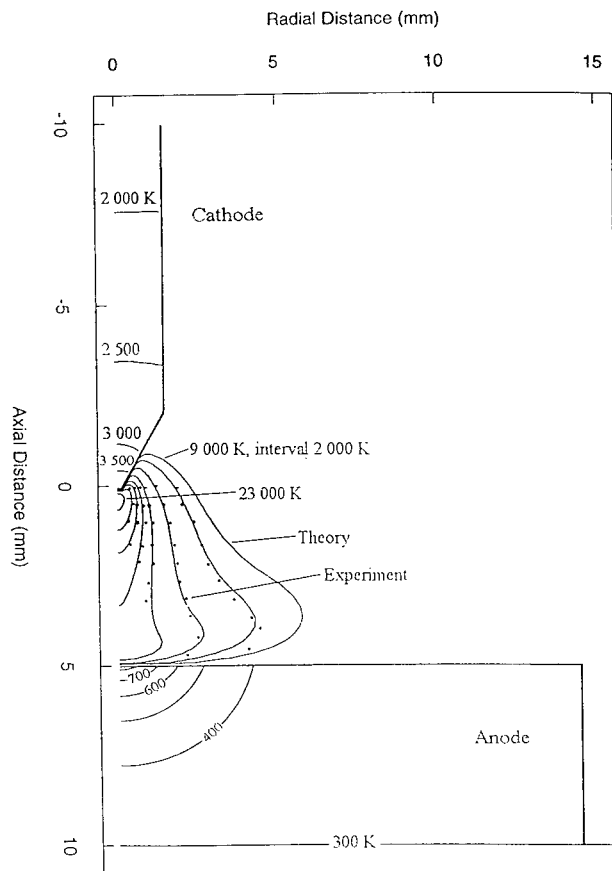


Fig. 2 Predicted temperature contours for a 200 A arc [11], compared with experiment [18].

#### 4. ANODES AND ANODE SHEATHS

At the anode surface we change the sign of the term in  $\phi$  of equation (7) as electrons heat the anode due to the work function potential. We assume that there is no ion current and hence no ion heating at the anode. For the anode it is not possible to calculate the resistance of the anode sheath by using the same ambipolar diffusion treatment as used for the cathode. It is usual to set the charged particle densities to zero as a boundary condition at any absorbing anode surface. However, the calculated electric field at

the anode surface with  $n_e = 0$  from equation (9) would be infinite. If current due to diffusion is included in the analysis, it is found that because of the large density gradients, the diffusion current is so large that the electric field immediately in front of the anode reverses sign. This effect has been found by Dinulescu and Pfender [20]. Our use of  $j = \sigma E$  in the main iteration algorithm requires a negative value of  $\sigma$  if there is a reversal in the sign of  $E$  to maintain positive current. However, our method for the solution of the current continuity equation (6) is unstable for negative values of  $\sigma$ .

Thus in our solutions of the equations we have omitted sheath effects at the anode and simply taken the local values of the electrical conductivity near the anode. Numerical solutions are a function of the grid spacing at the anode, as can be understood by considering that in the limit of a very fine mesh at the anode, the plasma temperature would approach that of the anode, and the electrical conductivity would approach zero. The calculated current density at the anode as a function of the mesh size in the  $z$  direction at the anode for a 200 A arc gives agreement with the experimental results of Nestor [21] if the mesh size near the anode is about 0.05 cm. This mesh size corresponds to an ambipolar sheath thickness of 0.05 cm [11] calculated from  $(DA/\eta_e)^{1/2}$  if we use values of  $\gamma$  from [16]. The maximum arc temperature and properties of the arc at the cathode are largely unaffected by the mesh size at the anode since the plasma flow is directed towards the anode. The arc voltage is, however, influenced by the anode sheath and is reduced by about a volt when the anode mesh size increases from 0.01 to 0.05 cm.

Fig. 4 shows calculated sheath properties at the anode [3] for a 200 A arc, taking account of space charge effects, through a solution of equations (10) - (13), discussed in the next section. The electric field in the sheath is reversed, producing a negative anode fall, and electron and ion densities are equal to within a few percent to distances of 0.0002 cm of the anode, which is much less than the electron mean free path.

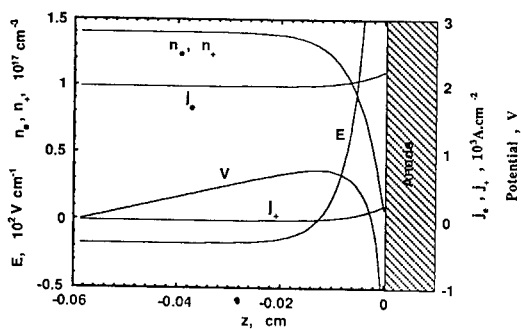


Fig. 4 Derived anode sheath properties for a 200 A arc [3].

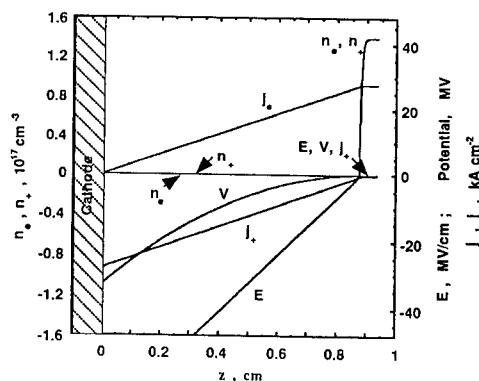


Fig. 5 Derived cathode sheath properties for  $S=2 \times 10^{23}$  [3].

## 5. NONTHERMIONIC CATHODES AND CATHODE SHEATHS

For nonthermionic cathodes there is little doubt that space charge effects in the cathode sheath are significant. The change in the electric field from these effects is determined by Poisson's equation.

$$\frac{dE}{dz} = \frac{e}{\epsilon} (n_i - n_e) \quad (10)$$

where  $\epsilon = 8.85 \times 10^{-14} \text{ C V}^{-1} \text{ cm}^{-1}$  is the permittivity of free space. The voltage,  $V$ , across the sheath is obtained by integrating the electric field. Calculations of sheath properties using transport coefficients have recently been made by Lowke and Quartel [3]. For non-thermionic cathodes there is a major question as to how the electrons are produced at the cathode for the arc. The mechanisms of (a) field emission, (b) electron impact ionisation, (c) thermal ionisation and (d) photo-ionisation by ion radiation, are now discussed in turn.

**(a) Field emission.** The usual view is that electrons are drawn from the cathode by field emission [5], as is generally accepted for vacuum arcs [6]. Electrons moving away from the cathode and positive ions moving toward the cathode produce a layer of high density positive ions next to the cathode which produces a high electric field. The electric field,  $E_s$ , necessary for field emission is generally taken to



be  $4 \times 10^7$  /cm for a typical work function of 4.5 eV [22]. Typical cathode sheath voltages,  $V_s$ , are 20 V or less [4]. By integration of equation (10) twice, neglecting the term in  $n_e$ , we obtain  $E_s = en_i b/\epsilon$ , and  $V_s = en_i b^2/2\epsilon$ , where  $b$  is the sheath thickness. Then using the values of  $E_s = 4 \times 10^7$  V/cm and  $V_s = 20$  V, we obtain  $b = 10^{-6}$  cm and  $n_i = 4 \times 10^{19}$ /cm<sup>3</sup>. Considering that the equilibrium ion density in the arc is approximately  $10^{17}$ /cm<sup>3</sup> and that ions will be accelerated and have a lower density on approaching the cathode, densities of  $4 \times 10^{19}$ /cm<sup>3</sup> to produce field emission seem most unlikely. Studies to obtain consistency with fields for field emission and experimental sheath voltages have also been made by other workers [23-24].

**(b) Electron impact ionisation.** A further possibility is that the electrons are produced by ionisation from electrons accelerated by the high electric field in the sheath. But the secondary emission coefficient for the production of initiating electrons at the cathode surface is only of the order of 0.1. Electron currents can at the very most be doubled for a voltage drop in the sheath equal to the ionisation potential. With a secondary emission coefficient of 0.1 we need a doubling of more than 3 times, which would imply sheath voltages of 50 volts or more for argon, where the ionisation potential is 15.8 V.

**(c) Thermal ionisation.** A further possibility is that electrons are produced by thermal ionisation in the sheath of neutral atoms. These atoms would be brought to a very high temperatures because of the proximity of the arc plasma. Such thermal ionisation must exist in the arc, to balance electron ion recombination, and is represented by a source term,  $S$ , just as in equation (8). For the general case where electron and ion densities may not be equal, the electron and ion continuity equations are given by

$$\frac{dj_e}{dz} = eS - e\gamma n_e n_i \quad \text{and} \quad \frac{dj_i}{dz} = eS - e\gamma n_e n_i. \quad (11)$$

In our calculations we have determined  $S$  using  $n_{eq} = 1.4 \times 10^{17}$  cm<sup>-3</sup>, which is the equilibrium electron density for argon at 15000 K at 1 bar. An approximate estimate of the minimum sheath thickness,  $b$ , can be obtained by integration of equations (11) to obtain  $b = j_e/eS$ , assuming a constant value of  $S$  for the sheath. The term in  $\gamma$  is neglected because values of  $n_e$  will be small in the sheath because of the high electron mobility. Furthermore, inclusion of the term in  $\gamma$  increases the derived value of  $b$ . Using a value of  $\gamma = 10^{-11}$  cm<sup>3</sup>s<sup>-1</sup> from [10] and  $n_{eq} = 1.4 \times 10^{17}$ , we obtain  $b \sim 1$  cm, which is much greater than experimental values. We conclude that thermal ionisation is insufficient to provide the required electrons.

Complete solutions for  $n_e$ ,  $n_i$ ,  $E$ ,  $j_e$ , and  $j_i$  for the sheath for the above parameters were obtained in [3] by solving equations (10) and (11) and in addition equations (12) and (13) for the electron and ion current densities;

$$j_e = -e n_e \mu_e E - e D_e \frac{dn_e}{dz} \quad (12)$$

$$j_i = -e n_i \mu_i E. \quad (13)$$

Such a solution, given in Figure 5. All of the spatial derivatives of the five basic variables  $j_e$ ,  $j_i$ ,  $n_e$ ,  $n_i$  and  $E$ , are set to zero in the plasma and solutions are obtained for a given value of  $j$  by integration of the simultaneous equations (10) - (13) from equilibrium values in the plasma to the cathode. The solution of Figure 5 is unrealistic as the sheath thickness is  $\sim 1$  cm, in agreement with the approximate calculation.

**(d) Photo-ionisation by ion radiation.** It is possible that electrons could be produced by photo-ionisation of neutral atoms in front of the cathode by ultra violet radiation from ions in the plasma [3]. Neutral atoms will exist at the cathode surface from the neutralisation of positive argon ions impinging on the cathode and also from background neutral gas. Ultra violet radiation from the equilibrium arc plasma is insufficient to produce the required source electrons as the total emission coefficient for argon at 1 bar and 20 000 K and a thickness of 1 mm is  $10^3$  W cm<sup>-3</sup> ster<sup>-1</sup> [27]. Then, for a 1 mm thick plasma and an ionisation potential of 10V, there is only a sufficient energy flux to produce an electron current density of 10 A/cm<sup>2</sup>, whereas experimental cathode current densities are  $\sim 10^4$  A/cm<sup>2</sup>.

However, electrons produced by photo-ionisation of neutral atoms at the cathode will be accelerated across the cathode sheath to have an energy equivalent to the sheath voltage, as it is anticipated that the sheath thickness will be of the order of an electron mean free path so that transit across the sheath will be collisionless. Such electrons can excite ions which then radiate. The threshold potential to excite

radiation from ions is  $\sim 18$  V, so that the sheath voltage is sufficient for the excitation of radiation. The sum of the cross-sections for the first 5 radiation levels for argon ions, all with thresholds of  $\sim 18$  V, is of the order of  $0.2 \times 10^{-16} \text{ cm}^2$  [25], so that for ion densities in the plasma of  $2 \times 10^{17} \text{ cm}^{-3}$ , the absorption distance of the electrons will be  $\sim 0.2$  cm. This radiation has photon energies greater than the ionisation threshold of 16 V of neutral atoms, so that it will cause photo-ionisation of the atoms at the cathode. The absorption distance of the radiation is small, ie  $\sim 0.03$  cm for a neutral density of  $10^{18} \text{ cm}^{-3}$  as the photo-absorption cross-section in argon at this electron energy is  $\sim 0.3 \times 10^{-16} \text{ cm}^2$  [26]. It is suggested that this photo-ionisation is a principal source of electrons at the cathode for arcs with non-thermionic cathodes.

## 6. SPECIFIC PREDICTIONS

### 6.1 Cathode tip melting

A striking effect occurs with tungsten cathodes having a narrow conical tip, in that at high currents a temperature maximum and melting occurs several mm from the tip. Thus if the tungsten electrode in "Gas Tungsten Arc Welding" accidentally touches the workpiece, producing high current, the tip of the tungsten can "break" off, as shown in Fig. 6, and become embedded in the weld, forming what is known as a tungsten "inclusion". Systematic surface temperature measurements [28] have shown that there is a maximum in the surface temperature several mm from the tip, as shown in Figure 7. Theoretical predictions [11], also shown in Figure 8, also predict a maximum in the surface temperature away from the tip. Thus the tungsten tip actually melts off rather than breaks off. The minimum in the temperature near the tip is due to cooling of the electrode by thermionic emission, and the maximum away from the tip is due to Ohmic heating by the current within the narrow tip of the electrode [11].

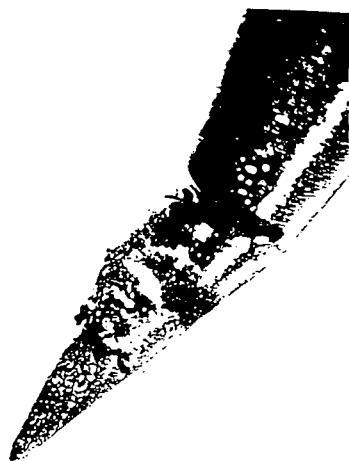


Fig. 6 Tungsten cathode melting away from the tip for 200 A [28].

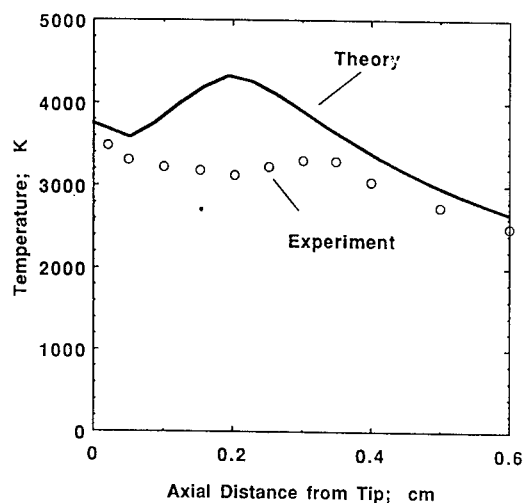


Fig. 7 Theoretical [11] and experimental [28] temperatures at 200 A for a tungsten cathode of 16 degrees.

### 6.2 Effect of 10% Hydrogen in Argon Arcs

It is found, in studies related to arc welding [29] that a few percent of hydrogen added to argon causes higher arc temperatures, arc constriction, a higher arc voltage, and a significantly larger volume of molten metal at the workpiece for a given arc current. Such variations can be predicted using the present theory, omitting convection in the molten anode. Figures 8 and 9 show similar calculations to Figure 2 but with an electrode separation of 3 mm and an anode of mild steel [30]. Figure 8 is for pure argon and Figure 9 is for a mixture of argon and 10 % hydrogen. It is found that the addition of 10 % hydrogen causes a marked increase in the volume of the molten steel, the arc is slightly more constricted and has a slightly increased central temperature and voltage.

The only difference in the calculations of Figures 8 and 9 are those of the material functions of argon and argon with 10% hydrogen. These material functions generally differ by only the order of 10%, but with one exception, namely the values of thermal conductivity. At temperatures of around 3500 K, where the dissociation of molecular hydrogen is significant, the thermal conductivity is almost a factor of 10 higher for the mixture than for pure argon [30]. It is this increased thermal conductivity which causes the increased volume of molten metal for the mixture containing hydrogen. The larger thermal conduction also causes a slightly more constricted arc with a higher central temperature and arc voltage.

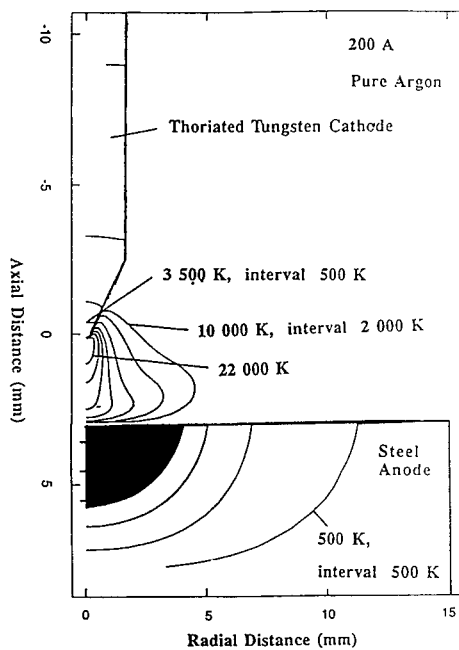


Fig. 8 Calculated Contours, 200A, Ar, steel workpiece, molten volume black [30].

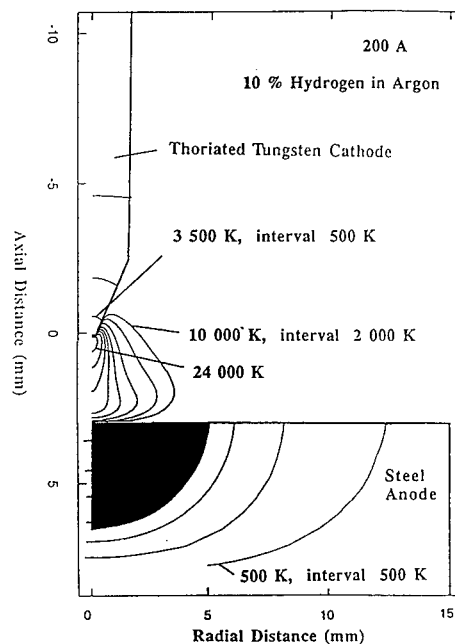


Fig. 9 Calculated contours, 200A, Ar+10% H<sub>2</sub> steel workpiece, molten volume black [30].

### 6.3 Globular and Spray modes in Arc Welding

One of the most striking properties found experimentally in "Gas Metal Arc Welding", where an arc is struck between the welding wire, as the anode, and the workpiece, as the cathode, is that at low currents the wire melts producing large molten drops or globules which generally have a diameter which is larger than the diameter of the wire. Then, above a discrete current, usually about 300A for an arc in argon with 1.6 mm diameter wire, there is a sudden mode change in the metal transfer, in that diameter of the drops is then smaller than the diameter of the wire. This mode is described as "spray" transfer; Lancaster [31]. The size of the droplets has a marked influence on the properties of the weld.

These differing modes of metal transfer have been obtained theoretically by Haidar and Lowke [32] using the present theoretical methods. The equations used are the same as equations (1) - (6) except that in addition account must be made of the molten liquid phase. Also the calculations must be time dependent as the arc and electrode properties vary in time as each drop is produced from the wire and is detached into the arc. The effect of surface tension acting in the surface of the liquid is to compress the drop and effectively increase the pressure at the surface of the drop by  $P_s$ , where

$$P_s = \Gamma \left( \frac{1}{R_1} + \frac{1}{R_2} \right); \quad (14)$$

$\Gamma$  is the surface tension coefficient and  $R_1$  and  $R_2$  are principal radii of curvature of the surface [33]. Thus the effect of surface tension is to introduce in equations (3) and (4) a step function increase in the pressure  $P$  from the plasma to the liquid at the drop surface of an amount given by  $P_s$  from equation (14). For a spherical surface of radius  $R$ , this pressure is  $P_s = 2\Gamma/R$ .

In the theoretical predictions of the time dependence of drop formation, again in a unified arc-electrode treatment, it is necessary to make accurate predictions of the curvature of the droplet surface as a function of time, in order to accurately account for the surface tension pressure from equation (6). Such a treatment is possible using the "Volume of Fluid" method [32]. Figure 10 shows the prediction of a large diameter drop, just before detachment, corresponding to the globular mode, for a current of 275 A in argon, with a wire diameter of 1.6 mm. Figure 11 shows a small droplet, just before detachment, corresponding to the spray mode, for a current of 325 A, also in argon for a wire diameter of 1.6 mm. For currents near the transition current, the calculations usually give a mixture of small and large drops, occurring at different times [32].

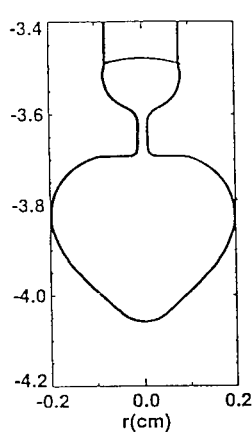


Fig. 10 Calculated drop, 275A, 1.6mm wire [32].

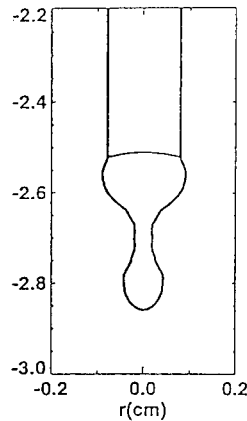


Fig. 11 Calculated drop 325 A, 1.6mm wire [32].

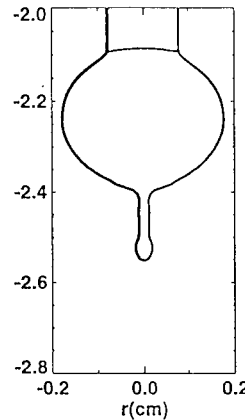


Fig. 13 Calculated drop development, Carbon dioxide, 325 A [40].

From the detailed calculations of droplet formation of Figures 10 and 11 it is possible to assess the order of magnitude of the various physical forces influencing drop detachment. The force of surface tension tends to compress the drop and hold it on to the wire. At low currents, magnetic pinch forces due to the self magnetic field of the arc are small and drop sizes grow until gravitational forces overcome the surface tension force tending to hold the drop on to the wire. These drop sizes are larger in diameter than that of the wire, as in globular transfer.

The self magnetic field from the current in the drop exerts a pinch force which tends to increase the pressure inside of the drop. For current,  $I$ , flowing in a uniform cylinder, of radius  $R$ , Maecker [34] showed that this magnetic pinch force increases the effective pressure on the axis of the cylinder by an amount  $P_m$ , where  $P_m = \mu I^2 / 4\pi^2 R^2$ ;  $\mu = 4\pi \cdot 10^{-7} \text{ N/A}^2$  is the permeability. This pressure increase will tend to extrude liquid from the base of the drop if it is greater than the pressure of  $2\gamma/R$  from surface tension holding the hemisphere to the solid wire. As the current increases the magnetic pinch pressure increases so that there will be a critical current given by  $\mu I^2 / 4\pi^2 R^2 = 2\Gamma/R$  beyond which surface tension will no longer be able to support the drop of radius equal to the wire radius. Thus an approximate formula for the critical current for transition from the globular mode of transfer to the spray mode of transfer is given by

$$I = 2\pi (2\Gamma R / \mu)^{1/2} \quad (15)$$

The above derivation is highly approximate in that the effects of gravity, viscous drag forces of the gas surrounding the drop and the pressure of the arc on the drop are all neglected. Figure 12 shows curves of theoretical predictions from Equation (15) for the transition current as a function of wire

diameter for mild steel and aluminium. The curves marked 'Overhead' and 'Normal' were obtained by including a term  $\rho g$  for gravity, in the derivation. For steel the value of  $\Gamma$  was taken as 1.2 N/m. For aluminium the value of  $\Gamma$  was taken as 0.28 N/m. Experimental values for the transition current are shown as points from references [35 - 37] for steel and [38] for aluminium. The values of  $\Gamma$  that have been used have been taken for the boiling point of these metals from Smithell's Metals Reference Book [39]. It is seen that despite the approximations made in the theory, agreement between theory and experiment is very good. The approximate physical model used to derive equation (15), treated more thoroughly in [40], provides a simple physical picture of the reason for the onset of the small droplet mode of spray transfer in GMAW. For arcs in carbon dioxide, however, the simple physical picture at the basis of equation (7) does not apply. Arcs in carbon dioxide are much more constricted than arcs in pure argon and as a consequence the pressure of the arc on the drop is much larger. As a result drop development is different than in argon, as is discussed in the next section.

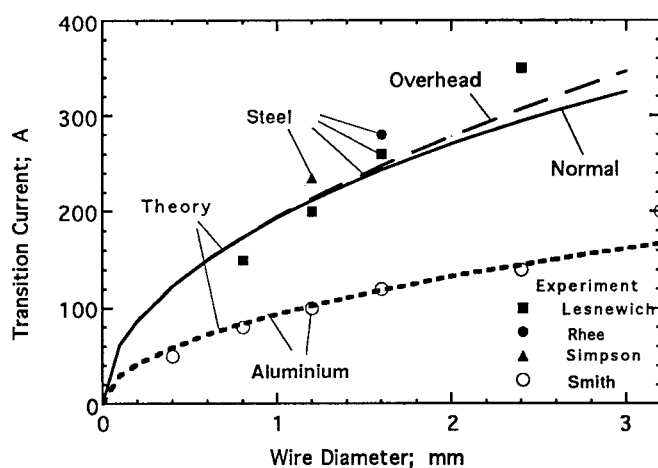


Figure 12: Comparison of experimental results of transition current for spray transfer with predictions from the approximate formula [40].

#### 6.4 Electrode Melting in Carbon Dioxide Arcs

It is well known that if arc welding is attempted using pure carbon dioxide gas, there is very different metal droplet behaviour compared with welding in argon [31]. In particular there is much "spatter" of molten electrode material and frequently metal droplets are repelled away from the workpiece and welding wire in a direction counter to the imposed gas flow towards the work piece.

When we make predictions of arc-electrode behaviour, similar to those in argon shown in Figures 2, 8 and 9, we obtain markedly different arc and droplet behaviour [41]. The central arc temperature for an arc current of 300 A is  $\sim 30\,000$  K in carbon dioxide compared with a temperature of  $24\,000$  K for argon and the arc is much more constricted in carbon dioxide. Instead of there being fairly distinct globular and spray modes of droplet behaviour, as shown for argon in Figures 10 and 11, in carbon dioxide we generally obtain both modes together, with very large drops, separated by the production of hundreds of very much smaller drops, as is shown in Fig. 13. The higher current density for arcs in carbon dioxide, produces a high arc pressure at the base of the drop, which for the very large drops can be larger than the pressure inside of the drop, tending to repel the drop towards the electrode. Of course our calculations [41] impose two dimensional symmetry, so that the "repelled transfer" mode of drop behaviour often observed in welding with high carbon dioxide concentrations, cannot be simulated theoretically.

### Acknowledgments

The author is most indebted to his colleagues and coworkers of the CSIRO Division of Telecommunications and Industrial Physics, namely Jawad Haidar, Dick Morrow, Tony Farmer, Gerry Haddad, and Tony Murphy, on whose work the present paper depends.

### References

- [1] Lowke J. J., Kovitya P. and Schmidt H. P. *J. Phys.D:Appl. Phys.* **25** (1992) 1600-1606.
- [2] Zhu P., Lowke J. J. and Morrow R. *J. Phys.D:Appl. Phys.* **25** (1992) 1221-1230.
- [3] Lowke J. J. and Quartel J. C. *Aust. J. Phys.* **50** (1997) 539-552.
- [4] Kesaev I. G. *Soviet Physics-Technical Physics* **9** (1965) 1146-1154.
- [5] Yokomizu Y., Matsumura T., Henmi R. and Kito Y. *J. Phys. D: Appl. Phys.* **29** (1996) 1260-1267.
- [6] Lafferty J. M. *Vacuum Arcs, Theory and Application*, (Wiley, New York, 1980).
- [7] Finkelburg W. and Maecker H., *Handbuch der Physik* **22** (1956) 254-444.
- [8] Winters H. F., Coufal H., Rettner C. T. and Bethune D. S. *Phys.Rev. B* **41** (1990) 6240-6256.
- [9] Morrow R. and Lowke J. J. *J. Phys. D: Appl.Phys.* **26** (1993) 634-642.
- [10] Zhu P., Lowke J. J., Morrow R., and Haidar J., *J. Phys. D:Appl. Phys.* **28** (1995) 1369-1376.
- [11] Lowke J. J. Morrow R. and Haidar J. *J. Phys. D:Appl. Phys.* accepted for publication.
- [12] Cobine J. (1958). *Gaseous Conductors*, (Dover, New York, 1958).
- [13] Hinno E and Hirschberg J. G. *Phys. Rev.* **125** (1962) 795-801.
- [14] Mitchner M. and Kruger C. H. Jr. *Partially Ionized Gases* (Wiley, New York, 1973).
- [15] Biberman L. M., Vorob'ev V. S. and Yakubov I. T. *Soviet Physics Uspekhi* **15** (1973) 375-394.
- [16] Hoffert M. and Lien H. *Phys. Fluids* **10** (1967) 1769-1777.
- [17] Murphy A. B. and Arundell C. J. *Plasma Chem. Plasma Processing* **14** (1994) 451-490.
- [18] Haddad G. N. and Farmer A. J. D., *J. Phys.D:Appl. Phys.* **17** (1984) 1189-1196.
- [19] Haidar J. and Farmer A. J. D., *Rev. Sci. Instrum.* **64** (1993) 542-547.
- [20] Dinulescu H. A. and Pfender E. *J.Appl.Phys.* **51** (1980) 3149-3157.
- [21] Nestor O. H. *J. Appl. Phys.* **33** (1962) 1638-1648.
- [22] Coulombe S. and Meunier J. L. *J. Phys.D:Appl. Phys.* **30** (1997) 776-780.
- [23] Zhou X. and Heberlein, J. *Plasma Sources Sc. Technol.* **3** (1994) 564-574.
- [24] Benilov M. S. and A. Marotta A. *J. Phys.D:Appl. Phys.* **28** (1995) 1869-1882.
- [25] Zapesochnyi I. P., Imre A. I., Dashchenko A. I., Vukstich V. S., Danch F. F., and Kel'man V. A. *Soviet Physics JETP* **36** (1973) 1056-1060.
- [26] Ditchburn R. W. *J. Quant. Spectrosc. Radiative Transfer* **2** (1962) 361-368.
- [27] Boulous M. I., Fauchais, P. and Pfender, E. *Thermal Plasmas: Fundamentals and Applications* (Plenum Press, New York, 1994).
- [28] Haidar J. and Farmer A. J. D. *J. Phys. D:Appl. Phys.* **27** (1994) 555-560.
- [29] Hoojmans J. W. *Hydrogen absorption in iron and steel during gas tungsten arc welding*, Thesis, Delft University of Technology, Delft, (1994).
- [30] Lowke J. J., Morrow R., Haidar J. and Murphy A. B. *IEEE Trans. Plasma Science*. Accepted for publication.
- [31] Lancaster, J. F., *The Physics of Welding*, (Pergamon Press, London, 1984), p 234.
- [32] Haidar J. and Lowke J. J. *J. Phys.D:Appl. Phys.* **29** (1996) 2951-2960 and *J. High Temp. Chem. Process.* Accepted for publication.
- [33] Starling S. G. and Woodall A. J., *Physics*, (Longmans, London, 1958), p104.
- [34] Maecker H., *Z. Phys.* **141** (1955) 198-216.
- [35] Lesnewitch A., *Welding Journal*, **37** (1958) 418s-425s.
- [36] Rhee R. and Kannatey-Asibu E., *Welding Journal*, **70** (1992) 381s-386s.
- [37] Simpson S. I., Zhu P., and Rados M., *Proc. 42nd National Welding Conference, Welding Technology Inst. Australia, Melbourne*, **2** (1994) p. 31.1.
- [38] Smith A. A. and Poley J. G. *British Welding Journal*, **6** (1959) 565-568.
- [39] Brandes E. A., *Smithell's Metals Reference Book*, 6th Edition, (Butterworths, London, 1983).
- [40] Lowke J. J., *Australasian Welding Journal*, **42** (1997) 1, 32-35.
- [41] Haidar J. and Lowke J. J. *IEEE Trans. Plasma Science*. Accepted for publication.

## High-Frequency Magnetoplasmas in Electronegative Gases

J. Margot, M. Chaker\*, L. St-Onge\*\*, M. Tabbal\*, A. Aliouchouche\*, O. Pauna\*\*\*, C. Alinot\* and C. Kliagine

*Groupe de Physique des Plasmas, Université de Montréal, C.P. 6128, Succ. Centre Ville, Montréal, Québec, H3C 3J7, Canada*

*\* INRS-Énergie et Matériaux, 1650 boulevard Lionel Boulet, Varennes, Québec, J3X 1S2, Canada*

*\*\* Institut des Matériaux Industriels, National Research Council, 75 boulevard de Mortagne, Boucherville, Québec, J4B 6Y4, Canada*

*\*\*\* Université de Montréal and CPAT, Université Paul Sabatier, 118 route de Narbonne, 31062 Toulouse, France*

**Abstract.** Discharges in electronegative gases are routinely used for the sub-micron etching of thin films in the microelectronics industry. Because of the strong electronegative character of these gases, negative ions constitute a significant fraction of the charged particles content of the discharge. The presence of these negative charge carriers affects the whole behavior of the discharge and, in particular, its electron power balance. This article compares a few characteristics of a high-density plasma produced either in  $\text{SF}_6$  or in  $\text{Cl}_2$  with those of an argon plasma under similar experimental conditions. We show that the plasma presents characteristics when the gas is electronegative that significantly differ from those observed in argon.

### 1. INTRODUCTION

The last decade has seen the development of high-density plasma sources aimed at improving the performances of sub-micron etching in the microelectronics industry [1,2]. These reactors operate at very low pressure yielding rather high ion-to-neutral flux ratios, and they allow an independent control of the energy of the ions impinging on the substrate surface. These features are expected to circumvent the limitations of RF capacitive discharges when highly anisotropic sub-micron etching is required. Such high-density plasma sources are thus operated in fluorinated and chlorinated gases such as  $\text{BCl}_3$ ,  $\text{SF}_6$  or  $\text{Cl}_2$ . These highly electronegative gases are chosen for their ability to produce atoms and radicals that chemically react with various microelectronics materials thus enhancing their etch rate as compared with pure ion bombardment. However, the high electronegativity and consequently the strong electron affinity of these gases also result in large concentrations of negative ions in the plasma. In general, negative ions do not play a direct role in the etching process since they are repelled by the sheath potential which develops on the substrate surface. However, their presence greatly influences the discharge behavior. For example, the creation of these negatively charged species lowers the total production of electrons so that, for the same amount of absorbed power, these discharges are usually poorer than electropositive plasmas (e.g. argon) in terms of electron population. The presence of negative ions also has an impact on the charged particles transport. For example, the value of the effective diffusion coefficient strongly depends on their concentration. Finally, the value of the sheath potential significantly is significantly decreased by the presence of negative ions in the discharge.

While the production of neutral atoms and radicals in high density plasmas is relatively well documented in the literature, it is not the case with the charged particles content of the discharge. This is because most studies report the charged particles concentration and distributions in rare gases like argon. Then, these studies are often incorrectly extrapolated to reactive gases for optimizing the reactor design and performances (unless the optimization is performed by a trial-and-error method). The presence of negative ions in the reactive plasmas used for etching has been known for long time, but they remain the least studied species in such discharges. This is particularly true for discharges in very low pressure conditions (10 mtorr or less). Indeed, reactive gases possess a complex chemistry as they lead to the formation in the plasma volume of many fragments such as radicals, atoms and ions hence complicating their experimental investigation and modeling.

The lack of exhaustive experimental investigations of high-density plasmas in electronegative gases has prompted us to undertake the characterization of a microwave-excited magnetoplasma designed for the etching of thin films. Started a few years ago, this work was initially carried out using  $\text{SF}_6$  gas at a wave frequency of 2.45 GHz and led to the successful sub-quarter micron etching of tungsten thin films [3,4,5]. However, because of the great difficulty in modeling  $\text{SF}_6$  discharges, we came to the conclusion that the use of a simpler gas (i.e. where the number of species is limited and the reaction rates are known with better accuracy) would be more suitable for the development of a model describing the physics and chemistry of the plasma as well as its interaction with the substrate surface. This has led us to investigate the properties of chlorine plasmas which are relevant for etching of many materials but possess a simpler chemistry than  $\text{SF}_6$ ; for example, in a first approximation, the sole species to be considered in the gas phase are  $\text{Cl}_2$ ,  $\text{Cl}$ ,  $\text{Cl}_2^+$ ,  $\text{Cl}^+$ , and  $\text{Cl}^-$ . Furthermore, taking advantage of the flexibility of surface-wave plasmas, we also decided to operate at a lower frequency, namely 200 MHz. This frequency allows a larger latitude in plasma operation: very stable and reproducible plasmas can be obtained over a large range of magnetic fields (0-1 kG) even at very low pressure. This is in contrast with operation at 2.45 GHz where easy ignition and good plasma stability require the magnetic field being close to Electron Cyclotron Resonance (ECR) conditions (i.e. at 875 gauss). It is thus possible to study the influence of the magnetic field on the plasma characteristics, a feature which can give some insight in the differences observed between various high-density plasmas (e.g. ECR and helicon).

In this article, we study some of the characteristics of magnetized high-frequency discharges operated in electronegative gases of interest for etching of thin films, namely  $\text{SF}_6$  and  $\text{Cl}_2$ . We emphasize the quantitative differences of several plasma parameters such as the neutral atom concentration, the positive and negative ion densities, and the electron power balance, using Ar as a reference gas in some cases. In Sec. 2, we present the experimental setup used for the experiments. Section 3 is devoted to the presentation of neutral atom concentrations while Sec. 4 concerns the positive ion density. In Sec. 5, we examine the negative ion content of the plasma and in Sec. 6, we determine the electron density and the electron power balance of the discharge to finally conclude in Sec. 7.

## 2. EXPERIMENTAL SETUP

The plasma used is based on the propagation of pseudo-surface waves [6] and was described in various publications [3-7]. The experimental setup is shown schematically in Fig. 1. The discharge is ignited in a 6''-diameter fused silica tube connected to a 11''-diameter stainless-steel chamber in which the plasma penetrates. Both in the source region and in the downstream chamber, the plasma is subjected to the action of an axial magnetic field of high axial and radial uniformity.

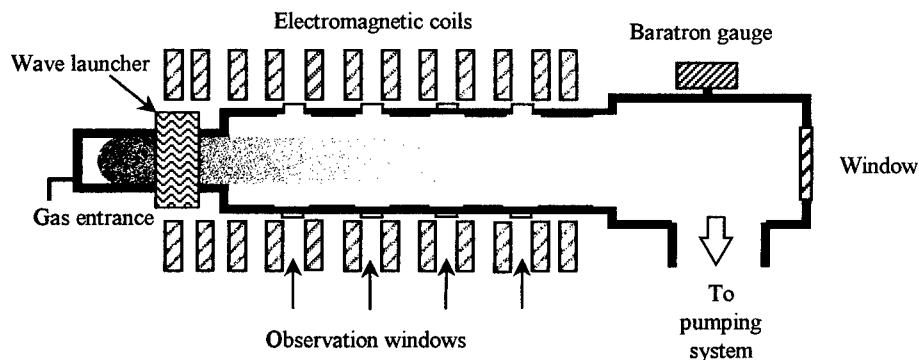


Figure 1: Schematic drawing of the plasma reactor

Two gases ( $\text{SF}_6$  and  $\text{Cl}_2$ ) were investigated. The  $\text{SF}_6$  plasma was produced at 2.45 GHz using a modified waveguide-surfatron [8] as a wave launcher while the chlorine plasma was generated at 200



MHz, using a Ro-Box [9]. At 2.45 GHz, the magnetic field was set close to the ECR condition, i.e. 875 gauss, which allows for  $\text{SF}_6$  plasma a much easier breakdown and a better plasma stability. At 200 MHz, the intensity of the magnetic field can be changed continuously from 0 to about 1 kgauss without significantly affecting either the ignition of the discharge or its stability. The range of pressures investigated is typically 0.1-10 mtorr, i.e. a domain pertinent for etching studies in magnetoplasmas.

The diagnostics used for plasma investigation were electrostatic probes, ion acoustic waves, laser photodetachment, and emission spectroscopy (in particular actinometry). The validity and application of most these diagnostic techniques to our experimental conditions are described in other publications [5,7,10,11,12]. A brief description of the various diagnostic techniques used in our studies are provided in the following sections.

### 3. FLUORINE AND CHLORINE ATOM DENSITY

Actinometry was performed for determining the relative F and Cl atom density in  $\text{SF}_6$  and  $\text{Cl}_2$  respectively, using argon as actinometer gas in a proportion varying between 2.5 and 5 % of the total gas pressure. This technique [13,14,15] allows in a simple way to determine the relative concentration of ground state species which cannot easily be measured by other techniques. It has been shown to provide reliable results for determining the dependence of the fluorine atom concentration upon plasma conditions [15]. In the case of fluorine, we used the lines F I 703.7 nm and Ar I 750.4 nm. In chlorine, two different Cl lines were examined (Cl I 808 nm and Cl I 837.6 nm) while the chosen argon line was Ar I 811.5 nm. In the specific case of chlorine, the actinometry technique can also be applied to the determination of the absolute density of molecules according to a method recently proposed by Donnelly [16]. Actinometry was then performed on molecular chlorine using 5 % xenon as actinometer by monitoring the  $\text{Cl}_2$  band at 306 nm and the Xe I line at 823.2 nm.

The pressure dependence of the concentration of F atoms in  $\text{SF}_6$  and of Cl atoms in  $\text{Cl}_2$  is shown in Figs. 2 and 3, respectively. In both cases, the magnetic field intensity was 875 gauss. As can be seen for both fluorine and chlorine, the neutral atom concentration increases with gas pressure. We note that for  $\text{SF}_6$ , the F atom density increases rapidly with pressure up to about 1 mtorr and then shows a linear increase. This is related to a higher dissociation degree below 1 mtorr, with this dissociation degree becoming constant at higher pressure [10]. For chlorine, the Cl atom density increases linearly with pressure up to 5 mtorr, the two Cl lines used yielding the same result. However at higher pressure ( $p > 5$  mtorr), we observe a slight discrepancy. This may be due to an overestimation of the Cl concentration

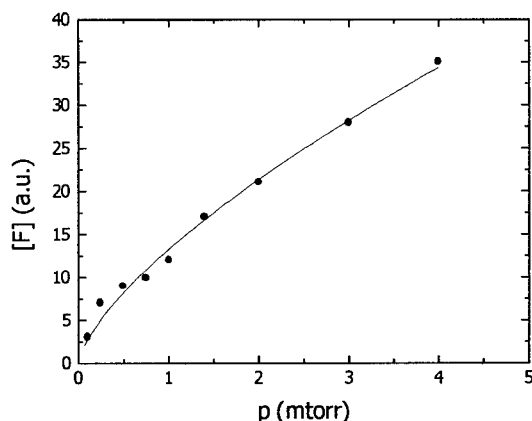


**Figure 2:** Relative concentration of F atoms in a pure  $\text{SF}_6$  plasma as a function of the initial gas pressure. The measurements were obtained for a wave frequency of 2.45 GHz, at 35 cm from the wave launcher gap. The absorbed power was 475 W and the magnetic field intensity was set to 875 gauss.

obtained from the Cl I 808 nm line. One possible explanation could be that the upper level of the transition is populated by radiative cascade from higher levels or by  $\text{Cl}_2$  dissociation (dissociative excitation).

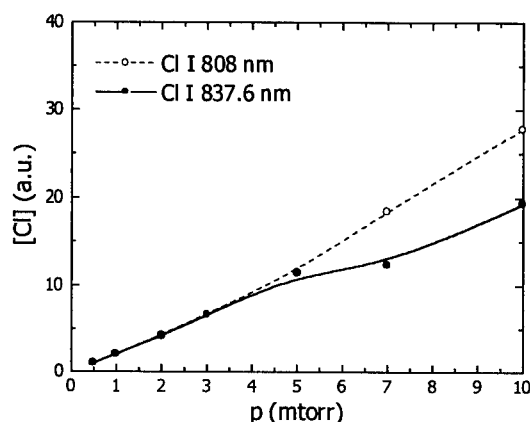


**Figure 3:** Relative concentration of Cl atoms in a pure chlorine plasma as a function of the initial gas pressure. The measurements were taken for a wave frequency of 200 MHz, at 20 cm from the wave launcher gap. The absorbed power was 270 W and the magnetic field intensity was set to 875 gauss.

In  $\text{SF}_6$ , there is no straightforward method of determining the absolute concentration of fluorine atoms. In contrast, for chlorine, as already mentioned, the absolute value of the Cl atom concentration can be determined from the actinometry measurement of the molecular chlorine density [16]. This allows in particular the determination of the dissociation degree of  $\text{Cl}_2$  molecules as a function of the experimental conditions. Such a dissociation degree measured as a function of the gas pressure for a magnetic field intensity of 875 gauss and 350 W absorbed power is shown in Fig. 4. As can be seen, it decreases linearly as gas pressure increases going from almost 90% at 0.2 mtorr down to 20% at 8 mtorr. The data obtained at p larger than 5 mtorr should however be considered with caution since we have observed a discrepancy in the results obtained from direct Cl actinometry and the indirect method from the  $\text{Cl}_2$  actinometry. We suspect that it may be due to the failure of Cl actinometry.

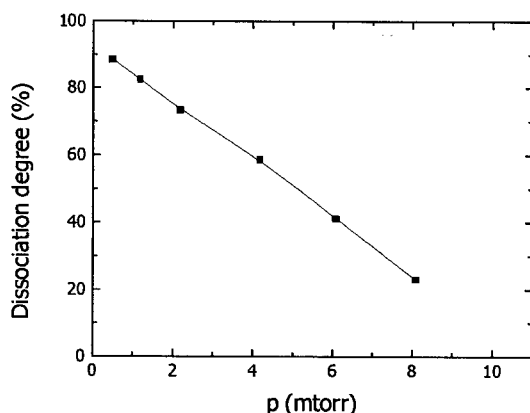


**Figure 4:** Dissociation degree of chlorine as a function of the initial gas pressure in a pure chlorine plasma. The data were obtained for a wave frequency of 200 MHz, at 20 cm from the wave launcher gap. The absorbed power was 350 W and the magnetic field intensity was set to 875 gauss.

#### 4. POSITIVE ION DENSITY

The positive ion concentration was determined from electrostatic probe measurements. The density was calculated from the ion saturation current of the probe characteristics. The measured current was related to the positive ion density using either the Laframboise or the ABR theory (in general both theories provide similar density values). In the case of  $\text{SF}_6$  where a large number of different ions can be present, we used an average weighted mass  $M_+$  of 50 a.m.u. based on the mass spectra obtained by Petit and Pelletier in low pressure magnetoplasmas [17]. In the case of chlorine, depending on the relative concentrations of  $\text{Cl}^+$  and  $\text{Cl}_2^+$ , the average weighted mass should vary between 35.5 and 71 a.m.u.. However, we assumed that the dominant ions should be atomic chlorine ions and we considered  $M_+=35.5$ . This assumption is supported by the high dissociation degree observed in our experiment and by the model recently developed by Lymberopoulos et al. [18] for a high-density chlorine plasma. In this work, they found that  $\text{Cl}^+$  is the dominant ion even at a pressure of 10 mtorr and in the presence of a very weak magnetic field (about 50 G).

Figure 5 shows the variation of the positive ion density  $n_+$  with gas pressure in  $\text{SF}_6$  and argon. Clearly, while  $n_+$  monotonously increases with pressure in argon, it is almost constant at lower pressure in  $\text{SF}_6$  and then strongly decreases. For example, at 4 mtorr, the positive ion density is two orders of magnitude lower in  $\text{SF}_6$  than in Ar. As will be seen later, this feature is correlated to the less favorable electron power balance in electronegative gases that results from additional losses as compared to rare gases, in particular through electron attachment.

In Fig. 6, we present the positive ion density measured in chlorine under the same magnetic field conditions as in  $\text{SF}_6$  (875 gauss). The pressure dependence of the positive ion density is similar to that observed in  $\text{SF}_6$ , i.e. an almost constant density at lower pressure and then a decrease. Combining these results with those presented in the previous section, and considering that the ions ( $\text{Cl}^+$ ) strike the substrate surface with a typical 20 eV energy while the neutrals (Cl) have only 0.025 eV, one can calculate that at 1 mtorr, the ion-to-neutral flux ratio is about 5% for an absorbed power of 270 W. In addition, taking advantage of the flexibility of the 200 MHz plasma in terms of magnetic field intensity, we have studied the dependence of the ion density on this parameter. We found that for an absorbed power of 270 W and a gas pressure of 0.5 mtorr, the positive ion density increases rapidly up to 200 gauss (by about a factor of 5) and then increases more slowly (a factor of 2 from 200 to 900 gauss).

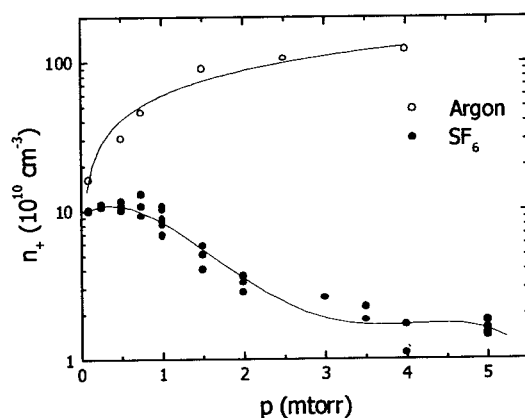


**Figure 5:** Variation with initial gas pressure of the positive ion density at the plasma axis in pure  $\text{SF}_6$  and pure argon. The data were obtained at a wave frequency of 2.45 GHz, at 35 cm from the wave launcher gap. The absorbed power was 475 W and the magnetic field intensity was set to 875 gauss and 950 gauss for  $\text{SF}_6$  and Ar, respectively.

The electron temperature  $T_e$  was also derived from probe measurements for  $\text{SF}_6$ ,  $\text{Cl}_2$  and Ar. We found that  $T_e$  was decreasing with increasing pressure for  $\text{SF}_6$  (typically from 4.5 to 3 eV between 0.25 and 5 mtorr) and Ar (from 4 to 2.5 eV between .1 and 4 mtorr). In the case of chlorine, this decrease was much less important (2.8 eV for  $p=0.1$  mtorr and 2.5 eV for  $p=2$  mtorr).

The data presented in Figs. 5 and 6 were analyzed by assuming that  $M_i=50$  and 35.5 a.m.u. for  $\text{SF}_6$  and  $\text{Cl}_2$  respectively. An increase by a factor of two of these masses would yield a density higher by about 40%. Despite these uncertainties, we see however that the positive ion density in chlorine is higher than in  $\text{SF}_6$  by factor of 2 to 4. These results suggest that the electron power balance is more favorable in chlorine presumably because volume losses such as electron attachment, dissociative attachment and recombination are less important.

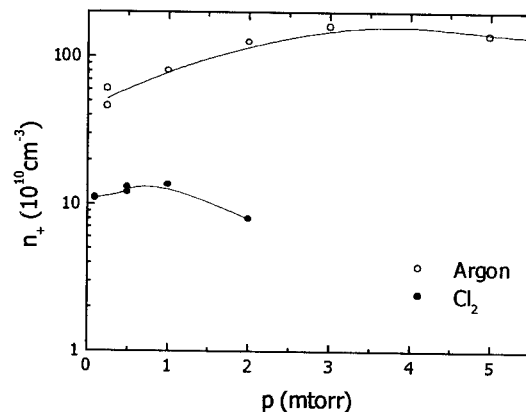


**Figure 6:** Variation with initial gas pressure of the positive ion density at the plasma axis in pure chlorine. The data were obtained for a wave frequency of 200 MHz, at 20 cm from the wave launcher gap. The absorbed power was 270 W and the magnetic field intensity was set to 875 gauss.

The results presented here clearly demonstrate that the characterization of an argon plasma cannot be simply extrapolated to electronegative gases. While in argon, the highest positive ion concentration is observed above a few mtorr, the maximum density in  $\text{SF}_6$  and  $\text{Cl}_2$  is at lower pressure. As we will show in the following section, the formation of negative ions in  $\text{SF}_6$  and  $\text{Cl}_2$  yields a discharge behavior which drastically differs from that of electropositive plasmas.

## 5. NEGATIVE ION DENSITY

Negative ion concentrations were measured using two diagnostic techniques: laser photodetachment (LPD) by means of a XeCl laser and ion acoustic waves (IAW). Laser photodetachment consists in detaching electrons from negative ions by means of a high energy laser beam. Following the detachment, an excess of electrons is present in the discharge for a few microseconds. These electrons are then detected, for example by an electrostatic probe biased in the electron saturation regime. This technique is very sensitive and its analysis rather straightforward. However, it necessitates a complex and costly experimental setup. The ion acoustic wave (IAW) diagnostic was recently proposed by St-Onge et al. [12] as a simple and cost-effective technique which allows a correct determination of the negative-to-positive ion concentration ratio provided the mass ratio of these ions and the electron temperature are known. This technique was validated in  $\text{SF}_6$  by comparison with laser photodetachment. In the case of complex gases which yield a large number of fragments like  $\text{SF}_6$ , it was found that the two methods were in good agreement above about 1 mtorr while the IAW method was underestimating the negative ion concentration at lower pressures. The cause of this discrepancy was shown to be probably due to the uncertainty on the positive ion mass used to analyze the data. In a much simpler gas like chlorine, we expect that this

uncertainty should be less important since the dominant ion should be atomic chlorine. Laser photodetachment experiments in chlorine are presently in progress in order to validate this assumption.

Figure 7 shows the variation with gas pressure of the ratio between the negative and positive ion concentration in the  $\text{SF}_6$  plasma at two different axial positions. Keeping in mind that  $n_- + n_e = n_+$ , these data, obtained from the laser photodetachment technique, clearly show that over the range of pressures investigated (0.25-5 mtorr), the majority of the negative charges are negative ions rather than electrons. For example, at a gas pressure of 4 mtorr, the negative ions constitute about 80% of the negatively charged particles even for a relatively short distance from the wave launcher gap. Even at pressures as low as 0.25 mtorr, they still are more numerous than electrons. The formation of this important population of negative ions is detrimental to the maintenance of electrons in the plasma and results as will be seen later in larger electron power losses. Figure 7 shows that the negative ion concentration is larger as the distance from the wave launcher increases. This can be explained by a larger formation rate (through electron attachment) and/or a smaller destruction rate (through ion-ion recombination or electron detachment).

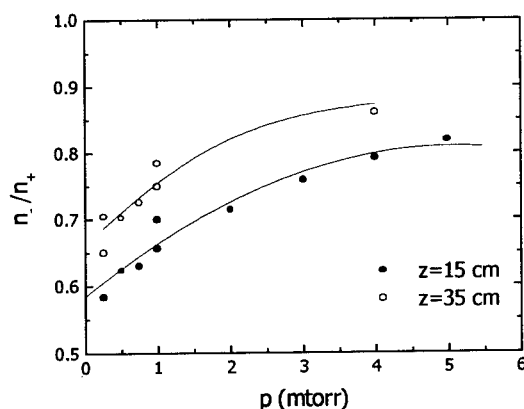


**Figure 7:** Negative-to-positive ion density ratio in  $\text{SF}_6$  as a function of the initial gas pressure at the plasma axis and for two different axial positions ( $z=15$  cm and  $z=35$  cm). The data were obtained from laser photodetachment for a wave frequency of 2.45 GHz. The absorbed power was 475 W and the magnetic field intensity was set to 875 gauss.

The formation of negative ions due to the strong electronegative character of  $\text{SF}_6$  is well illustrated when adding progressively  $\text{SF}_6$  to an argon discharge. The ratio  $n_-/n_+$  is presented in Fig. 8 as a function of the  $\text{SF}_6$  dilution in argon ( $X=[\text{SF}_6]/([\text{SF}_6]+[\text{Ar}])$ ). These results show that the negative ion percentage is almost that of a pure  $\text{SF}_6$  plasma even when argon constitutes 90% of the gas mixture.

In the case of chlorine, we observe similar tendencies, but the relative concentration of negative ions is found to be less important than in  $\text{SF}_6$ . This is because chlorine is less electronegative than  $\text{SF}_6$ . Figure 9 presents the variation of the negative-to-positive ion density ratio with gas pressure in pure chlorine as determined from ion acoustic wave measurements assuming  $\text{Cl}^+$  as the dominant positive ion. This ratio varies from about 0.18 at 0.2 mtorr to 0.3 at 2 mtorr. Over the same range of gas pressure the positive ion density varies from  $10^{11}$  to  $8 \times 10^{10} \text{ cm}^{-3}$  (see Fig. 6), yielding a negative ion concentration close to  $2 \times 10^{10} \text{ cm}^{-3}$  in both cases. In  $\text{SF}_6$ , over the same range of gas pressure, the negative ion density decreases from  $7 \times 10^{10}$  to  $3 \times 10^{10} \text{ cm}^{-3}$ , i. e. a value 2 to 4 times larger than in chlorine.

## 6. ELECTRON DENSITY AND POWER BALANCE

From the measurement of both positive and negative ion densities, one can deduce the electron density in the discharge. Figure 10 shows the variation of the electron density with gas pressure in pure  $\text{SF}_6$  and pure chlorine. We see that in both gases, it is almost independent of gas pressure up to 1 mtorr and then decreases

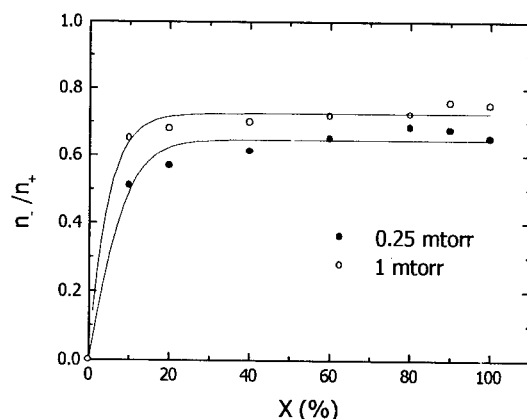


**Figure 8:** Negative-to-positive ion density ratio in  $\text{SF}_6$  at the plasma axis as a function of the partial  $\text{SF}_6$  pressure in  $\text{SF}_6/\text{argon}$  mixtures ( $X = [\text{SF}_6]/([\text{SF}_6] + [\text{Ar}])$ ). The data were obtained from laser photodetachment for a wave frequency of 2.45 GHz, at 35 cm from the wave launcher gap. The absorbed power was 475 W and the magnetic field intensity was set to 875 gauss.

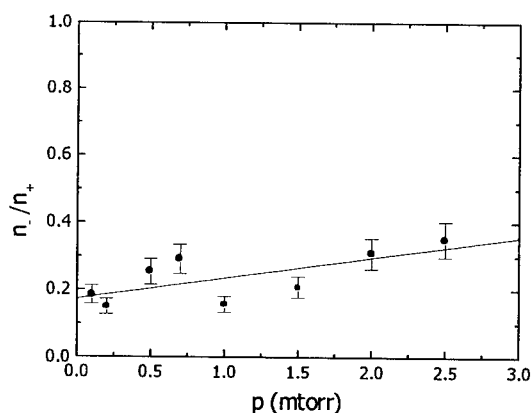


**Figure 9:** Negative-to-positive ion density ratio at the plasma axis as a function of the initial gas pressure in pure chlorine. The data were obtained at 200 MHz from ion acoustic wave measurements at 35 cm from the wave launcher gap. The absorbed power was 270 W and the magnetic field intensity was set to 875 gauss.

rapidly. The electron density determined in the electronegative gases reaches a maximum value of  $(5-10) \times 10^{10} \text{ cm}^{-3}$  at about 0.5 mtorr, a value ten to twenty times lower than the maximum electron density achieved in argon (see Figs. 5 and 6). This considerable depletion of the electron population essentially results from the electronegative character of  $\text{SF}_6$  and  $\text{Cl}_2$ .

From the electron density measurement we can easily calculate the power lost (or equivalently absorbed) per electron,  $\theta$ , which represents the power dissipated on the average to maintain an electron in the plasma. Introduced for the first time by Glaude et al. [19], this parameter plays a major role in the characterization of high-frequency discharges. It is given by the ratio between the total power absorbed by the plasma and the total number of electrons in the discharge. To estimate  $\theta$  from our local electron density measurements in  $\text{SF}_6$  and  $\text{Cl}_2$ , we have assumed that the electron density was almost constant over a diameter corresponding to the source dimension (6'') and all along the plasma reactor and that it was zero elsewhere. A more accurate determination of  $\theta$  would obviously require a complete mapping of the

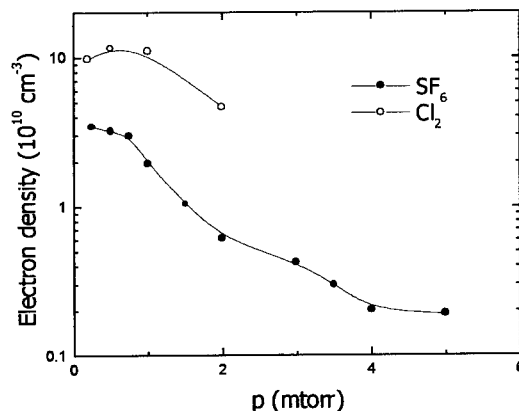


**Figure 10:** Electron density at the plasma axis as a function of the initial gas pressure in pure  $\text{SF}_6$  and pure chlorine. For  $\text{SF}_6$ , the data were obtained for a wave frequency of 2.45 GHz and an absorbed power of 475 W. In chlorine, the wave frequency was 200 MHz and the absorbed power 270 W. In both cases, the magnetic field intensity was set 875 gauss and the distance to the wave launcher gap to 35 cm.

spatial distribution of the electron density in the reactor. Figure 11 shows the value of  $\theta$  normalized to the gas pressure when the plasma is produced in Ar,  $\text{SF}_6$  and  $\text{Cl}_2$ . One notes that in the case of  $\text{SF}_6$ ,  $\theta/p$  is always larger than in the two other gases (up to one order of magnitude). In addition, its value is only weakly dependent on the gas pressure. In contrast, Ar yields  $\theta/p$  values which strongly decrease as  $p$  increases. The decrease of  $\theta/p$  with increasing gas pressure observed in argon is typical of a diffusion-controlled plasma [20]. Under such conditions, it can be shown that the electron temperature decreases as  $p$  increases thus inducing a decrease of  $\theta/p$ . Chlorine possesses an intermediate character, since the value of  $\theta/p$  is very close to that measured in argon at lower pressure while it is substantially larger at higher pressure. The differences observed between the two electronegative gases investigated can be explained by the fact that in  $\text{SF}_6$ , the electron energy is spent in the large number of  $\text{SF}_6$  fragmentation reactions and that electrons are more subject to attachment than in chlorine, thus enhancing the energy losses.

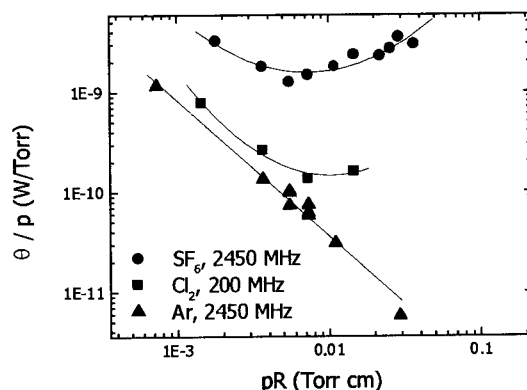


**Figure 11:** Power absorbed per electron normalized to the initial gas pressure as a function of gas pressure times plasma radius in argon, pure  $\text{SF}_6$  and pure chlorine. In  $\text{SF}_6$  and Ar, the wave frequency was 2.45 GHz while in  $\text{Cl}_2$  it was 200 MHz. The magnetic field intensity was set to 875 gauss for  $\text{Cl}_2$  and  $\text{SF}_6$  and 950 gauss for Ar.

## 7. CONCLUSION

In this article, we have compared the characteristics of two electronegative gases of interest for the sub-micron etching of thin films, namely  $\text{SF}_6$  and  $\text{Cl}_2$ . We have determined the dependence of the fluorine and chlorine atom concentration on the gas pressure in these two gases and shown that it increases almost linearly with pressure for  $p$  less than a few mtorr. We have also shown that in chlorine the dissociation degree can be as high as 90% at low pressure and large magnetic field intensity. In both  $\text{SF}_6$  and  $\text{Cl}_2$ , the positive ion density is comparable to that of argon only for pressures below 1 mtorr. Above this pressure, it decreases significantly for electronegative gases while it further increases for argon. Experiments have shown that the negative ion content of the  $\text{SF}_6$  and  $\text{Cl}_2$  plasmas is quite significant. For  $\text{SF}_6$ , the negative ion density was found to be higher than the electron density even at very low pressure (0.25 mtorr). In the case of chlorine, the negative ion density is lower than in  $\text{SF}_6$  but still far from being negligible. From positive and negative ion density measurements, we were able to determine the electron density which was found to decrease as the gas pressure increases for  $p > 1$  mtorr. This behavior is similar to that of the positive ion density but the values of the electron density of  $\text{SF}_6$  and  $\text{Cl}_2$  are 10 to 20 times lower than in argon for a gas pressure of only 5 mtorr. Finally, we have demonstrated that the lower positive ion and electron density observed in electronegative gases results from a much less favorable electron power balance and is related to additional charged particles losses through attachment.

## Acknowledgments

The authors are grateful to R. Grenier, R. Lemay, R. Martel, F. Roy and C. Sirois for their exceptional technical support. They also would like to thank the Natural Sciences and Engineering Research Council of Canada (NSERC) and the Network of Centers of Excellence in Microelectronics (MICRONET) for their financial support.

## References

- [1] Popov O.A., *High Density Plasma Sources: Design, Physics and Performances* (Noyes Publications, N.J., USA, 1995)
- [2] Lieberman M.A. and Gottscho R.A., "Design of High-Density Plasma Sources for Materials Processing", *Plasma Sources for Thin Film Deposition and Etching, Physics of Thin Films* vol. 18, M.H. Francombe and J.L. Vossen Eds. (Academic Press, N.Y., 1994).
- [3] Bounasri F., Gat E., Chaker M., Moisan M., Margot J. and Ravet M.F., *J. Appl. Phys.* **78** (1995) 6780-6783.
- [4] Gat E., Bounasri F., Chaker M., Ravet M.F., Moisan M. and Margot J., *Microelec. Eng.* **30** (1996) 337-340.
- [5] Margot J., Chaker M., Moisan M., St-Onge L., Bounasri F., Dallaire A and Gat E., "Magnetized surface-wave discharges for submicrometer pattern transfer", *Plasma Processing of Semiconductors*, NATO ASI, Series E: Appl. Sciences, vol. 336 (Kluwer 1997) pp. 491-513.
- [6] Margot J., "Etching of thin films using magnetised plasmas", 3<sup>rd</sup> International Workshop on Microwave Discharges: Fundamentals and Applications, Abbaye Royale de Fontevraud 20-25 April, 1997; in press (Les Éditions de Physique, Les Ulis, 1997).
- [7] Bounasri F., Moisan M., St-Onge L., Margot J., Chaker M., El Khakani M.A. and Gat E., *J. Appl. Phys.* **77** (1995) 4030-4038.
- [8] Moisan M., Chaker M., Zakrzewski Z. and Paraszczak J., *J. Phys. E: Sci Instrum.* **26** (1987) 1356-1361.
- [9] Moisan M. and Zakrzewski Z., *Rev. Sci Instrum.* **58** (1987) 1895-1904.
- [10] St-Onge L., "Physico-chimie d'un magnétoplasma de  $\text{SF}_6$ ", Ph.D thesis, Université de Montréal (1996).



- [11] St-Onge L., Margot J. and Chaker M., "Experimental investigation of a large volume SF<sub>6</sub> magnetoplasma based on surface-wave propagation, submitted to Plasma Sources Sci. Technol. (October 1997).
- [12] St-Onge L., Margot J. and Chaker M., "Characterization of the negative ion fraction in SF<sub>6</sub> and SF<sub>6</sub>/Ar magnetoplasmas using ion acoustic waves", submitted to Appl. Phys. Lett. (July 1997).
- [13] Coburn J.W. and Chen M., J. Appl. Phys. **51** (1980) 3134-3136.
- [14] d'Agostino R., Cramarossa F., De Benedictis S. and Ferraro G., J. Appl. Phys. **52** (1981) 1259-1265.
- [15] Donnelly V. M., Flamm D.I., Dautremont-Smith W.C. and Werder D.J., J. Appl. Phys. **55** (1984) 242-252.
- [16] Donnelly V.M., J. Vac. Sci. Technol. **14** (1996) 1076-1087.
- [17] Petit B. and Pelletier J., Jpn. J. Appl. Phys. **26** (1987) 825-834.
- [18] Lymberopoulos D.P. and Economou D.J., IEEE Trans. Plasma Sci. **23** (1995) 573-590.
- [19] Glaude V.M.M., Moisan M., Pantel R., Leprince P. and Marec J., J. Appl. Phys. **51** (1980) 5693-5698.
- [20] Pérès I. and Margot J., Plasma Sources Sci Technol. **5** (1996) 653-661.

## Laboratory Observations of Wave-Induced Radial Transport within an "Artificial Radiation Belt"

M.E. Mauel

*Department of Applied Physics, Columbia University, New York, NY 10027, U.S.A.*

**Abstract.** Wave-induced radial transport of energetic electrons has been observed in a laboratory terrella. In the experiment, electron-cyclotron-resonance heating (ECRH) is used to create a localized population of trapped energetic electrons ( $1 \text{ keV} < E_h < 50 \text{ keV}$ ) within a low-density discharge which we refer to as an "artificial radiation belt." As the intensity of the radiation belt increases, quasiperiodic bursts of drift-resonant fluctuations,  $\omega \simeq \omega_{dh}$ , are excited. The frequency spectrum of this instability is time-varying and complex, and global chaotic radial transport is induced whenever the frequency spectrum is both intense and compact. High-speed measurements of the energetic electron transport are made with particle detectors, and these measurements can be directly compared with nonlinear and self-consistent simulations. We find quasilinear transport simulations do not reproduce the experimental measurements. In contrast, simulations which retain the electron's guiding-center Hamiltonian dynamics and which preserve the first,  $\mu$ , and second,  $J$ , adiabatic invariants reproduce key temporal characteristics of the experimental measurements. The resemblance between simulation and experiment suggests that persistent phase-space structures strongly modulate the energetic electron transport and contribute to the growth and saturation of the instability.

### 1 INTRODUCTION

Since the early years of space exploration, models of fluctuation-induced radial transport of energetic particles trapped in dipolar magnetic fields have been used to describe the evolution of the planetary radiation belts [1]. When nonaxisymmetric fluctuations of geomagnetic [2] or electric [3] fields resonant with the magnetic drifts of trapped particles, the third adiabatic invariant,  $\psi$ , can become time-varying. Drift-resonant fluctuations mix the inner and outer regions of resonant particle distributions. In certain instances, the time-variation of  $\psi$  may become stochastic [4]. Drift-resonant transport has been used to explain the profiles of the inner radiation belt [5], the injection of energetic particles during magnetic storms and substorms [6], and the radial transport coefficients of the magnetospheric ring current [7]. When combined with other, higher-frequency wave-particle interactions in the Earth's magnetosphere, the inward and outward radial transport of energetic electrons, or adiabatic "recirculation" [8], may explain the flux intensification of very energetic electrons ( $E > 1 \text{ MeV}$ ) at geosynchronous orbit thought to result in the failure of electronic components on spacecraft [9].

For strongly-magnetized particles within a dipole, the radial transport induced by low frequency fluctuations also provides an opportunity for detailed study of wave-particle interactions within a plasma. When the ratio of the gyroradius,  $\rho$ , to the equatorial radius of the particle's field line,  $L$ , is small,  $\rho/L \ll 0.1$ , the particle's three characteristic frequencies of motion, the cyclotron,  $\omega_c$ , the bounce,  $\omega_b$ , and the drift,  $\omega_d$  frequency, separate [10]. Wave-particle interactions with low-frequency drift-resonant waves,  $\omega \sim \omega_d \ll \omega_b \ll \omega_c$ , preserve the first two adiabatic invariants [11] even when combinations of these waves create chaotic evolution of the third adiabatic invariant [12]. When collisionless energetic particles interact with low-frequency waves which preserve  $\mu$  and  $J$ , their time-evolution can be described by a one-dimensional Vlasov fluid. Furthermore, when the particles are confined by a magnetic dipole, the relevant Hamiltonian phase-space is directly and easily observable. The canonical action is the magnetic flux,  $\psi \sim 1/L$ , and the conjugate coordinate is the azimuthal angle,  $\varphi$ .

Previously, we reported the first observations of wave-induced chaotic radial transport in a laboratory terrella, the Collisionless Terrella Experiment (CTX) [13, 14]. The primary goal of CTX is to provide a laboratory test of guiding-center Hamiltonian methods used to predict and understand collisionless radial transport induced by low-frequency fluctuations in dipole-confined plasmas. By investigating the correlations between the observed transport and fluctuation spectrum and by comparing these correlations with guiding-center simulations, we see that strong radial transport only occurs when the amplitude, frequency, and azimuthal mode number of the fluctuations meet the conditions for global chaos [14]. Greatly diminished transport is observed when the fluctuations lead to thin, radially-localized bands of chaos.

Although the presence or absence of strong radial transport can be determined by evaluating global conditions for phase-space chaos, the temporal features of the observed flux can not. We find the flux to be strongly modulated in time ( $\approx 100\%$ ) near the drift frequency of the energetic electrons,  $\omega_{dh}$ . These modulations are related (but not equivalent) to the “drift-echoes” observed by satellites following magnetic storms and substorms [15, 16]. In CTX, the temporal modulations of the energetic electron flux can be reproduced by computing the induced Hamiltonian phase-space flows as a function of time beginning with an initially axisymmetric electron distribution. The simulations show the modulations are due to circulating phase-space structures generated by resonant wave-particle interactions which are detected at a fixed location in the laboratory frame of reference.

In this paper, we present a more detailed interpretation of both the nonlinear growth and saturation of the low-frequency drift-resonant instabilities observed in CTX and the self-consistent dynamics of the energetic electrons. This description is both complete and relatively simple because (1) the low-frequency, electrostatic instabilities are flute-like, (2) the geometry of a dipole magnetic field is relatively simple to characterize, and (3) the dynamics of the energetic electrons are one-dimensional. We introduce a fully self-consistent, nonlinear model for the evolution of a quasineutral plasma consisting of cold ions and a mixture of hot and cold electrons confined by a dipole magnetic field. Representative numerical solutions are presented and compared with experimental observations.

We believe it highly significant that the nonlinear model reproduces the frequency sweeping observed experimentally. Examination of the Hamiltonian phase-space flows of the energetic electrons during the nonlinear saturation of the instability suggests that the rising tones seen experimentally are due to the inward propagation of “phase-space holes.” The creation and dynamical evolution of phase-space structures including “holes” may be essential to the nonlinear saturation of certain instabilities [17, 18] and of drift-turbulence [19]. For the experiments described in this paper, both the observations and the numerical simulations appear to be explained by a generalized nonlinear theory recently developed by Berk and co-workers [20, 21]. In this theory, the growth and nonlinear saturation of collisionless resonant particle instabilities are dominated by three competing processes: (1) linear growth of the instability due to resonant particle effects,  $\gamma_L$ , (2) linear dissipation due to nonresonant effects,  $\gamma_d$ , and (3) nonlinear effects represented by the wave-particle trapping frequency,  $\omega_{tr} \propto \sqrt{\Phi}$ , where  $\Phi$  is the fluctuating potential of the instability. For strongly unstable plasmas,  $\gamma_L \gg \gamma_d$ , instabilities grow rapidly and saturate when the linear growth rate is balanced by nonlinear trapping,  $\omega_{tr} \sim \gamma_L$  [22]. On the other hand, for weakly unstable plasmas,  $\gamma_L \sim \gamma_d$ , nonlinear effects quickly overcome linear effects, and waves with both rising and falling frequencies are generated as the instability grows rapidly and nonlinearly to a large collective amplitude,  $\omega_{tr} \sim \gamma_L$ . At saturation, the wave frequencies continue to change as energy nonlinearly extracted from the resonant particles is balanced by nonresonant dissipation. Berk and co-workers suggest frequency sweeping to be a general nonlinear wave-particle effect. They note frequency sweeping has been observed experimentally during the saturated stages of several instabilities found in magnetized plasmas driven by energetic resonant particles. “Fishbone” instabilities [23] and toroidal Alfvén eigenmodes [24] excited by energetic ions in tokamaks are examples of drift-resonant magnetostatic instabilities where frequency sweeping occurs.

This paper is organized into five additional sections. Section 2 presents a brief description of the experimental device, diagnostics, and method used to produce an “artificial radiation belt” using microwave heating. Observations of the drift-resonant fluctuations using multiple electrostatic probes are summarized in Section 3. In Section 4, we introduce a self-consistent nonlinear model of the hot electron interchange instability (or HEI) [25] in the magnetic coordinates appropriate to an idealized dipole field. In Section 5, example solutions to the linearized and fully nonlinear descriptions of the HEI are presented. The nonlinear simulations illustrate frequency sweeping, and the computed phase-space flows of the energetic electrons clearly illustrate the inward propagation of “holes.” At a prescribed nonresonant dissipation, these phase-

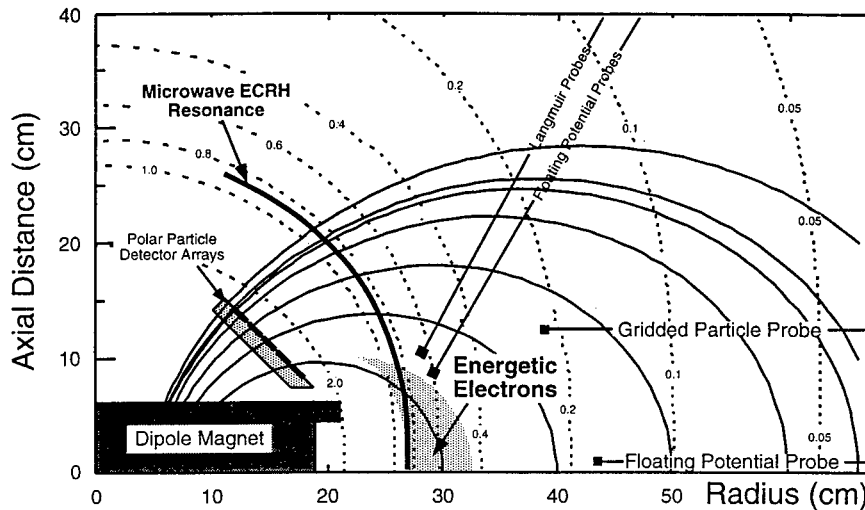


Figure 1: The magnetic field geometry of CTX. Solid lines represent magnetic field lines, and the dotted lines correspond to surfaces of constant magnetic field strength. The location of the fundamental microwave cyclotron resonance, the “artificial radiation belt”, and some key diagnostics are shown.

space holes extract energetic electron energy (by causing an outward expansion of energetic electrons) while maintaining nearly constant wave amplitude. The temporal features of the energetic particle flux computed by the simulation resemble those observed experimentally. Finally, in Section 6, we summarize key conclusions and suggest new opportunities for further investigations of the nonlinear evolution of resonant particle instabilities both in the laboratory and in space.

## 2 PRODUCTION OF AN “ARTIFICIAL RADIATION BELT”

The goal and purpose of the Collisionless Terrella Experiment (CTX) is to study the basic dynamical plasma processes which lead to collisionless radial transport of energetic particles. This is accomplished by creating an “artificial radiation belt” consisting of a population of energetic, deeply-trapped electrons as a result of cyclotron resonance absorption of microwaves within a low-density discharge.

The collisionless plasma dynamics within CTX differ from those observed in axisymmetric terrella built by Birkeland [26, 27] and Il'in and Il'ina [28]. Birkeland's terrella were used to study untrapped charged-particle orbits such as those followed by cosmic rays near Earth. For untrapped, very high energy particles, the normalized gyroradius satisfies the condition  $\rho/L > 0.3$ . Il'in and Il'ina demonstrated the Dragt condition for adiabaticity (*i.e.* the conservation of  $\mu$ ) [29], and, in their device,  $\rho/L \leq 0.1$ . In CTX,  $\rho/L \sim 0.01$ . At this normalized energy, the energetic particles in CTX are strongly trapped, adiabatic, and characterized by well-separated cyclotron, bounce, and drift frequencies.

Although the energetic electrons produced in CTX are referred to as a “radiation belt,” the plasmas created within CTX do not simulate planetary magnetospheres. This is because the effects of electron-plasma and electron-neutral collisions have been minimized by decreasing the plasma density and increasing the magnetic field. Although electrons are energetic,  $1 \text{ keV} < E_h \leq 20 \text{ keV}$ , the total plasma beta is low,  $\beta \simeq 1\%$ . The low plasma density allows the energetic electrons to execute thousands of drift-orbits within a collision time,  $\omega_{dh}\tau_{col} \sim 10^4$ , but the first Alfvén field line resonance occurs at high-frequency, near  $V_A/L \sim 50 \text{ MHz} \gg \omega_{dh} \sim 1 \text{ MHz}$ . In the laboratory, low-frequency drift-resonant fluctuations are electrostatic; whereas, in the Earth's magnetosphere they are Alfvénic.

Plasma is created in CTX using a 2.45 GHz 1 kW microwave power source illuminating a high-field water-cooled electromagnet suspended mechanically in an axisymmetric vacuum chamber approximately 140 cm in diameter. The magnet is surrounded by a stainless steel enclosure electrically grounded to the vacuum chamber. The magnetic field strength reaches 15 kG at the pole faces and falls to 50 G at the outer

vacuum vessel wall. As shown in Figure 1, the fundamental microwave cyclotron resonance,  $B_0 \equiv B \simeq 875$  G, intersects nearly all flux surfaces of the dipole magnet, but only electrons which mirror near  $L_0 \equiv L \simeq 30$  cm absorb microwave energy continuously and reach high energy. Although the CTX device is capable of long pulse discharges, the microwave discharges are usually pulsed for periods slightly less than one second which corresponds to peak x-ray emission.

The energetic electrons are measured with a krypton proportional counter viewing the equatorial mid-plane of the terrella and several XUV diodes and photodiodes viewing cords parallel to the dipole axis but at different radial positions. At one of the poles, arrays of biased Faraday cups, localized net current detectors, and gridded particle analyzers are used to monitor the azimuthal and radial evolution of plasma and electron profiles [30]. Langmuir probes are able to measure the density and temperature of the cooler plasma at all locations except at those occupied by the most intense energetic electrons.

The intensity of the energetic electron population is characterized by the hard x-ray emission produced by electron-ion and electron-neutral bremsstrahlung. Pulse-height analysis of the x-rays detected with the proportional counter show the distribution of energetic electrons to be non-Maxwellian, a characteristic of microwave-heated mirror-trapped electrons [31]. The electrons with energies between 1–10 keV are often referred to as the “warm” population and those electrons with energies above 10 keV are called “hot”. When the microwave power is switched off, the “hot” population persists for 5–20 ms, defining a relatively long “afterglow.” By inserting probes into the region occupied by the “artificial radiation belt,” the x-ray intensity decreases rapidly, and this information is used to estimate the belt’s spatial extent. Additional information describing the plasma and the energetic electrons has appeared elsewhere [13, 14, 30].

### 3 OBSERVATION OF DRIFT-RESONANT FLUCTUATIONS

When intense energetic electrons are produced, drift-resonant fluctuations ( $\omega \sim \omega_{dh}$ ) are observed both while the ECR heating is on and in the afterglow. During microwave heating, the fluctuations appear in quasiperiodic bursts lasting approximately 300–500  $\mu$ s. During the afterglow, the drift-resonant oscillations persist for several milliseconds. These electrostatic fluctuations are simultaneously measured with four movable probes with high-impedance tips and matched, low-noise, wide-band preamplifiers. The observed frequencies correspond to the drift-frequencies of both the “warm” and the “hot” energetic electrons,  $0.1 \text{ MHz} \leq f \leq 20 \text{ MHz}$ . The saturated wave amplitudes typically range from 100–200 V.

Correlations between multiple probes show that the waves (1) propagate azimuthally in the direction of the electron  $\nabla B$  drift, (2) are flute-like with constant phase along a field line, and (3) have a broad radial structure extending throughout the plasma [32]. Fourier analysis shows the fluctuations have a time-varying and complex frequency spectrum consisting of several coherent and sometimes incoherent modes. Figure 2 shows a spectrogram of the electrostatic fluctuations during microwave heating (showing several quasiperiodic instability bursts) and during the initial period of the hot electron afterglow. Multiple waves with rising frequencies are present. Comparing the phase differences measured between probes separated azimuthally show that the azimuthal mode number of the most intense modes is  $m = 1$ , although large amplitude instability bursts also have waves with  $m = 2$ , and waves observed during the afterglow have been detected with  $m \leq 6$ . It is observed that (1) multiple modes with different frequencies often have the same azimuthal mode structure, and (2) modes present at the same time but with different  $m$  often appear to be independent since the ratio of their frequencies are not harmonically related and change in time.

Coincident with the drift-resonant fluctuations is an outward expansion of the energetic electrons. This is shown in Figure 2, where the electron flux to the movable gridded particle analyzer shows a rapid increase during the instability bursts. Measurements using the photodiode and polar detector arrays, reported elsewhere [30], support this interpretation.

Analysis of the electron transport induced by the fluctuation’s time-evolving frequency spectrum results in two significant conclusions. First, the presence or absence of the induced radial flux of energetic electrons depends on the spectral characteristics of the fluctuations and not simply on the amplitude [13, 14]. Intense radial transport is observed only when the frequency spectrum of the fluctuations induced global chaotic drift-motion of the resonant energetic electrons. When the frequency spectrum of the fluctuations consists of isolated coherent modes, bands of chaotic motion are predicted to occur only in thin radial bands and greatly diminished transport is observed. Secondly, the flux of electrons impacting a small movable gridded particle detector is strongly modulated. A simple quasilinear picture of phase-space diffusion averages over phase-

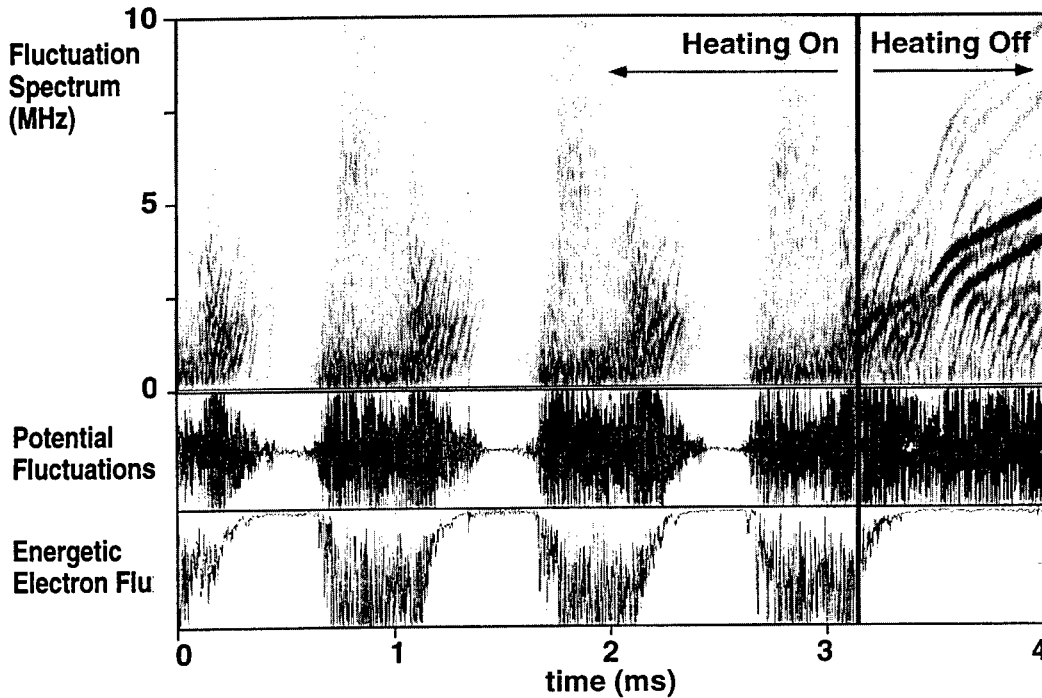


Figure 2: The measured electrostatic fluctuations and the flux of energetic electrons to the movable gridded particle detector. A spectrogram showing the time-evolving spectral amplitude of the fluctuations is also shown.

space correlations and fails to reproduce the modulated flux seen by the detector. However, a transport simulation based on the Hamiltonian motion of energetic electrons following the drift-motion induced by the measured fluctuation spectrum reproduces the frequency and modulation depth of the observations [14, 30].

#### 4 HOT ELECTRON INTERCHANGE INSTABILITY

The analyses of collisionless transport in CTX referred to in Section 3 were based on computed particle dynamics in the presence of a collection of electrostatic waves with fixed frequencies. The wave frequencies were measured within a relatively short time interval during an instability burst when the time-variation of the spectrum could reasonably be ignored. Although the energetic electron response to these fluctuations could be understood, we did not explain why the frequency of the drift-resonant instability increases on longer time periods nor did we identify the source or describe the evolution of the phase-space structures detected by the gridded particle detector. Possible answers to these questions are addressed in this section. A fully self-consistent model for the growth and saturation of the unstable waves is introduced which includes the Hamiltonian motion of the energetic electrons to drift-resonant electrostatic fluctuations.

In the following, the basic equations used to describe flute-like electrostatic fluctuations within a dipole magnetic field are described. Since  $\mu$  and  $J$  are preserved, the electron dynamics are described by a two-dimensional canonical phase-space, and the colder ions and electrons are described by field-line averaged particle continuity equations. When linearized, these equations describe the hot electron interchange instability (HEI) in a dipole confined plasma. Fully nonlinear solutions are computed numerically. The nonlinear solutions illustrate frequency sweeping for saturated instabilities and strong modulation of local energetic particle flux due to the transport of "phase-space holes." A more detailed description of the models presented in this section will be published elsewhere [33].

#### 4.1 Basic Equations

In the following, we summarize a self-consistent, nonlinear model for the flute-like electrostatic hot electron interchange instability in dipole magnetic flux coordinates.

##### 4.1.1 The Dipole Magnetic Field

A curl-free, axisymmetric dipole magnetic field can be represented in magnetic coordinates  $\mathbf{B} = \nabla\varphi \times \nabla\psi = \nabla\chi$ , where  $(\psi, \varphi)$  defines a field line and  $\chi$  relates to a position along a field line. In spherical coordinates,  $\psi = M \sin^2 \theta / r$ , and  $\chi = M \cos \theta / r^2$ , where  $M \equiv B_0 L_0^3$  is the moment of the dipole magnet defined in terms of the field strength at an equatorial ( $\theta = \pi/2$ ) reference radius,  $L_0$ .

Restricting our model to flute-like interchange instabilities, integrals along a field line incorporate the geometry of the dipole magnetic field. For example, the volume of a tube per unit flux is  $\delta V(\psi) = \int d\chi / B^2$  with the magnetic field strength expressible as  $B = (M/r^3)\sqrt{1 + 3\cos^2 \theta}$ . Integrals of this type are performed by first transforming the variable of integration from  $\chi$  to  $\xi \equiv \sin^2 \theta$  using the relations:

$$r = \frac{M\xi}{\psi}, \quad \chi = \frac{\psi^2}{M} \sqrt{\frac{1-\xi}{\xi^4}}, \quad \text{and} \quad \left. \frac{d\chi}{d\xi} \right|_{\psi, \varphi} = \frac{\psi^2}{M} \frac{3\xi - 4}{2\xi^3 \sqrt{1-\xi}}. \quad (1)$$

For a ideal dipole field, we find

$$\delta V(\psi) = \frac{M^3}{\psi^4} \int_0^1 \frac{d\xi \xi^3}{\sqrt{1-\xi}} \approx 0.91 \frac{M^3}{\psi^4}. \quad (2)$$

The flux-tube average,  $\langle A \rangle$ , and the density-weighted average,  $\|A\|$ , are defined as

$$\langle A \rangle \equiv \frac{1}{\delta V(\psi)} \int \frac{d\chi A}{B^2}, \quad \text{and} \quad \|A\| \equiv \frac{\langle An \rangle}{\langle n \rangle} = \frac{1}{N} \int \frac{d\chi}{B^2} n A, \quad (3)$$

where  $n$  is the plasma density, and  $N \equiv \langle n \rangle \delta V$  is the total particles on a tube per unit flux.

##### 4.1.2 Electron Dynamics

We model the electrons as consisting of anisotropic energetic electrons ( $p_\perp \gg p_\parallel$ ) equatorially trapped near the microwave cyclotron resonance (*i.e.* as shown in Figure 1) and cold electrons more uniformly distributed along the field lines. Since the instability of interest is flute-like with a frequency much higher than the cold electron drift frequency, the essential dynamics of the electrons is represented by assigning  $J = 0$  to the energetic electrons while preserving their total electron number density on a given flux tube. The energetic electrons form a “disk” encircling the terrella and immersed within the larger quasineutral cold plasma [14].

The interaction of nonrelativistic energetic electrons with the drift-resonant electrostatic waves are described by the guiding center drift Hamiltonian [34],  $\mathcal{H} = \mu c B / e - c \Phi$ , where  $e$  is the magnitude of its charge,  $c$  is the speed of light,  $B$  is the local strength of the dipole magnetic field,  $\mu \equiv m_e v_\perp^2 / 2B$  is the magnetic moment,  $m_e$  is the electron mass, and  $\Phi$  is the electrostatic potential. Particle motion is confined to trajectories in a two-dimensional phase-plane,  $(\psi, \varphi)$ , and the equations of motion take a particularly simple form:

$$\dot{\varphi} = \frac{\partial \mathcal{H}}{\partial \psi} = \mu \frac{c}{e} \frac{\partial B}{\partial \psi} - c \frac{\partial \Phi}{\partial \psi}, \quad (4)$$

$$\dot{\psi} = -\frac{\partial \mathcal{H}}{\partial \varphi} = c \frac{\partial \Phi}{\partial \varphi}. \quad (5)$$

For these equatorial particles, the magnetic precessional drift frequency is  $\omega_{dh} = 3c\mu B / e\psi$ , which scales as  $\omega_{dh} = 3\mu B_0 / m_e \omega_{ce0} L^2$  using  $\omega_{ce0} = eB_0 / m_e c$  and  $L \equiv M/\psi$  to label a flux surface and a particle's equatorial radial position. Cold electrons execute radial and azimuthal  $\mathbf{E} \times \mathbf{B}$  motion; whereas, the energetic electron drifts are Doppler-shifted according by the magnetic drift,  $\omega_{dh}$ . When  $\Phi$  consists of azimuthally propagating waves, the wave-particle resonance condition,  $\omega = m\omega_{dh}$ , relates a particle's energy,  $\mu$ , to a resonant flux surface,  $L \propto \sqrt{m\mu/\omega}$ . As  $\omega$  increases, the wave-particle drift-resonance moves inward.

When describing the complete dynamics of a population of trapped electrons, we use the bounce-averaged distribution,  $F(\mu, J, \psi, \varphi, t)$ , with adiabatic constants,  $(\mu, J = 0)$ . The collisionless evolution of  $F$  is described with the following equation

$$\frac{\partial F}{\partial t} + \frac{\partial}{\partial \varphi}(\dot{\varphi}F) + \frac{\partial}{\partial \psi}(\dot{\psi}F) = 0. \quad (6)$$

When the particle distribution is expressed in terms of the adiabatic invariants, the number of electrons on a tube of given flux  $\delta\psi\delta\varphi$  is  $N_e = \int d\mu dJ F$ , and the volume-averaged electron density is  $\langle n_e \rangle = N_e/\delta V(\psi)$ .

#### 4.1.3 Electrostatic Fluctuations

The potential fluctuations are modeled as constant along a field line and purely electrostatic. In flux coordinates, the flux-tube-averaged form of Poisson's equation becomes

$$\frac{\partial}{\partial \varphi} \left( h_\varphi \frac{\partial \Phi}{\partial \varphi} \right) + \frac{\partial}{\partial \psi} \left( h_\psi \frac{\partial \Phi}{\partial \psi} \right) = -4\pi e(N_i - N_e) \quad (7)$$

which determines the electrostatic potential,  $\Phi(\psi, \varphi, t)$ , in terms of the difference of electron and ion numbers within a flux-tube. Two geometric terms define the transformation of the Laplacian operator into field-line averaged flux-coordinates:

$$h_\varphi \equiv \int \frac{d\chi}{|\nabla\psi|^2} = 2\frac{M}{\psi^2}, \text{ and } h_\psi \equiv \int \frac{d\chi}{|\nabla\varphi|^2} = 4M. \quad (8)$$

#### 4.1.4 Cold Ion Dynamics

The plasma ions are modeled as a cold, neutralizing ion-fluid convected by  $\mathbf{E} \times \mathbf{B}$  and polarization drifts. This description assumes that the fluctuation frequency is much smaller than the ion cyclotron frequency,  $\omega \sim \omega_{dh}/2 \ll \omega_{ci} = eB/M_i c$  where  $M_i$  is the ion mass. For drift-resonant fluctuations, this condition is equivalent to  $\rho/L \ll \sqrt{m_e/M_i}$ .

The field-line averaged continuity equation is

$$\frac{\partial N_i}{\partial t} + \frac{\partial}{\partial \varphi} (N_i \|\nabla\varphi \cdot \mathbf{V}\|) + \frac{\partial}{\partial \psi} (N_i \|\nabla\psi \cdot \mathbf{V}\|) = 0. \quad (9)$$

Using  $\mathbf{E} = -\nabla\Phi$ , the particle-conserving cold ion flow can be written as

$$\frac{\partial N_i}{\partial t} + \frac{\partial}{\partial \varphi} \left[ cN_i \left( -\frac{\partial \Phi}{\partial \psi} - \left\| \frac{|\nabla\varphi|^2}{\omega_{ci} B} \right\| \frac{\partial^2 \Phi}{\partial \varphi \partial t} \right) \right] + \frac{\partial}{\partial \psi} \left[ cN_i \left( \frac{\partial \Phi}{\partial \varphi} - \left\| \frac{|\nabla\psi|^2}{\omega_{ci} B} \right\| \frac{\partial^2 \Phi}{\partial \psi \partial t} \right) \right] = 0 \quad (10)$$

which neglects the parallel flow of plasma lost to the poles. The first term in parentheses is the  $\mathbf{E} \times \mathbf{B}$  drift, and the second term is the polarization drift.

The field-line averaged ion polarization drift terms require knowledge of the density profile along a field line. This profile has not yet been measured in CTX; however, these density-weighted field-line integrals are only weakly profile dependent for a reasonable range of possible profiles. For the examples reported here, the density profile is assumed to be moderately broad along a field line,  $n \sim \sqrt{\xi} = \sin \theta$ , and  $\| |\nabla\varphi|^2 / \omega_{ci} B \| \approx 0.66 M^2 B_0 / \psi^4 \omega_{ci0}$ ,  $\| |\nabla\psi|^2 / \omega_{ci} B \| \approx 0.77 M^2 B_0 / \psi^2 \omega_{ci0}$ , where  $\omega_{ci0}$  is the ion cyclotron frequency at  $B = B_0$ .

#### 4.2 Linear Dispersion Relation

The linear dispersion relation for low-frequency, flute-like modes in a hot-electron, dipole plasma can be derived from the equations presented in the previous section. We use several simplifications. First, the electron distribution is assumed to be separable with  $\alpha(\psi)$  defined as the fractional density of energetic electrons. Secondly, solutions to Poisson's equation are restricted to be traveling waves localized on a flux surface where  $\partial\Phi/\partial\psi \approx 0$ . With these assumptions, the unperturbed electron distribution function,  $F_0$ , takes the form

$$F_0(\mu, J, \psi) = N_{i0}(\psi)[1 - \alpha(\psi)]\delta(\mu)\delta(J) + N_{i0}(\psi)\alpha(\psi)G(\mu)\delta(J) \quad (11)$$



where  $\int d\mu G(\mu) = 1$ , and the linear potential fluctuations are:

$$\Phi(\psi, \varphi, t) \approx \Phi_m(\psi^*) \cos(m\varphi - \omega t + \varphi_m) \left[ 1 - \left( \frac{\psi - \psi^*}{\Delta\psi} \right)^2 + \dots \right], \quad (12)$$

with  $m$  the azimuthal mode number,  $\varphi_m$  an arbitrary phase, and  $\psi^* = B^* L^2$  is the flux surface of peak mode amplitude (*i.e.* where  $\partial\Phi/\partial\psi = 0$ ). Only two significant terms of an expansion of the radial mode structure are retained. We refer to the radial mode width as  $\Delta\psi \equiv 2\psi^*/k_L L$ , and we define the total perpendicular mode number as  $m_\perp^2 \equiv m^2 + 0.58(k_L L)^2$ .

The Fourier-Laplace transform of the linearized fluctuating electron number,  $\tilde{N}_e$ , is equal to

$$\tilde{N}_e = cm\Phi_m \frac{1}{\omega} \frac{\partial N_{i0}}{\partial \psi} + cm^2\Phi_m \frac{\partial(N_{i0}\alpha)}{\partial \psi} \int d\mu \frac{\omega_d G}{\omega(\omega - m\omega_d)}. \quad (13)$$

The linearized ion fluctuation number is

$$\tilde{N}_i = cm\Phi_m \frac{1}{\omega} \frac{\partial N_{i0}}{\partial \psi} - cm^2\Phi_m \left\| \frac{|\nabla\varphi|^2}{\omega_{ci}B} \right\| N_{i0} + c \frac{\partial^2 \Phi_m}{\partial \psi^2} \left\| \frac{|\nabla\psi|^2}{\omega_{ci}B} \right\| N_{i0}. \quad (14)$$

On the same surface, the field-line averaged Poisson's equation becomes

$$\left[ m^2 + (k_L L)^2 \right] \Phi_m = \frac{4\pi e\psi^{*2}}{2M} (\tilde{N}_i - \tilde{N}_e), \quad (15)$$

which defines the local dispersion relation in terms of the radial gradients of the hot and cold plasma and the distribution of energetic drift frequencies,  $\omega_{dh}(\mu)$ .

The hot electron interchange mode is usually described [25] in the high-density limit where  $\langle \omega_{pi}^2 \rangle / \omega_{ci}^{*2} \approx 4\pi e c N_{i0} \psi^* / 0.91M \gg 1$ . For CTX,  $\langle \omega_{pi}^2 \rangle / \omega_{ci}^{*2} \simeq 10^3$ . When we further note that the observed instabilities have  $m \sim 1$  and a broad radial structure, the local dispersion is determined by the zeros of

$$D(\omega, m, m_\perp) \approx 1 + 1.5 \frac{m^2}{m_\perp^2} \frac{\psi^*}{N_{i0}} \frac{\partial(N_{i0}\alpha)}{\partial \psi} \int d\mu \frac{\omega_{ci}^* \omega_d G}{\omega(\omega - m\omega_d)} \quad (16)$$

This dispersion relation is easily examined using two relatively simple forms for  $G(\mu)$ . When  $G(\mu) = \delta(\mu - \mu_0)$ , the energetic electrons are mono-energetic.  $D$  is a simple quadratic function of  $\omega$ ,

$$D \approx 1 + \frac{m^2}{m_\perp^2} \frac{\Gamma_h^2}{\omega(\omega - m\omega_{d0})}. \quad (17)$$

In Eq. 17,  $\omega_{d0}$  is the hot electron drift frequency, and  $\Gamma_h^2 = 1.5 \omega_{ci}^* \omega_{d0} (\psi^*/N_{i0}) (\partial N_{i0} \alpha / \partial \psi)$  is the hot electron interchange drive. This reproduces the form of the HEI dispersion relation derived by Krall [25]. Instability results whenever  $\Gamma_h^2 > m_\perp^2 \omega_{d0}^2$  corresponding to unstable coupling of the negative energy precessional mode with the positive energy drift mode. The hot electron density gradient must exceed a stability threshold due to the competition between the stabilizing azimuthal ion polarization flows and the destabilizing net radial electron flows. For unstable modes, the real frequency is  $m\omega_{d0}/2$ . Low values of  $m$  and broad radial mode structures ( $m_\perp^2 \ll 1$ ) are more unstable than higher values of  $m$  or  $m_\perp$ . For mono-energetic electrons, local, linear theory does not produce a wave-particle resonance, and Eq. 17 is purely reactive.

The linear stability of energetic electrons having a distribution of energies can be investigated using a model such as

$$G(\mu) = \frac{\mu^{l-1} l!}{\mu_0^l \Gamma(l)} \exp(-\mu l / \mu_0), \quad (18)$$

where  $l$  is a positive integer. When  $l = 1$ , Eq. 18 represents a Maxwellian distribution of energetic electrons. When  $l \rightarrow \infty$ ,  $G$  becomes mono-energetic. For all  $l$ ,  $\int d\mu \mu G = \mu_0$ . Using Eq. 18,  $D$  can be expressed in terms of the exponential integral combined with the usual Landau prescription for evaluating the energy exchanged by the wave-particle drift-resonance,  $\omega = m\omega_{dh}(\mu)$ . The existence of the wave-particle resonance destabilizes the HEI (and eliminates the instability threshold) for a plasma with any unstable gradient,  $d\alpha/d\psi > 0$ . Numerical solution of the finite-temperature dispersion relation shows the growth rate is small until the Krall instability threshold is approached; however, it is significant that distinct intervals of stability are observed in CTX even with a radially-localized population of electrons having a broad energy distribution. These stable periods implies the presence of nonresonant wave dissipation not included within Eq. 17.

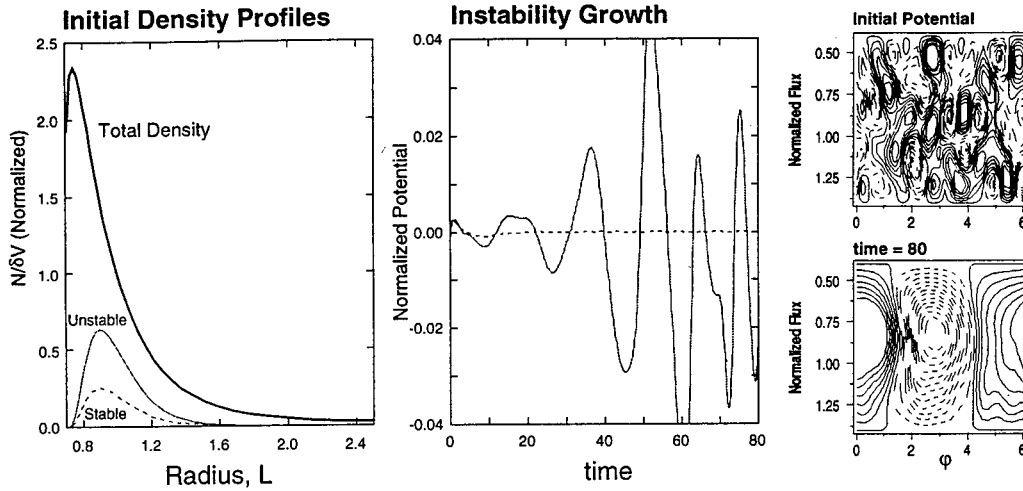


Figure 3: The evolution of the electrostatic potential during the growth and saturation of the HEI. Large amplitude waves dominated by  $m = 1$  grow from the initially random fluctuations when the energetic electrons are sufficiently intense. Stable and unstable hot electron densities are shown.

### 4.3 Self-Consistent Nonlinear Evolution of the HEI

The nonlinear evolution of the hot electron interchange instability has been simulated by computing simultaneously solutions to Eqs. 5, 7 and 10. These solutions exhibit frequency chirping and strong modulation of energetic electron flux as observed in the experiment. The simulation indicates a correspondence between the rising frequency of the instability and the inward motion of phase-space "holes."

Since the self-consistent dynamics of the HEI can be described on the  $(\psi, \varphi)$  phase-plane, the two-dimensional time evolution of  $N_i$ ,  $\Phi$ , and  $F(\mu)$  can be solved using relatively standard numerical techniques on a desktop computer workstation. We incorporate an important simplification. Since  $\mu$  is a constant of the motion, the electron distribution can be considered to consist of a continuum of two-dimensional phase-planes which interact only through their mutual and collective effects on the fluctuating potential. However, the computation of the entire Vlasov time evolution of  $F(\mu, t)$  would be time-consuming and unnecessary. In the simulations reported here, we represent the hot electrons as a finite number of hot-electron phase-planes distributed at various values of  $\mu$ ,  $F(\mu, \varphi, \psi, t) \approx \sum_i g_i(\varphi, \psi, t) \delta(\mu - \mu_i)$ . Since our potential fluctuations extend from the terrella to the outer vacuum chamber wall, each hot electron phase-plane resonates with the potential fluctuations at some radial location. This simplification, therefore, retains a complete description of the nonlinear wave-particle resonance without the need for excessive computation. Furthermore, the same numerical algorithm used for the evolution of the ion fluid flow can be used to compute the hot-electron phase-space flow for each value of  $\mu$ .

For a given electrostatic potential,  $\Phi$ , and its first time derivative,  $\Phi' \equiv \partial\Phi/\partial t$ , the ion and electron density is advanced using a flux-corrected transport algorithm [35] modified by Zalesak [36, 37]. Zalesak demonstrated the effectiveness of this numerical technique by computing the growth of electrostatic drift instability in a plasma following a magnetospheric release of barium.

The potential fluctuations are computed by recasting Poisson's equation using an equation for the conservation of charge derived from the ion and electron dynamical equations. The ion polarization currents are used to define a field-line averaged dielectric,  $\epsilon_\varphi(\psi)$ ,  $\epsilon_\psi(\psi)$  proportional to the axisymmetric part of the ion number density,  $\bar{N}_i \equiv \int d\varphi N_i/2\pi$ . This gives an elliptic equation for the time derivative of the potential,  $\Phi'$ , in terms of the divergence of the nonaxisymmetric ion polarization currents, the  $\mathbf{E} \times \mathbf{B}$  convection of the fluctuating charge density, and the magnetic precession of the hot electrons [33]. Since  $\epsilon_\varphi$  and  $\epsilon_\psi$  depend

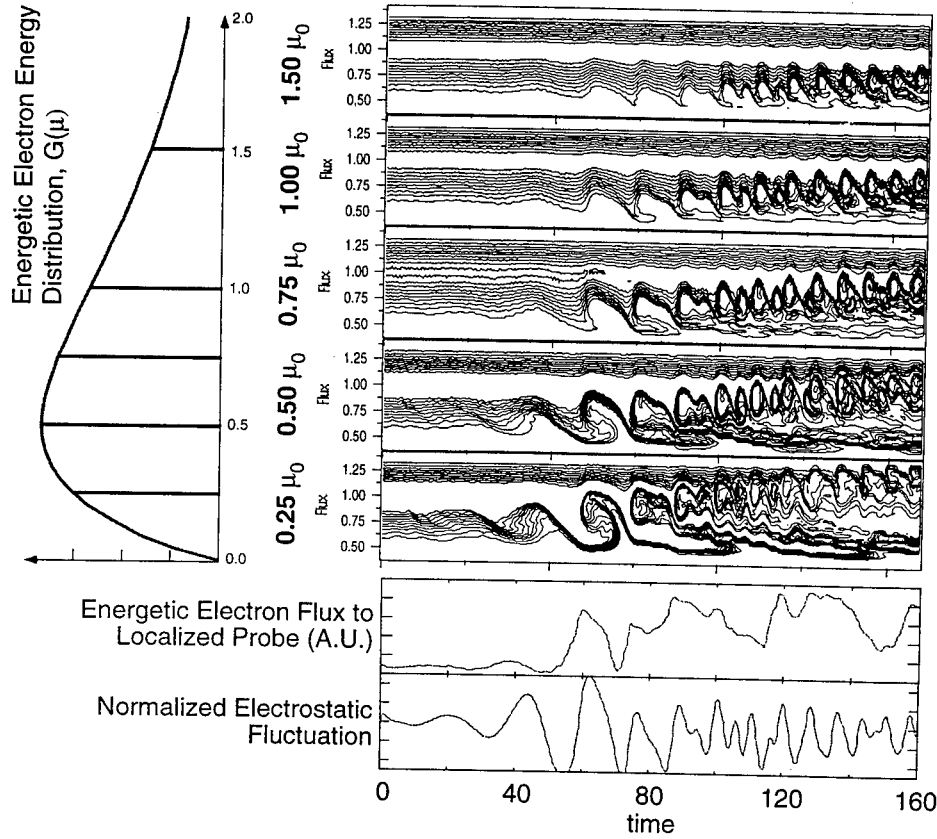


Figure 4: The evolution energetic electrons showing the modulations of the local electron flux (bottom) and the time-evolution of five hot electron "phase-planes" clearly illustrating the inward propagation of "holes" (top).

only upon  $\psi$ , the equation for  $\Phi'$  is solved efficiently using fast Fourier transforms of the azimuthal variations of potential and charge.

Nonresonant dissipation of the electrostatic fluctuations is required both for numerical stability and to produce frequency sweeping. Since the flux-corrected transport of electrons and ions introduces very little numerical dissipation, an explicit damping of the potential fluctuations is needed. After computing a solution for  $\Phi'$  as described above, the potential is advanced in time, from  $t$  to  $t + \Delta t$ , according to the rule:

$$\Phi(t + \Delta t) = \Phi(t) + \Delta t \Phi' - (-1)^k \Delta t \nu \nabla^{2k} \Phi(t), \quad (19)$$

where  $\nu$  is a specified constant, and  $k = 0, 1, 2, \dots$  sets the scale-length for dissipation.

Figure 3 shows the time evolution of the electrostatic potential from a representative simulation. Initially, the potential fluctuations are small and random. If the density of energetic electrons is below a threshold set by dissipation, the fluctuations decay. As the intensity of the energetic electrons increase, rapidly growing fluctuations appear dominated by a broad,  $m = 1$  structure. The frequency of potential fluctuations increase as the instability saturates. The peak amplitude of the instability corresponds to a trapping frequency having  $\omega_{tr} \sim \gamma_L \approx \omega_{dh}/4$ .

Figure 4 shows the evolution of the energetic electron phase-space distributed over five values of  $\mu$  and weighted according to Eq. 18 with  $l = 2$ . Since the initial frequency of the HEI is low, the low-energy electrons are the first to experience strong resonant diffusion. As the amplitude of the instability saturates,

the frequency increases and electrons with higher energies begin to resonate with the waves. Since the location of the resonance changes with frequency,  $\psi \propto 1/L \propto \sqrt{\omega/m\mu}$ , the drift resonance moves inward. Trapped within the resonances are low phase-space densities originating in the outer regions of the plasma. As these phase-space "holes" move inward, they displace hot and denser electrons at lower  $L$  and cause transport. For the low-energy electrons, phase-space structures exist at the outer regions of the plasma which circulate at low frequency. The location of the phase-space holes within each phase-plane (*i. e.* for each value of  $\mu$ ) are separated in radius but not in azimuth. As the frequency spectrum of the instability evolves, the dynamics of lower energy electrons appear chaotic. By summing the electron flux from all five phase-planes, the simulated signal from a stationary detector is strongly modulated.

## 5 CONCLUSIONS AND OPPORTUNITIES

An "artificial radiation belt" consisting of energetic electrons deeply trapped by a strong dipole electromagnet has been produced in the laboratory using microwave heating. As the intensity of the radiation belt increases, quasiperiodic bursts of hot electron interchange instability are excited which resonate with the magnetic drifts of the energetic electrons,  $\omega \simeq \omega_{dh}$ . High-speed measurements of the induced energetic electron transport are made with particle detectors, and these measurements show strong temporal modulations indicating the presence of circulating phase-space structures. The frequency spectrum of the nonlinear phase of the HEI is complex with slowly rising tones. We have introduced a self-consistent nonlinear simulation of the flute-like electrostatic response to a steep radial gradient of energetic electrons confined in an ideal dipole magnetic field. The simulation reproduces the temporal features of the energetic electron flux and the increasing frequency of the saturated instability. The simulation shows that a wave with rising frequency traps outer regions of low-density phase-space, called "holes," and transports these regions inward. The inner regions of high-density phase-space are displaced to lower  $B$  leading to energetic electron transport. The energy released during the frequency rise does not lead to significant wave growth due to nonresonant dissipation [21].

The comparison between measurements and simulation lead to interesting questions for further investigation in the laboratory and in the Earth's magnetosphere. In the laboratory, two experiments are in progress to better measure and understand the phase-space structures created by the HEI. First, a 72-element particle analyzer is being installed at one magnetic pole in CTX in order to detect the circulation of phase-space "holes." Secondly, at the opposite pole, a high-frequency and high-power antenna has been installed in order to launch both low-frequency (electrostatic and Alfvénic) and high-frequency (whistler and electron cyclotron) waves into the plasma. These waves will provide a tool for direct interaction with the electron phase-space. For example, excitation of bounce-resonances may result in wave-induced velocity scattering and the destruction of the phase-space "holes." Finally, we can not avoid asking the questions: "Are low-frequency waves within the Earth's magnetosphere driven unstable by energetic particles? And, if so, is frequency sweeping associated with the saturation of these instabilities?" Although most magnetospheric waves which resonate with energetic particles are externally driven by solar wind variability and plasma flows near the magnetosphere [38], theory and observation have indicated the possibility of drift-bounce resonant excitation of Pc 4-5 pulsations by energetic ring-current ions [39]. If low-frequency Alfvén waves are excited by drift-bounce resonances, they will have a relatively short perpendicular wavelength, and the detection of frequency sweeping will require multiple satellites. Unlike the HEI, localized Alfvén pulsations in space would propagate radially if their frequency were to be changed by resonant particle phase-space structures.

## Acknowledgment

The author is grateful to the contributions and enlightening suggestions from H. Warren, A. Boozer, H. Berk, and B. Breizman, and of the support of AFOSR Grant F96-2097-1-0026 and NASA Grant NAWG-3539.

## References

- [1] M. Schulz and L. Lanzerotti, *Particle Diffusion in the Radiation Belts*, (Springer-Verlag, 1974).
- [2] M. P. Nakada and G. D. Mead, *J. Geophys. Res.* **70** (1965) 4777.

- [3] T. J. Birmingham, *J. Geophys. Res.* **74** (1969) 2169.
- [4] A. A. Chan, L. Chen, and R. B. White, *Geophys. Res. Lett.* **16** (1989) 1133.
- [5] T. A. Farley, A. D. Thomassian, and M. Walt, *Phys. Rev. Lett.* **25** (1970) 47.
- [6] X. Li, *et al.*, *Geophys. Res. Lett.* **20** (1993) 2423.
- [7] M. Chen, L. Lyons, and M. Schulz, *J. Geophys. Res.* **99** (1994) 5745.
- [8] D. Baker, *et al.*, *Geophys. Res. Lett.* **16** (1989) 559.
- [9] D. Baker, *et al.*, *Geophys. Res. Lett.* **21** (1994) 409.
- [10] T. G. Northrup and E. Teller, *Phys. Rev.* **117** (1960) 215.
- [11] S. Murakami, T. Sato, and A. Hasegawa, *Phys. Fluids B* **2** (1990) 715.
- [12] H. P. Warren, A. Bhattacharjee, and M. E. Mauel, *Geophys. Res. Lett.* **19** (1992) 941.
- [13] H. P. Warren and M. E. Mauel, *Phys. Rev. Lett.* **74** (1995) 1351.
- [14] H. P. Warren and M. E. Mauel, *Phys. Plasmas* **2** (1995) 4185.
- [15] L. J. Lanzerotti, C. S. Roberts, and W. L. Brown, *J. Geophys. Res.* **72** (1967) 5893.
- [16] A. L. Vampola and A. Korth, *Geophys. Res. Lett.* **19** (1992) 625.
- [17] H. L. Berk, C. E. Nielsen, and K. V. Roberts, *Phys. Fluids* **13** (1970) 980.
- [18] T. O'Neil, J. H. Wfey, and J. Malmberg, *Phys. Fluids* **14** (1971) 1204.
- [19] P. W. Terry, P. H. Diamond, and T. S. Hahm, *Phys. Fluids B* **2** (1990) 2048.
- [20] H. L. Berk, B. Breizman, and M. Pekker, *Phys. Rev. Lett.* **76** (1996) 1256.
- [21] B. Breizman, *et al.*, *Phys. Plasmas* **4** (1997) 1559.
- [22] T. O'Neil, *Phys. Fluids* **8** (1965) 2255.
- [23] M. F. F. Nave, *et al.*, *Nuc. Fusion* **31** (1991) 697.
- [24] W. W. Heidbrink and J. R. Danielson, *Phys. Plasmas* **1** (1994) 4120.
- [25] N. A. Krall, *Phys. Fluids* **9** (1966) 820.
- [26] D. P. Stern, *Rev. of Geophys.* **27** (1989) 103.
- [27] C. Störmer, *The Polar Aurora*, (Oxford, 1995).
- [28] V. D. Il'in and A. N. Il'ina, *Sov. Phys. JETP* **43** (1976) 661.
- [29] A. J. Dragt and J. M. Finn, *J. Geophys. Res.* **81** (1976) 2327.
- [30] H. P. Warren, *et al.*, *Phys. of Plasmas* **3** (1996) 2143.
- [31] M. E. Mauel, *Phys. Fluids* **27** (1984) 2899.
- [32] M. E. Mauel and H. P. Warren, "Observation of Drift-Resonant Fluctuations in the Collisionless Terrella Experiment," in *Physics of Space Plasmas (1993)*, eds. T. Chang and J. Jaserse, Proc. of the 1993 Cambridge Workshop in Geoplasma Physics, (MIT, 1995).
- [33] Mauel, M. E., and Warren, H. P., "Hot electron interchange instability in a plasma confined by a dipole magnetic field," to be submitted to *Phys. Plasmas*.
- [34] A. H. Boozer, *Phys. Fluids* **23** (1980) 904.
- [35] J. P. Boris and D. L. Book, *J. Comput. Phys.* **20** (1976) 397.
- [36] S. T. Zalesak, *J. Comput. Phys.* **31** (1979) 335.
- [37] S. T. Zalesak, *J. Comput. Phys.* **40** (1981) 497.
- [38] W. J. Hughes, "Magnetospheric ULF Waves: A Tutorial with a Historical Perspective," in *Solar Wind Sources of Magnetospheric ULF Waves*, M. J. Engebretson, K. Takahashi, M. Scholer, eds. (Geophysical Monograph, 9817, AGU, 1994).
- [39] K. Takahashi, "ULF Waves in the Magnetosphere," in *Rev. of Geophys.*, U.S. Report to the IUGG (April, 1991) 1066.

## Measurements of High Density Plasmas after Pulsed Discharges in Liquid Helium

W. Qin, K. Minami, A.W. DeSilva\* and F. Tomimoto

*Graduate School of Science and Technology, Niigata University, Niigata 950-21, Japan*

*\* Institute for Plasma Research, University of Maryland, College Park, MD 20742, U.S.A.*

**Abstract.** High density plasmas created by high-voltage pulsed discharges in liquid helium below 4.2 K, 1 atm, and cryogenic helium gas near 4.2 K, 1 atm, have been investigated by spectroscopic measurements in the visible spectral range. The well known atomic lines exhibit strong and broadened profiles with underlying continua at early stages. Several experimental findings indicate that this broadening is dominated by Stark broadening caused by the presence of the transient plasmas. The spectral profiles are therefore used to deduce the plasma densities, which are on the order of  $10^{18} \text{ cm}^{-3}$  at 0.2  $\mu\text{s}$  after the breakdown. The electron temperatures are measured from the ratios of total spectral line intensities to continuum intensities. It turns out to be about 35,000 K at 0.2  $\mu\text{s}$ . The measured plasma parameters suggest that the observed plasmas are moderately strongly coupled plasmas with Coulomb coupling coefficients around 0.1. In addition, some strong spectral features are observed near 430 nm, which can be assigned to  $\text{He}_2$  transition ( $g^3\Sigma_g^+ \rightarrow a^3\Sigma_u^+$ ). The reaction mechanisms are discussed in this paper.

### 1. INTRODUCTION

For many years, a variety of high-density plasmas that were beyond the scope of conventional laboratory experiments have been generated by novel methods such as laser implosion of a small target [1, 2]. Azechi *et al.* [2] generated a strongly coupled (non-ideal) and partly degenerated plasma with density on the order of  $10^{26} \text{ cm}^{-3}$  and electron temperature of 0.5 keV attained by the laser implosion. Here, the strongly coupled plasma means that the Coulomb coupling coefficient  $\Gamma$  defined by the ratio of the average Coulomb energy to the average kinetic energy is not much less than unity. Shock wave compression in gases or solid materials have been measured to generate non-ideal plasmas with densities on the order of  $10^{18} \text{ cm}^{-3}$  and electron temperature around 1 eV [3]. One of the authors (A. W. DeSilva) and his collaborator measured by means of laser scattering a plasma with densities  $10^{17} \text{ cm}^{-3}$  and electron temperature 2 eV [4]. Peaked spectra caused by ion-acoustic fluctuations in the collision dominated plasmas were detected and fitted to Bhatnagar-Gross-Krook model among various versions.

On the other hand, spectroscopic measurements have been employed extensively to investigate properties of dissolved impurities in liquid helium (LHe). Spectroscopic measurements were carried out to measure dissolved clusters from metal target caused by laser ablation [5]. Laser-generated sparks have been employed to analyze liquids spectroscopically [6]. Our spectroscopic study presented here was motivated by a possible existence of cryogenic plasma states generated by high-voltage pulsed discharges in LHe [7]. The cryogenic plasma, *i.e.*, positive and negative ion mixture with temperature below 4.2 K dissolved in LHe, may be an unknown subject in physics of condensed matter. Time-resolved emission spectra resulting from sparks in LHe and cryogenic helium (He) gas are here measured in the visible spectral region from 380 nm to 720 nm. In LHe, a high power discharge will create a gaseous He bubble between the electrodes, as occurred in other liquids [6]. The measurements we made, in fact, are limited to transient gaseous He plasmas in cryogenic environments immediately after the pulsed discharge. The results show that the well known neutral He atomic lines are strong and broadened with underlying continua at the early stages. Several experimental findings indicate that this broadening is dominated by Stark broadening caused by the presence of the transient plasmas. The

spectral profiles are therefore used to deduce the plasma densities. The electron temperatures are measured from the ratios of total spectral line intensities to continuum intensities. These data suggest that the observed plasma with relatively high density and low electron temperature due to rapid cooling are moderately strongly coupled plasmas beyond the scope of conventional discharges in gas at room temperature. In addition, there are some strong spectral features near 430 nm ( $23300\text{ cm}^{-1}$ ), which can be assigned to the  $\text{He}_2$  transition ( $g^3\Sigma_g^+ - a^3\Sigma_u^+$ ). They are not observed in 77 K and 300 K, 1 atm, He gas under the same experimental conditions. By analyzing these spectral data, the emissions of neutral atomic He are estimated to be from the hot core of the plasma while the strong molecular  $\text{He}_2$  transitions occur at the rapid cooling edge layers, where the molecular He ions become dominant positive ions.

The outline of this paper is as follows: the experiment is described in section 2, analyses and discussions of the measured results are given in section 3, and conclusions are presented in section 4.

## 2. EXPERIMENTS

Pulsed discharges of -22 kV are made between tungsten rod electrodes separated by 1.5 mm in a Dewar bottle filled with LHe or with cryogenic He gas. The peak discharge current measured by a Rogowski coil is about 50 A with 0.5  $\mu\text{s}$  duration as shown in Figure 1. The states of He examined are (1) superfluid LHe II with temperature 1.62 K and pressure 5.8 Torr, (2) normal fluid LHe with 4.2 K and 1 atm, (3) cryogenic He gas near 4.2 K and 1 atm, (4) He gas near 77 K and 1 atm, and (5) He gas at 300 K, 1 atm. The case (1) is attained by evacuation cooling, *i.e.*, the pressure of He gas above the LHe surface is kept at 5.8 Torr. The cases (4) and (5) are investigated for comparison.

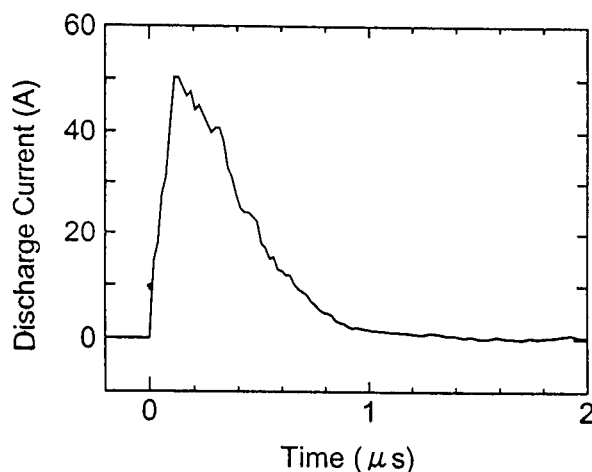


Figure 1: The discharge current vs time measured by a Rogowski coil.

The light emissions from the spark are collected through a vertical transparent slit made on the Dewar bottle by a lens and focused into the entrance slit of a 0.25 m monochromator fitted with a 1200 grooves/mm grating. The detector is a MCP high-speed gated image intensifier head combined with a multichannel detecting system. The 1024 channels cover a spectral region of 46 nm when the center wavelength of the monochromator is set to 550 nm. Spectra at various delay times  $t_d$  after the discharge can be measured in a certain spectral range without the necessity for scanning the spectrometer. The time resolution is 0.4  $\mu\text{s}$ . No particular efforts have been made for getting spatial resolution. The data are average values of all line-of-sight emissions. The calibration of the spectral response is carried out by using a tungsten-filament 2,854 K standard lamp.

### 3. ANALYSES AND DISCUSSIONS

#### 3.1 Determination of Plasma Densities

##### 3.1.1 Spectral Line Broadening

The emissions from discharges in all five cases (1)–(5) in a spectral region from 380 nm to 720 nm last typically about 6–8  $\mu$ s. In the low temperature cases (1)–(3), the spectra show extremely broadened neutral He atomic lines together with a very strong continuum background at the early stage after the discharge. Then, the continua gradually disappear. Most of the strong atomic lines 388.9 nm ( $3p^3P-2s^3S$ ), 447.1 nm ( $4d^3D-2p^3P$ ), 501.7 nm ( $3p^1P-2s^1S$ ), 587.6 nm ( $3d^3D-2p^3P$ ), 667.8 nm ( $3d^1D-2p^1P$ ) and 706.5 nm ( $3s^3S-2p^3P$ ) in this spectral region appear and become increasingly narrow in line width as time elapses. An example of case (1) near the spectral line 587.6 nm is shown in Figure 2.

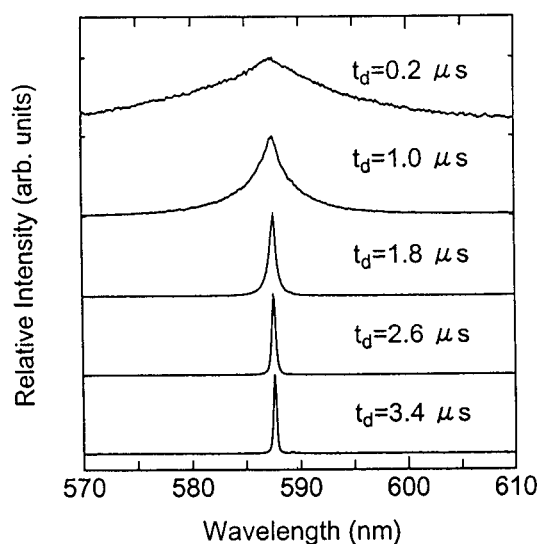


Figure 2: Time-resolved emission spectra near 587.6 nm ( $3d^3D-2p^3P$ ) in 1.62 K, 5.8 Torr liquid helium. Note the line broadening and continuum at early stage.

For the gas cases in our conditions, the observed spectral line broadening can be considered to be dominated by Stark broadening as in usual dense plasmas. The plasma densities can be accordingly calculated with the use of the theory developed by Griem and his co-workers [8–10]. In LHe cases (1) and (2), however, the plasma is believed to be located in the gas bubble bounded by LHe, in which the pressure may be very high and decreases rapidly as time progresses [6]. The line width, therefore, may result partially from the effects other than that of the local electrons and ions. Nevertheless, the following experimental findings indicate that the broadening in LHe is also dominated by Stark broadening.

Firstly, the measured spectral line profiles and numerically calculated Stark profiles can be well fitted with each other. The numerical calculations of the Stark spectral line profiles are based on the impact approximation for electrons and quasi-static approximation for ions as were described by Griem and the co-workers [8–10]. Two examples of the fittings for the spectral line 587.6 nm at delay time 0.2  $\mu$ s and 1.4  $\mu$ s, respectively, in the case (1) are shown in Figure 3. The poor fit at the line center is probably due to contributions from low-density edge layers because of the spatial and temporal nonuniformity of plasma parameters in the discharge region.



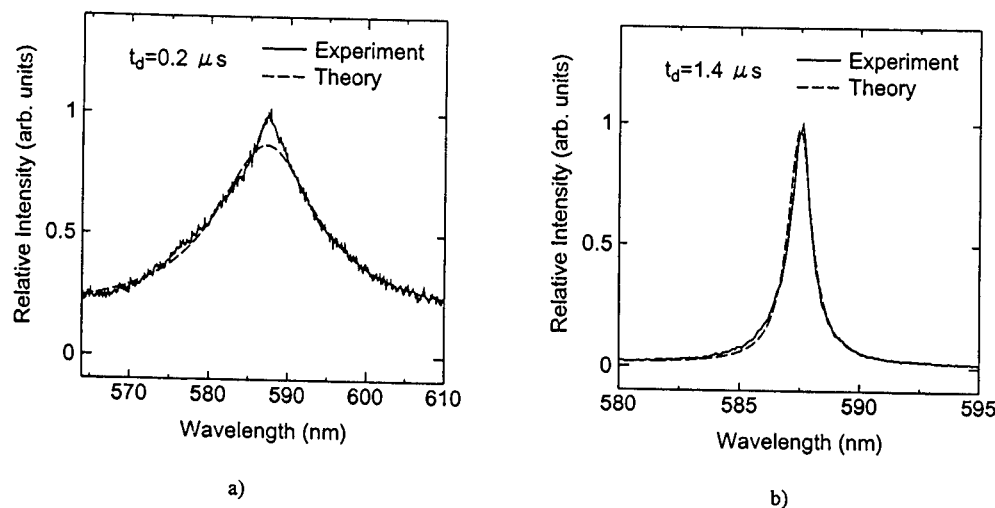


Figure 3: The comparison between theoretically calculated Stark profiles and the measured spectral line shapes of spectral line 587.6 nm at delay time a) 0.2  $\mu$ s and b) 1.4  $\mu$ s in 1.62 K, 5.8 Torr superfluid liquid helium.

Secondly, the plasma densities deduced from a few different isolated lines by fitting the line profiles exhibit consistency within an error limit under the assumption that the mechanism of Stark broadening dominates the spectral line profiles. The results after Debye shielding correction [9] of spectral lines 388.9 nm, 587.6 nm, 667.8 nm and 706.5 nm in case (1) are given in Table I. Some of the data have large deviations from others. For example, the density obtained from line 667.8 nm at the delay time  $t_d = 1.0 \mu$ s is very low. However, these inconsistencies are not worse than those in gas cases. Taking into account the experimental errors, *e.g.*, time jitter ( $\sim 0.1 \mu$ s) of MCP delay in our single shot measurements and the accuracy of numerical calculation according to Refs. 8—10, errors in density determination from He neutral atomic lines can be estimated to be as large as 35%.

Table I: Plasma densities obtained by fitting different emission spectral lines for 1.62 K, 5.8 Torr, liquid helium.

Spectral line (nm)	$3p^3P-2s^3S$ 388.9	$3d^3D-2p^3P$ 587.6	$3d^1D-2p^1P$ 667.8	$3s^3S-2p^3P$ 706.5	Average
Delay time $t_d$ ( $\mu$ s)	Plasma density ( $10^{17} \text{ cm}^{-3}$ )				
0.2	—	44	—	—	44
0.6	19	24	18	18	20
1.0	7.3	8.9	5.7	9.0	7.7
1.4	3.4	3.2	2.8	2.9	3.1
1.8	1.9	2.2	1.9	2.1	2.0
2.2	1.5	1.7	1.4	—	1.5
2.6	1.2	1.1	0.83	—	1.0
3.0	1.0	1.0	—	—	1.0
3.4	0.91	0.88	—	—	0.90
3.8	0.81	0.75	—	—	0.78

“—” The experimental spectral line profile is too difficult to obtain because of strong continuum background or poor signal-to-noise ratio.

Finally, the average plasma densities deduced from spectral line shifts and those obtained from the line widths show consistency within the error limit under the assumption that the mechanism of Stark broadening and shift dominates the spectral line profiles. When there exist a large number of free charged particles near the He atom emitters, the spectral lines will not only be broadened, but also shifted [8—10]. Our experimental results show such shifts, just as was expected theoretically. Despite the large error inherent in line shifts theoretically and experimentally [8—9], the plasma densities can roughly be deduced from the fitting values of the shifts. The average densities in the cases (1) obtained from shifts and widths of 388.9 nm, 587.6 nm, 667.8 nm and 706.5 nm are depicted in Figure 4.

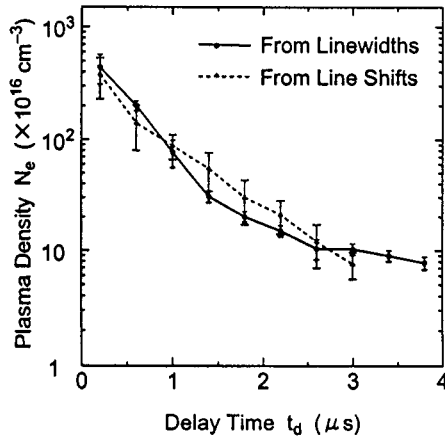


Figure 4: Comparison between average plasma densities obtained from shifts and profiles of spectral lines 388.9 nm, 587.6 nm, 667.8 nm and 706.5 nm in 1.62 K, 5.8 Torr superfluid liquid helium.

### 3.1.2 Determination of plasma densities

Plasma density is one of the important parameters that are used to describe a plasma environment. The value is also very important for establishing the equilibrium in the plasma. One of the advantages of measuring the density through Stark broadening is that the density can be calculated with good accuracy, even when the electron temperature  $T_e$  is not accurately known because Stark broadening is insensitive to  $T_e$ .

In Figure 5, the average densities after Debye shielding correction, determined from line profiles of neutral lines 388.9 nm, 587.6 nm, 667.8 nm and 706.5 nm, are plotted for the cases (1)—(3) as functions of the delay time  $t_d$ . The plasma densities are  $4.4 \times 10^{18}$  cm $^{-3}$ ,  $3.6 \times 10^{18}$  cm $^{-3}$  and  $1.3 \times 10^{18}$  cm $^{-3}$  at the earliest stage of  $t_d = 0.2$   $\mu$ s in the cases (1), (2) and (3), respectively. They are  $8 \times 10^{16}$  cm $^{-3}$ ,  $6 \times 10^{16}$  cm $^{-3}$  and  $6 \times 10^{16}$  cm $^{-3}$ , respectively, at  $t_d = 3.8$   $\mu$ s. Such plasma densities, on the order of  $10^{18}$  cm $^{-3}$ , are much higher than the values,  $1.4 \times 10^{17}$  cm $^{-3}$  and  $1.1 \times 10^{17}$  cm $^{-3}$ , produced, respectively, in the cases (4) and (5), at  $t_d = 0.2$   $\mu$ s. Here, it should be mentioned that, at  $t_d = 0.2$   $\mu$ s, the measured line profile may be influenced by the remains of the discharge electric field strength. However, this effect is estimated to be minor, because much lower densities are acquired under the same discharge conditions in the cases (4) and (5), and the plasma formed may also shield itself from this effect. After 3  $\mu$ s, the electron densities in the cases (2) and (3) converge to about  $6 \times 10^{16}$  cm $^{-3}$ . For the case (1), however, they remain above  $7 \times 10^{16}$  cm $^{-3}$  for a long time. Subsequent decreased emission intensities result in poor signal-to-noise ratios, and there exists a limitation in the instrumental spectral resolution. Accordingly, this phenomenon requires further investigation.

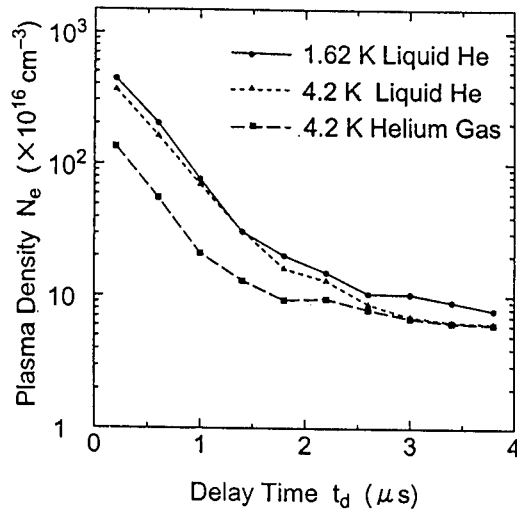


Figure 5: Plasma densities as functions of delay time  $t_d$  in cases (1) 1.62 K, 5.8 Torr superfluid liquid helium (He), (2) 4.2 K, 1 atm normal fluid liquid He and (3) 1 atm He gas near 4.2 K.

In addition, in terms of the plasma densities obtained here and electron temperatures, which will be discussed in the next section, the densities of neutral He atoms at the breakdown region can be estimated by Saha equation. It turns out that the density of neutral ground-state He atoms at delay time  $t_d = 0.2 \mu\text{s}$  is on the order of  $10^{16} \text{ cm}^{-3}$ , while typical plasma density at this moment is  $10^{18} \text{ cm}^{-3}$  in the cases (1)–(3). This fact provides another evidence for dominant mechanism of Stark broadening.

### 3.2 Determination of Electron Temperatures

#### 3.2.1 Measurement of Electron Temperatures

The observed underlying continuum light in our measurements is considered mainly to arise from recombination radiation and bremsstrahlung due to atomic processes. By using the observed continuum, the electron temperatures can be deduced by relative line-to-continuum intensities described by Griem in Ref. 8. The procedure of this method is to calculate the ratio of the measured total spectral line intensity to the continuum intensity in a certain wavelength band, *e.g.* 10 nm, centered at the line. This result is then compared with the calculated one [8]. The ratio is a function of electron temperature and is independent of the plasma density. Comparing with other spectroscopic methods for electron temperature determination, this method is normally restricted to simple pure gases such as hydrogen and He, because continuum intensities can be precisely calculated. However, it permits rather precise temperature determinations in relatively low temperatures ( $15,000 \text{ K} < T_e < 30,000 \text{ K}$ ). As in most of other spectroscopic methods, this method is also only applied to local thermodynamic equilibrium (LTE) plasmas. The validity of LTE under our conditions will be discussed in the next subsection.

Figure 6 shows the measured  $T_e$  as functions of delay time  $t_d$  in the cases (1)–(3). It is found that, at delay time  $t_d = 0.6 \mu\text{s}$ ,  $T_e \approx 32,000 \text{ K}$ ,  $33,000 \text{ K}$  and  $25,600 \text{ K}$  for the cases (1)–(3), respectively. They are  $19,100 \text{ K}$ ,  $15,900 \text{ K}$  and  $17,500 \text{ K}$ , respectively, at  $t_d = 3.0 \mu\text{s}$ . The decay time of  $T_e$  in the case (1) has some similarities to that for the case (3). In the case (2), however, the decay seems to be somewhat faster than others. The theoretical [8] and experimental uncertainty in the temperature measurements is estimated to be 20% for the delay time  $t_d$  between  $0.6 \mu\text{s}$  and  $3.0 \mu\text{s}$  in the cases (1)–(2).

and between 0.2  $\mu\text{s}$  and 3.0  $\mu\text{s}$  in the case (3). Before 0.6  $\mu\text{s}$  in LHe cases, a very strong continuum background and extremely broadened emission line profiles prevent the determination of  $T_e$ . On the other hand, after 3.0  $\mu\text{s}$ , the continuum background becomes too weak to obtain electron temperature within error 30%.

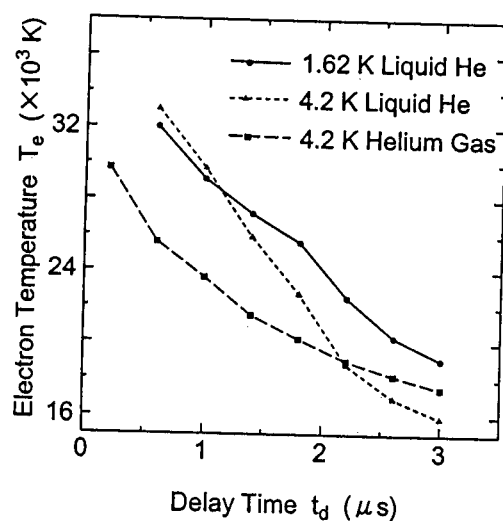


Figure 6: Electron temperatures as functions of delay time in cases (1) 1.62 K, 5.8 Torr superfluid liquid helium (He), (2) 4.2 K, 1 atm normal fluid liquid He and (3) 1 atm He gas near 4.2 K.

### 3.2.2 Equilibrium Discussions

In order to determine electron temperature  $T_e$  by using the method described above, it is necessary to assume that the plasma establishes a state of LTE soon after its formation. Although it is not certain that LTE exists in this transient plasma, there are some general arguments for the existence of LTE. Firstly, the lower criterion imposed on plasma density, for which the plasma will be within 10% at LTE for the excitation and ionization distributions, is  $2 \times 10^{16} \text{ cm}^{-3}$ . From our experimental results up to 3.8  $\mu\text{s}$ , the electron densities satisfy this criterion. This suggests that LTE can be attained during this time. The high plasma density and high pressure in the bubble formed by breakdown in LHe imply high collision frequencies between constituent particles. Secondly, the criterion of the time for the excitation and ionization distributions to establish equilibrium is estimated to be less than 70 ns in our LHe cases at  $t_d = 0.2 \mu\text{s}$  [8, 11]. The time for establishing a kinetic equilibrium between electrons, heavier neutral atoms and ions turns out to be less than 1 ns at  $t_d = 0.2 \mu\text{s}$  [8, 12]. Therefore, LTE is suggested in the plasmas produced in our experiments, although it is not yet possible for us to make an experimental comparison between three temperatures, *i.e.*, ionization, excitation and electron temperatures, directly. Nonetheless, some deviations from LTE cause no great errors in temperature determination by the method of relative line-to-continuum intensities for all neutral He lines which we have used, as long as densities are above  $10^{15} \text{ cm}^{-3}$  [8].

### 3.3 Coulomb Coupling Coefficient $\Gamma$

The Coulomb coupling coefficient  $\Gamma$  of a plasma defined as the ratio of the average Coulomb energy to the average kinetic energy can be calculated from measured plasma densities and electron temperatures.

According to the plasma parameters measured in the cases (1), (2) and (3), the  $\Gamma$  factors of the transient plasmas are around 0.1 which is about 5 times greater than that for the case (5). Therefore, our plasmas in cryogenic environments are considered to be moderately strongly coupled plasmas.

### 3.4 Analyses of Reaction Dynamics

As one of advantages, the spectroscopic observations can provide not only plasma parameters such as density and electron temperature but also the information on reaction dynamics of the plasma.

In our experiments, the observed emissions from excited neutral atoms are very intense. These emissions were, however, completely absent in Kimura's spectra of nitrogen ion-impinged cryogenic He gas in this spectral range [13]. Only transitions of atomic He 706.5 nm ( $3s^3S-2p^3P$ ) and 728.1 nm ( $3s^1S-2p^1P$ ) occurred in Brooks and Hunt's proton beam irradiated cryogenic He gas [14]. The failure to observe atomic lines was considered to arise from associative ionization reaction (Hornbeck-Molnar process) [15],



In our case, the concentration of neutral ground-state He atoms in the center part of breakdown is relatively low. It is reasonable that most of excited atomic He transitions occur with significant intensities as in the case (5) at the hot core of the transient plasma.

In addition to the neutral atomic spectra, some strong spectral features are observed near  $23300 \text{ cm}^{-1}$  ( $\sim 430 \text{ nm}$ ) in the cases (1)–(4). Here, for the convenience of assignment, unit of frequency is used. The time-resolved spectra from  $22100 \text{ cm}^{-1}$  to  $24400 \text{ cm}^{-1}$  ( $\sim 410\text{--}450 \text{ nm}$ ) for the cases (1) and (2) are shown in Figure 7. According to the spectral data given by Orth and Ginter [16], they consist primarily of spectra of  $\text{He}_2$  transitions,  $P$  branch,  $g^3\Sigma_g^+(\nu=0)-a^3\Sigma_u^+(\nu=0)$  as marked in Figure 7. A few weak peaks

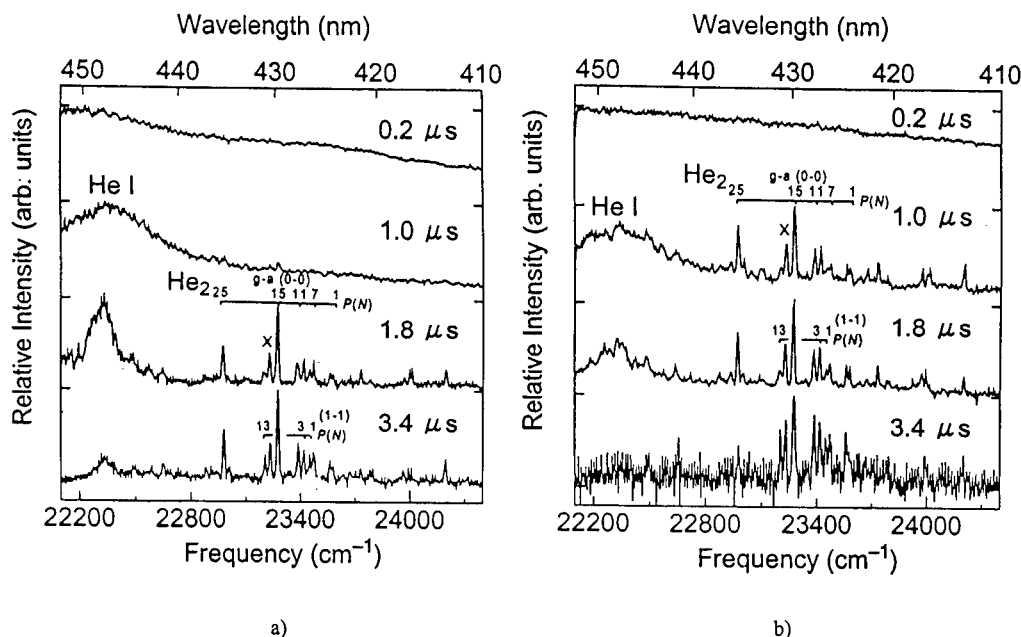


Figure 7: The time-resolved emission spectra from  $22100 \text{ cm}^{-1}$  to  $24400 \text{ cm}^{-1}$  ( $\sim 410\text{--}450 \text{ nm}$ ) at delay time  $0.2 \mu\text{s}$ ,  $1.0 \mu\text{s}$ ,  $1.8 \mu\text{s}$  and  $3.4 \mu\text{s}$  after discharges in cases a)  $1.62 \text{ K}$ ,  $5.8 \text{ Torr}$  liquid helium (LHe), and b)  $4.2 \text{ K}$ ,  $1 \text{ atm}$  LHe.

can be assigned to  $\nu(1-1)$  vibrational band with  $N=1, 3$  and  $13$ . No lines of the  $R$  branch are identified. Here, it should be mentioned that the spectral resolution and frequency precision of our system is about  $6 \text{ cm}^{-1}$  at  $18182 \text{ cm}^{-1}$  ( $550 \text{ nm}$ ). The assignments are accordingly limited to this precision. Some lines of the band may be ruled out because of line shift due to high pressure or line mixing. The line marked  $x$  is probably caused by the transition  $g-a$  ( $0-0$ ),  $N=17$ . However, the frequency discrepancy is as large as  $11 \text{ cm}^{-1}$ .

The only reasonable source of excited  $\text{He}_2^+(g^3\Sigma_g^+)$  seems to be neutralization of ionic species. No experimental observations and theoretical expectations about the formation of  $\text{He}_2^+(g^3\Sigma_g^+)$  by other way have been reported. One of possible ionic species is  $\text{He}_2^+$ . In plasmas of high neutral density,  $\text{He}^+$  ions are rapidly converted to  $\text{He}_2^+$  ions through ion conversion processes [15]:



The associative ionization process (1) also occurs rapidly for excited atoms with levels higher than  $n=2$ . It is commonly believed that the  $\text{He}_2^+$  ion formed from reactions (1)–(3) are in highly excited vibrational states [15, 17]. However, the spectra we observed in low temperature are found to be “hot” rotational distribution maximized at  $N=15$  with “cool” vibrational distribution ( $\nu=0$  and  $1$ ) of  $\text{He}_2^+$ . The resultant molecules of the transition should be rotationally excited molecules in  $a^3\Sigma_u^+$  state. As a progenitor of  $\text{He}_2^+(g^3\Sigma_g^+)$ ,  $\text{He}_2^+$  ion probably relaxes to its ground vibrational state very fast. However, it is very difficult to picture a mechanism to explain the formation of  $\text{He}_2^+(g^3\Sigma_g^+)$  or its progenitor,  $\text{He}_2^+$  ion, in highly rotationally excited states.

Rotational distribution of non-thermal equilibrium was observed in temperature lower than about  $200 \text{ K}$  by Callear and Hedges [18]. Infrared absorption spectra from metastable He molecules ( $a^3\Sigma_u^+$ ) were previously examined with proton beam irradiation by Brooks, Hunt and Tokaryk [17, 19]. It was observed that the vibrational-rotational distribution within the  $a^3\Sigma_u^+$  state was far from thermal equilibrium. There were three different vibrational-rotational groups: thermal molecules ( $\nu=0$ ,  $N=1$ ), rotationally excited molecules ( $\nu=0$ ,  $9 \leq N \leq 21$ ) and vibrationally excited molecules ( $10 \leq \nu \leq 12$ ,  $N=1$ ). They suggested that the rotationally excited molecules were the products of neutralization of  $\text{He}_3^+$  ions rather than  $\text{He}_2^+$  ions, which were considered to be progenitor for the vibrational excited ones.

Evidence of the existence of  $\text{He}_3^+$  ions in low temperatures was given by Patterson [20]. It was proposed that the reaction leading to a stable  $\text{He}_3^+$  was a three-body process or a four-body reaction [17],



The rate of formation of  $\text{He}_3^+$  from  $\text{He}_2^+$  was found to be faster than the formation of  $\text{He}_2^+$  through reaction (2) and (3) at  $76 \text{ K}$ . Further studies made by other researchers indicated that  $\text{He}_3^+$  ion was, in fact, the dominant ion in  $76 \text{ K}$  He afterglow and the neutralization of these ion species produced  $\text{He}_2^+$  and He [21].

Obviously, this reaction model can explain our spectra very well. However, it seems to be impossible to estimate that the molecular emissions come from the hot core of the plasma. At edge layers, where the density of neutral He atoms is very high and all kinds of particles are undergoing a rapid cooling,  $\text{He}_3^+$  ions are formed quite readily. According to the intensities of the spectra presented here,  $\text{He}_3^+$  ions may be created very copiously in outer layers during and after the discharge. They lead to recombination within the time resolution of  $0.4 \mu\text{s}$ .

In conclusions, as schematically illustrated in Fig. 8, the intense neutral atomic He spectra are considered to be from the hot core of the plasma, where the dominant positive ions are  $\text{He}^+$ . The obtained plasma densities and electron temperatures in this work are spatial average values of the line-of-

sight in this region. In contrast, the strong molecular  $\text{He}_2$  transitions are considered to occur at rapid cooling edge layers. They are suggested to be a subsequent process of neutralization of  $\text{He}_3^+$  ions. In other words, in edge region of the plasma,  $\text{He}_3^+$  are the dominant positive ions. Here, it should be noted that the so-called "hot core" and "rapid cooling edge layer" are two extreme conditions. Between these two conditions, there may exist some region where both excited atoms and molecules are emitting and the kinetics are much more complicated. The object we viewed is a very dense transient plasma with extremely large temperature and density gradients.

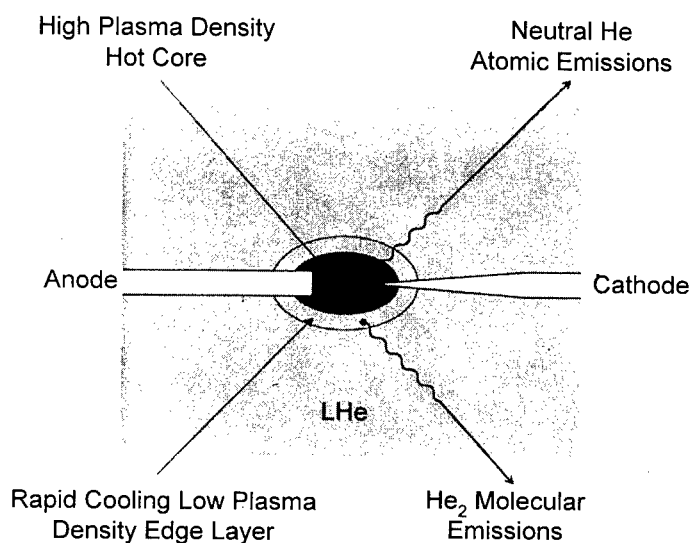


Figure 8: The schematic diagram of the discharge region.

#### 4. CONCLUSIONS

The time-resolved emission spectra from high-voltage pulsed discharges in LHe below 4.2 K, 1 atm, and cryogenic helium gas near 4.2 K, 1 atm, have been examined in a spectral region from 380 to 720 nm. The spectra exhibit both the well known neutral atomic lines, which are strong and broadened with underlying continua at early stages, and intense molecular  $\text{He}_2$  transitions.

Several experimental findings indicate that the broadening of neutral atomic lines in LHe cases is dominated by Stark broadening. The spectral profiles are therefore used to deduce the plasma densities, which are on the order of  $10^{18} \text{ cm}^{-3}$  at 0.2  $\mu\text{s}$  after breakdown. The electron temperatures are measured from the ratios of total spectral line intensities to continuum intensities. It turns out to be about 35,000 K at 0.2  $\mu\text{s}$ . The gaseous plasma state with relatively high density and low electron temperature is obtained in cryogenic environments. According to the plasma parameters obtained here, the Coulomb coupling coefficient  $\Gamma$  are around 0.1 which is about 5 times greater than that in the room temperature He gas case. Therefore, the plasmas are considered to be moderately strongly coupled plasmas.

However, the obtained plasma parameters are limited to the region of the plasma hot core, where the emissions of neutral excited atoms are substantial. At rapid cooling outer layers,  $\text{He}_3^+$  ions are proposed to be dominant positive ions. The strong molecular  $\text{He}_2$  transitions are estimated to be a subsequent process of neutralization of  $\text{He}_3^+$  ions.

The present work makes the first investigation on a transient plasma produced by pulsed discharge in LHe environment. The present results would be helpful to understand the physics of very dense helium plasmas.

### Acknowledgements

The authors would like to acknowledge profoundly Professor H. R. Griem, the University of Maryland, for his interest and encouragement to present work.

### References

- [1] Hooper C. F., Jr., Mancini R. C., Haynes D. A., Jr. and Garber D. T., Elementary processes in dense plasmas, eds. Ichimaru. S and Ogata. S (Addison-Wesley, Tokyo, 1995) pp. 403-414.
- [2] Azechi H. *et al.*, *Laser & Particle Beams* **9** (1991) 193-207.
- [3] Fortov V. E., Bushman A. V., Filimonov A. S., Kvitov S. V., Kulish M. I., Lebedev M. E., Polischuk A. Ya. and Ternovoi V. Ya., Shock compression of condensed matters (Elsevier Science Publishers, New York, 1992) pp. 745-748.
- [4] Mostovych A. N. and DeSilva A. W., *Phys. Rev. A* **34** (1986) 3238-3252.
- [5] Fujisaki A., Sano K., Kinoshita T., Takahashi Y. and Yabusaki T., *Phys. Rev. Lett.* **71** (1993) 1039-1042.
- [6] Cremers D. A., Radziemski L. J. and Loree T. R., *Appl. Spectrosc.* **38** (1984) 721-729.
- [7] Minami K., Watanabe S., Qin W., Tomimoto F., Kuwabara S., Ruhul Amin Md., Kato K., and Satow T., *Jpn. J. Appl. Phys.* **34** (1995) 271-276.
- [8] Griem H. R., Plasma spectroscopy (McGraw-Hill, New York, 1964) pp. 63-455.
- [9] Griem H. R., Spectra line broadening by plasmas (Academic Press, New York and London, 1974) pp. 1-320.
- [10] Griem H. R., Baranger M., Kolb A. C., and Oertel G., *Phys. Rev.* **125** (1962) 177-195.
- [11] Griem H. R., *Phys. Rev.* **131** (1963) 1170-1176.
- [12] Lochte-Holtgreven W., Plasma diagnostics, ed. Lochte-Holtgreven W. (Wiley, New York, 1968) pp. 180-182.
- [13] Kimura K., *J. Chem. Phys.* **84** (1986) 2002-2009.
- [14] Brooks R. L. and Hunt J. L., *J. Chem. Phys.* **88** (1988) 7267-7272.
- [15] Déloche R., Monchicourt P., Cheret M. and Lambert F., *Phys. Rev. A* **13** (1976) 1140-1176.
- [16] Orth F. B. and Ginter M. L., *J. Mol. Spectrosc.* **61** (1976) 282-288.
- [17] Tokaryk D. W., Brooks R. L. and Hunt J. L., *Phys. Rev. A* **48** (1993) 364-381.
- [18] Callear A. B. and Hedges R. E. M., *Trans. Faraday Soc.* **66** (1970) 2921-2935.
- [19] Brooks R. L. and Hunt J. L. and Tokaryk D. W., *J. Chem. Phys.* **91** (1989) 7408-7414.
- [20] Patterson P. L., *J. Chem. Phys.* **48** (1968) 3625-3631.
- [21] Gerber R. A. and Gusinow M. A., *Phys. Rev. A* **4** (1971) 2027-2033.



## Generation of Supersonic Plasma Flow by Means of Unipolar RF Discharges

M. Novák, M. Šícha\*, V. Kapička\*\*, L. Jastrabík, L. Soukup, Z. Hubička\*, M. Klíma\*\*, P. Slaviček\*\* and A. Brablec\*\*

*Institute of Physics, Division of Optics, Academy of Sciences of the Czech Republic, Na Slovance 2, 180 40 Prague 8, Czech Republic*

*\* Department of Electronics and Vacuum Physics, Faculty of Mathematics and Physics, Charles University, V. Holešovičkách 2, 180 00 Prague 8, Czech Republic*

*\*\* Department of Physical Electronics, Faculty of Science, Masaryk University, Kotlářská 2, 611 37 Brno, Czech Republic*

**Abstract.** Recently the unipolar discharges has been used as a plasma source which employ the flow of the working gas for the creation of plasma channels: At first the radio frequency unipolar one hollow cathode discharge the cathode of which acts simultaneously as a nozzle for working gas inlet to the reactor chamber has been used in the particular applications.[1,2]. On the base of this reactor the plasma-chemical reactor with a system of unipolar multi-hollow-cathode discharges has been developed. This reactor is able to deposit the composite thin films and multi-layer structures onto internal walls of cavities, tubes and on the components with complicated shapes. Secondly the RF unipolar torch discharge has been used as a source of the plasma channel. The advantage of this system is that it is possible to use it up to atmospheric pressure of the working gas and even in the liquid environment[3],[4]. In the present report the generation of the plasma channels by means of mentioned RF unipolar plasma discharges is discussed. At first the devices with RF unipolar hollow cathode discharge are presented and after that the device with the torch discharge is mentioned.

### 1. RF LOW PRESSURE PLASMA CHEMICAL REACTOR WITH UNIPOLAR HOLLOW CATHODE DISCHARGE

#### 1.1 The plasma-chemical reactor with one unipolar hollow-cathode discharge

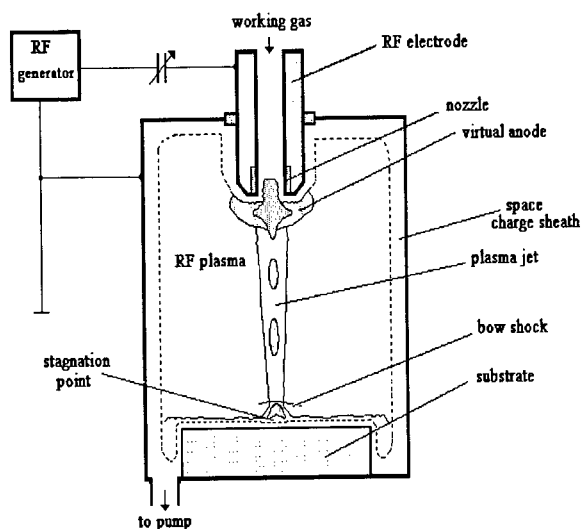


Fig.1. Schematic drawing of the unipolar hollow cathode discharge device.

In the plasma-chemical reactors with unipolar hollow cathode discharge [1,5] the working gas flows through the hollow cathode which acts simultaneously for working gas as a nozzle. According to the working gas velocity in the hollow cathode these systems can be roughly divided into two groups: The system with subsonic working gas flow in the reactor chamber and with supersonic one (RPJ).

The unipolar hollow cathode discharge is induced by potential drop across the space charge sheath around the RF electrode. The space charge sheath is created by the customary two electrode RF discharge (Fig.1). The substrate is placed on the grounded electrode. The nozzle in the RF electrode connected with radiofrequency signal admits the working gas into the continuously pumped vacuum reactor.

At the RF power below a certain limit (for example < 20 W) the value of the potential drop is not sufficient to induce the additional hollow-cathode discharge. In this case only an

ordinary RF discharge is generated in the reactor chamber. However at conditions when the RF power

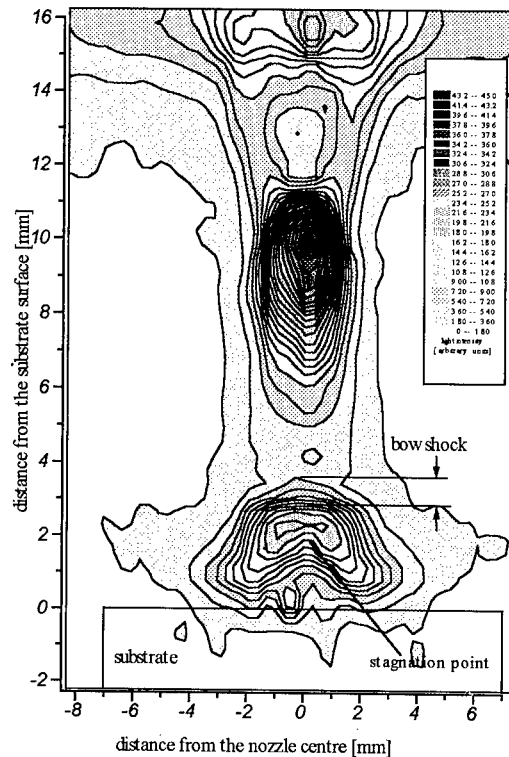


Fig 2. Lines of equal light intensity in the supersonic plasma jet channel. Working gas  $N_2$  pressure 75 Pa, gas flow 900 sccm, RF power 60 W

exceeds this limit the potential drop induces an intensive unipolar hollow cathode discharge inside the nozzle.

The potential drop across the space charge sheath around the powered RF electrode which is created by RF discharge represents the source of electromotive force for the unipolar hollow cathode discharge induced inside the nozzle. Because the RF power for generation of the RF plasma inside the reactor is fed to the electrode through a serial capacitor the DC component of the unipolar hollow cathode discharge cannot flow through external circuit. For this reason the virtual anode is created in the neighbourhood of the RF electrode. According to [1,5,6] the AC current component also flows to the virtual anode.

The working gas pressure is maintained at several tens or hundreds of Pa and the working gas flow is adjusted in such a manner that the flow inside the reactor chamber is supersonic.

The incoming working gas forces this discharge supersonically from the nozzle into the reactor and a well-defined plasma jet channel is created inside the primary RF plasma [6,7]:(see Fig.2)

The simplified condition for the plasma jet generation has been described in [5]. The processes inside the nozzle are described with more precision in [1]. If we take into account the hollow cathode effect then

according the paper [1] we obtain for the breakdown condition of the discharge inside the nozzle the following expression:

$$\langle K \rangle = \frac{1+\gamma}{\gamma+G} \frac{1-\frac{G_S}{\gamma}}{1-\frac{G_S}{\gamma+G}}; \quad (1)$$

where:

$$\langle K \rangle = \exp \left( \frac{1}{T} \int_0^T \int_0^d \alpha(x, t) dx dt \right), \quad (2)$$

and  $\alpha$  and  $\gamma$  are the first and the third Townsend coefficients,  $T$  is the period of the RF voltage,  $d$  is the thickness of the cathode fall region inside the nozzle, the coefficient  $G$  expresses the electron emission from the nozzle surface due to the hollow cathode effect and the coefficient  $G_S$  expresses the particular process of electrons secondary emitted from the nozzle surface by means of ions created by pendulum high energetic electrons inside the cathode fall region.

The described radio frequency plasma jet reactor with supersonic flow of the working gas inside the nozzle (RPJ) was developed for deposition of thin films into the hollow substrates and substrates of complicated shapes because the plasma channel is forced by supersonic flow to the substrate.

Depending on experimental conditions the nozzle outlet can be sputtered or evaporated by the hollow cathode discharge inside the nozzle. The deposition of the thin films can be carried out by two basic ways:

a.) Plasma Chemical Vapour Deposition (PCVD) when a mixture of reactive gas is activated in the plasma stream and the chemically activated species recombine on the substrate surface to form the thin film. Typical example of PCVD thin film deposition by means of RPJ is the deposition of the silicon nitride thin films. The working gas mixture is composed from nitrogen and 3% silane diluted in argon [8].

b.) Physical Vapour Deposition (PVD) when the components which are necessary for growth of the thin film is supplied by an erosion of the nozzle for example by reactive sputtering or by an arc evaporation. Typical example of (PVD) by means of RPJ deposition is deposition of the germanium nitride thin film [2]. In these cases has been experimentally found that by means of the RPJ reactor the thin films with defined stoichiometry have been achieved  $\text{Ge}_3\text{N}_4$  [2]. Recently thin films with defined stoichiometry have been obtained for  $\text{Cu}_3\text{N}$  [9] and  $\text{Al}_2\text{O}_3$  [10] thin films.

## 1.2 The plasma-chemical reactor with a system of unipolar multi-hollow-cathode discharges

The results that have been obtained in the deposition of thin films by means of RPJ reactors with one unipolar hollow cathode discharge indicate, that the plasma-chemical reactor with multi-hollow-cathode system [11] should be able to deposit the composite thin films and multi-layer structures onto internal walls of cavities, tubes and on the components with complicated shapes. It can be also expected that this system could be able to deposit the composite thin films and multi-layer structures from various materials in dependence on the sort of working gases and nozzle's materials.

In the primary plasma channel and also inside the hollow cathode discharge takes place also the product of plasma-chemical reactions between the working gas particles and particles sputtered from the cathode. Therefore in the two primary plasma channels the intensive plasma-chemical reactions should be expected especially if the working gas is composed from several sorts of gases. This fact increases flexibility in the use of the reactor with multi-hollow-cathode system.

Until now for sake of simplicity we used the reactor with only two hollow cathodes. The schematic drawing of the experimental set up is shown in Fig. 3. The velocity of the working gases which flow through both nozzles were adjusted in such a manner that the flows from both nozzles are supersonic. Both nozzles are connected to the different RF generators (in Fig.3. generator RF1 and RF2). By means of these generators two plasma jets are created inside the reactor chamber in the same way as in one hollow cathode reactor. The advantage of such experimental set up is that both plasma-jet channels are created by independent sources and the working conditions of each

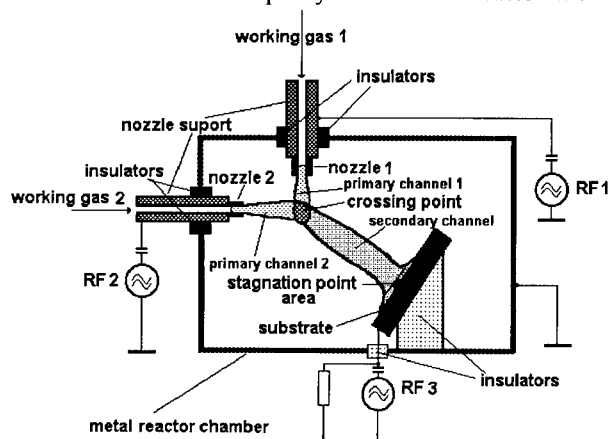


Fig. 3. Schematic drawing of the system of two unipolar hollow cathode discharges

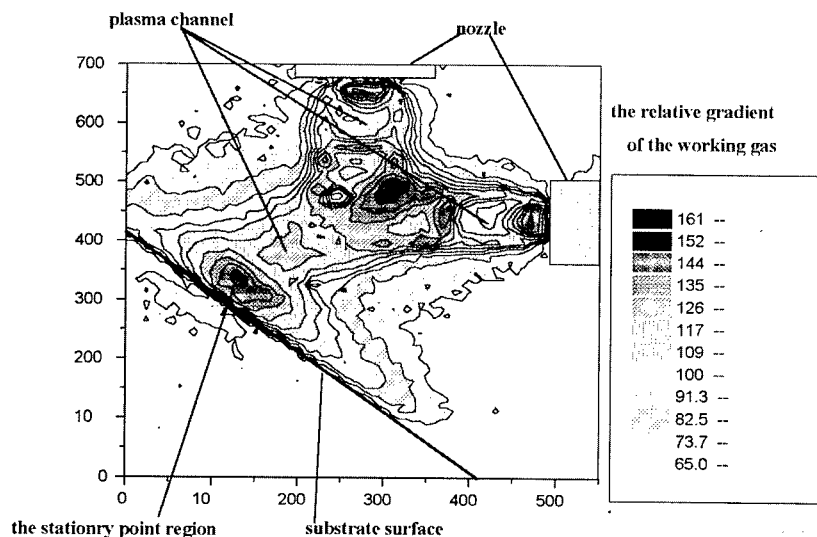


Fig. 4. Lines of equal relative working gas density gradient in a system of two unipolar hollow cathode discharges taken by Schlieren method.

hollow cathode discharge and primary plasma-jet channels can be independently adjusted.

The substrate is isolated from the metallic wall of the reactor chamber and it is connected with the output of the third RF generator (in Fig 3. RF3). Within certain limits it is possible by means of the output voltage of this generator to adjust the self-bias voltage of the substrate.

In order to study the neutral gas flow in the plasma channels and in the crossing point we used the Schlieren method (for example [12]) supplemented by the CCD camera. The data processing computer software has been used in order to obtain the lines of the same value of the relative working gas density gradient and hence to get an idea of the structure of gas flows in the plasma channels and in the crossing point region.

An example of the experiment is shown on Fig.4. Experimental results presented in this figure show that if the gas flows in the primary plasma channels are supersonic in the crossing point of primary plasma

channels the shock wave is created. This shock wave bend the primary channels to one direction and secondary plasma channel is created.

Furthermore experimentally has been found that the direction of the secondary plasma channel depends on the magnitude of the flows of working gases in the primary plasma channels (see Fig.4). It has been found that it is possible to deviate the secondary plasma channel by the variation of the gas flow (drift velocity) in both nozzles. The secondary plasma channel could be deviated up to  $70^\circ$  from the vertical direction if the ratio of the flows in the horizontal nozzle with respect to the flow in vertical one increases approx. four times.

The deviation of the secondary plasma channel allowed to deposit the thin film in the defined part of the substrate. For this reason by means of the multi-hollow-cathode system it is possible to deposit the composite thin films and multi-layer structures onto internal walls of cavities, tubes and on the components with complicated shapes.

In order to study the homogeneity of the secondary plasma channel argon and nitrogen have been used as working gases. The radial distributions of the ratio of the two spectral lines of Ar (826.4 nm) and N<sub>2</sub> (371 nm) have been measured across the crossing point (see Fig.5(a)) and at the stagnation point near the substrate (see Fig. 5 (b)). From Fig. 5(b) it is seen that near the substrate the secondary plasma channel is homogeneous.

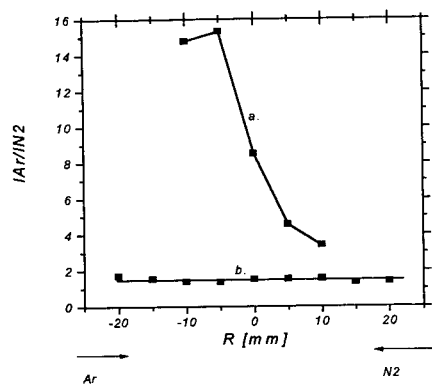


Fig. 5. Radial distributions of the ratio of the spectral lines of Ar and N<sub>2</sub> across the crossing point (a) and the stagnation point near the substrate (b).

### 1.3 The plasma-chemical processes in the plasma channels.

The scheme of the particles and their interactions inside the reactor with the two-hollow-cathode system is presented in Fig.6. In the primary plasma channels due to hollow cathode discharges there are the neutral ( $A_1, B_1$ ), excited ( $A_1^*, B_1^*$ ) and ionised ( $A_1^+, B_1^+$ ) particles of the working gas and the particles sputtered from nozzle surface: ( $A_2, B_2, A_2^*, B_2^*, A_2^+, B_2^+$ ). Therefore in the two primary plasma channels and also inside the hollow cathode discharges intensive plasma-chemical reactions take place. That should be expected especially if the working gas is composed from several sorts of gases.

In the crossing point, in the secondary plasma channel and in the stagnation point (that is the point of the interaction between the substrate and the secondary channel) one should expect intensive plasma-chemical reactions between the particles from both primary channels. This fact increases flexibility in the use of the reactor with multi-hollow-cathode system.

As an example of plasma-chemical reactions in the plasma channel the plasma-chemical ion-molecular reaction of ions ( $A^+$ ) with the neutral molecules ( $B_n$ ) will be investigated in more detail. The intensity of the particular plasma-chemical ion-molecular reaction of ions ( $A^+$ ) with the neutral molecules ( $B_n$ ) can be estimated under assumption that in the supersonic channel the plasma is approximately in the condition of the flowing afterglow. The radial diffusion of the particles does not play a substantial role due to supersonic axial velocity and shock waves on the boundary of the channel. The density of the neutral molecules [ $B_n$ ] is customary several orders higher with respect to the density of ions [ $A^+$ ] so that the variation of the density [ $B_n$ ] due to reactions with ions ( $A^+$ ) can be in our estimation neglected. Then for the variation of the ion density [ $A^+$ ] along the secondary channel can be written assuming that radial diffusion is negligible:

$$\frac{d[A^+(t)]}{dt} \approx -k_r [A^+(t)][B_n] \quad (3)$$

where  $[A^+]$  and  $[B_n]$  are the densities of ions and molecules respectively,  $k_r$  is the rate coefficient of the ion-molecular reaction between  $A^+$  and  $B_n$ .

The solution of the equation (3) is:

$$[A^+(t)] \approx [A^+(0)] \exp \{-k_r [B_n] t\}, \quad (4)$$

where  $t$  is the reaction time and  $[A^+(0)]$  is the density of the ions in the crossing point. Because the plasma in the secondary channel is flowing with drift velocity  $V_D$  for the reaction time  $t$  can be approximately written:

$$t \approx \frac{x}{V_D} \quad (5)$$

$x$  is the distance from the crossing point where the reaction time is  $t = 0$ .

By means of equation (4) it is possible to determine the decay of the ion density  $[A^+]$  due to reactions with molecules ( $B_n$ )

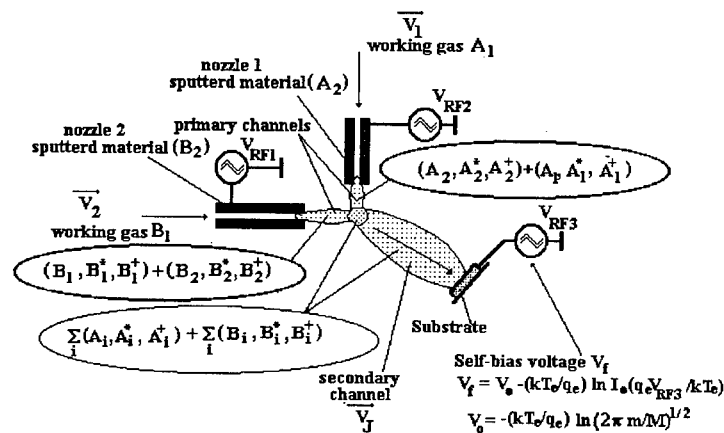


Fig. 6. Scheme of particles and their interactions inside the two-hollow-cathode system

and from obtained results roughly estimate the intensity of the investigated ion molecular reactions.

For example we assume that the rate coefficient  $k_i$  of the investigated ion-molecular reaction is of the order of  $10^{-9} \text{ cm}^3 \text{ sec}^{-1}$ , the density of the neutral molecules  $[B_n]$  is of the order of  $10^{14} - 10^{16} \text{ cm}^{-3}$ . The density of the ions  $A^+$  in the secondary channel decreases on 1 % of the value on the beginning of the channel  $[A^+(0)]$  (in the crossing point) after the reaction time of about  $t \approx 0.04 - 40 \text{ } \mu\text{sec}$ . For supersonic velocity of the particles in the secondary plasma channel the average drift velocity is of the order of  $V_D \approx 3 \cdot 10^4 \text{ cm/sec}$ . If we assume the distance between substrate and crossing point in the order of several cm the life time of the particles in the plasma channel is of the order of several tenth till hundred  $\mu\text{sec}$ . For the exact calculations of the reaction intensity along the channel it is necessary to take into account the recombination, the radial diffusion of the ions  $A^+$  and also the variation of the drift velocity in the supersonic channel. Nevertheless from above mentioned simplified consideration it could be seen that the density of the reaction product at the end of the secondary channel reaches the value which is in the order approximately the same as the value  $[A^+]$  of ion density at the beginning of the channel.

By means of the above presented considerations dealing with plasma-chemical processes in the plasma channels could be explained the experimental fact that by means of the reactor with hollow cathode it is possible to deposit thin films with defined stoichiometry. As it has been mentioned above up to now the  $\text{Ge}_3\text{N}_4$  [2] and more recently the  $\text{Cu}_3\text{N}$  [9], and  $\text{Al}_2\text{O}_3$  [10] stoichiometric thin films have been achieved.

## 2. THE HIGH PRESSURE TORCH DISCHARGE PLASMA SOURCE

This plasma source is based on the RF arc torch discharge. For this reason we will at first shortly describe the phenomena of the RF corona and the torch discharge and the transition of the corona to the torch discharge and transition to the arc torch discharge. Furthermore the plasma source which employ the high pressure RF torch discharge will be described.

## 2.1 The RF corona and the torch discharge

Generally the RF corona discharge is generated due to the strong intensity of the RF electric field in the neighbourhood of a sharp electrode edge where the discharge originates. This fact is confirmed by the spectrum of the discharge. Thus the main ionisation processes of neutral particles in the RF corona discharge are the ionisation collisions of the electrons accelerated in the strong electric field region.

When the RF power dissipated in the discharge in the polyatomic working gas increases then the vibrational temperature of excited neutral molecules also increases [13,14]. Due to the increase of the vibrational temperature increases also the role of thermal ionisation of the excited neutral molecules (with higher vibrational temperature). This thermal ionisation causes the decrease of the electric field intensity in the neighbourhood of the electrode and as a consequence also the ionisation caused by accelerated electrons decreases. In the region where the electron temperature and the vibrational temperature of the excited neutral molecules takes approximately the same value the corona discharge transits to the torch discharge. The transition between the corona and the torch discharge is not abrupt, but gradual [13,14]. At small RF power absorbed in discharge the discharge corresponds to the corona discharge while at higher power the torch discharge occurs. In Fig. 7 it is seen the dependence of neutral particles and electron temperatures on the RF power in the transition region between the corona and the torch discharge. The plasma of the torch discharge in the monoatomic working gas differs from that burning in the polyatomic gases. The transfer of the electron energy to the neutral particles in this case has been studied in [15]

When the RF power which is dissipated in the torch discharge increases above certain limit at which the temperature of the sharp electrode edge is so high that the electrode material is evaporated the plasma of the torch discharge is formed in the mixture of working gas and vapours of the evaporated electrode material. The properties of such torch discharge do not resemble those of a glow discharge but they are more like those of an arc discharge. For this reason it is necessary to consider such torch discharge as the arc torch discharge [14,16].

## 2.2 The plasma source with the arc torch discharge

The scheme of the experimental set up [3,4] is shown in Fig 8. The powered electrode of the arc torch discharge is made from the thin pipe the inner diameter of which is 1-2 mm and length several cm. The support for the electrode has been cooled by flowing water. The electrode was connected through the matching unit to the RF generator the frequency of which was 13,56 MHz. The RF power absorbed in torch discharge has been adjusted in such a manner that at the electrode edge the arc torch discharge was created. The working gas which flows from the nozzle stabilizes the arc torch discharge and well-defined plasma channel is created downstream the gas flow. It is important to notice that for generation of the plasma channel at the atmospheric pressure it is not necessary to place the torch arc discharge electrode nozzle inside the closed plasma-reactor chamber.

The pressure in our reactor chamber was maintained in the range approx. from  $10^3$  Pa up to atmospheric pressure. In such pressure range the nozzle of the powered electrode (thin pipe) cannot act as a hollow cathode [17] and only the edge of the electrode is involved in the discharge processes. Due to this phenomenon the torch plasma source differs from the source in the reactor with the hollow cathode [1,5] in which

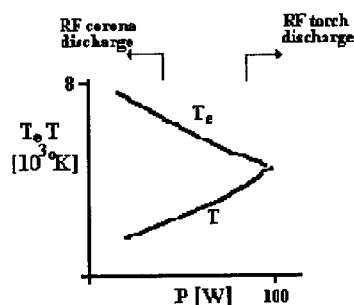


Fig. 7. Dependence of the neutral particles (T) and electron ( $T_e$ ) temperatures on the RF power

the primary RF plasma inside the reactor chamber induces the additional discharge inside the hollow cathode.

For atmospheric pressure of the working gas the RF power absorbed in torch discharge has been adjusted above 100 W and so at the electrode edge the arc torch discharge was created. At lower pressure approx.  $10^3$  Pa the RF power which was necessary to create the arc torch discharge was in the order of several tens of watts.

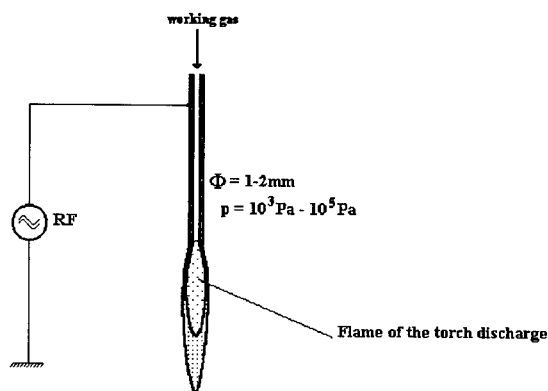


Fig. 8. Schematic drawing of the torch discharge device.

close to the electron temperature has been determined from molecular band of  $N_2$  second positive system. The magnitude of the vibrational temperature has been found approx.  $T_v \approx 2000$  K. For rotational temperature which was determined from the OH 306,4 nm band has been found the magnitude approx.  $T_r \approx 500$  K. The rotational temperature was assumed to be close to the temperature of the neutral gas in the place of the discharge.

The plasma source with the arc torch discharge can be fasten in the dielectric holder and used for surface treatments as a "RF plasma pencil". Up to now such plasma pencil has been used for treatment of archaeological artefacts in liquid environments [4].

### Acknowledgements

This work has been done in frame of the Association for Education, Research and Application in Plasma-Chemical Processes and was financially supported by grant 202/95/1222 of Grant Agency of Czech Republic and by project COST 515<sup>50</sup>.

### References

- [1] M. Šícha, L. Soukup, L. Jastrabík, M. Novák, M. Tichý, Surface and Coatings Technology 74-75 (1995) 212
- [2] L. Soukup, V. Peřina, L. Jastrabík, M. Šícha, P. Pokorný, R.J. Soukup, M. Novák, J. Zemek, Surface and Coating Technology, (1996) 280
- [3] A. Brablec, P. Slaviček, M. Klíma, V. Kapička, Proc. 18th Symposium on Plasma Physics and Technology Prague (1997) 193
- [4] Klíma M., Janča J., Zajíčková L., Brablec A., Sulovský P., Alberti M., Proc. 18th Symposium on Plasma Physics and Technology Prague (1997) 285
- [5] Šícha M., Bárdoš L., Tichý M., Soukup L., Jastrabík L., Baránková H., Soukup R.J., Touš J., Contrib. Plasma Phys. 34 (1994) 794.
- [6] M. Tichý, M. Šícha, L. Bárdoš, L. Soukup, L. Jastrabík, K. Kapoun, J. Touš, Z. Mazanec, R.J. Soukup, Contrib. Plasma Phys. 34 (1994) 765



- [7] M. Šícha, Z. Hubička, M. Tichý, M. Novák, L. Soukup, L. Jastrabík, J.F. Behnke, V. Kapička, K. Kapoun, M. Šerý, *Contrib. Plasma Phys.* 36 (1996) 605
- [8] L. Bárdoš, V. Dušek, *Thin Solid Films* 159 (1988) 265
- [9] L. Soukup, L. Jastrabík, M. Šícha, Z. Hubička, M. Novák, H. Šíchová, F. Fendrych, V. Valvoda, The deposition of the  $\text{Cu}_3\text{N}$  thin films by means of hollow cathode plasma-chemical reactor. (to be published)
- [10] L. Soukup, L. Jastrabík, M. Šícha, Z. Hubička, M. Novák, H. Šíchová, F. Fendrych, V. Valvoda, The deposition of the  $\text{Al}_2\text{O}_3$  thin films by means of hollow cathode plasma-chemical reactor (to be published)
- [11] Z. Hubička, M. Šícha, M. Novák, L. Soukup, L. Jastrabík, K. Kapoun, M. Šerý, V. Kapička, The RF Plasma-Chemical Reactor with the System of Multi-Hollow-Cathodes for the Surface and Coating Technologies (to be published).
- [12] *Plasma Diagnostics Techniques*, (ed. Huddelstone R.H., Leonard S.L.), Academic Press, New York, London, (1965)
- [13] El Gammal M., *Proc. VIII. ICPIG (Contributed papers) Vienna* (1967) 237.
- [14] Truneček V., *Proc. Conf. Unipolar High-Frequency Discharges, Brno* (Folia Sci. Nat. University Brno, Physica ) (1971) 3.
- [15] Janča J., *Folia Fac. Sci. Nat. University Brno*, 9 (1968) 31.
- [16] Popov V., Stolov A. L., *Učon. Zap. Kazan. Univerziteta, Kazan* 113 (1953) 53 (in russian).
- [17] Delcroix H. I., Mino H., Popovici C., *Proc. Int. Conf. Hollow Cathode Discharge Appl.* ( 1971) 18

## **Negative Differential Resistance, Oscillations and Constrictions of Low Pressure, Low Current Discharges**

Z.Lj. Petrović, I. Stefanović, S. Vrhovac and J. Živković

*Institute of Physics, University of Belgrade, P.O. Box 57, 11001 Belgrade, Yugoslavia*

**Abstract:** A brief review is given of the recent experimental and theoretical studies of low current diffuse discharges. Two models are developed, one that is based on phenomenological description by effective discharge circuit parameters and the other which is based on the calculation of the field profile from the ion distribution for uniform field. In the first case the physical process responsible for the development of the negative differential resistance is the dependence of the secondary electron yield on current through modification of the field close to the cathode. Experimental systems were developed to provide observables that include: breakdown voltage, volt-ampere characteristics (which in the low current limit is represented very well by a negative differential resistance), limits and the profile of the low current oscillations, frequency and damping of the induced oscillations, current growth coefficient and the onsets for constrictions. All of the observables are very well predicted by the theory based on the data taken from independent sources, once the steady state secondary electron yield has been fitted to predict the breakdown voltage.

### **1. INTRODUCTION**

In this paper we describe the results of studies of low-pressure, low-current but very high  $E/N$  discharges operating in the low current diffuse (Townsend dark) regime and of their transitions to constricted (normal) glow discharge. The experimental procedure and models were initially developed at the University of Colorado by Phelps and coworkers [1-4] and were further developed at the University of Belgrade [5,6]. The discharges studied here are obstructed or cathode dominated and are a good model for cathode fall or for some of the processes occurring in rf discharge sheaths.

The primary motive for these studies came from experimental observations that these discharges are inherently unstable (oscillate) even at very low currents, below the transition to constriction. Thus since we could not beat (remove) the oscillations we have joined them (started studying). While some evidence of negative differential resistance, which could lead to self sustained oscillations, existed in the literature [7-9] we believed that the effect so far has not been fully understood and generally appreciated.

### **2. EXPERIMENTAL SETUP AND PROCEDURE**

The discharge vessel (see Figure 1a) consists of parallel plane electrodes placed inside a quartz cylinder that prevents the long path breakdown. Thus we are able to operate both to the left and to the right of the Paschen minimum. The parallel electrodes can be positioned at several fixed distances ranging between 1 and 3 cm, but it is necessary to open the system to adjust the gap. In order to provide parallel surfaces, one electrode is fixed to a dielectric supports with different thicknesses. The test whether the surfaces are sufficiently parallel is performed by observing the radial distribution of emission in the diffuse low current regime (Townsend regime) and making sure that the discharge is not confined to one region only. The diameter of the electrodes in both experiments was of the order of 8 cm (area=50 cm<sup>2</sup>) while the gap was 1.05 cm. In the variable gap measurements, gaps of 1, 2 and 3 cm were used.

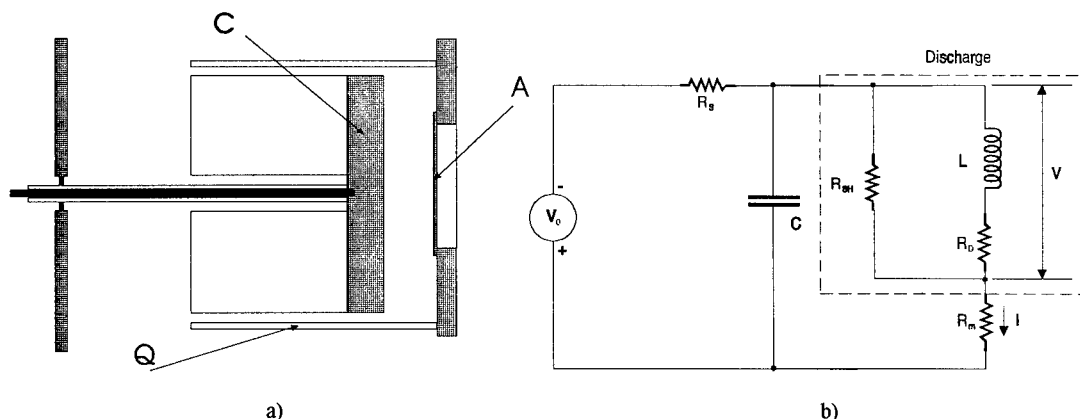


Figure 1: a) Discharge vessel: C-cathode, A-anode, Q-quartz tube and b) equivalent electrical circuit of the discharge.

The electrical circuit of the experiment is shown in Figure 1b. The system has provision for producing a pulse of current (up to 20 mA) in addition to a very small dc current (3-10  $\mu\text{A}$ ). The dc current is required to remove the breakdown time delays and achieve reproducible operating conditions. The dc current is as small as possible in order to avoid heating and/or significant conditioning of the cathode during the measurements. Yet it is not possible to maintain a stable dc current under all conditions (pressure, gap, gas).

Initial mode of operation was to use laser induced perturbation [1]. Discharge was operated at a low dc current. A pulse of a Q switched YAG laser, quadrupled in frequency, lasting 10-15 ns was focused onto the cathode inducing secondary electrons from the cathode and producing a pulse of current. This mode did not provide a possibility to record voltage current characteristic over a wide range of currents. It also required averaging over several shots to produce a smooth signal with a possible uncertainty due to the jitter. Yet laser pulsing provided data for ringing frequencies and damping corresponding exactly to the dc operating conditions, i.e. without questions whether the discharge has fully relaxed which may be relevant to the voltage pulsing technique. The voltage pulsing, on the other hand, is more versatile [2,5] and easier to perform. All the data presented here were obtained by voltage pulsing.

Before measurements, the surfaces of electrodes were treated by a relatively high current of the order of few mA until a stable breakdown voltage  $V_b$  was achieved. Initially, gold plated cathodes were used. We found that it is possible to achieve stable and reproducible operating conditions after treating the cathode to a hydrogen or argon discharge. Gold plated cathodes gave rise to quite large variations of operating conditions during the treatment, with breakdown voltages changing by a factor even greater than two. Gold plated electrodes had to be treated every day. Using a copper cathode, without gold, gives smaller variations of the breakdown voltage and it was possible to achieve reproducible conditions over periods of several weeks. The behavior of the two types of electrodes is consistent with formation of a very thin film of yet unknown nature on gold which is removed by ion bombardment. On the other hand the copper has a stable oxide layer which determines its secondary electron yield. If not treated, gold plated cathode will significantly change its properties during the measurements. In case of the copper cathode, even a treatment of the surface by currents of few mA over periods of up to one hour is not sufficient to remove the oxide film. The presence of a thin oxide layer may give stable operating conditions but may make it difficult to apply secondary electron yield measurements from an independent experiment due to a possible Malter effect.

We usually use a monitoring resistor  $R_m$  to determine the current in the low voltage circuit between the anode and the ground, but it is possible to run the discharge with zero resistance and still obtain the value of the current by applying a low input impedance amplifier. After a stable, low dc current, operation is achieved, pulses of higher current are triggered lasting only sufficiently long to make a reliable recording of voltage and current. Voltage is measured by two probes, as a difference, when a relatively

high monitoring resistor is used in the low voltage anode circuit to determine the current. Probes are connected directly to the discharge electrode terminals and remain connected even when not used. The effective capacitance of the electrode system and of the terminals is measured by pulsing the system without the discharge operating. The voltage and current transients are recorded by a digital oscilloscope and stored in a computer. In Figure 2 we show an example of voltage and current pulses recorded by the technique. It should be noted that even though the external voltage pulse is positive, the voltage change at the discharge is negative indicating a negative differential resistance.

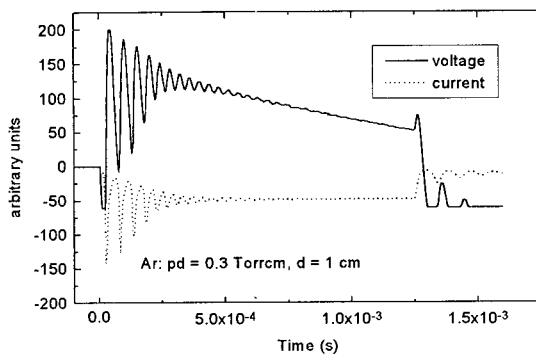


**Figure 2:** Voltage and current waveforms. The sloping voltage pulse is due to the discharging of capacitor, extrapolation to zero time is used to establish the voltage drop.

Recorded waveforms are fitted to obtain voltage and current before and after the pulse. The signal in the transient region is used to obtain the frequency and damping of damped oscillations induced by the high current pulse. When transition is made to the self-sustained oscillations the duration of the pulse is extended as much as possible to verify the regime and the waveform is recorded to give the frequency and for comparisons with calculations. The onset of self-sustained oscillations is recorded both by using a pulsed technique and by using dc measurements. Another observable that is recorded is the rate of increase of current when the pulse is applied [3,4]. It is recorded over sufficiently short time so it is possible to assume that it corresponds to a linear increase in voltage. In order to avoid a possible effect of the voltage pulse on detection of current, a differential amplifier is used with compensation adjusted for pulses when no discharge is created.

One of the electrodes can be made transparent by depositing a thin metallic film on glass. Such electrodes are used to study constrictions with a CCD camera that was needed to record the spatial distribution of light. This method gave only a limited possibility of getting a time resolved results so a photomultiplier was used to record the emission through the electrode as well.

So, to summarize, the observables in the experiment are: breakdown voltage, voltage-current characteristics and consequently the negative differential resistance, range of oscillations (damped and self sustained), frequency and damping of damped oscillations and the rate of rise of current. It is also possible to record the onset of constrictions which also corresponds to the behavior of the discharge in the low current regime.

### 3. MODELS

The basis for the model developed to describe the phenomena in low-pressure, low-current cathode dominated diffuse discharges is the idea that under those conditions a gradual accumulation of the space-charge effects affects the uniformity of the electric field. The field increases close to the cathode due to the shielding by charged particles and decreases elsewhere (see Figure 3). An increase in the field in a small region leads to a drastic increase of electron production due to the  $E/N$  dependence of the ionization

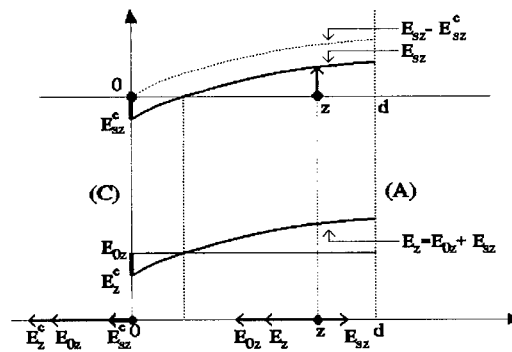


**Figure 3:** Electric field distribution in the gap between electrodes. Space charge effect (s) is integrated and added to the homogeneous field. Field at the cathode is denoted by the superscript 'c'.

coefficient. Thus the decrease in other regions may be greater and the overall voltage decreases giving rise to a negative differential resistance. The perturbation of the field is assumed to be small so the initial distribution of charges used for calculation of the space charge effects is that for the unperturbed field. Another assumption is that of locality. It has two aspects. One is that we can represent the ionization rate coefficient by its local field value, which may be questionable for very high  $E/N$  conditions. Yet it was shown by Stojanović and Petrović [10] that even when electron beams develop it is still possible to assign a reasonably well defined value to the ionization coefficient up to very high  $E/N$ , much higher than the upper limit covered here. A more important aspect of locality is that the secondary electron yield at the cathode is determined by the field right at the cathode, implying equilibrium for ions. This assumption may fail for large mean free paths.

Two different models were developed to analyze the experimental data [3]. The first is a phenomenological model which basically means that some of the physical phenomena were assigned to effective circuit parameters of the discharge. The second model is more physical as it attempts to correlate observables with physical parameters such as ionization and secondary electron yield coefficients and their dependence on  $E/N$ .

### 3.1 Phenomenological Model

The basis for the phenomenological model is an idea that the secondary electron yield may be represented as a function of both voltage and current:

$$\gamma = \gamma_p + k_v V + k_I I. \quad (1)$$

The first assumption is easily understood, while the second requires further explanation. The current dependence of gamma is due to the fact that increasing of the current leads to an increased space charge shielding effect and consequently a higher field close to the electrode (while overall voltage may drop). Thus in principle both dependencies are associated with the field close to the cathode.

Another assumption of the model is that the changes occur on the time scales greater than the ion transit time  $T$ . Thus it is possible to associate the electron current  $I_e$  at the cathode (at time  $t+T$ ) with the current at the time  $t$  by equation:

$$I_e(0, t+T) = I_p(0, t+T) + \gamma I_e(0, t) [\exp(\alpha(t)T) - 1] + \delta \gamma I_e(0, t) \exp(\alpha(t)T), \quad (2)$$

where  $I_p(0, t+T)$  is the photoelectric current produced by irradiation of the cathode and  $\delta$  is the secondary electron production term due to impact of fast electrons on anode surface.

After applying Taylor expansion and using definitions of coefficients this equation may be converted to:

$$\frac{dI}{dt} = \left[ \frac{(1+\gamma)I_p}{\gamma T} + \frac{(g-1)I}{T} - \frac{Ik_v}{\gamma(1+\gamma)} \frac{dV}{dt} \right] \left[ 1 + \frac{Ik_I}{\gamma(1+\gamma)} \right]^{-1}, \quad (3)$$

where  $g$  is the round trip charge multiplication factor that may be associated with the breakdown condition:

$$g(t) = \gamma[(1+\delta)\exp(\alpha(t)T) - 1]. \quad (4)$$

The electric circuit of the discharge with effective representation of the discharge is shown in Fig. 1b and when we solve the equations for that circuit, another differential equation is obtained:

$$\frac{dV(t)}{dt} = \frac{1}{R_s C} [V_0(t) - V(t) - I(t)(R_s + R_m)] - R_m \frac{dI(t)}{dt}. \quad (5)$$

The circuit parameters correspond to those defined in Fig. 1b.

Equations (3) and (5) are a complete set of equations which may be solved numerically for any signal provided that initial assumptions are acceptable. Analytical solutions may be obtained for a small

signal theory using the ac component as a small perturbation on the steady state (SS) current ( $I = I_{ss} + \beta i$ ;  $V = V_{ss} + \beta v$ ). The corresponding equations are:

$$\left[ 1 + \frac{I_{ss} k_I}{\gamma_{ss}(1 + \gamma_{ss})} \right] \frac{di}{dt} = \frac{I_{ss}}{T} \frac{\partial g}{\partial V} v - \frac{I_{ss} k_V}{\gamma (1 + \gamma)} \frac{dv}{dt} + \frac{I_{ss} k_I}{T \gamma_{ss}} i, \quad (6)$$

$$\frac{dv}{dt} = - \frac{v}{R_s C} - \frac{i}{C} \left[ 1 + \frac{R_m}{R_s} \right] - R_m \frac{di}{dt}, \quad (7)$$

which give formulae for the frequency and damping of induced oscillations:

$$\omega^2 = \frac{I_{ss}}{R_s C T} \left[ (R_s + R_m) \frac{\partial g}{\partial V} - \frac{k_I}{\gamma_{ss}} \right] \times \left[ 1 + \frac{I_{ss} (k_I - R_m k_V)}{\gamma_{ss} (1 + \gamma_{ss})} \right]^{-1} - k^2, \quad (8)$$

$$k = \frac{1}{2 R_s C} \left[ 1 + \frac{I_{ss} (k_I - (R_s + R_m) k_V)}{\gamma_{ss} (1 + \gamma_{ss})} - \frac{R_s C I_{ss}}{T} \left( \frac{k_I}{\gamma_{ss}} - R_m \frac{\partial g}{\partial V} \right) \right] \times \left[ 1 + \frac{I_{ss} (k_I - R_m k_V)}{\gamma_{ss} (1 + \gamma_{ss})} \right]^{-1}, \quad (9)$$

limits of selfsustained oscillations:

$$I_{ss}^{tr} = \left[ \frac{R_s C}{T} \left( \frac{k_I}{\gamma_{ss}} - R_m \frac{\partial g}{\partial V} \right) + \frac{(R_s + R_m) k_V - k_I}{\gamma_{ss} (1 + \gamma_{ss})} \right]^{-1}, \quad (10)$$

and most importantly clearly indicate that the primary cause for the effect of negative differential resistance is the dependence of the secondary electron yield on current ( $k_I$ ):

$$R_D = \frac{-k_I}{\gamma_{ss} \partial g / \partial V} \left[ 1 + \frac{I_{ss} k_I}{\gamma_{ss} (1 + \gamma_{ss})} \right] \times \left[ 1 + \frac{I_{ss} k_I}{\gamma_{ss} (1 + \gamma_{ss})} \left[ 1 - \frac{k_V}{\gamma_{ss} \partial g / \partial V} \right] \right]^{-1}. \quad (11)$$

These equations also reveal the influence of external circuit elements on experimental observables.

In the low current limit these equations become:

$$\omega^2 = \frac{1}{LC} \left[ 1 + \frac{(R_m + R_D)}{R_s} \right], \quad (12)$$

$$k = \frac{1}{2 R_s C} + \frac{(R_m + R_D)}{2 L}, \quad (13)$$

$$R_D = - \frac{k_I}{\gamma_{ss} \partial g / \partial V}. \quad (14)$$

### 3.2 Physical Model

It is more physical to represent the secondary yield dependence on the local electric field in front of the cathode rather than on voltage and current. In order to do so one should calculate the field distribution and the shift of the field at the cathode ( $E_s^c$ ) as well as the overall field distribution and the corresponding voltage change ( $\partial V$ ). This is the basis of the "physical model" of Phelps and coworkers [3]:

$$\delta V := - \int_0^d E_{sz}(z) dz = - \frac{\hat{\gamma}}{\hat{\gamma} + \gamma \alpha d \exp(\alpha d)} \frac{1}{\varepsilon_0} \frac{j}{W_+} f^{(1)}(\alpha_0, d), \quad (15)$$

where

$$f^{(1)}(\alpha_0, d) = d^2 \left[ \frac{1}{2} + \frac{\exp(-\alpha_0 d)}{\alpha_0 d} - \frac{(1 - \exp(-\alpha_0 d))}{(\alpha_0 d)^2} \right]. \quad (16)$$

Implicit assumption of the model is that the ion distribution is that which corresponds to the unperturbed field, which is used in the Poisson equation to determine the field distribution:

$$\frac{dE_{sz}}{dz} = \frac{1}{\varepsilon_0} \frac{j_z}{W_+} [1 - \exp(\alpha_0(z-d))]. \quad (17)$$

When linear terms are retained in Eq. (17) and both electron ionization and secondary yield coefficients are developed to the first term in the electric field (the latter only depends on the field at the cathode), one may obtain an explicit formula for the negative differential resistance normalized to the area ( $A$ ) of electrodes and the square of the interelectrode spacing ( $d$ ):

$$R_N := \frac{A \delta V}{I d^2}. \quad (18)$$

The correlation with the current dependence of the secondary electron yield may also be found:

$$k_I = \frac{d^2 f(\alpha d) \gamma \hat{\gamma}}{A V_0 \varepsilon_0 W_+} = \frac{df(\alpha d)}{A \varepsilon_0 W_+} \frac{d\gamma}{d|E|}. \quad (19)$$

At this point it is important to explain the relationship between the two models. Both models are certainly less accurate than numerical solutions to partial differential equations such as those used in fluid models of rf discharges. The two models described here, however, allow us to establish analytical relationships between different quantities and thus to provide physical insight into the main mechanisms. The phenomenological model gives differential equations for voltage and current waveforms which are used to fit the experimental waveforms and to determine the observables in the experiment. The physical model associates some of the measured quantities with the more fundamental properties of basic physical quantities such as dependence of the secondary electron yield on the electric field. It is not possible to maintain the same level of simplicity of analytical formulae if one attempts to include the electric circuit equations at the level of physical model. In addition the phenomenological model covers a broader range of physical quantities. Therefore it is necessary to maintain application of both models, the first in the analysis of raw experimental data and the second to study the basic causes of the negative differential resistance.

A similar but somewhat modified theory was developed for higher pressures where ions are not the only or the dominant feedback mechanism [11]. Under those conditions photons or metastables may provide a significant effect. For the present, ion dominated, conditions the effect of the modification of the field due to a small but still significant space charge effect is well represented by the formulae above. Calculations of the field profile and deviations from the uniform field distributions of electron and electron density show very small effects for all but the most severe conditions at the onset of transition to the glow (constriction) [3,4].

The present theory is similar, but less restrictive, to the theory of Naumov and Melekhin which was developed earlier and independently of our work, and which has been applied to a more narrow range of experimental data [12,13].

In the remaining of the text we shall compare the theoretical predictions with experimental results. The theory has only one fitting parameter, that is the value of the steady state secondary electron yield which is obtained by fitting the breakdown voltage. It is very strongly affected by surface conditions and therefore has to be obtained directly from the data. All other parameters (in case of hydrogen) are taken from independent sources, mostly experimental.

#### 4. U-I CHARACTERISTICS

The textbooks usually represent volt-ampere characteristics of Townsend dark discharges as a constant with a sudden (usually shown by dashed lines) transition to the constricted glow. The first point is that the negative differential resistance (NDR) i.e. negatively sloped characteristics is usually not discussed, sometimes even not indicated on the graph, even though it has been in the literature since the forties [8]. In fact it appears that a number of specialists in the field are not aware of the universality of the NDR in the dark Townsend regime.

Another point worth discussing is the smooth, uniquely defined appearance of the volt-ampere characteristics as usually presented in the textbooks. Phelps has compiled data for several gases [14] and there are very few examples that the data from different sources agree on the most important properties. In particular the current defining the transition to the constricted regime varies by several orders of magnitude and so does the shape of the dependence. One may, however, accept as expected, the variation of the actual value of the dc breakdown voltage, which is very sensitive to surface conditions.

We have performed a series of measurements for different gases under conditions that were more controlled than those for most other experiments reported in the literature. An essential item was to carefully control that the oscillations did not develop. Another assumed explanation for the large scatter of experimental data in the literature was that local heating of surfaces could cause inconsistencies between different experiments. However, we could not find any evidence of significant heating for currents up to 30 mA and for the configuration of our experiment [1] even when a thermocouple was positioned within one millimeter from the surface. We however discovered that discharge at moderate and higher currents could modify significantly the conditions at the surface and we had to develop a pulsed technique to limit such effects, which limited possible heating of the surface even further.

##### 4.1 Data for U-I characteristics

Gases that were studied include Ar, N<sub>2</sub>, H<sub>2</sub>, CH<sub>4</sub> and SF<sub>6</sub>. Thus we cover both atomic and molecular gases, with and without long lived metastables and we also have a representative of electronegative gases. It is also important to note that identity of ions may change for some gases depending on conditions, particular examples are H<sub>2</sub> and SF<sub>6</sub>.

In Figure 4. we show one example of a recorded volt ampere characteristics. As it is difficult to present small changes in voltage on top of a large breakdown voltage, we only present the difference. In Figure 5 voltage difference is shown as a function of  $id^2$ , which is expected scaling and the agreement between the two characteristics for a factor of three different gap lengths is excellent. The line corresponding to the unscaled negative differential resistance (i.e. as a function of  $i$  shown on  $id^2$ ) of the discharge is also shown. Most other characteristics for the low current regime for all gases agree very well. The differences in the glow region are however greater.

It is therefore, possible to determine accurately and with great reproducibility volt-ampere characteristics of gas discharges. The profiles agree well with the expected behavior. Through most of the low-current regime it is possible to define a constant negative differential resistance.

##### 4.2 Negative differential resistance

Measurements of volt-ampere characteristic show that it is possible to define a constant negative differential resistance (NDR) that describes well most of the characteristics, certainly its low current limit. The second model described here predicts  $d^2$  scaling for NDR and in Figure 6a we show experimental confirmation of that prediction in case of argon. The case of argon is particularly important as it has only one species of ions. For hydrogen the linearity starts to break down but only slightly at the highest  $d$  covered here, indicating a change in the identity of dominant ions as the pressure decreases. For SF<sub>6</sub> (see Figure 6b) there are two groups of lines in the  $R_D$  versus  $d^2$  graph. The low  $pd$  data agree and so do the high  $pd$  data, but the two corresponding lines differ. It appears that here, the identity of ions that carry the



feedback changes as the  $pd$  changes. In cases where relevant additional data are available it is possible to predict the values of NDR relatively accurately.

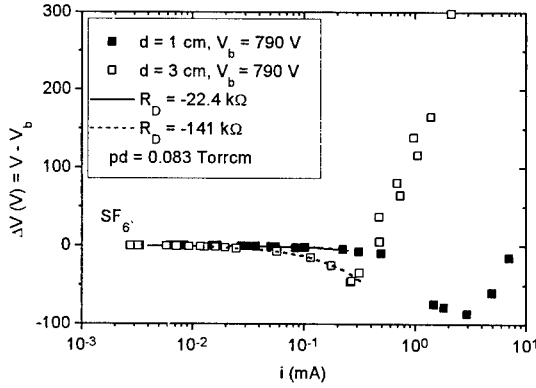


**Figure 4:** Volt-ampere characteristics for  $\text{SF}_6$ : symbols-experimental data for different  $d$ , lines-fits for  $R_D$  [5].

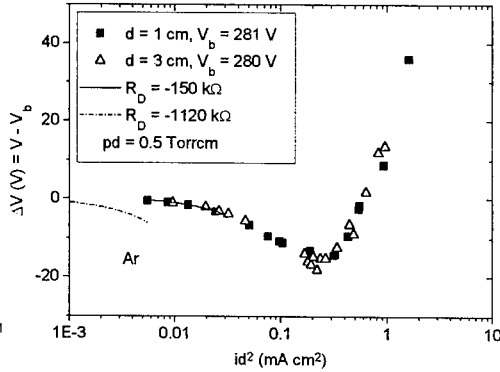


**Figure 5:** Voltage difference versus  $id^2$  for Ar: symbols-experimental data for different  $d$ , lines-fits for  $R_D$  [5].

We have found some situations where NDR starts increasing with a tendency to become infinite close to the onset of constriction. It is believed that this phenomenon is more universal than observed but that oscillations develop once it occurs preventing us from detecting it. The observation has, however prompted the development of a nonlinear theory.

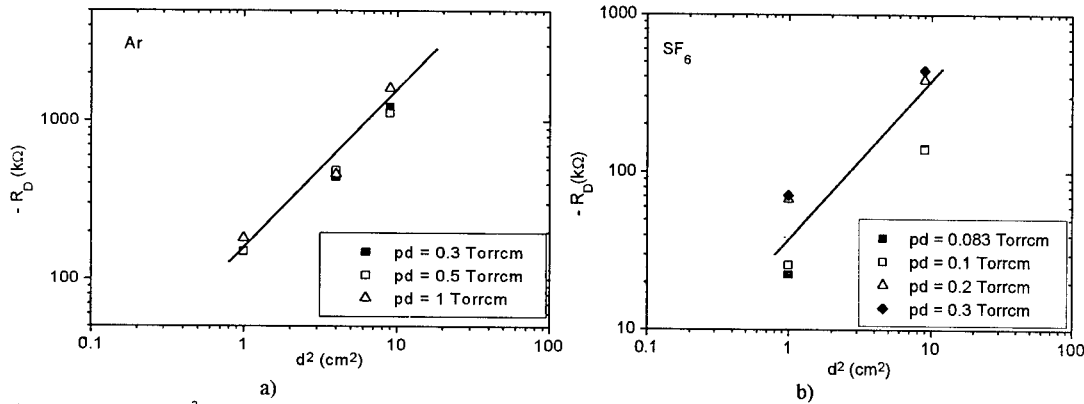


**Figure 6:**  $R_D$  versus  $d^2$  for Ar (a) and  $\text{SF}_6$  (b): symbols-experimental data for different values of  $pd$  [5]. Solid line indicates a linear dependence.

### 4.3 Nonlinear behavior

Extending development of ionization and secondary yield coefficients beyond the linear term, with a similar extension in the corresponding equations leads to:

$$\delta V \approx \delta V_s^{(1)} + \left( \frac{j_z}{\varepsilon_0 W_{+z}} \right)^2 \left[ \frac{k_6}{k_2} f^{(2)}(\alpha_0, d) + \left( \frac{k_3^2}{4k_1 k_2} - \frac{k_5}{k_2} \right) (f^{(2)}(\alpha_0, d))^2 \right], \quad (20)$$

where  $\delta V_s^{(1)}$  is given by Eq. (15) and

$$f^{(2)}(\alpha_0, d) = \frac{1}{\alpha_0^2} \left[ d \exp(-2\alpha_0 d) + \alpha_0 \exp(-\alpha_0 d) d^2 + \frac{1}{3} \alpha_0^2 d^3 - 2d + \frac{2}{\alpha_0} (1 - \exp(-\alpha_0 d))^2 + \frac{1}{2\alpha_0} (1 - \exp(-2\alpha_0 d)) \right], \quad (21)$$

$$k_6 = -d^2 \gamma_0^2 (\exp(\alpha_0 d)) \alpha'' , \quad (22)$$

$$k_2 = 2d^2 \gamma_0^2 (\exp(\alpha_0 d)) \alpha' + 2d \gamma' . \quad (23)$$

We do not have enough room here to explicitly define the remaining terms in equation (20), a more detailed explanation is given as a contributed paper to this conference [15]. The terms presented here will dominate in case that  $f^{(2)}$  is small. The two terms presented here are given explicitly to point out that non-linearities depend directly on derivatives of ionization coefficient and secondary electron yield.

In principle it is also possible to expect non-linearities due to modification of the spatial distribution of ions away from that for the uniform field, due to non-equilibrium effects and also due to emission of resonant photons or metastable diffusion to the surface.

In all measurements, the volt-ampere characteristics is linear in the low current limit, linearity extending quite close to the onset of free running oscillations or transition to constrictions. Nevertheless there are few examples of nonlinear behavior away from that transition resulting in a strong current dependence of the negative differential resistance (NDR) [16]. It appears that NDR would have a tendency to extend to very high values right at the transition. It is however not certain yet what the actual cause for the non-constant NDR is, for those examples.

The ultimate non-linearity of course, occurs at the transition to constriction. The point of transition appears to be very accurately defined and there is also a well defined hysteresis.

## 5. OSCILLATIONS

Presence of NDR, leaves a possibility that free running oscillations may be generated when the overall resistance in a closed loop becomes less than zero. The loop is usually formed with the stray capacitance which is generally significantly larger than the electrode capacitance. Equations (8) and (9) are able to predict the shape of the oscillations in the low current range. We have however observed one or two transitions with a significant change in the shape of the self sustained oscillations which presumably correspond to transition to the glow regime. The model developed here cannot describe the glow conditions as it assumes almost uniform electric field. In any case, the low current free running oscillations are one of the observables that can be used. For practical purposes it is important to establish ranges of oscillations and stable operation of low current diffuse discharges as a function of the series resistance. Such ranges can be predicted very accurately from the theory [1,3] on the low current end, again the high current limit requires model that includes selfconsistent calculation of the field in the glow regime.

If, however, one wants to obtain reliable data for modeling and consequently obtaining an insight into the relevant processes, it is better to use damped oscillations because they can be made small enough in order not to make large perturbations on the steady state discharge. In addition it is possible to obtain analytic solutions for their properties. In Figure 7, we show an example of experimental data and calculations of the frequency ( $\omega$ ) and the damping coefficient ( $k$ ) of such oscillations for hydrogen. Theory gives a very good prediction of the experimental data in most cases. For most gases, however, additional experimental data for secondary electron yields and its dependence on  $E/N$  are lacking so fitting of the characteristics of induced oscillations may be a satisfactory source of data needed to predict other properties of the discharge.

It has been shown experimentally [14] that it is possible to damp the oscillations and extend the region of stable operation by increasing the monitoring resistor  $R_m$  which is within the loop where oscillations may occur. The condition for stable operation is  $R_m > R_D$  and in most cases it is efficient though very high values of  $R_m$  are not practical to use. However, as discussed earlier  $R_D$  may increase towards the onset of constrictions making it impossible to remove oscillations.

It has been predicted [17] that for mixtures of electronegative and electropositive gases a special type of oscillations will develop in glow and with a frequency much lower than that for the ion feedback driven oscillations that were discussed above. We have observed occurrence of low frequency self sustained oscillations in the glow regime for pure  $SF_6$  only at very low  $pd$  (see Figure 8.). We could not

operate the discharge in the exact conditions (10 Torr) used in the theoretical model so it is still uncertain whether the causes for the two low frequency self sustained oscillations are the same.

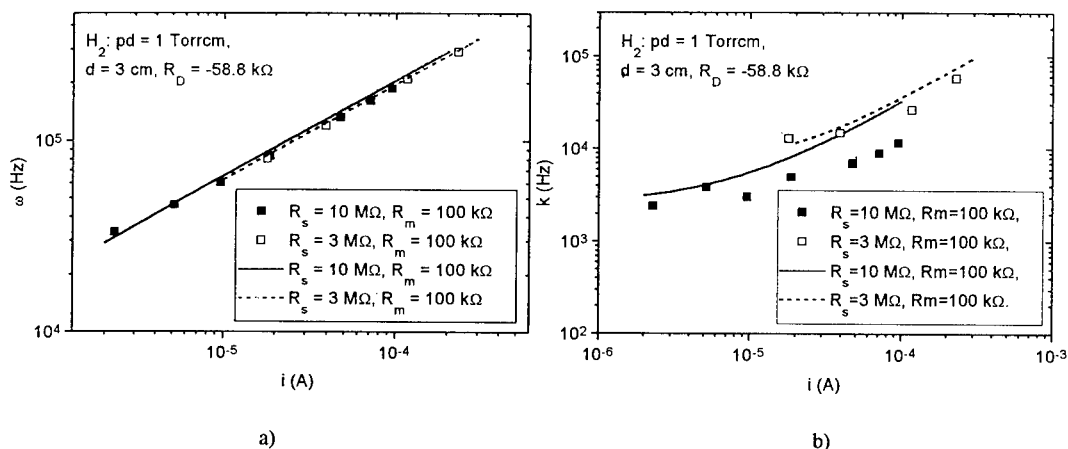


Figure 7: Experimental data and calculations of the a) frequency ( $\omega$ ) and b) damping coefficient ( $k$ ) for hydrogen.

## 6. CONSTRICTIONS

Low frequency oscillations are also observed associated with the beginning of constrictions. It was possible to make a pulse of voltage and current into the region close to the onset of constrictions. The pulse stabilizes in the diffuse mode and after some time a transition is made to the constricted discharge. The transition goes through a series of initially-growing low-frequency oscillations. Later, as the mean value of the voltage changes, oscillations are damped. The frequency may be associated with the main process driving the transition. The regime is not identified on the basis of time resolved emission, which is time averaged and the constricted mode dominates. We conclude that the discharge starts in the diffuse mode on the basis of smooth extension from the diffuse conditions. When pulse increases only a little further, the transition is made directly to the constricted discharge.

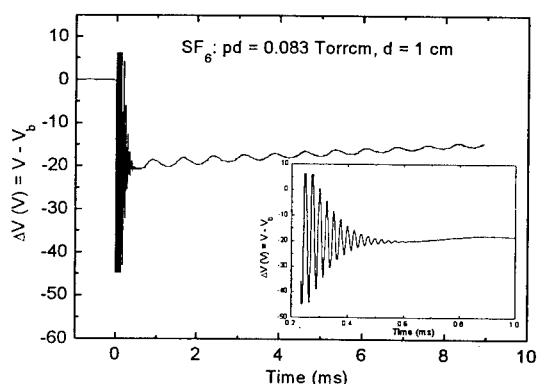


Figure 8: Voltage waveform in  $\text{SF}_6$  with both the high and low frequency oscillations. The insert shows the first millisecond magnified.

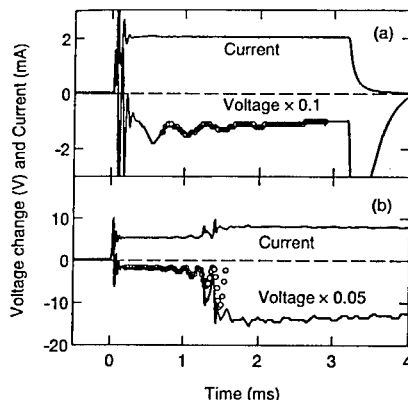


Figure 9: Voltage and current transients in Ar for pressure of 0.12 Torr. The upper trace in each pair shows the discharge current, while the lower trace shows the voltage change. These traces show the transition from a diffuse to constricted regime occurring during the pulse [4].

We have made a systematic study of the onsets of constrictions in a number of gases, hydrogen, argon and nitrogen in particular. Some differences in the behavior of constricted glow discharges are

observed, as well as the differences due to different  $E/N$  or  $pd$  values. A particularly interesting situation occurs in argon at 0.12 Torr cm [4]. The discharge seems to concentrate close to the walls with very small intensity of emission at the axis which is unlike the behavior of other gases and even of the same gas at different  $pd$ . The observation was labeled as "donut" constriction and it actually proved to be a regular constriction rotating close to the walls with a frequency slightly larger than 1 kHz. The reasons for rotation were not fully understood yet.

Comparisons between our observations and some of the available theories indicate that the emission normalized to current remains constant over a wide range of currents [4].

## 7. CONCLUSION: WHY AND WHAT NEXT?

Low current diffuse, or dark Townsend discharges are the simplest form of discharges. Therefore it is essential to achieve a full understanding of their basic physics and to use them to test the models for more complex discharges with strongly inhomogeneous field [18]. For this purpose we need reproducible data obtained under controlled and well defined conditions and we hope that our work may be a step towards providing such data. In particular, such discharges have been used to study low pressure, high  $E/N$  situations [10] with a strong non-equilibrium which to a large degree represent the non-equilibrium non-local electron transport found in sheaths of dc and rf discharges. The most difficult parameter to control is the secondary electron yield from the cathode surface that varies over a large range of values depending on the conditions at the surface. Therefore the only technique that takes care of this problem would be to use the breakdown voltage to establish its value. Even gold plated surfaces have a strongly variable conditions that may be stabilized by running a discharge.

Low current diffuse discharges are also often used to perform swarm experiments [19] and therefore determine data on atomic and molecular processes. Assumption of uniform field that may be essential for such purposes should be verified by following some of the procedures described in this paper. Such experiments are the only method to sufficiently simplify the discharge in order to be able to rule out competing processes and identify some of the physical phenomena such as heavy particle excitation [20], excitation after surface reflection of heavy particles [21] and electron backscattering [10] and its influence on discharge kinetics. Those are just few examples of processes which are usually neglected in discharge modeling but which may be significant under special circumstances and which have been studied in low current discharges i.e. in swarm-like situations.

In addition to our work there is a number of recent theoretical [16,17,22] and experimental [23] studies of low current diffuse discharges which illustrates a continuing interest. Unfortunately we have no room in this paper to give a more detailed review of the entire field.

Finally we may still expect to find and understand some new physics even in such simple systems, and being simple it could even make them well suited for studies of such processes. Constrictions are usually associated with the glow discharge conditions and thus modeled from that viewpoint. Yet the "decision" to change into constriction is "made" in the low current Townsend discharge as a result of processes described here. In particular it is the accuracy and stability of the current where transition takes place that has to be explained on the basis of the low current regime physics, not the glow. Constriction is in fact one of the simplest and first studied forms of selforganization. A simple one dimensional model of competing current channels with the addition of a small perturbation gives the constriction and approximately accurate conditions for the onset of constriction [24]. It is based on the  $E/N$  dependence of the ionization coefficient only. Of course, it cannot give accurate properties of the discharge once the constriction is achieved but it still describes the basic aspect of selforganization of the charges. Important and still puzzling aspect of the process is the fact that charges do not interact directly under the low current conditions. Interaction exists, as described in this paper but it is indirect, through shielding of the field and with additional nonlinearity brought in by the  $E/N$  dependence of the ionization coefficient.

### Acknowledgements

The authors are grateful to Dr. A.V. Phelps who initiated this program and gave us considerable help and advice in addition to permission to use some of his data. Part of this work was performed during the stay of one of the authors (Z.Lj.P) at Joint Institute for Laboratory Astrophysics, University of Colorado at Boulder. Ministry of Science and Technology of Serbia funded to a small degree part of the project carried out at the Institute of Physics, University of Belgrade. Authors are also grateful to Slobodan Manola and MTT INFIZ for partial support.

### References

- [1] Z.Lj. Petrović and A. V. Phelps, *Phys. Rev. E* **47** (1993) 2806-2815.
- [2] B. M. Jelenković, K. Rózsa and A. V. Phelps, *Phys. Rev. E* **47** (1993) 2816-2824.
- [3] A. V. Phelps, Z. Lj. Petrović and B. M. Jelenković, *Phys. Rev. E* **47** (1993) 2825-2838.
- [4] Z.Lj. Petrović and A. V. Phelps, (submitted for publication) *Phys. Rev. E*.
- [5] I. Stefanović and Z.Lj. Petrović, *Jpn. J. Appl. Phys.* **36** (1997) 225-259.
- [6] I. Stefanović, Z. Velikić and Z.Lj. Petrović, in Contributed Papers of the 22<sup>nd</sup> International Conference on Phenomena in Ionized Gases, Hoboken, New Jersey, USA (1995) pp. 123-124.
- [7] R. S. Sigmond, in Proceedings of the 4<sup>th</sup> International Conference on Ionization Phenomena in Gases, Uppsala (1959), ed. N. R. Nilsson (North-Holland, Amsterdam, 1960) pp. 189-194.
- [8] M. J. Druyvesteyn and F. M. Penning, *Rev. Mod. Phys.* **12** (1940) 87-174.
- [9] M. Hayashi and Y. Miyoshi, *Bulletin Nagoya Inst. Technology* **13** (1962) 339-345.
- [10] V. Stojanović and Z.Lj. Petrović, (to be published).
- [11] A. V. Phelps, (unpublished).
- [12] V. N. Melekhin and N. Yu. Naumov, *Sov. Phys. Tech. Phys.* **29** (1984) 888-892.
- [13] V. N. Melekhin, N. Yu. Naumov and N. P. Tkachenko, *Sov. Phys. Tech. Phys.* **32** (1987) 274-279.
- [14] A. V. Phelps, *JILA Data Center Report* **35** (1993)
- [15] S.B. Vrhovac, I. Stefanović and Z.Lj. Petrović, *Proc. XXIII ICPIG (Toulouse) II* (1997) 44-45.
- [16] Z.Lj. Petrović and A. V. Phelps, (unpublished).
- [17] I. Pérès and L. C. Pitchford, *J. Appl. Phys.* **78** (1995) 774-782.
- [18] V. I. Kolobov and A. Fiala, *Phys. Rev. E* **50** (1994) 3018-3032.
- [19] Z.M. Jelenak, Z.B. Velikić, J.V. Božin, Z.Lj. Petrović and B.M. Jelenković, *Phys. Rev. E* **47** (1993) 3566-3573.
- [20] V.D. Stojanović, B.M. Jelenković and Z.Lj. Petrović, *J. Appl. Phys.* **81** (1997) 1601-1603.
- [21] Z.Lj. Petrović, B.M. Jelenković and A.V. Phelps, *Phys. Rev. Lett.* **68** (1992) 325-327.
- [22] I.D. Kaganovich, M.A. Fedotov and L.D. Tsendin, *Tech. Phys.* **39** (1994) 241-245.
- [23] K. Rózsa, L. Szalai and Z. Donko, *Europhys. Abstracts* **20 E** (1996) 161-162.
- [24] Z.Lj. Petrović, (unpublished).

## Progress in the Development of Table-Top Discharge-Pumped Soft X-Ray Lasers

J.J. Rocca, F.G. Tomasel<sup>1</sup>, C.H. Moreno<sup>2</sup>, V.N. Shlyaptsev<sup>3</sup>, M.C. Marconi<sup>4</sup>, B.R. Benware, J.J. Gonzalez, J.L.A. Chilla<sup>5</sup> and C.D. Macchietto

*Department of Electrical Engineering, Colorado State University, Fort Collins, CO 80521, U.S.A.*

**Abstract.** The demonstration of large soft x-ray amplification in a discharge-created plasma has opened a new path to the development of compact and practical soft x-ray lasers. We review our progress in the development and study of these ultrashort wavelength lasers. The field has advanced from the first observation of large amplification in a discharge-created plasma in Ne-like Ar [J.J. Rocca, V.N. Shlyaptsev, F.G. Tomasel, O.D. Cortazar, D. Hartshorn, and J.L.A. Chilla, *Phys. Rev. Lett.* **73**, 2192 (1994)], to the demonstration of an extremely compact saturated laser at 46.9 nm. In this paper we give an overview of these and other selected results. They include the observation of large amplification (gain-length product of 7.5) in Ne-like S at 60.8 nm in material ablated from a solid target by a discharge, and preliminary results of the search for gain at a shorter wavelength in Ne-like Ca. A recent study of the spatial coherence of the capillary discharge 46.9 nm Ne-like Ar laser, which provides the first experimental measurement of a monotonic increase of the spatial coherence with length in a soft x-ray amplifier, is also summarized.

### 1. INTRODUCTION

Following the first demonstrations of soft x-ray lasing in plasmas generated by large laser facilities in 1984 [1,2], the goal of realizing more compact and efficient soft x-ray lasers that could have widespread use in applications has received much attention. With this motivation considerable effort has been devoted to explore amplification schemes that use smaller laser drivers, leading to significant progress in the past few years [3-7]. Alternatively, it has been recognized that direct discharge excitation of the gain medium could result in increased laser efficiency and simplicity. However, in pulse-power driven plasmas a major obstacle has been axial inhomogeneities produced by non-symmetric compressions and instabilities, which result in severe distortion of the plasma column that destroys the amplification. To efficiently generate axially uniform plasma columns with the large densities of multicharged ions necessary for soft x-ray amplification we have proposed the use of fast capillary discharges [8, 9]. This approach was successful in obtaining for the first time large soft x-ray amplification in a discharge-created plasma [10], and has led to the demonstration of the first saturated table-top soft x-ray laser, in Ne-like Ar [11].

In the capillary discharge scheme an elongated, needle-like plasma with remarkable axial uniformity is created by a fast current pulse that excites preionized material contained in a capillary channel defined by insulating walls. In the fast capillary discharges we use for excitation of collisional soft x-ray lasers, the electromagnetic forces of the rapidly rising current pulse compress the plasma creating a shock wave. The current distribution is influenced by the wall plasma created by plasma radiation and heat conduction [11, 12]. Following the initial phase of the discharge, the soft x-ray emitting region of the plasma is rapidly compressed to form a plasma column 200-300  $\mu\text{m}$  in diameter [13]. The optimum plasma temperature and density for lasing occur several nanoseconds before stagnation, when the first compression shock wave reaches the axis. Subsequently, the plasma density continues to increase as the plasma stagnates, and laser action ceases due to increased refraction and collisional thermalization. The high efficiency with which these fast capillary discharges can generate highly ionized plasma columns is illustrated by the remarkable similarity of the two argon spectra shown in Fig. 1. The spectrum in Fig. 1a) corresponds to a 43 kA, 30 ns full width at half maximum (FWHM) discharge through a 2.5-mm-diam Ar-filled capillary channel, while the spectrum in Fig. 1b) is for a 1 MA current implosion in a multi-Terawatt pulse power generator (Gamble II, see Ref. [14]). Moreover, the capillary discharge structure has the advantages of providing a very good initial plasma

<sup>1</sup> On leave from Departamento de Física, Facultad de Ingeniería, Universidad Nacional de Mar del Plata, Argentina

<sup>2</sup> Permanent address: Instituto de Física del Plasma, Universidad de Buenos Aires, CONICET, Argentina

<sup>3</sup> Present address: Lawrence Livermore National Laboratory, U.S.A.

<sup>4</sup> Present address: Departamento de Física, Universidad de Buenos Aires, CONICET, Argentina

<sup>5</sup> Present address: Coherent Inc., U.S.A.

symmetry, and a short compression time which leads to stable plasma columns. This has allowed us to generate axially uniform plasma columns with a very large length-to-diameter ratio ( $l/d=500-1000$ ) and up to 20 cm in length.

In the following two Sections we summarize laser results obtained in Ne-like Ar using these discharges, and the following Section discusses lasing in Ne-like S. Preliminary results of the search for gain in Ne-like Ca are reported in Section 5, followed by a discussion of the measurement of the spatial coherence of the Ne-like Ar laser.

## 2. AMPLIFICATION IN Ne-LIKE Ar

The first observation of large soft x-ray amplification in a discharge-pumped amplifier was realized in the  $J=0-1$  line Ne-like Ar at 46.9 nm [10, 15]. In this initial experiment a fast discharge, having a half-period of 60 ns and a peak current of approximately 40 kA, was used to excite Ar plasma columns in 4-mm-diameter channels drilled in polyacetal. The capillary channel was placed in the axis of a 3 nF liquid-dielectric circular-parallel-plate capacitor. The capacitor was charged by a Marx generator and rapidly discharged through the capillary channel by closing a spark gap switch pressurized with SF<sub>6</sub>. The gain at 46.9 nm was determined by measuring the integrated line intensity as a function of plasma column length. The spectra of Fig. 2 show the dramatic increase of the laser line intensity as a function of capillary length. In the spectrum of the 3-cm-long capillary, the intensity of the  $J=0-1$  line of the Ne-like Ar is observed to be smaller than the intensity of the surrounding lines. In the 6-cm-long capillary amplification makes this line more intense than the many neighboring lines, and in the 12-cm-long plasma column the laser line totally dominates the spectrum. Analysis of the data of this first experiment yielded a gain coefficient of 0.6 cm<sup>-1</sup> and a gain-length product of 7.2 for the 12-cm-long capillaries. As summarized in the next Section, subsequent experiments conducted utilizing longer plasma columns under optimized discharge conditions and double-pass amplification yielded an effective gain-length product of 27, the largest reported to date for a table-top soft x-ray amplifier [11]. Also, spectra we obtained for different capillary lengths in the wavelength region corresponding to the  $J=2-1$  line of Ne-like Ar at 69.8 nm showed a supralinear increase of this line, indicative of gain. However, the gain in this line was much smaller than for the  $J=0-1$  line [15], and a significant increase in the amplification is still required to make it of practical interest. Small amplification in this line in a capillary discharge was more recently also observed by Hildebrand *et al.* [16].

## 3. SATURATED OPERATION OF THE Ne-LIKE Ar AMPLIFIER

A major step in the development of compact ultrashort wavelength lasers consists in saturating the gain in the amplifier and in demonstrating substantial output energies. At this condition, which occurs when the laser

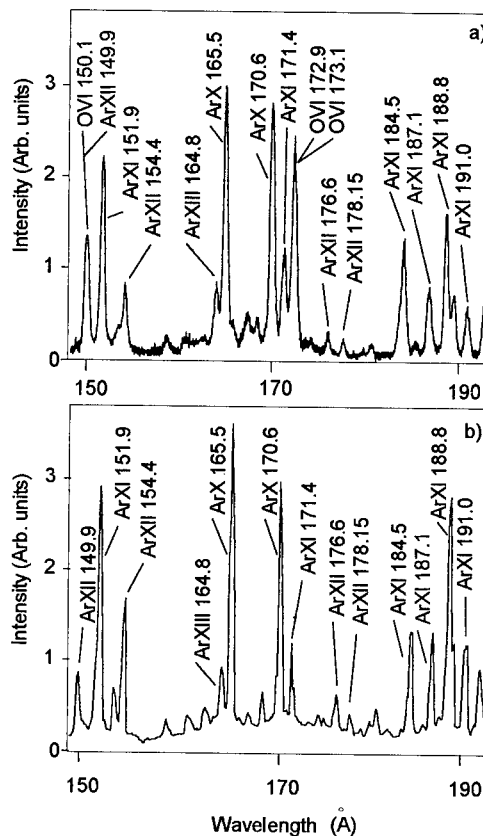


Figure 1. Argon spectra corresponding to a) 43-kA, 30-ns FWHM discharge current pulse through a 2.5-mm-diam capillary [9], b) 1 MA current implosion in the Gamble II generator [14]. Transition wavelengths are in Å.

intensity reaches the saturation intensity, an important fraction of the energy stored in the laser's upper level can be extracted. Depending on the specific amplifier characteristics, this amounts to overcome barriers that are imposed by the small gain volumes and short plasma lengths, by the short duration of the gain, or by plasma inhomogeneities and limiting refraction effects. To reach gain saturation in our discharge-pumped Ne-like Ar laser we conducted experiments in longer plasma columns, and used an iridium mirror to implement double-pass amplification measurements. This resulted in the first clear observation of gain saturation in a table-top soft X-ray amplifier [11, 17].

The experiments were conducted exciting 4-mm-diam capillaries filled with 700 mTorr of Ar gas with current pulses of approximately 39 kA peak current having a half cycle duration of about 70 ns. A detection system consisting of a 2.2 m grazing incidence spectrograph with a microchannel plate (MCP) intensified CCD array detector was used to measure the relative variation of the laser energy as a function of plasma column length. Absolute measurements of the laser output pulse energy were performed using a fast vacuum photodiode having a calibrated Al photocathode [11]. The results of single-pass amplification measurements for capillary plasma columns up to 15.8 cm in length are shown as open circles in Fig. 3. At these discharge conditions, the energy of the laser pulse is observed to increase exponentially for lengths up to about 12 cm, where it begins to saturate. A fit of the data corresponding to plasma columns up to 11.5 cm with the Linford formula [18] yields a gain coefficient of  $1.16 \text{ cm}^{-1}$ . Saturation of the intensity is observed at gain-length products of about 14. Laser pulse energies of  $6 \mu\text{J}$  were measured to exit the 15.8-cm-long plasma columns.

Double-pass amplification experiments allowed us to substantially increase the laser pulse energy and to study the saturation behavior for significantly longer effective plasma column lengths. The double-pass amplification measurements were performed using a flat iridium mirror for two different plasma column lengths: 9 and 14 cm. In the 9-cm-long capillaries the laser intensity enhancement due to the mirror was measured to be 63x. In contrast, the enhancement observed in the 14-cm-long capillaries was in the average only 8x. This behavior is indicative of saturation of the amplification in the second pass. The increase in the laser energy measured in the double-pass experiments in the 14-cm-long capillaries corresponds to laser pulse energies of up to  $30 \mu\text{J}$  and to beam intensities larger than the computed saturation intensities of  $56\text{--}78 \text{ MW/cm}^2$ . The saturation intensity was calculated considering an ion temperature of 100 eV, and an effective-to-radiative lifetime ratio for the laser upper level between 20 and 30 for plasma densities of  $5\text{--}8 \times 10^{18} \text{ cm}^{-3}$ , as computed by our magnetohydrodynamic calculations for these discharge conditions [11].

The measured saturation behavior is in good agreement with the result of two independent radiation

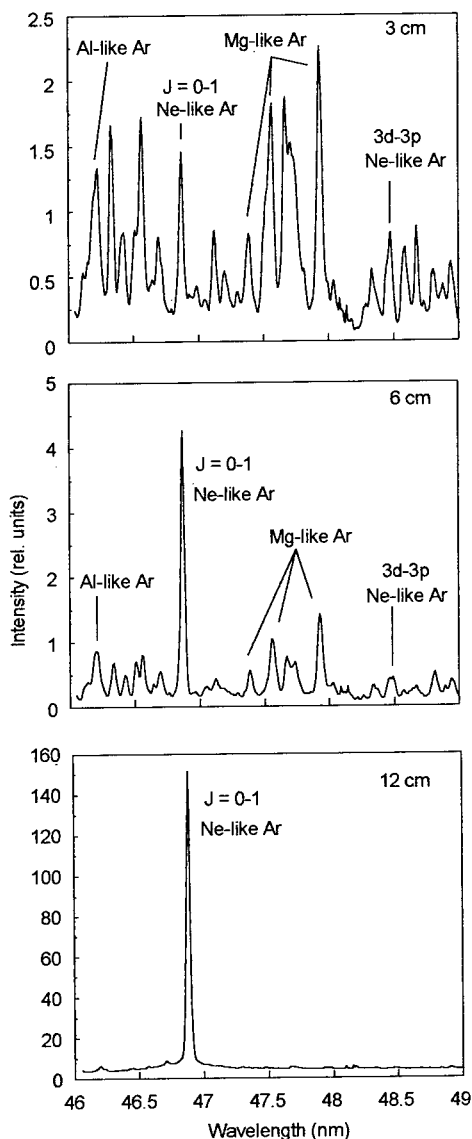


Figure 2. Axial spectra from Ar plasma columns 3-, 6-, and 12-cm-long. A dramatic increase of the  $J=0-1$  line of Ar IX at 46.9 nm as a function of length is observed. The spectra correspond to  $38 \pm 1 \text{ kA}$  discharges through 4-mm-diam capillaries.



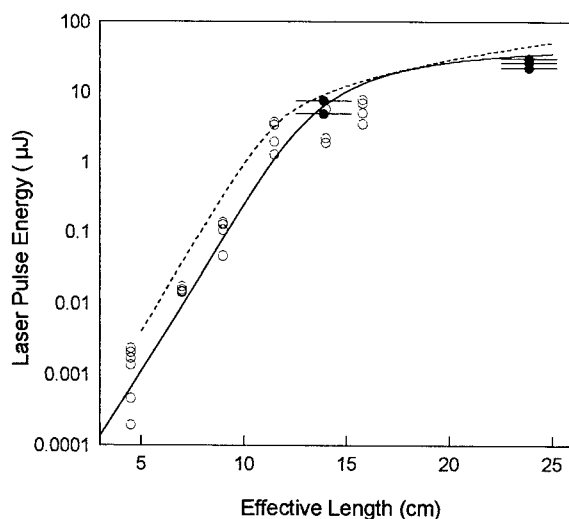


Figure 3. Measured and computed 46.9 nm laser output energy as a function of capillary discharge plasma column length. Single- and double-pass measurements are indicated by open and full circles, respectively. The solid line is the result of simple radiation transport calculations assuming parabolic gain and density profiles. The dashed line was computed with a hydrodynamic/atomic physics code.

transport models for the capillary plasma columns. Computations of the variation of the laser energy as a function of plasma column length were conducted by solving the radiation transport equation for an inhomogeneously broadened transition, taking into account line narrowing, refraction effects, and gain saturation. It should be noticed that consideration of refraction losses is essential to adequately describe the measured energy dependence on plasma column length. The solid line in Fig. 3 is the result of calculations performed assuming parabolic gain and density profiles, while the dashed line corresponds to computations conducted for the time dependent electron density and gain profiles obtained from magnetohydrodynamic and atomic physics calculations conducted with the code Radex [19]. We have also studied the influence of an externally applied axial magnetic field on the capillary discharge soft x-ray laser performance. An optimized magnetic field of about 0.15 T was observed to increase the uniformity and intensity of the soft x-ray laser beam by decreasing the plasma density gradients at the time of lasing [20].

Based on these results, we have succeeded in developing a very compact saturated 46.9 nm laser of size comparable with that of many widely utilized visible and ultraviolet gas lasers. This laser generates subnanosecond pulses with energies up to 25  $\mu\text{J}$  and with a beam divergence that varies between 3.5 and 6.5 mrad depending on the discharge conditions [21].

#### 4. DEMONSTRATION OF LASING IN VAPOR CREATED BY ABLATION OF A SOLID MATERIAL: AMPLIFICATION IN Ne-LIKE S

Recently, we have also demonstrated lasing in the  $J=0-1$  transition of Ne-like sulfur ions at 60.8 nm in vapor produced by discharge ablation of a solid target [22]. This result is of particular interest because it shows the feasibility of also obtaining ultrashort wavelength amplification by discharge excitation in materials that are solid at room temperature. For this experiment our original discharge setup [9] was modified to allow the injection of the sulfur vapor into the capillary channel through a hole in the ground electrode. The sulfur vapor was produced ablating the wall of a 5-mm-diam, 2-cm-long secondary capillary channel drilled in a sulfur rod with a slow current pulse delivering 200 J in about 50  $\mu\text{s}$ . The vapor generated by this capillary discharge was injected into the main capillary channel and was subsequently excited by a fast current pulse of 35-37 kA peak amplitude to generate a narrow plasma column with the necessary conditions for amplification.

Under optimized conditions, strong lasing was expected to occur in the  $3s\ ^1P_1 - 3p\ ^1S_0$  line, as is the case in the discharge pumped Ne-like Ar laser [10]. This  $J=0-1$  line has been accurately identified at 60.84 nm in spectra obtained from laser-created sulfur plasmas [23], and has recently been observed to lase in laser-created plasmas generated using the Asterix iodine laser facility at the Max Planck Institute for Quantum Optics [24]. Figure 4 shows a spectrum obtained under optimized laser conditions in the spectral region spanning from 58.8 to 61.2 nm using a tin filter. The spectrum corresponds to a 37 kA discharge through a 4-mm-diam, 16.8-cm-long channel filled with 460 mTorr of sulfur vapor. The spectrum is completely dominated by the  $J=0-1$  line transition of Ne-like sulfur, which appears at  $60.84 \pm 0.015$  nm. Another line of Ne-like sulfur (the  $3p\ ^1P_1 - 3d\ ^1P_1^0$  transition at 60.12 nm [23]), that in absence of amplification should have similar intensity, also falls in the spectral range of Fig. 4. The fact that in our plasma column the intensity ratio of these two lines is observed to be at least 100 is clear evidence of amplification in the  $J=0-1$  line.

Figure 5 shows the measured variation of the integrated line intensity of the  $J=0-1$  line of Ne-like sulfur as a function of plasma column length. An increase of about 1.6 in the plasma column length is observed to increase the integrated intensity of the line by a factor 13. This corresponds to a gain coefficient of  $0.45\text{ cm}^{-1}$ , and a gain-length product of 7.55 for 16.8-cm-long capillaries. Strong amplification was observed for a broad range of pressures, from 300 to 700 mTorr and for currents between 33 and 38 kA.

Lasing occurs shortly before stagnation of the plasma column, as in the case of Ne-like Ar [11]. The region of gain is a narrow plasma column of about 0.03 cm in diameter surrounded by a lower-density plasma containing sulfur ions of a lower degree of ionization, which in turn is surrounded by material ablated from the capillary walls. The deceleration of the plasma column near the axis prior to stagnation results in a velocity gradient that, due to motional Doppler broadening, considerably facilitates the radial escape of the lower laser level radiation. At the time of lasing, which for our discharge conditions is observed to occur near the time

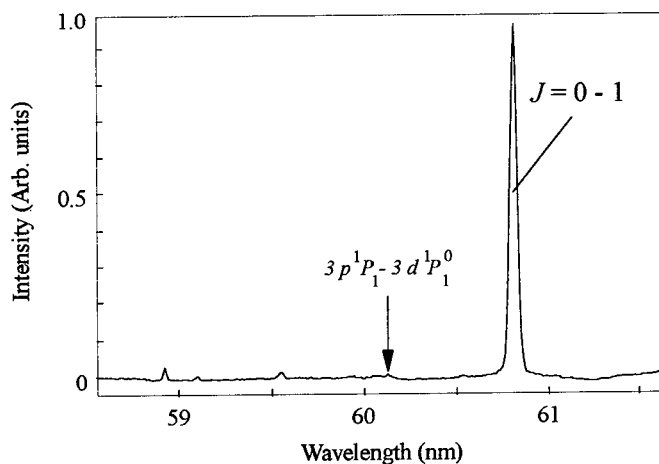


Figure 4. Spectrum of the axial emission of the sulfur plasma column in the region between 58.5 and 61.5 nm. The spectrum corresponds to a 37 kA discharge through a 4-mm-diam, 16.8-cm-long capillary filled with 460 mTorr of ablated sulfur vapor. The  $3s\ ^1P_1 - 3p\ ^1S_0$  line of Ne-like sulfur completely dominates the spectrum, while the 60.12 nm  $3p\ ^1P_1 - 3d\ ^1P_1^0$  line of the same ion, that in absence of amplification should have similar intensity, is not observed.

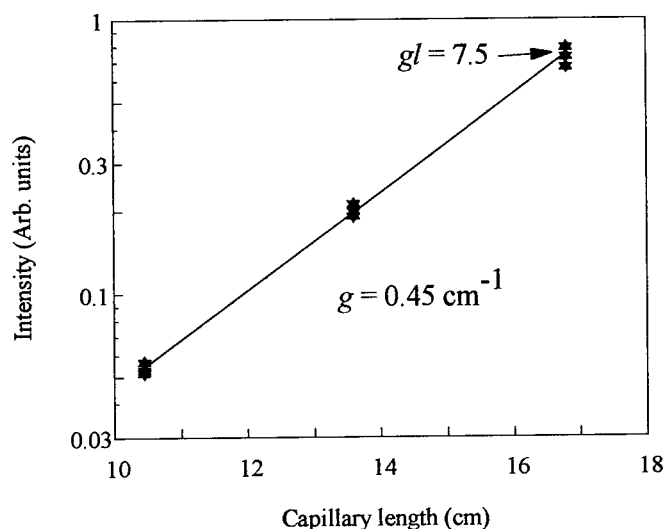


Figure 5. Variation of the integrated intensity of the  $J=0-1$  line of Ne-like sulfur as a function of plasma column length. The line is a fit with the Linford formula [18], which results in a gain coefficient of  $0.45 \pm 0.01\text{ cm}^{-1}$ , and to a  $gl$  product of  $7.5 \pm 0.15$  for the 16.8-cm-long plasma column.

of maximum current, the electron density and temperature in the gain region are computed to be about  $2\text{-}3 \times 10^{18} \text{ cm}^{-3}$  and 60-80 eV, respectively. As described below, this temperature corresponds to a plasma that is overheated with respect to the temperature range  $T_e = 20\text{-}40$  eV for maximum Ne-like sulfur abundance in a steady-state plasma.

According to the approximate scaling laws of atomic kinetics valid for lasing in Ne-like ions in steady-state conditions the gain scales for ions of charge  $Z$  approximately as  $G \sim Z^{4.5}$  [25]. Consequently for sulfur, a gain  $\sim 3$  times smaller than that for the  $J=0-1$  line of argon could be estimated. As mentioned above, in the case of the  $J=0-1$  line of argon the effective gain was measured to reach  $1.16 \text{ cm}^{-1}$  [11], value that is smaller than the maximum computed gain of  $1.5\text{-}1.8 \text{ cm}^{-1}$  due to refraction. According to the above scaling law the effective gain in Ne-like sulfur would be expected to be rather small, less than  $0.3 \text{ cm}^{-1}$ . Our computations using the code Radex [12, 19, 26] indicate important contributions to the generation of the population inversion by plasma overheating and transient population effects. Due to the exponential dependence of the excitation rates on the electron temperature, a larger population inversion and, consequently a larger gain, arises from overheating. Such overheating of the plasma respect to steady-state ionization conditions can be more easily achieved in low- $Z$  elements like sulfur, due to a large decrease of the ionization time with ion charge. In addition, in this sulfur laser transient population effects are found to play a more important role than in the argon laser. A transient increase in the population inversion can arise when the characteristic time of the rise of the excitation is of the order of the effective lifetime of the laser upper level [27]. While in these relatively long-lived discharge plasmas transient effects are not nearly as dramatic as in plasmas produced by subpicosecond lasers [4], their contributions to the gain can be noticeable. The computations indicate that, in the case of sulfur, transient population effects can increase the gain by 20-40%. As a result of plasma overheating and transient population effects the maximum gain in the  $J=0-1$  line of Ne-like sulfur is computed to approach  $1 \text{ cm}^{-1}$ , a value which taking into account refraction losses is in satisfactory agreement with the measured effective gain of  $0.45 \text{ cm}^{-1}$ .

## 5. SEARCH FOR GAIN IN Ne-LIKE Ca

The natural extension of the work summarized in the previous Sections is the search for gain in capillary plasmas at shorter wavelengths [15]. The demonstration of lasing in Ne-like sulfur at 60.8 nm showed the feasibility of obtaining amplification by collisional excitation in discharge-created plasmas produced by ablation of solid targets. To obtain lasing by collisional excitation at wavelengths shorter than that of the Ne-like Ar, 46.9 nm, it is necessary to search for amplification in elements heavier than Ar [15]. We have obtained spectra of Ca plasmas with the objectives of identifying the  $J=0-1$  line of Ne-like Ca and searching for amplification. The  $3s^1P^0_1 - 3p^1S_0$  line of Ne-like Ca at 38.327 nm was first identified in laser created-plasmas [28], and later observed by us in a discharge-created plasma [29]. It was also observed to lase in plasmas created in the Asterix iodine laser [30].

For the calcium experiments discussed herein, capillaries were made by pressing a mixture of CaO and  $\text{Ca}_3\text{N}_2$  powder in a 2:1 ratio to 65 MPa. Plasmas containing Ca were produced by ablating the walls of these capillaries with a slow current pulse, followed by a fast high current pulse that ionizes and compresses the plasma as in the previous experiments. Figure 6 shows a time-resolved spectrum of the axial plasma emission in the neighborhood of

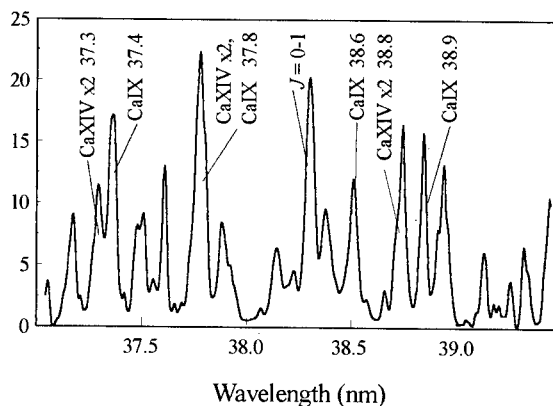


Figure 6. Time-resolved spectrum of capillary plasma containing Ca ions in the region between 37 and 39.5 nm showing line emission at 38.3 nm, the wavelength of the  $J=0-1$  line of Ne-like calcium.

38.3 nm for a 75 kA discharge through a 3.5-mm-diam, 5-cm-long capillary channel. The first half-cycle duration of the current pulse was 56 ns. The spectrum corresponds to the emission 33 ns after the initiation of the current pulse and has a time resolution of about 5 ns. A strong line is observed at  $38.33 \pm 0.015$  nm, which corresponds well with the wavelength of the  $J=0-1$  laser line of Ne-like Ca. The line has an intensity comparable to that of neighboring resonant lines of CaIX (Mg-like Ca) and CaX (Na-like Ca). The second order of CaXIV (N-like Ca) lines is also observed, confirming that the plasma is sufficiently hot to create a high abundance of Ne-like Ca. Experiments with CaH<sub>2</sub> capillaries have yielded similar spectra, encouraging further experiments.

## 6. STUDY OF THE SPATIAL COHERENCE OF THE Ne-LIKE Ar LASER

Good transverse spatial coherence will be essential in realizing the full potential of these sources in some important applications. Current soft x-ray lasers face the difficulty of achieving a good coherence without the aid of an optical cavity, mainly due to their short gain duration. Measurements of the spatial coherence of laser pumped soft x-ray lasers have been reported [31-33], but most of them correspond to a single amplifier length of the particular laser studied. Several theoretical studies have been conducted to understand the spatial coherence of soft x-ray amplifiers [34-38]. In general, they predict an improvement of the coherence with amplifier length. This is the result of a decreasing number of modes guided along the amplifier column due to gain guiding and refractive anti-guiding [34]. Such build-up of the coherence is essential in achieving very good spatial coherence in cavity-less soft x-ray amplifiers. However, this monotonic increase of the spatial coherence with amplifier lengths had not been previously experimentally observed in soft x-ray lasers. We have measured a monotonic increase of the spatial coherence as a function of plasma column length in a capillary discharge soft x-ray amplifier.

The measurements were conducted in the 46.9 nm line of Ne-like Ar for capillary plasma column lengths up to 16.4 cm. The spatial coherence was measured recording the diffraction produced when the soft x-ray laser beam intersects a knife edge (Fig. 7, left) [39]. This technique has been recently utilized to observe an improvement in the coherence of a laser pumped Ne-like Zn laser when a reflecting multilayer mirror was used [40]. It has the advantage of determining in a single shot the degree of coherence for any two points on the illuminated region of the detector plane that correspond to a line perpendicular to the knife edge. The interference fringes were recorded with a gated detector consisting of the combination of a gated MCP, phosphor screen, image intensifier, and a CCD array. To conduct the measurements of the spatial coherence as a function of plasma column length, the knife edge was placed in a radial position respect to the beam. This gives a measurement of the coherence in the tangential direction. The measurements were conducted in 4-mm-diam polyacetal capillaries filled with Ar gas at pressures of 600 mTorr. The plasma was excited by current pulses of approximately 37 kA peak current, having a first half cycle duration of about 70 ns.

Figures 7a) and 7b) (right) show the measured diffraction patterns corresponding to capillaries with length between 8 and 16.4 cm. The improvement of the coherence with amplifier length is evident in the increased fringe visibility observed in the diffraction patterns corresponding to the longer plasma columns. The observed diffraction patterns compare well with those obtained numerically using the results of a wave-optics model for the generation and propagation of the radiation in the capillary plasma column, shown in Fig. 7c) (right). The model used to calculate the coherence of the beam produced by the capillary discharge soft x-ray laser is similar to that developed by Feit and Fleg [37], but takes into account the temporal variation of the electron density and of the gain coefficient, and was extended to two dimensions.

The data of Fig. 7, and that corresponding to other similar series of measurements, were analyzed to quantify the coherence function and its dependence on amplifier length. The result is shown in Fig. 8. The coherence is observed to increase monotonically with capillary length. Good agreement is observed with the result of wave-optics calculations, represented by a line in the same figure. This is, to our knowledge, the first observation of a monotonic increase of the transverse spatial coherence with amplifier length in a soft x-ray laser. For the longest capillaries studied, 16.4 cm, the coherence length in the tangential direction was determined to be about 4.5 mm in the detector plane situated at 5.89 m from the exit of the amplifier. This corresponds to an effective coherence angle of 0.8 mrad and to an effective source size of 26  $\mu$ m FWHM. The total beam divergence of about 5 mrad is caused by refraction due to the electron density gradients.

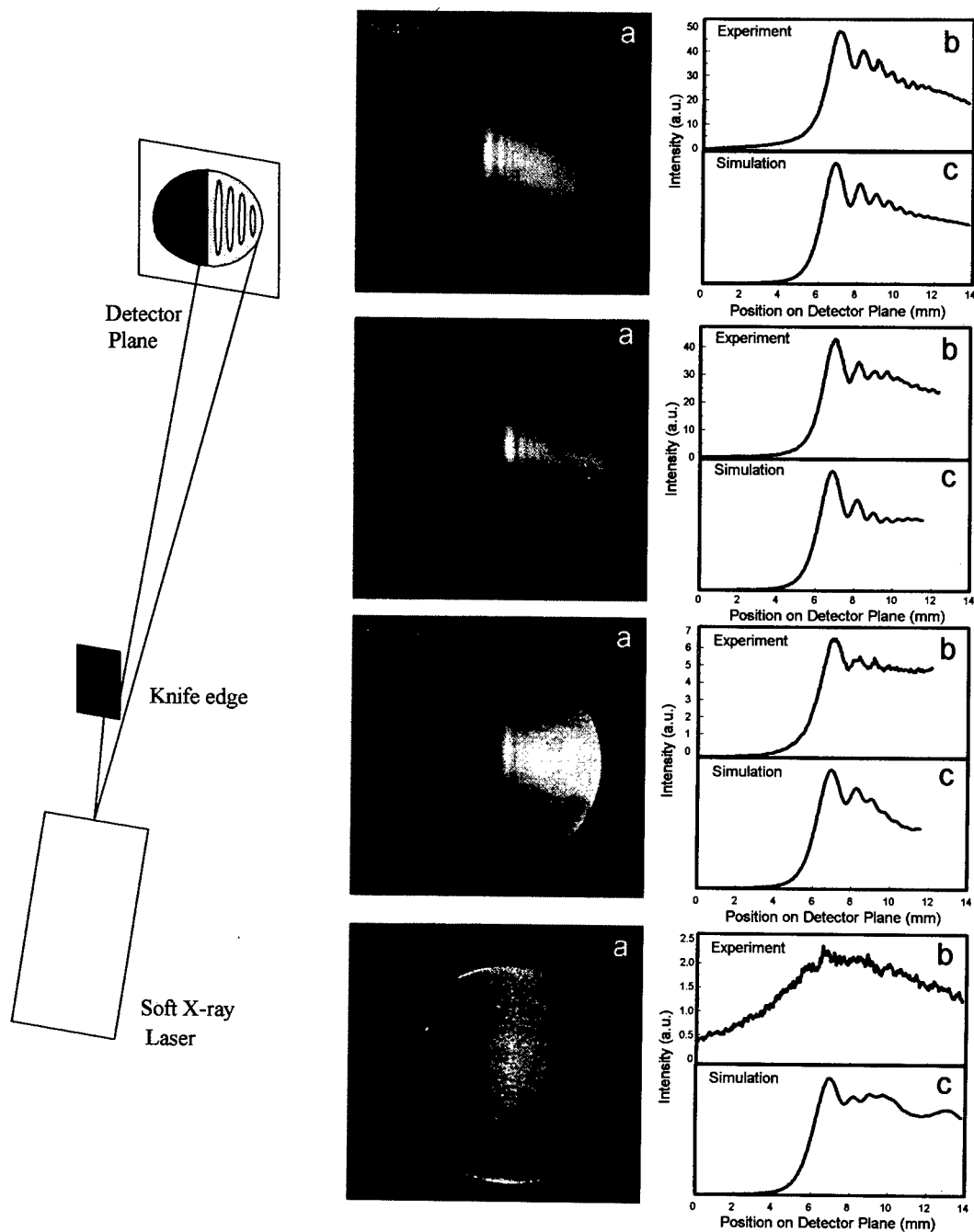


Figure 7. Left. Schematic representation of the set up used to measure the spatial coherence of the Ne-like Ar laser. The knife edge and the detector were placed at 56 cm and 589 cm from the exit of the amplifier respectively. Right a) Measured diffraction patterns corresponding to capillaries with lengths between 8 and 16.4 cm. b) Cross sections of the diffraction patterns of a) obtained by vertically integrating 50 pixels of the CCD in the region of maximum fringe visibility. c) Corresponding diffraction patterns computed using the result of the wave-optics model.

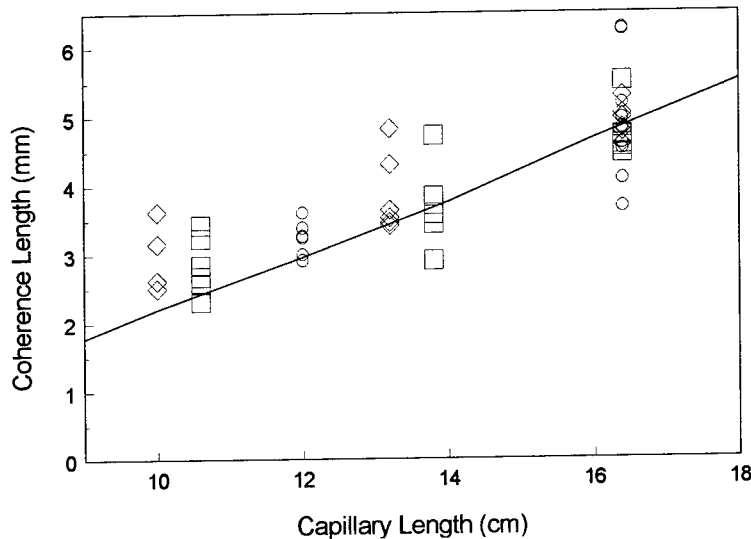


Figure 8. Variation of the coherence length in the tangential direction as a function of plasma column length. Different symbols correspond to series of measurements conducted in several identical capillaries. The line is the result of wave-model calculations.

To study the uniformity of the coherence properties across the beam profile, we performed measurements placing the knife edge in different positions relative to the laser beam. Measurements conducted placing the knife edge along a diameter of the beam (on-axis) showed that the coherence is the same in the two orthogonal directions. Measurements off-axis showed that the coherence length in the radial direction is 30-50 % shorter than in the tangential direction. The wave-model computations suggest that a likely cause of the observed anisotropy of the spatial coherence is the change of the electron density during the laser pulse. As curves of constant phase are circles concentric with the beam, the dephasing due to a change in the curvature of the wavefront is more significant off-axis and in the radial direction. This effect is clearly shown by our simulations that use parabolic profiles and a time varying electron density. It is nevertheless possible that the observed anisotropy could be caused by a non parabolic density profile in which the curvature is radially dependent.

In summary, we have studied the spatial coherence of a discharge pumped 46.9 nm table-top amplifier for plasma columns up to 16.4 cm in length. We have observed a monotonic increase of the spatial coherence with amplifier length, in agreement with the result of wave-model computations measurement in the tangential direction yield a coherence angle of 0.8 mrad and an effective source size of 26  $\mu\text{m}$  for a capillary length of 16.4 cm.

## 7. CONCLUSIONS

We have developed and characterized compact soft x-ray lasers based on fast discharge excitation of capillary plasmas. This was made possible by capillary discharge generation of hot and dense needle-like plasma columns of remarkable stability. A saturated 46.9 nm laser was developed by collisional excitation of Ne-like Ar and large amplification was also obtained at 60.8 nm in Ne-like S. The large amplification measured and the observed monotonic increase of the spatial coherence, both of which approach their theoretical values, are direct and clear evidence of the very high stability and uniformity of these plasma columns. These results have shattered the notion that discharge-created plasmas are insufficiently stable and uniform for soft x-ray lasing, and have opened a new road to practical soft x-ray lasers for applications.

### Acknowledgements

We want to thank the contributions of D. Clark, D. Burd, O.D. Cortazar and M. Frati. This work was supported by NSF grants ECS-9713297 and DMR-9512282, and the NSF Optoelectronic Computing Systems Center. Part of the soft x-ray optics used developed in collaboration with Hyperfine Inc. (Boulder, CO), with the support of the Colorado Advance Technology Institute.

### References

- [1] D.L. Matthews, P.L. Hagelstein, M.D. Rosen, M.J. Eckart, N.M. Ceglio, A.U. Hazi, M. Medeck, B.J. MacGowan, J.E. Trebes, B.L. Whitten, E.M. Campbell, C.W. Hatcher, A.M. Hawryluk, R.L. Kauffman, L.D. Pleasance, G. Rambach, J.H. Scofield, G. Stone, and T.A. Weaver, *Phys. Rev. Lett.* **54**, 110 (1985).
- [2] S. Suckewer, C.H. Skinner, H. Milchberg, C. Keane, and D. Voorhees, *Phys. Rev. Lett.* **55**, 1753 (1985).
- [3] B.E. Lemoff, G.Y. Lin, C.L. Gordon III, C.P. Barty, and S.E. Harris, *Phys. Rev. Lett.* **74**, 1574 (1995).
- [4] P.V. Nickles, V.N. Shlyaptsev, M. Kalachnikov, M. Schnurer, I. Will, and W. Sandner, *Phys. Rev. Lett.* **78**, 27498 (1997).
- [5] D.V. Korobkin, C.H. Nam, S. Suckewer, and A. Goltsov, *Phys. Rev. Lett.* **77**, 5206 (1996).
- [6] Y. Nagata, K. Midorikawa, S. Kubodera, M. Obara, H. Tashiro, and K. Toyoda, *Phys. Rev. Lett.* **71**, 3774 (1993).
- [7] S. Basu, P.L. Hagelstein, and J.G. Goodberlet, *Appl. Phys. B* **57**, 303 (1993).
- [8] J.J. Rocca, D.C. Beethe, and M.C. Marconi, *Opt. Lett.* **13**, 565 (1988).
- [9] J.J. Rocca, O.D. Cortazar, B. Szapiro, K. Floyd, and F.G. Tomasel, *Phys. Rev. E* **47**, 1299 (1993).
- [10] J.J. Rocca, V.N. Shlyaptsev, F.G. Tomasel, O.D. Cortazar, D. Hartshorn, and J.L.A. Chilla, *Phys. Rev. Lett.* **73**, 2192 (1994).
- [11] J.J. Rocca, D.P. Clark, J.L.A. Chilla, and V.N. Shlyaptsev, *Phys. Rev. Lett.* **77**, 1476 (1996).
- [12] V.N. Shlyaptsev, J.J. Rocca, P.V. Nickles, M.P. Kalashnikov, and A.L. Osterheld, in *X-Ray Lasers 1996*, S. Svanberg and C.-G. Wahlström Eds (IoP, Bristol, 1996).
- [13] F.G. Tomasel, J.J. Rocca, and V.N. Shlyaptsev, *IEEE Trans. Plasma Sci.* **24**, 49 (1996).
- [14] P.G. Burkhalter, G. Mehlman, F.C. Young, S.J. Stephanakis, V.E. Scherrer, and D.A. Newman, *J. Physique Colloque C6*, 247 (1986).
- [15] J.J. Rocca, F.G. Tomasel, M.C. Marconi, V.N. Shlyaptsev, J.L.A. Chilla, B.T. Szapiro, and G. Giudice, *Phys. Plasmas* **2**, 2547 (1995).
- [16] A. Hildebrand, A. Ruhmann, and H.-J. Kunze, *Phys. Lett. A* **221**, 335 (1996).
- [17] J.J. Rocca, D. Clark, F.G. Tomasel, V.N. Shlyaptsev, B. Benware, C.H. Moreno, D. Burd, and J.J. Gonzalez, in *X-Ray Lasers 1996*, S. Svanberg and C.-G. Wahlström Eds (IoP, Bristol, 1996).
- [18] G.L. Linford, E.R. Peressini, W.R. Sooy, and M.L. Spaeth, *Appl. Opt.* **13**, 379 (1974).
- [19] V.N. Shlyaptsev, A.V. Gerusov, A.V. Vinogradov, J.J. Rocca, O.D. Cortazar, F.G. Tomasel, and B.T. Szapiro, *SPIE J.* **2012**, 99 (1993).
- [20] F.G. Tomasel, V.N. Shlyaptsev, and J.J. Rocca, *Phys. Rev. A* **54**, 2474 (1996).
- [21] B. Benware, C.H. Moreno, D. Burd, and J.J. Rocca, *Opt. Lett.* **22**, 796 (1997).
- [22] F.G. Tomasel, J.J. Rocca, V.N. Shlyaptsev, and C.D. Macchietto, *Phys. Rev. A* **55**, 1437 (1997).
- [23] R.R. Gayazov, A.E. Kramida, L.I. Podobedova, E.N. Ragozin, and V.A. Chirkov, in *X-Ray Plasma Spectroscopy and the Properties of Multiply-charged Ions*, (Nova Science, NY, 1988).
- [24] Y. Li, P. Lu, G. Pretzler, and E.E. Fill, *Optics Commun.* **133**, 196 (1997).
- [25] A.V. Vinogradov and V.N. Shlyaptsev, *Sov. J. Quantum Electron.* **13**, 1511 (1983).
- [26] V.N. Shlyaptsev, J.J. Rocca, and A.L. Osterheld, *SPIE J.* **2520**, 365 (1995).
- [27] Yu. V. Afanas'ev and V.N. Shlyaptsev, *Sov. J. Quantum Electron.* **19**, 1606 (1989).

- [28] E.N. Ragozin, S.S. Churilov, E.Ya. Kononov, A.N. Ryabtsev, and Yu.F. Zayikin, *Phys. Scr.* **36**, 586 (1987).
- [29] J.J. Rocca, O.D. Cortazar, F.G. Tomasel, and B.T. Szapiro, *Phys. Rev. E* **48**, R2378 (1993).
- [30] Y. Li, G. Pretzler, and E.É. Fill, *Phys. Rev. A* **52**, R3433 (1995).
- [31] See for example *X-Ray Lasers 1996*, S. Svanberg and C.-G. Wahlström Eds (IoP, Bristol, 1996), and *Soft X-ray Lasers and Applications*, SPIE J. **2520**, J.J. Rocca and P.L. Hagelstein, Eds.
- [32] A. Carrillon, H.Z. Chen, P. Dhez, L. Dwivedi, J. Jacobi, P. Jaegle, G. Jamelot, J. Zhang, M.H. Key, A. Kidd, A. Klishnick, R. Kodama, J. Krishnan, C.L.S. Lewis, D. Neely, P. Norreys, D. O'Neill, G.J. Pert, S.A. Ramsden, J.P. Rancourt, G.J. Tallents, and J. Uhmohibhi, *Phys. Rev. Lett.* **68**, 2917 (1992).
- [33] R. Kodama, D. Neely, Y. Kato, H. Daido, K. Murai, G. Yuan, A. MacPhee, and C.L.S. Lewis, *Phys. Rev. Lett.* **73**, 3215 (1994).
- [34] R.A. London, M. Strauss, and M.D. Rosen, *Phys. Rev. Lett.* **65**, 563 (1990).
- [35] R.P. Ratowsky and R.A. London, *Phys. Rev. A* **51**, 2361 (1995).
- [36] G. Hazak and A. Bar-Shalom, *Phys. Rev. A* **40**, 7055 (1989).
- [37] M.D. Feit and J.J.A. Fleck, *Opt. Lett.* **16**, 76 (1991).
- [38] M.D. Feit and J.J.A. Fleck, *J. Opt. Soc. Am. B* **7**, 2048 (1990).
- [39] M.C. Marconi, J.L.A. Chilla, C.H. Moreno, B.R. Benware, and J.J. Rocca, "Measurement of the spatial coherence build-up in a discharge pumped table-top soft x-ray laser", submitted to *Phys. Rev. Lett.* (1997).
- [40] F. Albert, B. Rus, Ph. Zeitoun, A. Carrillon, P. Jaegle, G. Jamelot, A. Klishnick, D. Ros, and S. Sebban, in *X-Ray Lasers 1996*, S. Svanberg and C.-G. Wahlström Eds (IoP, Bristol, 1996).



## Quasistatic Plasma Sources: Physical Principles, Modelling Experiments, Application Aspects

K.P. Shamraj, A.F. Aleksandrov\*, G.E. Bougrov\*, V.F. Virko, V.P. Katiukha, S.K. Koh\*\*,  
E.A. Kralkina\*, G.S. Kirichenko and A.A. Rukhadze\*

*Institute for Nuclear Research, National Academy of Sciences, Kiev 252022, Ukraine*

*\* Moscow State University, Moscow 117942, Russia*

*\*\* KIST, Cheongryang, Seoul, Korea*

**Abstract.** Magnetic field enhanced rf plasma sources excited by frame-type antennas (quasistatic plasma sources) are treated theoretically and experimentally. The theoretical model predicts that a significant part of the rf power is absorbed in a source plasma via the excitation of quasi-electrostatic waves. The dependences of absorption on plasma density, external magnetic field, driving frequency, and source dimensions (scaling laws) are obtained. Special experiments on low-power rf signal absorption in a preformed dense plasma corroborate well the theory. Results of test experiments with different sources have shown that a behaviour of the discharge in quasistatic sources is in good agreement with theoretical predictions. Using this knowledge, a compact low-power ion source was designed and optimized. Detailed testing of its parameters has shown that this device has good prospects for use as an ion thruster, and for various materials processing applications.

### 1. INTRODUCTION

Radio-frequency (rf) inductive methods of plasma production are used on various fields of technology from materials processing [1] to fusion devices [2,3]. These methods have many advantages for applications including a high efficiency of power utilization; a high efficiency of plasma generation, and thus a low ion production cost, and a high efficiency of gas utilization; flexibility in a source design; etc. Indeed, the density of inductively coupled plasmas grows linearly with input power [4], in contrast with capacitive discharges where the density scales as a square root of power. Plasmas with densities above  $10^{12} \text{ cm}^{-3}$  can be produced at a rather moderate specific input power of 50-100 mW/cm<sup>3</sup>. Inductive sources are capable of running in a wide range of aspect (length-to-radius) ratios and magnetic fields, and in downstream regimes. They can also work at very low gas pressures (below 1 mTorr), and to produce low-energy (< 60 eV) ion fluxes onto a substrate which is favourable for highly anisotropic and damage-free processing.

Inductive sources have become the dominant tool for high aspect-ratio dry etching of sub-micron patterns [4], and for high density plasma deposition [5]. They have also good prospects for utilization as ion sources for ion thrusters [6], for gas laser pumping, plasma particle accelerators etc. [7].

Inductively coupled plasmas are known to run with or without the external magnetic field. Except for an obvious increase of plasma confinement and thus of plasma density, imposing a magnetic field improves the source operation at least in two respects [8]. First, the magnetic field increases the resistance of the plasma load, and thus the efficiency of rf power utilization and the stability of a discharge in electronegative gases. Second, it permits the discharge ignition at lower gas pressures.

From the physical viewpoint, the magnetic field gives rise to specific plasma waves, and thus changes substantially the coupling of rf power to the plasma. Excitation of waves increases the depth of rf field penetration into the plasma, which results in enhanced bulk power absorption.

Inductive sources can be excited by helices, flat spirals [4], or frame-type antennas enveloping a plasma column [7,9-12]. In the latter case, the plasma production turns out to be the most efficient, probably due to a better coupling of driving antenna to waves. The usual name for devices of this type is *helicon* source.

In the range of plasma parameters typical for inductive sources enhanced by magnetic field, one can find in plasmas the electromagnetic (helicon) and quasi-electrostatic (Trivelpiece-Gould) waves [13-15]. Both may be excited by a frame-type antenna, but it turns out that a significant fraction of rf power is

absorbed in helicon sources via electrostatic waves [15,16]. Moreover, devices of this type can operate at densities below the cut-off for helicon waves [17]. For this reason, we call a magnetic field enhanced inductively coupled plasma with a frame-type antenna as *quasistatic* source.

We report here the results of research on the physics and applications of quasistatic sources. Two groups of sources are treated. Low aspect-ratio (AR) sources and their applications for ground and space technologies are examined at Moscow State University. High AR sources with applications to materials processing are studied at Kiev Institute for Nuclear Research. In its physical part, this report is aimed at finding out general principles, especially scaling laws, governing source operation, and in the experimental verifying of these principles by comparing the results from sources of different design.

## 2. THEORY OF A RF FIELD INTERACTION WITH A MAGNETIZED PLASMA COLUMN

### 2.1. Propagation and damping of waves in a source plasma

In the range of plasma parameters and magnetic fields typical for the operation regimes of quasistatic sources, the following relations between the frequency of driving generator  $\omega$  and characteristic plasma frequencies hold

$$k_z v_{th} \ll \omega_{LH} < \omega < \omega_c \ll \omega_p \quad (1)$$

where  $\omega_p$ ,  $\omega_c$ , and  $v_{th}$  are plasma and gyro-frequencies, and thermal velocity of electrons, respectively;  $\omega_{LH}$  is the lower hybrid frequency; and  $k_z$  is a characteristic number (along the external magnetic field  $B_0$ ) of waves excited by a driving antenna in plasma.

Waves of two types exist in plasma in the range (1) [13]. Both belong to a magnetosonic mode but differ in wavelength. A long-wave magnetosonic mode,  $k_t c \ll \omega_p$ , is a helicon (whistler) wave. In a short-wave limit,  $k_t c \gg \omega_p$ , the magnetosonic mode is a quasi-electrostatic (Trivelpiece-Gould) wave. The dispersion relations for these wave are respectively

$$\omega_H = \omega_c \cos \theta_H \frac{k_t^2 c^2}{\omega_p^2}, \quad \omega_{TG} = \omega_c \cos \theta_{TG} \quad (2)$$

where  $\mathbf{k}_t$  is a total wave-vector making an angle  $\theta$  with the external magnetic field.

Helicon waves can propagate in a plasma provided that a magnetic field is not very low, so that  $\omega_c > 2\omega$ , and a plasma density lies in the interval which is defined by relations

$$\omega_{\min} < \omega_p < \omega_{\max} \quad (3)$$

where

$$\omega_{\min} = k_z c \left( \frac{\omega_c}{\omega} - 1 \right)^{1/2} \quad \text{and} \quad \omega_{\max} = k_z c \frac{\omega_c}{2\omega} \quad (4)$$

Electrostatic Trivelpiece-Gould (TG) waves need  $\omega_c > \omega$ , and not very high plasma density. In the range  $\omega < \omega_c < 2\omega$ , the condition for TG waves to propagate reads  $\omega_p < \omega_{\min}$ , whereas at  $\omega_c > 2\omega$  it is  $\omega_p < \omega_{\max}$ . Thus, TG waves have no the lower limit for density.

The regions where the waves can propagate are shown in Fig. 1. One can see that densities accessible for electrostatic TG waves extend far below those for helicons.

Helicon and electrostatic waves reserve the energy in different components. Almost all the energy of helicons is concentrated in a magnetic field, whereas electrostatic waves reserve it mostly in a kinetic

energy of electrons oscillations [16]. For this reason, any electron collisions (both with neutrals and ions) are extremely effective for the electrostatic wave as destroying the principal (kinetic) part of its energy. On the contrary, any dissipation mechanism destroying either the kinetic energy of electrons (binary or anomalous collisions), or the electric field (Landau damping, or trapping of electrons by a longitudinal electric field) is ineffective for helicons. To be efficient, a mechanism of damping should destroy the magnetic field of helicon wave. Such a mechanism is absent among wave - particle interactions in plasmas of quasistatic sources.

Efficient mechanisms for the helicon dissipation are provided by wave - wave interactions, both linear and non-linear. The non-linear damping of helicon wave can arise as the beam-like parametric instability with the growth rate few-fold exceeding the driving frequency [18]. In a linear case, these mechanisms arise due to coupling of helicon wave to the electrostatic wave [15,16], that is are displayed as the mode conversion. It may occur both at the surface of a bounded plasma, or in a plasma bulk.

A bulk conversion arises if the plasma is not too dense and includes the surface  $\omega_p = \omega_{\max}$  with  $\omega_{\max}$  defined in Eq. (4). At this surface, merging (degeneration) of helicon and electrostatic waves results in the efficient conversion.

If the helicon wave is excited in a bounded plasma column, it gives rise to a redundant polarization of plasma at the edge which is cancelled by arising electrostatic wave. Such a mechanism of surface mode conversion results in that a principal fraction of the energy of helicon wave is transferred to the electrostatic wave. The efficiency of this mechanism is evaluated in terms of effective collision frequency which makes [16, 19]

$$\nu_{\text{eff}} \approx \omega_c (r_0 / \lambda_z) \quad (5)$$

where  $r_0$  is the plasma radius, and  $\lambda_z = 2\pi/k_z$  a characteristic axial wavelength excited by antenna. Being very efficient, the surface conversion dominates in many situations as the damping mechanism for helicons.

The efficiency of surface conversion may be low provided that the azimuthal electric field of helicon

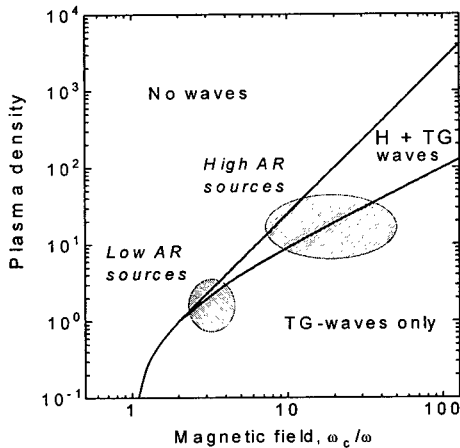


**Figure 1:** Regions accessible for helicon (H) and electrostatic (TG) waves. The plasma density is in  $\omega_p^2 / k_z^2 c^2$  units.

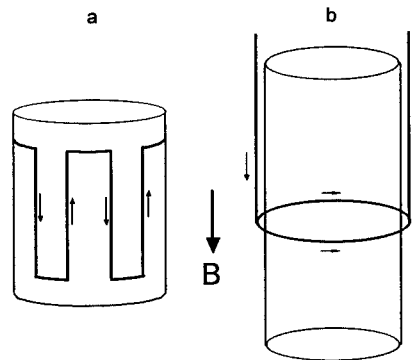


**Figure 2:** Antennas exciting low (a) and high (b) aspect-ratio sources.

wave has a node at the plasma edge. Then the redundant polarization does not arise, and the excitation of electrostatic wave is suppressed. This is the case if the plasma and wave parameters satisfy the condition of anti-resonance for the electrostatic wave excitation [20]

$$n = n_{AR} \approx \frac{2c}{e} \frac{B_0}{\omega r_0 \lambda_z} \quad (6)$$

Electrostatic waves excited at the plasma edge due to mode conversion propagate to the plasma centre and deposit energy via collisions. The depth of penetration is

$$\delta = r_0 \frac{B_{cr}}{B_0} \quad \text{where} \quad B_{cr} = \frac{m_e c}{2\pi e} \frac{\omega^2}{v} \frac{\lambda_z}{r_0} \quad (7)$$

An electrostatic wave can penetrate into the bulk plasma at low magnetic fields only,  $B_0 < B_{cr}$  [16].

## 2.2. Antenna-to-wave coupling and rf power absorption

Frame-type rf antennas of different design were shown to be efficient for driving quasistatic sources (e.g. [7,9-12]). Two of them used in experiments are shown in Fig. 2. Both are surface current-carrying contours including axial (along the magnetic field) and azimuthal parts.

Coupling of the rf driving system to the plasma may be inductive or capacitive [1]. The first is provided via rf currents whereas the second via rf charges induced in elements of the driving system. Both types of coupling are intrinsic for quasistatic sources [21]. A source can operate in a mode with low plasma density when a capacitive-type coupling is probably dominating. The plasma density in a capacitive mode is well below the cut-off for helicon waves,  $\omega_p < \omega_{min}$  with  $\omega_{min}$  defined by Eq. (4).

Much more interesting, however, is a high-density mode of quasistatic source which arises with strong inductive coupling. A transition between these modes occurs as abrupt density jump at smoothly varying input power [11,22]. In the high mode, the plasma density is normally well above the cut-off for helicons, and traveling waves may arise in the regions of plasma remote from antenna [21,23,24].

Inductive coupling is efficient provided that plasma density exceeds the cut-off value for helicons. To consider pure inductive coupling, one should put  $\nabla \cdot \mathbf{j}_a = 0$ , where  $\mathbf{j}_a$  is the density of antenna current. In this case, the antenna is found to be coupled to helicon waves only, and by azimuthal parts only [16]. Being excited by antenna, helicon waves transfer a principal part of energy, via surface or bulk mode conversion, to electrostatic waves which finally deposit the rf power in the plasma. Thus, helicon waves are a sort of transmission element between the antenna and electrostatic waves.

The surface mode conversion results in a bulk power absorption if the magnetic field is rather low,  $B_0 < B_{cr}$ , where  $B_{cr}$  is defined in Eq. (7). At higher fields, this mechanism gives a surface power absorption. The bulk mode conversion, if any, results normally in a bulk absorption.

With capacitive coupling  $\nabla \cdot \mathbf{j}_a \neq 0$ , and antenna charges can excite electrostatic waves directly [17]. This mechanism may be efficient especially in plasmas with density well below the cut-off for helicons.

## 2.3. The power absorbed with pure inductive coupling, and the discharge stability

The rf power absorbed in the plasma is defined by the Joule law

$$P_{abs} = (1/2) R_p I_a^2 \quad (8)$$

where  $R_p$  is the plasma resistance, and  $I_a$  is the amplitude of antenna current. The resistance is defined mainly by the excitation of waves. The model assuming that the plasma resistance is due to surface mode conversion yields the following scaling laws for the magnitude of resistance and for the location of its maxima

$$R_p \propto \frac{r_0 B_0}{\lambda_z^2 n} \quad \text{and} \quad r_0 \lambda_z \omega \frac{n}{B_0} = \text{const.} \quad (9)$$

The variation with density of power absorbed in the plasma is shown in Fig. 3 for a fixed magnetic field and some value of antenna current. It is calculated for the anti-symmetric antenna shown in Fig. 2b, and in the approximation of pure inductive coupling described in Refs. [16,19].

One can see a non-monotonic behaviour of absorbed power in Fig. 3. The peaks of absorption arise provided that the amplitude of helicon wave is a maximum at the plasma edge, so that the efficiency of surface conversion is high. The minima are due to anti-resonances of various spatial (axial and radial) modes. The first minimum is positioned where the density satisfies condition (6).

Power losses are shown in Fig. 3 as scaling linearly with density. This is so provided that axial losses are dominant [1] which is normally true for quasistatic sources. Of two equilibrium points satisfying the power balance condition  $P_{\text{abs}} = P_{\text{loss}}$ , the stable one belongs to the part of absorption curve where the rate of changing of absorbed power is lower than that of losses.

Increasing the antenna current results in increased absorbed power. For this reason, the power balance can be satisfied provided that the antenna current exceeds some critical value  $I_1$ . At  $I_a = I_1$ , a transition to inductive coupling occurs. This is shown in Fig. 4 for the absorption curve calculated at the external magnetic field  $B_1$ . The transition occurs as an abrupt jump of the plasma density to the value  $n_1$ .

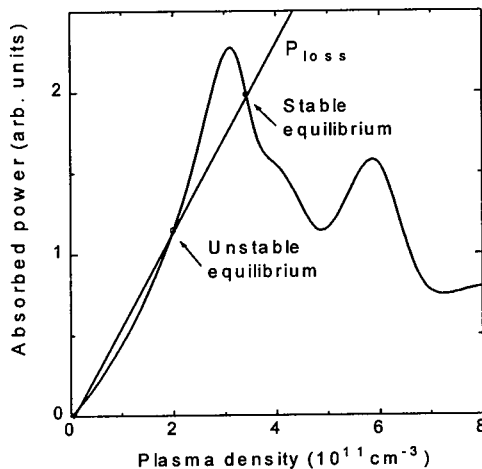


Figure 3: Stable and unstable equilibrium points for a quasi-static discharge with dominant axial losses.

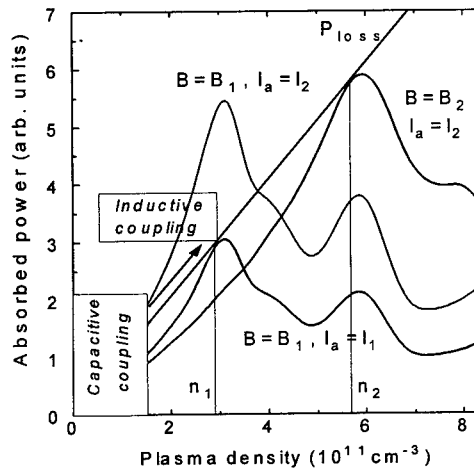


Figure 4: Transitions to inductive coupling at different magnetic fields.

Increasing the magnetic field shifts the absorption peaks to higher densities, as is seen from the second Eq. (9). As a result, at higher magnetic field,  $B_2 > B_1$ , a transition to inductive coupling has to occur at higher antenna current,  $I_2$ , that is at higher rf power. This is shown in Fig. 4. The plasma density after this transition is also higher,  $n_2 > n_1$ . Note that such a peculiarity of transitions was observed in a set of experiments including ours (see Sec. 3.3).

At purely inductive coupling, the absorbed power turns out to depend extremely weakly on collision frequency, as a result of a collisionless (conversion) nature of the absorption of helicon waves.

### 3. MODELLING AND TEST EXPERIMENTS

In this Section, experimental results are presented to confirm the theoretical understanding of rf power absorption in quasistatic sources, and thus to indicate the ways for finding the regimes of source operation most proper for that or another application. Experiments were conducted with various in size and design devices which are differentiated as high and low aspect-ratio (AR) devices.

Since the waves are of special importance for quasistatic sources, the most appropriate definition of the aspect ratio for these devices is as that of a characteristic wavelength excited by the antenna to the plasma radius,  $\lambda_z / r_0$ . Large devices like those which are used for dry etching and high-density plasma

deposition (e.g. [22,25]) are high AR sources with  $AR \geq 4-5$ , whereas small devices which can be used as thrusters are low AR ones with  $AR \approx 1$  (see Sec. 4). In short devices, the characteristic wavelength is approximately twice a device length,  $\lambda_z \approx 2L$ .

The regions of parameters typical for the operation modes of low and high AR sources are shown schematically in Fig. 1. High AR devices normally operate in the region accessible for helicon waves. For this reason, the power in these devices can be absorbed both via surface mode conversion, and via direct excitation of electrostatic waves arising due to capacitive coupling. The bulk conversion can work in high AR devices at low magnetic fields only. In low AR sources, all three mechanisms may be important, and especially direct excitation of electrostatic waves by a high-inductance antenna shown in Fig. 2a.

### 3.1. Experimental study of a low-power rf signal absorption in a preformed dense-plasma column

To refine the physical picture of rf field interaction with dense plasma, and to uncouple from specific discharge phenomena, we conducted experiments with a dense plasma preformed by a ECR discharge. A scheme of the experimental device is shown in Fig. 5. A quartz camera was filled by a dense plasma produced by a 2.45 GHz ECR source which worked in a pulsed regime,  $\tau_{imp} = 10$  ms, at a power up to 500 W. ECR source was magnetically and microwave isolated by a magnetic screen and a wire grid. A low rf power was supplied to the antenna in the frequency range of 8-26 MHz. A variable tuning capacitor permitted matching of antenna+plasma load to the generator. The plasma density was measured by a microwave interferometer.

Fig. 6 shows the interferometer trace and the variation of antenna voltage with time. One can see that the voltage varies non-monotonically, that is the plasma resistance depends non-monotonically on density. The minima of voltage correspond in Fig. 6 to maxima of plasma resistance (absorption peaks).

Fig. 6 permits one to determine the dependence of plasma resistance on density. The result is shown in Fig. 7 for different magnetic fields. Both the non-monotonic variation of resistance with density, and the location of resistance maxima, and shifting of them to higher densities with the increase of magnetic field confirm the theory of rf power absorption.

Fig. 8 demonstrates the dependence of plasma resistance at some maximum on the gas pressure. One can see that this dependence is extremely weak, as it is predicted by theory. Dropping of resistance at

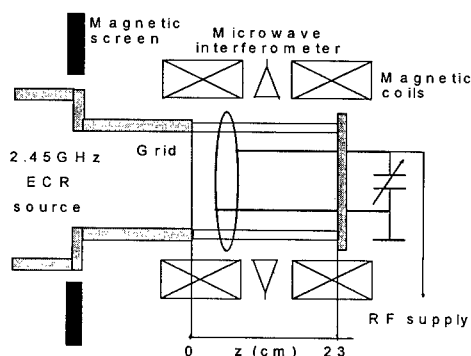


Figure 5: A scheme of experimental device for the low-power excitation of a preformed plasma column.

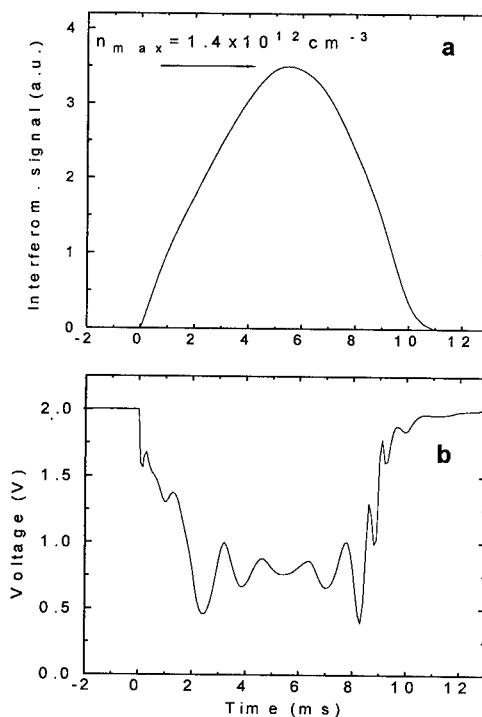
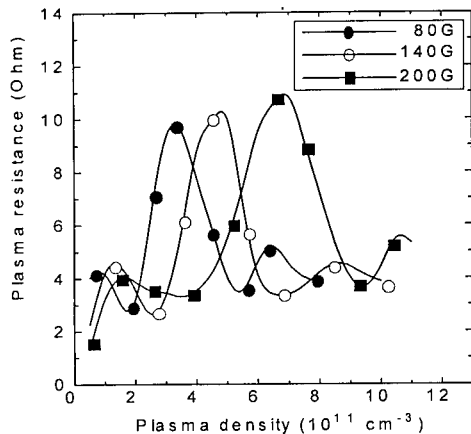


Figure 6: Interferometer trace (a) and variation of the antenna voltage (b) with time.



**Figure 7:** Resistance of a plasma load vs plasma density, at different magnetic fields.

pressures above 3 mTorr is the effect of the unstable ECR source operation at high pressures rather than some physical effect.

Relative amplitudes of different absorption peaks are shown in Fig. 9 vs axial position of the azimuthal part of antenna (double half-turn in Fig. 2b). The peaks are numbered starting from low densities (see Fig. 6). Such a behaviour is also predicted by theory supposing that each of peaks arises due to some spatial mode [16]. An exception is the first peak, its behaviour cannot be understood in the frame of purely inductive coupling. In addition, this peak lies at densities below the cut-off for helicon waves, so that it is likely the result of capacitive coupling giving rise to a direct excitation of electrostatic waves.

### 3.2. Operation parameters of high aspect-ratio sources

High aspect-ratio quasistatic sources are well known in applications related to materials processing where they are normally called helicon sources (e.g. [7,22,25]). A schematic diagram of a processing source operating at Kiev Institute for Nuclear Research is shown in Fig. 10 [12]. It includes a source chamber with an anti-symmetric antenna of design shown in Fig. 2b, and a processing chamber. Such a design is typical for processing devices (see, e. g. [22,26]).

The plasma density is shown in Fig. 11 vs magnetic field for various input powers. One can see a peak at low magnetic fields where a density of the order of  $2 \times 10^{11} \text{ cm}^{-3}$  is produced with a specific power input in a  $50 \text{ mW/cm}^3$  range. A low- $B$  density peak was also observed in other experiments [10]. It is most probably due to the bulk mode conversion which works at low fields as the additional mechanism of power absorption (see Sec. 2.2 and Fig. 1). A possibility to get high densities at low magnetic fields is important for applications as permitting the source to run with light magnetic systems.

One can see in Fig. 12 that a high AR source is capable of operating at gas pressures over a wide range from a few tenths to a few tens of mTorr without substantial change of plasma density. This may be understood from our theory (see Sec. 2) which predicts a weak dependence of the rf absorption on collision frequency.

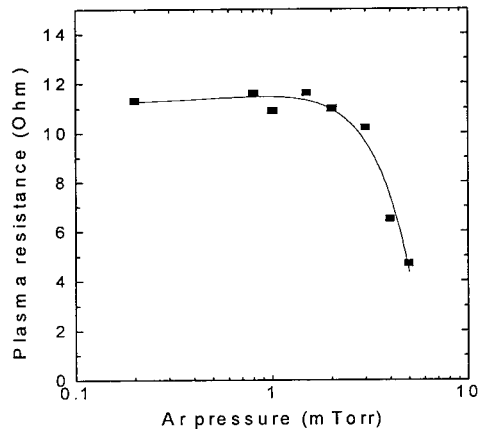


**Figure 8:** Dependence of a plasma resistance on Ar pressure.

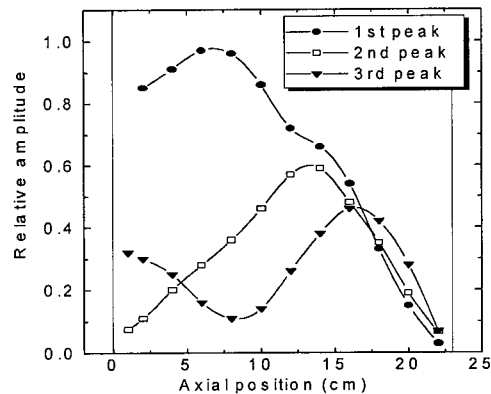


**Figure 9:** Amplitudes of absorption peaks as dependent on a position of antenna relative to the plasma column.

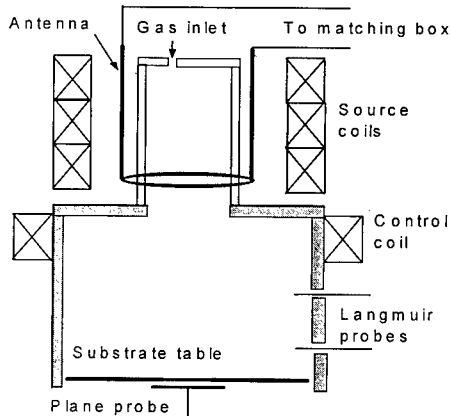


**Figure 10:** A scheme of a high aspect-ratio source for materials processing applications.

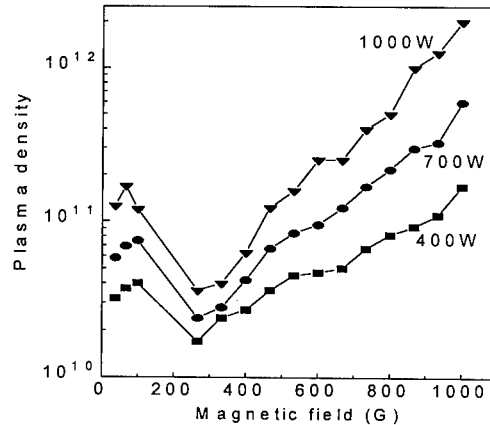


**Figure 11:** Variation of a plasma density with magnetic field in a high AR source, at different input powers.

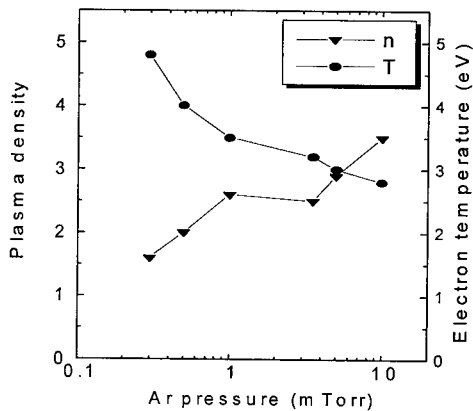


**Figure 12:** Plasma density (in  $10^{11} \text{ cm}^{-3}$ ) and electron temperature vs Ar pressure.

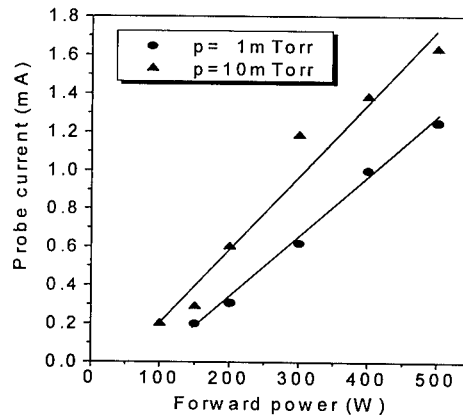


**Figure 13:** Ion current to probe vs forward power, at different Ar pressures.

A low sensitivity of a plasma density to the gas pressure is seen again from Fig. 13. This figure shows also a linear growth of density with input power, in agreement with the expectations of our theory. Such a growth is similar to that in a magnetic field-free source excited by a flat spiral rf coil [4].

### 3.3. Optimal regimes of a low aspect-ratio low power plasma source

Experiments with low aspect-ratio source were performed using two glass discharge tubes 9.2 cm in diameter and 8 and 4 cm long closed by end-flanges. A discharge was excited by an antenna of the type shown in Fig. 2a. It was fed by a rf generator operating at frequencies 20, 30, 40, 60, and 81 MHz, and at a power up to 200 W. A magnetic field in the range of 0 - 600 G was generated by a solenoid. Plasma parameters were measured by two cylindrical probes positioned at the tube axis and at a half of tube radius.

The dependences of ion saturation current on the magnetic field corresponding to the centre of the discharge tube are shown in Fig. 14 for different input powers. Dashed bands in Fig. 14 correspond to magnetic fields  $\omega_c = \omega$ , and  $\omega_c = 2\omega$ . Their finite widths are defined by a 20% non-uniformity of the magnetic field along the device.

One can see from Fig. 14 that the probe current does not change in the ECR region. However, it starts to grow rapidly at  $\omega_c = 2\omega$ , and reaches a maximum at some higher magnetic field. The increase of input



power shifts the location of this broad maximum towards higher fields. The plasma density and its rate of growth were found to be higher at the tube periphery.

As is seen from Fig. 14, the increase of the probe current and thus of plasma density starts at the magnetic field corresponding to the lower boundary for the excitation of helicon waves (see Fig. 1). In addition, a direct excitation of TG-waves is possible in the range  $\omega_c > \omega$ . We suppose this to be an evidence of efficient plasma production due to the excitation of waves in a quasistatic source.

Fig. 15 shows the variation of saturation ion current with input power at fixed values of magnetic field. One can see an abrupt increase of the current occurring at some threshold value of a rf power. This value is higher for higher magnetic fields. The further increase of power above the threshold does not result in a substantial change of ion current.

The jumps in discharge density are likely to be the abrupt transitions from capacitive to inductive coupling we discussed in section 2.3. Similar phenomena were observed in high aspect-ratio devices [22,25], and seem to be some universal property of quasistatic sources.

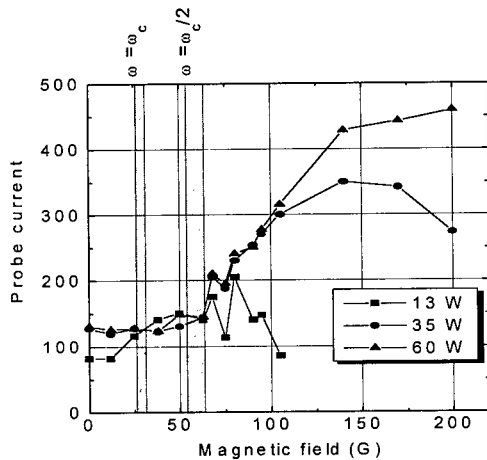


Figure 14: Dependences of saturation ion current to probe (in  $\mu\text{A}$ ) on magnetic field.

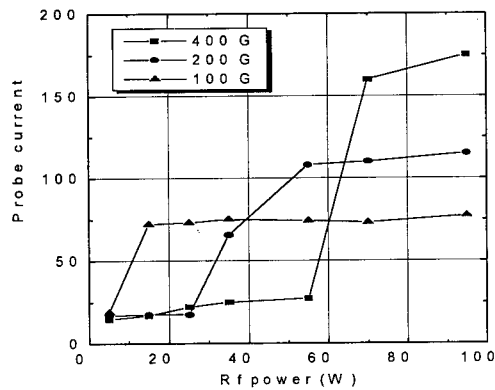


Figure 15: Dependences of saturation ion current (in  $\mu\text{A}$ ) on rf power.

#### 4. DESIGN AND OPTIMIZATION OF A LOW ASPECT-RATIO ION SOURCE

The idea of low power ion source development as ion propulsion system for light communication satellites was suggested by PROEL specialists in 1991 [27]. At the same time, the development of ground plasma technologies, such as sputtering, ion assisted deposition of thin films, surface modification of materials etc.[28,29], required the new generation of low-power ion sources capable of producing pure ion beams of inert and chemically reactive gases in the range of ion current densities of  $0.05 - 5 \text{ mA/cm}^2$ , and beam energies of 100-2500 eV. These two factors initiated the start at the end of 1992 of work developing a new ion source in RIAME MAI under a partial financial support of the firm PROEL TECHNOLOGIE. The evaluation of the ion source in ground plasma technologies started in 1995 in collaboration with KIST specialists.

The comparison of ion sources has shown that dc ion sources, for instance, ion sources with divergent magnetic field [30], were very effective from the viewpoint of power utilization. They found wide application both in space technology as space ion propulsion systems and in ground industry for various ion-beam processing technologies. However, in spite of the efforts of numerous specialists, dc ion sources still have problems with the lifetime of cathodes, which decrease the period of a source's continuous work, especially with using reactive gases, pollute the ion beam, and significantly complicate source design. Complicated design is also typical for microwave ion sources. From this point of view, rf ion sources are much more attractive. They provide a possibility of obtaining beams of inert and chemically reactive gases with a little amount of impurities; have large resource limited by the lifetime of

ion extraction system only, and relatively low power expenditures [28,29-31]. These advantages motivated the choice of a rf discharge for our needs, which was confirmed by that the rf ion source RITA was successfully used as an ion thruster during space mission EURECA [6]

We used the results described in Section 3.3 for designing the low-power ion source, and for choosing the region of parameters for its operation.

#### 4.1. Experimental installation

Tests of a low-power rf ion source were performed using the installation shown in Fig. 16. The source was fastened to an adjusting flange 8 of a large vacuum chamber 3.

We examined the ion source behaviour enhanced by magnetic field which was produced either by solenoid, or by permanent magnets. Fig. 17 shows schematically the source equipped by permanent magnets. The source with a solenoid was of similar design. The discharge chamber was a 9.2 cm in diam dielectric cylinder made of quartz, Pyrex, or glass ceramics, and closed at one of the ends.

The discharge was ignited by a silver or copper antenna located on the outer surface of the discharge chamber. The rf power up to 200 W was supplied through a matching network 13 (see Fig. 16) from a rf generator operating at frequencies 20, 30, 40, 60, or 81 MHz.

The ion optic system (IOS) was made as a three-electrode, three-grid system. It is non-flat and includes special "deflect" of grids and "pinched" acceleration electrode. The shape of electrode deflection is aimed at supporting the hole alignment under possible warping, minimizing the ion current density losses onto target, and achieving the necessary uniformity of the ion beam profile on the substrate. Both concave and convex grids were examined in this work.

The IOS was designed as one assembly unit. The electrodes are made of titanium alloy OT4-1. The 0.4 mm in width emission electrode has a transparency about 0.65 (the holes of 2 mm in diameter with distances of 0.5 mm between them). The acceleration electrode is a grid with holes of 0.8 mm in diameter and 0.8 mm in width. The transparency of this electrode is about 0.15. The deceleration electrode is a grid with holes of 2 mm in diameter and 0.8 mm in width. The gap between the emission and the acceleration electrode is about 1 mm; between the acceleration and the deceleration electrode 1.2 to 1.5 mm. The insulation unit consists of cups, where 2 insulators made of Alumina are aligned using the spacers. The insulation unit serves for electrode isolation (was tested to 5000 V), and carries also a mechanical load.

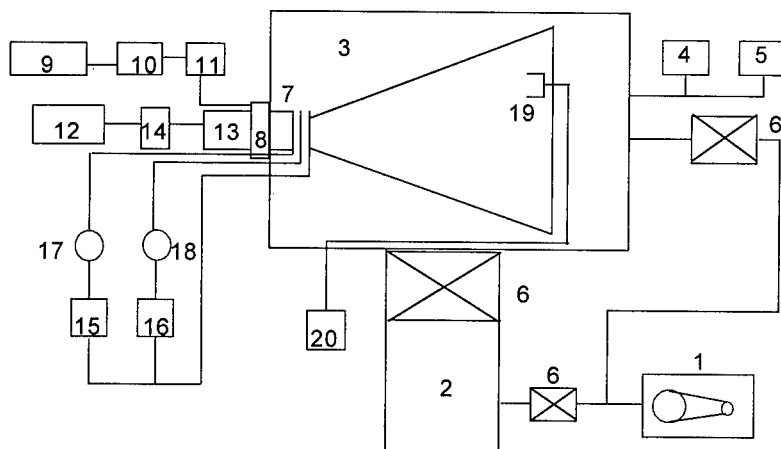


**Figure 16.** A scheme of experimental set-up.

1 - rotary pump; 2 - diffusion pump; 3 - vacuum chamber; 4 - thermocouple lamp; 5 - ionization lamp; 6 - vacuum seals; 7 - ion source; 8 - adjusting flange; 9 - tank with working gas; 10 - needle valve; 11 - gas flow meter; 12 - rf generator; 13 - matching box; 14 - power meter; 15, 16 - power supplies of emission and accelerating electrodes; 17, 18 - milliamperimeters, 19 - Faraday cup; 20 - PC computer.

Voltage supplies 15 and 16 (see Fig. 16) biased the emission and accelerating electrodes to potentials 0 - 1700 and 0-1000 V, respectively. The decelerating electrode was grounded. The circuit of emission electrode included a milliamperemeter 17 for measuring the ion current  $i_b$  extracted from the discharge. A milliamperemeter 18 measured the current  $i_{ac}$  from the acceleration electrode for controlling the quality of the beam optics.

To analyze the ion beam profile, a Faraday cup 19 biased to -30 V was used (see Fig. 16). It could move normally to the beam axis at distances 5, 22, and 45 cm from the source outlet. The dependencies of ion beam density on absorbed power, gas flow rate, and acceleration potential were measured for different gases (Ar, Kr, Xe, the mixture of Kr with H<sub>2</sub>, N<sub>2</sub>, O<sub>2</sub> and air). Data were processed using PC computer equipped by Analog-Digital and Digital-Analog cards.

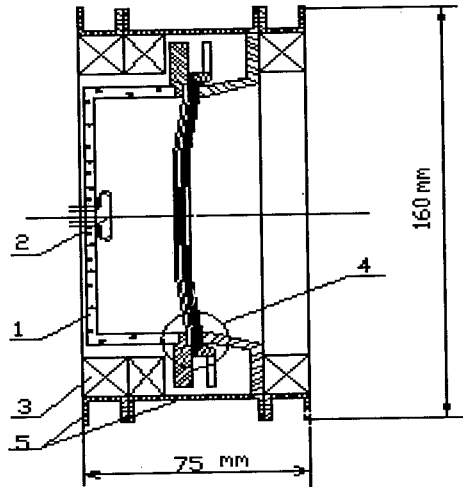


**Figure 17.** A schematic diagram of the rf ion source with magnetic system based on permanent magnets.  
1 - discharge chamber; 2 - gas distributor; 3 - magnetic rings; 4 - ion optical system.

#### 4.2. Results from a source with a solenoid

This set of experiments was performed to identify the range of magnetic fields optimal for the source operation. The source used a 8 cm long discharge chamber and was equipped by a solenoid producing the magnetic field up to 300 G at the source axis. The emission and accelerating electrodes were normally biased to +1000 V and -300 V, respectively. The experiments were conducted with a Xe consumption  $m_g = 0.7$  to 1.0 sccm.

Fig. 18a shows the variation of extracted ion beam current with magnetic field, at different input powers. One can see in this figure a low- $B$  peak corresponding to near-ECR region (compare with Fig. 14). At higher fields, the ion current increases without saturation.

Fig. 18b shows that the coefficient of gas utilization  $\beta$  (that is the ratio of extracted ion current to a gas consumption in current units,  $\beta = i_b / e m_g$ ) behaves in a similar non-monotonic manner, and grows at rather high fields. Fig. 18c demonstrates that increasing of magnetic field above 30 G results in the decrease of a power ion cost  $C_i$  (a power needed for producing a unit ion current).

Figs. 18b and 18c jointly show that at fields above 200 G the designed device can serve as an efficient ion source. The problem with high power losses in the solenoid (about 1 kW) was overcome by substituting the coil by permanent magnets.

#### 4.3. Optimization and tests of a source with permanent magnets

A design of a source with permanent magnets is shown in Fig. 17. The magnetic system included magnetized rings with inner and outer diameters of 11 and 16 cm, respectively. The rings were fabricated of a magnetically soft steel with sectors of samarium-cobalt magnets pressed in.

Increasing the magnetic field and thus the extracted current is possible in such a design by (i) using the magnetic core; (ii) decreasing the distances between rings; and (iii) increasing the number of rings. The source operation was tested with one, two, and three magnetic rings in different combinations, as well as with and without the magnetic cores. The axial magnetic field was at its largest, about 350 G, with three rings, and at its least, about 170 G, with one ring.

The basic source model used two magnetic rings and various in length discharge chambers. The results from this model have shown that the effect of magnetic core on the beam current is low. On the

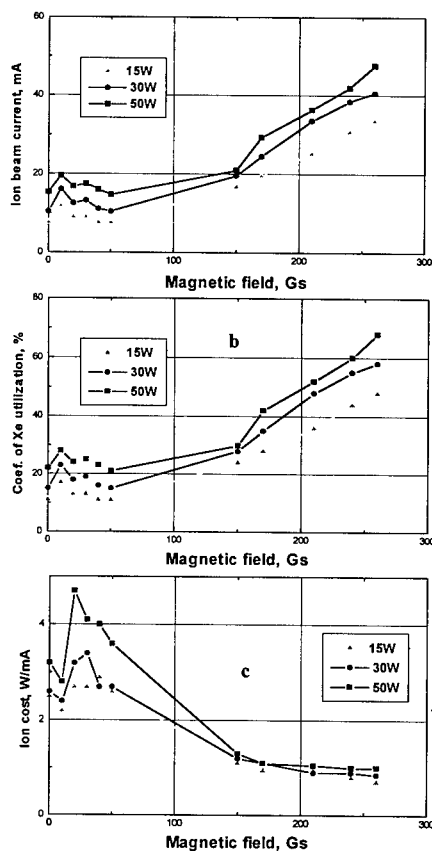


Figure 18. Dependences of Xe ion current (a), coefficient of Xe utilization (b), and ion cost (c) on magnetic field.

contrary, bringing the rings together and thus increasing the magnetic field gives a substantial growth of beam current.

This is seen from Fig. 19 where the ion current cost is plotted as a function of distance between the rings. Note that shorter discharge chambers were used in configurations with closer rings. Decreasing the chamber length is known to result in a decrease of power losses outside the source [32], but to reduce the lifetime of neutrals in the discharge chamber. Bearing in mind these results and those shown in Fig. 19, we come to the conclusion that a source of optimal design should be based on a 3 cm long discharge chamber, and on a magnetic configuration with minimal distance between rings.

The ion current extracted from a 3-cm source was measured at a fixed input power for various gases and with different magnetic systems. Imposing a single-ring magnetic field gave a 3-fold gain in ion current, whereas adding more rings resulted in a 20-30% further increase of current only. This means that a source for technological needs may use one or two rings only. But a source for an ion thruster has to include three magnetic rings because of very strict claims to power and gas utilization efficiency.

Fig. 20 shows the variation of ion beam current with absorbed power, for different gases. Approximately linear growth of current is seen at power above 20 W. Such behaviour was observed in large aspect-ratio sources (see e.g. Fig. 13), and thus is an intrinsic property of quasistatic sources. The data presented in Fig. 20 for Xe are used in Sec. 5 for estimating the ion source as the ion thruster. Note that in all cases considered the current in the circuit of accelerating electrode did not exceed 1-3% of the total beam current.

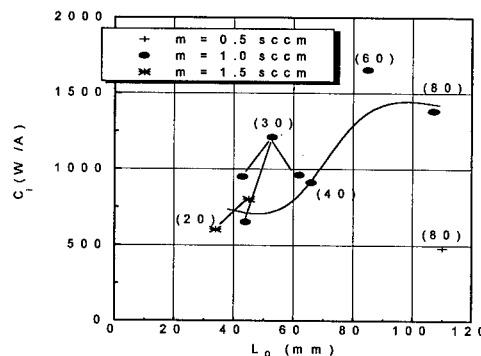


Figure 19. Dependences of Xe ion cost on the distance between magnetic rings for a coefficient of Xe utilization 0.7. In brackets, the length of gas discharge chambers is indicated (in mm).

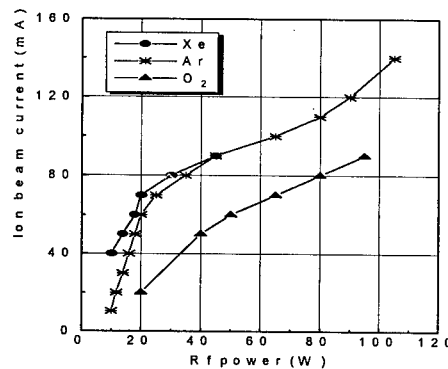


Figure 20. Dependence of ion beam current on a rf power. Magnetic system consists of three magnetic rings.

One can see from Fig. 20 the possibility of obtaining at rather low input power ion beams of inert and chemically active gases with densities in a 0.05 - 2.5 mA range. These are enough for sputtering, ion beam-assisted deposition of thin films [28,29], and other materials applications.

One more important characteristic for technological applications is beam uniformity. It is defined by three factors, that is (i) by the plasma uniformity near the IOS; (ii) by the divergence of an elementary beam extracted from a single IOS hole; and (iii) by the shape of IOS grids. Far from the source, the last two factors govern the beam profile, whereas closer to the source the first and the third factors are important.

Ion beam profiles measured close to the IOS are shown in Fig. 21. One can see a rather high uniformity, and especially for large accelerating potentials. The slight structure of the profiles is probably due to a spatial non-uniformity of fields of excited waves. The beam profile was found to be practically independent of gas, and to depend slightly on accelerating potential.

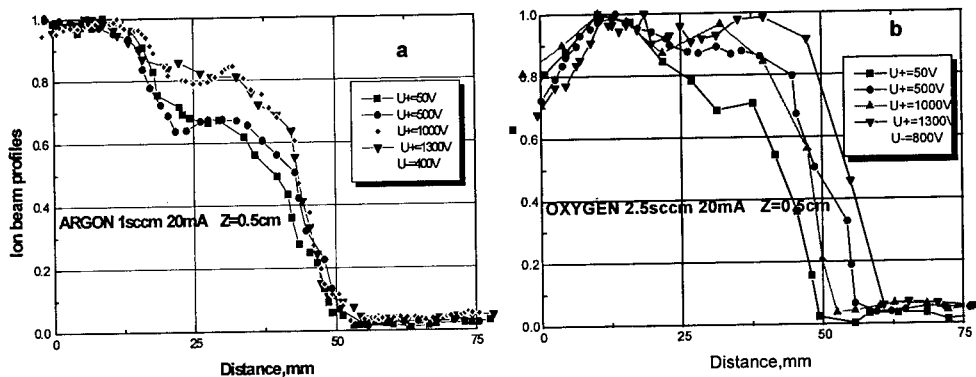


Figure 21. Ion beam profiles measured close to the exit of IOS.

The beam profiles measured at 5 and 22 cm distances from the source with concave IOS are shown in Fig. 22 for different magnetic configurations. The effect of magnetic configuration is of no account at 22 cm, but plays an essential role closer to the source. This results from a divergence of elementary beams produced by each of IOS holes. The divergence of the whole beam extracted from the source with a concave IOS was measured to be within 13 to 15%.

The geometry of IOS grids has a dramatic effect on the beam profile. This is seen from Fig. 23 where plotted are the profiles of beams extracted from the source with concave and convex ion optics systems.

## 5. ESTIMATING QUASISTATIC SOURCES FOR APPLICATIONS

### 5.1. A prototype of an ion thruster

To estimate a capability of the ion source with permanent magnets to serve as the ion thruster for space applications, we use the data obtained with Xe and partly presented in Fig. 20. The results are listed in Table 1. One can see that the values of power ion cost,  $C_i = P/i_b$ , where  $P$  is the input power, and  $i_b$  the

Table 1

Ion current mA	Gas efficiency %	Ion cost W/mA	Specific impulse	Thrust mN	Cost of thrust W/mN
60	70	670	3200	3.9	33
70	70	500	3000	4.5	34
100	70	700	3200	6.7	34

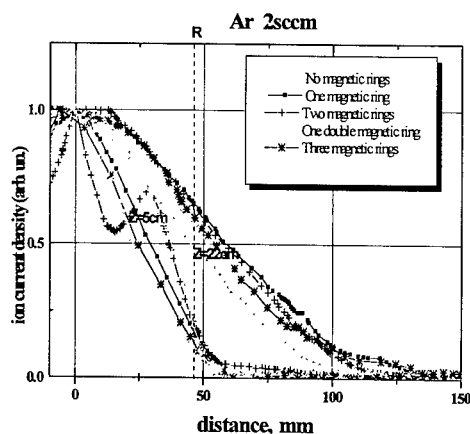


Figure 22. Ion beam profiles obtained with different magnetic systems and concave-type IOS.

beam current, and of gas efficiency,  $\beta = 0.7$  ( $\beta = i_b / m$  with  $m$  being a gas flow rate in current units) are compatible with those obtained with RITA [6], and meet the requirements listed in [27].

Comparison of our prototype thruster with other devices can be made using Table 2 where the parameters of different low-power (the power below 1 kW) ion engines are presented. All thrusters listed in this table are based on the dc discharges excepting RIT-10 which uses a rf discharge.

Table 2

Ion engine	IDOR-100 USSR	ARFA Russia	RIT-10 Germany	UK-10 UK-France	SIT-8 USA	XIES
Thrust mN	20	20	10	25	4.98	18
Specific impulse	3300	3000	4800	3200	2600	2585
Power W	500	500	440	650	120	439
Ion current mA	420	300	156		72	405
Working gas	Cs	Ar	Xe	Xe	Hg	Xe
Gas efficiency %			70	85	77	79
Power efficiency %			71		72	69
Total efficiency %	76	73	49	76	55	51
Resource hrs	1,000	10,000	8,150	6,000		12,000

## 5.2. A compact ion source for surface modifications of materials

A scheme of experiments is shown in Fig. 24. Surfaces of metals and polymers were irradiated by ions of different gases accelerated to energies ranging 100 to 1500 eV. The ion beam current was controlled by the rf power and gas flow rate, and was measured by a Faraday cup biased to -30 V. Doses of ions in a  $5 \times 10^{14}$  to  $5 \times 10^{16}$  ions/cm<sup>2</sup> range were exposed by varying the irradiation time at fixed ion beam current.

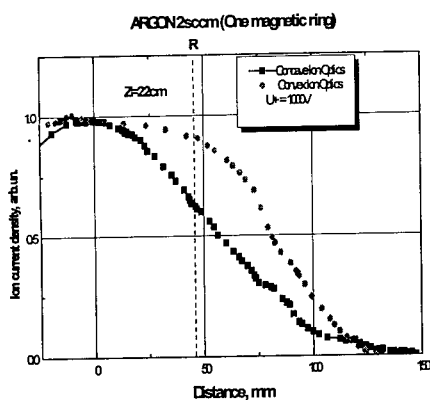


Figure 23. Ion beam profiles obtained with concave and convex grids.

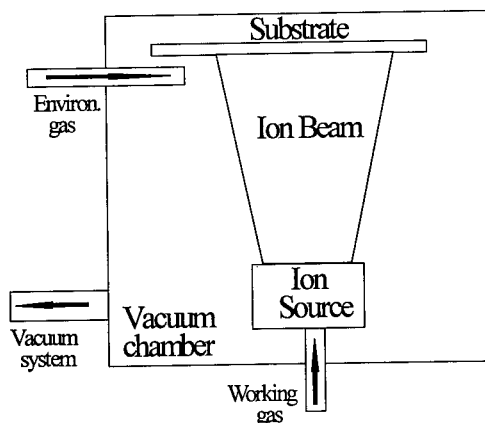


Figure 24. A diagram of the technological installation.

Environment gas was introduced near the surface of substrate during its irradiation. A wettability of irradiated samples was measured by a contact angle meter (ERMA, Goniometer Type). The measurement was done with triply distilled water by dropping of 0.25 ml distilled water on three different places of the substrate surface and averaging the contact angles. Polymer as well as aluminum surfaces were treated by the ion beam of different gases, with and without environment gas. Typical results of measurements for Al samples are shown in Fig. 25. One can see that the increase of ion dose up to  $2 \times 10^{17}$  ions/cm<sup>2</sup> leads to a significant decrease of the contact angle with hydrogen environment gas or hydrogen ions at the substrate.

The modification of Al surface was conducted using ions of inert gases and nitrogen. The modification of polymer surfaces needs also the utilization of reactive gases [33]. Fig. 26 shows the best contact angles achieved for polycarbonate in experiments with ions of both inert and chemically active gases. The results for argon and oxygen ions are close to those presented in [33,34]. The results for carbon dioxide and freon gases are new.

The operation of the ion source was stable for all gases used. The input power was less than 100 W, and the gas flow rate did not exceed 3 sccm.

## 6. CONCLUSION

In conclusion, we designed and optimized a compact, low-power (input power below 100 W) and economical (gas efficiency above 0.7) ion source based on a quasistatic discharge. It was shown to have a good potential as an ion thruster in a mN range, and as a device for surface modifications of both metals (Al) and polymers.

We established some general physical principles governing the operation of quasistatic sources, and verified their appropriateness in designing. These principles define the rf power absorption in source plasmas and permit one to predict the peculiarities of the source operation as dependent on the external magnetic field, driving frequency, and source geometry (scaling laws). Using these principles may contribute to improving the discharge stability and plasma parameters, that is to increasing the source controllability, as well as to designing new devices capable to serve as flexible instruments for various applications.

## Acknowledgements

This work was partly supported by the Ministry of Science, Technologies and Industrial Policy of Ukraine (MSTIPU), Grant No 2.4/997. One of the authors (K. P. S.) acknowledges a support of his trip to the ICPG XXIII by MSTIPU.

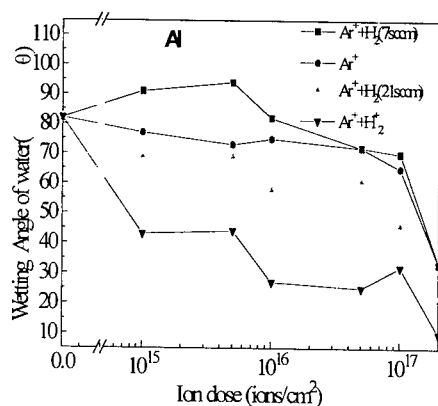


**Figure 25.** Change of contact angles of water for Al as a function of  $\text{Ar}^+$  and  $\text{Ar}^+ + \text{H}_2^+$  ion dose at 1 keV with and without flowing  $\text{H}_2$ .

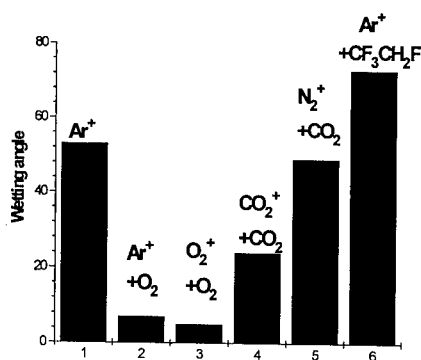


**Figure 26.** The best achieved contact angles for polycarbonate in experiments with ions of inert and chemically active gases.

## References

- [1] Lieberman M. A. and Lichtenberg A. J., Principles of Plasma Discharges and Materials Processing (Wiley, New York, 1994) pp. 387-411.
- [2] Nazarov N. I., Plyusnin V. V., Ranyuk T. Yu. et al., *Sov. J. Plasma Phys.* **13** (1987) 871-874.
- [3] Loewenhardt P. K., Blackwell B. D., and Boswell R. W., *Phys Rev. Lett.* **67** (1991) 2792-2794.
- [4] Keller J. H., *Plasma Sources Sci. Technol.* **5** (1996) 166-172.
- [5] Korczynski E., *Solid State Technol.* # 4 (1996) 63-73.
- [6] Bassner H. P., Berg H. P., et al., "Flight test results of the RITA experiment on EURECA", AIAA Papers, Sept 13-16 (1993) JEPC.
- [7] Chen F. F., "Helicon plasma sources", in High Density Plasma Sources, ed. O. A. Popov (Noyes, Park Ridge, NJ, 1996) chap. 1.
- [8] Keller J. H., *Plasma Phys. Control. Fusion* **39** (1997) A437-A442.
- [9] Boswell R. W., Porteous R. K., Prytz A., Bouchoule A., and Ranson P., *Phys Lett. A* **91** (1982) 163-164.
- [10] Chen F. F. and Chevalier G., *J. Vac. Sci. Technol. A* **10** (1992) 1389-1401.
- [11] Shoji T., Sakawa Y., Nakazawa S., Kadota K., and Sato T., *Plasma Sources Sci. Technol.* **2** (1993) 5-10.
- [12] Kat'yukha V. P., Kirichenko G. S., Taranov V. B., and Shamrai K. P., *Rev. Sci. Instrum.* **65** (1994) 1368-1370.
- [13] Aleksandrov A. F., Bogdankevich L. G., Rukhadze A. A., Principles of Plasma Electrodynamics (Springer, Heidelberg, 1984) chap. 7.
- [14] Shamrai K. P. and Taranov V. B., *Plasma Phys. Control. Fusion* **36** (1994) 1719-1735.
- [15] Vorob'ev N. F. and Rukhadze A. A., *Plasma Phys. Reports* **20** (1994) 1065-1077.
- [16] Shamrai K. P. and Taranov V. B., *Plasma Sources Sci. Technol.* **5** (1996) 474-491.
- [17] Aleksandrov A. F., Vorob'ev N. F., Kral'kina E. A., Obukhov V. A., and Rukhadze A. A., *Zh. Tech. Fiz.* **64** (1994) 53-67.
- [18] Kitsenko A. B., Panchenko V. I., Stepanov K. N., and Tarasenko V. F., *Nucl. Fusion* **13** (1973) 557-562.
- [19] Shamrai K. P., Pavlenko V. P., and Taranov V. B., *Plasma Phys. Control. Fusion* **39** (1997) 505-529.
- [20] Shamrai K. P. and Taranov V. B., *Phys. Lett. A* **204** (1995) 139-147.



- [21] Ellingboe A. R. and Boswell R. W., *Phys Plasmas* **3** (1996) 2797-2804.
- [22] Perry A. J., Vender D., and Boswell R. W., *J. Vac. Sci. Technol.* **B 9** (1991) 310-317.
- [23] Boswell R. W., *Plasma Phys. Control. Fusion* **26** (1982) 1147-1162.
- [24] Chen F. F., Sudit I. D., and Light M., *Plasma Sources Sci. Technol.* **4** (1995) 173-181.
- [25] Charles C. and Boswell R. W., *J. Vac. Sci. Technol.* **A 13** (1995) 2067-2073.
- [26] Shamrai K. P., Virko V. F., Blom H.-O., Pavlenko V. P., Taranov V. B., Jonsson L. B., Hedlund C., and Berg S., submitted for publ. in *J. Vac. Sci. Technol* (1997).
- [27] Perrota G., Bianconi M., Bicci A., Capacci M., Cirri G. F., and Matticari G., "Orbital control and manoeuvring of lightsats / Synchronous satellites: Assessment of new ion propulsion technologies, based on electron cyclotron resonance phenomenon, to improve the performances of thrusters in the millinewton range", AIDAA/AIAA/DGLR/JSASSS 22nd Int. Electric Propulsion Conference, Viareggio, Italy, October 14-17, 1991.
- [28] Rossnagel S. M., Cuomo J. J., and Westwood W. D., *Handbook of plasma processing technology: fundamentals, etching, deposition, and surface interactions* (Noyes, Park Ridge, NJ, 1990) 523p.
- [29] Cuomo J. J., Rossnagel S. M., and Kaufman H. R., *Handbook of ion beam processing technology: fundamentals, principles, deposition, film modification and synthesis* (Noyes, Park Ridge, NJ, 1989), p.362.
- [30] Kaufman H. R., *J. Vac. Sci. Technol.*, **21** (1982) 725-731.
- [31] Eberius M., et al., "Electric propulsion engines and their technical applications", Proc. 2nd German-Russian Conference, Moscow, Russia, July 16-21, 1993.
- [32] Alexandrov A. F., Kondranin S. G., Bougrov G. E., Vorobjev N. F., Kralkina E. A., Obukhov V. A., and Rukhadze A. A., *Appl. Phys.* **1** (1995) 3-25.
- [33] Koh S. K., Choi W. K., Cho J. S., Song S. K., Kim Y. M., Jung H. J., *J. Mater. Res.* **11** (1996) 2933-2943.
- [34] Choi W. K., Koh S. K., and Jung H. J., *J. Vac. Sci. Technol.* **A 14** (1996) 2366-2378.

## The Oscillations of the Positive Glow Corona

R.S. Sigmond

*The Electron and Ion Physics Group, Physics Department, Norwegian University of Science and Technology, 7034 Trondheim, Norway*

**Abstract.** The paper treats experiments, computer simulations, and the physical explanation of the oscillatory behaviour of positive glow coronas at or below atmospheric density. Experiments show that most positive glows have ionization regions that oscillate with frequencies depending on the gas, geometry, and average discharge current. Our circuit simulating program CIRCSIM with the general gas discharge element GPCS1 reproduces quantitatively Beattie's sphere-to-plane coronas in air, and also our cylindrical coronas in air and in argon with additives. The oscillations demand a fast secondary ionization (feedback) mechanism, and are damped or inhibited by slower feedback processes like positive ion or metastable feedback, and detachment from negative ions. Linear damped oscillations are due to ionization region capacitance and equivalent inductance. Nonlinear self-sustained oscillations are formed by periodic quenching by the generated positive ions.

### 1. INTRODUCTION

This paper treats the oscillatory behaviour of positive glow corona discharges in gases at or below atmospheric density, as studied by experiments, computer simulations, and physical reasoning. I believe that it provides a general physical answer to what has been, in my opinion, the last remaining major mystery of classical corona physics. The paper is organized as follows:

1. Introductory remarks and selected references for positive glow coronas.
2. Experimental observations of free and forced positive corona oscillations: typical recordings, and experimental indications for connections between oscillation types and discharge parameters.
3. Computer simulations: the simulation model, some important simulations of positive glow coronas, and simulation indications for connections between oscillation types and discharge parameters.
4. The physical mechanism of the positive glow oscillations: the impedances of the ionization and drift regions of coronas, passive oscillatory properties, linear and nonlinear free-running oscillations.
5. Conclusion: when and why positive glow oscillation and pulses occur.

All gases used in experiments and simulations in this paper have room temperature. The letter  $g$  is used for gas density instead of the customary  $n_g$ , to save one letter in all simulation screens.

A *corona discharge* is a low current ( $\approx \mu\text{A}$ ) gas discharge where the electrode geometry concentrates all ionization processes in a region close to the high field corona electrode. The rest of the discharge space forms a drift region where few charges are created but where electrons, ions and excited neutrals drift and react on their way towards the other, low field electrode [1,2]. A *positive glow corona* has a positive corona electrode, and is characterized by an ionization region that evenly covers the high-field surface area of the electrode. In positive wire-cylinder coronas the whole wire surface is glowing, in contrast to negative Trichel type coronas, which burns in contracted, nearly evenly spaced spots along the wire. Figure 1 illustrates such a positive cylindrical corona and its commonly used external electrical supply circuit. (The other common positive corona type, the positive streamer corona, occurs when the glow ionization region produces more ions and electrons than can be conducted away to the electrode. The conducting plasma column thus formed pushes the ionization region away from the corona electrode surface and permits it to propagate into and through the drift region. This type of corona will not be further discussed here.)

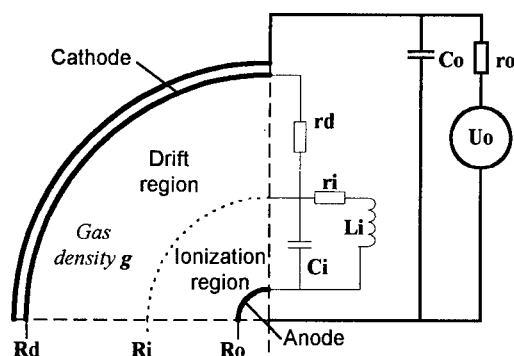


Figure 1. Schematic drawing of a quadrant of a cylindrical positive corona configuration with anode radius  $R_o$  and cathode radius  $R_d$ .  $C_o$ ,  $r_o$  and  $U_o$  forms the real external circuit, while  $r_d$ ,  $r_i$ ,  $C_i$  and  $L_i$  represent components of a simplified corona stability model, to be discussed in later sections. The ionization region is drawn abnormally large, for clarity.

As reported in the 1965 book by Loeb [3], the early investigators found positive coronas at and just above the onset voltage to consist of burst pulses and occasional weak "pre-onset" streamers. At higher voltages (and currents) these pulses either developed into streamers, or melted together on the oscilloscope screen to form the steady positive glow corona, often called the "Hermstein glow" [4] or "Uhlig ultracorona" [5].

In these early works the positive glow was generally described as "steady", with no systematic reports of oscillations. Colli et al [6] in 1954 reported on oscillatory behaviour of positive cylindrical coronas. It was, however, Beattie who in 1975 [7] pointed out that most apparently steady positive glow coronas really had violently oscillating or self-pulsed ionization regions. This pulsing is fast, in the 100 kHz range, and does not much affect the corona current, which is induced mainly by the slowly drifting positive ions. When observed by a free-running oscilloscope the pulses are easily mis-read as ordinary discharge current noise. Only by observing and triggering on the light emission from the coronas the pulses are readily visible.

Following Beattie, the positive glow oscillations were most actively studied in Trondheim, and sometimes reported upon [8–10]. We found that the oscillations were very dependent upon the corona gas composition. For example, pure argon gave no oscillations at all, but small additions of gases like  $N_2$ ,  $CO_2$ , or  $SF_6$  made it oscillatory. Air in the same corona vessel gave strong oscillations, but at appreciably higher frequency than with argon as the main gas. In all cases the oscillations were practically unaffected by changes in the external electric circuit parameters. This gave us two motives for further studies: to exploit the sensitivity to gas composition in a cheap detector for trace gases, and to find the physical mechanism responsible for the oscillations. As will be told below, the latter was not at all evident.

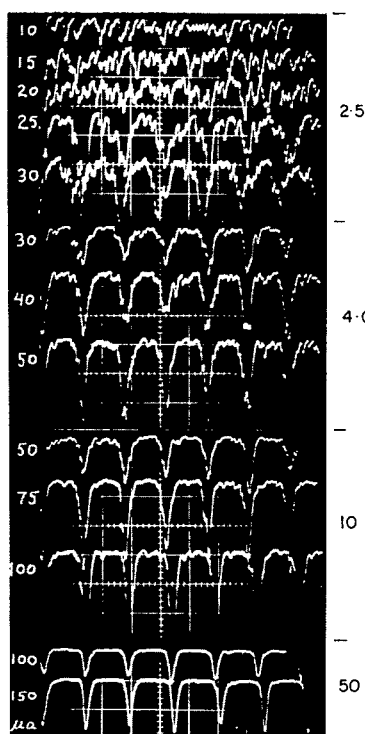


Figure 2. Beattie's photomultiplier oscillograms of the light from a positive glow corona, at increasing values of the average discharge current. Sphere-to-plane geometry with sphere radius 16 mm and the plane 24 mm away. Gas: 1 bar of  $O_2/N_2=10\%/90\%$ . Voltage around 40 kV. Time scale 5  $\mu s$  per major division. The average (DC) current is noted to the left of the oscillograms, while the relative light output scale is printed to the right. The pulses are completely spontaneous and free-running, and strongly nonlinear (no light emitted between the pulses).

## 2. SOME TYPICAL EXPERIMENTAL RECORDS OF POSITIVE GLOW OSCILLATIONS

Figure 2 shows Beattie's oscillograms [7] of the light output from the positive glow corona between a spherical anode of 16 mm radius and a plane cathode 24 mm away, in a 10% / 90%  $O_2/N_2$  mixture at

1 bar pressure, at DC currents 10–150  $\mu\text{A}$ . In this particular case the free-running pulses had a remarkably current-independent period of about 8  $\mu\text{s}$  and amplitudes increasing proportionally to the current. (Note the contrast to negative corona Trichel pulses, which tend to hold the amplitude constant while their repetition frequency increases proportionally with the current). It should be mentioned that some other of Beattie's observations show a more "normal" frequency increase with the current.

Beattie ascertained that each individual ionization region pulse occurred simultaneously over the complete anode surface, i.e., it was the whole ionization region that was "turned on and off". He noted further that the pulse repetition period was considerably longer than the electron transit time and considerably shorter than the ion transit time between anode and cathode, but coincided well with the positive ion transit time across the ionization region. Beattie also found that some electronegative gas

constituent seemed to be needed for oscillations to occur, and concluded that the oscillations had to be due to photodetachment from negative ions arriving in front of the ionization region. This conclusion was disputed by me [1] because the relevant cross sections seemed far too small.

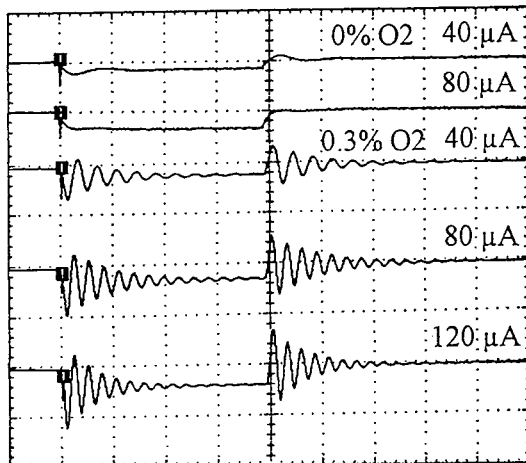


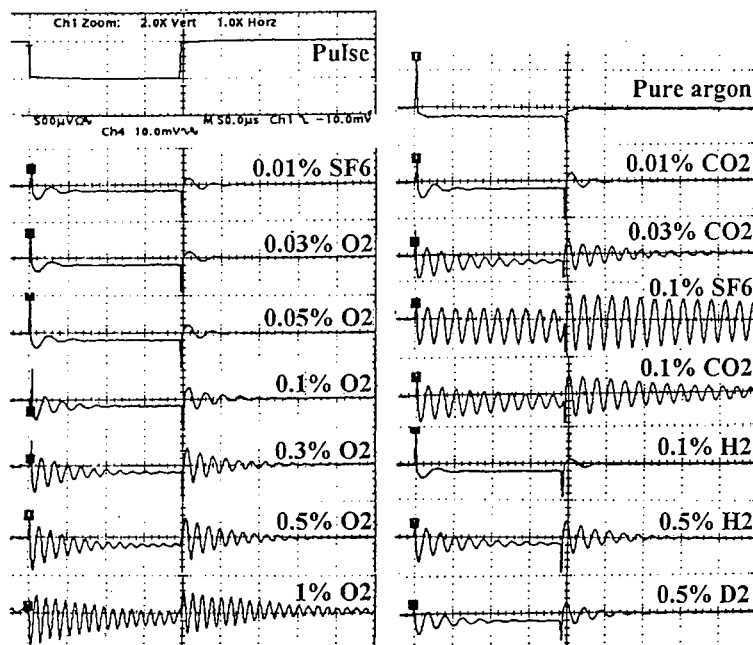
Figure 3. Voltage pulse excited current oscillations in cylindrical positive glow coronas in 1/4 bar argon and argon with 0.3% oxygen for different average (DC) corona currents (values typed above the curves) [11]. Anode radius  $R_0=0.8$  mm, cathode  $R_d=13$  mm, guard-ring shielded cylinder length 80 mm. Excitation pulse to the cathode 10 V 200  $\mu\text{s}$  negative. Time scale 50  $\mu\text{s}/\text{div}$ , current scale 10  $\mu\text{A}/\text{div}$ . The current is negative. Traces are averaged over about 100 sweeps.

The experimental work in Trondheim has covered both point-to-plane coronas in  $\text{N}_2\text{--O}_2$

mixtures [10], and concentric cylinder coronas in argon with additives and in air. The cylindrical coronas had guard sections to eliminate end effects, and are directly comparable with one-dimensional calculations, see Section 3 below.

Figure 3 shows the effect of corona current variation for pure argon and for  $\text{Ar} + 0.3\%$   $\text{O}_2$ , while in Figure 4 the gas composition is varied at a constant 50  $\mu\text{A}$  corona current [11].

Figure 4. Voltage pulse excited current oscillations in cylindrical positive glow coronas in 1/4 bar argon with different trace gases added [11] (concentrations typed above the curves), all at 50  $\mu\text{A}$  average corona current. Scales and other data as in Figure 3.



The excitation is a 10 V 200  $\mu$ s negative pulse applied to the outer (cathode) cylinder, which ensures that the unavoidable capacitive current pulse has the opposite polarity of an absolute increase in the (negative) discharge current.

Notable features of the Figures 3 and 4 and of all our other similar experiments are:

- Pure Ar shows a nearly pure RC relaxation response, without oscillatory tendency.
- 0.01% of the highly electronegative SF<sub>6</sub> in Ar has the same effect as 0.05% of the correspondingly less electronegative O<sub>2</sub>, – but also the same effect as 0.01% of the very weakly electronegative CO<sub>2</sub>.
- Hydrogen additives also induce oscillatory behaviour, but D<sub>2</sub> gives lower frequencies than H<sub>2</sub>.
- An increase of additive concentration increases the oscillation frequency.
- At higher concentrations of O<sub>2</sub>, SF<sub>6</sub>, and CO<sub>2</sub> the oscillations become free, and then become nonlinear.
- For all linear oscillations in a given gas mixture, the frequency increases proportionally to the square root of the DC discharge current:  $f \propto \sqrt{I}$ . (1)

Please note that any changes in current or gas composition also entail changes in the corona voltage, with corresponding changes in electron and ion transit times and discharge reaction times.

### 3. COMPUTER SIMULATIONS OF POSITIVE GLOW CORONAS

The computer simulations form an all-important part of the present study. The simulation engine is quite unique, and to judge its conclusions, it is essential that the reader know its basic principles, its strengths and its weaknesses. It differs from more conventional computer models of gas discharges by:

- treating discharges as elements in a general electrical circuit simulation program
- handling small numbers of charged particles as Poisson distributed integers
- handling drift by shuffling particles as bunches from one computing cell to another without splitting.

#### 3.1. Gas discharges and the CIRCSIM circuit simulation system

A given corona discharge may have concentrated regions containing millions of electrons and ions in non-linear Coulomb interaction, and other regions where one single electron is the seed that spawns new millions elsewhere. Our gas discharge simulation model GPCS1 [12] handles both the continuum aspects of the many as well as the stochastic integer nature of the few. The external electrical circuit feeding the discharge is often essential to its stability and mode, and is therefore included in the modeling.

GPCS1 forms one special circuit element in the general-purpose electrical circuit simulation program CIRCSIM developed by me and my students for PC type microcomputers. The CIRCSIM algorithm calculates the circuit voltages and currents by intelligent trial-and-error adjustments of all node voltages until the Kirchhoff current law is satisfied for all nodes to a specified accuracy. It solves no explicit matrices and does no linearizations at all. Circuits may be built from one or more discharge elements combined with all common passive and active electronic circuit components, like R, C, L, thermistors, diodes, Zeners, transistors, transformers, transmission lines, operational amplifiers, and voltage and current waveform supplies.

At every time step  $k$ , the main CIRCSIM algorithm gives each circuit element  $i$  its input voltages  $V_{i,k}$ . On the basis of these, and previous voltages  $V_{i,k-1}$  and currents  $I_{i,k-1}$  stored by the elements, each element is required to give back the present currents  $I_{i,k}$ . These are then used by the CIRCSIM algorithm to calculate the deviations from Kirchhoff's current law for each node, and to estimate the next iterative set of node voltages within the same time step.

#### 3.2. The GPCS1 gas discharge element

##### 3.2.1. Geometries, space and time subdivisions, inputs and outputs

The GPCS1 element has a selectable geometry with one space coordinate. GP1 has plane parallel electrodes, GC1 has concentric cylinders, and GS1 has concentric spheres. The discharge volume is subdivided along the space coordinate  $R$  into 50 or 120 computing shells of widths inversely proportional

to the Laplacian electric field. For each CIRCSIM time step  $dTi$  the electrons, negative ions, positive ions, and metastables are moved between these shells according to the local electric field, mobilities and diffusion coefficients; and excite, ionize, attach, and detach. The electric field  $E$  is recalculated for each time step by the Poisson equation. The electrode current is calculated by the Shockley-Ramo theorem and added to the current due to the electrode capacitance, to give the element output current.

To speed up the simulation, the GPCS1 element may change the CIRCSIM time step  $dTi$  according to the speed of the discharge processes. Also, it may internally subdivide  $dTi$  into  $DivT$  local time steps  $dTe$ , usually 10-100. Inside each CIRCSIM time step  $dTi$  only the electrons are moved and react, while heavy particles and imposed voltages are frozen. Interaction with the external circuit can only take place each main time step  $dTi$ .

The discharge elements have two main circuit terminals A and B for connection to the normal electrical supply circuit. In addition they have particle input and output (signal) terminals. The particle input terminals accept voltages as signals, equal to currents of electrons or ions to be liberated from the electrodes by external means (like photoelectrons). By connecting these terminals to CIRCSIM voltage waveform generators, any combination of ion and electron pulses can be liberated from the electrodes. Likewise, electrons, ions and metastables arriving at a discharge electrode may be selected to generate output signal voltages equal to the particle currents (in equivalent amperes, even for neutrals).

The GPCS1 circuit element, inserted into a typical voltage supply and current recording circuit, is illustrated in the Figure 5 below.

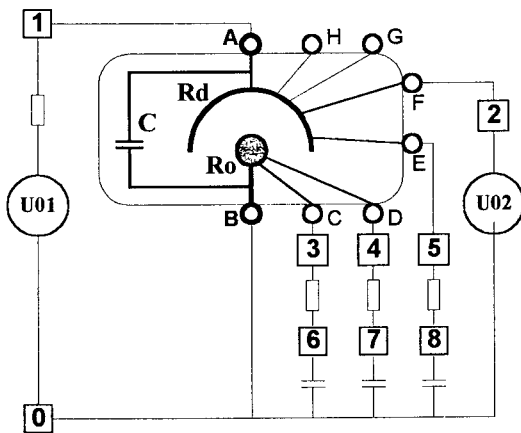


Figure 5. The CIRCSIM GPCS1 plane/cylindrical/spherical discharge element, inserted in a typical voltage supply and current recording circuit.

The anode radius is  $R_0$ , the cathode radius  $R_d$ , and the gap capacitance  $C$ .  $U01$  is the applied voltage with internal resistance  $r01$ , while  $U02$  injects an electron current from the cathode.  $A$  and  $B$  are the real corona current terminals.  $C$ ,  $D$ , and  $E$  give out signal voltages numerically equal to the currents of electrons and negative and positive ions hitting the electrodes, while nodes 6, 7, and 8 give out the corresponding RC-filtered signals.  $F$  is a signal terminal used for injecting an electron current from the cathode.  $G$  and  $H$  are signal terminals which can be used for particle input or output, but which are not used in the present circuit.

### 3.2.2. The charged particle drift algorithm

The charged particle drift algorithm is the main engine inside the GPCS1 discharge model. The plane, cylindrical, and spherical electrode geometries are all mathematically one-dimensional, i.e., the discharges develop along one space coordinate only. This coordinate is called  $R$ , or  $Rk$  when we refer to the  $R$  of the space shell no.  $k$ . The inner electrode is at  $R=R_0$ , and the outer electrode at  $R=R_d$ . The discharge volume is subdivided into  $TM$  shells,  $k = 1..TM$ , where at present  $TM=50$  or 120. The shells are represented by elements in the TrArrays (for Transit Arrays). Each type of charged particles uses two array rows, i.e., two array elements per space shell, while neutral diffusing particles use one.

The drift of any charged particle type  $i$  is simulated by retaining the particles in each half-shell for half the time needed to cross the shell, and then transferring *all* those particles to the next half-shell. Thus, by this *two-step drift algorithm* the particles move in bunches which may be added, but never split up. The use of two array elements (half-shells) per shell is necessary in order to avoid particle runaway in case of slowly decreasing particle velocity downflow. When below a selected number, the content of any cell is treated as a stochastic integer. In this way unphysical fractional particles are never created, and the ordinary numeric diffusion effect is avoided. The two-step drift algorithm has two drawbacks, however: a certain scatter in the charged particle transit time, and comparatively large particle current fluctuations (numerical noise) due to the creation of occasional empty shells.

### 3.2.3. Particle diffusion and reactions

Particle diffusion and reactions (like ionization and attachment) are computed separately from the drift. The algorithm scans through the TrArrays and calculates the reactions in each cell from the reaction rate functions (see below), and then simulates diffusion by three-point averaging weighed according to the diffusion coefficient to be simulated.

All reactions that may create particles in critical feedback positions, like electrode processes, detachment, and photoionization are sent through a random Poisson integer distribution routine if the particles created in one step are few. Thus, fractional electrons are avoided where they could have caused numerically important but completely unphysical avalanches.

### 3.2.4. The current induced in the external circuit

The current in the external circuit is due to two sources: the current induced by the moving particles, and the current due to the capacitance of the gap. CIRCSIM treats the latter as an ordinary capacitor.

The electrode current  $I_{qk}$  induced by a charge  $q$  moving with a radial velocity  $v$  in a shell number  $k$  at position  $Rk$  is given by the Shockley-Ramo theorem:

$$I_{qk} = qvE_{Lk}^I, \quad \text{where } E_{Lk}^I \text{ is the Laplacian field at } Rk \text{ due to 1 V across the gap.} \quad (2)$$

The total charge-induced current can be found simply by summing this equation over all charges moving in all shells. This may be called the charge drift method.

A mathematically equivalent and much more elegant method is found by taking the partial derivative of the charge drift method formula. The resulting charge derivative method will only contain a sum over the changes in the net shell charges from time step to time step, and computes appreciably faster. However, in GPCS1 it gives too much noise to be used, because of the two-step charged particle drift algorithm with infrequent transfers of particles from cell to cell.

### 3.2.5. Basic physical processes included in the GPCS1

The GPCS1 handles the basic discharge processes as follows:

- Transport equilibrium is assumed for all processes
- Mobilities and diffusion coefficients are field independent
- No-barrier interaction processes are always exothermic, and will have maximum and field-independent reaction rates at low fields, falling off at higher fields. Three-body electron attachment in air is of this type. Reaction rates from literature are used.
- Barrier processes, like electron impact ionization and dissociative attachment, need a certain energy to occur. For these reaction rates GPCS1 uses Townsend-type formulas:

$$\frac{\varphi}{g} = v \cdot \frac{A}{g} \cdot \exp\left(-\frac{B/g}{E/g}\right) \quad v: \text{ drift velocity, } E: \text{ el. field, } g: \text{ gas density, } A/g \text{ and } B/g: \text{ constants.} \quad (3)$$

### 3.2.6. Comparison with other, more conventional models

The CIRCSIM / GPCS1 model has proven to be very flexible, stable and reliable. It handles all types of external circuits, and all types of applied voltages: DC, AC HF, pulsed. At high plasma densities it may develop a fatal instability, probably because the plasma frequency gets too high in relation to the time step. This, however, never happens in coronas. Its main weakness derives from its main strength: it simulates discharges so well that it also simulates the discharge noise. In experiments using digital oscilloscopes, like Figures 3 and 4, one has to remove the noise by averaging over 20–200 sweeps. At a simulation speed of one millisecond per day such noise reduction by averaging is prohibitively slow.

Other, more conventional discharge simulation models, like the corona computations of Morrow [13], use continuous mathematics and often more implicit algorithms. They usually allow avalanche multiplication and feedback of fractional electrons and ions, and must be reprogrammed for each change of the external circuit, if included at all. These models are usually faster and have much less noise than GPCS1. Thus, the most efficient simulation strategy is probably to use CIRCSIM / GPCS1 for initial

surveys, external circuit changes, varying applied voltage types, and for checking continuous models; and to use the checked continuous models for series runs.

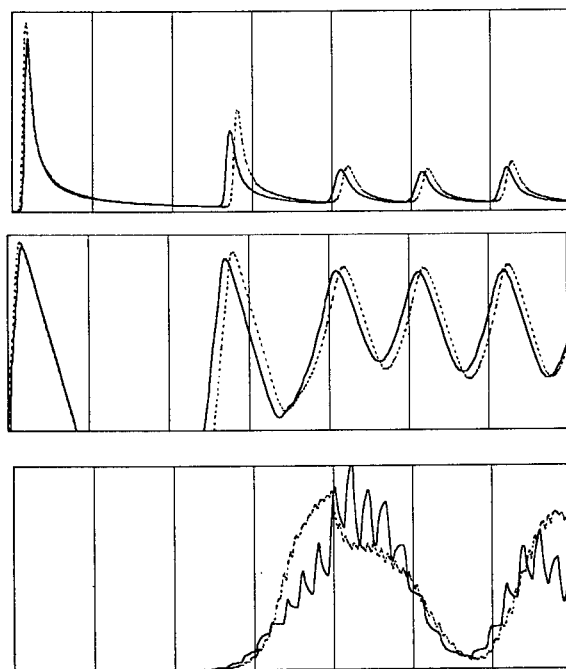
### 3.3. Selected GPCS1 simulations of positive coronas

The GPCS1 discharge model has about 40 adjustable parameters representing gas discharge process parameters. The strategy for searching for sets of parameters giving simulations which fitted experiments was to let well-published coefficients (like ionization and attachment coefficients, drift velocities, and diffusion coefficients) keep their values, select some few (like detachment, secondary ionization coefficients, and photoionization) for systematic variation, and put the rest equal to zero. The main experimental features to be reproduced were current-voltage characteristics, current-frequency curves, and oscillation damping. The systems simulated were our concentric cylinder corona chamber (data in Figure 6) filled with argon+additives or air at 1/4, 1/8, and 1/16 bar, and Beattie's sphere-plane system (data in Figure 8). The same set of discharge parameters for a given gas had to fit at all pressures.

The usual procedure was to adjust the sum of the secondary ionization and photoionization coefficients to make the current-voltage characteristics fit quantitatively over the pressure range, and then adjust the individual components of this sum to make the oscillation characteristics fit as well.

In this way the positive corona discharge systems described in Section 2 has been simulated running two 200 MHz Pentium PCs for more than one year. Even at a simulation speed of about one day per millisecond the number of runs recorded is large, and only the most important ones may be displayed here.

Figure 6 shows simulations of the initiation of a positive corona in the cylindrical corona chamber used for Figures 3 and 4, done both with the 50 shell and the 120 shell models. The agreement between the models is satisfactory, and the 50 shell model has been used for nearly all further simulations.



Corona current, linear scale 0–1800  $\mu\text{A}$ . Solid curves 50 shell, dotted curves 120 shell models. The corona current is computed from the Shockley-Ramo theorem, and is due to all charges moving in the corona gap between the inner anode at  $R_0=0.8$  mm and the outer cathode at  $R_d=13$  mm. The length of the corona section is 80 mm.

Electron current arriving at the anode, logarithmic scale  $10^{-8}$ – $10^{-2}$  A (6 decades!). The negative ions arriving at the anode follows the same curve, one decade lower.

With time the corona current and the electron current to the anode settle into regular, highly nonlinear oscillations of period about 11  $\mu\text{s}$ , against observed about 3  $\mu\text{s}$ . This is due to the photon feedback to the cathode. Photoionization gives the observed period.

Positive ion current arriving at the cathode, linear scale 0–400  $\mu\text{A}$ . The first positive ion cloud inhibits ionization for about 30  $\mu\text{s}$ , and then the second, smaller peak follows. With time the positive ion flow gets stationary. The ripple on the 50 shell curve is computational noise due to the special drift algorithm.

Time scale 0–70  $\mu\text{s}$ , common for all curves.

Figure 6. GC1 simulation of cylindrical corona in 1/4 bar "air", with ionization and attachment, but without detachment and photoionization. The secondary processes included are about 99% photon and 1% positive ion feedback to the cathode.

Figures 7a, b present computer simulations for the same cylindrical corona with respectively photon feedback to the cathode (a) and to the gas (photoionization, b), and with a stepwise increasing electron current injected from the cathode. In both cases the externally injected electron current damped the



oscillations, but only case b), with photoionization as the main feedback mechanism, gave current-voltage and oscillation characteristics in quantitative agreement with our air corona measurements. In other simulations the discharge current was varied. All linear oscillations followed the  $f \propto \sqrt{I}$  law.

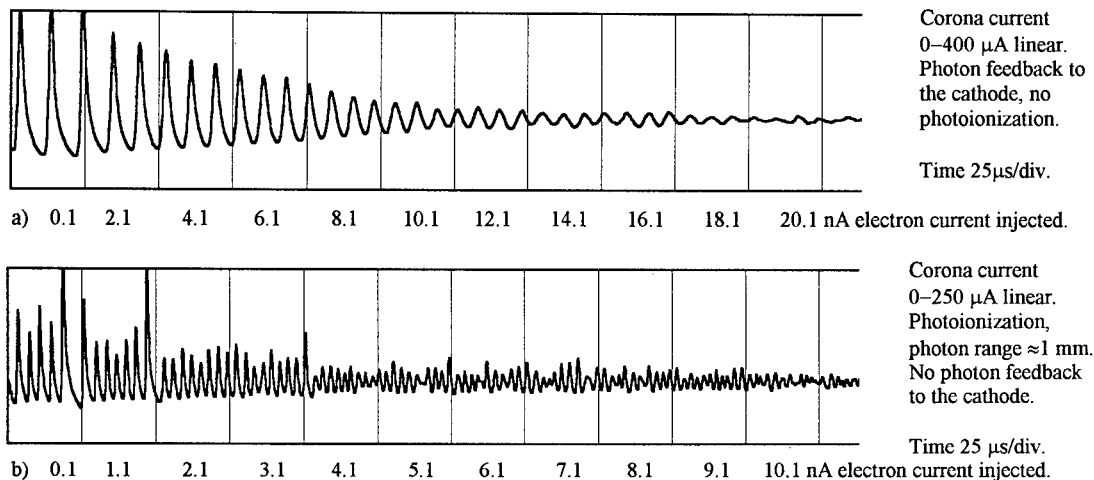


Figure 7 a-b. GC1 simulation of cylindrical corona in  $\frac{1}{4}$  bar “air”, with ionization and attachment, but without detachment. In both cases a steady injected electron current quenches the oscillations. Case b) has oscillation period in agreement with exp.

Similar simulations were made of the cylindrical corona chamber filled with argon plus additives, using a suitably pulsed voltage source. For pure argon a strong metastable feedback to the cathode had to be introduced to get agreement with experimental current-voltage characteristics and absence of oscillations. Some photon feedback to the cathode was also included, but played no role for pure argon. Additive gases were successfully simulated by quenching the metastable population while retaining the photon feedback to the cathode. Photoionization gave too short oscillation periods for the argon-based mixtures. Again all linear oscillations followed the  $f \propto \sqrt{I}$  law.

Finally, attempts were made to simulate the Beattie corona shown in Figure 2 above, using the GS1 spherical geometry model. The 16 mm radius spherical anode was simulated by a sphere, but the plane cathode 24 mm away had to be simulated by a second concentric sphere of 40 mm radius. These simulations used a slowly rising voltage ramp, in order to find parameter values that gave approximately current independent oscillation frequencies. Such oscillations necessarily had to be strongly non-linear, to escape from the  $f \propto \sqrt{I}$  law. The quite successful result is shown in Figure 8.

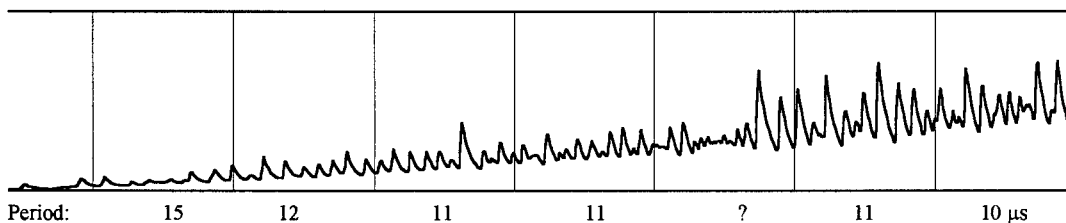


Figure 8. GS1 simulations of the Beattie corona of Figure 2 using concentric spheres of 16 and 40 mm radius, and ionization and attachment corresponding to 1 bar of  $\text{O}_2/\text{N}_2 = 10\% / 90\%$ , no detachment, and photoionization of the same specific range as for the other air corona simulations. Supply voltage linearly rising from 45 to 58 kV. Time scale 100  $\mu\text{s}/\text{div}$ , corona current scale 0–10 mA. The approximate oscillation period is shown under the graph, along the time axis.

### 3.4. Main results from the computer simulations

- 1) The most important conclusion from the simulations is that *Beattie's and our own positive corona measurements can be simulated quantitatively using consistent and reasonable sets of discharge parameters, and without postulating unproven or controversial discharge processes.*
- 2) The old accepted sets of primary ionization and attachment coefficients for both air [14] and argon [15] could be used without modification. Detachment in air, which has always been a subject of debate, had to be put close to zero, see below. In pure argon the metastable feedback coefficient had to be chosen so large that the corona onset occurred at an avalanche multiplication as low as 2.
- 3) Positive glow oscillations occurred whenever the main secondary (feedback) processes in the discharge were fast, i.e., had avalanche generation time distance  $T_g$  appreciably less than the positive ion transit time across the ionization region  $T_{pi}$ .
- 4) The oscillation or pulse period was roughly proportional to  $T_g$ , and usually of the order of  $T_{pi}$ . Linear oscillations (usually pulse excited) always had frequencies following the  $f \propto \sqrt{I}$  law. Non-linear pulses had longer periods, which usually were close to the positive ion transit time across the ionization region  $T_{pi}$ .
- 5) Positive glow oscillations were damped or completely eliminated by all slow electron feedback processes, i.e., processes that gave secondary electrons with delay greater than  $T_{pi}$ . Processes like constant electron injection (Figures 7 a-b), metastable feedback, positive ion feedback, and electron detachment from negative ions, all inhibited positive glow oscillations.
- 6) For the air coronas, the main feedback process had to be photoionization, to make  $T_g$  small enough to reproduce the high experimental oscillation frequencies.
- 7) For argon, feedback by metastables had to be the main secondary ionization process, with a small amount of photon feedback to the cathode added. Additives caused oscillations by quenching the metastable feedback, thus increasing the importance of the remaining photon feedback. Photoionization would give oscillation periods 3 times shorter than observed, and could not be a main secondary process in the argon based coronas.
- 8) Linear, pulse excited oscillations did not always readily transform into free-running nonlinear pulses, even when the parameters should encourage this. Often a larger pulse shock had to be given to start free-running pulses. (The computer, like me, could not always find any reason for positive feedback in the linear regime!)

## 4. THE PHYSICAL MECHANISM OF THE POSITIVE GLOW OSCILLATIONS

There are three different features of positive glow coronas that must be explained: the passive oscillatory response to a disturbance, the negative damping that in some cases makes free-running linear (sinusoidal) oscillations, and the completely nonlinear glow pulses. The third is simple, see Section 4.6., but the first two require discussion of the small signal equivalent circuit parameters of the corona regions.

### 4.1. The effects of a positive space charge shell. The ionization region capacitance

To discuss the oscillatory properties of the positive corona, we need the real and equivalent circuits drawn in Figure 1, as well as two new figures 9 and 10 which illustrate the effects of a shell of positive space charge on the field distribution and on the ionization integral of a low-current positive glow corona. The spherical simulated Beattie corona of Figure 8 has been chosen for convenience, but our cylindrical corona geometries show the same general features.

Figure 9 shows that a shell of positive charge  $Q$  around a positive inner electrode always will diminish the field inside and increase the field outside the charge shell. The net effect of  $Q$  on the ionization integral  $I_i = \int_{R_0}^{R_d} (\alpha - \eta) dR$  will always be detrimental, as long as the curve of the effective ionization coefficient  $\alpha' = \alpha - \eta$  vs. the reduced field  $E/g$  has a positive curvature. This is the case for all coronas treated in this paper. For the Beattie corona model of Figures 8-10 the ionization region limit, where  $\alpha' = 0$ , is at  $R_i = 22$  mm, so a  $Q$  at this position certainly will diminish  $I_i$ . However, the important point is that this does *not* make a negative, resistive  $180^\circ$  feedback, but a *capacitive*  $90^\circ$  feedback.

The proof is that a current increase  $\Delta I$  does not give a proportional reduction  $\Delta Vq$  of the ionization region voltage, while a charge increase  $\Delta Q = \int \Delta I dt$  does. The capacitance  $Cq = \Delta Q / \Delta Vq$  at  $Rq$  is easily calculated, and equals 12 pF for  $Rq = Ri = 22$  mm at the edge of the ionization region in the Beattie corona model of Figs. 8–10. This identifies the ionization region equivalent capacitance  $Ci$  in Figure 1.

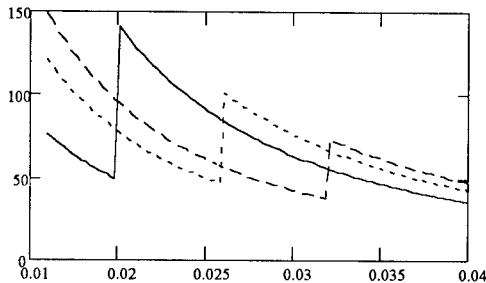
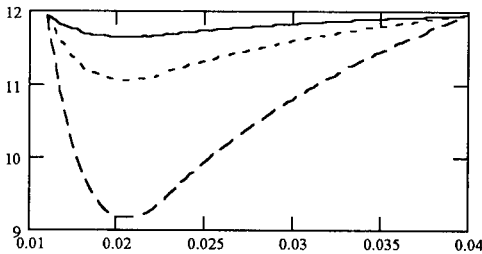


Figure 9. The effect of a given spherical, positive shell charge  $Q$  on the reduced electric field  $E/g$  distribution between the anode and the cathode spheres in the GS1 approximation to the Beattie geometry (see Figure 8 legend), as function of its position  $Rq$ . Anode radius 16 mm, cathode radius 40 mm, 40 kV gap voltage, and  $E/g$  scale 0–150 Td. No other space charges are present.

$Q$  will always diminish the field inside it and increase it outside. Its effect diminishes with the distance from the anode. The curve for  $Q=0$  (not drawn, for clarity) goes mid-between the right part of the solid curve and the left part of the dashed.



The ionization region limit, where  $(\alpha - \eta) = 0$ , is at  $R = 22$  mm.

Figure 10. The effect of a shell charge  $Q$  on the ionization integral  $Ii = \int_{Ro}^{Rd} (\alpha - \eta) dR$ , as function of the shell charge position  $Rq$ , for three values of  $Q$ , in the GS1 approximation to the Beattie geometry. Anode radius 16 mm, cathode radius 40 mm, 40 kV gap voltage. No other space charges are present. Note that the effect of a positively charged shell will always be detrimental for the corona gaps of this paper. Only for much smaller inner electrode radii will the ionization integral show a weak maximum for  $Q$  positions close to the inner electrode.

#### 4.2. The drift region equivalent resistance

A resistive effect  $rd$  of the drift region is defined by the drift region's immediate current change  $\Delta I$  when the drift region voltage is changed by  $\Delta Vd$ ,  $rd = \Delta Vd / \Delta I$ . At any given moment the corona drift region will contain numbers of positive and negative charges that are roughly proportional to the corona average current  $I_o$ . As no ionizations take place here, the only immediate effect of a voltage change  $\Delta Vd$  is to increase the charge particle speeds proportionally. The  $Ni$  positive ions dominate the drift region, and we can thus write:

$$\Delta I \approx N_i \mu_i \Delta Vd \propto I_o \Delta Vd \quad rd \propto 1/I_o \quad (4)$$

This allows an estimate of the drift region equivalent resistance  $rd$  in Figure 1 and its current dependence.

#### 4.3. The ionization region equivalent inductance and resistance

To show oscillatory behaviour, any electrical system must have two internal elements with opposite-phase current-voltage characteristics (like capacitance and inductance). For the cases of a parallel-plate DC Townsend discharge or a corona ionization region, the first of these required circuit elements is the capacitance  $Ci$  of the region, see Section 4.1. For a short time this capacitance is able to sustain a discharge current different from the imposed DC current. The voltage will lag behind any current change.

The second required element for oscillations is the equivalent inductance  $Li$  of the discharge or ionization region. This inductance is due to the delay between the application of a voltage step to the discharge DC voltage and the subsequent discharge current change. Any DC discharge burns with a reproduction factor  $\mu = 1$ ; i.e., each electron that leaves the cathode will on the average be replaced by exactly one new electron in the next avalanche generation. A voltage step  $\Delta Vi$  added to the DC sustaining voltage will increase the reproduction factor from 1 to  $1 + \Delta \mu$ , which will make each new avalanche generation  $1 + \Delta \mu$  larger than the preceding one. If the mean time between the avalanche generations is  $Tg$  (equal to the electron transit time in case of photon feedback alone), then the current will change with time as:

$$I_i(t) = I_{i0} \exp\left(\frac{\Delta\mu}{T_g} t\right) \quad \left(\frac{dI_i}{dt}\right)_0 = I_{i0} \frac{\Delta\mu}{T_g} = \frac{I_{i0}}{T_g} \frac{\partial\mu}{\partial V_i} \Delta V_i \quad (5)$$

If we, for comparison, take a real coil of inductance  $L$  and impose a voltage step  $\Delta V_i$  across it, then a linear current change will result:

$$\frac{dI}{dt} = \frac{\Delta V_i}{L} \quad (6)$$

Thus, for small voltage deviations from the DC sustainment voltage, the discharge or ionization region will act as inductances:

$$L_i = \frac{T_g}{I_{i0} \frac{\partial\mu}{\partial V_i}} \quad (7)$$

Note that  $L_i$  is proportional to  $T_g$  and inversely proportional to the DC sustainment current  $I_{i0}$ .

Will the Townsend discharge or corona ionization region also have an equivalent resistance  $ri$ , meaning that a change of current  $\Delta I_i$  will cause a fairly immediate change  $\Delta V_i$  in burning voltage? Yes, one insignificant part due to the increase of charge velocities caused by field increase, and one important part due to the change of the secondary ionization processes caused by space charge distortion of the field in the region. The space charges will usually increase the ionization efficiency in a parallel plate Townsend discharge, and this makes  $ri$  negative. For the ionization region in a positive corona, the effect depends on the types of secondary processes. From Figure 9 it is seen that a positive charge shell will increase the cathode field, and thus photon feedback to the cathode, while it might easily reduce the photoionization feedback to the gas near the anode. Thus the sign of  $ri$  for a positive corona depends on a quantitative balance between several discharge processes, and is not at all obvious.

#### 4.4. The passive oscillatory properties of the positive glow corona

If we at first neglect the equivalent resistance effects in Figure 1 by letting  $rd$  be very large and  $ri$  very small, then the small signal characteristics of the Townsend discharge and the corona ionization region may be modeled by the gap or region capacitance  $C_i$  in parallel with the discharge inductance  $L_i$ . A voltage pulse added to the discharge sustainment voltage will then induce a train of current oscillations with the angular frequency  $\omega_i$ :

$$\omega_i = \frac{1}{\sqrt{L_i C_i}} \propto \sqrt{\frac{I_{i0}}{T_g}} \quad (8)$$

This  $\sqrt{I_{i0}}$  frequency dependence has previously been observed in plane parallel Townsend discharges [16] and in positive concentric cylinder coronas [6], and is a main feature of all linear oscillations observed in the present experiments and simulations.

Please note from eq.(7) that the equivalent inductance  $L_i$  also is proportional to the effective avalanche generation duration  $T_g$ , and inversely proportional to the sensitivity of the reproduction factor to changes in the ionization region voltage  $\partial\mu/\partial V_i$ . The oscillation period is *not* determined by the positive ion transit time across the ionization region (but oscillations with longer periods become highly damped, see below). For linear oscillations the positive ions will affect  $ri$  but not  $\omega_i$ .

It is immaterial whether the oscillations are induced by applied pulses or by the natural stochastic fluctuations of the discharge current. In all cases a resistive impedance  $ro$  in the external circuit will damp these oscillations, as will the effective equivalent resistance  $rd$  of a corona drift region.

#### 4.5. Linear free-running positive glow oscillations?

In no way may the (positive) series impedances  $ro$  and  $rd$  make the oscillations self-sustained. For this, a negative effective resistance must exist. In a plane parallel Townsend discharge or in the ionization region of a negative corona, such a negative resistance may be provided by the space charge field of the positive ions, which will increase the cathode field and thus the efficiency of the secondary cathode processes. This will reduce the voltage necessary to sustain the discharge, and the  $V_i(I_i)$  curve will get a

negative slope. In the ionization region of a positive corona, on the other hand, Section 4.4. concluded that the sign of  $ri$  is more difficult to predict.

We now can discuss the complete small-signal equivalent network for a corona discharge shown in Figure 1. For a parallel-plate Townsend discharge the value of  $ri$  is readily measured, being the slope of the  $V(I)$  curve at small ( $\mu A$ ) currents. For a corona ionization region,  $ri$  will usually be masked by the drift region impedance  $rd$ , since it is the sum  $ri+rd$  that is accessible as the slope of the  $V(I)$  characteristic of the corona. Only when  $ri$  is negative and  $rd+ro$  sufficiently large will  $ri$  reveal itself, not by the slope but by making the current oscillatory.

It is easily shown [16] that the equivalent circuit of Figure 1 has two possibilities of instability. Both demand negative  $ri$ :

Catastrophic:  $r_i + r_d + r_o < 0$  (when  $Co$  is some picofarads only), leading to spark. (9a)

If  $Co$  is much larger:  $r_i + r_d < 0$  leading to recurrent spark discharging of  $Co$ . (9b)

Oscillatory:  $r_d > \frac{L_i}{C_i |r_i|}$  for  $Co$  greater than some ten picofarads. (10)

A high drift region resistance, i.e., a low corona current, should encourage growing linear oscillations. However, the sign of  $ri$  may change from one positive corona to another, as born out by the reluctance of our simulations to give growing oscillations in the linear, small signal range. This is radically different from negative coronas, where the positive ions formed by a first avalanche obviously increases the cathode field and all secondary processes, making  $ri$  so negative that the current growth becomes exponential even in the small-current range. Trichel pulses have no growth inhibitions.

#### 4.6. The nonlinear positive glow pulses

In contrast to linear positive glow oscillations, these are easy to predict and explain. Let us assume, in Figure 10, that the corona has such secondary (feedback) processes that the corona on the average needs an ionization integral  $Ii=11$  to burn with a reproduction factor  $\mu=1$ . We start the reasoning and the corona without any space charge, with an electron at the edge of the ionization region at  $R=22$  mm. This makes an avalanche on its way to the anode. As then  $Ii=12$  and  $\mu>1$  the ionization grows, and *if the feedback processes are fast enough* a substantial positive charge  $Q$  will have time to form before  $Ii$  falls below 11 (look at the  $Ii$  curve for the largest  $Q$ ). After  $Q$  has reached this point it continues to drift outwards, and  $\mu$  falls significantly below 1. All ionization ceases, and in simulations the corona dies out if not *some* slow feedback also exists to start the next pulse. A new pulse then starts when the  $Q$  has drifted out far enough to again make  $Ii>11$ , i.e.,  $\mu>1$ .

### 5. CONCLUSIONS

The oscillatory behaviour of positive glow corona discharges in gases at or below atmospheric density has been investigated using experiments, computer simulations, and physical reasoning. The combined results should provide a general answer to this last remaining major problem of classical corona physics:

- 1) The positive glow corona gets oscillatory behaviour when the dominating secondary feedback processes of the corona are fast compared to the transit time of positive ions across the ionization region. A minute amount of slow feedback or external electron generation may be necessary continuously to provide initiatory electrons in the case of nonlinearly self-pulsed coronas.
- 2) It is immaterial whether the feedback is photoelectron emission from the cathode or photoionization of the gas outside the ionization region, as long as the feedback fulfills the speed criterion 1). The linear oscillation periods may thus be much shorter than the positive ion transit time across the ionization region, but not much longer because of condition 1).
- 3) Linear positive corona oscillations generally have oscillation frequencies proportional to the square root of the average corona current. Nonlinear repetitive positive glow pulses temporarily quench all ionization (see point 6), resulting in lower and less current dependent repetition rates.
- 4) Slow secondary processes, like positive ion or metastable feedback, or detachment from negative ions, inhibit the oscillations, so that the reaction of the corona to pulse excitations becomes oscillatory

damped or exponentially damped. Pure argon coronas, with mainly metastable atom feedback, show no oscillatory behaviour at all.

- 5) Free-running linear positive glow oscillations may or may not occur, according to whether the ionization region has a negative resistance, and the drift region resistance is large enough.
- 6) Nonlinear positive glow pulses are formed because a positive ion shell, once formed close to the anode, first decreases and then increases the corona ionization when it drifts toward the outer electrode. The first decrease quenches all ionization. The next ionization pulse may start when the first positive ion shell has drifted sufficiently far out to restore the corona reproduction factor, if initiatory electrons are to be found.

### Acknowledgements

The present paper owes much to discussions with and experimental results from visitors, staff and students in the ELION laboratory in Trondheim: A and M Goldman (Laboratoire de Physique des Décharges, Gif-sur-Yvette, France); M Laan and K Kudu (Gas Discharge Laboratory, Tartu University, Estonia); B Kurdelova, M Kurdel and K Hensel (Comenius University, Bratislava, Slovakia); B Bjones, I H (Olsen) Lågstad, R T Randeberg, and G Løfsgård (ELION).

### References

- [1] Sigmond R S "Corona Discharges", Chapt. 4 in Meek J M and Craggs J D (eds) "Electrical Breakdown of Gases", (Wiley: London 1978) pp 319-84.
- [2] Goldman M, Sigmond R S "Corona Discharges and Applications", in Kunhardt E E and Luessen L H (eds) "Electrical Breakdown and Discharges in Gases", NATO ASI Series B: Physics, Vol.89B (Plenum: New York 1983) pp 1-64.
- [3] Loeb L B "Electrical Coronas", Univ. of California Press 1965
- [4] Hermstein W, Archiv für Elektrotechnik **44** 209-224 and 279-288 (1960)
- [5] Uhlig C A E, Proc. High Voltage Symp., Nat. Res. Council Pub. No 4313 pp 15-1 – 15-13 and 16-1 – 16-11, Ottawa 1956
- [6] Colli L, Facchini U, Gatti E, Persano A "Dynamics of corona discharge between cylindrical electrodes", J.Appl.Phys. **25** 429-435 (1954)
- [7] Beattie J "The Positive Glow Discharge", Ph.D. thesis, Univ. of Waterloo, Canada 1975
- [8] Linhjell D, Sigmond R S "Sampling image intensifier camera study of the glow pulses of positive point-to-plane coronas", Proc. 9<sup>th</sup> Int. Conf. on Gas Discharges and Their Applications, Venezia (Benetton) 1988 pp 403-406
- [9] Sigmond R S "Corona physics and diagnostics", Proc. 22. Int. Conf. on Phenomena in Ionized Gases, AIP Conf. Procs. 363, New York 1995 pp 332-344
- [10] Kudu K, Lågstad I H, Sigmond R S "About the positive corona discharge forms in O<sub>2</sub>-N<sub>2</sub> mixtures", Proc. 23. Int. Conf. on Phenomena in Ionized Gases, Toulouse 1997 pp IV-34 – 35
- [11] These measurements were done in my Trondheim laboratory by students K Hensel from Comenius University, Bratislava, and I H Lågstad and T Randeberg, NTNU.
- [12] Sigmond R S "GPCS1: A discharge model for all seasons", Proc. 8<sup>th</sup> Int. Conf. on Electrostatics, Poitiers June 4-6 1977 (ed. G Touchard), Additional Issue pp 58-63. CIRCSIM with GPCS1 is free, available from the author (one 1.44 Mb diskette), email [sigmond@phys.ntnu.no](mailto:sigmond@phys.ntnu.no).
- [13] Morrow R, personal communication "Positive glow corona theory", to be presented as topical invited lecture at 12<sup>th</sup> Int. Conf. on Gas Discharges and Their Applications, Greifswald Sept. 1997.
- [14] Sigmond R S "Basic corona phenomena" Proc. 16. Int. Conf. on Phenomena in Ionized Gases (Duesseldorf 1983) Invited Papers Volume pp 174-186.
- [15] Brown S C "Basic Data of Plasma Physics" Wiley: New York 1959.
- [16] Sigmond R S, "On the static and quasistatic characteristics of the self-sustained low pressure Townsend discharge in hydrogen", Proc. 5<sup>th</sup> Int. Conf. on Phenomena in Ionized Gases (North-Holland), 1962, pp 1359-1363.

## Langmuir Probe Diagnostics for Medium Pressure and Magnetised Low-Temperature Plasma

M. Tichý, P. Kudrna, J.F. Behnke\*, C. Csambal\* and S. Klagge\*\*

*Department of Electronics and Vacuum Physics, Faculty of Mathematics and Physics, Charles University, V. Holešovickách 2, 180 00 Prague 8, Czech Republic*

*\* Institute of Physics, Faculty of Mathematics and Natural Sciences, Ernst-Moritz-Arndt University, Domstrasse 10a, 17487 Greifswald, Germany*

*\*\* Rosenweg 7, 17489 Greifswald, Germany*

**Abstract.** In this contribution we aim at presenting the overview of the work that has been done in expanding the applicability of the probe method to low-temperature plasma at the pressure range when the collisions of charged particles with neutrals start to be important (we call this pressure range medium pressures) and to plasma under the influence of the weak-to-medium magnetic field that is commonly used in plasma enhanced technologies. Most of the discussion is devoted to simple case of a plasma consisting of electrons and of one kind of positive ions. Our review also mostly concerns the cylindrical Langmuir probe. The first part of the article is devoted to discussion on the influence of the positive-ion-neutral collisions on the interpretation of the ion current part of the probe characteristic in order to get the true value of the plasma number density. In the second part one of the theories that take account of this effect is used to assess the influence of the weak magnetic field to the interpretation of the probe data. Finally we discuss the anisotropy of the electron velocity distribution function due to the effect of the magnetic field. The discussion is supported by the new experimental data.

### 1. INTRODUCTION

Langmuir and Mott-Smith [1-5] firstly showed that it is possible to analyse properly the current-voltage probe characteristic in order to deduce plasma parameters in the vicinity of the probe. In particular, that it is possible to determine the plasma potential, the electron and ion densities and the electron energy distribution function. Assuming that the energy distribution of electrons is Maxwellian it is possible to determine the electron temperature too.

There are several potentially serious sources of errors in measurement of the probe characteristics in a DC plasma without the magnetic field. Some of them are coupled with the processing of the signal from the probe, some are effects that are coupled with the interaction of the probe and the plasma being investigated. Of the "apparatus" effects is worthy to mention the magnitude of the resistance in the probe circuit that should be much lower than the lowest differential resistance of the probe characteristic; the effect has been discussed in [6]. Among the second group we can list (i) too high probe collection area [7-9], (ii) the change of the work function over the probe surface (especially due to contamination of the probe surface) [10], (iii) the secondary emission of electrons from the probe surface, e.g. [11] and (iv) the collisions of charged particles with neutrals within the space charge sheath. If a magnetic field is applied to a plasma, then, in addition, (v) the orientation of the probe to the direction of the magnetic field is of prior importance. The effects (i,ii,v) cause "rounding off" the probe characteristic near the plasma potential and subsequently uncertainty in determination of the plasma potential and electron energy distribution function (EEDF). The effects (iii,iv) are at low-to-medium pressures mostly important in the positive-ion-current part of the probe characteristic and can cause changes of the measured value of the floating potential and of the estimated value of plasma number density. Our review concentrates on the effect of collisions and on the effect of magnetic field with regard to their influence of the probe data interpretation.

The working regime of the probe in a plasma without the magnetic field is usually described by two parameters (see e.g. [12]) namely by the Knudsen number for ions and electrons  $K_{i,e} = \lambda_{i,e}/R_p$  (where  $\lambda_{i,e}$  is the mean free path for ions/electrons and  $R_p$  the probe radius) and by the Debye number  $D_\lambda = R_p/\lambda_D$ ,  $\lambda_D = (\epsilon_0 k T_e / (q_0^2 n_e))^{1/2}$  is the Debye length,  $\epsilon_0$  is the permittivity of vacuum,  $k$  the Boltzmann constant,  $T_e$  the electron temperature,  $q_0$  the elementary charge and  $n_e$  the electron density). Another parameter which influences the collection of charged particles by a probe is the "anisothermicity parameter" of a plasma namely the ratio of the electron to ion temperature,  $\tau = T_e/T_i$ . The introduction of this parameter (and also of  $\lambda_D$ ) already implies the Maxwellian distribution of electron and (for the case  $T_i > 0$ ) of ion energies. The Maxwellian distribution of electron and ion energies is assumed also throughout the present paper except where stated otherwise. We restrict ourselves further to the case of a cylindrical probe which is easy to manufacture and is applicable in all cases where the distribution of electron and ion energies can be assumed isotropic. We also assume anisothermic plasma for which  $\tau \gg 1$ .

For most experimental conditions relevant to plasma-aided technologies the thickness of the probe sheath is proportional to the Debye length. Because  $K_{i,e}$  characterises the magnitude of the ion and electron mean free path the quantity  $(D_\lambda K_{i,e})^{-1}$  is proportional to the number of collisions of these particles with neutrals in the sheath. Since the thickness of the sheath depends on the probe potential the proportionality coefficient is a function of the probe potential too. For a given probe potential the number of collisions of electrons and ions in the sheath can be visualised by means of the  $D_\lambda$  vs  $K_i$  plot. Such graph for  $D_\lambda \leq 3$  is depicted in Fig. 1. Similar plot has been introduced in [12] and [13]. From the graph in Fig. 1 it is seen that the working regime of the probe could be roughly divided into three regions separated by the lines depicting the number of collisions of ions/electrons with neutrals in the probe sheath for which are  $X_{i,e} \approx 0.1$ . The reasoning behind it is a simple consideration that in such case one can expect that the relative error in the measured ion or electron current due to collisions in the space charge sheath does not exceed 10 %, which is an acceptable error for most probe measurements.

In the probe working regime where  $X_{i,e} \leq 0.1$  the influence of ion and electron collisions in the space charge sheath around the probe can be neglected. In this case the ion and electron probe currents can be described by a theoretical model that does not take the collisions between charged and neutral particles into account (shortly "collisionless model"). In case of  $X_i \geq 0.1$  and  $X_e \leq 0.1$  the electron probe current can be described by the collisionless model while in the ion current model the collisions in the space charge sheath should be taken into account. In the last case where both  $X_i$  and  $X_e$  are higher than 0.1 the collisions of both electrons and ions have to be taken into account in the probe current model.

The probe measurements in the medium pressure discharge correspond mostly to the transition and collision regimes. For this reason in order to analyse properly the current-voltage probe characteristics it is necessary to have the models of the probe current for these two regimes. The model for transition pressure regime is based on the collisionless model. In this model the electron current corresponds to the collisionless one and the positive ion current is corrected with respect to the collisionless one by the factor which expresses the influence of ion collisions in the space charge sheath around the probe.

In a magnetic field further parameter  $\beta$  characterises the magnetic field strength with respect to the probe dimension,  $\beta = r_L/R_p$ , where  $r_L$  is the mean Larmor radius that is for charged particles with a Maxwellian EEDF given by  $r_L = \frac{1}{eB} \sqrt{\frac{\pi m_e k T_{e,i}}{2}}$ . We do not have enough space in this report to describe in detail "classical" probe theories that analyse the collection of charged particles under the ideal,

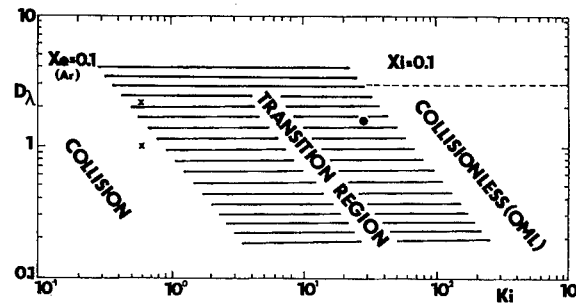


Figure 1. The division of the  $D_\lambda$ - $K_i$  plane to the collisionless, transition and collision probe regimes calculated for  $\eta = 15$  [12]. Working gas argon. The horizontal dashed line indicates the boundary of OML case [22].  $\times$ ...data from [60] taken at 62 Pa,  $\bullet$ ...datum from [61] taken at 7.5 Pa.



i.e. collision-free conditions; the reader should refer either to relevant books [9,11-15], or to original journal publications. For the case of so-called OML regime of the Langmuir probe that is most relevant for plasmas commonly used in plasma-aided technologies, i.e. when the sheath thickness is much larger than the probe radius, we would recommend the sources [3,16-20] and for the double probe method [21].

## 2. LANGMUIR PROBE IN THE TRANSITION REGIME OF PRESSURES

The collisionless OML model has been found satisfactory by experimenters for the electron collection by the probe for comparatively wide range of experimental conditions. However, the positive ion current was underestimated in this model that leads to overestimation of the positive ion density with respect to the electron one when determined from the same probe characteristic even at conditions when the plasma could be assumed as quasineutral. This has been found in non-isothermal discharge plasma, see e.g. [25] as well as in isothermal afterglow plasma [26]. Moreover the Bernstein-Rabinowitz [21] and Laframboise [22] theories predict that the ion saturation current should be for the orbital motion limited conditions (OML) independent of the Debye number  $D_\lambda$  if the probe potential is constant. The calculated dependence of the ion current for the probe potential  $\eta=(\eta_F+10)$  ( $\eta$  is the probe,  $\eta_F$  the floating potential normalised to the electron temperature in eV) is shown in Fig. 2 together with the curve presented by Chen [20] on the basis of Allen et al. theory [19]. In Fig. 2 the theoretical curves are compared with the experimental results presented in [27] and [28]. A comparison of the theoretical and experimental results has shown that in contrary to the Bernstein-Rabinowitz [21] and Laframboise [22] theories the ion saturation current depends on the Debye number  $D_\lambda$  at orbital motion limited (OML) conditions and that its magnitude is larger than that predicted theoretically.

Experimental results obtained by several authors [26,29,30] have been summarised by Smith and Plumb [26]. They have shown that the ion density  $n_i$  determined from the ion current  $I_i$  may be expressed in terms of the electron density  $n_e$  determined from the electron current  $I_e$  by the empirical relationship of the form  $n_i \approx (1 + 0.07 \sqrt{m_i}) n_e$  ( $[m_i]=\text{a.m.u.}$ ). From the quasineutrality of the plasma follows, however, that the electron density  $n_e$  should be equal to the positive ion density  $n_i$  assuming that no negative ions are present within the plasma. The discrepancy between  $n_i$  and  $n_e$  has been observed in [26] even in the flowing afterglow plasma where the condition for the stable space charge sheath  $T_i > (1/2)T_e$  (see e.g. [14]) is satisfied. The experimental results obtained in [26,29,30] indicate therefore an inaccuracy in the assumptions of the OML model of the positive ion collection for the used experimental conditions. The discrepancy of  $n_i$  and  $n_e$  determination cannot lead back to an end-effect phenomenon (transition to spherical-like sheath configuration) [31].

We believe that these discrepancies can be, at least at certain simple experimental conditions, explained if the collisions of positive ions with neutrals in the space charge sheath around the probe are taken into account. Monte Carlo simulations [32] have shown, that already a small number of collisions in the sheath can destroy the orbital motion. The next paragraph is therefore devoted to discussion of probe theories that take account of the ion-neutral collisions in the sheath around the Langmuir probe.

### 2.1 The collection of positive ions by the probe under the influence of ion-neutral collisions

This effect has already been studied for many years; examples of earlier papers on this subject are [33-39]. The theories that treat the problem of the positive-ion collection by a Langmuir probe under the influence

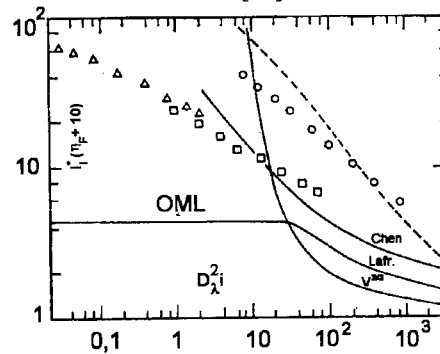


Figure 2. Comparison of the different collision-free-theories with experiment. ----- spherical probe theory [20,22], — cylindrical probe theories: Chen [20], Lafr. [22],  $V^{3/2}$  [60]. Experiment:  $\circ$   $R_p=1$  mm,  $\Delta$   $R_p=37.5$   $\mu\text{m}$ ,  $l_p=7$  mm,  $\square$   $R_p=0.375$  mm, measured in the positive column of He glow discharge at 25 Pa. Current normalized with  $n_e$  determined from the electron probe current at the plasma potential. From [27].

of collisions of ions with neutrals in the probe sheath can be divided into kinetic and continuum theories; we shall call such theoretical models "collision models" or "collision theories". The kinetic theories aim at description of the influence of the individual collision processes to the ion collection; the continuum theories use the hydrodynamical description. The kinetic approach can be regarded as more general since it describes the collisionless conditions too while the continuum theories require the supposition of many collisions. The kinetic theories discussed in this review present the effect of collisions in form of a correction to a collisionless ion collection model. Two collisionless models are used: Laframboise's [22] model that includes the classical Langmuir's orbital motion limited model (OML) [3] and the radial motion cold ion approximation model, so-called ABR-Chen [19,20]. We shall not present the thin sheath collision models such as "continuum plus free fall theory" [41,42] since they require higher plasma density than what is usually used in plasma-aided technologies.

The collision probe theory of the positive ion as well as of electron current to a cylindrical (spherical) probe has been presented by Chou, Talbot and Willis [43,44] and describes the Langmuir probe characteristics at an arbitrary Knudsen number  $0 \leq K_i \leq \infty$ . The result of this theory is a reduction of the ion as well as of the electron probe current due to elastic scattering of these particles caused by collisions with neutrals in the probe sheath. The influence of collisions is calculated as correction to Laframboise's collisionless ion current  $I_i^{*L}$ . This correction was in a form more suitable for practical calculations presented by Talbot and Chou [43] and by Kirchhoff, Peterson and Talbot [45]. Similar as in Laframboise theory in the Talbot et al. theory [43,44] the ion current is normalised using the factor  $I^*$  so that  $I_i^* = I_i/I^*$ ,

where  $I^* = A_p \sqrt{\frac{kT_e}{2\pi m_i}} n q_0$  with  $m_i$  being the mass of the ion and  $A_p$  the surface collecting area of the probe.

The correction factor  $F_T$  which expresses the reduction of the ion current due to the elastic scattering can be written according to the theory by Talbot and Chou [43] as  $F_T = \frac{I_i^{*L}}{I_i^*} = 1 + \frac{\tau^{1/2} J_i I_i^{*L}}{K_i}$ . In these expressions

$J_i = \int_0^1 \frac{\exp(-\tau\eta)}{Z} dZ$ ,  $I_i^{*L}$  and  $I_i^*$  are the normalised ion currents in the collisionless and collision case

respectively,  $\eta$  is the probe potential normalised to electron temperature in eV,  $Z$  is the reciprocal of the radial distance from the probe  $r$ , normalised to the probe radius  $R_p$ ,  $Z = (R_p/r)$ . Talbot and Chou [43] proposed to determine the integral  $J_i$  at an arbitrary value of  $K_i$  using an *ad hoc* interpolation formula  $J_i = J_{i\infty} + (J_{i0} - J_{i\infty})(1 + K_i)^{-1}$ , where  $J_{i\infty}$  and  $J_{i0}$  are the integrals  $J_i$  calculated at the collisionless and continuum limit respectively. The calculation procedure of these integrals is described in detail in [43], therefore we limit ourselves here only to the comments concerning the applicability of this procedure in the OML conditions. In the calculations of the collisionless limit of this integral,  $J_{i\infty}$ , the authors use the Bernstein and Rabinowitz theory [21] which assumes the monoenergetic ion distribution. In case of a cylindrical probe Laframboise's calculations [22] showed that the ion current calculated assuming Maxwellian and monoenergetic ion energy distribution differ very little from each other in the OML regime ( $D_\lambda < 3$ ). This fact supports the applicability of the procedure calculating the integral  $J_{i\infty}$  described in [43] in case of a cylindrical probe also in the OML regime. Since the calculation of the continuum limit of the integral  $J_{i0}$  does not present any problems concerning the applicability at OML conditions the overall conclusions is that for cylindrical probe the approximate Talbot and Chou procedure [43] can be applied in the OML regime.

It is to be noted that there were also other kinetic models for the description of the charged particle collection by a Langmuir probe. Bienkowski and Chang [46] found the solution of Poisson and Boltzmann equation with the collision term for the limiting case  $D_\lambda \rightarrow \infty$  while Wasserstrom et al. [47] only in the limiting case of  $\eta \rightarrow 0$ . Both limits can be, however, derived from the Talbot and Chou theory with the same results. Substantially simpler than the Talbot and Chou theory is the procedure employed by Self and Shih [48] that modified the ABR radial model (for spherical probe) [19] by introduction of the "friction term". The results are presented as dependencies of the normalised ion current at a certain probe

voltage on the  $D_\lambda$  and the ion-neutral collision frequency  $\nu_{in}$ . The same procedure is applied for cylindrical probe to the ABR-Chen [19,20] radial model in [49].

Klagge and Tichý in the paper [27] carried out a set of numerical calculations of the positive ion current as a function of the Knudsen number  $K_i$  at the normalised potential  $\eta = \eta_F + 10$  based on the procedure [43]. The difference from the original Talbot and Chou paper [43] consisted in the fact that they used the ABR-Chen [19,20] collisionless current  $I_i^{*A}$  in place of  $I_i^{*L}$  in  $F_T$  calculation. The reason for this was that this model ( $I_i^{*A}$ ) with a reasonable accuracy described the experimental results at conditions close to collision-free. The authors used their own analytical approximation for the numerical Chen [20] currents. This approximation has been presented in [48] and can be written as  $I_i^{*A}(\eta_w) = a(\eta_w/b)^\alpha$ , where  $a = (D_\lambda + 0.6)^{0.05} + 0.04$ ,  $b = 0.09[\exp(-D_\lambda^{-1}) + 0.08]$  and  $\alpha = (D_\lambda + 3.1)^{-0.6}$ . At a given  $\eta_w$  (so-called working point, usually  $\eta_w = \eta_F + 10$  or  $\eta_w = 15$  is selected for the calculation) this formula presents the dependence of the  $I_i^{*A}$  on  $D_\lambda$ , or in turn, on  $D_\lambda^2 I_i^{*A}$  in accordance with [20] with a fairly negligible error. The parameter  $D_\lambda^2 I_i^{*A}$  has the advantage that it does not depend on the electron density and can be therefore directly evaluated from the experimental data using the experimentally determined electron temperature. The dependence  $I_i^*$  vs  $D_\lambda^2 I_i^{*A}$  is generally called Sonin-plot [23]. The results of the corrections presented in [27] are shown in Fig. 3. From this figure it is possible to determine the correction factor  $F_T$  by means of which the experimental value of the ion probe current can be corrected with respect to collisions. The exact step-by-step procedure described in [27] enables to set-up a program that calculates this correction directly without the necessity to analytically approximate the data in Fig. 3.

Zakrzewski and Kopiczynski [51] have introduced the other model in which elastic collisions of ions with neutral particles have on the contrary to Talbot and Chou theory two consequences: the destruction of the orbital motion of ions and the elastic scattering of positive ions. As compared to the Talbot and Chou theory the destruction of the orbital motion can lead to an increase of the positive ion current. The effect of the orbital motion destruction predominates for lower pressures when the mean free path of positive ions is greater or comparable to the sheath thickness. The elastic scattering of the positive ions causes a monotonous decrease of the positive ion current and dominates for higher pressures. As a result the current peak appears at a pressure when approximately one collision of the ion with the neutral in the space charge sheath occurs. The resulting normalised dimensionless ion current  $I_i^*$  to a cylindrical probe is then  $I_i^* = \gamma_1 \gamma_2 I_i^{*L}$ , where  $\gamma_1$  describes the rate of increase of ion current due to destruction of orbital motion and  $\gamma_2$  corresponds to the rate of reduction of ion due to scattering,  $I_i^{*L}$  is the normalised collisionless ion probe current predicted by Laframboise [22]. The correction factor  $F_Z$  is given as

$$F_Z = \frac{1}{\gamma_1 \gamma_2}. \text{ Zakrzewski and Kopiczynski have derived the coefficient } \gamma_1 \text{ under assumptions that at the}$$

orbital motion limited conditions the positive ion current collected by a perfectly absorbing probe is saturated and it is described by Laframboise theory. This physical argument can be expressed analytically. They assumed that the dimensionless ion current at the sheath edge  $I_i^{*A}$  is given approximately by Allen et al. theory [19]. In the collisionless limit only the current  $I_i^{*L}$  predicted by Laframboise reaches the probe surface. The current  $(I_i^{*A} - I_i^{*L})$  leaves the sheath due to the orbital motion.

When an orbiting positive ion undergoes a collision with neutral particle in the space charge sheath it loses energy and is attracted to the probe. An average ion makes  $X_i = S/\lambda_i$  collisions in the sheath if we denote by  $S$  the thickness of the sheath and by  $\lambda_i$  the ion mean free path. According to Zakrzewski and Kopiczynski the rate of increase of the positive ion current due to the destruction of the orbital motion by

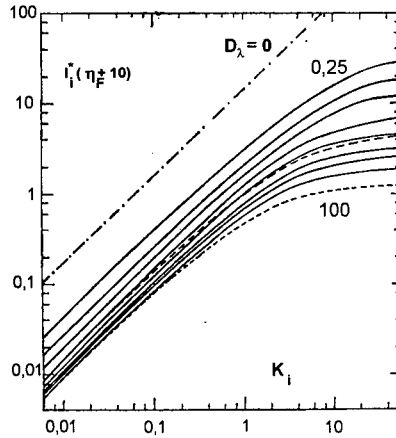


Figure 3. Normalised ion saturation currents at  $\eta = \eta_F + 10$  in dependence on  $K_i$ . -----  $D_\lambda = 2, 8, 100$  calculated with Laframboise collisionless current [22], —  $D_\lambda = 0, 25, 0, 5, 1, 2, 5, 5, 10, 20, 70$  calculated with ABR-Chen collisionless current [19,20], -.-.-  $D_\lambda = 0$  calculated according [63].  $\tau = 10$ ,  $K_e = 10K_i$ ,  $l_p/R_p = 100$ ,  $(m_i/m_e)^{1/2} = 100$ . From [27].

elastic collision is  $\gamma_1 = 1 + \left( \frac{I_i^A}{I_i^L} - 1 \right) \frac{S}{\lambda_i}$ . This equation is valid for  $S/\lambda_i < 1$ . For  $S/\lambda_i \geq 1$  total destruction of

the ion orbital motion occurs and  $\gamma_1 = \frac{I_i^A}{I_i^L}$ . The average amount of the ion collisions with the neutral

particles within the sheath equals roughly  $X_i = S/\lambda_i$ . Kopiczynski [52] determined the thickness of the

sheath  $S$  on the basis of numerical calculations carried out by Basu and Sen [53]. Then  $X_i = \frac{S}{\lambda_i} = \frac{\sqrt{\eta}}{D_\lambda K_i}$ ,

where  $\bar{\eta} = m(\eta + 3.5) - 4$  and  $m \approx 0.59 + 1.86(D_\lambda)^{0.47}$ . The corresponding reduction rate of the ion current

due to the elastic scattering  $\gamma_2$  Zakrzewski and Kopiczynski estimated according to Schulz and Brown [54] and Jakubowski [55]. It should be noticed that for a given probe potential  $\gamma_1$  and  $\gamma_2$  are function of both  $R_p/\lambda_D$  and  $\lambda_i/R_p$ .

For normalised probe potential  $\eta_w = 15$  Kopiczynski [52] carried out extensive numerical calculation of the dependence of the quantity  $I_i^* D_\lambda^2$  on the ion Knudsen number  $K_i$  with the Debye number  $D_\lambda$  as a parameter. David [56] and David et al. [57] extended these calculations towards lower Knudsen numbers  $K_i$  occurring in a medium pressure discharge. The comparison of the already mentioned theories of the ion current collection by the probe in the transition regime has been made by David [56]. The results of his calculations are depicted in Fig. 4.

It can be deduced from this figure that the results of Talbot and Chou and those of Zakrzewski and Kopiczynski are not in contradiction within the region  $2 \leq D_\lambda \leq 3$  since the ion current maximum predicted by Zakrzewski and Kopiczynski is within this region very flat and the results of both theories differ only a little from each other. For lower  $D_\lambda$  ( $D_\lambda < 2$ ) the ion current calculated by using the Zakrzewski and Kopiczynski theory [51,52] exhibits a well pronounced maximum at  $X_i \approx 1$ . At higher values of  $X_i \gg 1$  the ion current decreases with decreasing  $K_i$  more rapidly in comparison with the ion current obtained from theory [43,44] in which no current peak is observed.

Since the Chou and Talbot theory does not take into account the effect of the probe current increase due to the orbital motion destruction caused by ion collisions with neutrals within the probe sheath, the

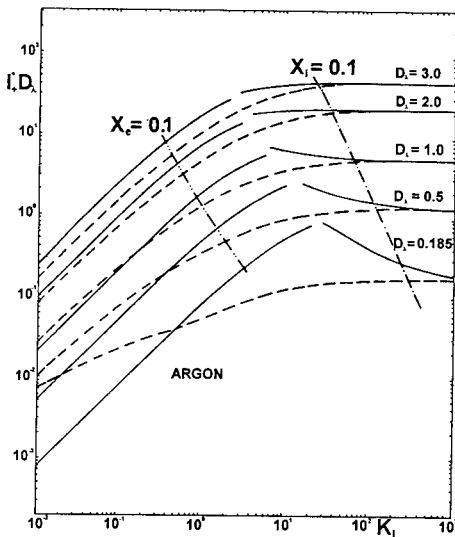
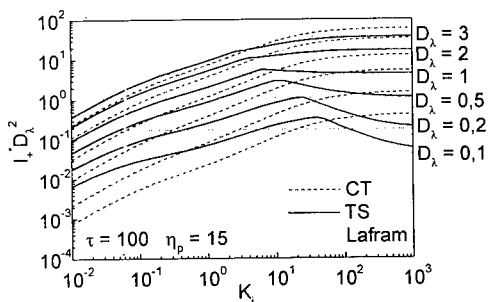


Figure 4. The dependence of the directly measurable quantity  $I_i^* D_\lambda^2$  on  $K_i$  with  $D_\lambda$  as a parameter calculated in [56] using the theory [51] (full line) and the theory [43,44] (broken line). The chain lines indicate the boundaries of the transition probe regime in the same way as in Fig. 1.

theory developed by Zakrzewski and Kopiczynski describes at OML conditions the ion collection by a Langmuir probe in the region where not all the ions suffer a collision with a neutral particle within the probe sheath ( $X_i < 1$ ) more precisely than the Talbot and Chou theory. On the other side for larger number of ion collisions within the sheath ( $X_i \gg 1$ ) the theory developed by Zakrzewski and Kopiczynski is not applicable at OML conditions since it uses for the evaluation of the factor  $F_Z$  the formulae which have been derived in [55] under the assumption of only a few ion collisions within the probe sheath. In order to extend the validity of the theory developed by Zakrzewski and Kopiczynski [51,52] for an arbitrary  $K_i$  we suggested in [12] to apply the Talbot and Chou theory [43,44] for determination of the factor (or its equivalent) describing the effect of scattering of ions due to their collisions with neutrals within the probe sheath. The corresponding expression following the model used by Zakrzewski and Kopiczynski (see eq.(5)) is  $I_i^* = \gamma_1 \gamma_2^* I_i^{*L}$ , where  $\gamma_2^*$  is the coefficient describing the effect of the ions scattering due to collisions with neutrals within the probe sheath determined from Talbot

and Chou model [43]. The advantage of the new model [12] of the ion collection by a cylindrical Langmuir probe consists mainly in the fact that it is valid for any  $K_i$  i.e. for  $0 \leq K_i < \infty$  as long as the condition of the OML regime of the probe is fulfilled ( $D_\lambda \leq 3$ ). On the contrary to the calculations of the  $\gamma_2$  factor which have been made by Zakrzewski and Kopiczynski the correction factor  $\gamma_2^*$  depends on the ratio of the electron to ion temperature  $\tau = (T_e/T_i)$ . We suggested in [12] to call this new model the "modified Talbot and Chou model" since it refines the "classical" kinetic Chou and Talbot theory [43,44].

Comparison of the theory [12] with the Chen-Talbot [27] and with the Zakrzewski-Kopiczynski [51,52] theories has been made by Kudrna in [58]. He calculated also the dependence of the directly measurable quantity  $D_\lambda^2 I_i^*$  on  $K_i$  with  $D_\lambda$  as a parameter. Samples of his results are presented in Fig. 5ab.



**Figure 5a.** Comparison of the Chen-Talbot positive ion current model [27] with modified Chou-Talbot model [12]. For comparison also collisionless current by Laframboise [22] is shown.

Note that in both figures the ion current calculated according [12] decreases at lower  $K_i$  with decreasing  $K_i$  slower than that from both theories [27] and [51,52].

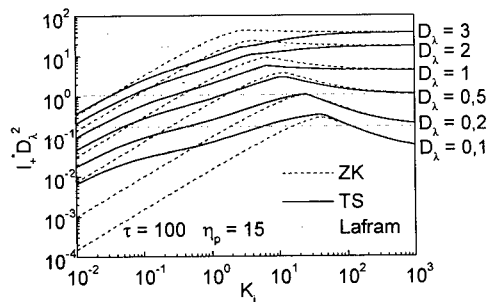


**Figure 5b.** Comparison of the Zakrzewski-Kopiczynski positive ion current model [51] with modified Chou-Talbot model [12]. For comparison also collisionless current by Laframboise [22] is shown.

## 2.2 Comparison of "collision theories" of positive ion collection by the probe with experiment

Up to now the Zakrzewski and Kopiczynski model [51] has been tested in several papers [12,52,59,60]. In [12,52] the authors used the X-band microwave interferometer for the independent determination of the relative values of the electron density. The double probe technique was used for the determination of the electron temperature. A set of single cylindrical probes was applied to obtain the probe characteristics. The reasonable quantitative agreement supports the model of ion collection carried out by Zakrzewski and Kopiczynski in the region of  $X_i < 1$ . For support of this theory speak also results of the work [60] obtained in an argon afterglow discharge at the pressure 62 Pa and of [61] measured in an RF argon discharge at the pressures around 10 Pa.

Thorough assessment of the applicability of all mentioned collision theories has been presented in [59]. The measurements have been done in a low pressure flowing afterglow system with a Langmuir probe and downstream mass analysis (FALP). The experiments have been done in collaboration with the Innsbruck University where the FALP system was available as well as on the FALP system at the Charles University in Prague. Several kinds of ions have been

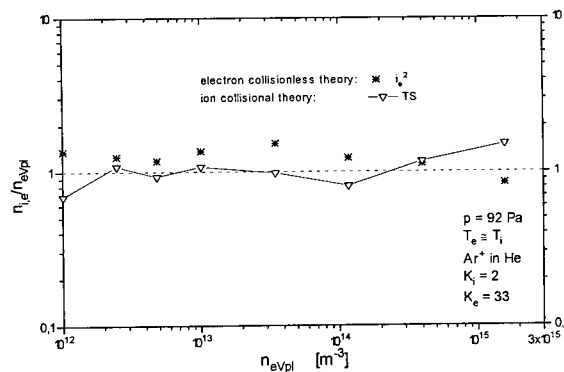


**Figure 6.** The comparison between the electron density calculated from the OML theory and the ion density calculated using theory [12] (denoted as TS) plotted as a ratio to the electron number density evaluated from the electron current at the space potential (also plotted on x-axis) at isothermal conditions. (From [59].)

used for this study. Fig. 6 presents typical results that have been obtained with rare gas ions ( $\text{Ar}^+$  and  $\text{Kr}^+$ ) in the He carrier gas. The plot shows the numerical values of the ratio of ion density according the theory [12] to the electron density estimated from the electron current at the plasma potential vs the numerical value of the electron density estimated from the electron current at the plasma potential ( $n_{eV_{pl}}$ ). In addition also the ratio of the electron density estimated from the  $I_e^2$  vs  $V_p$  plot ( $n_{elesqr}$ ), see e.g. [26] to the  $n_{eV_{pl}}$  is plotted on the ordinate axis (\* points) in order to support the choice of the density value  $n_{eV_{pl}}$  as the reference one.

There is a steady effort to improve the understanding of the probe method in order to obtain more reliable data from the probe diagnostic [64-67]. The present state of knowledge on the influence of positive ion-neutral collisions in the probe sheath does not, however, allow to recommend the universally applicable theory that would give satisfactory results in a broad range of experimental conditions; for afterglow conditions the theory [12] yields fairly consistent results, for an active plasma (also when the supposition of the Maxwellian EEDF is not quite satisfied) the ABR-Chen theory with the collision correction [27] gives the best agreement with the experiment. More general results might bring the Monte-Carlo simulation of the ion motion in the probe vicinity; the first steps have been done in [32].

### 3. LANGMUIR PROBE IN A MAGNETISED PLASMA

The low-temperature-plasma-aided creation and etching of thin films are due to their broad applications possibilities very important parts of plasma-chemistry. Important drawback of many plasma enhanced surface treatments is the comparatively low grow/etch rate compared to classical chemical or electrochemical processes. In many technological applications of the low-temperature plasma to creation and etching of thin films is therefore used magnetic field that helps the plasma confinement and increases the grow/etch rate. The magnetic field in these systems can be either non-homogeneous (created typically by permanent magnets; one example is the planar unbalanced magnetron) or almost homogeneous (created by coils) and its strength does not usually reach too high values. When using the Langmuir probe as a diagnostic tool in these systems the question arises up to what limit of the ratio  $B/p$  (magnetic field strength to the working pressure; this is a similarity parameter in magnetised plasma) it is possible to use the conventional methods for evaluation of the basic plasma parameters such as charged particle density and electron energy distribution function (EEDF) from the Langmuir probe data.

Although the first discussions on the Langmuir probe saturated currents in a magnetic field have been published already at the end of forties [15,18] the more intensive research on the use of the probe diagnostics in a low-temperature plasma in a magnetic field begun at the end of sixties [67-93] and proceeds up to the present time [11,94-99]. The decisive arguments have been given in the paragraph above, additional reasons are that the Langmuir probe is also often used to study the edge plasma in large magnetic fields in hot plasma devices such as tokamaks [100-107]. Not too many papers are devoted to the more complicated case of concerted action of higher pressures and magnetic field to the probe measurements [108-110] even if this case is from the viewpoint of technological applications the most interesting one.

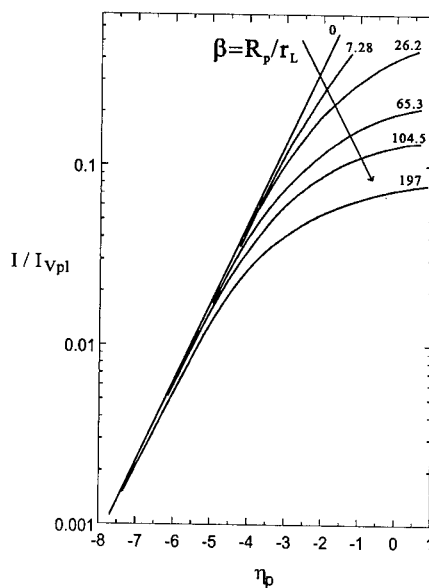


Figure 7. The influence of the magnetic field characterised by the parameter  $\beta$  on the spherical probe electron current (normalised to that at the space potential  $V_{p0}$ ). From [74].

The discussion of the influence of the magnetic field to probe measurement in the collision-free case can be, in accord with [16] divided in 4 categories in dependence on the parameter  $\beta = R_p/r_L$ : (i) At  $\beta \ll 1$ , weak  $B$ , the influence is small and can be neglected (rare case of technologically interesting applications), (ii) at  $\beta \approx 1$  the  $B$  is still weak, but it is sometimes necessary to introduce small corrections (frequent case in plasma-aided technologies), (iii) at  $\beta > 1$  the  $B$  is strong but it is still possible to interpret at least part of the Langmuir probe characteristic (case of tokamak edge plasma) and (iv) at  $\beta \gg 1$ , i.e. at very strong  $B$  the probe characteristic is no longer interpretable. From the definition of the parameter  $\beta$  it is evident that  $\beta$  decreases with increasing charged particle velocity and mass; therefore the faster electrons and the ions are less influenced by the magnetic field during their collection by the probe. In other words, least distorted part of the probe characteristic due to the effect of magnetic field shall be that for very negative probe with respect to plasma, see e.g. [74,77]. The changes in the probe characteristic when the probe is applied in a magnetized plasma are therefore most apparent in the region close to the plasma potential. The directional movement of charged particles along the magnetic field lines reduces the diffusion of particles in direction across the field lines. If we consider the electron motion that is mostly influenced by the magnetic field then their diffusion coefficient across the field  $D_\perp$  reduces to  $D_\perp = D_0 / (1 + \Omega_e^2 \tau_{en}^2)$  with  $D_0 = v_{th}^2 \tau_{en}$ , where  $\Omega_e = q_0 B / m_e$ ,  $\tau_{en} = 1 / \nu_{en}$  and  $v_{th}$  are the electron cyclotron frequency, electron-neutral collision time and electron thermal velocity respectively [113]. In case of  $\Omega_e \tau_{en} \gg 1$  (magnetized plasma at low pressures) that is the case of most technologically used plasmas the expression for  $D_\perp$  reduces to  $D_\perp \approx v_{th}^2 / \Omega_e^2 \tau_{en} = r_L^2 / \tau_{en}$ . In other words in direction perpendicular to the magnetic field the effective mean free path of electrons is roughly equal to the Larmor radius. If the probe draws too much current at probe potentials close to the plasma potential the electrons are absorbed by the probe more rapidly than they can be supplied by diffusion from the distant regions where they are produced. Further effect concerns the change of the effective collecting area of the probe, since the charged particles flow to the probe mostly from the direction of the field lines reducing hence the original probe area to double of its projection to the field direction. Finally, at higher magnetic fields, e.g. in tokamaks, the probe is connected to its reference electrode only by the "current tube", that reduces the ratio of the reference-electrode-probe surface collecting areas. All three effect then lead to "blurring of the knee" of the probe characteristic near the space potential as it is seen in Fig. 7. When for the data analysis from such affected probe the conventional methods are used the resulting plasma number density is underestimated, plasma potential shifted towards probe retarding voltages and the electron temperature deduced from the slope in the electron retarding regime is overestimated (the slope is slower). Note that this effect does not depend on the magnetic field strength only, but rather on the ratio  $\Omega_e / \nu_{en}$ , or on  $B/p$ . The degree of anisotropy of the problem (and hence of the influence to the probe measurements) will therefore depend also on  $B/p$  and not on  $B$  itself. The assessment of the error caused by the effect of magnetic field to the probe data and

consequently to accuracy of estimated plasma parameters is therefore most interesting.

Recent experimental assessment of this effect at weak-to-medium magnetic fields has been presented in [11,100]. The work was based on the assumption that at the range of the pressure and the magnetic field employed the influence of the magnetic field on the positive ion collection by the probe is negligible. The comparison of the positive ion density estimated from the ion accelerating region of the probe

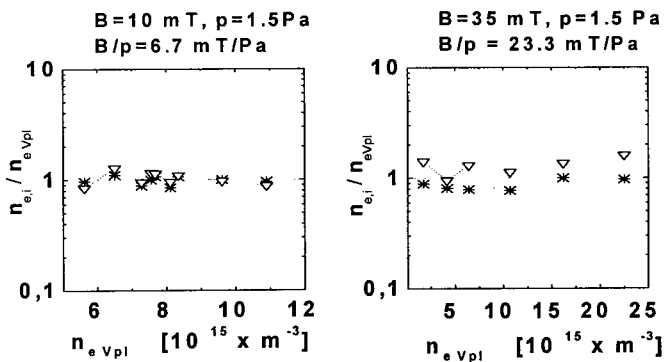


Figure 8. Comparison of the relative positive ion ( $-\nabla$ , theory [27]) and electron densities ( $*$ , OML theory [3,22]) estimated from the same probe data at different magnetic fields. DC cylindrical magnetron discharge, working gas argon. Reference electron density from the electron current at plasma potential. From [95].

characteristic with the electron density estimated from the electron current at the plasma potential (by conventional method, i.e. without any correction to the magnetic field) at lower and higher  $B/p$  should then give an idea of the magnitude of this influence. Sample of the results from [100] is given in Fig. 8. The figure is arranged in a similar manner as Fig. 6. It is seen that while at the low  $B/p$  there is an agreement between the estimated values of ion and electron density, at higher  $B/p$  the electron density estimated from the electron current at the space potential is systematically underestimated; the difference gives a measure of the error due to the magnetic field.

Anisotropy of the electron temperature in a magnetic fields has been studied e.g. in [112-114]. Of those we shall briefly mention that by Aikawa [113]. He used two Langmuir probes for determination of the perpendicular and the parallel components of the electron temperature, what represents the first approximation of a direction-resolved probe diagnostic. Both components of the electron temperature,  $T_{\parallel}$  and  $T_{\perp}$  he obtained by the "conventional" method, i.e. from the slope of the semilogarithmic plot of the current drawn either by the planar probe whose surface was perpendicular to the  $B$ -field lines or by the cylindrical Langmuir probe whose axis was parallel to the  $B$ -field lines in the electron retarding regime respectively. His typical results taken at the argon pressure  $1.6 \cdot 10^{-2}$  Pa are shown in Fig. 9 ( $\Theta$  is the angle between the probe axis and the magnetic field lines). The electron temperature measured at the angle  $\Theta$  exceeds up to several times the parallel one  $T_{\parallel}$ . Aikawa further computed that depending on the ratio of the probe radius  $R_p$  to the sheath radius  $r_s$ , the ratio of  $T_{\perp}/T_{\parallel}$  can at the same  $B$  and  $p$  as in Fig. 9 exceed the value 10 (at  $R_p/r_s \approx 0.1$ , i.e. at large sheath radius compared to the probe one). It is to be noted, that the Aikawa-theories for cylindrical and plane probe are selfconsistent. Both yield the same values for space potential and plasma density, while the cylindrical probe indicates  $T_{\perp}$  and the plane probe indicates  $T_{\parallel}$ .

The work [115] studied the radial distribution of the EEDF in the positive column of a glow discharge in neon in the magnetic field collinear with the electric field. The authors used the "conventional" second harmonic method to obtain the second derivative of the probe characteristic from which they calculated the electron density and the electron mean energy. They found that even at comparatively low values of  $B/p$  of the order of  $1 \cdot 10^{-3}$  T/Pa the magnetic field influences the radial distribution of the mean electron energy in the sense that higher  $B/p$  causes the increase of the mean electron energy at larger radii.

The recent work by Arslanbekov et al. [116] discusses the EEDF measurements by a Langmuir probe at elevated pressures and in magnetic field. He creates an analogy between the effect of an increased pressure and the effect of the magnetic field on the probe characteristic. However in the analysis of the influence of the magnetic field on the cylindrical probe in a plasma the case of a thin sheath is assumed and hence this work is not directly applicable to the low temperature discharge plasma of technological interest since in such case the sheath thickness is usually large or comparable to the probe radius.

#### 4. EXPERIMENTAL ASSESSMENT OF THE ANISOTROPY OF THE EEDF IN A MAGNETIC FIELD

Under the assumption that the EEDF is isotropic there exist many papers that are devoted to its probe studies in different experimental conditions, e.g. [116-118]. For the experimental study of the anisotropy of the EEDF the use of the method suggested by Mesentsev et al. [119-126] and by Klagge and Lunk

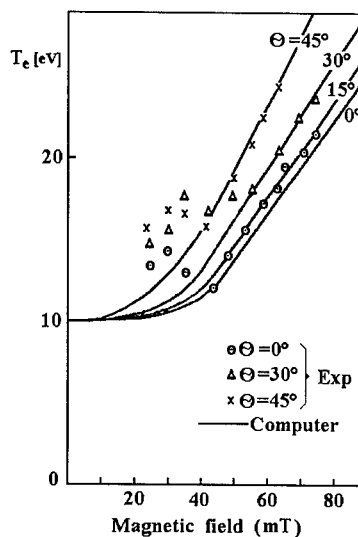


Figure 9. Computed (solid lines) and measured (points)  $T_e$  by Aikawa [113] at  $B/p \approx 3$  T/Pa and assumed  $T_{\parallel} = 10$  eV.



[127] is proposed. This method consists in the expansion of the anisotropic electron velocity distribution function (EVDF) in a series of spherical (Legendre) polynomials

$$f(v, \Theta) = \sum_{i=0}^{\infty} f_i(v) P_i(\cos \Theta). \quad (1)$$

Basic assumptions for the implementation of the procedure are:

- collisionless movement of the particles collected by the probe,
- negligibility of reflection and secondary emission of electrons from the probe,
- cylindrical symmetry of the EVDF around the preferred direction.



Figure 10. Possible orientation of the planar probe.

The coefficients in the expansion series are determined from the measurements by the planar Langmuir probe at different angles to the preferred direction, in this case to the direction of the magnetic field vector. Generally one obtains so many coefficients  $f_i$  for the into Legendre polynomial expanded EVDF as probe position is used. The accuracy of the determination of the probe data does not usually allow to determine more than the first two or three coefficients of this series, the first one being the isotropic one the second one characterizing the drift and the third one characterizing the second order anisotropy. For determination of the first three coefficients we need the probe data measured in three directions, see Fig. 10.

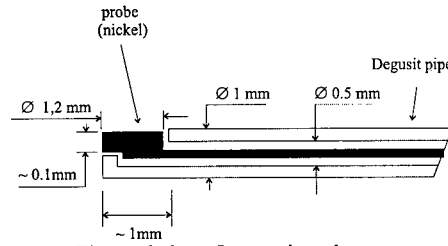


Figure 11. The used planar Langmuir probe.

From the probe data we get the required quantities as follows:

$$1. \text{ The electron density } n_e = \left(\frac{1}{3}\right) 2^{1/2} m_e^{-1/2} e^{-3/2} S^{-1} \int_0^\infty V^{1/2} (I_0'' + 4I_{90}'' + I_{180}'') dV$$

$$2. \text{ The isotropic part of the electron velocity distribution function (EVDF)}$$

$$F_0\left(\sqrt{\frac{2eV}{m_e}}\right) = \left(\frac{2}{3}\right) e^{-2} m_e n_e^{-1} S^{-1} V (I_0'' + 4I_{90}'' + I_{180}'')$$

or the isotropic part of EEDF

$$f_0(eV) = \left(\frac{1}{3}\right) 2^{1/2} e^{-5/2} m_e^{-1/2} n_e^{-1} S^{-1} V^{1/2} (I_0'' + 4I_{90}'' + I_{180}'')$$

$$3. \text{ The first order anisotropy of the EEDF}$$

$$f_1(eV) = 2^{1/2} e^{-5/2} m_e^{-1/2} n_e^{-1} S^{-1} V^{1/2} g_1(eV), \quad g_1(eV) = G_1 + (2eV)^{-1} \int_{eV}^\infty G_1 d\varepsilon, \quad \text{where } G_1 = (I_0'' - I_{180}'')$$

$$4. \text{ The second order anisotropy of the EEDF } f_2(eV) = \left(\frac{2}{3}\right) 2^{1/2} e^{-5/2} m_e^{-1/2} n_e^{-1} S^{-1} V^{1/2} g_2(eV), \quad \text{where}$$

$$g_2(eV) = G_2 + \left(\frac{3}{2}\right) (eV)^{-3/2} \int_{eV}^\infty \varepsilon^{1/2} G_2 d\varepsilon, \quad G_2 = (I_0'' - 2I_{90}'' + I_{180}'').$$

(2)

For detailed description of the procedure with 5 probe orientations see e.g. [121, 127]. It is to be noted that the anisotropy of the EEDF in the magnetic field should be regarded in similar manner as the anisotropy of the electron temperature in [113], i.e. as the anisotropy of the electron velocity components. The expansion (1) requires the EVDF to be symmetrical around the preferred direction and hence cannot be used generally. In magneto-plasmas without drift the preferred directions  $\vec{B}$  and  $-\vec{B}$  are equivalent. However, the measurement at  $\Theta=0$  and  $\Theta=180^\circ$  are advantageous for discharge end-effect studies. In our case of the measurement in a positive column of a DC magnetron discharge, where the electric field is very small the poloidal asymmetry of the EEDF due to the  $\vec{E} \times \vec{B}$  drift could be neglected.

The experiment has been performed on the DC cylindrical magnetron discharge system in the Institute of Physics, University of Greifswald, Germany. The system differed from that described in [11] only by the used probe. In the presented measurements the probe was planar, see Fig. 11. The 3 orientations with regard to the vector of the magnetic field were adjusted by rotating the probe along its axis that was positioned perpendicular to magnetic field lines. Hence  $f_0$  and  $f_2$  were obtained in the expansion (1);  $f_1$  and generally all odd terms should vanish, if the plasma anisotropy is produced only by the magnetic field, see Eq. (2). Because of discharge instabilities we could not operate with pressures lower than 0.3 Pa.

We present two sets of data, at higher and lower value of  $B/p$ . The results are presented as polar plots of the magnitude of the EEDF obtained from Eq. (1) at several different energies.

In Fig. 12 there is the EEDF at  $B/p = 3.3 \cdot 10^{-3}$  T/Pa. The data have been acquired in the cylindrical magnetron discharge in xenon at the pressure 6 Pa, discharge current 60 mA and the magnetic field strength  $2.10^{-2}$  T. The probe was positioned approximately in the middle between cathode and anode. The polar plots resemble circles even at lower energies what indicates almost isotropic EEDF. Qualitatively this is due to the effect of collisions of electrons with neutrals that randomise the directional movement of electrons caused by the magnetic field. When the pressure is lowered down to 0.71 Pa then at the same magnetic field  $2.10^{-2}$  T and the same discharge current the picture changes. In Fig. 13 we present the numerically calculated second derivatives of the experimentally measured probe characteristics with respect to the probe voltage in three different angles to magnetic field. The curves taken at  $0^\circ$  and  $180^\circ$

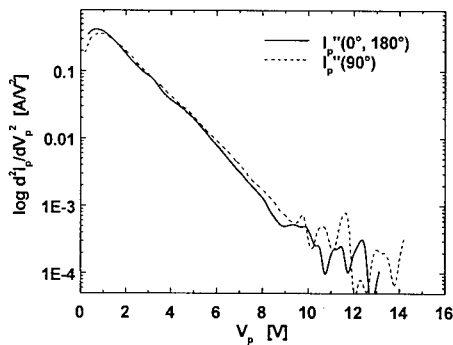


Figure 13. Second derivatives of the measured probe data in 3 different orientations at the conditions of Fig. 14.

coincide. It is seen that at  $90^\circ$  angle to  $B$  the second derivative has smaller amplitude, its maximum is shifted towards higher energies and its tail decays slower with energy. This indicates higher mean electron energy in direction perpendicular to  $B$ . The polar plot in Fig. 14 shows already anisotropy of the EEDF that can be qualitatively described as deficit of the low energy electrons in direction perpendicular to  $B$ . This deficit is compensated by larger apparent temperature of electrons coming from this direction.

## 5. CONCLUSION

We presented our viewpoint on the problems that arise from the use of probe method in the transition regime of pressures and in a magnetic field. We used the method of comparison of the density values obtained from the electron and positive ion current part of the probe characteristic with certain success,

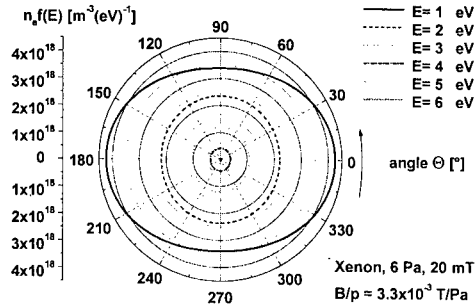


Figure 12. Polar plot of the EEDF in xenon at 6 Pa and  $B = 2.10^{-2}$  T.

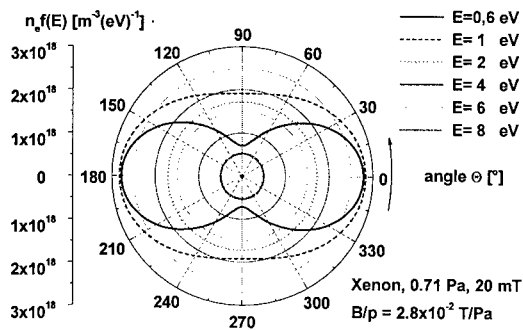


Figure 14. Polar plot of the EEDF in xenon at 0.71 Pa and  $B = 2.10^{-2}$  T.

however at higher pressures it is very difficult to fulfil the assumptions of the used theories. The presented method of the assessment of the anisotropy of EEDF in a magnetic field yields also the fairly simple method how to assure the quality of the experimental probe data under such conditions. In the presented contribution we concentrated on the measurement of the EEDF in non-isotropic plasma. The Mesentsev method [124] brings, however, also advantage when measuring the plasma density, since it solves by itself the problem of the reduction of the effective probe collecting area when the magnetic field strength is increased from  $B=0$  (isotropic case) to highly magnetised plasma (non-isotropic case). The authors constructed a computer program under Microsoft Windows® that carries out the probe data processing in continuous interaction with the experimenter. The program is available, together with its fairly detailed description, on request on the e-mail of one of us (P.K.). In the future we would like to compare the presented theories with numerical simulations that are under way.

### Acknowledgements

The work in Czech Republic was partially financially supported by the Grant Agency of Czech Republic, Grant No. GAČR-202/971011, by Grant Agency of Charles University, Grant No. GAUK-181/96 and by the EU Grant COPERNICUS CIPA-CT94-0183. The work in Germany was financially supported by the Deutsche Forschungsgemeinschaft (DFG) in frame of the project SFB 198 Greifswald "Kinetik partiell ionisierter Plasmen".

### References

- [1] Langmuir I., Mott-Smith H.M., *Gen. Elec. Rev.* **26**(1923)731.
- [2] Langmuir I., Mott-Smith H.M., *Gen. Elec. Rev.* **27**(1924)449, 538, 616, 762, 810.
- [3] Mott-Smith, H.M., Langmuir I., *Phys. Rev.* **28**(1926)727.
- [4] Langmuir I., *Phys. Rev.* **28**(1926)104.
- [5] Langmuir I., *Phys. Rev.* **31**(1928)357.
- [6] Godyak V.A., Piejak R.B., Alexandrovich B.M., *Plasma Sources Sci. Technol.* **1**(1992)36.
- [7] Waymouth J.F., *Phys. Fluids* **7**(1964)1893; *Phys. Fluids* **9**(1966)801.
- [8] Swift J.D., Schwar M.J.R., *Electrical Probes for Plasma Diagnostics* (Ilfie books, London, 1970).
- [9] Waymouth J.F., *J.Appl. Phys.* **37**(1966)4493.
- [10] Godyak V.A., in *Plasma-Surface Interaction and Processing of Materials*, NATO ASI, Ser. E, vol. 176, O. Auciello et al., ed. (Kluwer Academic, Dordrecht, 1990) pp 95-134.
- [11] Passoth E., Kudrna P., Csambal C., Behnke J.F., Tichý M., Helbig, V., *J.Phys. D (Appl. Phys.)* **30**(1997)1763.
- [12] Tichý M., Šícha M., David P., David T., *Contrib. Plasma Phys.* **34**(1994)59.
- [13] Tichý M., Šícha M., David P., *Proc. XX. ICPIG, Il Ciocco, Barga (Italy), July 8-12, 1991*, V. Palleschi, M. Vaselli, Eds., *Contributed Papers*, p. 839.
- [14] Chen F.F., in *Plasma Diagnostics Techniques*, ed. Huddelstone R.H., Leonard S.L., (Academic Press, New York, London 1965).
- [15] Granovskij V.L., *Električeskij tok v gaze* (GITTL, Moskva 1952), in russian, available also in german as Granowski, W.L., *Der elektrische Strom im Gas* (Akademie-Verlag, Berlin 1955).
- [16] Chung P.M., Talbot L., Touryan K.J., *Electrical Probes in Stationary and Flowing Plasmas, Theory and Application* (Springer-Verlag, Berlin, Heidelberg, New York, 1975).
- [17] Kapcov N. A., *Elektronika* (GITTL, Moskva 1953), in russian.
- [18] Bohm D., Burhop E.H.S., Massey H.S.W., *The Characteristics of Electrical Discharges in Magnetic Fields*, A. Guthrie, R.K. Wakerling, Eds., (McGraw-Hill, New York 1949).
- [19] Allen J. E., Boyd R.L.F., Reynolds., *Proc. Phys. Soc.* **B70**(1957)297.
- [20] Chen F.F., *Plasma Phys.* **7**(1965)47.
- [21] Bernstein I.B., Rabinowitz J.N., *Phys. Fluids* **2**(1959)112.
- [22] Laframboise J.G., Univ. of Toronto, Institute for Aerospace Studies (UTIAS), Report No. 100, (1966).
- [23] Sonin A.A., *AIAA Journal* **4**(1966)1588.
- [24] Johnson E., Malter L., *Phys. Rev.* **80**(1950)59.
- [25] Hopkins M.B., Graham W.B., *Rev.Sci.Instr.* **57**(1986)2210.

- [26] Smith D., Plumb I.C., *J. Phys.D (Appl.Phys.)* **6**(1973)196.
- [27] Klagge S., Tichý M., *Czech. J. Phys. B* **35**(1985)988.
- [28] Shulz G.J., Brown S. C., *Phys. Rev.* **98**(1955)1642.
- [29] Tonks L., Langmuir I., *Phys. Rev.* **34**(1929)876.
- [30] Shaeffer J.F., PhD Thesis, University of St. Louis (1971).
- [31] Virmont J., Proc. ICPIG -IX (Bucharest, Bulgaria 1969), Contrib. papers, p. 609.
- [32] Trunec D., Španěl P., Smith D., *Contrib. Plasma Phys.* **35**(1995)203.
- [33] Goodall C.V., Smith D., *Plasma Physics* **10**(1968)249.
- [34] Goodall C.V., Polychronopoulos B., *Planet. Space Sci.* **22**(1974)1585.
- [35] Dunn M.G., Lordi J.A., *AIAA Journal* **7**(1969)1458.
- [36] Dunn M.G., Lordi J.A., *AIAA Journal* **8**(1970)1077.
- [37] Johnson R.A., DeBoer P.C.T., *AIAA Journal* **10**(1972)664.
- [38] Thornton J.A., *AIAA Journal* **9**(1971)342.
- [39] Zakharova V.M., Kagan J.M., Mustafin K.S., Perel V.I., *Sov. Phys. Tech. Phys.* **5**(1960)411.
- [40] Chen S-L, Goodings J.M., *J. Appl. Phys.* **39**(1968)3300.
- [41] Swift J.D., *Proc. Phys. Soc.* **79**(1969)697.
- [42] Waymouth J.F., *Phys. Fluids* **7**(1964)1843.
- [43] Talbot L., Chou Y. S., *Rarefied Gas Dynamics* (Academic Press, 1966) p. 1723.
- [44] Chou Y. S., Talbot L., Willis D. R., *Phys. Fluids* **9**(1966) 2150.
- [45] Kirchhoff R. H., Peterson E. W., Talbot L., *AIAA Journ.* **9**(1971)1686.
- [46] Bienkowski K.G., Chang K.W., *Phys. Fluids* **11**(1968)784.
- [47] Wasserstrom E., Su C.H., Probst R.F., *Phys. Fluids* **8**(1965)56.
- [48] Self S.A., Shih C.H., *Phys. Fluids* **11**(1968)1532.
- [49] Shih C.H., Levi E., *AIAA Journal* **9**(1971)1673, *AIAA Journal* **9**(1971)2417.
- [50] Klagge S., DSc Thesis (Greifswald University, 1988).
- [51] Zakrzewski Z., Kopiczynski T., *Plasma Physics* **16**(1974)1195.
- [52] Kopiczynski T., PhD Thesis IMP PAN (Institute of Fluid-Flow Machines Polish Academy of Sciences, Gdansk, 1977).
- [53] Basu J., Sen C., *Japan J. Appl. Phys.* **12**(1973)1081.
- [54] Schulz G. J., Brown S. C., *Phys. Rev.* **98**(1955)1642.
- [55] Jakubowski A. K., *AIAA Journal* **8**(1972)988.
- [56] David P., CSc Thesis (Faculty of Mathematics and Physics, Charles University, Prague 1985).
- [57] David P., Šícha M., Tichý M., Kopiczynski T., Zakrzewski Z., *Contrib. Plasma Phys.* **30**(1990)167.
- [58] Kudrna, P., PhD Thesis, (Faculty Mathematics and Physics, Charles University, Prague 1996).
- [59] Chudáček O., Kudrna P., Glosík J., Šícha M., Tichý M., *Contrib. Plasma Phys.* **35**(1995)503.
- [60] Šícha M., Zu Cham Sun, Glosík J., Tichý M., *Contrib. Plasma Phys.* **30**(1990)195.
- [61] Šícha M., Špatenka P., Tichý M., *Contrib. Plasma Phys.* **31**(1991)43.
- [62] Kagan J.M., Perel V.S., *Uspekhi Fizicheskikh Nauk* **81**(1963)409, in russian.
- [63] Chang J.S., Laframboise J.G., *Phys. Fluids* **19**(1976)25.
- [64] Rogers J.H., DeGroot J.S., Hwang D.Q., *Rev. Sci. Instr.* **63**(1992)31.
- [65] Overzet L.J., Hopkins M.B., *J. Appl. Phys.* **74**(1993)4323.
- [66] Sudit I.D., Woods R.D., *J. Appl. Phys.* **76**(1994)4488.
- [67] Johnsen R., Shun'ko E.V., Gougousi T., Golde M.F., *Phys. Rev. E* **50**(1994)3994.
- [68] Feld L., Litvinov I.I., *Zhurnal Tekhnicheskoi fiziki* **12**(1968)1589, in russian.
- [69] Sugawara M., Hatta Y., *J. Appl. Phys.* **36**(1965)2361.
- [70] Sugawara M., *Phys. Fluids* **9**(1966)797.
- [71] Litvinov I.I., *Journal of Technical Physics* **37**(1967)2160, in russian.
- [72] Kagan J.M., Perel V.I., *Journal of Technical Physics USSR* **38**(1968)1663, (in russian).
- [73] Litvinov I.I., *Journal of Technical Physics USSR* **40**(1970)2018, in russian.
- [74] Sanmartin J.R., *Phys.Fluids* **13**(1970)103.
- [75] Sato M., *Phys. Fluids* **15**(1972)2427.
- [76] Sato M., *Phys. Fluids* **17**(1974)1903.
- [77] Laframboise J.G., Rubinstein J., *Phys. Fluids* **19**(1976)1900.
- [78] Rubinstein J., Laframboise J.G., *Phys. Fluids* **21**(1978)1655.
- [79] Rubinstein J., Laframboise J.G., *Phys. Fluids* **25**(1982)1174.

- [80] Rubinstein J., Laframboise J.G., *Phys. Fluids* **26**(1983)3624.
- [81] Sonmor L.J., Laframboise J.G., *Phys. Fluids* **33**(1991)2472.
- [82] Rozhanski V.A., Tsendin L.D., *Journal of Technical Physics USSR* **48**(1978)1647, in russian.
- [83] Vagner S.D., Shliaev B.V., *Journal of Technical Physics USSR* **48**(1978)675, in russian.
- [84] Vorobieva N.A., Zakharova V.M. Kagan J.M., Proceedings IX ICPIG, Bucharest (Bulgaria, 1969), p. 620.
- [85] Dobe T., Amemiya H., *J. Phys. Soc. Japan* **19**(1964)1915.
- [86] Ichimiya M., *Japan. Jour. Appl. Phys.* **3**(1964)789.
- [87] Amemiya H., Dobe T., *Japan. Jour. Appl. Phys.* **7**(1968)956.
- [88] Amemiya H., Dobe T., *Japan. Jour. Appl. Phys.* **8**(1969)818.
- [89] Shilinsky A.P., Kubeiev B.V., Sacharov V.V., Smirnov A.S., *Fizika plazmy* **3**(1977)1028, in russian.
- [90] Demirchanov R.A., Leontiev N.J., Kosy J.A., *Zhurnal tekhnicheskoi fiziki* **32**(1962)180, in russian.
- [91] Jones H., Sanders P., *J. Sci. Instr.* **37**(1960)457.
- [92] Clements R.M., Skavsgard H.M., *Can. J. Phys.* **45**(1967)3199.
- [93] Ishi S., Miyoshi S., Okamoto K., Sakamoto Y., Proceedings IX ICPIG, Bucharest (Bulgaria, 1969), p. 563.
- [94] Ishi S., Miyoshi S., *Japan. J. Appl. Phys.* **19**(1980)719.
- [95] Gyergyek T., Čerček M., Jelić N., Stanojević M., *Contrib. Plasma Phys.* **33**(1993)53.
- [96] Stanojević M., Čerček M., Gyergyek T., Jelić N., *Contrib. Plasma Phys.* **33**(1993)241.
- [97] Stanojević M., Čerček M., Gyergyek T., Jelić N., *Contrib. Plasma Phys.* **34**(1994)607.
- [98] Hansen K., Klinger T., Piel A., *Rev. Sci. Instr.* **65**(1994)2615.
- [99] Špatenka P., Leipner I., Vlček J., Musil J., *Plasma Sources Sci. Technol.* **6**(1997)1.
- [100] Kudrna P., Passoth E., *Contrib. Plasma Phys.* **37**(1997) in print.
- [101] Bertotty B., *Phys. Fluids* **4**(1961)1010.
- [102] Bertotty B., *Phys. Fluids* **4**(1961)1047.
- [103] Peter G., Rybarsch H., *Beitr. Plasmaphys.* **16**(1976)333.
- [104] Stangeby P.C., *J.Phys. D Appl. Phys.* **20**(1987)1472.
- [105] Stangeby P.C., in *Physics of plasma-wall interaction in controlled fusion*, D.E. Post, R. Behrsch, Eds. (Plenum publishing corporation, 1986).
- [106] Stangeby P.C., *J.Phys. B* **15**(1982)1007.
- [107] Stangeby P.C., *Phys. Fluids* **27**(1984)682.
- [108] Brown J.G., Compber A.B., Kunkel W.B., *Phys Fluids* **14**(1971)1377.
- [109] Cohen I.M., *Phys. Fluids* **12**(1969)2356.
- [110] Lam S.H., *Phys. Fluids* **8**(1965)1002.
- [111] Ditte U., Müller K.G., Proceedings XVI. ICPIG, Contributed Papers, Düsseldorf (Germany, 1983), p. 124.
- [112] Blancod J.C., Golovanievski K.S., Kravchov T.P., Proceedings X. ICPIG, Oxford (UK, 1971) p. 25.
- [113] Aikawa H., *J. Phys. Soc. Japan* **40**, 1741 (1976).
- [114] Brown J.G., Compber A.B., Ehlers K.W., Hopkins D.F., Kunkel W.B., Rostler P.S., *Plasma Phys.* **13**(1971)47.
- [115] Zakrzewski Z., Kopiczynski T., Lubanski M., *Czech.J.Phys. B* **30**(1980)1167.
- [116] Arslanbekov R.R., Khromov N.A., Kudryavtsev A.A., *Plasma Sources Sci. Technol.* **3**(1994)528.
- [117] Godyak V.A., Piejak R.B., Alexandrovich B.M., *J. Appl. Phys.* **73**(1993)3657.
- [118] Fernández Palop J.I., Ballésteros J., Colomer V., Hernández M.A., *Rev. Sci. Instr.* **66**(1995)1.
- [119] Mesentsev A.P., Mustafaev A.S., Federov V.L., *J.Tech.Phys. USSR (Sov.Phys. Tech.Phys)* **55**(1985)544, in russian.
- [120] Mesentsev A.P., Mustafaev A.S., Federov V.L., *J.Tech.Phys. USSR (Sov.Phys. Tech.Phys.)* **55**(1985)2232, in russian.
- [121] Mesentsev A.P., Mustafaev A.S., Federov V.L., *J.Phys.D* **21**(1988)1464.
- [122] Federov V.L., *J.Tech.Phys. USSR (Sov.Phys. Tech.Phys)* **55**(1985)926, in russian.
- [123] Laphshin V.F., Mesentsev A.P., Mustafaev A.S., Federov V.L., Proceedings ESCAMPIG-IX, C.M. Ferreira, Ed., Lisabon, (Portugal, 1988), p 141.
- [124] Mesentsev A.P., Mustafaev A.S., Laphshin V.F., Federov V.L., *J.Phys.B* **20**(1987)L723, *J.Phys.B* **20**(1987)L923.
- [125] Laphshin V.F., Mustafaev A.S., *J.Tech.Phys. USSR (Sov.Phys. Tech.Phys)* **59**(1989)35.
- [126] Federov V.L., Mesentsev A.P., *J.Tech.Phys. USSR (Sov.Phys. Tech.Phys)* **57**(1987)595.
- [127] Klagge S., Lunk A., *J. Appl.Phys.* **70**(1991)99.

## Nonlinear Wave Phenomena in an Electron-Beam Plasma

K. Yamagiwa, T. Itoh and T. Nakayama

Department of Physics, Faculty of Science, Shizuoka University, Shizuoka 422, Japan

**Abstract.** An experiment has been carried out to investigate one-dimensional nonlinear evolution and formation of the localized structure of unstable waves in an electron-beam plasma. The plasma system is linearly unstable against electrostatic perturbations of frequencies lower than the critical frequency  $\omega_{ce}$  ( $\approx \omega_{pe}$ , plasma frequency), but is stabilized in its nonlinear stage by generating wave packets irregularly. The amplitude of each wave packet never grows infinitely. The average time width of the packets is inversely proportional to the linear growth rate  $\gamma$ , where  $\gamma \propto (n_b/n_0)^{1/3} \omega_{pe}$  ( $n_b$ : beam density,  $n_0$ : plasma density). The system is also unstable for an external rf-burst with a narrow time-width, and then finally becomes stable by the emission of a series of burst waves. The number of emitted bursts increases with the beam density.

### 1. INTRODUCTION

Since the pioneering work on nonlinear phenomena of Langmuir waves was done by Zakharov [1], considerable progress has been made in this area [2]. There have also been growing interests [3-8] on nonlinear wave phenomena of unstable modes. Wong and Cheung [3] experimentally investigated nonlinear evolution and collapse of the electron-beam-instability. They explained their observed results with the theory of three dimensional Langmuir collapse in which the beam effect is not included.

The dispersion properties of unstable modes [4-9], however, are quite different from stable ones. Intrator *et al.* [4] observed unstable electron-beam wave packets. They tentatively explained their experimental results by a nonlinear geometrical optics theory, not by Zakharov Langmuir-wave collapse. N. Yajima and Tanaka [5] predicted the existence of soliton modes of unstable electron-beam waves which are described by a nonlinear Schrödinger equation with the beam correction. T. Yajima and Wadati [6] also theoretically showed that solitons arise as a result of the competition between instability and nonlinearity in unstable systems. We [7] have studied nonlinear evolution of one-dimensional perturbations in a weak electron-beam plasma ( $n_b/n_0 < 0.1\%$ ). Then we found that the initial growth of unstable modes and the formation of soliton-like excitation are characterized by the spatial linear growth rate  $k$ . In the case of a medium electron-beam ( $0.5\% > n_b/n_0 \geq 0.1\%$ ) [8], beam modes were initially unstable against frequencies lower than  $\omega_{ce}$ , and finally they were stabilized by generating nonlinear wave packets. The characteristic time for formation of the structure was much shorter than the ion response time ( $\approx 1/\omega_{pi}$ : inverse of ion plasma frequency).

In this paper we will present our recent observations on nonlinear wave phenomena in an electron-beam plasma and discuss them with theories on the soliton modes in unstable systems.

### 2. PLASMA DEVICE AND EXPERIMENTAL SETUP

A target plasma is produced by a dc discharge in a so called multi-dipole plasma device shown in Fig. 1(a). An additional magnetic field ( $\approx 90$ G) is externally applied parallel to the axis of the plasma chamber to observe the one-dimensional behavior of the beam modes. The working pressure of Ar gas for the discharge is adjusted to  $1 \times 10^{-5}$  Torr to reduce collisional loss of beam electrons with neutral particles. We inject a pulse electron beam with duration of  $7 \times 10^{-6}$ s into a target plasma along the external magnetic field. Figure 1(b) shows the experimental setup. The beam current  $I_b$  passing through the plasma is measured by using a collector located at the opposite end from the beam gun.

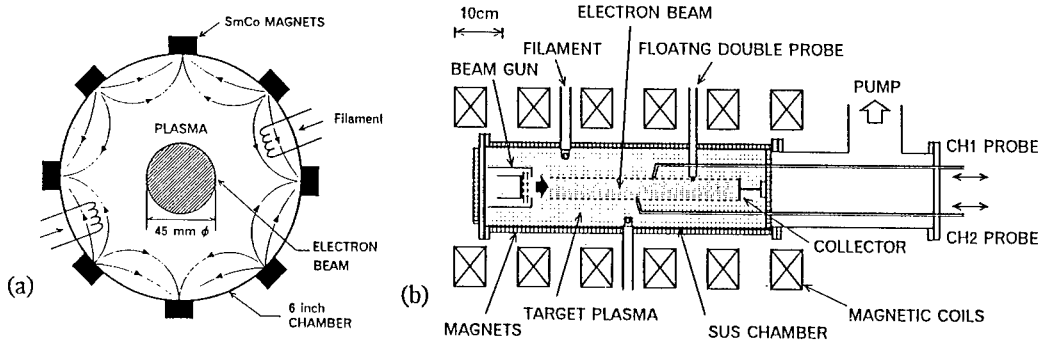


Figure 1: (a) Electron-beam plasma device. (b) Experimental setup.

Density fluctuations  $\tilde{n}(t)$  are picked up with two small plane probes (Mo disks of 3mm in diameter) located at different positions,  $z_1$  and  $z_2$ , measured from the beam gun and then two sets of realtime data are captured by a fast digitizing oscilloscope (HP54510A, 1GSa/s, 2ch, 8kW/ch). The maximum amplitude of the density fluctuations normalized by the equilibrium plasma density,  $\tilde{n}(t)/n_0$ , seems to be over ten percent in the present experiment. However we find it difficult to determine the exact value of it because of the high frequency ( $\omega \approx \omega_{pe}$ ). So that we will show the data of  $\tilde{n}(t)$  in relative units. Typical experimental parameters are summarized in Table 1.

Table 1. Experimental parameters

Working pressure (Ar)	$p$	$= 1 \times 10^{-3}$ Torr
Plasma density	$n_0$	$= 3 \times 10^{14}$ m <sup>-3</sup>
Electron temperature	$T_e$	$= 3 \sim 4$ eV
Plasma frequency	$\omega_{pe}/2\pi$	$= 150 \sim 160$ MHz
Debye length	$\lambda_D$	$= 0.9$ mm
Beam density	$n_b/n_0$	$= 0.02 \sim 0.5\%$
Beam velocity	$v_b/v_t$	$= 4 \sim 6$ (thermal velocity of electrons)
Unstable wavenumber	$k\lambda_D$	$= 0.2$ (typical value)
Beam diameter	$2r_b$	$= 45$ mm ( $kr_b = 7$ )
Beam duration	$t$	$= 7 \times 10^{-6}$ s ( $\omega_{pe} t = 20$ )
System length for beam path	$l$	$= 50$ cm

### 3. EXPERIMENTAL RESULTS

#### 3.1 Fundamental properties of unstable beam modes

When an electron beam is injected into the target plasma, unstable noise patterns are initially excited along the beam path and the rms-density fluctuation  $\langle \tilde{n}(t)/n_0 \rangle_{rms}$  grows to several percent in the

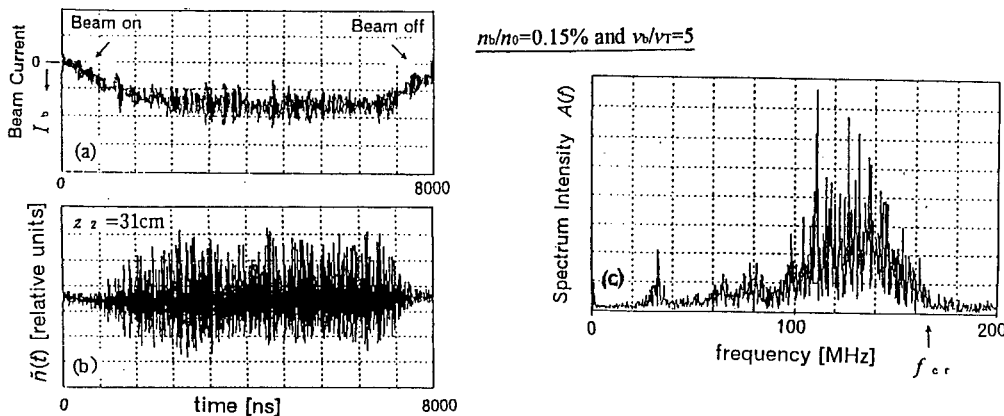


Figure 2: (a) Beam current  $I_b(t)$ , (b) density fluctuations  $\tilde{n}(t)$  and (c) Fourier spectrum  $A(f)$  of  $\tilde{n}(t)$ .

downstream region. Finally the system becomes stable in its nonlinear stage by generating nonlinear wave packets. Typical data of the beam current  $I_b(t)$ , density fluctuations  $\tilde{n}(t)$  and its Fourier spectrum  $A(f)$  are shown in Figs. 2(a), (b) and (c), where beam density  $n_b/n_0 = 0.15\%$ , beam velocity  $v_b/v_T = 5$  and the probe position  $z_2 = 31\text{cm}$ . The critical frequency  $f_{cr}$ , indicated by an arrow in Fig. 2(c) is nearly equal to the plasma frequency  $f_{pe} (\approx 160\text{MHz})$ . The plasma system should be unstable in a frequency range lower than the critical frequency  $f_{cr}$ .

In order to observe evolution of unstable beam waves we repetitively inject pulse electron beams and simultaneously apply small rf-signals as initial perturbations to the control grid of the beam gun. The spatial development of unstable waves is measured by an interferometry method, with a boxcar integrator as a low pass filter. In the initial stage of propagation, excited beam waves are linearly unstable, that is, their amplitudes exponentially increase along the beam path, but saturate in the downstream region. Finally a symmetric envelope ( $\propto k_i \text{sech}[k_i(z-z_0)]$ ) is produced [7]. The sets of dispersion data extracted from the linear phase are plotted with closed circles in Fig. 3.

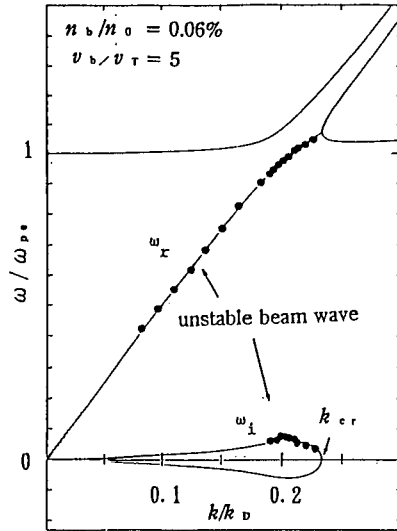


Figure 3: Dispersion relation. Closed circles: Experimental data in the linear phase. Solid curves: Calculated from eq.(1).

The temporal growth rate  $\omega_i$  is given by the product  $|k_i v_k|$ , where  $k_i$  is the spatial growth rate in the linear stage and  $v_k$  is the group velocity. Solid curves indicate the dispersion relation for linear waves in an electron-beam plasma given by [9]

$$1 = - \frac{\omega_{pe}^2}{(\omega^2 - k^2 v_T^2)} - \frac{\omega_{pb}^2}{(\omega - kv_b)^2} \quad (1)$$

The equation has a pair of complex conjugate roots,  $\omega_r \pm i\omega_i$ , for a fixed wave number  $k$  less than the critical value  $k_{cr} (\equiv \omega_{pe}/v_b)$ . One of these roots,  $\omega_r + i\omega_i$  corresponds to unstable modes. Experimental sets of data agree very well with these unstable modes. This dispersion relation also well explains the behavior of self-excited beam modes in the linear phase as shown below.

### 3.2 Nonlinear evolution and stabilization of beam modes: formation of nonlinear wave packets

Density fluctuations in Fig. 2(b) appear very spiky when viewed on the oscilloscope. Similar data sets are observed at  $z_1 = 28\text{cm}$ . In Fig. 4, both data sets of the density fluctuations detected at 28cm and 31cm are magnified by 16 times in time scale on the horizontal axis. It is found that (1) irregular wave packets with a narrow width shorter than 20ns are generated, (2) wave packets at  $z_2 = 31\text{cm}$  are delayed by 12ns compared with ones at  $z_1 = 28\text{cm}$ , that is, they propagate downstream with the group velocity  $v_g = 2.5 \times 10^6 \text{ m/s}$  and (3) the phase velocity  $v_\phi = 3.7 \times 10^6 \text{ m/s}$  (calculated from the cross-correlation between both realtime sets of data). The facts of (2) and (3) are consistent with the dispersion relation of unstable modes in the electron-beam plasma shown in Fig. 3. However we find it very difficult to obtain the time-width and amplitude of those wave packets because of their irregularity.



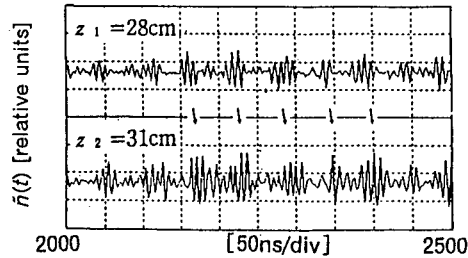


Figure 4: Density fluctuations  $\tilde{n}(t)$  at  $z_1 = 28\text{cm}$  and  $z_2 = 31\text{cm}$ , where  $n_b/n_0 = 0.15\%$  and  $v_b/v_T = 5$ ;  $t = 2000 - 2500\text{ns}$

Figures 5(a) and 5(b) show realtime data  $\tilde{n}(t)$  and self-correlation  $c(t)$ , respectively. We can estimate the average value of the time-width  $\Delta t$  by calculating the correlation time  $\Delta\tau_c$ . In this case, the correlation time  $\Delta\tau_c = 21.5\text{ns}$  corresponds to the average time-width  $\Delta t$  of the wave packets. With this method we tried to measure the average value of  $\Delta t$  varying the beam density  $n_b/n_0$ .

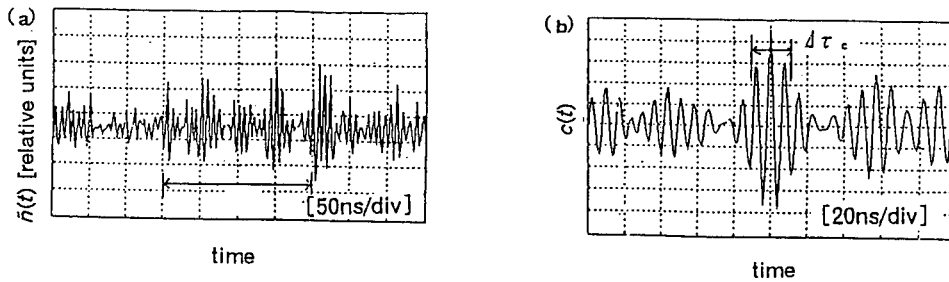


Figure 5: (a) Realtime data  $\tilde{n}(t)$  and (b) self-correlation  $c(t)$ :  $n_b/n_0 = 0.12\%$ ,  $v_b/v_T = 5$ .

In Fig. 6, experimental values of  $\Delta t$  are plotted on a logarithmic graph with closed circles as a function of beam density  $n_b/n_0$  ( $= 0.10 \sim 0.45\%$ ). In this graph we also draw the best fit line with a gradient of  $-1/3$ . Thus we find the empirical relation given by

$$\Delta t \propto (n_b/n_0)^{-1/3} \quad (2)$$

It is well known [9] that the linear growth rate  $\gamma$  of the beam modes is proportional to  $(n_b/n_0)^{1/3}$  and the maximum growth rate  $\gamma_{\max}$  is given by  $3^{1/2} 2^{4/3} (n_b/n_0)^{1/3} \omega_{pe}$  for  $\omega \approx \omega_{pe}$ . Observed values  $\Delta t$  ( $= 10 \sim 20\text{ns}$ ) are proportional to  $\gamma^{-1}$ , and their magnitudes are 2 times  $(\gamma_{\max})^{-1}$ . This indicates that the structure of the nonlinear wave packets is determined by the linear growth rate.

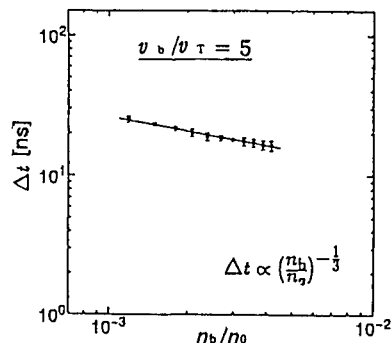


Figure 6: Average time-width  $\Delta t$  of wave packets as a function of beam density  $n_b/n_0$ .

### 3.3 Evolution of a single rf-burst and stabilization by the emission of bursts

We present interesting results of the test wave experiment. When a small rf-burst signal with the time width of 50ns as an initial perturbation is applied to the control grid of the beam gun, a single burst wave is excited from the noise level. This burst wave initially grows linearly along the electron stream and the amplitude of the unstable burst gradually saturates in its nonlinear stage. Finally the system becomes stable by the emission of a series of burst waves. In Figs. 7(a), (b) and (c) we show how a single rf-burst grows, saturates and generates new burst waves. In the case of a weak-beam injection ( $n_b/n_0 = 0.03\%$ ) a single burst wave only grows from noise level along the beam path. In this case

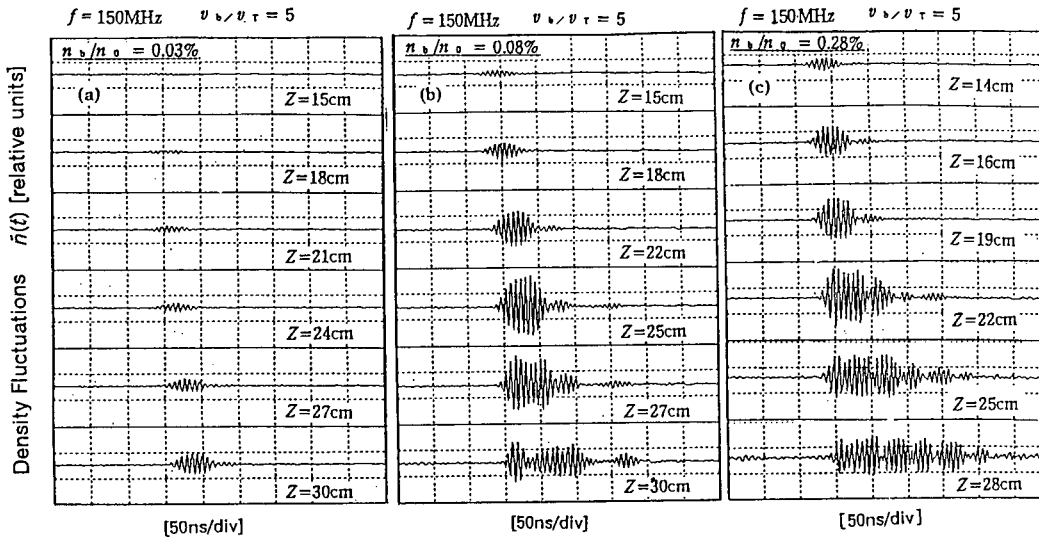


Figure 7: Nonlinear evolution of a single burst wave and the emission of a series of burst waves.

(a)  $n_b/n_0 = 0.03\%$ , (b)  $n_b/n_0 = 0.08\%$ , (c)  $n_b/n_0 = 0.28\%$ .

nonlinear saturation is very rare. On the other hand, in the case of a medium beam injection ( $n_b/n_0 \geq 0.05\%$ ), a single burst wave initially grows linearly along the electron stream and the amplitude of the

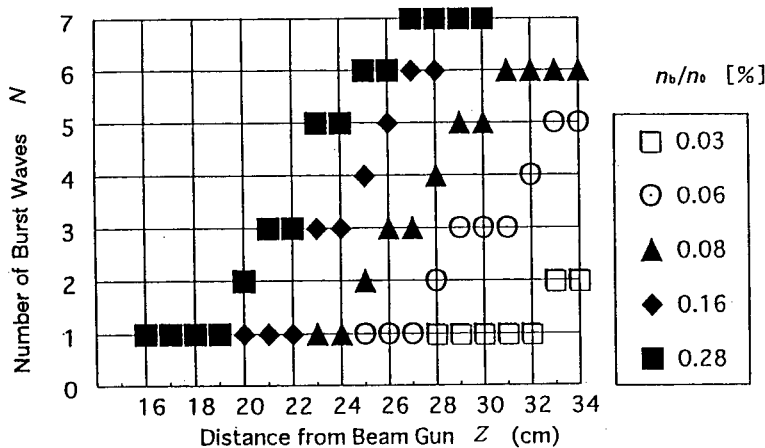


Figure 8: Number of burst waves as a function of the distance from beam gun, for several values of  $n_b/n_0$ .

unstable burst gradually saturates in its nonlinear stage. Finally the system becomes stable by the emission of a series of burst waves along the beam path as shown in Figs. 7(b) and (c). Ion motion has no effect on the phenomena because the ion response time ( $1/\omega_{pi} \approx 300\text{ns}$ ) is longer than the observed time scale ( $10 \sim 200\text{ns}$ ).

Figure 8 shows the number  $N$  of emitted burst waves as a function of probe position  $z$ , the distance from the beam gun, where the beam density  $n_b/n_0$  is varied from 0.03 to 0.28%. It is noticeable that the number of emitted bursts increases with the beam density  $n_b/n_0$  and the electron-beam plasma system becomes stable by emitting a series of burst waves. Therefore it never remains unstable for an infinite period of time.

#### 4. DISCUSSION

N. Yajima and M. Tanaka [5] theoretically studied nonlinear evolution of unstable electron beam waves in an electron beam plasma. When the beam velocity  $v_b$  is sufficiently large compared with the thermal velocity of electrons  $v_T$ , the system is governed by a nonlinear Schrödinger equation with an additional term of beam correction (the right hand side of the first equation):

$$(i \partial_t - 1 + \partial_z^2/2 + |f|^2) f = -[(n_b/n_0)/2] g \quad (3)$$

$$(\partial_t + v \partial_z)^2 g = f$$

$$; E = 4(2\pi n_0 T)^{1/2} f, \quad n_b = 2^{3/2} n_b \partial_z g, \quad v = v_b/v_T$$

They showed that the system is linearly unstable against electrostatic perturbations of large wavelengths but is stabilized in its nonlinear stage due to the ponderomotive force of high frequency fields. The amplitude of an unstable wave behaves in proportion to  $\gamma \text{sech}(\gamma t)$  as a function of time  $t$ , where  $\gamma$  is the temporal linear growth rate at  $k \approx k_c$  (critical wave number  $\approx \omega_{pe}/v_b$ ). They also showed that the plane wave is unstable for long wavelength modulation and is stabilized by the emission of a series of envelope solitons. Their theoretical study predicts that the structure of the soliton modes is determined by the initial growth rate but not by the amplitude of initial perturbations, as in stable systems. T. Yajima and M. Wadati [6] also showed that solitons arise as a result of the competition between instability and nonlinearity.

The present experiment showed that the unstable modes with localized structures are soliton-like excitations. They can exist in an electron-beam plasma, which is a weakly dispersive medium. Their dynamical processes are developed differently from the usual soliton processes in which the number of solitons and their identities are conserved. These soliton-like localized modes are completely different from Zakharov's Langmuir solitons which arise in a rather strong dispersive medium. The present observations shown in Figs. 4, 6, 7 and 8 are qualitatively in agreement with their theoretical predictions [5, 6].

#### 5. CONCLUSIONS

The electron-beam plasma is linearly unstable in a frequency range lower than the critical frequency ( $\approx \omega_{pe}$ ). The beam plasma system is stabilized in its nonlinear stage by generating nonlinear wave packets, the average space-time width of which is inversely proportional to the linear growth rate  $\gamma$  ( $\propto (n_b/n_0)^{1/2}$ ). The system is also linearly unstable for a single rf-burst wave and becomes stable by emission of burst waves along the beam path. The number of emitted burst waves increases with the beam density  $n_b/n_0$ . The results indicate that the nonlinear structures of the unstable electron-beam waves are determined by the linear growth rate. The characteristic time for formation of the structure is much shorter than the ion response time ( $\approx 1/\omega_{pi}$ ).

#### Acknowledgments

The authors gratefully acknowledge valuable discussions of Professor M. Tanaka of NIFS, Toki (JAPAN), stimulating discussions of Professor M. Wadati and Dr. T. Yajima of Tokyo University and careful observations of Mr. H. Takeshita (Msc) and Miss K. Hirahama (Msc) for this work. They also thank Mr. Nick Brown of Sussex University for his kind inspection of the English of this paper. The present work was partially supported by a Grand-in-Aid for Scientific Research from the Ministry of Education.

## References

- [1] Zakharov V. E., Sov. Phys. JETP **35** (1972) 908.
- [2] Goldman M. V., Rev. Mod. Phys. **56** (1984) 709.
- [3] Wong A. Y. and Cheung P. Y., Phys. Rev. Lett. **52** (1984) 1222.  
Cheung P. Y. and Wong A. Y., Phys. Fluids **28** (1985) 1538.
- [4] Intrator T., Chan C., Hershkowitz N. and Diebold D., Phys. Rev. Lett. **53** (1984) 1233.
- [5] Yajima N. and Tanaka M., Prog. Theor. Phys. Suppl. No. **94** (1988) 138.
- [6] Yajima T. and Wadati M., J. Phys. Soc. Jpn. **59** (1990) 41.  
Yajima T. and Wadati M., J. Phys. Soc. Jpn. **59** (1990) 3237.
- [7] Yamagiwa K., Mieno T. and Tanaka M., Proc. 1992-ICPP (Innsbruck, 1992) Part **III** 1859.
- [8] Yamagiwa K., Tanaka M., Itoh T. and Nakayama T., Proc. 1996-ICPP (Nagoya, 1996) Vol. **1** 774.  
Yamagiwa K., Itoh T. and Nakayama T., Proc. PFNL-96(Sendai, 1996), to be published in "*Double Layers-Potential Formation and Related Nonlinear Phenomena in Plasmas*" (World Scientific Publishing Co., Singapore) p.407.
- [9] Briggs R. J., "*Electron-Stream Interaction with Plasmas*" in Research Monograph No. **29** (M.I.T. Press, Cambridge, 1964) and "*Two-Stream Instabilities*" in Advance in Plasma Physics, Edited by A. Simon and W. B. Thompson (Interscience Publisher, New York, 1971) Vol. **4**, p.43.

## Author Index

Aleksandrov A.F. C4-365  
Alinot C. C4-295  
Aliouchouche A. C4-295  
Alves L.L. C4-143  
Annaratone B.M. C4-155

Behnke J.F. C4-397  
Benware B.R. C4-353  
Bouchoule A. VII  
Bœuf J.P. C4-3  
Bougrov G.E. C4-365  
Brablec A. C4-331  
Brunet H. VII  
Brundtland T. C4-113  
Buzak T.S. C4-225

Capitelli M. C4-271  
Carman R.J. C4-167  
Chaker M. C4-295  
Chilla J.L.A. C4-353  
Coudert J.F. C4-187  
Csambal C. C4-397  
Czarnetzki U. C4-175

d'Agostino R. C4-199  
DeSilva A.W. C4-319  
Doyeux H. C4-3

Egli W. C4-47  
Eliasson B. C4-47

Fauchais P. C4-187  
Favia P. C4-199  
Ferreira C.M. C4-143  
Freearde T.G.M. C4-15

Gonzalez J.J. C4-353  
Gousset G. C4-143  
Graham W.G. C4-209

Hancock G. C4-15  
Hassouni K. C4-271  
Hirech A. C4-3

Hubička Z. C4-331

Ignatov A.M. C4-215  
Ilcisin K.J. C4-225  
Itoh T. C4-413

Jastrabík L. C4-331  
Jüttner B. C4-31

Kapička V. C4-331  
Katiukha V.P. C4-365  
Kawai Y. C4-235  
Kirichenko G.S. C4-365  
Klagge S. C4-397  
Kliagine C. C4-295  
Klíma M. C4-331  
Kogelschatz U. C4-47  
Koh S.K. C4-365  
Konjević N. C4-247  
Kralkina E.A. C4-365  
Kruger C.H. C4-67  
Kudrna P. C4-397  
Kuraica M.M. C4-247

Laan M. C4-259  
Laux C.O. C4-67  
Longo S. C4-271  
Lowke J.J. C4-283

Macchietto C.D. C4-353  
Mahony C.M.O. C4-209  
Marconi M.C. C4-353  
Margot J. C4-295  
Mauel M.E. C4-307  
Mesyats G.A. C4-93  
Minami K. C4-319  
Moreno C.H. C4-353

Nakayama T. C4-413  
Novák M. C4-331

Owano T.G. C4-67

Palumbo F. C4-199  
Paris P. C4-259  
Parker G.J. C4-225  
Pauna O. C4-295  
Petrović Z.Lj. C4-341  
Pitchford L.C. VII  
Punset C. C4-3

Qin W. C4-319

Repán V. C4-259  
Rocca J.J. C4-353  
Rukhadze A.A. C4-365  
Rypdal K. C4-113

Shamrai K.P. C4-365  
Shlyaptsev V.N. C4-353  
Šícha M. C4-331  
Sigmond R.S. C4-383  
Slaviček P. C4-331  
Soukup L. C4-331  
Stefanović I. C4-341  
St-Onge L. C4-295

Tabbal M. C4-295  
Takeda S. C4-133  
Tichý M. C4-397  
Tomasel F.G. C4-353  
Tomimoto F. C4-319

Ueda Y. C4-235

Vardelle M. C4-187  
Videnović I.R. C4-247  
Virko V.F. C4-365  
Vrhovac S. C4-341

Yamagiwa K. C4-413

Zare R.N. C4-67  
Živković J. C4-341

Commission paritaire N° 57920

---

© EDP Sciences 1997

*Directeur de la Publication : Jean-Marc QUILBÉ*

---

*Imprimé en France. — JOUVE, 18, rue Saint-Denis, 75001 PARIS*  
N° 252550R. Dépôt légal : Décembre 1997